Petrochronology and mineral chemistry of mid-crustal shear zones: new tools for tectonics and mineral exploration

Konstantinos Papapavlou

The thesis is submitted in partial fulfilment of the requirements for the award of the degree of Doctor of Philosophy of the University of Portsmouth

February 2017

Abstract

Dating ductile shear zones is daunting because we have to demonstrate either that the chronometer of choice grew during shear zone operation or that crystal-plastic deformation induced age resetting. By adopting a petrochronological approach in this project combining petrographic, geochemical, U-Pb isotopic, and quantitative microstructural data U-Pb isotopic dates are linked with certain shear zone processes. The study area is the South Range of the world-class Sudbury Impact Structure.

Specifically, mylonitic shear zones at the Creighton Mine (South Range, Sudbury) operated during three distinct tectonothermal events at ca. 1.75 Ga, 1.65 Ga, and 1.45 Ga. The age dating of texturally and geochemically characterised titanite grains from a shear zone exposed at the 5400 level of the Creighton Mine, indicates operation of the shear during the Mazatzalian – Labradorian orogeny (1.7 – 1.6 Ga). Meso-scale sulphide structures of mechanical remobilization, within the main body of the examined shear zone, show that this event facilitated the local-scale transfer of sulphides to satellite positions. Three age populations of ca. 1.75 Ga, 1.65 Ga, and 1.45 Ga are also prevalent in shear zones from deeper levels of the Creighton Mine. These age populations yield new insights into the orogenic history of the South Range and the Southern Province, and provide further constraints on the comparison of accretionary provinces of the North American Mid-continent and the Southwest United States. Taking into consideration the fluid-mediated and crystal-plasticity textural features in the examined titanite populations it is suggested that these dates record events of syndeformational fluid percolation.

Within the 1.75 Ga textural population of titanite grains survived inclusions of inherited titanite grains with shock-metamorphic features. Microstructural and micro to nano-scale crosscutting relationships suggest that the shock wave during the 1.85 Ga impact event induced in these grains the growth of 75°/<010> and 108°/<010> shock microtwins. The nucleation of twins induced a work hardening effect that allowed their survival during the later polyorogenic reworking of the basin (1.75 to 1.45 Ga). U-Pb age dating of these grains yield accurately the age of impact (i.e. 1851 ± 12 Ma). In comparison, titanite grains located within Archaean target rocks ofthe Vredefort structure show identical crystallographic features and partial age resetting. The differential response is attributed to the different distance of the samples from the base of the impact melt sheet that was the dominant heat

source.

The ore-controlling character of the examined shear zones in the Sudbury mining camp can provide critical information about the exploration potential of these structures in metallogenetic settings. Preliminary mineral-chemical analysis, from major to trace element level, of fabric-forming silicates show distinct trends in the abundance of pathfinder elements (e.g. transition metals). Further, work that will collate the different datasets using multivariable statistical methods will be pursued in order to untangle the vectoring potential of different elements.

Table of Contents

Declaration

Whilst registered as a candidate for the above degree, I have not been registered for any other research award. The results and conclusions embodied in this thesis are the work of me and have not been submitted for any other academic award.

Konstantinos Papapavlou, February 2017

Word count: 50495

List of Tables

List of Figures

Chapter 2:

Chapter 3:

Chapter 4:

Figure 2. Simplified cross-section of the Creighton mine (modified from Vale ltd internal report), that depicts the spatial relationship of ductile shear zones with sulphide mineralization. The exact location of the cross section is depicted in the geological map (Figure 1, traverse A-B). With black bold letters is indicated the location of the Six Shaft Shear Zone in the 5400 level. The thickness of the ore bodies in the cross section is apparent since the location of the ore bodies has been projected on the cross-section using a wide clipping technique.

Figure 3. Simplified structural map of the Six Shaft Shear Zone at the 5400 level of the Creighton mine. The rectangular area in the inset depicts the NNW-striking domain of the Six Shaft Shear Zone and the spatial relationship of the shear with the 401 contact-style ore body. With red and black lines are depicted the foliation trajectories in the low (foliated-metagranitoid) and high strain domains of the shear zone, respectively. The pole figures show orientation data of stretching lineations and mylonitic foliations from the biotite-rich mylonitic domain. The black circles denote the location of each sample. The samples with underscored names were chosen for U-Pb titanite geochronology.

Figure 4. Field photographs from the Six Shaft Shear Zone that show: (a) Quartz porphyroclast with asymmetric strain shadows that indicate top-up-to-the-SW sense of shear (looking normal to the foliation and parallel to the stretching lineation), (b) Deflected quartz vein and quartz sigmoids that indicate southward translation at the contact of the foliated meta-granitoid with the biotite-rich mylonitic core, (c) cm-scale, eye-shaped, sheath folds developed at the YZ plane of strain ellipsoid (normal to the foliation and stretching lineation). The closure of the fold hinge lines is indicated with arrows. The tip of the pencil for scale is approximately 2 cm. (d) durchbeweng-style brecciated sulphides with quartz and biotite-rich mylonitic clasts in a pyrrhotite-rich matrix. Note that the chalcopyrite grains wrap around the more competent biotite and quartz clasts while pentlandite grains define porphyroblasts in the pyrrhotite-rich matrix

Figure 5. Photomicrographs from the marginal foliated metagranitoid of the Six Shaft Shear Zone that depict: (a) titanite replacing epidote in a plagioclase and K-feldspar-rich matrix, (b) titanite in textural disequilibrium at the marginal domains of a plagioclase grain, (c) titanite rimming epidote adjacent to K-feldspar that exhibits myrmekitic texture, (d) reflected light image of the photomicrograph c that shows titanite (brighter) rimming the epidote grain.

Figure 6. Shear sense indicators from the Six Shaft Shear Zone: (a) polycrystalline quartz aggregate with stair stepping geometry and asymmetric tails that indicate top-to-the-SW sense of shear, (b) C'-S composite fabrics that indicate top-to-the-SW sense of shear, (c) biotite sigmoids with top-to-the SW sense of shear, (d) feldspar porphyroclast with asymmetric wings that are defined by hornblende and titanite grains that show top-to-the-SW sense of shear, (e) rhomboidal biotite fish that indicates

top-to-the-SW sense of shear. All the shear sense indicators were recognized in thin sections oriented normal to the foliation and parallel to the stretching lineation (XZ plane of strain ellipsoid).

Figure 7. Compositional plots from fabric forming amphiboles and biotites of the Six Shaft Shear Zone: (a) Mineral chemical data of calcic amphiboles that are plotted with different colors according to the intra-grain location of the analytical spot (core-rim) and the textural relationship of the grains with the deformation fabrics, (b) Mineral chemical data of biotites from different structural levels of the shear zone.

Figure 8. Backscatter electron images of titanite grains from the Six Shaft Shear Zone : (a) Darker sector zoned titanite grains (Group 1 grains) overgrown by titanite grains with ilmenite inclusions, (b) titanite grains with ilmenite, allanite, and apatite inclusions that show a strong shape preferred orientation and are hosted in bands of recrystallized feldspar (Group 2 grains), (c) darker embayed titanite cores (Group 1 grains) overgrown by euhedral titanite rims (Group 2 grains) with the latter in textural equilibrium with apatite and biotite grains, (d) patchily zoned titanite grain with ilmenite inclusion and porphyroclastic texture (Group2 grains), (e) blocky anhedral titanite grains that exhibit faint zoning and host ilmenite and silicate inclusions (Group 3 grains). (f) apatite grain in contact with a titanite grain that hosts an allanite inclusion

Figure 9. Misorientation maps of representative titanite grains from the Six Shaft Shear Zone that show from (a) to (d): Misorientation maps of Group 2 dynamically recrystallized titanite grains hosted within plagioclase and biotite-rich matrices. Black lines denote high-angle grain boundaries and red low angle. (e) Blocky titanite grain (Group 3 grain) with abrupt transition between misorientation domains and maximum cumulative misorientation values up to 5 degrees relative to the white cross. In the upper-right part of the map is depicted the pole figure of the {100} crystallographic plane, (f) Anhedral titanite that shows amalgamation and local crystal-plastic deformation that is expressed with the development of low-angle grain boundaries. Note that the maximum cumulative misorientation value of 8 degrees is observed in association with low angle grain boundaries at the upper right part of the grain.

Figure 10. Misorientation and Phase map of a dynamically recrystallized titanite grain (Group 2) in a plagioclase-rich matrix. Both maps overlay a band contrast map. Below each map are depicted pole figures (lower hemisphere-equal area diagrams) for titanite (red) and plagioclase (blue) of the principal crystallographic axes.

Figure 11. Plot of selected trace elements from titanite and apatite grains of the Six Shaft Shear Zone. From top to bottom are depicted the following: U versus Sm/Yb scatter plot from the different titanite textural populations, REE diagram from titanite grains of Group 1 (resorbed dark cores), REE diagram from titanite grains the belong to the Group 2 (patchy zoning with ilmenite inclusions), and at the bottom REE diagram from apatite grains hosted in a biotite-rich matrix of the shear zone.

Figure 12. Terra Wasserburg concordia diagrams that show: (a) U-Pb ellipses colored in different shades of grey for different samples and (b) the same diagram colored based on the presence of Europium anomalies. Note that in figure 12b is presented also a REE diagram from titanite grains of the plagioclase-rich sample SSS11A. With red outlines in Figure 12b are depicted the two grains in the misorientation maps of Figure 9 (9a and 9c). The X and Y axes depict the total 207Pb/206Pb and 238U/206Pb isotopic ratios.

Chapter 5 :

Figure 1. Synthetic figure that depicts : (a) The location of the Sudbury impact structure relative to the main orogenic provinces in North America. With A-A' is indicated a schematic crustal-scale cross section., (b) Schematic cross section A-A' that shows the location of the Sudbury impact structure relative to Superior, Southern, and Grenville provinces (modified from Crofu and Easton., 2000), (c) Simplified map of the Sudbury impact structure modified from Ames et al., 2008. With B-B' is indicated the cross section of Creighton Mine in Figure 2.

Figure 2. Cross section of Creighton Mine that depicts the relation of mylonitic shear zones with Ni-Cu-PGE sulphide ore bodies at the basal contact of the Sudbury Igneous Complex and the footwall of the South Range. In the rectangle is shown schematically the spatial relationship between the 118 and Hodder/315 shear zone systems.

Figure 3. Model of Creighton Deep Mine constructed in DataMine that depicts the orientation relationships of the examined shear zones from the 118 and Hodder/315 families. The F1 denotes interpreted folds that produced during the deformation phase D1 whereas with F2 folds that produced during the deformation phase D2.

Figure 4. Drillcore samples from the Plum, RAR, and 315 shear zones of the Creighton Mine that depict : (a) Centimetre-scale strain gradients in quartzofeldspathic domains of the Plum shear zone. Note the intensification of the planar fabrics in the domain with higher modal abundance of biotite, (b) Isoclinally folded F1 carbonate vein with development of the S1m mylonitic fabric parallel to its axial plane, (c) Quartz sigmoid in the biotite-rich mylonitic domains of the Plum shear zone, (d) biotite-rich mylonitic domain of the RAR shear zone with ϕ-type porphyroclasts, (e) biotite-rich mylonitic domain

of the RAR shear zone with σ-type quartz porphyroclasts, (f) Ultramylonitic band in the 315 shear zone with alternation of feldspar, amphibole, and biotite-rich domains. Note the strong shape preferred orientation of chalcopyrite grains parallel to the high-strain S2m fabric.

Figure 5. Phototomicrographs from the the RAR, Plum, and 315 shear zone samples that show : (a) A penetrative mylonitic fabric defined by hornblende and biotite grains in the RAR shear zone. Note the C' planes, indicated with red color, oblique to the high-strain S1m fabric, (b) Boundary between two domains with different fabric intensity on the RAR shear zone. In the lower strain domain (right) is observed titanite porphyroclast with weak shape preferred orientation. In the higher strain domain with the higher abundance of biotite and amphibole grains (left) is observed a penetrative S1m fabric, (c) Feldspar porphyroclast in the Plum shear zone that exhibits recrystallization in the rims. Recrystallized areas are observed also within linear intragrain bands (indicated with red triangles). Chalcopyrite grains are preferentially located along the dynamically recrystallized rims of the feldspar porphyroclasts (d) Folded S1 fabric in the Plum shear zone defined by hornblende grains. Chalcopyrite and pyrrhotite grains with strong shape preferred orientation define also the S1 fabric, (e) S2 folded fabric in the 315 shear zone defined by hornblende, quartz, and sulphide grains, (f) High-strain S2m fabric defined by biotite in the 315 shear zone. Note the band of recrystallized feldspar at the lower part of the photograph.

Figure 6. Backscatter electron (BSE) images of titanite grains from the RAR, Plum and 315 shear zones that show : (a) Anhedral titanite grain with patchy zoning and ilmenite core from the low-strain domains of the RAR shear zone, (b) titanite grain with ilmenite inclusions from the high-strain domains of the RAR shear zone that is in textural equilibrium with fabric-forming biotite. Note the sharp optical contacts between titanite and biotite matrix, (c) patchily zoned titanite grains with ilmenite and apatite inclusions from the Plum shear zone. The apatite grains show also patchy zoning and are rimmed by allanite grains, (d) titanite grain with ilmenite inclusions from the Plum shear zone. The subgrains in this grain are decorated by darker films with anastomosing geometry, (e) Sector zoned titanite grain from the 315 shear zone with discontinuous core-mantle-rim domains with variable BSE response, (f) patchily zoned titanite grain with ilmenite inclusions from the 315 shear zone that shows a strong shape preferred orientation and is in textural equilibrium with the fabric-forming biotite.

Figure 7. Terra-Wasserburg U-Pb concordia diagrams that show isotopic data from: (Upper panel left) titanite grains hosted within the low-strain domains of the RAR shear zone. The analysed grains are variably enriched in common Pb components and show spread. (Upper panel right) titanite grains hosted with the higher strain domains of the RAR shear zone. Note that this generation of grains is more radiogenic and doesn’t show spread in Terra-Wasserburg space. (Lower panel – left) titanite

grains with patchy zoning from the 315 shear zone. (Lower panel - right) titanite grains with sector zoning from the 315 shear zone.

Figure 8. Terra-Wasserburg U-Pb concordia diagram that shows U-Pb isotopic data from titanite grains of the D1 Plum shear zone.

Chapter 6 :

Figure 1. Simplified geological maps of the Vredefort (A) and Sudbury (B) impact structures. With black stars is denoted the location of the samples (look also Item DR1) examined in this study. Note that in Figure 1B, the sample of the South Range is projected at the surface.

Figure 2. Collage of photographs that depicts in the first column band contrast maps (A,C,E), in the second misorientation maps (B,D,F), and in the third pole figures. In the first row the EBSD crystallographic data are from Type 1 titanite grains of the North Range, in the second row are depicted Type 1 and Type 2 grains from the South Range, and in the third Type 1 grains from the Vredefort structure.

Figure 3. Wetherill – Concordia diagrams the depict U-Pb isotopic data from Type 1 titanite grains from the South Range of the Sudbury structure (diagram A) and the Vredefort structure (diagram B), respectively.

Chapter 7 :

Figure 1. Simplified geological map of the Sudbury impact structure modified from Ames et al., (2005). With blue stitched lines is denoted the Cliff Lake Fault and with yellow stars the sampling locations of the structure. At the upper right part of the figure is depicted the simplified cross section A-B across the Cliff Lake fault. The cross section is modified from Vale internal report.

Figure 2. Schematic cross sections that depict the relationship of the examined shear zones with Ni-Cu-PGE sulphide ore bodies.

Figure 3. Plot that shows the relationship of Ni content relative to FeO in biotite grains from the Cliff Lake Fault

Figure 4. Plot that shows the relationship of Ni content relative to FeO in chlorite grains from the Cliff Lake Fault

Figure 5. Simplified map of the Six Shaft Shear Zone that shows the location of the biotite-rich mylonitic samples studied for mineral-chemical analysis and the concentration of nickel in each sample

Acknowledgements

The PhD thesis “Petrochronology and mineral-chemistry of mid-crustal shear zones: new tools for tectonics and mineral exploration” is a multidisciplinary work. That means that the interaction with different researchers and industry geologists that provided guidance, assistance, and support was of essential importance for the successful completion of the project. At this point I wish to thank the people that contributed to that. First, I would like to thank my PhD supervisor, Senior Lecturer, Dr. James Darling for trusting me this demanding project, giving me the space to follow my ideas and interests, and providing critical guidance on the subjects of isotopic, chemical, and crystallographic microanalysis. My second supervisor, Dr. Craig Storey for all the stimulating conversations and suggestions on different parts of the project and on a variety of isotopic and microstructural geology topics. Dr. Peter Lightfoot, Adjunct Professor, assisted on the field and sampling expeditions in Sudbury, taught me a lot of things about the geology of Sudbury structure, and provided critical information about the mineralization systems of the mining camp. Dr. Desmond Moser, Associate Professor, organized and accompanied me on my first fieldtrip in Sudbury and provided critical information on topics pertaining to the absolute age dating of ductile deformation induced by tectonic or impact phenomena. Dr. Stuart Kearns, at the University of Bristol, helped me extensively with his didactic stance and deep knowledge to understand complex topics in electron microprobe analysis. Dr. Richard Hinton, at the Ion Microprobe Facility (University of Edinburgh), helped to complete smoothly all the analytical sessions of data collection and provided useful feedback. Dr. Stephanie Lasalle helped on the smooth operation of the LA-ICP-MS at the University of Portsmouth. Mr. Ivan Barker, SEM technician at the University of Western Ontario, helped on the collection of quantitative microstructural data and provided feedback on the internal workings of electron microscopy and microstructural analysis. Mr. Joseph Dunlop, SEM technician at the University of Portsmouth, provided very useful feedback on a variety of electron microscopy and sample preparation topics. Mr. Geoff Long, specialist technician at the University of Portsmouth, prepared excellent quality thin- thick sections and grain mounts, always on time. The following industry geologists of VALE ltd: Lisa Gibson, Rob Pelkey, Ian Fieldhouse, Craig Arlt, Enrick Tremblay, and Michael Macburnie are thanked for extensive feedback on different aspects of Sudbury geology and help on the finding and collection of drillcore samples. All the members of crustal

evolution research group at the University of Portsmouth are thanked for their help on different analytical aspects of my work and discussion of scientific and other topics. I gratefully acknowledge also the University of Portsmouth that provided a PhD studentship to me in order to accomplish this research study, the Science faculty, and the School of Earth and Environmental Sciences that supported parts of my research after the duration of my three-year bursary funding.

Dissemination

1. Poster presentation at the Tectonic Studies Group, Annual Research In progress conference, London, January 2016. Poster title: Titanite petrochronology of ore-controlling shear zones: Insights from the Sudbury mining camp (Sudbury, ON).

2. Oral presentation at the Metamorphic Studies Group, Annual Research in progress conference, Nottingham, March 2016. Oral presentation title: Titanite petrochronology and microstructural analysis of ore-controlling shear zones from the Sudbury impact structure (Sudbury, ON).

3. Oral presentation at Goldschmidt 2016, Yokohama, Japan, June – July 2016. Oral presentation title: Direct dating of shear zone operation and sulphide mineralization using titanite.

4. Research article in the Journal Precambrian Research, February, 2017 with the title : Dating shear zones with plastically deformed titanite : New insights into the orogenic evolution of the Sudbury impact structure (Ontario ,Canada).

Chapter 1. Introduction

1.1 Thesis aims and structure

The PhD project **''Petrochronology and mineral chemistry of mid-crustal shear zones: new tools for tectonics and mineral exploration''** is focused in the wider area of the Sudbury impact structure (Ontario, Canada). The main aims of the project were to understand better by using a variety of microanalytical techniques: (a) the syn and post-impact orogenic evolution of the Sudbury impact structure through shear zone geochronology and (b) the prospectivity of mylonitic shear zones, that are spatially associated with magmatic Ni-Cu-PGE sulphide ore bodies, through their mineral-chemical signatures. A third major component of the project emerged through an unexpected finding. This finding is interpreted as the first microstructurally-justified example, to our present knowledge, of shock metamorphism in the accessory phase titanite ($CaTiSiO_5$). Hence, another objective that was included in the project was to understand better the role of this important accessory phase as recorder and chronometer of impact bombardment. Consequently, a significant part of the thesis (**Chapter 6**) presents and compares U-Pb isotopic and microstructural data of shock-metamorphosed titanite grains from the two largest impact structures on the planet, the 2.02 Ga Vredefort and the 1.85 Ga Sudbury craters. Main aims of this part of the thesis, was to trace the microstructural fingerprints of shock deformation and understand better the role of this refractory mineral as a chronometer of shock metamorphism.

The main part of the research project was to understand better the orogenic history of the Sudbury impact structure through the *in-situ* U-Pb geochronology of different ore-controlling mylonitic shear zones using the accessory phase of titanite. The syn and post-impact orogenic history of the Sudbury structure remains obscure and many researchers invoke the Penokean orogeny (1.9 – 1.8 Ga) as the main event that induced the deformation and collapse of the crater. To test the hypothesis of polyorogenic activity in the Sudbury structure different mylonitic shear zones from the South Range of the Sudbury structure were chosen for detailed isotopic, microstructural and petrographic analysis with main aim to reveal their orogenic affinity. In some parts of the project a petrochronological approach was followed (**Chapter 4**) whereas in others U-Pb titanite geochronological data are tied with detailed petrographic-microtectonic and electron beam imaging (SEM/BSE) observations (**Chapter 5**) in order to understand the age significance of the isotopic dates. Petrochronology

is the understanding of isotopic dates in the light of complementary geochemical (major to trace element), petrographic-microtectonic, quantitative microstructural (EBSD), and/or thermobarometric information gleaned from the same accessory phase. This approach was followed in the study of a mylonitic shear zone from the Creighton Mine, the Six Shaft Shear Zone (**Chapter 4**), by U-Pb isotopic, trace element, and quantitative microstructural analysis of shear-hosted titanite grains. The Six Shaft Shear Zone is exposed underground at the 5400 level (ca 1.65km) of the Creighton Mine in the South Range of the Sudbury structure. The main objectives in the study of the Six Shaft Shear Zone were: (a) to characterise in detail this unique ore-controlling structure using mineral-chemistry, petrographic – microtectonic observations, and quantitative microstructural data of mylonitic sulphides, and (b) to bracket the timing of its operation by dating geochemically and microstructurally characterised titanite grains. The presence of plastic deformation microstructures in the shear-hosted sulphides are discussed also in the light of the new age data with the main aim of placing temporal constraints of sulphide remobilization in the Sudbury mining camp.

Moreover, in Creighton Mine at depths below 2km, are exposed two orientation families of ore-controlling mylonitic shear zones, the steeply dipping 118 family and the south-dipping Hodder/315 family. Borehole data indicate that the shear zones of the Hodder/315 system are related to the main deformation system of the Sudbury structure, the South Range Shear Zone, that comprises chiefly ductile and brittle-ductile top-to-the-NW thrusts. The movement history, their role on remobilization of ore bodies, and the tectonic implications that arise from the presence of these two structural families are not well understood. Thus, the mains aim of this part of the study (**Chapter 5**), were to place constraints on the operation-reworking history of these structures via the U-Pb dating of shear-hosted titanite grains. Detailed meso and micro-scale analysis of drillcore samples allowed as to place these two shear families in a structural framework and establish new temporal constraints on the operation of the main deformation system of the Sudbury structure, the South Range Shear Zone. The new geochronological data evidence a prolonged reactivation history of the two structural families. This allows as to understand better orogenic affinities that may exist between the orogenic province that bounds the South Range of the Sudbury structure, the so-called Southern Province, and the Transcontinental Proterozoic provinces that extend from the Southwest up to the Northern part of the United States. The other major component of the project was to test if mineral-chemistry can be

used as a pathfinder tool of shear-hosted mineralization (**Chapter 7**). The ore-controlling character of mylonitic shear zones from different mines of the heavily mineralised South Range (e.g. Creighton, Copper Cliff, Garson Mines) provide unique laboratories to test if variations in the mineral chemistry of fabric-forming silicates, from major to trace element level, can be used as a vectoring tool of Ni-Cu-PGE mineralization. Thus, different barren and ore-bearing shear zones were sampled and studied combining high-spatial resolution chemical microanalysis (EPMA and LA-ICP-MS) in order to map compositional variations focused mainly on the abundance of transition metals (i.e. Ni, Cu). The target minerals were chiefly phyllosilicates (i.e. biotite and chlorite) and calcic-amphiboles since they define the high-strain fabrics. Mineral chemistry data from accessory phases (i.e. epidote, titanite) were also collected and compared with that of the major phases.

Chapter 2. Geological framework of the Sudbury impact structure (Ontario, Canada)

2.1. Geographical Location and general features

The Sudbury structure is located North of Lake Huron at the southern part of Ontario Province (Great Lakes Region, 46°29'24"N, 81°00'36"W, 348m) and is globally famous for two reasons : (a) it is the second largest and oldest impact structure on Earth (1.85 Ga, Krogh., 1984), after the Vredefort structure (2.02 Ga, Kamo et al., 1996), and (b) it hosts one of the largest Ni-Cu-PGE mining camps on the planet. The Sudbury region has a humid continental climate, and belongs to the physiographic regions of Canada that are characterised as shield regions. The shield regions cover most of the land surface in Ontario and Quebec, and consist chiefly of Precambrian crystalline rocks. The Sudbury structure is elliptical and covers an area of more than 15.000 km^2 (**Figure 1**).

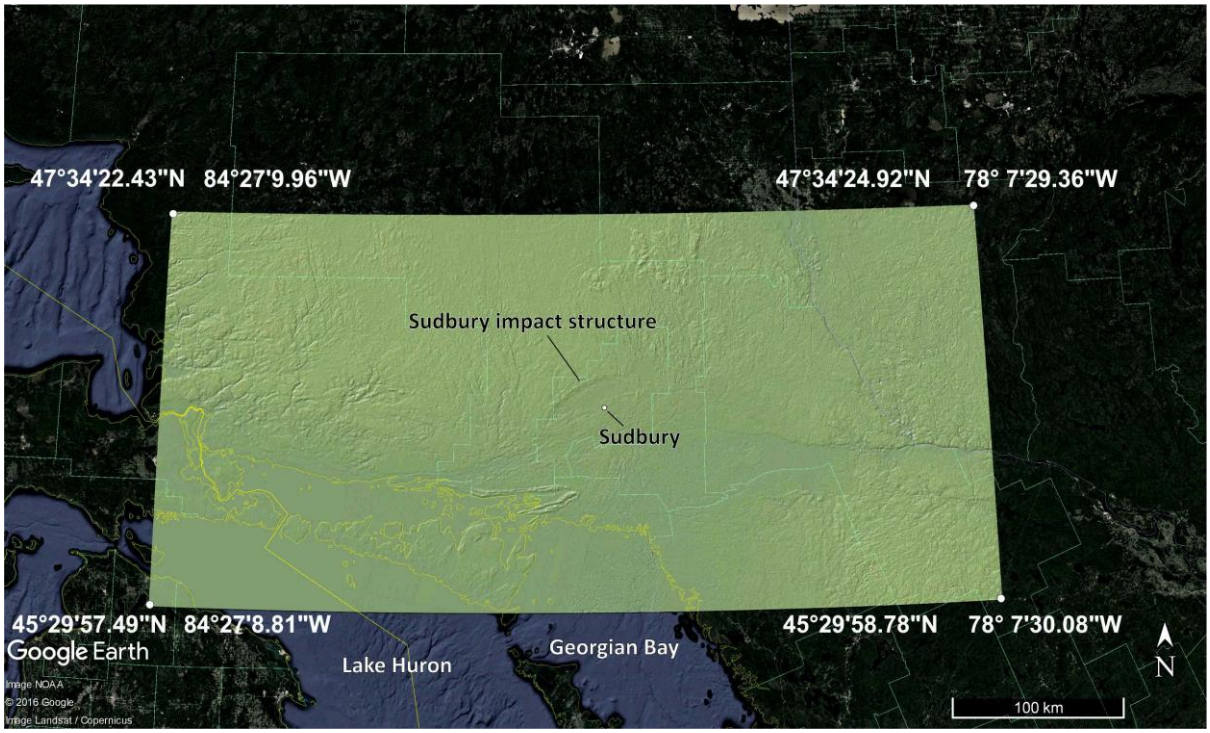

Figure 1. Location of the Sudbury impact structure and Sudbury town in Ontario (CA). Note the elliptical shape of the impact structure, with a long axis trending NE-SW, on the overlaid Shuttle Radar Topographic Mission (SRTM) digital elevation map.

2.2 Regional geology

The Sudbury impact structure is located at the intersection of two Precambrian accretionary provinces, the Archaean Superior and the Mesoproterozoic Southern Province (named also as the Penokean orogenic province, **Figure 2**). The orogenic front of the Late Mesoproterozoic Grenville Province is ~ 10km southofthe southern part of the Sudbury Structure (**Figure 2 and 3**). The deformational, metamorphic and magmatic records of these provinces record the growth, development, and assembly of the North American Craton (Laurentia) (Hoffman., 1988). The main geological features of each province are described in the following sections.

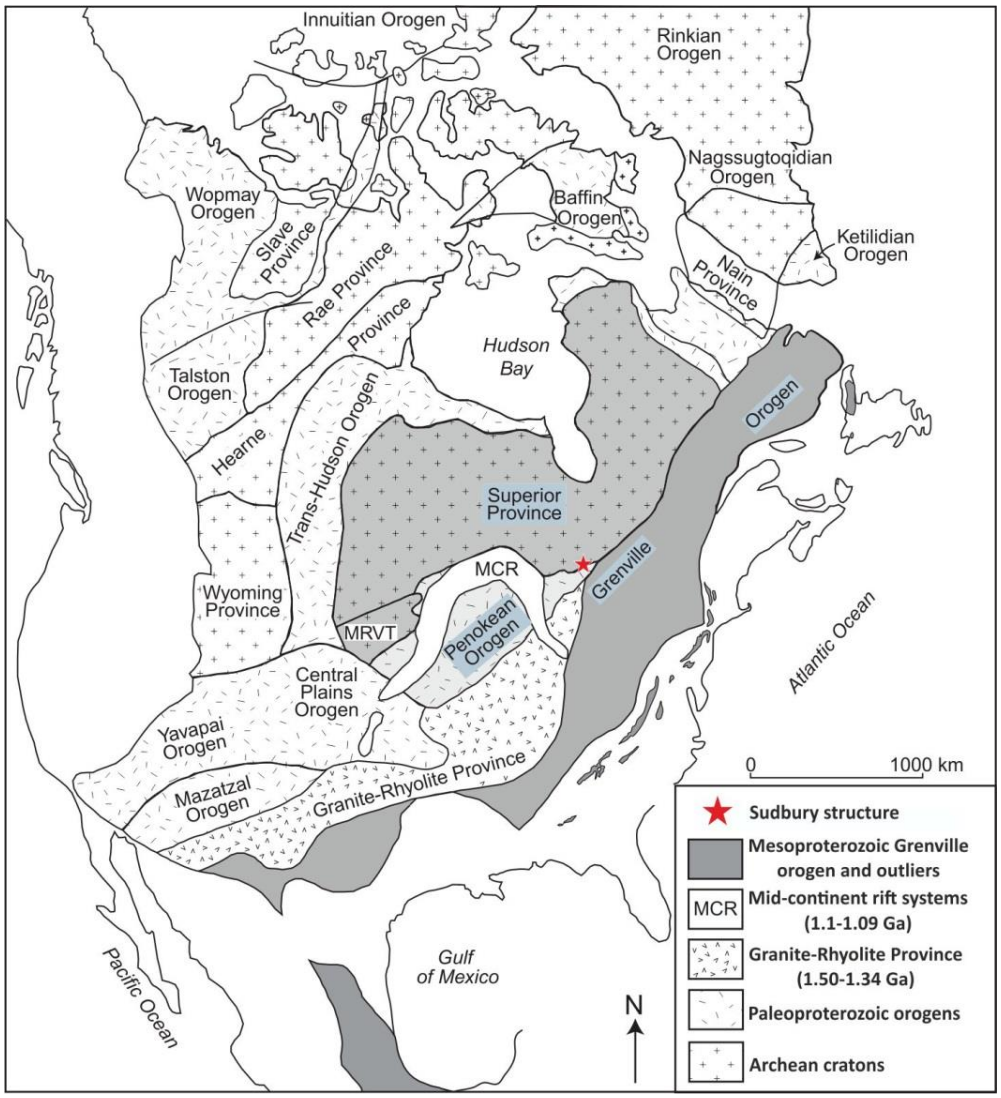

Figure 2. Simplified map of the North American and mid-continent orogenic provinces. The different provinces that bound the Sudbury impact structure are depicted with different shades of gray. The red star denotes the location of the Sudbury impact structure. Map modified from (Tollo et al.,2010).

2.2.1. The Superior Province

The Neoarchean Superior Province is the core of the North American craton and covers an area of approximately 2 million km^2 (~70% of the Canadian shield) (**Figure 2**). The Superior Province comprises different linear lithotectonic subprovinces that exhibit diverse deformation styles, metallogenetic features, tectonothermal, and geochronological characteristics (Hoffman, 1988, Card., 1990, Whitmeyer and Karlstrom., 2007*)*. The amalgamation of these terranes led to the characterization of the Superior province as a superterrane (Percival et al., 2006). The subprovinces of the Superior province are classified as volcano-plutonic (e.g. Wawa, Abitibi, Wabigoon), metasedimentary (e.g. Pontiac, Quetico, English River), and gneissic (e.g. Minessota River Valley, Kapuskasing structural zone, Pikwitonei) (Card., 1990).

The boundaries between the different subprovinces are domains of lithological contrast and strain localization that show reworking during different accretionary events (Percival and Williams, 1989). Proterozoic orogenic episodes that were accompanied by rifting and magmatism induced reactivation of structures located at the marginal domains of the different subprovinces (Percival and Easton, 2007). Specifically, U-Pb age dating of hydrothermal monazites from Neoarchean structures in Superior province (i.e. Abitibi subprovince) indicate their reworking at 1730 ± 5 Ma (Zhang et al., 2014). Hence, it is evident that Neoarchean structures were foci of strain accumulation and fluid-mediated mineralization (orogenic lode gold deposits) during later Proterozoic orogenies. The prevalent tectonic model for the build-up of the Superior province is the subduction-driven accretion of Archean terranes, that range in age from 3.1 to 2.6 Ga, similarto the modern style of subduction tectonics in the convergent margins of western Pacific (Card, 1990).

2.2.2. The Southern Province

The Southern Province hosts metamorphosed passive margin sediments that rest unconformably upon Archean basement rocks of the Superior province. This province extends for ~300km and consists mainly of volcanics, volcaniclastics, siliciclastics and limestones rocks of the Huronian Supergroup (2.6 – 2.2 Ga), that bound also the southern footwall of the Sudbury structure (**Figure 3**). Lithological members of the Huronian Supergroup are widespread in the wider area of the Great Lakes region (e.g. Minnesota, Wisconsin, Michigan). This package of supracrustals defines southwards-deepening clastic wedges with a maximum

thickness of 12km near Lake Huron. Along orogenic strike are recorded variations in the thickness and facies distribution of the Huronian metasediments that were caused chiefly by syntectonic processes (Zolnai et al., 1984). Whole-rock Sm-Nd and Pb isotopic data indicate that the provenance of the Huronian sediments was predominantly the Archean rocks of the Superior province (Mclennan et al., 2000). Identified disturbances in the U-Pb isotope systematics of Huronian metasediments have revealed at least two episodes of post-depositional alteration. The first is related with diagenetic processes at ~ 2.2 Ga whereas the second with an episode of potassic metasomatism at ~ 1.7 Ga (Fedo et al., 1997, Mclennan et al., 2000). The deformation of the Huronian metasediments in the Southern province is attributed mainly to the Penokean orogeny (1.9-1.8 Ga; Sims et al., 1989). The metamorphic grade during the Penokean orogeny reached the staurolite-in isograd (amphibolite-facies conditions), with a strong spatial correlation between metamorphic grade and deformation intensity (Bennett et al., 1991). Gabbroic, granitic, and diabase intrusive bodies intruded the Southern province metasediments and are related to Pre-Penokean orogenic events and Post-Penokean anorogenic processes (Bennett et al., 1991).

2.2.3. The Grenville Province

The Grenville province (1.3 – 1 Ga) is a mosaic of geological terranes that record arc-continent and continent-continent collisional events along the south-eastern margin of proto-North America (Laurentia margin; Krogh., 1994, Tollo et al., 2004, Hynes and Rivers., 2009). The long-lived character (~100 Ma) and the development of high and prolonged thermal gradients (amphibolite to granulite-facies conditions) during the peak of the orogeny classify the Grenvillian as a large-hot orogen (Himalaya-type) *sensu* Beaumont et al., (2006). The Grenvillian orogenic cycle comprises two major orogenic episodes: (a) the arc-continent Elzevirian orogeny (1230 – 1180 Ma) and (b) the continent-continent Ottawan orogeny (1100 – 1000 Ma). Between the two events a widespread event of anorthosite-mangerite-

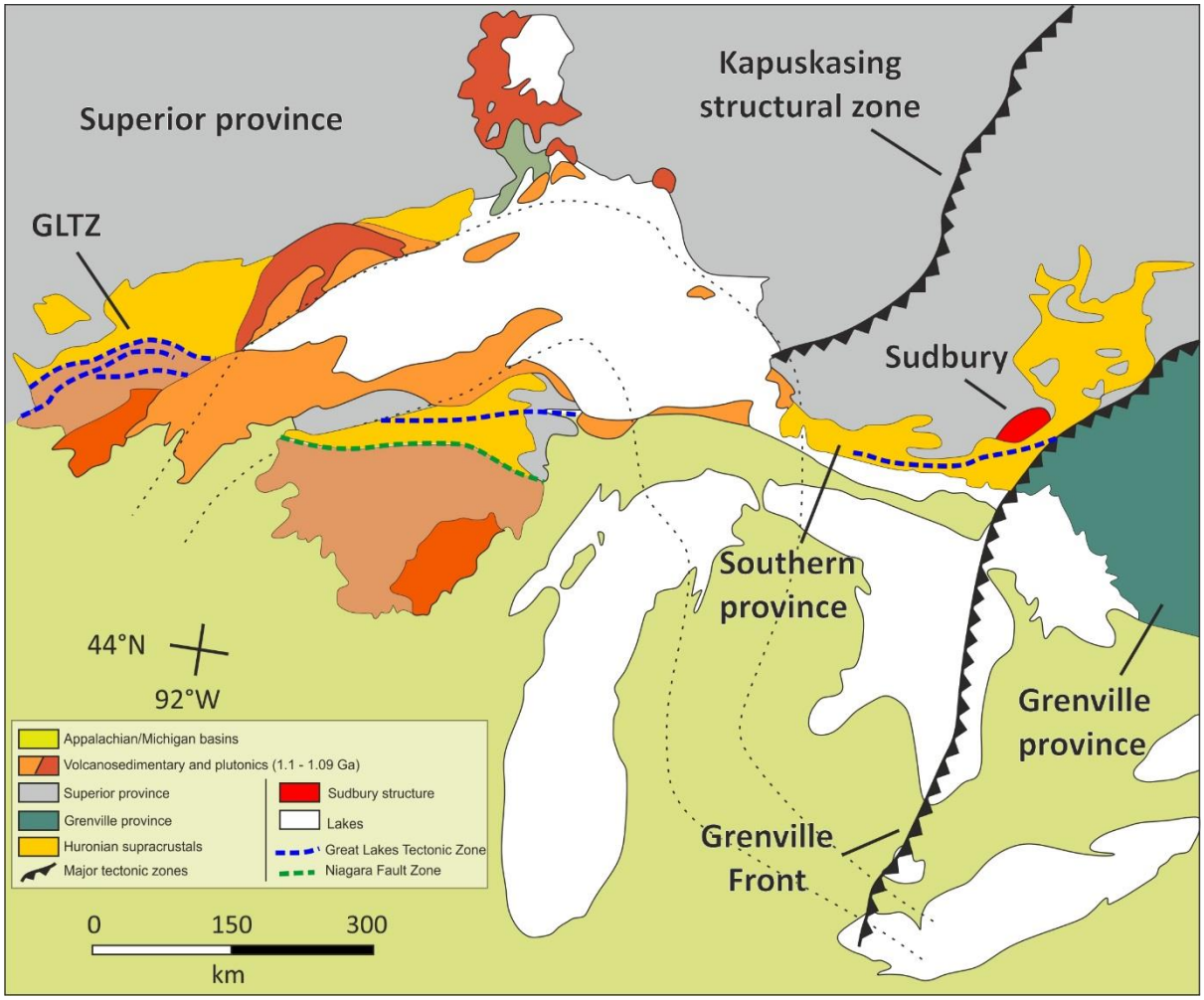

Figure 3. Simplified geological map of the Great Lakes Region that depicts the main lithostratigraphic units at the Southern part of the Superior province. With black stitched lines is depicted the location of the 1.1 Ga Mid-continent rift. Note that with white colour are depicted the lakes. Map modified from Thurston., (1991).

charnockite-granite magmatism is recorded (McLelland et al., 1996). Despite that the Grenvillian orogeny culminated between 1100 Ma and 1000 Ma, it is suggested that in different orogenic domains the peak conditions were attained at different times (Gower and Krogh., 2002).

The three lithotectonic segments of the Grenvillian province are arranged as a south-easterly dipping thrust stack and are: (a) the 'parautochtonous belt' composed of Archean, Paleoproterozoic, and Mesoproterozoic rocks, (b) the 'allochthonous polycyclic belt' that comprise transported Paleoproterozoic and Mesoproterozoic rocks, and (c) an 'allochthonous monocyclic belt' composed of rocks of Mesoproterozoic age (Carr et al., 2000). The orogenic front of the Grenvillian province is a crustal-scale, top-to-the-NW, amphibolite-facies shear

zone, termed as the 'Grenville front tectonic zone' (**Figure 3**) and is expressed by moderately dipping reflectors in deep seismics (Forsyth et al., 1994, Culshaw et al., 1997).

2.3. Lithostratigraphic architecture and mineralization of the Sudbury structure

2.3.1. The Sudbury Igneous Complex (SIC)

The Sudbury Structure is a folded multi-ring impact basin with initial diameter of ~ 250km (Riller., 2005). It is the only structure on the planet that hosts a differentiated impact melt sheet, the Sudbury Igneous Complex (SIC) (Naldrett and Hewins., 1984). The SIC is divided into three regions: (a) the South-dipping North Range (Northern part of the SIC), (b) the East Range (Eastern part of the SIC), and (c) the South Range (Southern part of the SIC) (**Figure 4**). The thickness of the SIC is 2.5 – 3 km and the estimated volume 8,000 to 14,000km^3 (Deutsch et al., 1995). From top to bottom, the Sudbury Igneous Complex is composed of four major units: (a) the upper unit (granophyre), (b) the middle unit (quartz gabbro), (c) the lower unit (norite), and (d) the contact sublayer (**Figure 5**) (Therriault et al., 2002). The main lithological and mineralogical features of each unit described in this section are according to Naldrett and Hewins., (1984), Lightfoot et al., (1997, 2001) and Therriault et al., (2002). The contact sublayer is a medium to coarse-grained noritic rock with hypidiomorphic texture and abundant monomineralic (quartz and plagioclase) and lithological inclusions (i.e. felsic gneisses, melanorites, ultramafics). The contact sublayer passes gradationally to the lower unit of the SIC. The lower unit consists of noritic rocks (Pl-Opx-Hyp-Aug-qtz-Mag-Ilm) with medium to coarse-grained hypidiomorphic granular texture and a ubiquitously developed planar lamination defined by plagioclase grains. The South Range norite is extensively altered with the one third of the unit lacking fresh pyroxenes. A quartz-rich noritic unit is observed also in the South Range that exhibits increasing modal abundance of quartz (~20%), relative to the South Range norite (~8%) with no evidence of magmatic foliation. In the North Range, the principal lithology of the lower unit is the Felsic norite (**Figure 5**). The felsic norite is characterised by hypidiomorphic, granular texture and shows elevated modal abundance of plagioclase and quartz (~25%). Stratigraphically below the felsic norite, is recorded the mafic

norite unit with increased hypersthene contents (~40-60%) (**Figure 5**). Stratigraphically upwards the lower unit passes transitionally to the Middle unit of quartz gabbro.

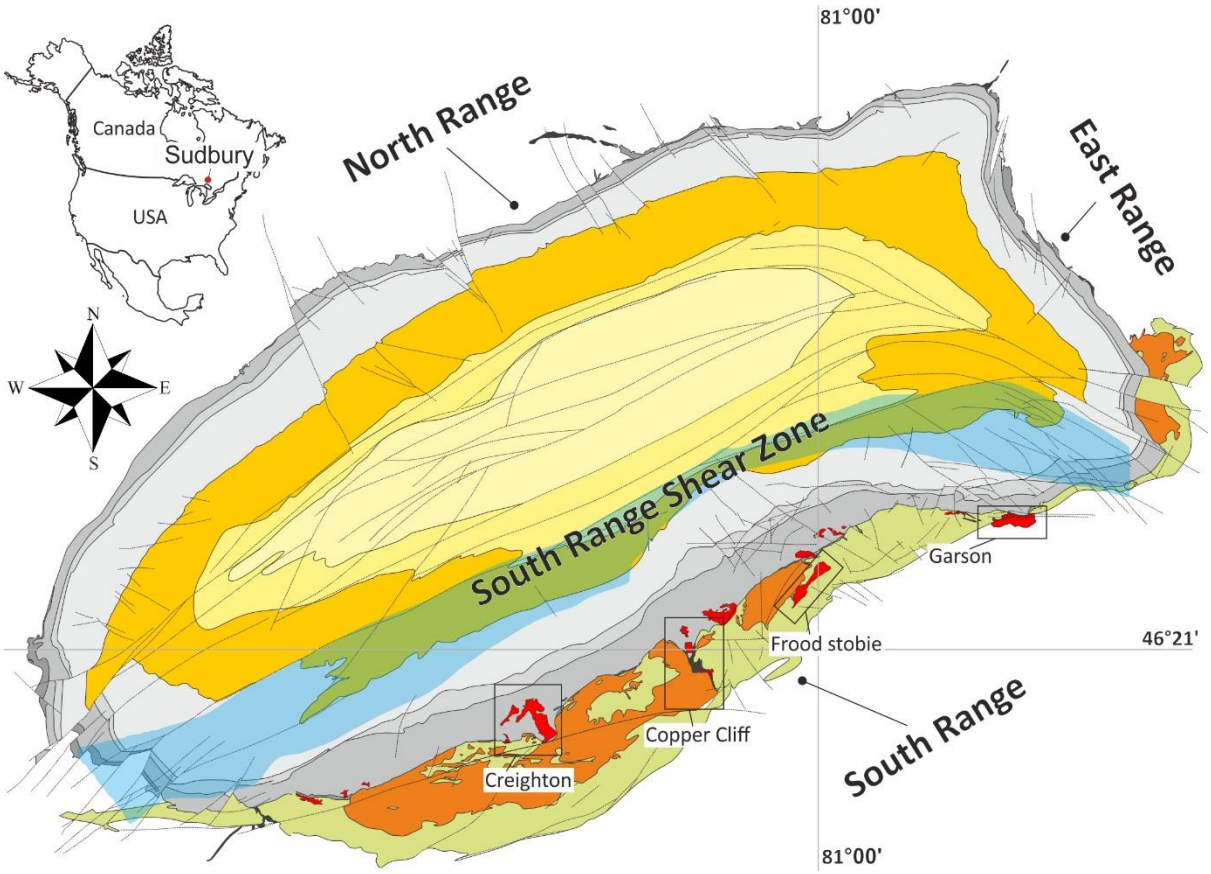

Figure 4. Simplified geological map of the Sudbury impact structure (see also chapter 4). In rectangle are marked the mines that host the largest sulphide deposits in the South Range (Creighton, Copper Cliff, Frood Stobie and Garson Mines).

The quartz gabbro unit exhibits similarities between the North and South Range of the Sudbury structure (**Figure 5**). A significant difference in the latter unit is the increased modal abundance of opaque minerals (~9%) in the North Range. Stratigraphically above the quartz gabbro unit develops gradationally the upper unit (granophyre) of the SIC. The transitional zone between the two units has a thickness of approximately 200m. Salient mineralogical features of the transitional zone are the increase in biotite abundance and the growth of cumulus apatite grains. The granophyre unit is coarse-grained and unlayered with characteristic development of micrographic and granophyric intergrowths between quartz and microcline. The contact between the Granophyre unit and the overlying sediments of the Sudbury basin is characterised also as gradational. A notable difference in the upper

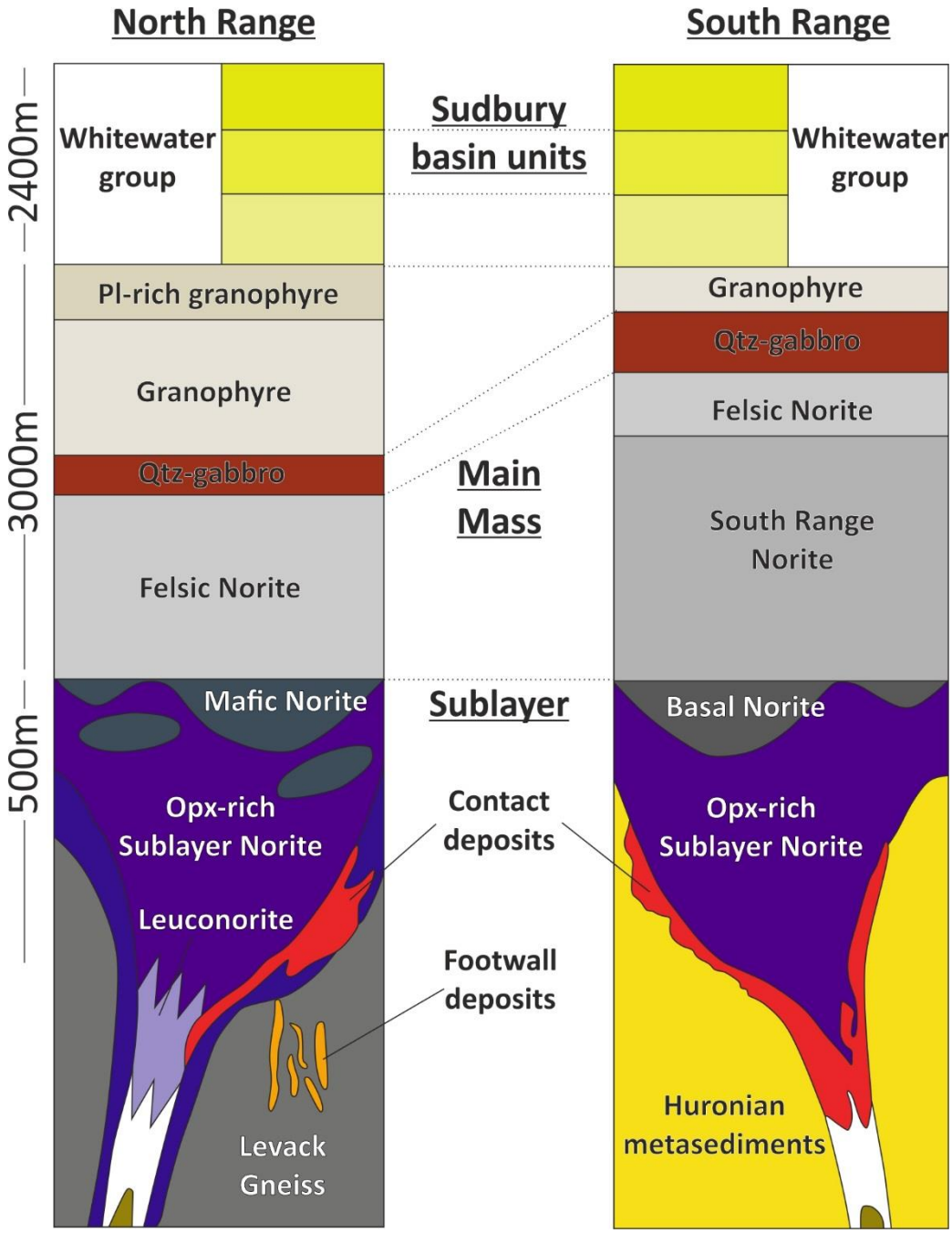

Figure 5. Principal lithostratigraphic units of the Sudbury Igneous Complex in the North and South Range, respectively. The lithostratigraphic columns were modified from Lightfoot et al., (1997).

unit between North and South Range is the intense shearing that is observed exclusively in the South Range, by a crustal-scale network of shear zones, the South Range Shear Zone (**Figure 4**).

The quartz diorite or ''offset'' dykes are 50 to 100m wide, extend radially and

concentrically around the complex, and constitute an important ore-bearing environment. Two varieties of quartz diorite dykes are recognised (Keays and Lightfoot., 2004): (a) inclusion and sulphide-free dykes that emplaced before the differentiation of the impact melt sheet and (b) inclusion-bearing dykes that also have geochemical features indicative of pre-differentiation emplacement (Darling et al., 2012). They show discontinuous and pinch and swell geometry and have a combined volume of ~ 100km^3 if projected to depth beneath the SIC. In many cases, they follow zones of pseudotachylitic breccia (e.g. Frood stobie deposit, South Range). Mineralised domains are observed often in spatial association with the swell zones and the discontinuities (Lightfoot and Zotov., 2005). Some of the dykes are mineralized (e.g. Copper Cliff deposits) whereas other are barren or host weakly disseminated sulphides (e.g. Foy and Ministic dykes) (Lightfoot., 2007). The barren dykes exhibit sharp contacts with the Huronian metasediments in the South Range (Keays and Lightfoot., 2004).

2.3.2 Sudbury basin

The Sudbury basin is located stratigraphically above the Sudbury Igneous Complex and comprises volcanosedimentary and fallback deposits that are collectively called : the Whitewater Group Formations. The latter are classified in the local literature as the: (a) Onaping, (b) Onwatin and (c) Chelmsford formations (Pye et al., 1984) (**Figure 5**). In more detail, the Onaping Formation is the lowest formation of the Whitewater Group with an estimated thickness of 1400 to 1600m. The contact of the Onaping Formation with the underlying granophyre unit is intrusive and with the overlying Onwatin formation gradational (Muir and Peredery., 1984). The presence of minerals with shock-metamorphic effects (e.g. planar deformation features in quartz, feldspar, and zircon grains), impact diamonds, and the documented iridium anomalies testify to the impact origin of this formation (Grieve et al., 2010 and references therein). The Onaping Formation has been characterised as a suevitic fallback breccia deposit, that is penetratively deformed in the South Range (**Figure 6A**), with abundant impact-produced melt bodies. Recent studies suggest that the Onaping Formation is a hydrothermally altered impact breccia that started as a fallback deposit but evolved by the interaction of the proto-igneous complex with the sea water that filled the impact structure soon after the impact event (Grieve et al., 2010). Recent mapping campaigns subdivide the Onaping Formation, based on the abundance and size of fragments versus matrix into three members the: (a) Garson (0-500m), (b) Sandcherry (~250m), and (c) Dowling

(~1000m) members (Ames et al., 2005). The Onwatin Formation is composed of pelagic sediments with a thickness of approximately 600m. These sediments are chiefly carbon-bearing argillites and siltstones with carbonate sediments at the lower parts of the formation. The contact with the underlying Onaping Formation is gradational (Rousell., 1984). Stratigraphically above the Onwatin Formation is a package of turbiditic sediments with an approximate thickness of 850m, the Chelmsford formation (Rousell., 1984). The deposition of this turbiditic sequence has been associated with a foreland basin depositional setting in front of the prograding Penokean orogen (Long., 1992).

2.4. Footwall units

2.4.1 The Huronian Supergroup

The Huronian Supergroup comprises an Early Paleoproterozoic (2600 Ma – 2200 Ma) sequence of siliciclastic rocks with a thickness that varies from ~8000 to 11000m around the Sudbury structure (Dressler., 1984). The Huronian Supergroup is subdivided into four main groups which in ascending stratigraphic order are the: (a) Elliot Lake, (b) Hough Lake, (c) Quirke lake, and (d) Cobalt groups (Bennett et al., 1991). The lower Elliot Lake unit is characterised by uranium-bearing quartz pebble conglomerates at the basal parts and volcanic rocks stratigraphically upwards. Members of the Elliot Lake unit, such as the pelite and metabasalt-dominated Elsie Mountain Formation, record perfectly the later medium-grade metamorphic evolution of the Huronian sequence (**Figure 6B**). Above the lower unit, cyclical repetitions of conglomerate, mudstone, wacke and quartz-feldspar arenites are recorded (Dressler., 1984). Specifically, each of these cyclical sequences contains glaciogenic diamictites (**Figure 6C**) that are followed by mudstone-dominated units and arenaceous deposits. The alternation of glacial and mudstone-dominated sequences record glaciation-deglaciation episodes that were accompanied by colossal atmospheric changes in the planet (e.g. oxygenation of the atmosphere, Young et al., 2001). The timing of deposition of the Huronian Supergroup during this interval makes this sequence one of the most important archives of crustal and atmospheric evolution at the transition from Archean to Proterozoic.

2.4.2 The South Range Breccia Belt

The South Range Breccia Belt is a zone of impact-produced pseudotachylite that developed sub-concentrically to the Sudbury Igneous Complex. This zone has a strike length of ~45km and thickness that varies from meter to kilometre scale (Scott and Spray., 2000).

This zone is hosted within the Huronian Supergroup and is composed of: (a) metasediments and metavolcanics the Elliot Lake Group, (b) Nipissing diabase fragments (2200 Ma), and (c) granitoid breccia fragments (2300 Ma – 2500 Ma). The entrained clasts of the Sudbury breccia are rounded to sub-rounded and are hosted in a grey to black fine-grained to aphanitic matrix (**Figure 6D**). Quartz diorite dykes and associated Ni-Cu-PGE sulphide mineralization are hosted within the Sudbury Breccia (e.g. Frood stobie, Vermillion and Kirkwood offset dykes, **Figure 6E**). Importantly, the South Range Breccia Belt is commonly localized within rheological boundaries defined by lithological units with different competency (e.g. contacts between metavolcanics and metasedimentary lithologies) (Scott and Spray., 2000). The genesis of the Sudbury breccia is attributed to the *in-situ* shock-induced compression and comminution of the host rocks during the shock wave passage (Lafrance and Kamber., 2010). Another hypothesis for the genesis of the Sudbury breccia is that it was produced by frictional melting and cataclasis along superfaults that accommodated large-scale (≥ 100m) displacements (Spray., 1997).

2.5 The Levack Gneiss Complex (North Range)

A complex of Neoarchean tonalitic gneisses, the Levack Gneiss Complex (LGC), underlies the northern half of the Sudbury Igneous Complex (Ames et al., 2005). The LGC complex exhibits arcuate shape, has a width of 0.5 to 5km, and bounds also the East Range of the Sudbury structure. This complex comprises migmatitic tonalites, orthogneisses, biotite paragneisses, diatexetic granitoids, gabbroic, dioritic, and pyroxenitic intrusions (Card., 1994). Thermobarometric studies on garnet-orthopyroxene-biotite, garnet-biotite, and garnet-cordierite-orthopyroxene symplectites indicate that a high-grade metamorphic event took place at 6-8 kbar and 750° - 800° C (granulite-facies conditions). U-Pb zircon geochronology (ID-TIMS) of pegmatite bodies hosted within the gneiss complex indicate that this high-grade event took place at 2.65 Ga (Krogh et al., 1984). The Levack Gneiss Complex underwent an amphibolite-facies event after the Neoarchean high temperature event that is associated with the exhumation of the complex from mid-crustal levels. Contact metamorphic effects induced by the 1.85 Ga impact melt sheet are expressed with the development of two zones of pyroxene and hornblende hornfels. The latter event is suggested to have taken place when the gneiss complex had already reached shallow crustal levels (5 – 10 km) (James et al., 1991).

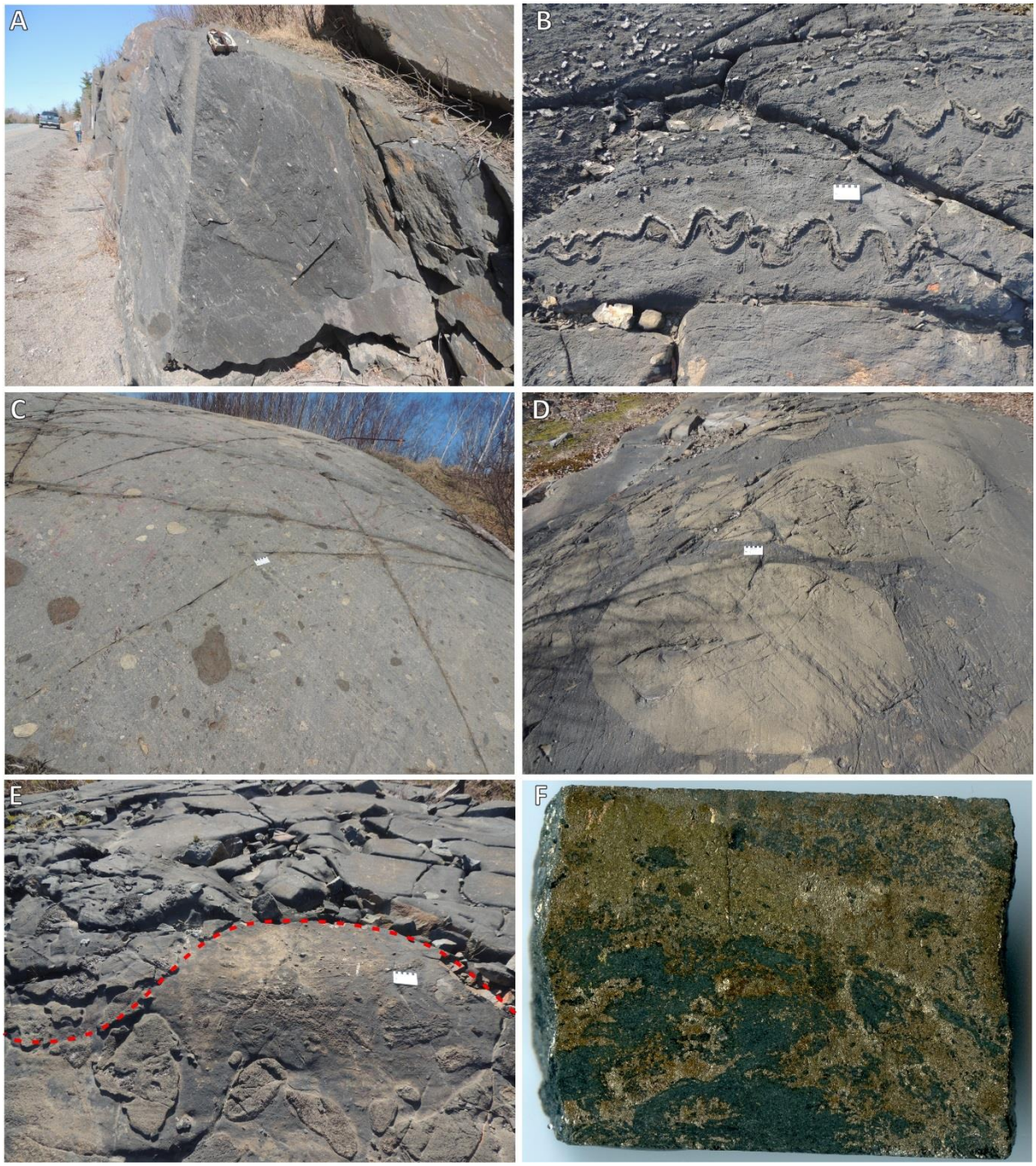

Figure 6. Collage of photographs that depicts: (A) Suevitic breccia along the highway 144 with a penetrative planar fabric. Within the foliated suevites are recorded asymmetric clasts, (B) carbon-rich metasediments of the Elsie Mountain Formation in the Frood Stobie area. Note the abundant presence of staurolite that define symmetrically folded layers, (C) Matrix-supported diamictites at the basal parts of the Huronian Supergroup, (D) Sudbury breccia with entrained rounded clasts in a dark grey aphanitic matrix, (E) lithological contact between the Sudbury breccia and the quartz diorite in the Frood Stobie, (F) pyrrhotite-rich ore body hosted within a foliated metabasalt in the #4 shear zone of the Garson Mine. In the photographs A to E the card for scale is 9 cm. In the photograph F the length of the drillcore interval is ~5cm.

2.6. Ni-Cu-PGE sulphide mineralization

The SIC hosts ~1.65 million metric tons (historic production plus present reserves and resources) of Ni-Cu-PGE mineralization at grades: Ni ~1.2 wt%, Cu ~ 1.03 wt%, Pt ~ 0.4 g/t, and Pd ~ 0.4 g/t (Lightfoot et al., 1997, Barnes and Lightfoot., 2005). In the following sections are described the main geological features of the four major ore-bearing/controlling environments of the Sudbury structure.

2.6.1 Contact-sublayer ore bodies

Disseminated to massive contact style ore bodies constitute ~50% of the magmatic Ni-Cu-PGE mineralization in the mining camp. They settled gravitationally as immiscible sulphide liquids in embayments at the base of the SIC and depleted the main mass units in chalcophile elements (Keays and Lightfoot., 2004). Contact-style deposits are observed also within the footwall breccia at the interface of the contact sublayer with the footwall rocks. These ore bodies are pyrrhotite-rich with Cu/Ni ratios < 1 and low PGE contents (Pt+Pd+Au < 1 g/t) (Ames and Farrow., 2007). In more detail, the contact sublayer contains two members the: (a) igneous-textured sublayer norite, and (b) fragment-bearing footwall breccia (Pattison., 1979). In a detailed study of the contact sublayer from different embayments, Lightfoot et al., (1997) show that this unit is characterised by significant geochemical differences from the main mass units. These differences resulted by the assimilation of compositionally heterogeneous country rocks at different proportions. The most abundant type of rock inclusions in the contact sublayer is diabase with ages of ~1.85 Ga (U-Pb in zircon and baddeleyite, Corfu and Lightfoot., 1996). Contact style deposits are located in South, East and North Ranges of the Sudbury structure (e.g. Victoria, Creighton, Garson, Victor, Whistle Mines. They formed as Fe-Ni monosulphide solid solution that was crystallized from the parent sulphide melt at ~ 1191°C (White., 2012).

2.6.2 Footwall-style ore bodies

The footwall deposits are high metal tenor Cu-PGE-rich vein systems hosted chiefly in pseudotachylite breccia and Archean footwall rocks in the South and North range, respectively. The most characteristic example in the mining camp is the Frood Stobie deposit (South Range) that is hosted with the South Range Breccia Belt (**Figure 4**). The upper part of the ore body contains blebby to disseminated sulphides with increasing modal abundance at depth of Cu-rich minerals such as cubanite and bornite. The bottom of the Frood Stobie

deposit is extremely enriched in PGE and shows quartz-rich alteration (Farrow and Lightfoot., 2002). The most well studied footwall-style deposits are located in the North Range (e.g. McReedy West, McReedy East, Coleman, Strathcona, Fraser Mines). The networks of mineralized veins and pods are characterised by the following phases: chalcopyrite, cubanite, pyrrhotite, pentlandite, millerite and magnetite. Compositionally, the footwall deposits are extremely enriched in copper with Cu/Ni ratios above 6, Cu contents above 6.5 wt%, and Pt+Pd+Au contents above 7g/t (Farrow and Lightfoot., 2002).

2.6.3 Offset dykes (quartz-diorite) ore bodies

The quartz diorite offset dykes were emplaced at the early stages, before the differentiation and sulphide saturation, of the impact melt sheet (Keays and Lightfoot., 2004). The mineralization in the offset dykes (e.g. Foy Dyke, North Range) occurs in disseminated and blebby form or as inclusion-bearing massive form and occurs dominantly in association with the inclusion-bearing variety of quartz diorite. The dominant sulphide phases are: pyrrhotite, pentlandite, chalcopyrite, pyrite, and bornite (Tuchscherer and Spray.,2002). The ore bodies have sheetlike geometry and develop either parallel to the trend of the dykes or as subvertical bodies (Tuchscherer and Spray.,2002). Offset-style ore bodies, in North and South Range, are severely faulted and displaced to deeper mining levels (e.g. Foy and Copper Cliff offset dykes).

2.6.4 Ore bodies related with mylonitic shear zones

Ductile shear zones displace and remobilise Ni-Cu-PGE magmatic sulphides in the Sudbury mining camp (**Figure 7**) (Bailey et al., 2004, Bailey et al., 2006, Mukwakwami et al., 2012, Mukwakwami et al., 2013, Gibson et al., 2010, Papapavlou et al., 2017). Specifically, Bailey et al., (2006) investigated the control of medium-grade metamorphism (amphibolite-facies conditions) and ductile shearing on Ni tenor (Wt% Ni in 100% sulphide) in a shear zone from the Thayer Lindsley Mine (South Range). The strongly sheared sulphides in Thayer Lindsley are characterised by depleted Ni contents and enriched Pt and Pd contents. The Ni depletion is attributed to the replacement of pentlandite by pyrrhotite and mobilization of the liberated Ni by channelized metamorphic fluids that permeated within the shear zone. In contrast, in a study of ore-controlling, amphibolite-facies shear zones from the Garson Mine (**Figure 4**) Mukwakwami et al., (2014) suggested that brecciated, shear-hosted sulphides in Garson Mine are not significantly modified by hydrothermal processes and compositionally

are similar with undeformed contact-style disseminated sulphides.

Recent exploration campaigns towards footwall-hosted ore bodies indicate the presence of structurally remobilized ore bodies that are characterised as ''Low Sulphide High Precious Metal'' ore bodies (Gibson et al., 2010). In this type of mineralization, shear zones control the distribution of platinum group elements (PGE) and acted as pathways for the transfer of metal-bearing fluids. Quantitative microstructural data (EBSD) that were collected in this study from shear-hosted ore bodies in Creighton (Six Shaft Shear Zone) and Garson (#4 shear zone) Mines show different microstructures produced during crystal-plastic deformation such as: low angle grain boundaries (2°-10°), strong crystallographic preferred orientation (CPO), high intracrystalline misorientation values.

2.7. Metamorphic events in the Sudbury structure

The Sudbury igneous complex and the bounding footwall lithologies underwent a regional metamorphic event or events that reached epidote-amphibolite up to greenschist facies conditions in the South and North Range, respectively (Thompson et al., 1985, Fleet et al., 1987). Thus, impact melt rocks in certain locations of the South Range are characterised as amphibolites and epidote-amphibolites (**see Chapter 4, Six Shaft Shear Zone**). Thermobarometric constraints on this event are sparse but recently Mukwakwami et al., (2012) using the garnet-hornblende thermometer in amphibolites from the Garson Mine suggest that this event reached 550° - 590°C. These estimates are in reasonable agreement with thermobarometric results from the Nipissing diabase dykes in the Sudbury area (May township) that underwent metamorphism in amphibolite-facies conditions. Specifically, Blonde., (1996) using the TWEEQU thermodynamic analysis (thermobarometry with estimation of equilibrium state) (Berman., 1991) and amphibole-plagioclase thermometry estimate equilibrium conditions of T = 580°C ± 60°C and P = 4.3 ± 0.8 kbar. The metamorphic gradients that are observed in the area of the impact crater led in the compartmentalization of the crater in four metamorphic zones. In these zones the central and northern part of the craters are characterised by greenschist facies assemblages whereas the southern part and southern footwall by amphibolite up to epidote-amphibolite-facies conditions (Fleet et al., 1987). Petrographic data in this study from a shear zone that marks the southern boundary of the South Range Shear Zone, called in the local literature as Cliff Lake Fault, show that greenschist-facies assemblages are dominant with chlorite as the main fabric-forming phase.

Moreover, quartz recrystallization microstructures are indicative of subgrain rotation recrystallization placing deformation temperatures at the greenschist facies field (~400° - 450°C, Stipp et al., 2002).

2.8. Previous geochronological studies of the Sudbury Igneous Complex

The geochronological studies of the Sudbury structure have focused mainly on the age dating of the impact melt units, using high temporal resolution analytical techniques (ID-TIMS, TE-TIMS). The accessory phases that were used for U-Pb age dating were predominantly magmatic zircon and baddeleyites. In more detail, ID-TIMS U-Pb age dating of zircons from the North Range Felsic Norite and the North Range mafic Norite (lower unit) yield crystallization ages of 1848.9 +4/-2.7 Ma and 1850 +3.4/-2.4 Ma (Krogh et al., 1984). Similar to the Noritic unit, the crystallization age of the North Range Granophyre (upper unit) is estimated at 1850 ± 3 Ma (**Table 1**). In a U-Pb geochronological study of the sublayer unit and the Copper Cliff offset dyke Corfu and Lightfoot., (1996) show that these two units yield indistinguishable $^{207}Pb/^{206}Pb$ ages that range from 1848.1 to 1849.8 Ma. In another study that investigated the age relationship of the offset dykes with units of the Sudbury igneous complex, Ostermann et al., (1996) show that the Foy offset dyke crystallized at 1852 +4/-3 Ma corroborating the previous studies. In another study, Davis., (2008) dated zircons from the Noritic unit of the South Range, using the technique of thermal extraction – thermal ionization mass spectrometry, and concluded that the crystallization age of this unit is 1849.5 ± 0.02 Ma. A recent geochronological study by Bleeker et al., (2015) show again that offset dykes crystallized within uncertainty during the crystallization of the melt sheet. Specifically, Bleeker et al., (2015) conclude to a weighted $^{207}Pb/^{206}Pb$ age of 1849.7 ± 0.2 Ma for the crystallization of a high-MgO Norite on the South Range and 1848.5 ± 0.8 Ma for the radial Pele oofset dyke on the North Range (see the summary in **Table 1**).

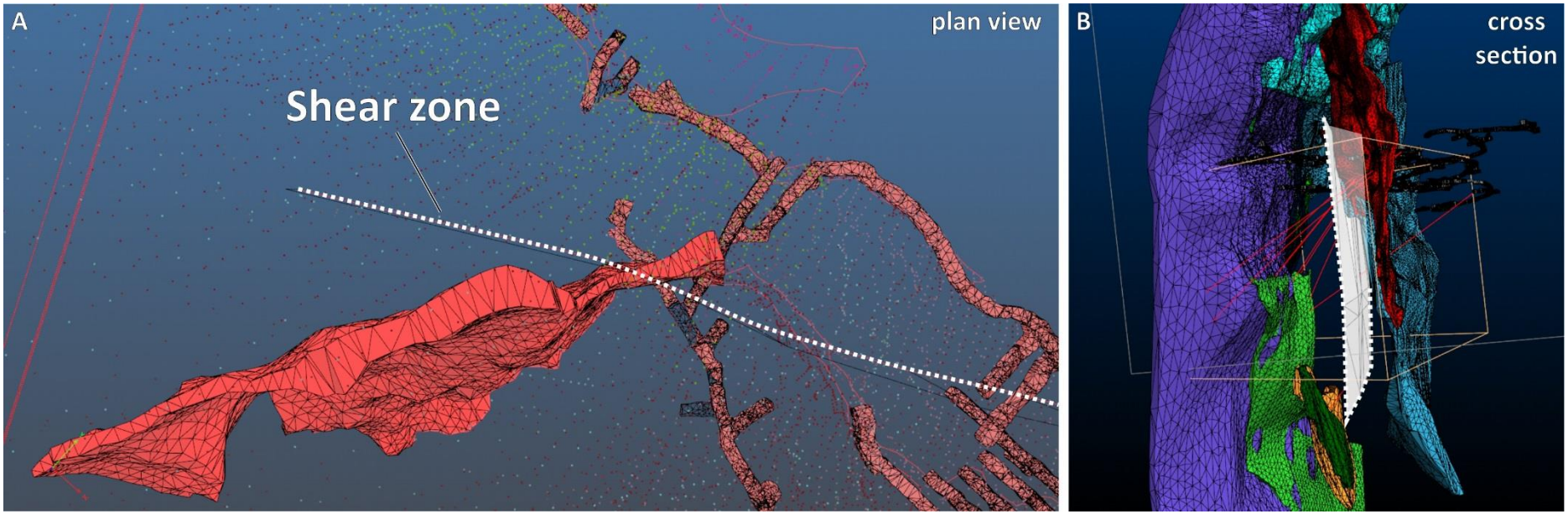

Figure 7. 3D models of Ni-Cu-PGE sulphide ore bodies spatially associated with ductile shear zones. In the photo A is depicted the trace of the RAR shear zone and the right-lateral displacement of the 461 ore body along this structure. In photo B is shown an oblique cross section of the RAR shear zone and its spatial relation with different ore bodies below the 7000ft level of the Creighton Mine.

2.9. Orogenic history in the wider area of the Sudbury structure

The main orogenic event in the southern province that predates the event of impact cratering is the Blezardian orogeny (2.4 – 2.2 Ga) (Stockwell., 1982). Specifically, Riller and Schwerdtner., (1997) suggest that this event was accompanied by metamorphism in amphibolite-facies conditions and development of magmatic and solid-state fabrics in the Creighton Pluton (2.3 Ga) and the hosting Huronian metasediments of the South Range. After the Blezardian, the next orogenic event, that is suggested as dominant on the construction of structural grain in the Sudbury structure, is the Penokean orogeny (1.9 – 1.8 Ga) (Boerner et al., 2000, Schulz and Cannon., 2007). The Penokean is characterised as an arc-continent accretionary event of an island arc, the Pembine – Wausau arc, with the southern margin of the Archean Superior craton (Sims et al., 1989). The Penokean is the oldest Proterozoic orogen at the margins of the Laurentian craton and comprises two domains: (a) an external domain that comprise foreland basin metasediments and supracrustals and (b) an internal that is composed of magmatic lithologies with island arc affinities. The two domains are separated by the Niagara Fault Zone that is regarded as a Penokean suture zone (Tohver et al., 2007) (**Figure 3**). Many researchers suggest that the syn-impact Penokean event induced localization of strain in a deformation system that displaced the lithological units of the Sudbury igneous complex and is named as the South Range Shear Zone (Riller et al., 1999, Boerner et al., 2000).

The southward addition of juvenile crust along the Laurentian convergent margin continued during the Proterozoic. Two major pulses of accretionary tectonics are related to the Yavapai (1.75 – 1.7 Ga) and Mazatzalian – Labradorian orogenies (1.7 – 1.6 Ga) (Whitmeyer and Karlstrom., 2007). The Yavapai accretionary province extends from Arizona to the southwest to the mid-continent areas at the northeast. The Yavapai orogenic province was produced by a series of docking events of juvenile arc crust with the peak of orogenic activity at ~ 1.71 – 1.68 Ga. In the southern province, in proximity with the Sudbury structure, Raharimarefa et al., 2014 report a U-Pb zircon crystallization age of 1744 ± 29 Ma for a deformed granitoid intrusion within the Huronian metasediments (Eden Lake complex) and an age of 1704 ± 13 Ma for an undeformed cross-cutting granitic dyke. Consequently, these researchers bracket the period of Yavapai tectonism between these two magmatic events.

The Mazatzalian – Labradorian accretionary province extends from Southwest United States up to Labrador in Canada (Whitmeyer and Karlstrom., 2007). Age data in proximity to

the Sudbury structure that record this event are sparse. In a study from the Thayer Lindsley Mine (South Range), Bailey et al., (2004) show that syntectonic titanite grains from a lower amphibolite-facies shear zone, the Thayer Lindsley shear zone, yield a mean $^{207}Pb/^{206}Pb$ age of 1658 ± 68 Ma that is attributed as evidence of shear zone reworking during the Mazatzalian – Labradorian orogeny. In this study, further constraints for the operation of shear zones during this event are provided in chapters 3 and 5 (i.e Creighton Mine shear zones).

Table 2.2. Synthesis of geochronological data from the Main Mass units. For comparison are noted also the geochronological results from shocked titanite grains that obtained in this study.

Unit	Location	Age (Ma)	Method	Reference
Lower unit (Norite)	North Range	1849.6 +3.4/-3	Zircon U-Pb (ID-TIMS)	Krogh et al., (1982)
Lower unit (Norite)	South Range	1849.4 + 1.9/ - 1.8	Zircon U-Pb (ID-TIMS)	Krogh et al., (1982)
Lower unit (Norite)	North Range	1848.9 + 4/- 2.7	Zircon U-Pb (ID-TIMS)	Krogh et al., (1984)
Lower unit (Norite)	North Range	1850 + 3.4/- 2.4	Zircon U-Pb (ID-TIMS)	Krogh et al., (1984)
Upper Unit (Granophyre)	North Range	1850.5 ± 3	Baddeleyite U-Pb (ID-TIMS)	Krogh et al., (1984)
Lower unit (Norite)	South Range	1849.7 ± 1.1	Zircon U-Pb (ID-TIMS)	Krogh et al., (1984)
Offset Dyke (Quartz-diorite)	Copper Cliff (South Range)	1849.8 ± 2	Zircon U-Pb (ID-TIMS)	Corfu and Lightfoot., (1996)
Offset Dyke (Quartz-diorite)	Foy (North Range)	1852 +4/-3	Zircon and Baddeleyite U-Pb (ID-TIMS)	Ostermann et al., (1996)
Sublayer (Norite)	Whistle (North Range)	1848.1 ± 1.8	Zircon and Baddeleyite (ID-TIMS)	Corfu and Lightfoot., (1996)
Sublayer (olivine melanorite)	Whistle (North Range)	1849.1 ± 1.1	Zircon and Baddeleyite (ID-TIMS)	Corfu and Lightfoot., (1996)
Sublayer (metapyroxenite)	Whistle (North Range)	1848.4 ± 1.4	Zircon U-Pb (ID-TIMS)	Corfu and Lightfoot., (1996)
Sublayer (melanorite)	Whistle (North Range)	1848.3 ± 1	Zircon U-Pb (ID-TIMS)	Corfu and Lightfoot., (1996)
Sublayer (melanorite)	Whistle (North Range)	1848.3 ± 1	Zircon and Baddeleyite (ID-TIMS)	Corfu and Lightfoot., (1996)
Sublayer (diabase)	Whistle (North Range)	1848.7 ± 1.1	Zircon U-Pb (ID-TIMS)	Corfu and Lightfoot., (1996)
Sudbury basin (Onaping fm.)	Joe Lake (North Range)	1848.4 +3.8/-1.8	hydrothermal titanite (U-Pb ID-TIMS)	Ames et al., (1998)
Lower unit (Norite)	North Range	1849.53 ± 0.21	Zircon U-Pb (TE-TIMS)	Davis., (2008)
Lower unit (Norite)	South Range	1849.11 ± 0.19	Zircon U-Pb (TE-TIMS)	Davis., (2008)
Lower unit (Norite)	South Range	1849.7 ± 0.2	Zircon U-Pb (TE and ID-TIMS)	Bleeker et al., (2015)
Offset Dyke (Quartz-diorite)	North Range	1849.1 ± 0.9	Baddeleyite U-Pb (ID-TIMS)	Bleeker et al., (2015)
Offset Dyke (Quartz-diorite)	North Range	1848.5 ± 0.8	Baddeleyite U-Pb (ID-TIMS)	Bleeker et al., (2015)
Sudbury metabreccia	South Range	1851 ± 12	shocked titanite (SIMS)	Papapavlou et al., (In prep, this study)

Chapter 3. Methodology

3.1. Electron Probe Microanalysis (EPMA)

Electron probe X-ray microanalysis is a high spatial resolution quantitative technique for the chemical microanalysis of solid materials. The bombardment of a solid material with a focused beam of electrons results in the emission by inelastic scattering of characteristic (i.e. element specific) X-rays. The discrimination of the emitted X-rays can be achieved either by their energy (energy dispersive X-ray spectroscopy) or their wavelength (wavelength dispersive x-ray spectroscopy). In the former method, all the emitted X-rays are measured simultaneously yielding a spectrum with the number of X-ray counts versus energy. The energy dispersive spectrometry is used mostly for the qualitative chemical analysis of materials. However, by following identical measurement protocols between standards and unknowns (i.e. *k* ratio protocol) accuracy and precision levels, equivalent with that of the more precise and sensitive wavelength dispersive x-ray spectroscopy (Newbury and Ritchie., 2013), can be achieved for major elements.

The foundation of quantitative chemical analysis is based on the wavelength dispersive X-ray spectroscopy (WDS). Every electron microprobe has three to five spectrometers with one to four crystals of natural or polysynthetic materials, with known interplanar spacing d, that operate as diffractometers. The diffraction of X-rays of a single wavelength is achieved when the bragg equation is satisfied ($n\lambda = 2d\sin\theta$ where n = order of reflection, λ = wavelength, d = interplanar spacing, and θ = incidence angle). For the analysis of a different element (i.e. different wavelength), the crystals are mechanically tuned relative to the point source of X-rays, resulting in the change of the incidence angle θ, and the diffraction of X-rays with different wavelength in the detector (Reed., 2005).

In the present study, electron probe microanalysis (EPMA) was used for the collection major, minor and trace element data from rock-forming and accessory silicates (i.e. amphibole, biotite, epidote, apatite, titanite). The analytical details and measurement protocols of data collection are provided in the following section.

3.1.1 Analytical protocols (Electron Probe Microanalysis)

The mineral chemistry data of the present study were collected during two analytical sessions using a Cameca SX-100 electron microprobe at the University of Bristol (UK). The instrument is equipped with five wavelength dispersive spectrometers with the setup shown in **Table 3.1**. The analysed samples were carbon-coated polished thin and thick sections. The calibration standards that were used are the: Amelia albite (Na and Si), Eifel sanidine (Al and K), St. Johns olivine (Mg), wollastonite (Ca), ilmenite (Ti), Cr_2O_3 (Cr), Manganese metal (Mn), Nickel metal (Ni), MgF_2 (F), $NaCl_2$ (Cl). The calibration involved measuring on the peak for 10 seconds for Na, Mg, Si, K, Ca, Ti, Fe and Ni, 20 seconds for Al and Mn, 30 seconds for for Cl, and 60 seconds for Cr and F. The background offsets were ± 800 for most of the elements and ± 1000 for Fe and Ni, with background measurement times from 5 to 30 seconds. Accelerating voltage of 20 kV with beam current of 10 nA and spot size of 10µm was used in all the analyses of the rock-forming silicates. The accuracy and precision of the analyses were monitored by analysing standards before each analytical session and comparing with long-term datasets.

Table 3.1. Spectrometer (EPMA) setting for collection of mineral-chemical data from silicates

Spectrometer	Crystal	Element
Spectrometer 1	LPET	K (Ka, 3.313), Cr (Ka, 5.414)
Spectrometer 2	TAP	Na (Ka, 1.040), F (Ka, 0.676)
Spectrometer 3	LPET	Ca (Ka, 3.691), Ti (Ka, 4.510), Cl (Ka, 2.622)
Spectrometer 4	TAP	Si (Ka, 1.739), Al (Ka, 1.486), Mg (Ka, 1.253)
Spectrometer 5	LLIF	Fe (Ka, 6.403), Mn (Ka, 5.898), Ni (Ka, 7.478)

Table 3.2. Spectrometer (EPMA) setting for the collection of mineral-chemical data from apatite

Spectrometer	Crystal	Element
Spectrometer 1	LPET	P (Ka, 2.013), S (Ka, 2.307)
Spectrometer 2	PC1	F (Ka, 0.676)
Spectrometer 3	LPET	Ca (Ka, 3.691), Cl (Ka, 2.622), Th (Ma, 2.996), U (Mb, 3.337)
Spectrometer 4	TAP	Na (Ka, 1.040), Al (Ka, 1.486), Si (Ka, 1.739)
Spectrometer 5	LLIF	Ce (La, 4.840), La (La, 4.650)

Apatite is a mineral susceptible to beam damage, thus the adopted analytical protocol aimed to mitigate the beam damage for the high abundance elements (e.g. Ca, P) and those susceptible to damage (e.g. alkalis and halogens). Thus, for the analysis of apatite, were

chosen two sets of analytical conditions. A set of lower beam power conditions with 20 kV accelerating voltage, 10 nA beam current and 20 μm spot size and a set with 20 kV accelerating voltage, 40 nA beam current and 20μm spot size. The higher beam current conditions were used for trace and minor constituents in order to yield more precise quantitation. The setup of spectrometers that was used is shown in **Table 3.2**. The calibration standards that were used in the analyses of apatite were the: Durango apatite (F, P, Ca), Amelia albite (Na, Si), Eifel sanidine (Al), Ce-glass (Ce), $NaCl_2$ (Cl), $BaSO_4$ (S), La-glass (La), ThO_2 (Th) and UO_2 (U). The calibration for the analysis of apatite involved measuring on the peak for 10 seconds for P, Ca, Th and U, 20 seconds for Na, Al, and Si, 30 seconds for La and S, 40 seconds for F and 60 seconds for Cl. The background offsets were ± 800 for the majority of the elements with background measurement times from 5 to 30 seconds.

3.2. Mass spectrometry techniques for U-Pb and trace element microanalysis

3.2.1 Laser Ablation - Inductively Coupled Plasma - Mass Spectrometry (LA-ICP-MS)

LA-ICP-MS is a solid state mass spectrometric technique that comprises three main parts: (a) a laser system for the in-situ sampling of solid materials, (b) the Inductively Coupled Plasma where the laser-generated particles are atomised, vaporised and ionized using a plasma formed by inductive heating of Ar gas in an electromagnetic field, and (c) a mass spectrometer that separates the ions based on their mass/charge ratio (Longerich., 2008). The laser systems that are suggested as optimal for the ablation of silicate minerals emit in the ultraviolet (100 - 400nm) and Vacuum ultraviolet (100 - 200nm) wavelengths (Sylvester and Jackson., 2016). Specifically, laser ablation using 213nm Nd:YAG and 193nm ArF excimer lasers generates aerosols that contain only a small fraction of large particles (diameter > 150nm) that is difficult to be vaporised in the ICP (Guillong and Gunther., 2002). In addition, lasers with wavelengths shorter than 213nm and shorter pulse duration (ns to fs), demonstrate stable transient signals, reduced time dependent elemental fractionation (i.e. non-stoichiometric ablation), and diminished thermal alteration of the samples (Guillong et al., 2003, Gunter and Hattendorf., 2005).

ICP-MS instruments consists of three basic components (a) the Ar plasma ion source, (b) an ion separator and (c) an ion detector. For most applications, the plasma operates at atmospheric pressure, temperature of ca. 8000K, and radiofrequency power of 1200 – 1300 W (Becker., 2007). In these conditions aerosol particles of the ablated material break down

into their atomic constituents and, depending on their first ionisation potential, are ionised. The ionization of argon plasma gas, at energy levels of 15.8ev (first ionization potential of argon), generates a mix of argon atoms, argon ions, and electrons producing an ICP plasma discharge that is adequate to ionize the majority of elements in the periodic table (Thomas, 2013). Elements with ionization potential less than about 8ev (e.g. Na, Mg, Fe, Ni, Cu, REE) are ionized with 100% yield whereas in elements with increasing ionization potential the ionization efficiency is decreasing (Taylor., 2001).

Different kinds of ion separators can communicate with an ICP ion source, such as a quadrupole mass analyser, Time-of-Flight (ToF) mass analyser, magnetic sector field or a combination of magnetic and electric sector field instruments. The ion separator operates at high vacuum conditions (ca. 10^{-6} Torr) and its main function is to separate the analyte ions according to their mass/charge ratios after their passage from an ion optics system. The most common ion separation device, and the one that has been used for the collection of isotopic and trace element data in this study, is the quadrupole mass filter. The quadrupole mass filter consists of four parallel metallic rods of cylindrical or hyperbolic geometry that operate as electrodes. In the oppositely located pairs of electrodes, a direct (DC) and an alternating (AC) current field is applied. By varying the AC/DC ratio, ions of the certain mass of choice accelerate along the space between the four rods and reach the detector. The rest of the ions follow an unstable trajectory and collide with the rods (Becker., 2007).

The ion detector converts the accelerated ion beam from the ion separators into electrical pulses in the range of 10^{-8} to 10^{-9} A (Becker., 2007). Ion detectors operate at ultra-high vacuum conditions and the most popular are Faraday detectors for high ion count rates, and electron multipliers for lower count rates. In order to increase the dynamic range of the instrument both detectors can be used in conjunction. The most popular ion detectors that are used extensively with ICP mass spectrometers are the secondary electron multipliers. The basic principle of secondary electron multipliers is the production (i.e. up to 10^8 electrons for each ion) and amplification of secondary electrons when a charged particle is impacting with one of the dynode plates of the detector. A significant advantage of this approach is that they can operate in dual detector mode (Longerich., 2008). That means that secondary electron multipliers can operate in analogue mode for high ion beam currents and in pulse counting mode for lower beam currents. This dual mode can increase the dynamic range of a mass

spectrometer up to nine orders of magnitude (i.e. ppt to ppm). However, the most common approach is to determine high and low ion counts in a single scan. This is achieved by measuring the lower counts in pulse counting mode and the higher counts in analog mode. For analytes with concentration levels between the two modes, a cross-calibration is performed (Thomas, 2013).

In the present study, LA-ICP-MS was used chiefly for the collection of U-Th-Pb isotopic and trace element data from rock-forming silicates and accessory phases. Analytical details and protocols for each part of data collection are described in the sections 1.3 and 1.4.

3.2.2 Secondary Ion Mass Spectrometry (SIMS)

SIMS is a high spatial resolution microanalytical technique that is based on the generation of secondary ions when solid materials are bombarded with a high energy primary ion beam (1keV to 20 keV). The ion beam, under high to ultra-high vacuum conditions, penetrates several atomic layers (~10nm) and induce an atom-scale structural disruption in the targeting material (Stern., 2009). The sputtered (i.e. ejected) atomic and molecular species that are ionized are analysed to a mass spectrometer according to their mass/charge ratios. SIMS has been used widely for the isotopic microanalysis of radiogenic (e.g. Al – Mg, Mn – Cr, Fe – Ni, U – Pb, Th – Pb, U – Th, Hf - W) and stable isotopes (e.g H, Li, B, C, N, O, Si, S, Cl, Ca, Cu). SIMS was used in this study (Chapter 6), because it provided: (a) accurate and precise U-Pb isotopic data of specific titanite microstructural domains with spot size of 15-20µm and (b) common lead corrected U-Pb isotopic data by measuring the ^{204}Pb mass. With LA-ICP-MS ^{204}Hg interferes with ^{204}Pb and swamps the signal making the common lead correction problematic.

3.2.3. Analytical protocols and sample preparation (U-Pb geochronology)

U-Pb isotopic analyses of the accessory mineral titanite ($CaTiSiO_5$) in this study were undertaken in polished thin sections, thick sections, and grain mounts. The titanite grains in the grain mounts were separated using standard heavy liquid and magnetic separation methods. Before each analytical session, the specimens were carbon-coated and imaged using scanning electron microscopy (SEM) for the targeting and characterisation of accessory phases. After the imaging the specimens were re-polished using 0.3 micron alumina slurry and then wiped clean using methanol. After the cleaning, the specimens were inspected in

reflected light in order to ensure that carbon flakes are not remaining above the selected targets. Before the insertion of the specimens into the chamber for LA-ICP-MS analysis, they were cleaned again using methanol and any dust from their surface was removed using nitrogen gas. A reflected light map of the whole specimen was prepared using the reflected light optics of the laser system, although a few were separately collected using standard optical microscopy. The reflected light maps were loaded on the software Geostar v.8.41 where every analytical point was preloaded. For every preloaded analytical point the spot size and in some cases information about the energy of ablation and/or frequency was noted.

The U-Pb isotopic data were collected in four analytical sessions. Three of the sessions took place at the University of Portsmouth using the technique of LA-ICP-MS, and the fourth at the Ion Microprobe Facility (University of Edinburgh, UK). LA-ICP-MS was used because it provided the capability to date *in-situ* geochemically and microstructurally characterised accessory minerals, the latter was crucial in order to apply a petrochronological approach in this study. Moreover, the precision levels achieved with LA-ICP-MS were adequate in order to resolve the timing of the different geological events. Two of the LA-ICP-MS sessions were performed using an ASI RESOlution 193 nm ArF excimer laser coupled to a quadrupole Agilent 7500cs ICP-MS, whereas the third using the same laser system attached to a higher-sensitivity PlasmaQuant Elite quadrupole ICP-MS that was acquired by the University of Portsmouth during this project. A standard approach to the tuning of the instrument was undertaken in all of the LA-ICP-MS sessions, by monitoring the following masses or isotopic ratios: ^{238}U, ^{235}U, ^{232}Th, ^{208}Pb, ^{207}Pb, ^{206}Pb, ^{204}Pb, ^{202}Hg, ^{43}Ca, ^{23}Na, $^{238}U/^{232}Th$, and $^{238}U^{16}O^{+}/^{232}Th$. The highest sensitivity levels were recorded with U/Th ratios of ca. 1 and UO/U < 0.2%.

All the LA-ICP-MS U-Pb titanite data of the unknowns are presented in Terra – Wasserburg space uncorrected for common lead. Any common lead correction was avoided because of the isobaric interference of ^{204}Hg on ^{204}Pb, which dominates the common lead budget. In the first and second session, the U-Pb isotopic data were collected in static ablation mode using spotsize between 20 and 30µm. The data were collected with a fluence (energy density) of 2 – 3 J/cm^2 and frequency (repetition rate) of 2 Hz. The dwell times (i.e. time interval that integrates the signal of an individual mass) for the analysed masses was 0.02 s, apart from ^{235}U that was 0.03sec in order to maximize detection limits for the this less

abundant uranium isotope. The acquisition of the data comprised 20 seconds of gas blank, 40 seconds of ablation, and 30 seconds of washout time.

The correction of instrument-induced mass bias was performed by sample-standard bracketing using the matrix-matched Khan titanite (ID-TIMS age of 522.2 ± 2.2 Ma) (Heaman., 2009) in all sessions. For quality control, the secondary reference materials that were used in the first session are the Bear Lake Ridge titanite (ID-TIMS age of 1047.1 ± 0.4 Ma) (Aleinikoff et al., 2007) and Fish Canyon Tuff titanite (ID-TIMS age of 28.40 ± 0.02 Ma) (Schmitz and Bowring., 2001). The Fish Canyon Tuff titanite yielded a regressed lower intercept of 23.2 ± 6.3 Ma (2σ, n = 36, MSWD = 3.9) anchored to a $^{207}Pb/^{206}Pb$ isotopic composition of 0.84 ± 0.05, which is the lead isotopic composition for that age based on the crustal lead evolution model of Stacey and Kramers., (1975) (**Figure 1 left**). The Bear Lake Ridge titanite yielded a regressed lower intercept age of 1044 ± 23 Ma (2σ, n = 28, MSWD = 7.1) anchored to a $^{207}Pb/^{206}Pb$ isotopic composition of 0.912 ± 0.05 (model lead isotopic composition for this age) (**Figure 1 right**). For both secondary standards, the lower intercept ages agree within uncertainty with the precise ID-TIMS ages.

The raw isotopic data were processed using the software Iolite (Paton et al., 2011). In the processing of data using Iolite the first step is to select the baseline signal that will be subtracted and will yield the raw (measured) signal. After that, is selected the signal that corresponds to the primary reference material (i.e. Khan titanite in this case) and then it follows the selection of signal on the unknowns (i.e. secondary standards and sample unknowns). The next step is the application of a down-hole fractionation correction model to to the time resolved signal of the unknowns. In this study, was applied an exponential correction model to the time-resoled data. After the down hole fractionation correction, the ratios are adjusted to the accepted values of the primary reference material. This is achieved with a spline interpolation of a correction factor through the analyses. The propagated uncertainty on the analyses is estimated based on the interspersed analyses of the primary standard which in this study is the Khan titanite. The standard file with the chemical and isotopic composition of the primary standard (Khan titanite) was created based on the published compositional and isotopic data of Heaman., 2009 (Table 3.3).

Table 3.3. Isotopic and chemical data that were used for the creation of a standard file in Iolite for the primary reference material (Khan titanite)

Parameter	Units	Value	Uncertainty
U	ppm	584	
Th	ppm	473	
Pb	ppm	57	
Th/U	-	0.81	0.05
$^{206}Pb/^{238}U$	-	0.8432	0.0008
$^{207}Pb/^{235}U$	-	0.6652	0.0008
$^{207}Pb/^{206}Pb$	-	0.0578	0.000073
$^{207}Pb/^{206}Pb$ initial	-	0.8714	-
$^{208}Pb/^{232}Th$	-	0.0261	-

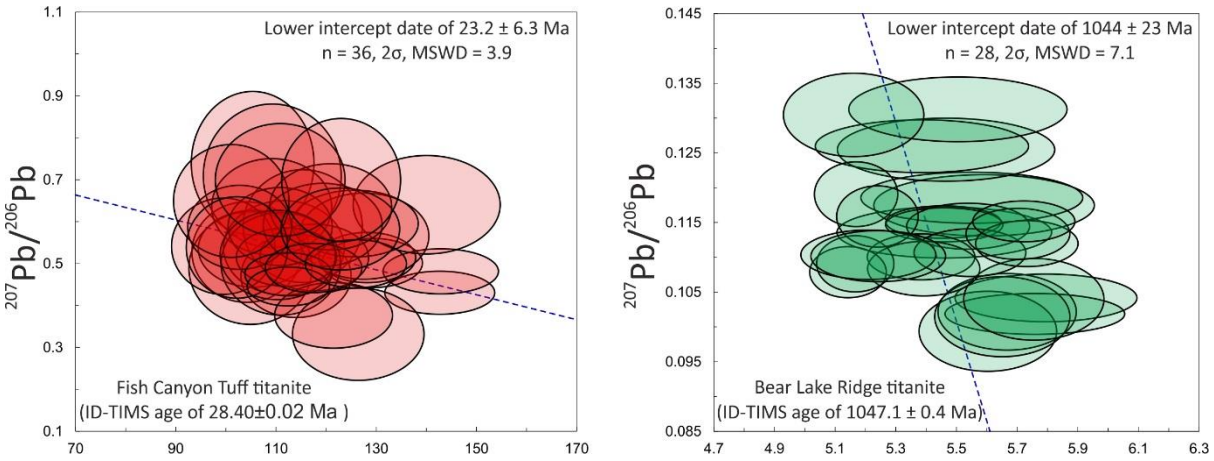

Figure 1. Terra-Wasserburg diagrams with U-Pb isotopic data of the secondary reference materials, Fish Canyon Tuff and Bear Lake Ridge titanite, that were included in the first analytical session

In the first session, the precision and the accuracy on the Fish Canyon Tuff titanite are very poor and are estimated at 27.3 % and 18.3 %, respectively. In contrast, analyses on the Bear Lake Ridge titanite grains show significantly better precision and accuracy levels, estimated at 2.2 % and 0.3 %, respectively.

In the second session, the U-Pb isotopic data were collected in static ablation mode, with a fluence of 2 J/cm^2 and frequency of 2Hz. The secondary standards that were used in this session are the Fish Canyon Tuff titanite, and the Sylvester Pluton titanite (ID-TIMS age of ~262 Ma, C.Storey pers. com). The $^{207}Pb/^{206}Pb$ anchored isochron for the Fish Canyon Tuff titanite yielded a lower intercept age 24 ± 7.3 Ma (2σ, n = 23, MSWD = 3.2) (**Figure 2 left**). The

non-anchored isochron for the Sylvester pluton titanite grains yielded a lower intercept age of 257 ± 13 Ma (2σ, n = 8, MSWD = 0.42) (**Figure 2 right**). In the second session, the precision and accuracy levels of the Fish Canyon Tuff titanite remain poor and are estimated at 30 % and 15 %, respectively. The analyses in Sylvester Pluton titanite, show precision and accuracy levels at 5 % and 1.91 %, respectively.

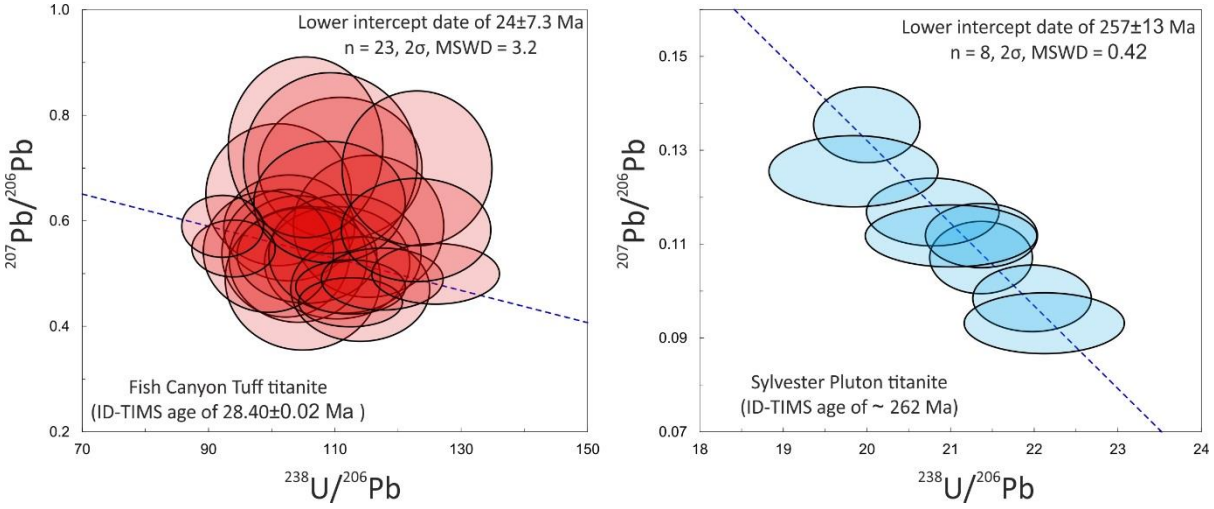

Figure 2. U-Pb isotopic data of the secondary reference materials, Fish Canyon Tuff and Sylvester pluton titanite, that were included in the second analytical session

In the third session, the U-Pb isotopic data were collected using a PlasmaQuant Elite ICP-MS (**please see Table 3.4 for tuning parameters**). The secondary standards that were used are the Fish Canyon Tuff titanite, the Sylvester Pluton titanite, the Bear Lake Ridge titanite, and the MKED 1 titanite (ID-TIMS age of 1517.32 ± 0.32 Ma) (Spandler et al., 2016). The analyses on Sylvester pluton titanite yielded a lower intercept age of 262.8 ± 9.2 Ma (2σ, n = 11, MSWD = 0.21) (**Figure 3 upper right**), non-anchored to an initial $^{207}Pb/^{206}Pb$ isotopic ratio, with precision of 3.5 % and accuracy of 0.3 %. The Fish Canyon Tuff titanite yielded a regressed lower intercept age of 27.5 ± 9.2 Ma (2σ, n = 7, MSWD = 2.8) (**Figure 3 upper left**), anchored to a model lead isotopic composition (0.84 ± 0.05), with estimated precision of 33 % and accuracy of 3.1 %. The Bear Lake Ridge titanite yielded a lower intercept age of 1051 ± 18 Ma (2σ, n = 12, MSWD = 12) (**Figure 3 lower left**), anchored to a model lead isotopic composition for this age (0.912 ± 0.05), with estimated precision of 1.71 % and accuracy of 0.37 %. The MKED1 standard is low in common lead components and the collected data were

plotted in Wetherill - Concordia diagram ($^{206}Pb/^{238}U$ – $^{207}Pb/^{235}U$). Twenty analyses yielded an age of 1524 ± 35 Ma (2σ, n = 20, MSWD = 0.61) (**Figure 3 lower right**) with precision of 2.3 % and accuracy of 0.44 %.

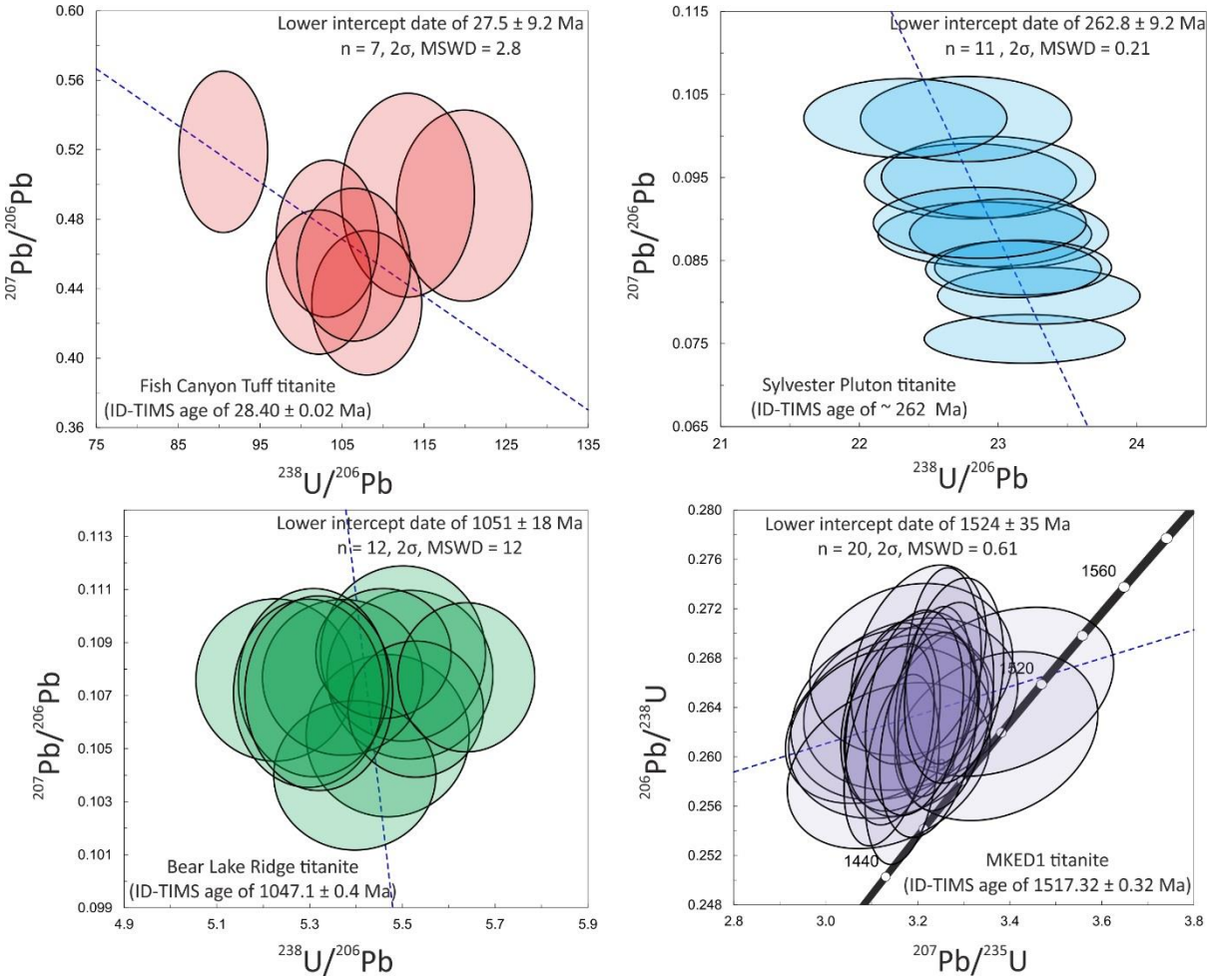

Figure 3. U-Pb isotopic data in Terra- Wasserburg and Wetherill-Concordia diagrams of the secondary reference material that were included in the third analytical session

The fourth analytical session took place at the Ion Microprobe Facility (University of Edinburgh, UK) using a Cameca ims-4f ion microprobe. The U-Pb isotopic data were collected using an O^{2-} ion beam inclined relative to the specimen with a spotsize of approximately 20µm. The primary beam current during the collection of the data was 6nA and the impact energy 22keV. The secondary standards that were used in this session were the MKED 1 titanite and the Ontario-2 titanite (ID-TIMS age of 1053.5 ± 1.3) (Spencer et al., 2013). The MKED1 titanite yielded an upper intercept in Wetherill-Concordia diagram of 1518 ± 11 Ma (2σ, n = 6, MSWD = 1.16) (**Figure 3.4**). The precision in the MKED1 analyses is estimated at 0.72 % and the accuracy 0.04 %. The Ontario – 2 standard yielded a weighted mean

$^{207}Pb/^{206}Pb$ age of 1057 ± 67 Ma (2σ, n = 5, MSWD = 6.5) with estimated precision of 6.34 % and accuracy of 0.35 %.

Table 3. LA-ICP-MS tuning settings in the third session of U-Pb data collection

Flow parameters (L/min)	
Plasma flow	10
Auxiliary flow	1.65
Sheath Gas	0
Nebulizer flow	0.87
Torch alignment (mm)	
Sampling depth	7
Other	
RF Power (kW)	1.3
Pump rate	0
Stabilization delay (s)	0
Ion optics (volts)	
First extraction lens	-150
Second extraction lens	-900
Third extraction lens	-580
Corner lens	-580
Mirror lens left	72
Mirror lens right	47
Mirror lens bottom	64
Entrance Lens	3
Fringe Bias	-4
Entrance Plate	-80
Pole bias	0
CRI (mL/min)	
Skimer Gas source	OFF
Skimmer Flow	0
Nitrox200	
Flow (mL/min)	0

Table 3.5 LA-ICP-MS tuning settings of trace element data collection

Plasma parameters	
RF power	1200W
Sampling depth	3mm
Torch (Horizontal)	-0.3mm
Torch (Verical)	0.1mm
Carrier gas	0.73 L/min
Makeup Gas	0 L/min
Nebulizer pump	0 rps
S/C temp	15 degrees
Ion Lenses	
Extract 1	4.4V
Extract 2	1V
omega bias	-50 V
omega lens	11.8 V
Cell entrance	-50 V
QP focus	8 V
Cell exit	-70 V
Q-pole parameters	
AMU Gain	123
AMU Offset	125
Axis Gain	1.0001
Axis offset	0.02
QP Bias	-2.7
Octpole parameters	
Octop RF	180V
Octop Bias	-3V
Reaction Cell	
Reaction Mode	Off
Detector parameters	
Discriminator	8mV
Analog HV	1770V
Pulse HV	1290v

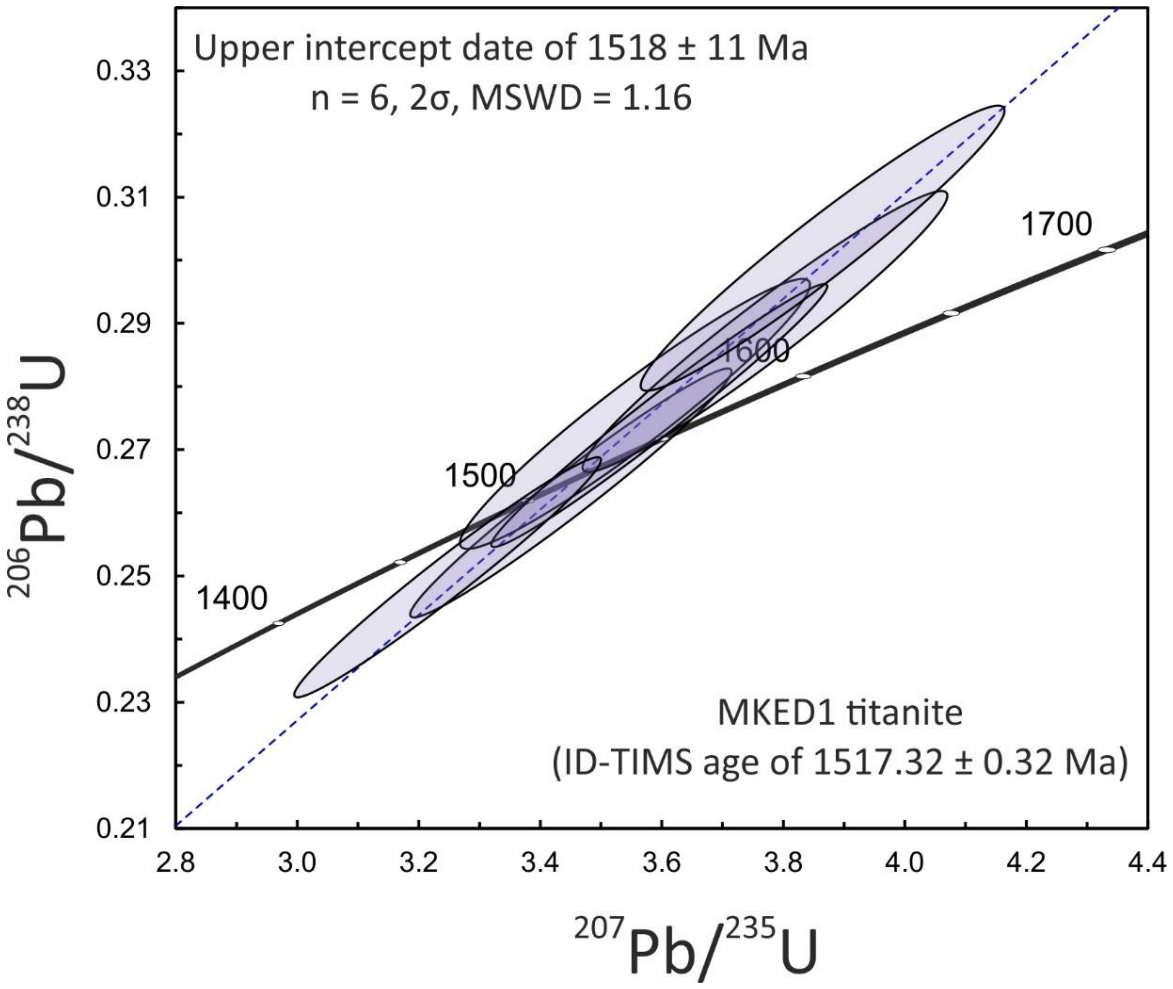

Figure 4. Wetherill-Concordia diagram of the U-Pb isotopic data that were collected in the fourth analytical session (SIMS)

3.2.4. Analytical protocols for trace element microanalysis by LA-ICP-MS

Trace element data in this study were collected for the following minerals: titanite, apatite, epidote, amphibole, and biotite. All the data were collected at the University of Portsmouth using an ASI RESOlution 193 nm ArF excimer laser coupled to a quadrupole Agilent 7500cs ICP-MS. The following isotopes were analysed ^{27}Al, ^{29}Si, ^{31}P, ^{43}Ca, ^{45}Sc, ^{49}Ti, ^{51}V, ^{53}Cr, ^{55}Mn, ^{59}Co, ^{60}Ni, ^{66}Zn, ^{69}Ga, ^{72}Ge, ^{85}Rb, ^{88}Sr, ^{89}Y, ^{90}Zr, ^{95}Mo, ^{118}Sn, ^{121}Sb, ^{137}Ba, ^{139}La, ^{140}Ce, ^{141}Pr, ^{146}Nd, ^{147}Sm, ^{151}Eu, ^{157}Gd, ^{159}Tb, ^{163}Dy, ^{165}Ho, ^{167}Er, ^{169}Tm, ^{173}Yb, ^{175}Lu, ^{177}Hf, ^{208}Pb, ^{232}Th, and ^{238}U. The following masses and isotopic ratios were monitored during the tuning of the instrument: ^{43}Ca, ^{202}Hg, ^{204}Hg, ^{51}V, ^{89}Y, ^{208}Pb, ^{232}Th, ^{235}U, ^{238}U, ^{238}U/^{232}Th, ^{238}U^{16}O^{+}/^{232}Th, ^{140}Ce, and ^{177}Hf.The highest sensitivity levels in the masses of interest was recorded with Th/U ~ 1 and UO/O ~0.12. For the collection of the data was used as primary reference material the NIST 612 silica glass (Jochum et al., 2011). The analytical data were collected using a fluence

of 4.5 J/cm^2, repetition rate of 4Hz and spotsize between 15 and 40μm (**please see Table 3.5 for tuning parameters**). For quality control, a series of secondary standards were analysed, including the Max Planck Institute silica glasses (MPIDING GOR128-G and MPIDING T1G) (Jochum et al., 2006), the Khan titanite (Heaman., 2009), and the Durango apatite (Marks et al., 2012). The internal standard that was used in order to compute the actual concentrations of the unknown analytes are the stoichiometric CaO concentration for titanite and apatite (28.6 Wt% and 55 Wt%, respectively) and the TiO_2 concentration for the major silicate minerals (biotite, epidote, amphibole). The TiO_2 concentration was measured at the analytical sites of interest with electron microprobe (EPMA).

The raw signals of the trace element data were reduced using the software Sills (Guillong et al., 2008). During the processing, the first step was to load the standard reference material (e.g. NIST glasses). After that is performed a spike elimination, to correct for potential outliers (e.g. inclusions), and then are selected integration intervals in the background and the unknown sample signals. In every run, three analyses of standard reference materials were performed at the start and three at the end. The next step is to load the unknowns, where again are selected first the background interval and then up to three different intervals of the sample's signal. The next main step is to assign, in the calculation settings, the concentration value of a chosen internal standard for the normalization of the different analytes. As a final step, the instrumental drift is corrected with an element that shows minimum drift in relative sensitivity (<5%).

The quantification of a trace element i is based on the following equation (Halter et al., 2002):

$$Ci\ (unk) = \frac{Ci\ (std) \times Ii\ (unk)}{Ii\ (std) \times RSF} \quad \text{Eq. (1a)}$$

Where $\mathrm{Ci\ (std)}$ is the concentration (ppm) of the i element in the standard, $\mathrm{Ii\ (unk)}$ is the intensity (cps) of the i element in the unknown sample, $\mathrm{Ii\ (std)}$ is the intensity of the i element in the standard, and RSF is the relative sensitivity factor that is given by the following equation:

$$RSF = \frac{Cis\ (std) \times Iis\ (unk)}{Iis\ (std) \times Cis\ (unk)} \quad \text{Eq. (1b)}$$

Where Cis (std) is the concentration of the internal standard in the sample, Iis (unk) is the intensity of the internal standard in the unknown sample, Iis (std) is the intensity of the internal standard in the standard reference material and Cis (unk) is the concentration of the internal standard in the unknown sample. From the equation 1a is evident that a concentration of a trace element can be determined as a function of a relative sensitivity factor. The relative sensitivity factor (Equation 1b) describes the ratio of sensitivities (cps/ppm), and is identical between the standard and the unknown for different elements. Thus, by estimating the concentration of an internal standard in the unknowns (e.g. Ca) by stoichiometry or microanalytical methods (e.g. EPMA), the concentration of different elements can be quantified. It is important to stress that the RSF is identical for every element in one analysis (Halter et al., 2002).

The limit of detection of an element i is given by the following expression:

$$LODi\ (unk) = 3\sigma i\ (Bkg) \sqrt{\frac{1}{N(Bkg)} + \frac{1}{N(unk)}} \times \frac{1}{RSF} \times \frac{Ci\ (std)}{Ii\ (std)}$$

Where σi (Bkg) is the uncertainty in the background in cps; N (Bkg) and N(unk) are the number of detector cycles in the background and sample integration windows (Pettke et al., 2012).

In the analyses of Khan titanite, the accuracy is within 10 %, for most of the elements, relative to the concentration values of Heaman., (2009), and the precision in the elements of interest (REE, Rare Earth Elements) is approximately 2 % (RSD %) (**Figure 5 and 6**). In the analyses of the MPIDING GOR128 glass, the precision up to the element with mass 66 (^{66}Zn) is approximately 1.5 %. For the rest of the element the precision deteriorates and can be up to 20 % (e.g.^{139}La) (**Figure 7**). In the MPIDING GOR128 is observed that the accuracy is poor for elements that belong to the transition metals (Ni, Cu, Zn) and deviate up to 30 % relative to the reference values (**Figure 8**). In comparison, data from the MPIDING T1G silica glass in

the same session show that the precision for most analytes is 1 – 5 % and the accuracy within 10 % relative to the published reference values (**Figure 9**).

Deviations from the ±10 % accuracy limit are observed in ^{63}Cu, ^{85}Rb and ^{95}Mo, ^{118}Sn, ^{121}Sb and ^{197}Au and in some of the heavy rare earth elements (Khan titanite). This deviation could be attributed: (a) to the presence of inclusions within the analytical volume and (b) the comparison with concentration values (e.g. Khan titanite data), that are not ubiquitously considered as accurate and precise.

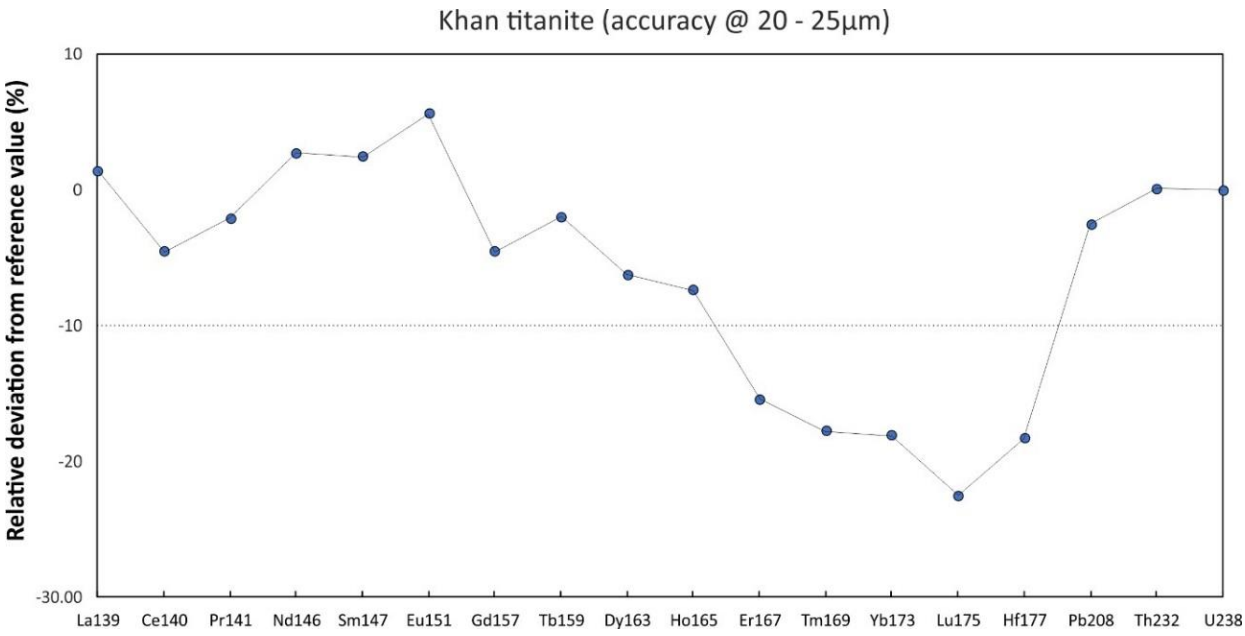

Figure 5. Plot that shows the deviations in accuracy in the trace element concentration of Khan titanite

3.3. Scanning electron microscopy (SEM)-based techniques

3.3.1 Electron microscopy (SEM/BSE)

The scanning electron microscopy is based on the interaction of a focused electron beam with solid materials using a scanning electron microscope (SEM). A SEM consists of the following components: an electron source, lenses for focusing the electron beam, instruments for the sweeping of the electron beam on the specimen, electron detectors and an image-display system (Reed., 2005). Different kind of radiation products are produced by the electron beam-specimen interactions such as: (a) secondary electrons; these are electrons with energies below 50 eV that are emitted from the near surface parts of the specimen

(~10nm) and reveal topographic contrast information of the specimen, (b) backscatter electrons; that provide atomic number – sensitive compositional information and sample deeper parts of the specimen; (c) cathodoluminescence; that is emission of photons when electrons transfer from the valence to the conduction band, and (d) X-rays; that are produced as an excess form of energy when an electron jumps from the outer to the inner shell to fill an electron vacancy (Goodhew et al., 2001).

The imaging of silicate and accessory phases in this study took place using different SEM at the University of Portsmouth and the University of Western Ontario. These phases were imaged using backscatter electron microscopy (BSE), in high contrast – low brightness mode in order to resolve different growth or compositionally distinct domains. The majority of the BSE images were recorded using 15 - 20 kV voltage and ca. 1nA beam current.

3.3.2 Quantitative microstructural analysis (Electron Backscatter Diffraction; EBSD)

Electron Backscatter Diffraction (EBSD) is a SEM-based technique of orientation microscopy that is used for the quantitative microstructural characterisation of inorganic crystalline materials. Different microstructural variables can be quantified using this technique such as: grain size, grain boundary character (low angle versus high angle grain boundaries), crystallographic preferred orientation (texture), phase identity, recrystallized fraction, and orientation gradients inter alia. The technique of EBSD is based on the automated evaluation of the Backscatter Kikuchi Patterns (BKP) or Electron Backscatter Diffraction Patterns (EBSP).

The Backscatter Kikuchi Patterns are produced when a stationary electron beam impinges, at a small angle (~20°), the specimen surface. The backscattered electrons that satisfy the Bragg equation (**look also section 1, EPMA**) are diffracted from the lattice planes of crystalline materials and define bands (BKP) that are captured by a fluorescent phosphor screen (**Figure 11 and 12**). These bands are gnomonic projections of diffracted cones of electrons (Kossel cones), that correspond to the lattice planes {hkl}, with the centre of projection the point of electron beam impingement on the specimen (Randle, 2000). The BKP are unique for particular crystal structures and crystallographic orientations. Hence, comparing the interplanar angles and spacing of the BKP with theoretical crystallographic datasets (match units) is possible to index each BKP through an image processing algorithm, the Hough transform.

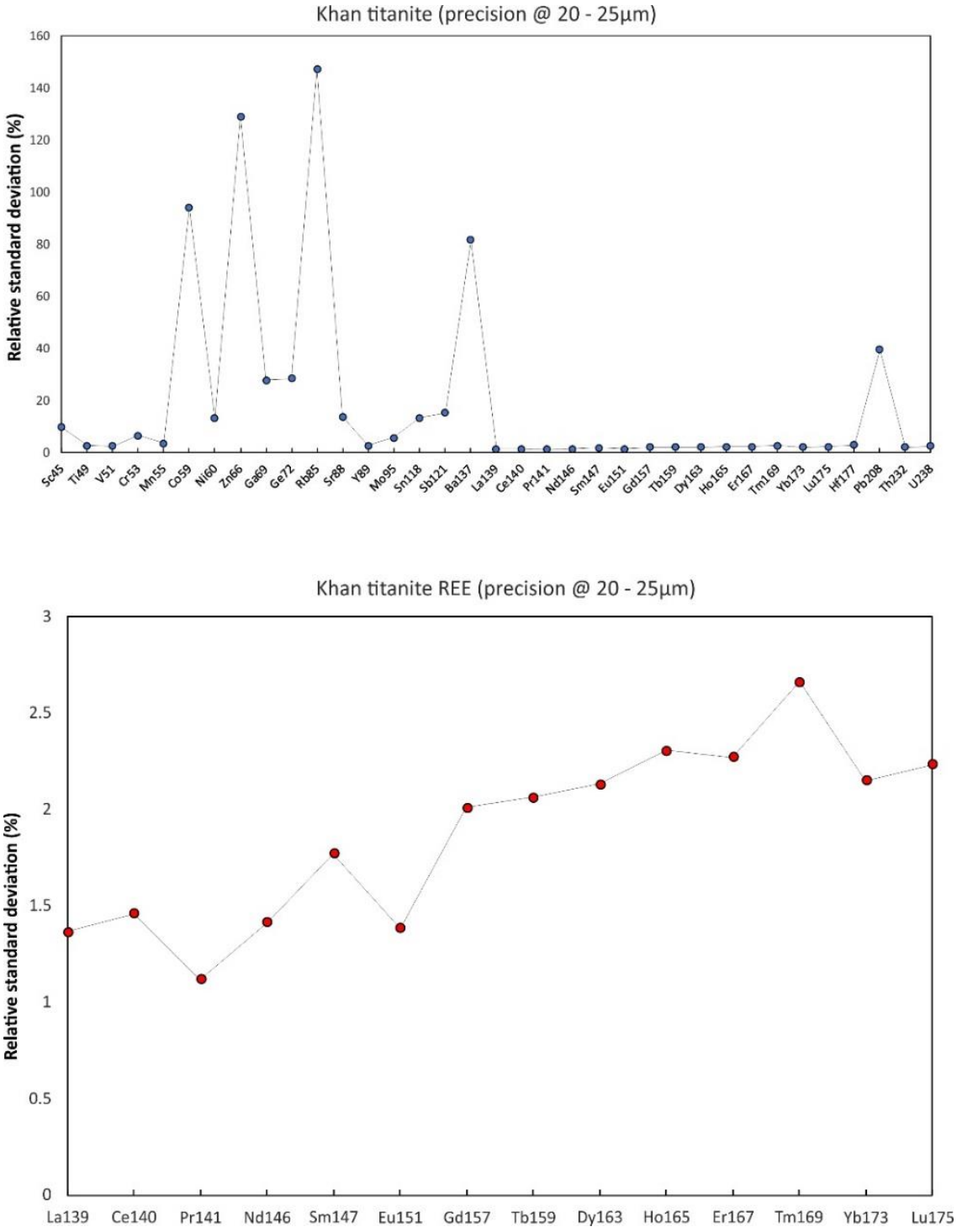

Figure 6. Plots that show the precision of Khan titanite in different trace elements with focus on the rare-earth elements

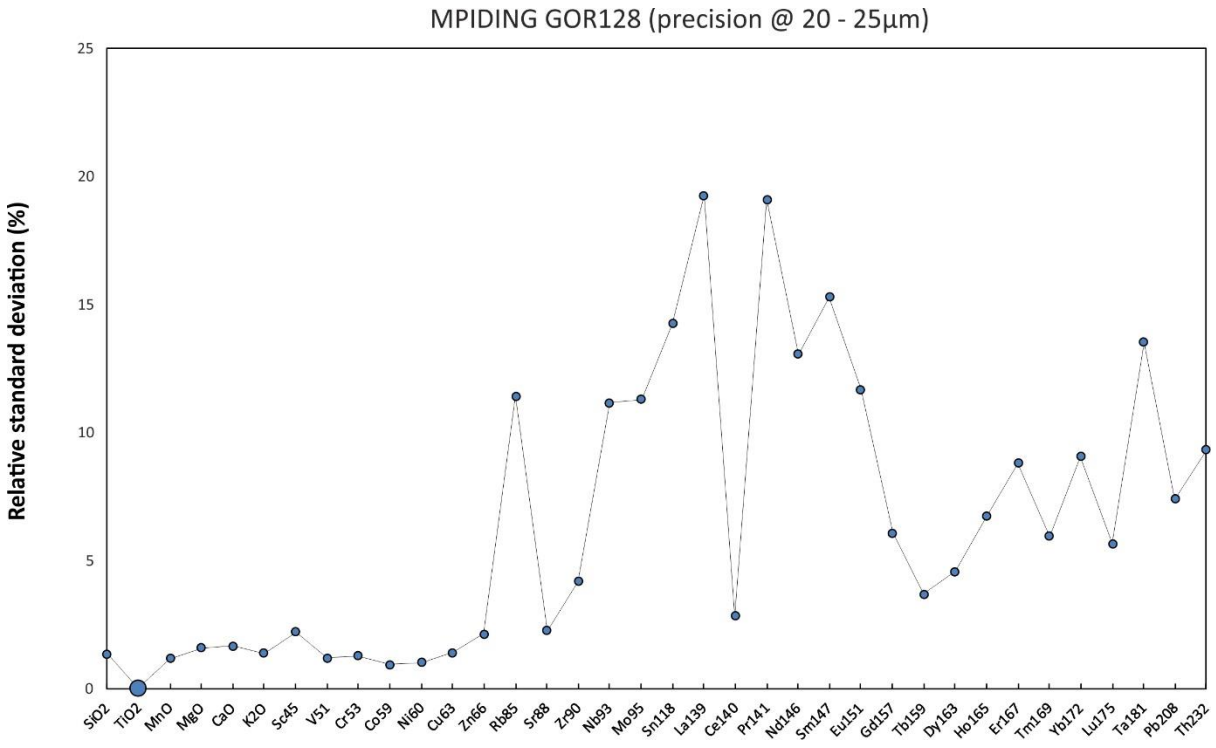

Figure 7. Plot that show the precision levels for different trace elements of the standard MPIDING GOR 128

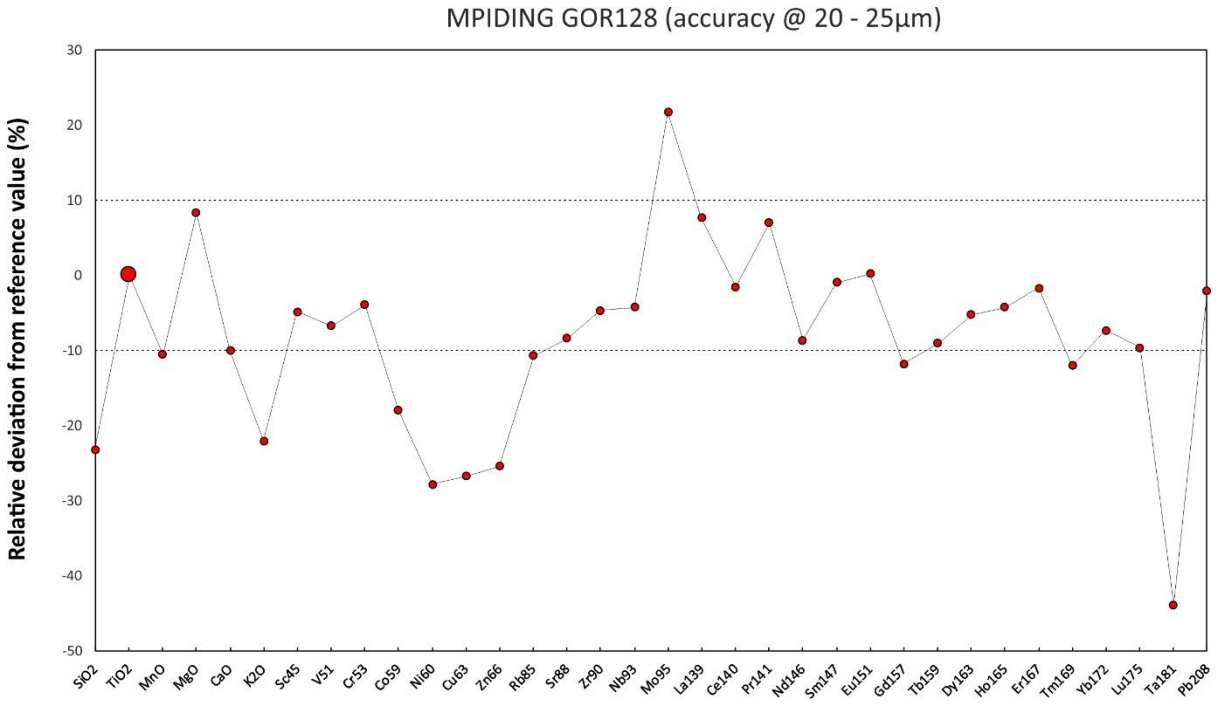

Figure 8. Plot that depicts the accuracy on the analysed trace elements of the standard MPIDING GOR128

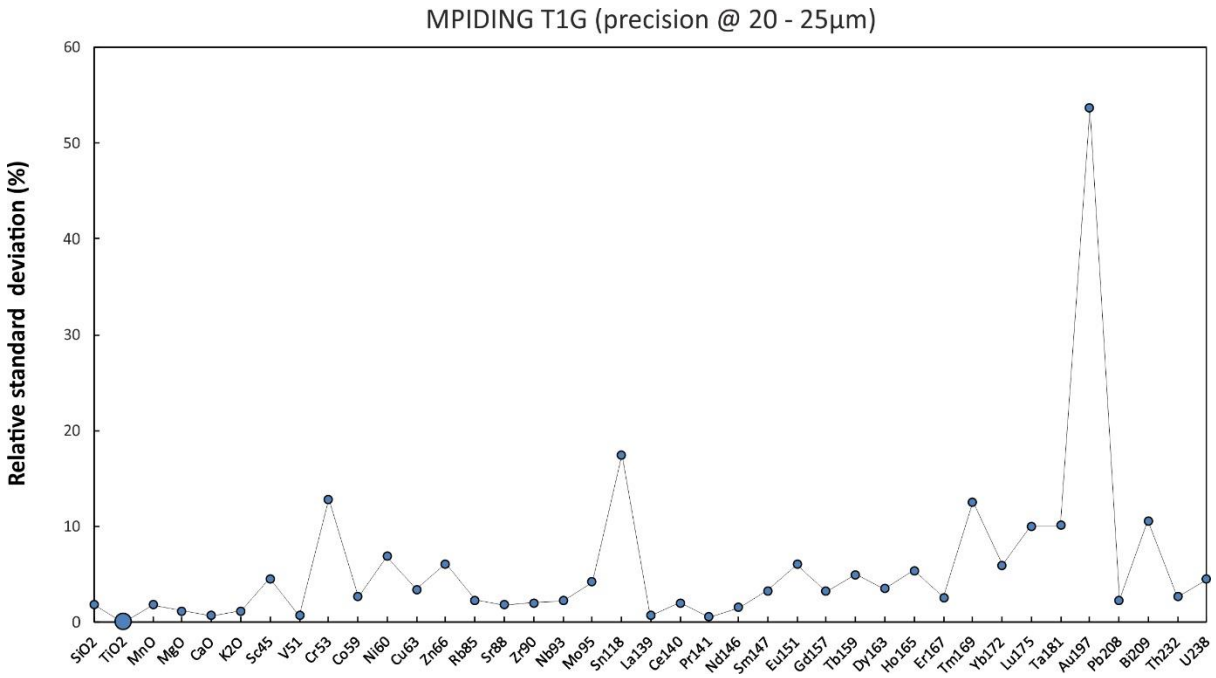

Figure 9. Plot that shows the precision on different trace elements of the MPIDING T1G standard

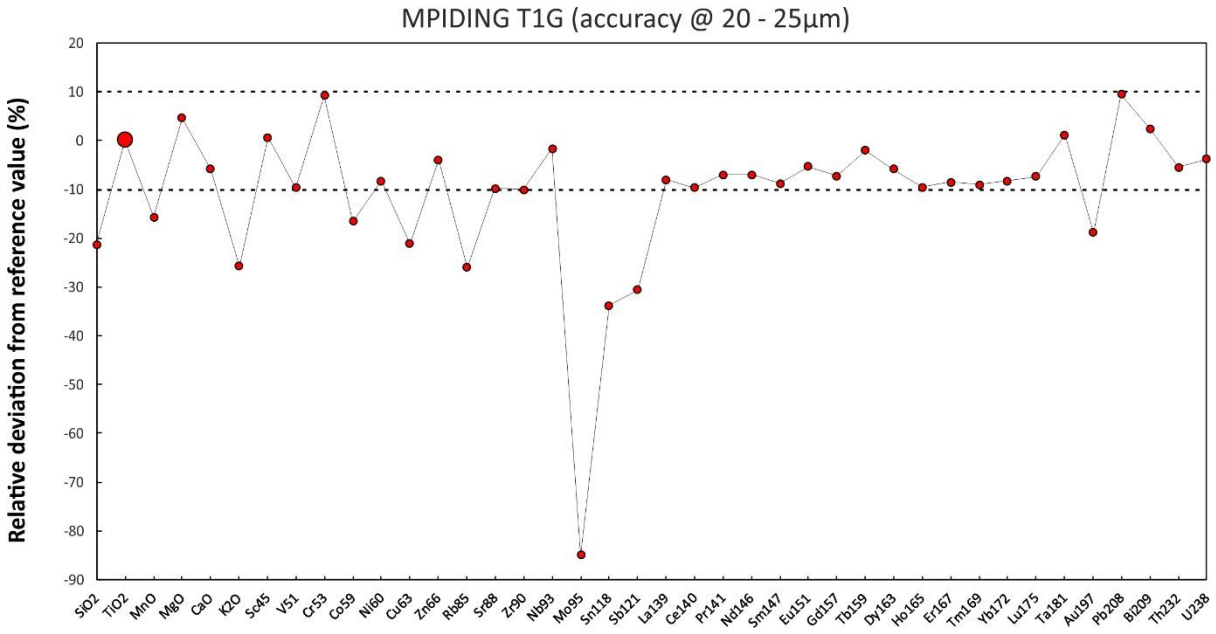

Figure 10. Plot that shows the accuracy levels in different trace elements of the MPIDING T1G secondary standard

The main orientation descriptors of crystallographic data are the: (a) pole figure, (b) inverse pole figure, (c) orientation matrix, (d) Miller-Bravais indices, (e) Euler angles, (f) angle/axis of rotation and (g) Rodrigues vector (Engler and Randle., 2010). In this study were used pole figures (**chapter 6**) and angle/axis of rotation (chapter xxx) as orientation descriptors of plastically deformed titanite and feldspar grains. In the produced EBSD maps can be overlaid different orientation microscopy components that entail different microstructural content. The three components that were chiefly used in this study are the band contrast, texture, and grain boundary component.

The band contrast component depicts in grey scale the quality of the diffraction pattern, with darker domains denoting lower quality patterns (e.g. grain boundaries) and vice versa. The factors that influence the quality of the pattern are: (a) the diffraction intensity of the phase, (b) dislocation density, and (c) crystallographic orientation (Maitland and Sitzman., 2006). The texture component colours each pixel for minimum misorientation relative to a user defined reference orientation (Reddy and Hough., 2013). The grain boundary component draws grain boundaries between map pixels when the interpixel orientation variation is higher than the user defined minimum (Maitland and Sitzman., 2006). In this study, grain boundaries with misorientation values between 2° to 10° are considered as low angle grain boundaries whereas those with misorientations above 10° are considered as high angle grain boundaries.

Another orientation microscopy tool that was used in this study is forescatter or orientation contrast imaging (Chapter 6). Up to six forescatter detectors can be fitted around the phosphor screen, that records the BKP, and record in gray scale, orientation contrast images that correspond to variations in crystallographic orientation (Prior et al., 1996). Orientation contrast imaging provided qualitative information and was used primarily for the selection of intragrain domains for further quantitative crystallographic analysis (EBSD). Another significant parameter that expresses the indexing confidence (i.e. the degree that a simulated BKP overlaps with the actual BKP) is the Mean Angular Deviation (MAD). In other words, the higher the MAD value the higher the misfit between actual and simulated BKP.

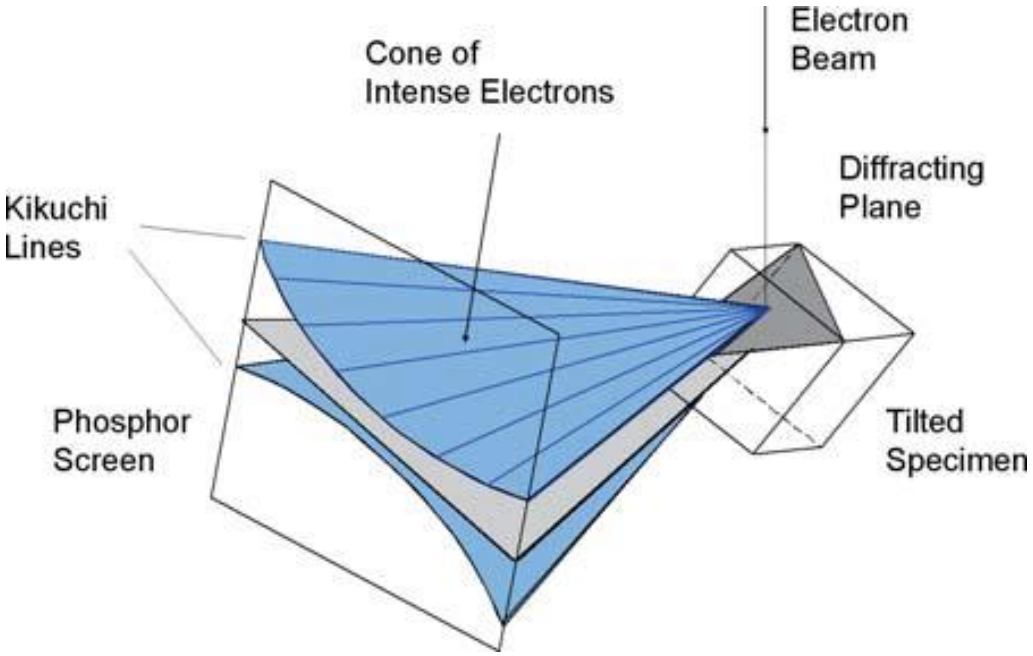

Figure 11. Schematic representation of the diffracted cones relative to a random crystallographic plane of the specimen and the phosphor screen. Modified after Schwarzer et al., 2009.

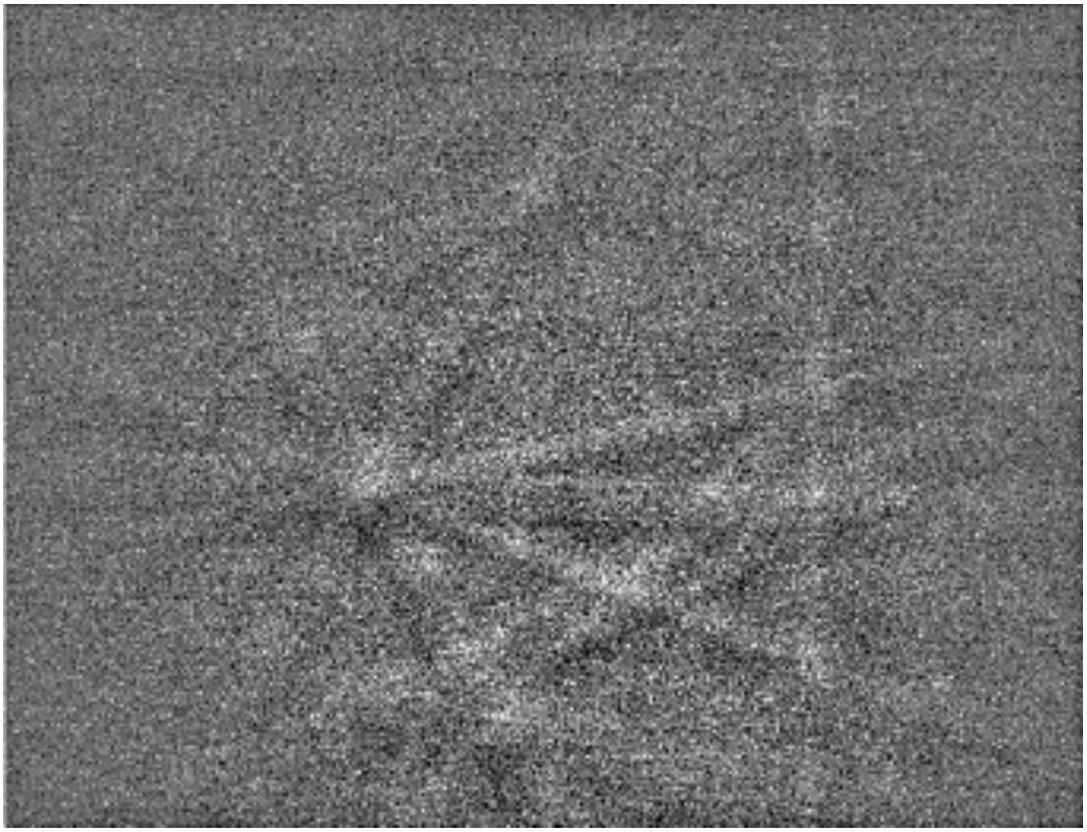

Figure 12. Example of an electron backscatter pattern (EBSP) from a titanite grain. Note the brighter diffraction bands.

3.3.3 Technical and analytical details of data collection and processing

The collection of quantitative microstructural data took place during two analytical sessions at the University of Western Ontario (ZAPLab, Canada) in May 2015, and the University of Portsmouth in September 2016. During the first analytical session four carbon coated, polished specimens (thin and thick sections) were analysed. The specimens were polished with a Buehler Vibromet 2 vibratory polisher using 0.05 µm alumina suspension. The EBSD analyses were performed using a Hitachi SU6600 FEG SEM equipped with an Oxfords instrument Nordlys EBSD detector. During the first session samples were tilted to 70° and analysed with a 20Kv and 8nA electron beam. The step size (pixel width) of the acquired BKP in the first session varied from 0.1 (titanite) to 5µm (sulphides). A grain mount of fifteen titanite grains was studied using orientation contrast imaging and EBSD analysis during the second session. The titanite grains were separated using standard heavy liquid and magnetic separation methods. Orientation contrast images were used a guide for the selection of specific intragrain domains for microstructural analysis.

The quantitative microstructural analysis during the second session took place using a Zeiss EVO MA10 LaB_6 SEM. The imaging and the crystallographic analysis were performed in an uncoated grain mount, in low vacuum mode, to avoid any charging effects. The specimen was tilted to 70° and analysed with a 20kV and 1nA electron beam. Further analytical and data collection details are provided in Table 3.6.

During both analytical sessions indexing with MAD values below 1° was acceptable. The crystallographic data sets were processed using the Tango (orientation map display and manipulation) and Mambo (pole figure and inverse pole figure) components of the HKL channel 5 software (Oxfords instruments). The only noise reduction operation that was applied to the raw crystallographic data was a 'wild-spikes' correction that replaces isolated, erroneously-indexed pixels, with zero solutions.

Table 3.6. Analytical details of EBSD data collection

Instrumentation		
Host Institute	Western University	Portsmouth University
SEM Model	Hitachi SU6600 FEG-SEM (Schottky electron source)	Zeiss EVO MA10 (LaB6 electron source)
EBSD System	Oxford Instruments Nordlys EBSD detector	Oxford Instrument Nordlys-Nano EBSD detector
EBSD Software	HKL Channel 5	Oxford Instruments AZTEC

SEM settings		
Carbon coat (<5nm)	Yes	No
Acc. Voltage (kV)	20	20
Working distance (mm)	19	14 to 20
Probe current (nA)	8	1
Tilt (^{o})	70	70

EBSD data collection and processing		
EBSP collection time per frame (m	80	< 120
Background (frames)	64	64
EBSP noise reduction (frames)	7	5
EBSP noise reduction (binning)	4x4	2x2
EBSP noise reduction (gain)	High	High
Hough resolution	60	70
Band detection min/max	4 to 7	10 to 12
Step size (nm)	50 to 150	80 to 200
Noise reduction	wildspike only	wildspike only

Chapter 4. Dating shear zones with plastically deformed titanite: New insights into the orogenic evolution of the Sudbury impact structure (Ontario, Canada)

Konstantinos Papapavlou[a*], James R. Darling[a], Craig D. Storey[a], Peter C. Lightfoot[b], Desmond E. Moser[c], and Stephanie Lasalle[a]

[a]School of Earth and Environmental Sciences, University of Portsmouth, Portsmouth PO1 3QL, UK

[b]Harquail School of Earth Sciences, Laurentian University, Sudbury, Ontario, P3E 2C6, Canada

[c]Department of Earth Sciences, University of Western Ontario, London N6A 5B7, Ontario, Canada

Abstract

The Sudbury structure is a mineralized impact crater that hosts different families of ore-controlling shear zones with poorly known orogenic affinities. Discriminating whether these deformation events relate to the 1.85 Ga crater modification stage or later regional tectonism, that collapsed the impact structure, is important both for crustal and mineral exploration studies. We have combined underground mapping with isotopic and microstructural analysis of titanite and host minerals in a benchmark ore-controlling mylonitic shear zone of the mining camp, the Six Shaft Shear Zone from the Creighton Mine. Three growth stages of chemically and microstructurally-characterised titanite grains were identified and related to the pre-, syn and late deformation stages. *In-situ* U-Pb age dating of the syndeformational grains demonstrates that a shearing event took place at 1645 ± 54 Ma during the Mazatzalian – Labradorian orogeny (1.7 – 1.6 Ga). This event led to the plastic deformation and local-scale remobilization of primary Ni-Cu-PGE sulphides in Creighton Mine (Sudbury, South Range). The adopted novel petrochronological approach can reveal the age significance of syn-deformational processes and holds promise for the untangling of complex syn-orogenic processes in Precambrian terranes globally.

Keywords: Shear zones, Titanite, Mineralization, Sudbury impact structure, Orogeny

*corresponding author (konstantinos.papapavlou@port.ac.uk)

1. Introduction

High-strain mylonitic shear zones control the location, geometry, and metal tenor of a range of ore-deposits in many mining camps around the world (McQueen, 1987, Phillips et al., 1987, Cook et al., 1993, Blenkinsop, 2004, Duuring et al., 2007). The world-class polymetallic Ni-Cu-PGE Sudbury mining camp (Ontario, Canada) is no exception. The structural architecture of this camp is controlled by a crustal-scale network of greenschist to amphibolite facies shear zones, collectively termed as the South Range Shear Zone (Shanks and Schwerdtner, 1990). The timing of operation and the orogenic affinity of the structures that define this system of shear zones remains unclear (Bailey et al., 2004). Better age constraints on their operation will provide new insights on the tectonothermal events that induced the orogenic deformation of the crater and remobilization of some of the magmatic sulphide ore bodies to satellite positions. In this regard, the concept of petrochronology has emerged as a novel means to understand the chronologic significance and constrain the rates of metamorphic and deformational processes in polyphase deformed terranes globally.

Petrochronology is the linkage of isotopic ages with microstructural, geochemical, and/or thermobarometric constraints from the same or adjacent intra-grain domains of accessory phases. Constraining the timing of deformation remains a challenging endeavour but U-Th-Pb-bearing accessory phases have revealed, in several cases, a great potential to resolve the timing of deformation and fluid flow events in mylonitic shear zones (Parrish et al., 1988, Storey et al., 2004, Clark et al., 2005, Mahan et al., 2006, Cenki-Tok., 2013). In this contribution, we focus on a uniquely exposed mylonitic shear zone from the Creighton mine (**Figure 1**) that is spatially related with magmatic and remobilized Ni-Cu-PGE sulphide ore bodies. The main aims of this study are to: (a) bracket the timing of operation and the orogenic affinity of the shear zone, by adopting a petrochronologic approach using the accessory phase titanite and (b) characterise in detail this ore-controlling deformation zone and the mineralization that it hosts with new field, kinematic, mineral-chemical, and quantitative microstructural data (electron backscatter diffraction; EBSD).

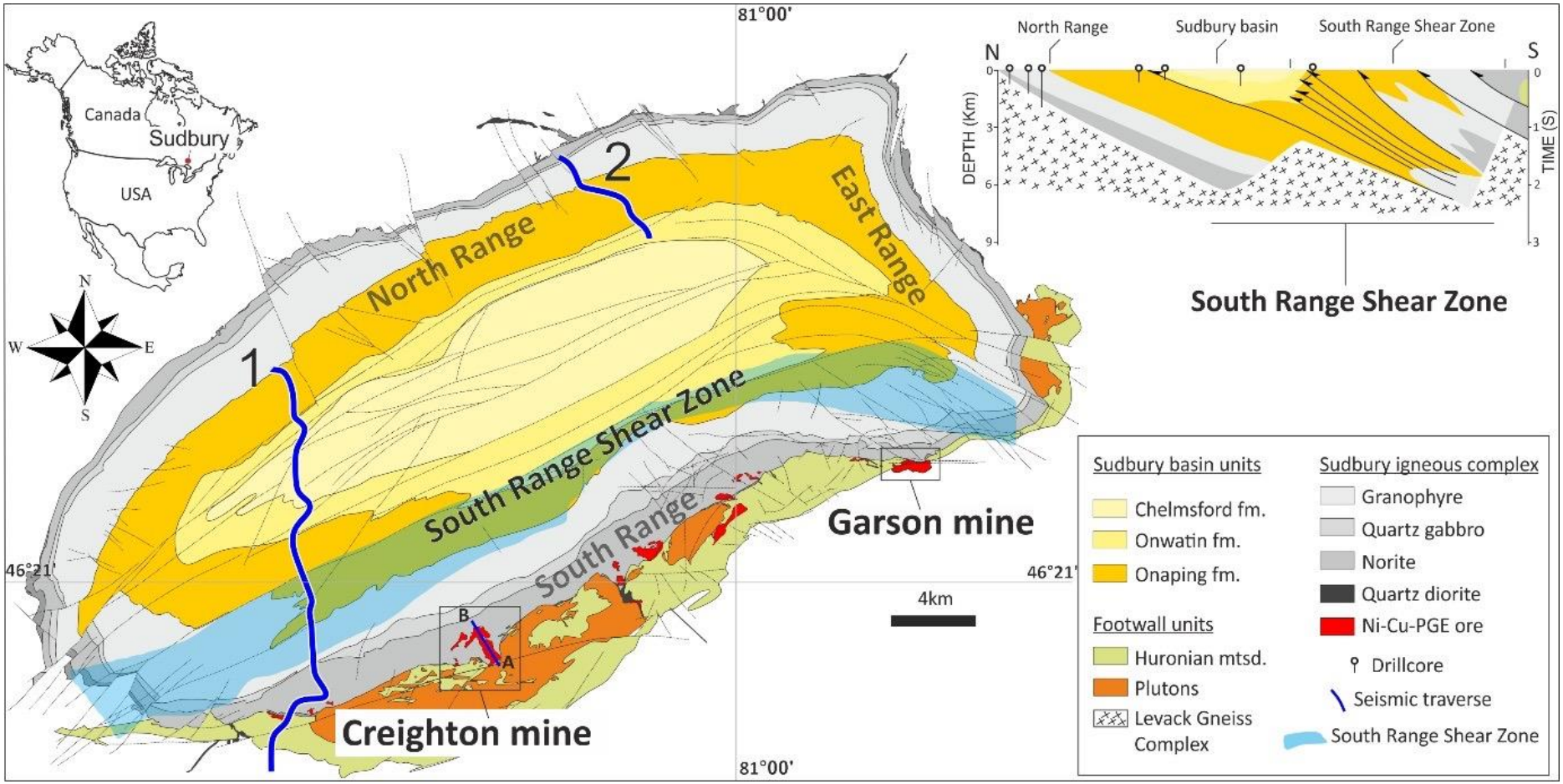

Figure 1. Simplified geological map of the Sudbury impact structure and composite North-South seismic cross section along the traverses 1 and 2 that are depicted with blue jagged lines (map modified from Ames et al 2008 and cross section from Adam et al., 2000).

2. The Sudbury impact structure

2.1 Geological setting and styles of mineralization

The 1.85 Ga Sudbury impact structure is a unique example of an ore-bearing terrestrial impact crater that underwent multiple orogenic events that extensively modified its structural architecture and metallogenic potential (Krogh et al., 1982; Riller, 2005). It is located at the junction of three Precambrian orogenic provinces (Superior, Grenville and Southern provinces), and is traditionally divided into the North, East, and South Ranges (**Figure 1**). The three major impact-related lithostratigraphic units of the Sudbury structure are: (a) the pseudotachylitic Sudbury Breccia (Spray, 1998, Rousell et al., 2003), (b) the Sudbury igneous complex (SIC) or Main Mass (Lightfoot et al., 1997), and (c) the elliptical Sudbury Basin (Pye et al., 1984 and references therein). In the South Range, Paleoproterozoic metamorphosed volcano-sedimentary rocks of the Huronian Supergroup form the footwall of the SIC (Card et al., 1984). In the North and East Ranges, the footwall of the SIC contains the 2.71 Ga Levack Gneiss Complex which consists of amphibolite to granulite facies tonalitic gneisses (Card et al., 1990; Ames and Farrow., 2007).

Four main types of sulphide mineralization are recorded in the Sudbury mining camp (Lightfoot et al., 1997; Mukwakwami et al., 2012). The dominant type comprises contact-style Ni-Cu-PGE sulphide ore bodies that accommodate more than 50 % of the Sudbury ores (Lightfoot et al., 2001). These are characterised by massive and disseminated sulphide ore bodies that settled gravitationally as immiscible liquids from a voluminous supra-liquidus silicate melt to thermally eroded embayments at the bottom of the SIC (Barnes and Lightfoot., 2005). The Offset-style deposits constitute the second major style of mineralization. These deposits are hosted within inclusion-bearing quartz diorite dykes (i.e. Offset Dykes) that exhibit pinch and swell geometry and thin away from the SIC (Lightfoot and Farrow., 2002). The third major ore-bearing environment comprises Cu-Ni-PGE footwall-style deposits that are hosted mainly within the Sudbury breccia (South Range) and the Archean gneiss complex (North Range) (Ames and Farrow., 2007). The fourth type is associated with mylonitic shear zones that host, displace and remobilize high metal tenor contact and footwall-style ore bodies and is exemplified mainly by deposits in Garson, Thayer Lindsley, Falconbridge and Creighton mines (Bailey et al., 2006; Gibson et al., 2010; Mukwakwami et al., 2012).

2.2.1 Structural and metamorphic evolution of the South Range

The main deformation system of the South Range is the South Range Shear Zone that comprises a moderately dipping array of top-to-the-north ductile and brittle-ductile structures that transect the SIC and the southern footwall of the Sudbury Structure (Shanks and Schwerdtner., 1990). Quantitative thermobarometric constraints and mineral-chemical analyses of amphiboles place the peak metamorphic conditions, and the operation of the South Range Shear Zone, within the epidote-amphibolite facies stability field (T = 550° - 600˚C, P = 4-5 Kbar) (Thomson et al., 1985, Fleet et al., 1987, Mukwakwami et al., 2014). The western segment of the South Range Shear Zone comprises ENE- trending, top-to-the-NW thrusts whereas the eastern exhibits a map-scale switch in the orientation of the structural grain with development of WNW-trending structures (**Figure 4.1**). These two structural domains are characterised by distinct kinematics (Santimano and Riller, 2012): a kinematic domain dominated by thrusting in the western part of the complex and a domain of dextral transpression in the eastern part (Riller et al., 1999). Generally, the following processes have been proposed to have influenced the deformation pattern of the South Range during and/or after the impact event : (a) the formation of syn-impact fractures (Siddorn and Ham., 2006), (b) the mechanical weakening of the crust by the impact event (Riller et al., 2010), (c) the orogenic buckling of the Sudbury Igneous Complex in a flexural – slip mode (Mukwakwami et al., 2012), and (d) a tri-shear fault – propagation folding of the crater units (Lenauer and Riller., 2012).

Despite recent advances on the structural characterization of the impact crater, the timing of syn and post-impact orogenic events and associated tectonic deformation is disputed. Specifically, high temporal resolution age dating (ID-TIMS) of syn-tectonic titanite grains from the #4 shear zone of the Garson mine (**Figure 1**), indicates operation of the shear zone at 1849 ±6 Ma (Mukwakwami et al., 2014). In contrast, titanite grains from the Thayer Lindsley shear zone, also from the south-eastern part of the complex, yielded a mean $^{207}Pb/^{206}Pb$ age of 1658 ± 68 Ma (Bailey et al., 2004). At the southwestern part of the complex, K-Ar and ^{40}Ar-^{39}Ar dates from fabric-forming biotite and muscovite grains yielded ages related to a thermal event between 1450 and 1480 Ma (Szentpeteri, 2009). Overall, the age dating of shear zones from the South Range of the Sudbury structure provides hints of three distinct thermal episodes related to the Penokean (ca. 1.9-1.8 Ga), the Mazatzalian-Labradorian (ca.

1.7-1.6 Ga), and the Chieflakian (ca. 1.5 – 1.4 Ga) orogenies. These results indicate that the impact event temporally may overlap with the Penokean orogeny (1.9 – 1.8 Ga) but the relative importance and control of post-impact events on the structural evolution of the crater remain far from well understood.

2.3 Shear zone families in the Creighton mine (South Range)

Creighton Mine is located at the southwestern margin of the Sudbury Structure (**Figure 1**) and hosts one of the largest contact-style deposits in the mining camp (i.e. the Creighton Deposit with 280 Mt of mined and unmined reserves). Many smaller contact and footwall-style ore bodies are located at depth in the Creighton Mine (e.g. 125, 126, 403, 461, 649 ore bodies, **Figure 2**) (Farrow and Lightfoot., 2002; Dare et al., 2010). Ductile shear zones exert a strong control on the geometry and location of these ore bodies (O'Donell., 1979). The following four main families of biotite-rich mylonitic shear zones are detected in the Creighton Mine (Snelling, 2009, Snelling et al., 2013): (a) the ENE-striking, steeply dipping 118 family of shear zones, (b) the NW-striking, moderately dipping family of footwall-type shear zones, (c) the steeply dipping family of E-W striking shear zones, and (d) the family of splay shears that link the NE-striking structures. The focus of this study is a deformation zone that is not categorized within any of the existing orientation families, exhibits listric geometry, and constitutes an important mechanical link between contact and footwall-style Ni-Cu-PGE magmatic ore bodies (**Figure 2, Six Shaft Shear Zone**).

3. Six Shaft Shear Zone (Creighton Mine, 5400 level)

3.1 Sampling

The Six Shaft Shear Zone is exposed underground from the 5000 (1524 m depth) to the 5400 (1767 m depth) level of the Creighton Mine and is also identified by multiple drillholes (**Figure 2**). Twenty-four samples of biotite-rich mylonite and two samples of shear-hosted ore were collected along a transect of approximately 25m from the 5400 level drift (**Figure 3**). The transect cross-cuts marginal lower strain and higher strain core domains of the Six Shaft Shear Zone. Eighteen of the mylonitic samples were collected for microtectonic and kinematic analysis. These samples were oriented normal to the foliation and parallel to the stretching lineation (XZ plane of the strain ellipsoid), taking into consideration field

observations that this plane hosts highly asymmetric kinematic indicators and can be regarded as the vorticity profile plane of the shear zone.

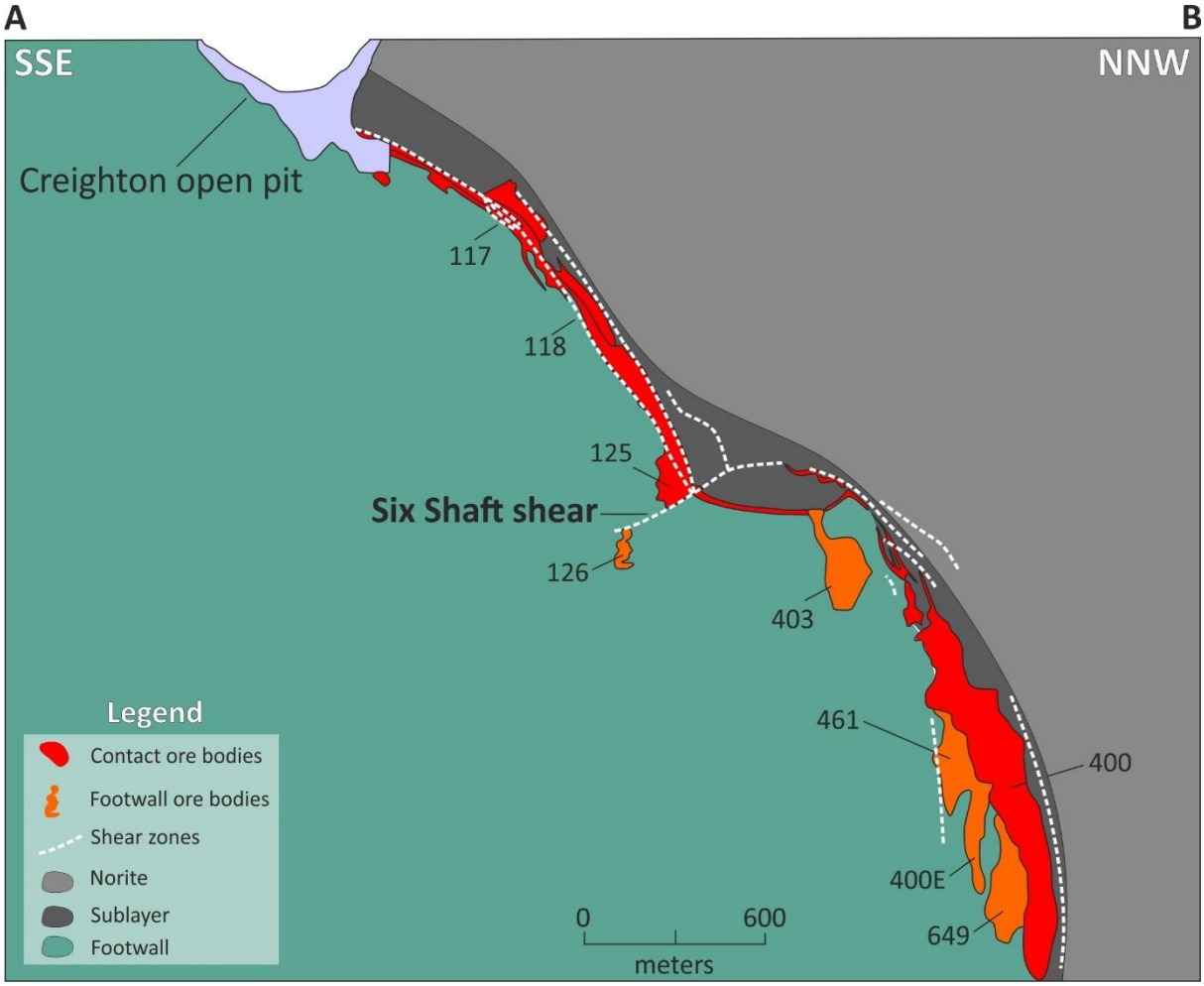

Figure 2. Simplified cross-section of the Creighton mine (modified from Vale ltd internal report), that depicts the spatial relationship of ductile shear zones with sulphide mineralization. The exact location of the cross section is depicted in the geological map (**Figure 1**, traverse A-B). With black bold letters is indicated the location of the Six Shaft Shear Zone in the 5400 level. The thickness of the ore bodies in the cross section is apparent since the location of the ore bodies has been projected on the cross-section using a wide clipping technique.

3.2 Field relationships

The Six Shaft Shear Zone is a km-scale mylonitic shear zone that exhibits a NNW to ENE strike swing (**Figure 3**). In this study the NNW-striking domain of the shear zone was accessed (**Figure 3**). This domain hosts a moderately dipping, high-strain fabric, defined by aligned biotite flakes and foliation-parallel, decimetre to meter-scale mylonitic quartz veins. A well-developed stretching lineation on the foliation planes is defined by elongate amphibole prisms and biotite flakes. The strong development of foliation and stretching lineation

characterise the biotite-rich mylonites as S-L tectonites. The average stretching lineation on the foliation planes plunges moderately towards the northeast and pitches around 80˚ (**Figure 3**, **pole figures**).

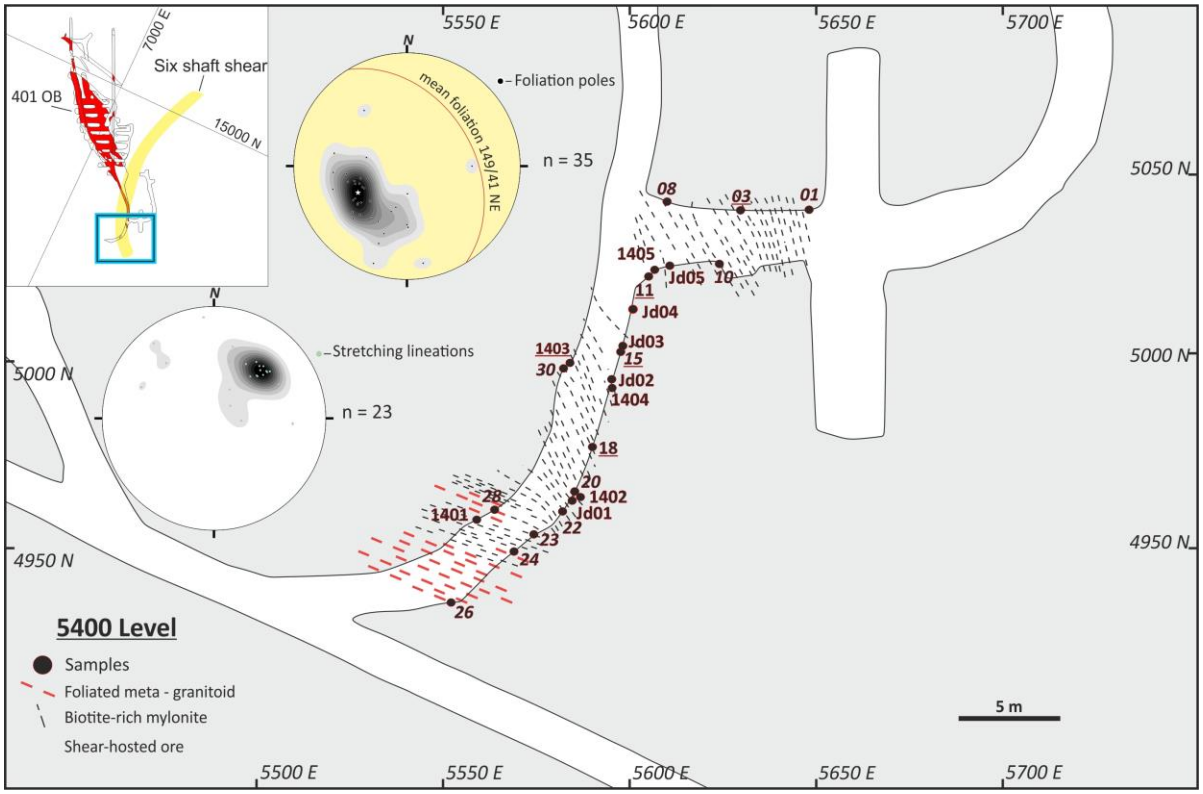

Figure 3. Simplified structural map of the Six Shaft Shear Zone at the 5400 level of the Creighton mine. The rectangular area in the inset depicts the NNW-striking domain of the Six Shaft Shear Zone and the spatial relationship of the shear with the 401 contact-style ore body. With red and black lines are depicted the foliation trajectories in the low (foliated-metagranitoid) and high strain domains of the shear zone, respectively. The pole figures show orientation data of stretching lineations and mylonitic foliations from the biotite-rich mylonitic domain. The black circles denote the location of each sample. The samples with underscored names were chosen for U-Pb titanite geochronology.

Parasitic folds defined by quartz-rich veins have axial planes sub-parallel to the mylonitic foliation. Refolded isoclinal quartz veins are observed also locally. Massive, quartz-rich, discordant veins occur in association with the biotite-rich mylonitic core. Marginally, the main body of the mylonitic zone is bounded by a weakly foliated meta-granitoid (i.e. black porphyry in the local literature). At the contact of the meta-granitoid with the mylonite, deflected quartz veins and quartz porphyroclasts with asymmetric strain shadows show a top-to-the-SW sense of shear (**Figure 4a, b).** Millimetre-scale asymmetric quartz veins also demonstrate a south-vergent sense of movement. Hand samples oriented normal to the

foliation and the stretching lineation (YZ plane of strain ellipsoid) exhibit cm-scale eye-shaped sheath folds defined by quartz veinlets (**Figure 4c**). Pyrrhotite-rich sulphide ore bodies with pentlandite porphyroblasts and durchbewegt-type structures are oriented sub-parallel to the mylonitic foliation at the core of the mylonitic zone (**Figure 4d**). These outcrop-scale ore slivers host in their pyrrhotite-rich matrix biotite, amphibole, and quartz-rich wallrock clasts that locally define a crude foliation.

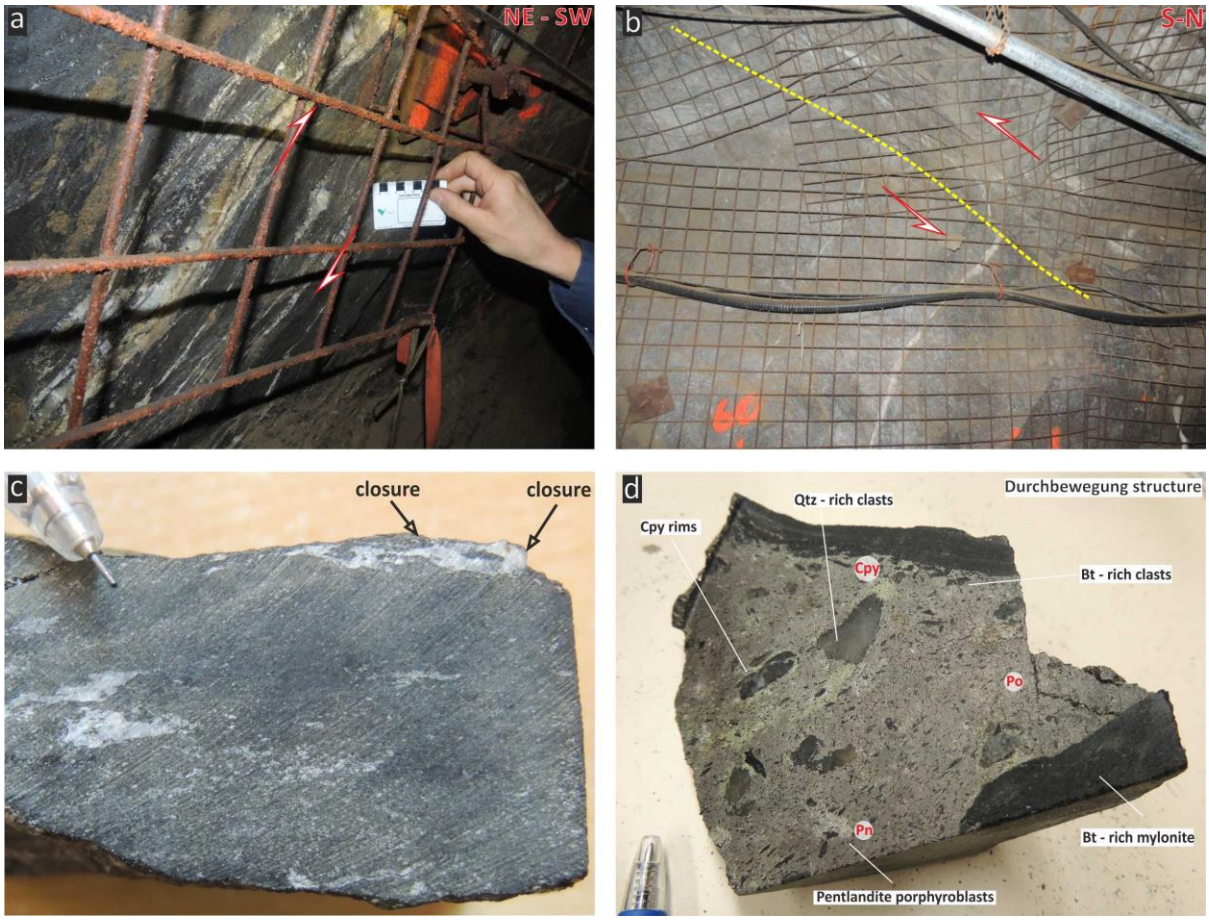

Figure 4. Field photographs from the Six Shaft Shear Zone that show: (a) Quartz porphyroclast with asymmetric strain shadows that indicate top-up-to-the-SW sense of shear (looking normal to the foliation and parallel to the stretching lineation), (b) Deflected quartz vein and quartz sigmoids that indicate southward translation at the contact of the foliated meta-granitoid with the biotite-rich mylonitic core, (c) cm-scale, eye-shaped, sheath folds developed at the YZ plane of strain ellipsoid (normal to the foliation and stretching lineation). The closure of the fold hinge lines is indicated with arrows. The tip of the pencil for scale is approximately 2 cm. (d) durchbeweng-style brecciated sulphides with quartz and biotite-rich mylonitic clasts in a pyrrhotite-rich matrix. Note that the chalcopyrite grains wrap around the more competent biotite and quartz clasts while pentlandite grains define porphyroblasts in the pyrrhotite-rich matrix

3.3 Petrography and microstructures

3.3.1 Petrographic features of the Six Shaft Shear Zone

Biotite is the most abundant mineral phase (70-80% modally) and defines the penetrative high-strain fabric. Hornblende grains aligned with the fabric are observed in textural equilibrium with the biotite flakes. Relict hornblendes with corroded boundaries locally exhibit pinch and swell microstructures. Titanite, allanite with epidote rims, and apatite grains are ubiquitous accessory phases and commonly occur in close spatial association with each other (**see section 5.2.2**). The titanite grains in the biotite-rich mylonitic domain have patchy zoning in reflected light and occur chiefly as fine-grained clusters that define bands parallel to the high-strain fabric. Recrystallized titanite grains that host accessory phase inclusions (i.e. apatite and epidote) are observed within mm-scale, plagioclase-rich ultramylonitic bands. Blocky, anhedral, millimetre-scale titanite grains are also observed locally. In the marginal meta-granitoid domain, biotite flakes and chalcopyrite-pyrrhotite grains wrap around feldspar and quartz-rich porphyroclasts.

Titanite grains in the quartzofeldspathic lithologies of this domain occur at the rims of epidote grains or in a textural disequilibrium with the rims of plagioclase porphyroclasts (**Figure 5**). Reflected light microscopy of the mylonitised sulphides reveals a pyrrhotite-rich matrix with millimetre-scale pentlandite and chalcopyrite grains. The chalcopyrites are commonly located at the boundaries of pentlandite grains or they fill intragranular fractures within pentlandite grains. Isolated, detached grains of biotite and zoned calcic amphiboles occur as inclusions in pentlandites and chalcopyrites. The detailed paragenetic relationships in the studied samples are described in **Table 1 (Supplementary material).**

3.3.2 Microstructures

Shear sense indicators in the biotite-rich mylonitic domain have monoclinic symmetry and consistently indicate a top-to-the-SW sense of shear (**Figure 6**). The main indicators are asymmetric polycrystalline quartz aggregates, feldspar porphyroclasts with asymmetric wings, biotite sigmoids, and C-S/C'-S composite fabrics (**Figure 6a-d**). Recrystallized feldspars with a strong grain shape fabric define millimetre-scale ultramylonitic bands between coarse-grained equigranular quartz grains with granoblastic texture. Undulose extinction and development of polycrystalline quartz aggregates with ribbon-shaped geometry are ubiquitous features in the quartz-rich domains.

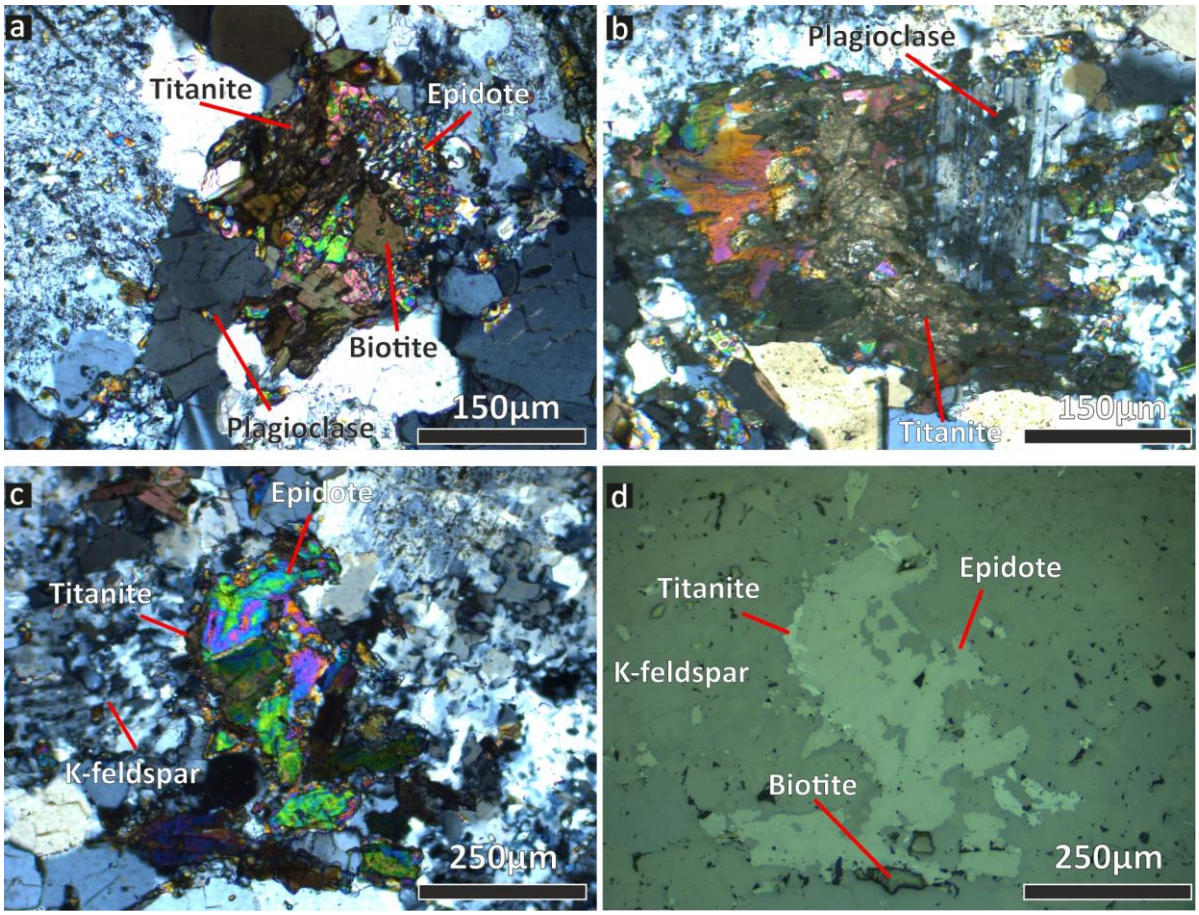

Figure 5. Photomicrographs from the marginal foliated metagranitoid of the Six Shaft Shear Zone that depict: (a) titanite replacing epidote in a plagioclase and K-feldspar-rich matrix, (b) titanite in textural disequilibrium at the marginal domains of a plagioclase grain, (c) titanite rimming epidote adjacent to K-feldspar that exhibits myrmekitic texture, (d) reflected light image of the photomicrograph c that shows titanite (brighter) rimming the epidote grain.

4. Analytical techniques and methodology

4.1 Electron beam imaging and microstructural analysis (SEM/EBSD)

Accessory phases were detected in thin section-scale reflected light maps and imaged using different scanning electron microscopes (SEM) at the University of Portsmouth (UK). The spectral composition and identification of different accessory phases was determined using a silicon drift (SDD) Oxford X-max 80mm^2 detector attached to a Zeiss EVO MA 10 LaB6 SEM at the University of Portsmouth. Electron backscatter diffraction analysis

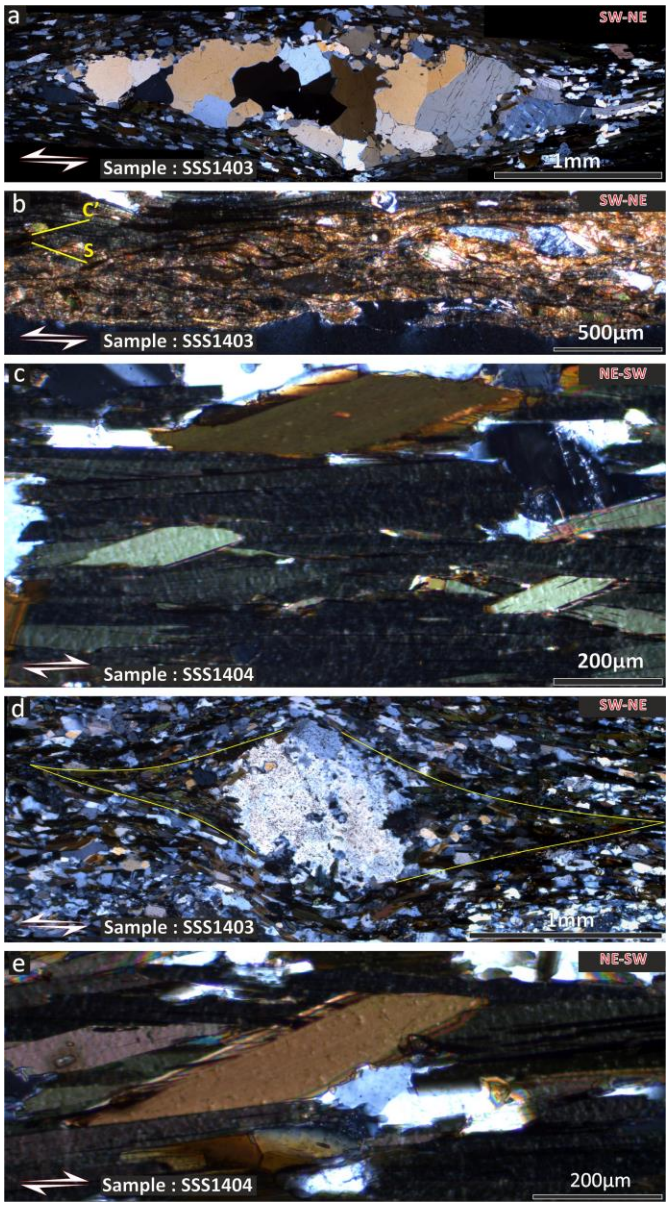

Figure 6. Shear sense indicators from the Six Shaft Shear Zone: (a) polycrystalline quartz aggregate with stair stepping geometry and asymmetric tails that indicate top-to-the-SW sense of shear, (b) C'-S composite fabrics that indicate top-to-the-SW sense of shear, (c) biotite sigmoids with top-to-the SW sense of shear, (d) feldspar porphyroclast with asymmetric wings that are defined by hornblende and titanite grains that show top-to-the-SW sense of shear, (e) rhomboidal biotite fish that indicates top-to-the-SW sense of shear. All the shear sense indicators were recognized in thin sections oriented normal to the foliation and parallel to the stretching lineation (XZ plane of strain ellipsoid).

(EBSD) of titanite grains was performed using a Hitachi SU6600 (variable pressure-field emission gun SEM) equipped with an Oxford Instruments Nordlys EBSD detector at the Zircon and Accessory Phase Laboratory (ZAPLab, University of Western Ontario). The thin sections were vibratory polished (Buehler VibroMet 2) using an 0.05 µm alumina suspension. During the EBSD analysis, specimens were tilted to 70° and analysed with a beam current of 8 nA and accelerating voltage of 20 kV. The only post-analysis noise reduction processing performed was to replace 'wild-spikes' (interpreted as isolated, erroneously-indexed pixels) with a zero solution. The EBSD data were processed using the Oxford Instruments software package Channel 5.

4.2 Mineral chemistry by electron probe microanalysis (EPMA)

Major element data from silicates were measured with a Cameca SX-100 at the University of Bristol using the TAP, LPET, and LLIF crystal spectrometers. An electron beam of 10µm diameter with 20 kV accelerating voltage and 20nA beam current was used in all the analyses. Natural silicates and synthetic materials were used as standards. Counting times for the analysed elements were from 10 to 60 seconds both at peak and background positions. The recalculation in the mineral-chemical analyses of calcic amphiboles was performed using the spreadsheet of Tindle and Webb (1994). The biotites were recalculated based on 22 oxygens per formula unit (**Table 1, supplementary material**). The amphiboles were recalculated based on 23 oxygens per formula unit with Fe^{+2}/Fe^{+3} estimation assuming 13 cations in total (**Table 2, supplementary material**). The amphibole mineral-chemical data were classified based on the method and nomenclature of Leake et al (1997).

4.3 Trace element micro-analysis by laser-ablation-inductively-coupled-mass-spectrometry. (LA-ICP-MS)

Trace element data from titanite and apatite grains were collected using an ASI RESOlution 193 nm ArF excimer laser coupled to an Agilent 7500cs quadrupole ICP-MS at the University of Portsmouth. The following isotopes were analysed ^{27}Al, ^{29}Si, ^{31}P, ^{43}Ca, ^{45}Sc, ^{49}Ti, ^{51}V, ^{53}Cr, ^{55}Mn, ^{59}Co, ^{60}Ni, ^{66}Zn, ^{69}Ga, ^{72}Ge, ^{85}Rb, ^{88}Sr, ^{89}Y, ^{95}Mo, ^{118}Sn, ^{121}Sb, ^{137}Ba, ^{139}La, ^{140}Ce, ^{141}Pr, ^{146}Nd, ^{147}Sm, ^{151}Eu, ^{157}Gd, ^{159}Tb, ^{163}Dy, ^{165}Ho, ^{167}Er, ^{169}Tm, ^{173}Yb, ^{175}Lu, ^{177}Hf, ^{208}Pb, ^{232}Th, ^{238}U. The laser spot size used in the analyses was between 15 and 40 µm. All the analyses were performed at frequency of 10 Hz and fluence of 4.5 J/cm^2. NIST 612 was used as the primary bracketing standard (Jochum et al., 2011). MPI-DING reference glasses (i.e. GOR128_G and T1G) Khan titanite (Heaman., 2009) and Durango apatite (Marks et al., 2012) were included as secondary standard every four or five unknowns. The analysed elements are within 10% in accuracy relative to published values for the MPI-DING reference glasses and the Khan titanite (Jochum et al., 2006, Heaman, 2009, **Table 3, supplementary material**). Six analyses were rejected because were positioned above ilmenite inclusions and cracks. Representative microprobe analyses demonstrate that titanites and apatites are stoichiometric in their CaO abundance (28.6 wt% for titanite and 55 wt % for apatite) (**Table 4**, **supplementary material**). Thus, the CaO value was used as the internal standard to

normalise the intensity of the unknown analytes. The raw data were reduced using the matlab-based software package SILLS (Guillong et al., 2008).

4.4 U-Pb geochronology by laser-ablation-inductively-coupled-plasma-mass-spectrometry (LA-ICP-MS)

U-Pb isotopic analyses on titanite were performed using an ASI RESOlution 193 nm ArF excimer laser coupled to a quadrupole Agilent 7500cs ICP-MS at the University of Portsmouth. Analytical and instrumentation parameters are provided in **Table 5 (supplementary material)**. All the analyses were performed with spot size between 15 and 30 µm. The laser fluence was approximately 3 J/cm^2 and the frequency 2 or 3 Hz. A sample-standard bracketing method was used to correct for mass fractionation, using Khan titanite (ID-TIMS age of 522.2 ± 2.2 Ma, Heaman.,2009) as the primary standard. Downhole U-Pb elemental fractionation was corrected using an exponential downhole correction fit to the time-resolved data for each analysis. A ^{207}Pb based correction scheme was applied to the variably common lead-bearing primary reference material (Khan titanite) using the Visuage_Ucompbine add-in for Iolite (Paton et al., 2010, Chew et al., 2014). The resulting corrections in the raw measured ratios of Khan titanite are negligible and within analytical uncertainty. Taking in consideration the recrystallization features in the unknown titanite grains, and the relatively high background signal of ^{204}Pb due to the interference of ^{204}Hg, a ^{204}Pb correction scheme based on crustal lead evolution models (Stacey and Kramers., 1975) was avoided. Thus, the U-Pb data (**Table 6, supplementary material**) are presented uncorrected for common lead in Tera-Wasserburg space. The Bear Lake Ridge Titanite (ID-TIMS age of 1047.4 ± 1.4 Ma, Aleinikoff et al., 2007) and Fish Canyon Tuff titanite (ID-TIMS age of 28.40 ± 0.02 Ma, Schmitz and Bowring., 2001) were analysed as secondary standards every four or five unknowns. The LA-ICP-MS analyses of the secondary standards are within uncertainty of the ID-TIMS values both for BLR and FCT titanite, yielding lower intercept ages of 1044 ± 23 Ma and 23.2 ± 6.3 Ma respectively on Tera-Wasserburg plots (**Table 5, supplementary material**). The isochrons of secondary standards were anchored to ^{207}Pb/^{206}Pb isotopic ratios of 0.912 ± 0.05 (Stacey and Kramers., 1975) and 0.84 ± 0.05 (Schmitz and Bowring., 2001), for BLR and FCT, respectively.

5. Results

5.1 Mineral chemistry of mylonitic fabrics

5.1.2 Amphiboles

The calcic amphiboles, according to their morphology and their relationship with the deformation fabrics, are classified in two micro-textural settings: (a) as relict, subhedral boudinaged grains, and (b) as pristine elongate grains that define the wings of feldspar porphyroclasts and the penetrative mylonitic fabric (S_m). The mineral-chemical analyses of these two textural populations manifest distinct differences. A core to rim zoning pattern is evident in the co-axially deformed amphiboles. The cores record an alternation of magnesio-hornblende, ferro-actinolite, and actinolitic hornblende domains (X_{Mg} = 0.49 – 0.66) (**Figure 7a**). The rims of the boudinaged amphiboles and the fabric-forming grains show compositional similarities and plot in the field of ferro-tschermakitic hornblende (X_{Mg} = 0.45-0.50). Comparatively, the fabric-forming grains have a marked increase in the ^{vi}Al, ^{iv}Al, $(Na + K)_{(A)}$ and Ti contents relative to the cores of the relict boudinaged amphiboles. Similar core to rim zoning patterns in calcic amphiboles are commonly attributed to amphibole growth at increasing P-T conditions along the prograde path of metamorphic terranes (Spear, 1993, Zenk and Schulz, 2004).

5.1.1 Biotite

The fabric-forming biotites of the Six Shaft Shear Zone show a progressive decrease in the X_{Fe} ($Fe^{+2}/Mg + Fe^{+2}$) from X_{Fe} = 0.62 to X_{Fe} = 0.53 (**Figure 7b**). This trend towards more phlogopitic compositions, along a traverse oblique to the strike of the mylonitic fabric, coincides with the exposure of foliation-parallel brecciated sulphides. The biotite grains are halogen-poor and have a slightly increasing trend in the abundance of chlorine from the marginal meta-granitoid (Cl = 0.14 wt %) to the biotite-bearing mylonitic core (Cl = 0.23 wt %).

5.2 Electron beam imaging and microstructural analysis of titanite (SEM/BSE-EBSD)

5.2.1 Electron beam imaging

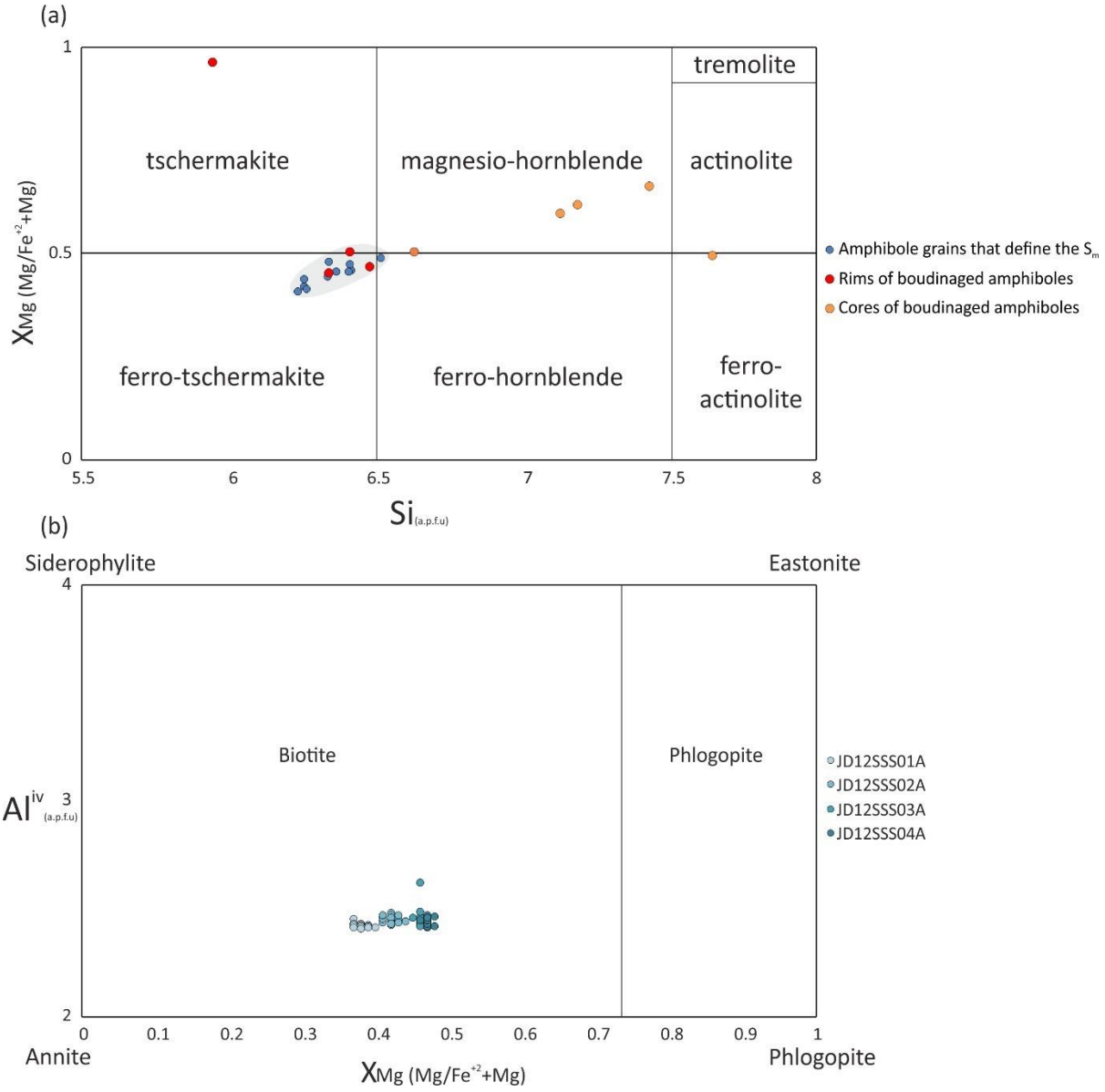

Figure 7. Compositional plots from fabric forming amphiboles and biotites of the Six Shaft Shear Zone: (a) Mineral chemical data of calcic amphiboles that are plotted with different colors according to the intra-grain location of the analytical spot (core-rim) and the textural relationship of the grains with the deformation fabrics, (b) Mineral chemical data of biotites from different structural levels of the shear zone.

Titanite grains were located in thin section-scale reflected light maps and imaged using backscatter electron microscopy (BSE). The majority of the imaged grains were classified based on their textural relationship with the deformation fabrics as pre-deformational relict cores (**Group 1**), syn-deformational (**Group 2**), and post/late-deformational grains (**Group 3**). A large population of grains though, has an ambiguous relationship with the deformation fabrics. Specifically, the **Group 1** grains are expressed as darker, sector-zoned cores, within grains that show overgrowth zoning **(Figure 8a)**. These grains commonly are decorated by a

sub-micrometer mantle zone with brighter BSE response that mimics their embayed geometry. The **Group 2** grains are characterised by strong shape preferred orientation, patchy BSE zoning, and micrometer-scale ilmenite, allanite, and apatite inclusions (**Figure 8b**).

These patchily-zoned grains commonly show amalgamation and define larger polycrystalline aggregates. Grains with overgrowth zoning and dissolution-precipitation features, such as darker sector zoned embayed cores (**Group 1 grains**), have idioblastic rims in textural equilibrium with fabric-forming silicates (**Figure 8c**) and are classified in the same textural population with the rest of the syn-deformational grains. In this population also occur locally grains with porphyroclastic texture and asymmetric wings (**Figure 8d**). The post/late-deformational population of titanite grains (**Group 3**) does not exhibit any systematic relationship with the deformation fabrics. These grains have blocky idioblastic habit, faint BSE zoning, and amphibole-biotite inclusions (**Figure 8e**). In addition, titanite grains from different textural populations are in mutual contact with allanite-cored epidotes and apatites indicating textural equilibrium during the growth of the three phases (**Figure 8f**).

5.2.2 Microstructural features of titanite and plagioclase grains

Titanite grains from the syn and post-deformational textural populations (**Groups 2 and 3**) were selected for quantitative microstructural analysis using the technique of electron backscatter diffraction (EBSD). The development of intragranular high-angle grain boundaries (i.e. boundaries with misorientation angles above 10˚) in the syndeformational, ribbon-shaped grains, induced the development of discrete crystallites (**Figure 9a-d**). These boundaries are evident also in BSE images as ovoid fractures (e.g. **Figure 8b**). Low angle grain boundaries (i.e. boundaries with misorientation angles between 2˚ and 10˚) are observed within the crystallites of both textural populations. The cumulative misorientation, relative to a reference point (white cross), differs considerably between grains of the two populations. In grains of Group 2 are recorded misorientation values up to 100° whereas in the blocky grains of Group 3 up to 8° (**Figure 9e-f**). Moreover, in grains of Group 3 the gradational increase in misorientation values is accommodated only locally by low-angle grain boundaries (**Figure 9f**).

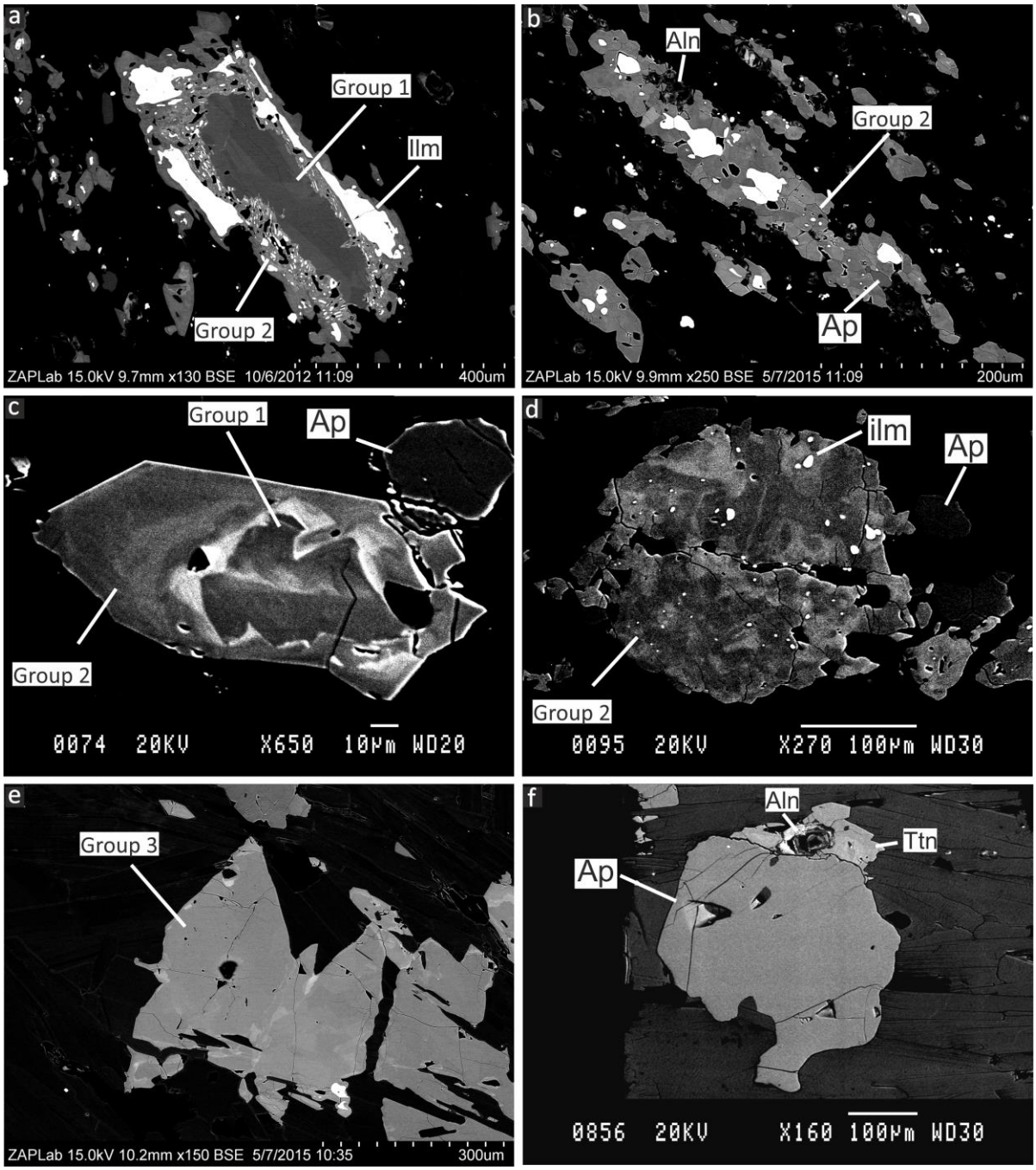

Figure 8. Backscatter electron images of titanite grains from the Six Shaft Shear Zone : (a) Darker sector zoned titanite grains (Group 1 grains) overgrown by titanite grains with ilmenite inclusions, (b) titanite grains with ilmenite, allanite, and apatite inclusions that show a strong shape preferred orientation and are hosted in bands of recrystallized feldspar (Group 2 grains), (c) darker embayed titanite cores (Group 1 grains) overgrown by euhedral titanite rims (Group 2 grains) with the latter in textural equilibrium with apatite and biotite grains, (d) patchily zoned titanite grain with ilmenite inclusion and porphyroclastic texture (Group2 grains), (e) blocky anhedral titanite grains that exhibit faint zoning and host ilmenite and silicate inclusions (Group 3 grains). (f) apatite grain in contact with a titanite grain that hosts an allanite inclusion

The blocky grains of **Group 3** exhibit a strong CPO (crystallographic preferred orientation) that is expressed by point maxima in the pole figures (**Figure 9e**). In stark contrast, in the recrystallized grains of **Group 2** the poles of the {100}, {010}, and {001} crystallographic planes show girdle-shaped patterns in lower hemisphere-equal area projections (**Figure 10a**). The grains of **Group 2**, that show a strong shape preferred orientation, have maximum MUD values up to 13 whereas the blocky grains of group 3 up to 165. The Multiples of Uniform Density value (MUD) is a parameter that characterise the fabric intensity, with MUD>1 indicative for the development of a fabric (Bland et al., 2011). Plagioclase grains have a different microstructural response relative to the **Group 2** titanite grains that they host (e.g. sample SSS18.4, **Figure 10a-b**). They show 120° triple junctions in band contrast maps and exhibit random CPO in pole figures of the {100), {010}, and {001} crystallographic planes (**Figure 10b**).

5.3 Titanite and apatite trace element geochemistry

In-situ trace element analyses were performed on titanite (n = 93) and apatite grains (n = 21) from different samples of the shear zone (**Table 7 and 8, supplementary material**). Eight apatite and five titanite analyses were rejected after inspection of the SEM images since they were located above or close to fractures. The analytical positions overlaid, where possible, the EPMA spots. Twenty-two (n=22) analyses in titanite grains of **Group 2** were located adjacent to spots that were selected for U-Pb isotopic microanalysis. A distinction between the different titanite groups can be inferred based on the uranium concentrations. Specifically, from the eighteen analyses in grains of **Group 1** twelve analyses show uranium contents below 1.5 ppm, and six between 2 and 6ppm. From forty-five analyses in grains of **Group 2** (patchy zoning and ilmenite inclusions), twenty-seven show uranium contents between 1.5 and 6.7 ppm. In addition, in twenty-five analyses from **Group 2** grains with overgrowth zoning eleven analyses show uranium contents between 5 and 11.8 ppm of uranium (**Figure 11**). The main compositional feature that is observed in the majority of the

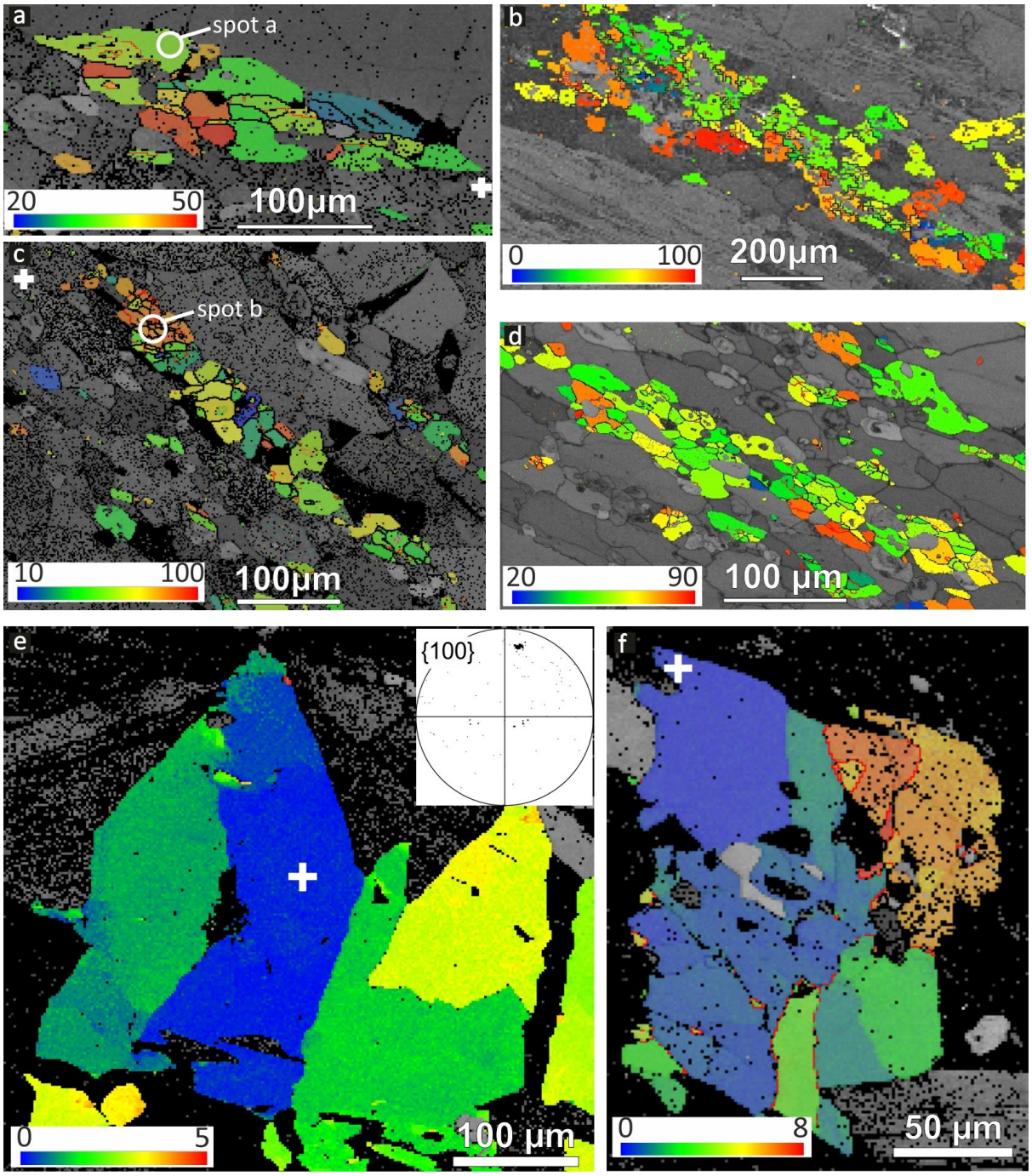

Figure 9. Misorientation maps of representative titanite grains from the Six Shaft Shear Zone that show from (a) to (d): Misorientation maps of Group 2 dynamically recrystallized titanite grains hosted within plagioclase and biotite-rich matrices. Black lines denote high-angle grain boundaries and red low angle. (e) Blocky titanite grain (Group 3 grain) with abrupt transition between misorientation domains and maximum cumulative misorientation values up to 5 degrees relative to the white cross. In the upper-right part of the map is depicted the pole figure of the {100} crystallographic plane, (f) Anhedral titanite that shows amalgamation and local crystal-plastic deformation that is expressed with the development of low-angle grain boundaries. Note that the maximum cumulative misorientation value of 8 degrees is observed in association with low angle grain boundaries at the upper right part of the grain.

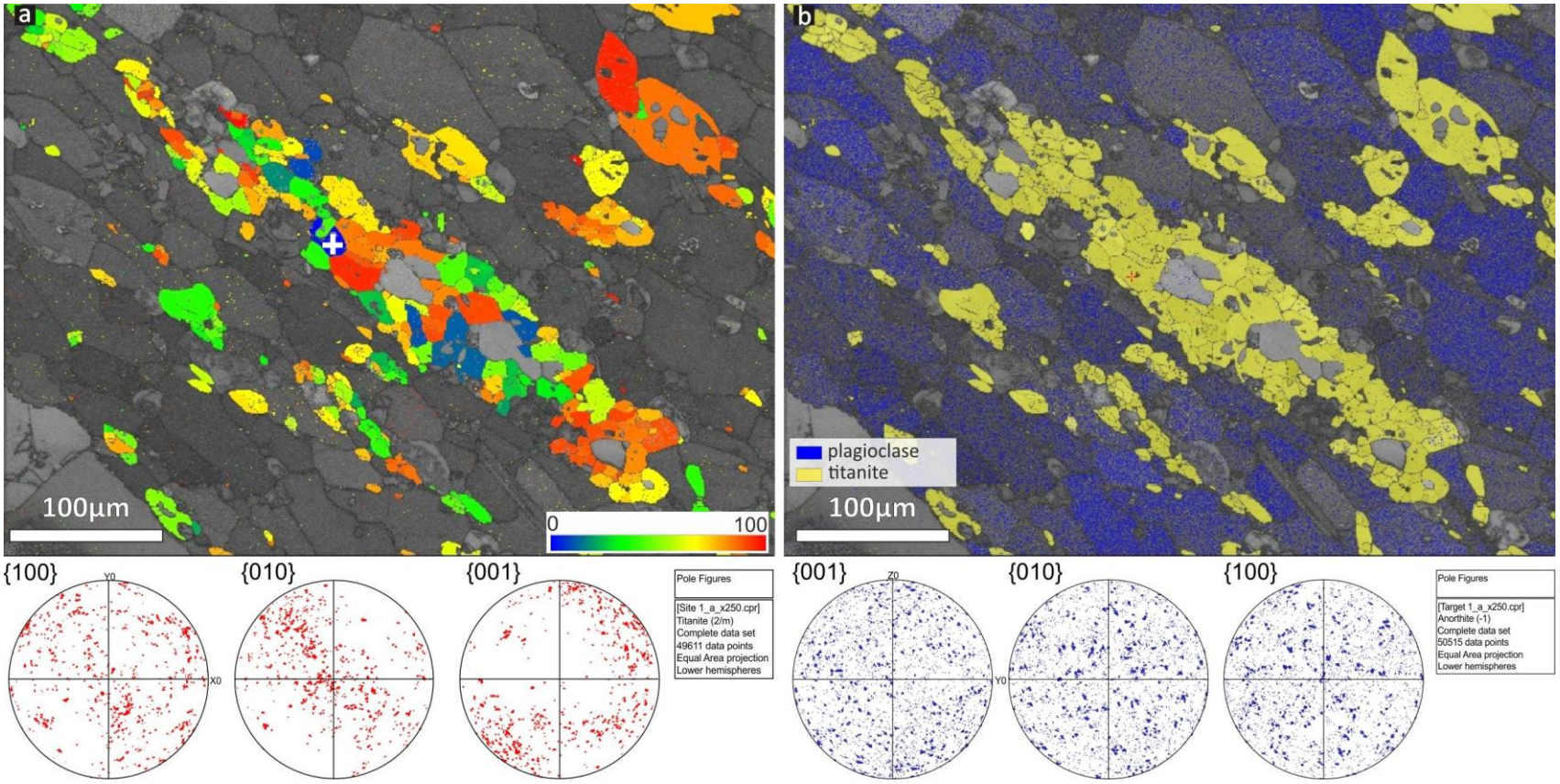

Figure 10. Misorientation and Phase map of a dynamically recrystallized titanite grain (Group 2) in a plagioclase-rich matrix. Both maps overlay a band contrast map. Below each map are depicted pole figures (lower hemisphere-equal area diagrams) for titanite (red) and plagioclase (blue) of the principal crystallographic axes.

grains (n=90), independently of zoning pattern and textural classification is depletion of LREE relative to HREE ($La/Yb_{(N)}$ = 0.001 – 0.041) (**Figure 11**). No or negative europium anomalies ($Eu/Eu_{(N)}$=0.56 – 1) are recorded in most of the grains (n = 76). Positive europium anomalies ($Eu/Eu_{(N)}$ = 1.25 – 2.25) are recorded chiefly in grains from a plagioclase-rich sample (i.e. sample SSS11A, n=11). Interestingly, titanite grains from this sample show also elevated Sm/Yb ratios (0.20 – 0.46) relative to grains from the other biotite-rich samples. In the titanite grains with overgrowth zoning, a slight increase of Y+REE contents from the darker in BSE resorbed cores (**Group 1** grains) to the lighter in BSE mantle and rim zones (**Group 2** grains) occurs (**Table 7**, **supplementary material**). In addition, thirteen analyses (n=13) of matrix-hosted fluorapatites (**Table 8, supplementary material**) exhibit also LREE-depleted patterns ($La/Yb_{(N)}$ = 0.01 – 0.16) with most of them (n=19) having negative europium anomalies ($Eu/Eu_{(N)}$ = 0.46-0.92) (**Figure 11, bottom**).

5.4 U-Pb titanite geochronology

Fifty-six analyses were performed in thin sections from six mylonitic samples (**Figure 12a**). The spots for U-Pb isotopic analysis were located primarily in fabric-forming titanite grains, free of fractures, which exhibit patchy zoning in BSE images (**Group 2 grains**). Four analyses were performed within the idioblastic rims of overgrowth zoned titanite grains that are in textural equilibrium with biotite (**Group 2 grains-overgrowth zoning**). U-Pb data from the texturally older populations of Group 1 grains were not collected since for the majority of the grains the trace element microanalysis showed that the ^{238}U content was below 1.5 ppm with a spot size of 20-30 μm. Thus, in order to get potentially meaningful age data, we would have needed to increase the spot size to 35-40 μm. In this case though, we would ablate cracked and/or inclusion-bearing domains. With the same rationale, age data from group 3 grains were not collected since they show uranium contents below 0.1 ppm. The uranium contents in the analysed grains vary from ca. 1 to 11 ppm. The U-Pb isotope data were plotted in Tera-Wasserburg concordia diagram taking into consideration that the analysed grains have cogenetic textural features and spread in U/Pb ratios (**Figure 12a-b**). The spread in the U/Pb isotopic ratios defines a single $^{238}U/^{206}Pb$ – $^{207}Pb/^{206}Pb$ isochron in Terra-Wasserburg space denoting that the selected targets belong to a single age population within uncertainty (**Figure 12**). The analysed grains yield a regressed lower

intercept date of 1645±54 Ma (2σ) (MSWD = 1.9) (**Figure 12a-b**). Excluding from the analyses the point with the lowest $^{207}Pb/^{206}Pb$ ratio, that has a strong bearing on the date, yields a lower intercept date of 1634±60 Ma (2σ) (MSWD = 1.9). The U-Pb isotopic data are uncorrected for common Pb and the intersection of a regression line through all the data points with the y axis represents the $^{207}Pb/^{206}Pb$ isotopic composition of common lead (Pb_{com}) that is estimated at 1.02 ± 0.02. The $^{207}Pb/^{206}Pb$ isotopic composition of common lead, based on crustal Pb evolution models for this age is estimated at 0.97 (Stacey and Kramers., 1975). In a plagioclase-rich sample (i.e. SSS11A), eleven trace element analyses in grains that were

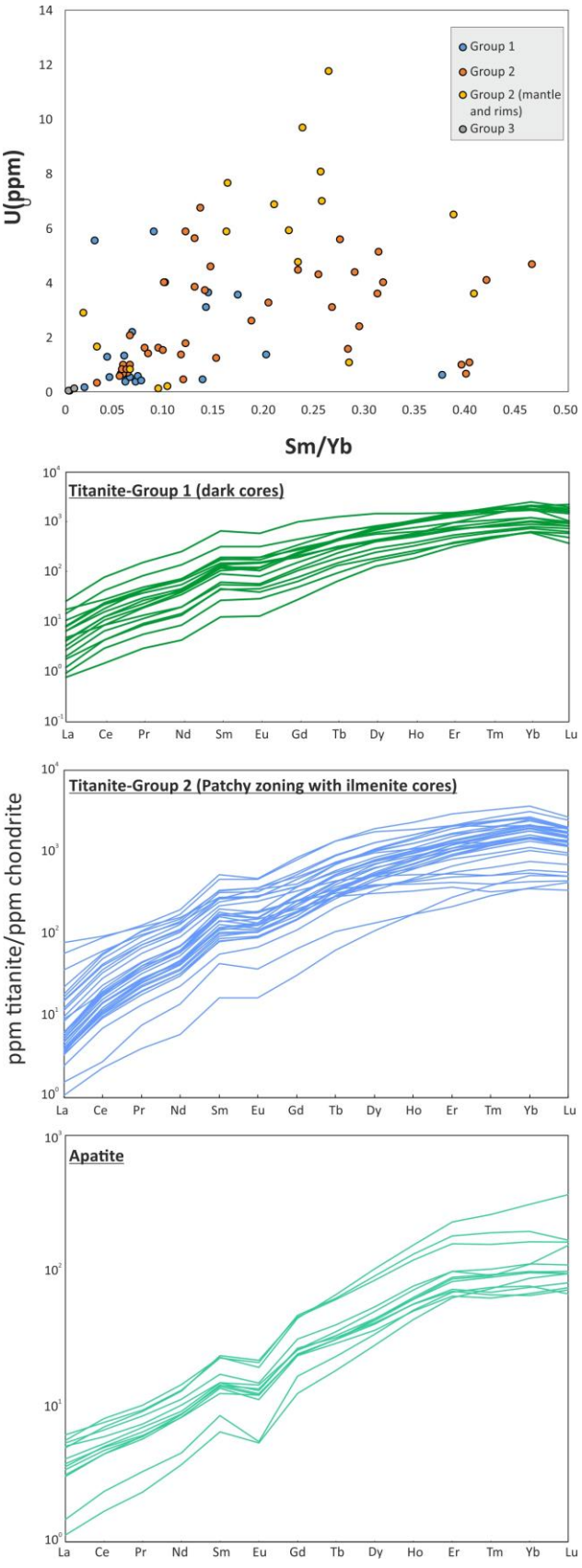

Figure 11. Plot of selected trace elements from titanite and apatite grains of the Six Shaft Shear Zone. From top to bottom are depicted the following: U versus Sm/Yb scatter plot from the different titanite textural populations, REE diagram from titanite grains of Group 1 (resorbed dark cores), REE diagram from titanite grains the belong to the Group 2 (patchy zoning with ilmenite inclusions), and at the bottom REE diagram from apatite grains hosted in a biotite-rich matrix of the shear zone.

used for U-Pb isotopic microanalysis consistently indicate the presence of positive europium anomalies (Eu* = 1.25 – 2.27, Table 2, **Figure 12b**). The rest of the samples, that are biotite or amphibole-rich, show no or negative Eu anomalies. U-Pb analyses of two microstructurally characterised (EBSD) titanite grains are depicted with red outline in order to demonstrate the relationship of the microstructurally characterised titanite grains with the grains that define the dominant age population (**Figure 12b**).

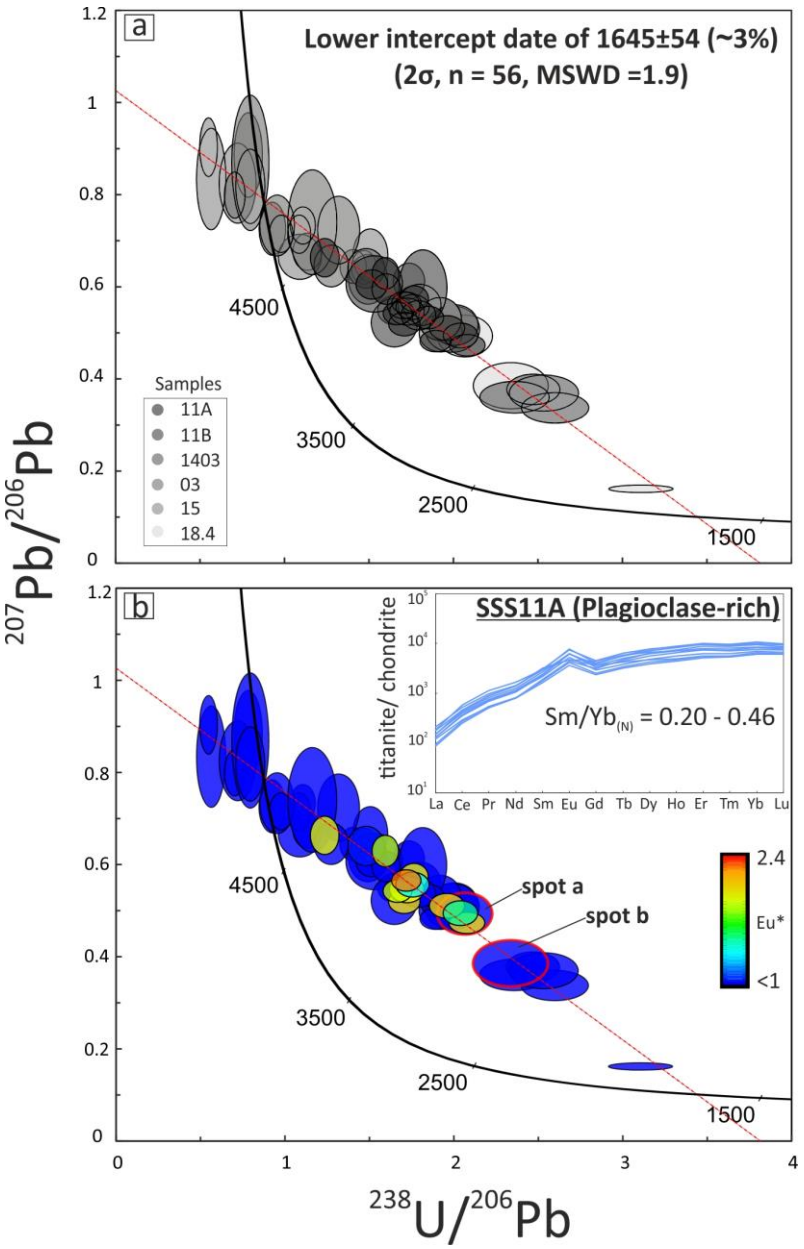

Figure 12. Terra Wasserburg concordia diagrams that show: (a) U-Pb ellipses colored in different shades of grey for different samples and (b) the same diagram colored based on the presence of europium anomalies. Note that in figure 12b is presented also a REE diagram from titanite grains of the plagioclase-rich sample SSS11A. With red outlines in Figure 12b are depicted the two grains in the misorientation maps of **Figure 9** (9a and 9c). The X and Y axes depict the total $^{207}Pb/^{206}Pb$ and $^{238}U/^{206}Pb$ isotopic ratios.

6. Discussion

6.1 Petrogenetic origin of the shear-hosted titanites

6.1.1 Titanite grains with ilmenite cores and patchy zoning

The presence of titanite grains with darker embayed cores (**Group 2** grains), patchy zoning, and ilmenite cores or inclusions are features that are attributed as evidence of intracrystalline dissolution and fluid-mediated growth (Harlov et al., 2006; Lucassen et al 2010; Villa and Williams., 2013).Specifically, Harlov et al., (2006) tested in amphibolite-facies samples if a H_20-rich fluid phase is responsible for the removal of Fe from ilmenite and the addition of Ca for the formation of titanite. By adopting a phase equilibria approach discussed mineral reactions in the CaO-FeO/Fe_2O_3-TiO_2-SiO_2-H_2O-O_2 (CFTSH) and CaO-FeO/Fe2O3-Al2O3-SiO2-H20-O2 (CFASH) systems, as function of H_20 and 0_2 fugacity. According to these researchers, in amphibole and clinopyroxene-absent samples the two main reactions that led to titanite formation are the: (a) plagioclase + ilmenite + H_20 = plagioclase + titanite + biotite and/or (b) 54 Anorthite + 6 Annite + 18 Titanite + 12 H_20 = 18 ilmenite + 36 Clinozoisite + 6 K-feldspar + 18 Quartz (for epidote-bearing samples). The presence of titanite in textural disequilibrium with plagioclase and epidote/clinozoisite (e.g. sample SSS 26, **Figure 5**) indicates that in the felsic domains of the shear zone the fluid-mediated break down of Ca-bearing phases led to the growth of titanite. Patchy zoning is a textural feature that indicates redistribution of the major structure-forming cations through open system recrystallization (Villa and Williams., 2013). In an experimental study, Lucassen et al., (2010) synthesized titanite in expense of rutile at run conditions of 600°C and 4Kbar (amphibolite-facies conditions) using a saline fluid phase to enhance solubility of rutile. In their results, titanite exhibits patchy compositional zoning in Ti-Al-F-OH, as a result of heterogeneities in the fluid composition. In the case of the Six Shaft Shear Zone, patchy zoning in BSE-compositional imaging is the main type of zoning and is interpreted as evidence for the existence of intragrain compositional heterogeneities. The presence of patchy zoning in grains with ilmenite inclusions possibly indicates that the fluid-induced breakdown of ilmenite and the development of irregular brighter and darker BSE domains are two interrelated processes.

6.1.2 Apatite and allanite inclusions in titanite

The nucleation of fluorapatite and allanite grains (LREE-enriched epidote) as inclusions in the LREE-depleted titanite grains is another textural line of evidence that can be related to the fluid-mediated petrogenesis of titanite in the Six Shaft Shear Zone. Similar micro-textural relationships between different REE-bearing accessory phases are attributed to the process of dissolution-reprecipitation in accessory phases from natural metasomatic settings (Pan et al., 1993, Dempster et al., 2006, Dempster and Macdonald, 2016). Experimental studies have also shown that permeating metasomatic fluids can exploit micro and nano-scale intragranular porosity paths (e.g. high-angle grain boundaries) and induce the development of analogous intragrain associations. For instance, the instantaneous growth, in geological timescales, of LREE-enriched monazite inclusions in fluorapatite (Harlov et al., 2005, Krenn et al., 2012, Harlov pers. com.).

In the case of the Six Shaft Shear Zone one scenario is that the LREE-depleted signature of both matrix-hosted apatite and titanite grains implies that pulses of fluid mobilized the LREE into other LREE-rich repositories such as allanite. Another scenario that seems more feasible in the examined shear zone, is that titanite co-crystallized with a LREE-enriched mineral, such as allanite, with the partitioning of LREE in allanite. BSE imaging provides support for the second scenario since both phases share sharp optical boundaries and are in textural equilibrium.

6.3 Chronologic significance of titanite age data

The suggested closure temperature of titanite, for typical cooling rates of most geological settings, varies from 600 to 800°C with fluid-assisted recrystallization rather than temperature-controlled thermal diffusion being also a controlling factor on the loss or exchange of radiogenic daughters (Cherniak, 1993, Verts et al., 1996, Villa, 1998, Frost et al., 2000, Rubatto and Herman, 2001, Spencer et al., 2013, Stearns et al., 2015, Kirkland et al., 2016). The syn-kinematic assemblage in the Six Shaft Shear Zone (i.e. Hbl-Pl-Ep-Qtz±Ttn±Ilm±Zr±Ap) indicates operation at epidote-amphibolite facies conditions (450 - 550°C). Further constraints are provided also by the microstructural data (EBSD) from plagioclase grains. The presence of annealing textures in band contrast maps and the absence of CPO (**i.e. Figure 10b**) indicate that plagioclase grains underwent crystal-plastic deformation via a dissolution-precipitation creep mechanism (Menegon et al., 2008, Mukai et al., 2014).

This deformation mechanism has been described again in deformed lithologies at epidote-amphibolite facies conditions and places the peak temperatures of shear zone operation at 600°C (Wintsch and Yi., 2002). The positive europium anomalies in titanite grains of Group 2, from the plagioclase-rich sample SSS11A, are interpreted to record the break-down of plagioclase via a dissolution-precipitation creep mechanism. This trace element signature suggests that titanite grains of Group 2 (higher U grains) grew during crystal-plastic deformation in the shear zone. These grains belong to the age population of 1645 ± 54 Ma (**Figure 12b**) and document the timing of crystal-plastic deformation and shear zone activity. In the case of the examined shear zone though, there is strong evidence for crystallite development and sub-grain formation in the titanite grains. These grain-scale modifications could have a strong impact on the diffusion characteristics of titanite and to the age significance of that date (i.e growth versus cooling age).

In a recent study, Kirkland et al., (2016) show through thermochronological modelling that titanite grains with length ≥ 210μm were not reset by a metamorphic event that reached 695 - 725°C demonstrating the critical role of grain size on preservation or resetting of isotopic information. Therefore, the relatively large grain size of the selected grains (i.e median length = 208μm, **Table 2 supplementary material**) possibly inhibited the modification of the closure temperature below the suggested range (600 - 800°C). On another note, the relatively high MSWD (Mean Square of Weighted Deviation) value (MSWD = 1.9) indicates that the titanite age data contain geologically meaningful scatter, possibly recording fluid-mediated and deformation processes throughout an orogenic cycle. The deviation in $^{207}Pb/^{206}Pb$ common lead ratios compared to model Pb estimates indicates that in shear zone settings localized fluid flow and deformation can induce fractionation of U/Pb, Th/Pb and Th/U ratios (e.g. Cenki-Tok et al., 2013).

6.4 Implications for the orogenic evolution of the South Range

The presence of top-to-the-SW monoclinic symmetry shear sense indicators in the Six Shaft Shear Zone indicate dominantly a non-coaxial strain path. Field-based mesoscale kinematic data are sparse in Creighton Mine, but biotite-rich shear zones from the deeper levels of the Mine show an opposite top-to-the-NW sense of shear (Snelling et al., 2013). Mineral phases with different rheological behavior and strain memory paint a more complex picture in the strain history of the examined shear zone. Paradoxically, feldspars with a diffuse

CPO host dynamically recrystallized titanites with a strong CPO. This denotes that titanite is a robust recorder of strain increments and resilient to fluid-mediated annealing and randomization of the CPO. The age dating of these syn-deformational titanite grains (Group 2 grains) from the Six Shaft Shear Zone indicate operation during an important, but under-recognised event, the Mazatzalian – Labradorian orogeny (1.7 – 1.6 Ga) (Romano et al., ,2000, Bailey et al., 2004). Structural data from the north-central United States show that during the Mazatzalian event a thin-skinned fold and thrust belt accommodated, via North and South-vergent structures, more than 600km of crustal shortening in 70 Myr (Craddock and McKiernan., 2007; Czeck et al., 2007, Duebendorfer et al., 2015). The new age data challenge the widely-held view that shear zones operated exclusively during the Penokean orogeny (ca. 1.9 – 1.8 Ga) (Shanks and Schwerdtner., 1991; Milkereit et al., 1992; Riller and Schwerdtner., 1997; Riller et al., 1999).

6.5 Implications for the mode and timing of sulphide remobilization in the Creighton mine

The extent of deformation-assisted remobilization of magmatic sulphides in Creighton Mine is not well constrained relative to other mines (e.g. Thayer Lindsley and Garson Mines, Bailey et al., 2006, Mukwakwami et al., 2014). However, the spatial relationship of the Six Shaft Shear Zone, with contact and footwall-style ore bodies suggests that this shear operated as a transfer pathway between contact (e.g. 125 ore body, **Figure 2**) and footwall-style deposits (e.g. 403 and 126 ore bodies, **Figure 2**) (O'Donell, 1979). The presence of meso-scale remobilization structures (i.e. durchbewegt) in the shear-hosted sulphides indicate a strong component of mechanical remobilization (Marshall and Gilligan., 1989, Marshall and Gilligan., 1993, Marshall et al., 1998). Unambiguous micro and meso-scale evidence does not exist though to support the hypothesis that the footwall ore system of the Creighton Mine was emplaced entirely via mylonitic shear zones. The more probable scenario is that ductile shear zones in the South Range, as foci of orogenic strain and fluid flow, led to a local-scale remobilization of primary contact and footwall-style Ni-Cu-PGE sulphide ore bodies. The texturally-controlled age dating of the Six Shaft Shear Zone demonstrates that this remobilization event can be linked with the Mazatzalian-Labradorian orogeny (1.7 – 1.6 Ga).

7. Conclusions

The Six Shaft shear zone is a top-to-the-SW ductile thrust that was active at epidote-amphibolite-facies conditions. The age dating of dynamically recrystallized titanite grains shows that this structure operated at 1645 ± 54 Ma during the Mazatzalian-Labradorian convergent orogeny (1.7 – 1.6 Ga). Syndeformational titanite grains with positive europium anomalies (Eu* = 1.25 – 2.25) record the breakdown of plagioclase grains with diffuse CPO via a dissolution-precipitation creep mechanism. The development of mechanical remobilization structures in sulphides at the mesoscopic scale indicates that the Six Shaft shear zone accommodated the local-scale transfer of contact and footwall-style Ni-Cu-PGE sulphide ore bodies. The synergistic approach on the study of the Six Shaft Shear Zone enhances our understanding of the operation of the structures that belong to the South Range Shear Zone and places maximum age constraints (1.7 – 1.6 Ga) on the local-scale remobilization of Ni-Cu-PGE sulphides during the orogenic deformation of the Sudbury impact structure.

Acknowledgements

K.P. acknowledges a university of Portsmouth research studentship. Vale Ltd is gratefully acknowledged for access to underground facilities and drillcore material. Vale geologists Lisa Gibson, Rob Pelkey and Collin Mecke are thanked for the provided unpublished material, samples and feedback. Dr. Stuart Kearns (University of Bristol) is also thanked for the assistance during the collection of electron microprobe data. J.D acknowledges Higher Education Innovation Fund and Researcher Development Fund grant from the University of Portsmouth. ZAPLab support from an NSERC Discovery Grant to D.M. is gratefully acknowledged, as is assistance from I. Barker (UWO) with SEM-EBSD analyses.

References

Adam, E., Perron, G., Milkereit, B., Wu, J., Calvert, A. J., Salisbury, M., … Dion, D.-J. (2000). A review of high-resolution seismic profiling across the Sudbury, Selbaie, Noranda, and Matagami mining camps. Canadian Journal of Earth Sciences, 37(2–3), 503–516. http://doi.org/10.1139/e99-064

Aleinikoff, J. N., Wintsch, R. P., Tollo, R. P., Unruh, D. M., Fanning, C. M., & Schmitz, M. D. (2007). Ages and origins of rocks of the Killingworth dome, south-central Connecticut: Implications for the tectonic evolution of southern New England. *American Journal of Science*, *307*(1), 63–118. doi:10.2475/01.2007.04

Ames, D.E. and Farrow, C.E.G. (2007). Metallogeny of the Sudbury mining camp, Ontario, in Goodfellow W.D., ed., Mineral deposits of Canada: A synthesis of major deposit-types, district metallogeny, the evolution of geological provinces, and exploration methods: Geological Association of Canada, Mineral Deposits Division, Special Publication no. 5, p. 329–350

Ames, D. E., Davidson, A., & Wodicka, N. (2008). Geology of the giant Sudbury polymetallic mining camp, Ontario, Canda. *Economic Geology*, *103*(5), 1057–1077. http://doi.org/10.2113/gsecongeo.103.5.1057

Bailey, J., Lafrance, B., McDonald, A. M., Fedorowich, J. S., Kamo, S., & W.J. Davis., D. A. A. (2004). Mazatzal–Labradorian-age (1.7–1.6 Ga) ductile deformation of the South Range Sudbury impact structure at the Thayer Lindsley mine, Ontario. *Canadian Journal of Earth Sciences* , *41* (12), 1491–1505. doi:10.1139/e04-098

Bailey, J., McDonald, A. M., Lafrance, B., & Fedorowich, J. S. (2006). Variations in Ni content in sheared magmatic sulfide ore at the Thayer Lindsley Mine, Sudbury, Ontario. *Canadian Mineralogist*, *44*(5), 1063–1077. doi:10.2113/gscanmin.44.5.1063

Barnes, S.-J., & Lightfoot, P. C. (2005). Formation of magmatic nickel-sulfide ore deposits and processses affecting their copper and platinum-group element contents. *Economic Geology*, 179–213.

Bland, P. a., Howard, L. E., Prior, D. J., Wheeler, J., Hough, R. M., & Dyl, K. a. (2011). Earliest rock fabric formed in the Solar System preserved in a chondrule rim. *Nature Geoscience*, *4*(4), 244–247. http://doi.org/10.1038/ngeo1120

Blenkinsop, T. G. (2004). Orebody geometry in lode gold deposits from Zimbabwe: Implications for fluid flow, deformation and mineralization. *Journal of Structural Geology*, *26*(6-7), 1293–1301. doi:10.1016/j.jsg.2003.11.010

Card K. D., Gupta P. H., McGrath P. H., and Gant F. S. (1984). The Sudbury structure: its regional geological and geophysical setting. In The geology and ore deposits of the Sudbury structure, edited by Pye E. G., Naldrett A. J., and Giblin P. E. Special Publication 1. Toronto: Ontario Geological Survey. pp. 25–43.

Card, K. D. (1990). A review of the Superior Province of the Canadian Shield, a product of Archean accretion. *Precambrian Research*, *48*(1-2), 99–156. doi:10.1016/0301-9268(90)90059-Y

Cenki-Tok, B., Darling, J. R., Rolland, Y., Dhuime, B., & Storey, C. D. (2014). Direct dating of mid-crustal shear zones with synkinematic allanite: new in situ U-Th-Pb geochronological approaches applied to the Mont Blanc massif. *Terra Nova*, *26*(1), 29–37. doi:10.1111/ter.12066

Cherniak, D. J. (1993). Lead diffusion in titanite and preliminary results on the effects of radiation damage on Pb transport. *Chemical Geology*, *110*(1–3), 177–194. http://doi.org/10.1016/0009-2541(93)90253-F

Chew, D. M., Petrus, J. A., & Kamber, B. S. (2014). U-Pb LA-ICPMS dating using accessory mineral standards with variable common Pb. *Chemical Geology*, *363*, 185–199. doi:10.1016/j.chemgeo.2013.11.006

Clark, C., Schmidt Mumm, A., & Faure, K. (2005). Timing and nature of fluid flow and alteration during Mesoproterozoic shear zone formation, Olary domain, South Australia. *Journal of Metamorphic Geology*, *23*(3), 147–164. doi:10.1111/j.1525-1314.2005.00568.x

Craddock, J. P., & McKiernan, A. W. (2007). Tectonic implications of finite strain variations in Baraboo-interval quartzites (ca. 1700 Ma), Mazatzal orogen, Wisconsin and Minnesota, USA. *Precambrian Research*, *156*(3-4), 175–194. doi:10.1016/j.precamres.2006.03.010

Cook, N.J., Halls, C., Boyle, A.P. (1993): Deformation and metamorphism of massive sulphides at Sulitjelma, Norway. *Mineralogical Magazine*, 57, 67-81.

Czeck, D. M., & Ormand, C. J. (2007). Geometry and folding history of the Baraboo Syncline: Implications for the Mazatzal Orogeny in the north-central U.S. *Precambrian Research*, *157*(1-4), 203–213. doi:10.1016/j.precamres.2007.02.017

Dempster, T. J., Campanile, D., & Holness, M. B. (2006). Imprinted textures on apatite: A guide to paleoporosity and metamorphic recrystallization. *Geology*, *34*(11), 897–900. http://doi.org/10.1130/G22299A.1

Dempster, T. J., & Macdonald, F. (2016). Controls on fluid movement in crustal lithologies: evidence from zircon in metaconglomerates from Shetland. *Geofluids*, *16*(3), 507–517. http://doi.org/10.1111/gfl.12172

Duebendorfer, E. M., Williams, M. L., & Chamberlain, K. R. (2015). Case for a temporally and spatially expanded Mazatzal orogeny. *Lithosphere*, *7*(6), L412.1. doi:10.1130/L412.1

Duuring, P., Bleeker, W., & Beresford, S. W. (2007). Structural modification of the komatiite-associated Harmony nickel sulfide deposit, Leinster, Western Australia. *Economic Geology*, *102*(2), 277–297. doi:10.2113/gsecongeo.102.2.277

Farrow CEG, Lightfoot PC (2002) Sudbury PGE Revisited: Toward an Integrated Model. Canadian Institute of Mining and Metallurgy Special Volume 54: 273- 297

Fleet, M. E., Barnett, R. L., & Morris, W. A. (1987). Prograde Metamorphism of the Sudbury Igneous Complex. *Canadian Mineralogist*, *25*, 499–514.

Gibson, A.M., Lightfoot, P.C., Evans, T.C., (2010). Contrasting styles of Low Sulphide High Precious Metal Mineralization in the 148 and 109 FW zones: North and South Ranges of the Sudbury Igneous Complex, Ontario, Canada. In Jugo, P.J., Lesher, C.M., and Mungall, J.E. (Eds): Abstracts, 11th International Platinum Symposium, Sudbury, Ontario, Canada. OGS Miscellaneous Release Data 269.

Guillong, M., Meier, D.L., Allan, M.M., Heinrich, C.A., Yardley, B.W.D., (2008). Sills: a Matlab-based program for the reduction of laser ablation ICP-MS data of homogeneous materials and inclusions. Laser Ablation-ICP-MS in the Earth Sciences: Current Practices and Outstanding Issues, 328–333

Harlov, D. E., Wirth, R., & Förster, H. J. (2005). An experimental study of dissolution-reprecipitation in fluorapatite: Fluid infiltration and the formation of monazite. *Contributions to Mineralogy and Petrology*, *150*(3), 268–286. doi:10.1007/s00410-005-0017-8

Harlov, D., Tropper, P., Seifert, W., Nijland, T., & Förster, H. J. (2006). Formation of Al-rich titanite (CaTiSiO4O-CaAlSiO4OH) reaction rims on ilmenite in metamorphic rocks as a function of fH2O and fO2. *Lithos*, *88*(1-4), 72–84. doi:10.1016/j.lithos.2005.08.005

Heaman, L. M. (2009). The application of U-Pb geochronology to mafic, ultramafic and alkaline rocks: An evaluation of three mineral standards. *Chemical Geology*, *261*(1-2), 42–51. doi:10.1016/j.chemgeo.2008.10.021

Jochum, K. P., Weis, U., Stoll, B., Kuzmin, D., Yang, Q., Raczek, I.,Enzweiler, J. (2011). Determination of reference values for NIST SRM 610-617 glasses following ISO guidelines. *Geostandards and Geoanalytical Research*, *35*(4), 397–429. doi:10.1111/j.1751-908X.2011.00120.x

Kirkland, C. L., Spaggiari, C. V., Johnson, T. E., Smithies, R. H., Danišík, M., Evans, N., … McDonald, B. J. (2016). Grain size matters: Implications for element and isotopic mobility in titanite. *Precambrian Research*, *278*, 283–302. http://doi.org/10.1016/j.precamres.2016.03.002

Krenn, E., Harlov, D. E., Finger, F., & Wunder, B. (2012). LREE-redistribution among fluorapatite, monazite, and allanite at high pressures and temperatures. *American Mineralogist*, *97*(11-12), 1881–1890. doi:10.2138/am.2012.4005

Krogh, T.E., MCNutt, R.H., and Davis, G.L. 1982. Two high precision U-Pb Zircon ages for the Sudbury Nickel Irruptive. Canadian Journal of Earth Sciences, 19, 723 – 728

Kylander-Clark, A. R. C., Hacker, B. R., & Cottle, J. M. (2013). Laser-ablation split-stream ICP petrochronology. *Chemical Geology*, *345*, 99–112. doi:10.1016/j.chemgeo.2013.02.019

Leake, B. E., Woolley, A. R., Arps, C. E. S., Birch, W. D., Gilbert, C. M., Grice, J. D., … Youzhi, G. (1997). Nomenclature of Amphiboles: Report of the Subcommittee of the International Commission on New Minerals and Mineral Names. *The Canadian Mineralogist*, *35*, 219–246.

Lightfoot, P. G., Keays, R. R., Morrison, G. G., Bite, A., & Farrell, K. P. (1997). Geochemical relationships in the sudbury igneous complex: Origin of the main mass and offset dikes. *Economic Geology*, *92*(3), 289–307. doi:10.2113/gsecongeo.92.3.289

Lightfoot, P. C., & Doherty, W. (2001). Chemical evolution and origin of nickel sulfide mineralization in the sudbury igneous complex, Ontario, Canada. *Economic Geology*, *96*(8), 1855–1875. doi:10.2113/gsecongeo.96.8.1855

Lightfoot, P. C., & Farrow, C. E. G. (2002). Geology, Geochemistry, and Mineralogy of the Worthington Offset Dike: A Genetic Model for Offset Dike Mineralization in the Sudbury Igneous Complex. *Economic Geology*, *97*(7), 1419–1446. doi:10.2113/gsecongeo.97.7.1419

Lenauer, I., & Riller, U. (2012). Geometric consequences of ductile fabric development from brittle shear faults in mafic melt sheets: Evidence from the Sudbury Igneous Complex, Canada. *Journal of Structural Geology*, *35*, 40–50. doi:10.1016/j.jsg.2011.11.012

Lucassen, F., Franz, G., Rhede, D., & Wirth, R. (2010). Ti-Al zoning of experimentally grown titanite in the system CaO-Al2O3-TiO2-SiO2- NaCl-H2O-(F): Evidence for small-scale fluid heterogeneity. *American Mineralogist*, *95*(10), 1365–1378. doi:10.2138/am.2010.3518

Marks, M. A. W., Wenzel, T., Whitehouse, M. J., Loose, M., Zack, T., Barth, M., … Markl, G. (2012). The volatile inventory (F, Cl, Br, S, C) of magmatic apatite: An integrated analytical approach. *Chemical Geology*, *291*, 241–255. doi:10.1016/j.chemgeo.2011.10.026

Marshall, B., & Gilligan, L. B. (1989). Durchbewegung structure, piercement cusps, and piercement veins in massive sulfide deposits; formation and interpretation. *Economic Geology*, *84*(8), 2311–2319. doi:10.2113/gsecongeo.84.8.2311

Marshall, B., & Gilligan, L. B. (1993). Remobilization, syn-tectonic processes and massive sulphide deposits. *Ore Geology Reviews*, *8*(1), 39–64. http://doi.org/10.1016/0169-1368(93)90027-V

Marshall, B., Vokes, F.M. & Larocque, A.C.L. 2000. Regional metamorphic remobilization: upgrading and formation of ore deposits. In: SPRY, P.G., MARSHALL, B. & VOKES, F.M. (eds) Metamorphosed and Metamorphogenic Ore Deposits. SEG Reviews in Economic Geology, 11, 19-38.

Mahan, K. H., Goncalves, P., Williams, M. L., & Jercinovic, M. J. (2006). Dating metamorphic reactions and fluid flow: Application to exhumation of high-P granulites in a crustal-scale

shear zone, western Canadian Shield. *Journal of Metamorphic Geology*, *24*(3), 193–217. doi:10.1111/j.1525-1314.2006.00633.x

McQueen, K. G. (1987). Deformation and remobilization in some Western Australian nickel ores. *Ore Geology Reviews*, *2*(1-3), 269–286. doi:10.1016/0169-1368(87)90032-1

Menegon, L., Pennacchioni, G., & Spiess, R. (2008). Dissolution-precipitation creep of K-feldspar in mid-crustal granite mylonites. *Journal of Structural Geology*, *30*(5), 565–579. http://doi.org/10.1016/j.jsg.2008.02.001

Mukai, H., Austrheim, H., Putnis, C. V., & Putnis, A. (2014). Textural evolution of plagioclase feldspar across a shear zone: Implications for deformation mechanism and rock strength. *Journal of Petrology*, *55*(8), 1457–1477. http://doi.org/10.1093/petrology/egu030

Mukwakwami, J., Lafrance, B., & Lesher, C. M. (2012). Back-thrusting and overturning of the southern margin of the 1.85Ga Sudbury Igneous Complex at the Garson mine, Sudbury, Ontario. *Precambrian Research*, *196-197*, 81–105. doi:10.1016/j.precamres.2011.10.020

Mukwakwami, J., Lafrance, B., Lesher, C. M., Tinkham, D., Rayner, N., & Ames, D. (2014). Deformation, metamorphism, and mobilization of Ni–Cu–PGE sulfide ores at Garson Mine, Sudbury. *Mineralium Deposita*, *49*(2), 175–198. doi:10.1007/s00126-013-0479-y

Milkereit, B., & Green, A. (1992). Deep geometry of the Sudbury structure from seismic reflection profiling. *Geology*, *20*(9), 807–811. doi:10.1130/0091-7613(1992)020

O'Donell. D., (1979). Creighton Mine orebody characteristics, Unpublished internal report to INCO, 88P.

Parrish, R. R., Carr, S. D., & Parkinson, D. L. (1988). Eocene extensional tectonics and geochronology of the Southern Omineca Belt, British Columbia and Washington. *Tectonics*, *7*(2), 181–212. doi:10.1029/TC007i002p00181

Pan, Y., Fleet, M. E., & MacRae, N. D. (1993). Late alteration in titanite (CaTiSiO5): Redistribution and remobilization of rare earth elements and implications for U/Pb and Th/Pb geochronology and nuclear waste disposal. *Geochimica et Cosmochimica Acta*, *57*(2), 355–367. doi:10.1016/0016-7037(93)90437-

Paton, C., Hellstrom, J., Paul, B., Woodhead, J., & Hergt, J. (2011). Iolite: Freeware for the visualisation and processing of mass spectrometric data. *Journal of Analytical Atomic Spectrometry*, *26*, 2508. doi:10.1039/c1ja10172b

Phillips, G. N., Groves, D. I., & Brown, I. J. (1987). Source requirements for the Golden Mile, Kalgoorlie: significance to the metamorphic replacement model for Archean gold deposits. *Canadian Journal of Earth Sciences*, *24*(8), 1643–1651. doi:10.1139/e87-158

Pye E. G., Naldrett A. J., and Giblin P. E., editors. (1984). The geology and ore deposits of the Sudbury structure. Special Publication 1. Toronto: Ontario Geological Survey. 603 p

Riller, U. (2005). Structural characteristics of the Sudbury impact structure, Canada: Impact-induced versus orogenic deformation-A review. *Meteoritics & Planetary Science*, *40*, 1723–1740. doi:10.1111/j.1945-5100.2005.tb00140.x

Riller, U., Boutelier, D., Schrank, C., & Cruden, A. R. (2010). Role of kilometer-scale weak circular heterogeneities on upper crustal deformation patterns: Evidence from scaled analogue modeling and the Sudbury Basin, Canada. *Earth and Planetary Science Letters*, *297*(3-4), 587–597. doi:10.1016/j.epsl.2010.07.009

Riller, U., Schwerdtner, W. M., Halls, H. C., & Card, K. D. (1999). Transpressive tectonism in the eastern Penokean orogen, Canada consequences for Proterozoic crustal kinematics and continental fragmentation. *Precambrian Research*, *93*(1), 51–70. doi:10.1016/S0301-9268(98)00097-7

Rousell, D. H., Fedorowich, J. S., & Dressler, B. O. (2003). Sudbury Breccia (Canada): A product of the 1850 Ma Sudbury Event and host to footwall Cu-Ni-PGE deposits. *Earth-Science Reviews*, *60*(3-4), 147–174. doi:10.1016/S0012-8252(02)00091-0

Riller, U., & Schwerdtner, W. M. (1997). Mid-crustal deformation at the southern flank of the Sudbury Basin, central Ontario, Canada. *Bulletin of the Geological Society of America*, *109*(7), 841–854. doi:10.1130/0016-7606(1997)109<0841:MCDATS>2.3.CO;2

Romano, D., Holm, D. K., & Foland, K. A. (2000). Determining the extent and nature of Mazatzal-related overprinting of the Penokean orogenic belt in the southern Lake Superior

region, north-central USA. *Precambrian Research*, *104*(1-2), 25–46. doi:10.1016/S0301-9268(00)00085-1

Rubatto, D., & Hermann, J. (2001). Exhumation as fast as subduction? *Geology*, *29*(1), 3–6. http://doi.org/10.1130/0091-7613(2001)?029<0003:EAFAS>?2.0.CO

Santimano, T., & Riller, U. (2012). Revisiting thrusting, reverse faulting and transpression in the southern Sudbury Basin, Ontario. *Precambrian Research*, *200-203*, 74–81. doi:10.1016/j.precamres.2012.01.012

Shanks, W. S., & Schwerdtner, W. M. (1991). Structural analysis of the central and southwestern Sudbury Structure, Southern Province, Canadian Shield. *Canadian Journal of Earth Sciences*, *28*(3), 411–430. doi:10.1139/e91-037

Siddorn, J.P., and Hamm A., (2006). Review of Garson Mine phase 3 exploration program. Unpublished SRK report for Vale, 53p.

Snelling, P.E., (2009). The influences of stress and structure on mining-induced seismicity in Creighton Mine, Sudbury, Canada. MSc thesis. Queens university, Canada, 225p.

Snelling, P. E., Godin, L., & McKinnon, S. D. (2013). The role of geologic structure and stress in triggering remote seismicity in Creighton Mine, Sudbury, Canada. *International Journal of Rock Mechanics and Mining Sciences*, *58*, 166–179. doi:10.1016/j.ijrmms.2012.10.005

Spear, F.S., (1993). Metamorphic phase equilibria and Pressure-Temperature-Time Paths. Mineralogical Society of America Monograph, Washington

Spray, J. G. (1998). Localized shock- and friction-induced melting in response to hypervelocity impact. *Geological Society, London, Special Publications*, *140*(1), 195–204. doi:10.1144/GSL.SP.1998.140.01.14

Spencer, K. J., Hacker, B. R., Kylander-Clark, A. R. C., Andersen, T. B., Cottle, J. M., Stearns, M. A., Seward, G. G. E. (2013). Campaign-style titanite U-Pb dating by laser-ablation ICP: Implications for crustal flow, phase transformations and titanite closure. *Chemical Geology*, *341*, 84–101. doi:10.1016/j.chemgeo.2012.11.012

Stacey, J. S., & Kramers, J. D. (1975). Approximation of terrestrial lead isotope evolution by a two-stage model. *Earth and Planetary Science Letters*, *26*(2), 207–221. doi:10.1016/0012-821X(75)90088-6

Stearns, M. A., Hacker, B. R., Ratschbacher, L., Lee, J., Cottle, J. M., & Kylander-Clark, A. (2013). Synchronous oligocene-miocene metamorphism of the pamir and the north himalaya driven by plate-scale dynamics. *Geology*, *41*(10), 1071–1074. doi:10.1130/G34451.1

Stearns, M. A., Hacker, B. R., Ratschbacher, L., Rutte, D., & Kylander-Clark, A. R. C. (2015). Titanite petrochronology of the Pamir gneiss domes: Implications for middle to deep crust exhumation and titanite closure to Pb and Zr diffusion. *Tectonics*, *34*(4), 784–802. doi:10.1002/2014TC003774

Storey, C. D., Brewer, T. S., & Parrish, R. R. (2004). Late-Proterozoic tectonics in northwest Scotland: One contractional orogeny or several? *Precambrian Research*, *134*(3-4), 227–247. doi:10.1016/j.precamres.2004.06.004

Szentpeteri, K., 2009. Geology and mineralization of the proximal Worthington offset area in the Sudbury igneous complex. Unpublished PhD thesis. Eotvos Lorand University, Hungary, 145p.

Tindle, A. G., & Webb, P. C. (1994). Probe-AMPH—A spreadsheet program to classify microprobe-derived amphibole analyses. *Computers & Geosciences*, *20*(7-8), 1201–1228. doi:10.1016/0098-3004(94)90071-X

Thomson, M. L., Barnett, R. L., Fleet, M. E., & Kerrich, R. (1985). Metamorphic assemblages in the South-Range norite and footwall mafic rocks near the Kirkwood mine, Sudbury, Ontario. *Canadian Mineralogist*.

Verts, L. A., Chamberlain, K. R., & Frost, C. D. (1996). U-Pb sphene dating of metamorphism: the importance of sphene growth in the contact aureole of the Red Mountain pluton, Laramie Mountains, Wyoming. *Contributions to Mineralogy and Petrology*, *125*(2–3), 186–199. http://doi.org/10.1007/s004100050215

Villa, I. M. (1998). Isotopic closure. *Terra Nova*, *10*(1), 42–47. http://doi.org/10.1046/j.1365-3121.1998.00156.x

Villa, I.M., & Williams, M.L. (2013). Geochronology of Metasomatic Events. In : Harlov, D. E., & Austrheim, H (Eds), *Metasomatism and the Chemical Transformation of Rock*. Berlin, Heidelberg: Springer Berlin Heidelberg. doi:10.1007/978-3-642-28394-9

Wintsch, R. P., & Yi, K. (2002). Dissolution and replacement creep: A significant deformation mechanism in mid-crustal rocks. *Journal of Structural Geology*, *24*(6–7), 1179–1193. http://doi.org/10.1016/S0191-8141(01)00100-6

Zenk, M., & Schulz, B. (2004). Zoned Ca-amphiboles and related P-T evolution in metabasites from the classical Barrovian metamorphic zones in Scotland. *Mineralogical Magazine*, *68*(October), 769–786. doi:10.1180/0026461046850218

Supplementary material of Chapter 4

Table 1. Petrographic relationships in the Six Shaft Shear Zone

Sample's name	Lithology	Mineral assemblage	Petrographic features of accessory phases
SSS01	Biotite-rich mylonite	Bt-Qtz-Pl-Hbl-Ep-Cal±Ttn±Ilm±Zr±Ap±Opq	Titanite grains in the sample are observed either as anhedral, stubby and randomly oriented or as fine-grained clusters that align with the mylonitic fabric
SSS03	Hornblende-rich mylonite	Hbl-Bt-Qtz±Ttn±Ilm±Zr±Ap±Opq	Titanite grains define µm-thick bands oriented sub-paralle to thehigh-strain fabric
SSS10	Feldspar-rich mylonite	Pl-Hbl-Qtz-Bt-Ep-Cal±Ttn±Ilm±Zr±Opq	Anhedral, fine grained titanites (10-45µm) align locally with the high-strain fabric
SSS11A	Feldspar-rich mylonite	Pl-Hbl-Qtz-Bt-Ep-Cal±Ttn±Ilm±Opq	Titanite grains with asymmetric wings that show stair-stepping geometry are observed in hornblende-rich domains of the sample
SSS11B	Biotite-rich mylonite	Bt-Hbl-Qtz-Cal-Pl-Ep-±Ttn±Ap±Ilm±Opq	Euhedral and subhedral titanite grains are observed in textural equilibrium with fabric-forming biotite and hornblende grains
SSS15	Biotite-rich mylonite	Bt-Qtz-Pl±Ttn±Ilm±Zr±Ep±Aln±Ap	Anhedral, stubby titanite grains with ilmenite cores show sharp optical boundaries with the biotite flakes.In reflected light mode titanite grains exhibit patchy zoning
SSS18	Quartz-rich mylonite	Qtz-Pl-Bt-Hbl-Ep-Cal±Ttn±Ilm±Ap	The dominant population of titanites in the sample are anhedral andrandomly oriented. A mm-scale subhedral titanite in association with elongated and radiating titanite grains is observed locally
SSS18.3	Biotite-rich mylonite	Bt-Hbl-Qtz-Cal-Pl-Ep-±Ttn±Zr±Aln±Opq	Accessory phases are not recognized in abundance in this sample
SSS18.4	Quartz-rich mylonite	Qtz-Bt-Hbl-Ep-Pl-Cal±Ttn±Ilm±Ap	Recrystallized titanites (10-20µm) are hosted in bands of recrystallized plagioclase. Anhedral 40-50µm size titanites are observed in the biotite-rich domains of the sample
SSS20	Plagioclase-rich mylonite	Pl-Bt-Qtz-Cal-Ep±Ttn±Aln±Zr±Ap	Anhedral and subhedral titanites with ilmenite cores align with the biotite-defined fabric
SSS23	Biotite-rich (proto)mylonite	Bt-Qtz-Kfs-Pl-Ep±Zr±Ttn	Accessory phases are not recognized in abundance in this sample
SSS24	Quartz-rich mylonite	Qtz-Bt-Cal-Ep-Kfs±Ttn±Ilm±Zr±Ap±Mag(?)	Titanite grains with ilmenite cores align with the fabric. Zircon grains are hosted mostly in the biotite flakes
SSS26	Metagranitoid	Qtz-Bt-Kfs-Pl-Ep±Ttn	Subhedral to anhedral titanite grains are observed in association with epidote and plagioclase grains
SSS28	Quartz-rich mylonite	Qtz-Bt-Kfs-Cal-Ep	Distinct petrographic features of accessory are not detected in this sample
SSS1401	Quartz -rich mylonite	Qtz-Bt-Ep-Cal-Pl±Ttn	Anhedral titanites with ilmenite cores align with the mylonitic fabric
SSS1402	Metagranitoid	Kfs-Qtz-Pl-Bt-Ep-Cal-Hbl±Ttn±Zr±Opq	Micrometer-scale zircon grains are hosted in the biotite flakes and show distinct radiation haloes
SSS1403	Biotite-rich mylonite	Bt-Hbl-Qtz-Pl-Ep-Cal±Ttn±Ilm±Ap±Aln	Subhedral to anhedral titanites are arranged in clustered and are preferentially located at the wings of feldspar porphyroclasts. Sharpoptical boundaries are observed also between titanite and biotite.
SSS1404	Biotite-rich mylonite	Bt-Qtz-Pl-Ep±Ttn±Ilm±Zr±Ap	Anhedral titanites with ilmenite cores are arranged in clusters

Table 1 (Supplementary material). Mineral-chemistry data of biotite grains

Locality	Creighton Mine (5400 lvl)	Creighton Mine (5400 lvl)	Creighton Mine (5400 lvl)	Creighton Mine (5400 lvl)	Creighton Mine (5400 lvl)	Creighton Mine (5400 lvl)
Sample	JD12SSS01A	JD12SSS01A	JD12SSS01A	JD12SSS01A	JD12SSS01A	JD12SSS01A
Mineral	Biotite	Biotite	Biotite	Biotite	Biotite	Biotite
SiO2	36.09	36.29	36.01	35.47	36.17	35.59
TiO2	1.63	1.70	1.70	1.72	1.52	2.36
Al2O3	16.64	16.46	16.43	15.86	16.33	15.86
FeO	23.63	23.62	23.66	23.44	23.94	24.17
MnO	0.29	0.28	0.31	0.28	0.29	0.27
MgO	8.18	8.49	8.23	8.23	8.40	7.92
CaO	0.04	bdl	0.03	bdl	bdl	0.16
Na2O	0.02	0.05	0.01	0.04	0.06	0.03
K2O	9.76	9.77	9.50	9.65	9.80	9.21
Cl	0.23	0.22	0.25	0.21	0.23	0.24
Total	96.51	96.88	96.13	94.90	96.74	95.81
Si	5.57	5.58	5.58	5.58	5.58	5.55
Al iv	2.43	2.42	2.42	2.42	2.42	2.45
Al vi	0.60	0.56	0.58	0.52	0.55	0.46
Ti	0.19	0.20	0.20	0.20	0.18	0.28
Fe	3.05	3.04	3.06	3.08	3.09	3.15
Mn	0.04	0.04	0.04	0.04	0.04	0.04
Mg	1.88	1.94	1.90	1.93	1.93	1.84
Ca	0.01	bdl	bdl	bdl	bdl	0.03
Na	0.01	0.01	bdl	0.01	0.02	0.01
K	1.92	1.91	1.88	1.94	1.93	1.83
OH*	4.00	4.00	4.00	4.00	4.00	4.00
Cl	0.06	0.06	0.06	0.06	0.06	0.06
TOTAL	19.69	19.70	19.66	19.72	19.73	19.64
Al total	3.03	2.98	3.00	2.94	2.97	2.91
Fe/Fe+Mg	0.62	0.61	0.62	0.62	0.62	0.63
Mn/Mn+Fe	0.01	0.01	0.01	0.01	0.01	0.01

Table 1 (Supplementary material; continue).

Creighton Mine (5400 lvl) JD12SSS01A Biotite	Creighton Mine (5400 lvl) JD12SSS01A Biotite	Creighton Mine (5400 lvl) JD12SSS01A Biotite	Creighton Mine (5400 lvl JD12SSS01A Biotite	Creighton Mine (5400 lvl) JD12SSS01A Biotite	Creighton Mine (5400 lvl) JD12SSS01A Biotite	Creighton Mine (5400 lvl) JD12SSS01A Biotite
35.79	36.12	36.46	36.34	35.94	36.02	36.39
1.73	1.75	1.52	1.57	1.57	1.77	1.16
16.25	16.22	16.56	16.86	16.47	16.52	17.23
23.54	23.52	23.71	23.10	23.69	23.89	23.12
0.26	0.30	0.31	0.28	0.28	0.30	0.31
8.08	8.36	8.58	8.49	8.06	7.95	8.07
bdl	0.10	bdl	bdl	bdl	bdl	0.20
0.03	0.03	0.04	0.03	0.02	0.13	0.02
9.84	9.84	9.68	9.45	9.78	9.65	9.83
0.22	0.24	0.20	0.24	0.20	0.26	0.28
95.74	96.48	97.06	96.36	96.01	96.49	96.61
5.58	5.58	5.59	5.59	5.58	5.57	5.59
2.42	2.42	2.41	2.41	2.42	2.43	2.41
0.56	0.54	0.58	0.64	0.60	0.58	0.72
0.20	0.20	0.18	0.18	0.18	0.21	0.13
3.07	3.04	3.04	2.97	3.08	3.09	2.97
0.03	0.04	0.04	0.04	0.04	0.04	0.04
1.88	1.93	1.96	1.95	1.87	1.83	1.85
0.00	0.02	bdl	bdl	bdl	bdl	0.03
0.01	0.01	0.01	0.01	0.01	0.04	0.01
1.96	1.94	1.89	1.85	1.94	1.90	1.93
4.00	4.00	4.00	4.00	4.00	4.00	4.00
0.06	0.06	0.05	0.06	0.05	0.07	0.07
19.71	19.71	19.69	19.64	19.70	19.69	19.68
2.98	2.95	2.99	3.05	3.01	3.01	3.12
0.62	0.61	0.61	0.60	0.62	0.63	0.62
0.01	0.01	0.01	0.01	0.01	0.01	0.01

Table 1 (Supplementary material; continue).

Creighton Mine (5400 lvl)	eighton Mine (5400 l	Creighton Mine (5400 lvl)	Creighton Mine (5400 lvl)	Creighton Mine (5400 lvl)	Creighton Mine (5400 lvl)	reighton Mine (5400 lv
JD12SSS01A	JD12SSS01A	JD12SSS01A	JD12SSS02A	JD12SSS02A	JD12SSS02A	JD12SSS02A
Biotite	Biotite	Biotite	Biotite	Biotite	Biotite	Biotite
36.39	36.06	36.28	35.680	36.150	36.540	36.160
1.16	1.70	1.65	1.700	1.750	1.920	2.010
17.23	16.63	16.57	16.830	17.200	17.170	17.290
23.12	23.75	24.12	21.660	21.860	21.860	21.950
0.31	0.31	0.3	0.200	0.200	0.190	0.240
8.07	7.88	7.96	8.590	8.750	8.890	8.730
0.20	0.01	0.02	bdl	0.020	0.020	0.010
0.02	0.10	0.13	0.260	0.080	0.110	0.050
9.83	9.61	9.53	9.380	9.520	9.440	9.590
0.28	0.27	0.25	0.190	0.160	0.170	0.140
96.61	96.32	96.81	94.490	95.690	96.310	96.170
5.59	5.58	5.59	5.567	5.561	5.576	5.537
2.41	2.42	2.41	2.433	2.439	2.424	2.463
0.72	0.61	0.59	0.662	0.680	0.664	0.658
0.13	0.20	0.19	0.199	0.202	0.220	0.231
2.97	3.07	3.11	2.826	2.812	2.790	2.811
0.04	0.04	0.04	0.026	0.026	0.025	0.031
1.85	1.82	1.83	1.998	2.007	2.022	1.993
0.03	0.00	0.00	bdl	0.003	0.003	0.002
0.01	0.03	0.04	0.079	0.024	0.033	0.015
1.93	1.90	1.87	1.867	1.868	1.837	1.873
4.00	4.00	4.00	3.950	3.958	3.956	3.964
0.07	0.07	0.06	0.050	0.042	0.044	0.036
19.68	19.67	19.67	19.658	19.623	19.595	19.615
3.12	3.03	3.01	3.095	3.119	3.088	3.121
0.62	0.63	0.63	0.586	0.584	0.580	0.585
0.01	0.01	0.01	0.009	0.009	0.009	0.011

Table 1 (Supplementary material; continue).

Creighton Mine (5400 lvl	reighton Mine (5400 lvl	Creighton Mine (5400 lvl)	Creighton Mine (5400 lvl)	Creighton Mine (5400 lvl)	Creighton Mine (5400 lvl)	Creighton Mine (5400 lvl)
JD12SSS02A	JD12SSS02A	JD12SSS02A	JD12SSS02A	JD12SSS02A	JD12SSS02A	JD12SSS02A
Biotite	Biotite	Biotite	Biotite	Biotite	Biotite	Biotite
35.750	35.700	36.350	36.320	36.190	35.760	36.610
1.840	1.840	1.750	1.740	1.770	1.770	1.710
16.990	16.980	17.300	17.310	17.090	17.140	17.140
22.180	22.090	21.570	22.020	21.920	21.880	22.110
0.200	0.190	0.210	0.220	0.210	0.220	0.210
8.870	8.660	9.090	9.110	9.090	8.820	9.230
0.080	bdl	0.050	0.030	0.050	0.040	0.030
0.090	0.060	0.130	0.040	0.130	0.120	0.070
9.450	9.730	9.350	9.530	9.350	9.260	9.470
0.240	0.180	0.180	0.190	0.180	0.220	0.190
95.690	95.430	95.980	96.510	95.980	95.230	96.770
5.521	5.531	5.560	5.541	5.550	5.533	5.568
2.479	2.469	2.440	2.459	2.450	2.467	2.432
0.614	0.632	0.679	0.654	0.639	0.659	0.640
0.214	0.214	0.201	0.200	0.204	0.206	0.196
2.865	2.862	2.759	2.810	2.811	2.831	2.812
0.026	0.025	0.027	0.028	0.027	0.029	0.027
2.042	2.000	2.073	2.072	2.078	2.034	2.092
0.013	bdl	0.008	0.005	0.008	0.007	0.005
0.027	0.018	0.039	0.012	0.039	0.036	0.021
1.862	1.923	1.824	1.855	1.829	1.828	1.837
3.937	3.953	3.953	3.951	3.953	3.942	3.951
0.063	0.047	0.047	0.049	0.047	0.058	0.049
19.663	19.675	19.611	19.636	19.635	19.630	19.630
3.093	3.101	3.119	3.113	3.089	3.126	3.072
0.584	0.589	0.571	0.576	0.575	0.582	0.573
0.009	0.009	0.010	0.010	0.010	0.010	0.010

Table 1 (Supplementary material; continue).

Creighton Mine (5400 lvl)	Creighton Mine (5400 lvl)	Creighton Mine (5400 lvl)	Creighton Mine (5400 lvl)	Creighton Mine (5400 lvl)	Creighton Mine (5400 lvl)	Creighton Mine (5400 lvl)
JD12SSS02A	JD12SSS02A	JD12SSS02A	JD12SSS02A	JD12SSS02A	JD12SSS02A	JD12SSS02A
Biotite	Biotite	Biotite	Biotite	Biotite	Biotite	Biotite
35.530	36.690	36.210	36.370	36.260	35.920	36.240
1.700	1.690	1.900	1.880	1.880	1.910	1.780
16.960	17.470	17.090	17.320	17.240	17.140	17.360
21.470	21.560	22.080	22.360	22.190	22.250	22.010
0.220	0.230	0.210	0.230	0.210	0.230	0.180
8.960	9.390	8.790	8.780	8.740	8.620	8.910
0.040	bdl	0.120	0.010	bdl	0.040	0.010
0.040	0.040	0.060	0.090	0.050	0.100	0.170
9.520	9.570	9.590	9.540	9.590	9.460	9.390
0.160	0.130	0.140	0.180	0.150	0.180	0.170
94.600	96.770	96.190	96.760	96.310	95.850	96.220
5.534	5.560	5.550	5.543	5.549	5.532	5.542
2.466	2.440	2.450	2.457	2.451	2.468	2.458
0.647	0.681	0.637	0.654	0.659	0.644	0.671
0.199	0.193	0.219	0.215	0.216	0.221	0.205
2.797	2.732	2.830	2.850	2.840	2.866	2.815
0.029	0.030	0.027	0.030	0.027	0.030	0.023
2.080	2.121	2.008	1.995	1.994	1.979	2.031
0.007	bdl	0.020	0.002	bdl	0.007	0.002
0.012	0.012	0.018	0.027	0.015	0.030	0.050
1.891	1.850	1.875	1.854	1.872	1.858	1.832
3.958	3.967	3.964	3.954	3.961	3.953	3.956
0.042	0.033	0.036	0.046	0.039	0.047	0.044
19.662	19.618	19.634	19.627	19.623	19.635	19.630
3.113	3.120	3.087	3.111	3.110	3.112	3.129
0.573	0.563	0.585	0.588	0.588	0.592	0.581
0.010	0.011	0.010	0.010	0.009	0.010	0.008

Table 1 (Supplementary material; continue).

Creighton Mine (5400 lvl) JD12SSS02A Biotite	Creighton Mine (5400 lvl) JD12SSS03A Biotite	Creighton Mine (5400 lvl) JD12SSS03A Biotite	Creighton Mine (5400 lvl) JD12SSS03A Biotite	Creighton Mine (5400 lvl) JD12SSS03A Biotite	Creighton Mine (5400 lvl) JD12SSS03A Biotite	Creighton Mine (5400 lvl) JD12SSS03A Biotite
36.500	36.320	36.580	36.450	36.270	36.240	34.640
1.740	1.990	1.980	2.030	2.000	2.020	1.820
17.210	16.540	16.740	16.660	16.690	16.720	16.910
21.990	20.920	20.810	20.880	20.970	21.110	22.010
0.240	0.190	0.210	0.210	0.220	0.200	0.260
8.910	10.050	9.930	10.030	9.900	9.940	10.630
0.030	bdl	bdl	0.010	0.010	bdl	bdl
0.050	0.120	0.080	0.110	0.080	0.120	0.050
9.520	9.260	9.510	9.360	9.530	9.520	8.060
0.140	0.150	0.140	0.130	0.130	0.120	0.130
96.330	95.540	95.980	95.870	95.800	95.990	94.510
5.574	5.567	5.578	5.565	5.553	5.540	5.383
2.426	2.433	2.422	2.435	2.447	2.460	2.617
0.671	0.555	0.587	0.564	0.564	0.553	0.480
0.200	0.229	0.227	0.233	0.230	0.232	0.213
2.808	2.682	2.654	2.666	2.685	2.699	2.860
0.031	0.025	0.027	0.027	0.029	0.026	0.034
2.028	2.296	2.257	2.283	2.259	2.265	2.462
0.005	0.000	0.000	0.002	0.002	0.000	0.000
0.015	0.036	0.024	0.033	0.024	0.036	0.015
1.854	1.810	1.850	1.823	1.861	1.856	1.598
3.964	3.961	3.964	3.966	3.966	3.969	3.966
0.036	0.039	0.036	0.034	0.034	0.031	0.034
19.612	19.633	19.627	19.630	19.654	19.667	19.662
3.098	2.988	3.009	2.998	3.012	3.013	3.097
0.581	0.539	0.540	0.539	0.543	0.544	0.537
0.011	0.009	0.010	0.010	0.011	0.010	0.012

Table 1 (Supplementary material; continue).

Creighton Mine (5400 lvl) JD12SSS03A Biotite	Creighton Mine (5400 lvl) JD12SSS03A Biotite	Creighton Mine (5400 lvl) JD12SSS03A Biotite	Creighton Mine (5400 lvl) JD12SSS03A Biotite	Creighton Mine (5400 lvl) JD12SSS03A Biotite	Creighton Mine (5400 lvl) JD12SSS03A Biotite	Creighton Mine (5400 lvl) JD12SSS03A Biotite
36.300	36.330	35.990	36.080	36.450	36.260	36.800
1.990	1.920	1.950	1.930	1.950	1.930	1.930
16.850	16.950	16.720	16.720	16.540	17.000	16.860
20.890	20.650	20.920	20.920	20.790	21.200	20.560
0.200	0.240	0.230	0.230	0.220	0.200	0.220
9.940	9.860	9.780	9.920	9.920	10.150	10.090
0.040	0.030	0.020	0.010	0.030	0.020	0.050
0.080	0.110	0.100	0.120	0.100	0.070	0.160
9.550	9.370	9.510	9.280	9.560	9.370	9.300
0.140	0.000	0.150	0.170	0.130	0.140	0.140
95.980	95.460	95.370	95.380	95.690	96.340	96.110
5.544	5.558	5.540	5.545	5.582	5.518	5.588
2.456	2.442	2.460	2.455	2.418	2.482	2.412
0.577	0.615	0.573	0.574	0.567	0.567	0.606
0.229	0.221	0.226	0.223	0.225	0.221	0.220
2.668	2.642	2.693	2.689	2.663	2.698	2.611
0.026	0.031	0.030	0.030	0.029	0.026	0.028
2.263	2.249	2.244	2.273	2.265	2.302	2.284
0.007	0.005	0.003	0.002	0.005	0.003	0.008
0.024	0.033	0.030	0.036	0.030	0.021	0.047
1.860	1.828	1.867	1.819	1.867	1.819	1.801
3.964	4.000	3.961	3.956	3.966	3.964	3.964
0.036	0.000	0.039	0.044	0.034	0.036	0.036
19.653	19.623	19.666	19.645	19.649	19.657	19.607
3.033	3.057	3.033	3.029	2.985	3.049	3.018
0.541	0.540	0.545	0.542	0.540	0.540	0.533
0.010	0.012	0.011	0.011	0.011	0.009	0.011

Table 1 (Supplementary material; continue).

Creighton Mine (5400 lvl)	Creighton Mine (5400 lvl)	Creighton Mine (5400 lvl)	Creighton Mine (5400 lvl)	Creighton Mine (5400 lvl)	Creighton Mine (5400 lvl)	Creighton Mine (5400 lvl)
JD12SSS04A	JD12SSS04A	JD12SSS04A	JD12SSS04A	JD12SSS04A	JD12SSS04A	JD12SSS04A
Biotite	Biotite	Biotite	Biotite	Biotite	Biotite	Biotite
35.610	36.570	36.670	36.390	36.320	36.580	35.840
1.630	1.630	1.630	1.650	1.600	1.610	1.640
16.420	16.740	16.680	16.750	16.720	16.620	16.710
20.860	20.850	20.810	20.990	20.220	21.110	20.220
0.240	0.200	0.220	0.210	0.200	0.220	0.200
10.340	10.390	10.250	10.430	10.280	10.320	10.520
bdl	bdl	bdl	bdl	bdl	0.020	0.040
0.120	0.110	0.140	0.110	0.110	0.060	0.110
9.090	9.560	9.480	9.530	9.460	9.510	9.170
0.150	0.140	0.150	0.110	0.130	0.180	0.170
94.460	96.190	96.030	96.170	95.040	96.230	94.620
5.530	5.568	5.589	5.546	5.582	5.576	5.535
2.470	2.432	2.411	2.454	2.418	2.424	2.465
0.535	0.573	0.586	0.556	0.610	0.562	0.577
0.190	0.187	0.187	0.189	0.185	0.185	0.190
2.709	2.655	2.653	2.676	2.599	2.691	2.612
0.032	0.026	0.028	0.027	0.026	0.028	0.026
2.393	2.358	2.329	2.370	2.355	2.345	2.422
bdl	bdl	bdl	bdl	bdl	0.003	0.007
0.036	0.032	0.041	0.033	0.033	0.018	0.033
1.800	1.857	1.843	1.853	1.854	1.849	1.806
3.961	3.964	3.961	3.972	3.966	3.953	3.955
0.039	0.036	0.039	0.028	0.034	0.047	0.045
19.696	19.688	19.668	19.702	19.663	19.680	19.673
3.005	3.004	2.997	3.009	3.029	2.986	3.042
0.531	0.530	0.532	0.530	0.525	0.534	0.519
0.012	0.010	0.011	0.010	0.010	0.010	0.010

Table 1 (Supplementary material; continue).

Creighton Mine (5400 lvl)	Creighton Mine (5400 lvl)	Creighton Mine (5400 lvl)	Creighton Mine (5400 lvl)	Creighton Mine (5400 lvl)	Creighton Mine (5400 lvl)	Creighton Mine (5400 lvl)
JD12SSS04A	JD12SSS04A	JD12SSS04A	JD12SSS04A	JD12SSS04A	JD12SSS04A	JD12SSS04A
Biotite	Biotite	Biotite	Biotite	Biotite	Biotite	Biotite
36.440	36.370	36.330	36.620	36.410	36.110	36.480
1.600	1.610	1.650	1.720	1.670	1.670	1.640
16.700	17.170	16.780	16.730	16.580	16.580	16.730
20.560	20.880	20.480	21.050	20.580	20.580	21.200
0.200	0.200	0.180	0.200	0.210	0.220	0.230
10.400	10.380	10.320	10.340	10.270	10.300	10.290
0.020	bdl	bdl	bdl	0.020	0.010	bdl
0.100	0.080	0.120	0.130	0.180	0.130	0.100
9.350	9.400	9.580	9.510	9.400	9.210	9.630
0.130	0.160	0.150	0.160	0.160	0.180	0.140
95.500	96.250	95.590	96.460	95.480	94.990	96.440
5.576	5.530	5.562	5.564	5.581	5.563	5.554
2.424	2.470	2.438	2.436	2.419	2.437	2.446
0.589	0.607	0.590	0.561	0.576	0.573	0.556
0.184	0.184	0.190	0.197	0.193	0.193	0.188
2.631	2.655	2.622	2.675	2.638	2.651	2.699
0.026	0.026	0.023	0.026	0.027	0.029	0.030
2.372	2.353	2.355	2.342	2.347	2.365	2.335
0.003	bdl	bdl	bdl	0.003	0.002	bdl
0.030	0.024	0.036	0.038	0.053	0.039	0.030
1.825	1.823	1.871	1.843	1.838	1.810	1.870
3.966	3.959	3.961	3.959	3.958	3.953	3.964
0.034	0.041	0.039	0.041	0.042	0.047	0.036
19.661	19.671	19.687	19.682	19.675	19.663	19.707
3.012	3.077	3.028	2.996	2.995	3.011	3.002
0.526	0.530	0.527	0.533	0.529	0.529	0.536
0.010	0.010	0.009	0.010	0.010	0.011	0.011

Table 1 (Supplementary material; continue).

Creighton Mine (5400 lvl) JD12SSS04A Biotite	Creighton Mine (5400 lvl) JD12SSS04A Biotite	Creighton Mine (5400 lvl) JD12SSS04A Biotite	Creighton Mine (5400 lvl) JD12SSS04A Biotite
36.390	36.680	36.060	36.220
1.740	1.670	1.690	1.780
16.610	17.090	16.620	16.650
20.670	20.800	20.600	20.840
0.210	0.200	0.200	0.230
10.230	10.370	10.260	10.320
0.010	0.010	0.010	bdl
0.100	0.100	0.180	0.140
9.450	9.620	9.300	9.550
0.160	0.140	0.130	0.140
95.570	96.680	95.050	95.870
5.575	5.552	5.553	5.542
2.425	2.448	2.447	2.458
0.574	0.601	0.570	0.544
0.200	0.190	0.196	0.205
2.648	2.633	2.653	2.667
0.027	0.026	0.026	0.030
2.336	2.340	2.355	2.354
0.002	0.002	0.002	bdl
0.030	0.029	0.054	0.042
1.846	1.857	1.827	1.864
3.958	3.964	3.966	3.964
0.042	0.036	0.034	0.036
19.664	19.677	19.683	19.705
2.999	3.049	3.017	3.003
0.531	0.529	0.530	0.531
0.010	0.010	0.010	0.011

Table 2 (Supplementary material). Mineral chemistry data of amphiboles from the Six Shaft Shear Zone

Locality	Creighton Mine (5400 lvl)	Creighton Mine (5400 lvl)	Creighton Mine (5400 lvl)	Creighton Mine (5400 lvl)	Creighton Mine (5400 lvl)
sample and analytical point	sss1403_Trgt1_Amph1	sss1403_Trgt1_Amph2	sss1403_Trgt1_Amph3	sss1403_Trgt1_Amph4	sss1403_Trgt1_Amph5
Mineral	Amphibole	Amphibole	Amphibole	Amphibole	Amphibole
Textural features	Defines the mylonitic fabric	Defines the mylonitic fabric	Defines the mylonitic fabric	Defines the mylonitic fabric	Defines the mylonitic fabric
SiO2	41.37	41.312	42.418	46.142	42.463
TiO2	0.412	0.416	0.374	0.31	0.449
Al2O3	14.056	14.009	13.341	10.058	13.175
FeO	20.561	20.63	20.761	18.672	20.252
MnO	0.345	0.311	0.327	0.39	0.278
MgO	6.833	6.688	7.296	9.074	7.499
CaO	11.827	11.817	11.929	11.962	11.839
Na2O	1.395	1.265	1.316	1.004	1.223
K2O	0.904	0.897	0.712	0.508	0.806
F	0.037	0.205	0.229	0.122	0.103
Cl	0.175	0.176	0.117	0.056	0.157
Cr2O3	0.008	0.009	0.012	0.015	0.008
NiO	0.043	0.08	0.077	0.088	0.048
Total	97.966	97.815	98.909	98.401	98.3
Si	6.256	6.267	6.338	6.833	6.365
Al ^{iv}	1.744	1.733	1.662	1.167	1.635
Al ^{vi}	0.762	0.772	0.687	0.589	0.693
Ti	0.047	0.772	0.042	0.035	0.051
Cr	0.001	0.047	0.001	0.002	0.001
Fe^{3+}	0.471	0.001	0.554	0.327	0.527
Fe^{2+}	2.130	0.478	2.040	1.985	2.011
Mn	0.044	2.140	0.041	0.049	0.035
Mg	1.541	0.040	1.625	2.003	1.676
Ni	0.005	1.513	0.009	0.010	0.006
Ca	1.916	1.921	1.910	1.898	1.901
Na	0.409	0.372	0.381	0.288	0.355
K	0.174	0.174	0.136	0.096	0.154
F	0.018	0.098	0.108	0.057	0.049
Cl	0.045	0.045	0.030	0.014	0.040
OH*	1.937	1.856	1.862	1.929	1.911
Total	17.500	17.466	17.427	17.282	17.411
Calculation scheme	∑13	∑13	∑13	∑13	∑13
Amphibole group	Calcic	Ca	Ca	Ca	Ca
$(Ca+Na)_{(B)}$	2.000	2.000	2.000	2	2
$Na_{(B)}$	0.084	0.079	0.090	0.102	0.099
$(Na+K)_{(A)}$	0.500	0.466	0.427	0.282	0.411
$Mg/(Mg+Fe^{+2})$	0.420	0.414	0.443	0.502	0.454
$Fe^{+3}/(Fe^{+3}+Al^{vi})$	0.382	0.382	0.446	0.357	0.432
Sum of S2	13.000	13.000	13.000	13.000	13

Table 2 (Supplementary material; continue).

Creighton Mine (5400 lvl)	Creighton Mine (5400 lvl)	Creighton Mine (5400 lvl)	Creighton Mine (5400 lvl)	Creighton Mine (5400 lvl)	Creighton Mine (5400 lvl)
sss1403_Amph6	sss1403_Amph7	sss1403_Amph8	sss1403_Amph9	sss1403_Amph10	sss1403_Amph11
Amphibole	Amphibole	Amphibole	Amphibole	Amphibole	Amphibole
Defines the mylonitic fabric	Defines the mylonitic fabric	Defines the mylonitic fabric	Defines the mylonitic fabric	Defines the mylonitic fabric	Defines the mylonitic fabric
42.423	43.871	41.732	43.068	40.948	42.94
0.375	0.389	0.486	0.429	0.347	0.397
12.62	12.002	13.91	12.933	14.146	12.658
20.009	19.712	20.838	20.28	20.945	20.23
0.346	0.32	0.313	0.358	0.348	0.326
7.558	8.327	7.023	7.636	6.438	7.803
11.792	11.922	11.762	11.949	11.725	11.815
1.122	1.167	1.29	1.248	1.278	1.166
0.695	0.673	0.912	0.758	0.788	0.764
0.178	0.083	0.213	0.192	-0.005	-0.016
0.132	0.11	0.207	0.156	0.179	0.127
0.026	0.012	0.014	0.017	0.026	0.017
0.018	0.035	0.051	0.058	0.033	0.059
97.294	98.623	98.751	99.082	97.196	98.286
6.420	6.517	6.257	6.410	6.238	6.413
1.580	1.483	1.743	1.590	1.762	1.587
0.670	0.618	0.715	0.679	0.778	0.641
0.043	0.043	0.055	0.048	0.040	0.045
0.003	0.001	0.002	0.002	0.003	0.002
0.534	0.518	0.588	0.497	0.544	0.590
1.998	1.930	2.025	2.027	2.125	1.936
0.044	0.040	0.040	0.045	0.045	0.041
1.705	1.844	1.570	1.694	1.462	1.737
0.002	0.004	0.006	0.007	0.004	0.007
1.912	1.897	1.889	1.906	1.914	1.891
0.329	0.336	0.375	0.360	0.377	0.338
0.134	0.128	0.174	0.144	0.153	0.146
0.085	0.039	0.101	0.090	-0.002	-0.008
0.034	0.028	0.053	0.039	0.046	0.032
1.881	1.933	1.846	1.870	1.956	1.975
17.375	17.361	17.439	17.410	17.444	17.374
∑13	∑13	∑13	∑13	∑13	∑13
Ca	Ca	Ca	Ca	Ca	Ca
2	2	2	2	2	2
0.088	0.103	0.111	0.094	0.086	0.109
0.375	0.361	0.439	0.410	0.444	0.374
0.460	0.489	0.437	0.455	0.408	0.473
0.443	0.456	0.451	0.423	0.411	0.479
13	13	13	13	13	13

Table 2 (Supplementary material; continue).

Creighton Mine (5400 lvl)	Creighton Mine (5400 lvl)	Creighton Mine (5400 lvl)	Creighton Mine (5400 lvl)	Creighton Mine (5400 lvl)	Creighton Mine (5400 lvl)
sss1403_Amph12	sss18_4_trgt4_Amph1	sss18_4_trgt4_Amph2	sss18_4_trgt4_Amph3	sss18_4_trgt4_Amph4	sss18_4_trgt4_Amph5
Amphibole	Amphibole	Amphibole	Amphibole	Amphibole	Amphibole
Defines the mylonitic fabric	rim of boudinaged grain	rim of boudinaged grain	rim of boudinaged grain	core of boudinaged grain	core of boudinaged grain
42.45	43.828	42.994	42.77	50.766	44.993
0.495	0.346	0.377	0.357	0.159	0.346
13.069	12.921	12.509	12.267	5.271	11.385
20.333	19.984	19.597	19.783	16.312	19.128
0.338	0.34	0.319	0.317	0.343	0.258
7.653	8.372	7.712	12.827	9.074	8.909
11.566	11.969	11.689	12.162	11.962	12.138
1.163	1.228	1.203	0.592	1.004	1.168
0.833	0.626	0.556	0.225	0.508	0.488
0.198	0.067	0.06	0.095	0.122	0.056
0.232	0.104	0.132	0.025	0.056	0.095
0.035	0.032	0.037	0.016	0.015	0.002
0.078	0.079	0.101	0.111	0.088	0.098
98.443	99.896	97.286	101.547	95.68	99.064
6.342	6.410	6.478	5.945	7.644	6.628
1.658	1.590	1.522	2.009	0.356	1.372
0.643	0.637	0.699	0.000	0.579	0.605
0.056	0.038	0.043	0.037	0.018	0.038
0.004	0.004	0.004	0.002	0.002	0.000
0.701	0.657	0.502	2.203	0.000	0.434
1.839	1.787	1.967	0.096	2.054	1.923
0.043	0.042	0.041	0.037	0.044	0.032
1.704	1.825	1.732	2.658	2.037	1.956
0.009	0.009	0.012	0.012	0.011	0.012
1.851	1.876	1.887	1.811	1.930	1.916
0.337	0.348	0.351	0.160	0.293	0.334
0.159	0.117	0.107	0.040	0.098	0.092
0.094	0.031	0.029	0.042	0.058	0.026
0.059	0.026	0.034	0.006	0.014	0.024
1.848	1.943	1.938	1.952	1.928	1.950
17.347	17.341	17.345	17.011	17.065	17.341
∑13	∑13	∑13	∑13	∑13	∑13
Ca	Ca	Ca	Ca	Ca	Ca
2	2	2	1.970631006	2	2
0.149	0.1245	0.1132	0.1595	0.0702	0.0842
0.347	0.3405	0.3451	0.0399	0.3205	0.3411
0.481	0.5053	0.4682	0.9651	0.4979	0.5043
0.522	0.5076	0.4181	1.0000	0.0000	0.4176
13	13	13	13	12.74436123	13

Table 2 (Supplementary material; continue).

Creighton Mine (5400 lvl) sss18_4_trgt4_Amph6 Amphibole core of boudinaged grain	Creighton Mine (5400 lvl) sss18_4_trgt4_Amph7 Amphibole core of boudinaged grain	Creighton Mine (5400 lvl) sss18_4_Amph8 Amphibole core of boudinaged grain	Creighton Mine (5400 lvl) sss18_4_Amph9 Amphibole core of boudinaged grain	Creighton Mine (5400 lvl) sss18_4_Amph10 Amphibole rim of boudinaged grain
51.577	49.584	48.712	48.712	41.858
0.169	0.215	0.248	0.248	0.371
4.296	6.55	6.931	6.931	13.093
15.951	16.731	17.154	17.154	20.359
0.295	0.354	0.328	0.328	0.289
13.294	11.994	11.459	11.459	7.299
12.094	12.208	12.182	12.182	11.788
0.413	0.688	0.683	0.683	1.172
0.222	0.256	0.381	0.381	0.656
0.247	-0.048	0.133	0.133	0.184
0.007	0.027	0.033	0.033	0.137
-0.006	0.007	0.018	0.018	0.039
0.13	0.106	0.109	0.109	0.105
98.689	98.672	98.371	98.371	97.35
7.427	7.184	7.125	7.125	6.340
0.573	0.816	0.875	0.875	1.660
0.156	0.302	0.320	0.320	0.677
0.018	0.023	0.027	0.027	0.042
-0.001	0.001	0.002	0.002	0.005
0.492	0.436	0.415	0.415	0.598
1.429	1.592	1.683	1.683	1.980
0.036	0.043	0.041	0.041	0.037
2.854	2.591	2.499	2.499	1.648
0.015	0.012	0.013	0.013	0.013
1.866	1.895	1.909	1.909	1.913
0.115	0.193	0.194	0.194	0.344
0.041	0.047	0.071	0.071	0.127
0.112	-0.022	0.062	0.062	0.088
0.002	0.007	0.008	0.008	0.035
1.886	2.015	1.930	1.930	1.877
17.022	17.136	17.174	17.174	17.384
∑13 Ca	∑13 Ca	∑13 Ca	∑13 Ca	∑13 Ca
1.981282555	2	2	2	2
0.1153	0.1050	0.0909	0.0909	0.0872
0.0408	0.1356	0.1739	0.1739	0.3837
0.6664	0.6194	0.5975	0.5975	0.4542
0.7588	0.5903	0.5646	0.5646	0.4692
13	13	13	13	13

Table 4 (Supplementary materials). Trace element analyses of secondary standards MPIDING and GOR128

Element	Mass	MPIDING_T1G (This study) Concentration (oxides in wt%, rest in ppm)
SiO2	oxide	71.03598992
TiO2	oxide	0.755
MnO	oxide	0.146938351
MgO	oxide	3.575836899
CaO	oxide	7.519086152
K2O	oxide	2.464865414
Sc45	45	26.71531797
V51	51	208.2862039
Cr53	53	18.96590741
Co59	59	22.02976409
Ni60	60	11.48132169
Cu63	63	22.7865482
Zn66	66	76.9112184
Rb85	85	100.4335954
Sr88	88	311.9589941
Zr90	90	158.5607453
Nb93	93	9.018565773
Mo95	95	7.76631834
Pd105	105	bdl
Ag107	107	bdl
Sn118	118	2.676671126
Sb121	121	0.326346653
La139	139	76.00520715
Ce140	140	136.0232115
Pr141	141	13.26956337
Nd146	146	44.3175448
Sm147	147	7.144145128
Eu151	151	1.274201276
Gd157	157	5.697225016
Tb159	159	0.785225496
Dy163	163	4.761655291
Ho165	165	0.941598685
Er167	167	2.703800749
Tm169	169	0.381792319
Yb172	172	2.576996077
Lu175	175	0.375787938
Ta181	181	0.454418302
Au197	197	0.118806873
Pb208	208	10.50115601
Bi209	209	0.097615963
Th232	232	33.0105361
U238	238	1.774235678

Table 5 (Supplementary materials; continue).

Standard deviation (1σ)	MPIDING_T1G (Literature values) Concentration (oxides in wt%, rest in ppm)	GOR128_G (This study) Concentration (oxides in wt%, rest in ppm)
1.192880484	58.6	56.78241447
0.015639813	0.755	0.288
0.002798607	0.127	0.194591976
0.072265268	3.75	23.85231436
0.204876265	7.1	6.869366272
0.040330447	1.96	0.043928464
0.892780477	26.9	33.65872828
4.38777963	190	201.7387773
3.340085212	20.9	2362.551734
0.587591693	18.9	109.0203783
0.948961097	10.6	1373.388928
0.828453183	18.8	80.86070669
3.356674998	74	93.71324426
1.724322158	79.7	0.449565005
6.321323163	284	32.52868584
3.41546912	144	10.46598911
0.263750616	8.87	0.103250993
0.458101529	4.2	0.556252197
bdl	bdl	bdl
bdl	0.1	bdl
0.364184039	2	1.291203905
0.118702609	0.25	bdl
1.505964384	70.4	0.111805589
2.788491851	124	0.457136783
0.283610314	12.4	0.093054048
1.182330176	41.4	0.85157936
0.372622594	6.57	0.530124162
0.086843279	1.21	0.263462394
0.32825118	5.31	1.308021588
0.046705394	0.77	0.270529018
0.248239857	4.5	2.084706476
0.053798306	0.86	0.461928934
0.173321002	2.49	1.424488101
0.032830402	0.35	0.228502125
0.169198208	2.38	1.513842193
0.032035779	0.35	0.22579877
0.032472982	0.46	0.027341771
0.04220515	0.1	bdl
0.354848392	11.6	0.35232948
0.039829849	0.1	bdl
0.701144041	31.3	0.016107735
0.092479928	1.71	bdl

Table 6 (Supplementary materials; continue).

Standard deviation (1σ)	GOR 128_G (Literature values) Concentration (oxides in wt%, rest in ppm)
1.131650244	46.1
0.007591447	0.288
0.004363855	0.176
0.529447195	26
0.195806378	6.24
0.001217663	0.036
1.048717083	32.1
4.948385795	189
55.7260576	2272
2.300222587	92.4
22.49212507	1074
1.762446966	63.8
3.657511904	74.7
0.059906288	0.406
0.78539345	30
0.357900909	10
0.030448421	0.099
0.160428716	0.71
bdl	bdl
bdl	<0.5
0.314992886	0.224
bdl	0.01
0.024979056	0.121
0.042213589	0.45
0.019235834	0.1
0.12732075	0.784
0.109017848	0.525
0.040981041	0.264
0.165954292	1.17
0.026832591	0.248
0.151336878	1.98
0.033492354	0.443
0.130535233	1.4
0.025623	0.204
0.149293214	1.41
0.026753181	0.206
0.01063265	0.019
bdl	0.024
0.06019682	0.345
bdl	0.0009
0.007200557	0.008
bdl	0.0123

Table 4 (Supplementary material). Titanite mineral chemistry data (EPMA)

Sample	**JD12SSS01A**	**JD12SSS01A**	**JD12SSS01A**	**JD12SSS01A**	**JD12SSS01A**
DataSet/Point	33 / 1 .	7 / 1 .	8 / 1 .	9 / 1 .	10 / 1 .
Comment	01A_site02_tit_01	01A_site04_tit_01	01A_site04_tit_02	01A_site04_tit_03	01A_site04_tit_04
SiO2	31.129	31.468	30.572	30.373	31.771
TiO2	36.870	30.528	36.103	36.202	32.726
Al2O3	1.708	5.886	1.763	1.982	5.110
CaO	29.001	29.189	28.723	28.789	29.696
FeO	0.754	0.922	0.985	0.933	0.587
MnO	0.048	0.062	0.059	0.035	0.015
MgO	0.006	0.079	0.005	0.014	0.008
Nb2O5	0.183	0.081	0.178	0.143	0.217
ZrO2	bdl	bdl	bdl	0.002	bdl
La2O3	bdl	bdl	bdl	bdl	bdl
Ce2O3	bdl	bdl	bdl	bdl	bdl
Nd2O3	bdl	0.002	0.045	bdl	bdl
Na2O	0.019	0.021	0.007	0.001	bdl
K2O	0.001	0.012	0.030	0.204	0.010
Cl	bdl	0.004	0.002	0.002	0.001
Total	99.718	98.253	98.473	98.680	100.143

Table 4 (Supplementary material; continue)

JD12SSS01A	**JD12SSS01A**	**JD12SSS01A**	**JD12SSS01A**	**JD12SSS01A**	**JD12SSS01A**
11 / 1 .	47 / 1 .	47 / 1 .	48 / 1 .	49 / 1 .	2 / 1 .
01A_site04_tit_05	01A_site07_tit_01	01A_site07_tit_01	01A_site07_tit_02	01A_site07_tit_03	01A_site09_tit_01
31.329	30.997	30.997	31.138	31.388	31.090
35.847	38.165	38.165	35.878	36.509	37.861
2.150	1.357	1.357	2.478	2.393	1.280
29.019	29.433	29.433	29.048	29.072	29.380
1.235	0.460	0.460	0.741	0.668	0.554
0.076	0.047	0.047	0.040	0.027	0.040
0.004	bdl	bdl	bdl	bdl	bdl
0.209	0.053	0.053	0.123	bdl	0.141
bdl	bdl	bdl	0.005	bdl	0.016
bdl	bdl	bdl	bdl	bdl	bdl
bdl	bdl	bdl	bdl	bdl	bdl
0.008	bdl	bdl	bdl	bdl	bdl
0.010	bdl	bdl	0.007	bdl	bdl
0.021	0.007	0.007	0.004	0.076	0.003
0.004	0.005	0.005	0.002	bdl	bdl
99.914	100.523	100.523	99.464	100.134	100.366

Table 4 (Supplementary material; continue)

JD12SSS01A 5 / 1 . 01A_site09_tit_02	**JD12SSS01A** 6 / 1 . 01A_site09_tit_03
30.917	31.025
35.911	37.752
1.926	1.214
28.717	29.206
1.094	0.586
0.059	0.042
bdl	bdl
0.174	0.168
bdl	bdl
bdl	bdl
bdl	bdl
0.029	0.037
0.004	bdl
0.016	0.004
0.010	0.006
98.856	100.041

Table 4 (Supplementary material; continue)

Sample	**JD12SSS02A**	**JD12SSS02A**	**JD12SSS02A**	**JD12SSS02A**	**JD12SSS02A**
DataSet/Point	24 / 1 .	25 / 1 .	26 / 1 .	26 / 1 .	26 / 1 .
Comment	02A_site04a_tit_01	02A_site04a_tit_02	02A_site04a_tit_03	02A_site04a_tit_03	02A_site04a_tit_03
SiO2	30.946	30.770	30.804	30.804	30.804
TiO2	38.105	38.184	37.035	37.035	37.035
Al2O3	1.123	1.105	1.731	1.731	1.731
CaO	29.224	29.250	28.755	28.755	28.755
FeO	0.459	0.478	0.409	0.409	0.409
MnO	0.073	0.050	0.042	0.042	0.042
MgO	bdl	bdl	bdl	bdl	bdl
Nb2O5	0.094	0.127	0.246	0.246	0.246
ZrO2	bdl	bdl	bdl	bdl	bdl
La2O3	bdl	bdl	bdl	bdl	bdl
Ce2O3	bdl	bdl	bdl	bdl	bdl
Nd2O3	bdl	bdl	bdl	bdl	bdl
Na2O	0.012	bdl	bdl	bdl	bdl
K2O	0.006	0.025	0.027	0.027	0.027
Cl	0.006	0.001	0.000	0.000	0.000
Total	100.049	99.990	99.048	99.048	99.048

Table 4 (Supplementary material; continue)

JD12SSS02A	**JD12SSS02A**	**JD12SSS02A**	**JD12SSS02A**	**JD12SSS02A**	**JD12SSS02A**	**JD12SSS02A**
50 / 1 .	51 / 1 .	52 / 1 .	60 / 1 .	61 / 1 .	62 / 1 .	63 / 1 .
02A_site05a_tit_01	02A_site05a_tit_02	02A_site05a_tit_03	02A_site08_tit_01	02A_site08_tit_02	02A_site10_tit_01	02A_site10_tit_02
30.859	31.063	30.847	30.938	31.069	30.924	31.011
37.101	33.822	37.160	37.862	37.648	37.969	37.966
1.627	3.718	1.653	1.412	1.679	1.303	1.309
28.946	28.413	28.952	29.172	29.296	29.104	29.180
0.488	1.011	0.520	0.368	0.411	0.536	0.441
0.085	0.066	0.045	0.050	0.029	0.022	0.064
bdl	0.057	bdl	bdl	bdl	bdl	bdl
0.291	0.493	0.566	0.354	0.277	0.095	0.171
bdl	0.080	0.019	0.012	0.004	bdl	bdl
bdl	bdl	bdl	bdl	bdl	bdl	bdl
bdl	bdl	bdl	bdl	bdl	bdl	bdl
bdl	bdl	bdl	bdl	0.004	0.020	0.016
bdl	bdl	bdl	bdl	0.009	0.001	0.000
0.000	0.063	0.004	0.018	0.024	0.004	0.000
0.005	0.018	0.006	0.002	0.006	0.000	0.002
99.423	98.826	99.772	100.189	100.458	99.977	100.162

Table 4 (Supplementary material; continue)

Sample	**JD12SSS04A**	**JD12SSS04A**	**JD12SSS04A**	**JD12SSS04A**	**JD12SSS04A**
DataSet/Point	103 / 1 .	104 / 1 .	105 / 1 .	106 / 1 .	107 / 1 .
Comment	04A_site_16b_tit_01	04A_site_16b_tit_02	04A_site_16b_tit_03	04A_site_16b_tit_04	04A_site_16b_tit_05
SiO2	30.460	30.648	30.547	30.465	30.410
TiO2	37.384	36.715	36.742	36.930	37.173
Al2O3	1.605	1.898	1.993	1.753	1.831
CaO	28.819	29.085	28.845	28.980	29.024
FeO	0.423	0.660	0.623	0.597	0.692
MnO	0.080	0.050	0.059	0.040	0.045
MgO	0.000	0.005	bdl	0.001	bdl
Nb2O5	0.375	0.230	0.197	0.119	0.123
ZrO2	bdl	bdl	0.005	0.000	0.019
La2O3	bdl	bdl	bdl	bdl	bdl
Ce2O3	bdl	bdl	bdl	bdl	bdl
Nd2O3	0.021	0.020	0.008	0.014	0.039
Na2O	0.014	0.007	0.033	0.000	0.012
K2O	0.016	0.020	0.066	0.095	0.119
Cl	bdl	0.004	bdl	0.004	0.004
Total	99.196	99.343	99.116	98.999	99.493

Table 4 (Supplementary material; continue)

JD12SSS04A 108 / 1 . 04A_site_16b_tit_06	**JD12SSS04A** 91 / 1 . 04A_site01_tit_01	**JD12SSS04A** 91 / 1 . 04A_site01_tit_01	**JD12SSS04A** 92 / 1 . 04A_site01_tit_02	**JD12SSS04A** 92 / 1 . 04A_site01_tit_02	**JD12SSS04A** 93 / 1 . 04A_site01_tit_03
30.506	30.969	30.969	30.588	30.588	30.545
37.488	37.202	37.202	37.034	37.034	36.636
1.751	1.657	1.657	1.642	1.642	1.718
28.944	28.769	28.769	28.446	28.446	28.240
0.661	0.568	0.568	0.519	0.519	0.578
0.050	0.060	0.060	0.068	0.068	0.055
0.013	bdl	bdl	bdl	bdl	bdl
0.100	0.347	0.347	0.429	0.429	0.352
0.000	0.000	0.000	0.000	0.000	0.000
bdl	bdl	bdl	bdl	bdl	bdl
bdl	bdl	bdl	bdl	bdl	bdl
0.024	0.023	0.023	0.026	0.026	0.005
0.000	0.011	0.011	0.014	0.014	0.000
0.194	0.015	0.015	0.005	0.005	0.020
0.005	bdl	bdl	bdl	bdl	bdl
99.735	99.622	99.622	98.771	98.771	98.149

Table 4 (Supplementary material; continue)

JD12SSS04A	**JD12SSS04A**	**JD12SSS04A**	**JD12SSS04A**	**JD12SSS04A**	**JD12SSS04A**
16 / 1 .	17 / 1 .	18 / 1 .	19 / 1 .	20 / 1 .	21 / 1 .
04A_site02a_tit_01	04A_site02a_tit_02	04A_site02a_tit_03	04A_site02a_tit_04	04A_site02a_tit_05	04A_site02a_tit_06
30.984	30.944	30.474	30.511	30.933	31.203
35.722	37.687	36.576	37.500	37.376	37.870
2.758	1.537	1.851	1.404	1.621	1.650
29.224	29.340	28.079	28.444	28.926	29.338
0.421	0.298	0.640	0.514	0.578	0.560
0.040	0.044	0.078	0.055	0.048	0.040
bdl	bdl	bdl	bdl	0.004	bdl
0.111	0.072	0.393	0.448	0.219	0.097
0.017	0.000	0.000	0.014	bdl	0.037
bdl	bdl	bdl	bdl	bdl	bdl
bdl	bdl	bdl	bdl	bdl	bdl
bdl	0.002	0.038	0.020	0.007	bdl
0.013	0.000	0.034	0.009	0.006	0.004
0.002	0.000	bdl	0.036	0.033	0.068
bdl	0.003	bdl	bdl	0.003	0.001
99.292	99.927	98.163	98.954	99.754	100.870

Table 4 (Supplementary material; continue)

JD12SSS04A 94 / 1 . 04A_site04a_tit_01	**JD12SSS04A** 95 / 1 . 04A_site04a_tit_02	**JD12SSS04A** 98 / 1 . 04A_site06a_tit_01	**JD12SSS04A** 99 / 1 . 04A_site06a_tit_02	**JD12SSS04A** 100 / 1 . 04A_site06a_tit_03
30.810	30.650	30.856	31.169	30.770
37.267	37.463	37.418	37.694	37.514
1.962	1.585	1.621	1.624	1.563
29.145	28.800	28.760	29.465	28.542
0.552	0.455	0.505	0.513	0.623
0.043	0.057	0.066	0.031	0.067
0.004	0.000	bdl	0.001	0.002
0.134	0.262	0.271	0.060	0.360
bdl	0.006	bdl	bdl	0.010
bdl	bdl	bdl	bdl	bdl
bdl	bdl	bdl	bdl	bdl
bdl	bdl	bdl	bdl	0.014
0.031	0.000	0.000	0.001	bdl
0.002	0.011	0.022	0.052	0.010
bdl	bdl	0.002	bdl	bdl
99.950	99.289	99.521	100.610	99.476

Table 5 (Supplementary material). LA-ICP-MS analytical conditions

	U-Pb	Trace elements
Instrument model	RESOlution SE ArF (Argon-Fluoride)	RESOlution SE ArF (Argon-Fluoride)
Ablation cell	Laurin S155 (dual volume design)	Laurin S155 (dual volume design)
Laser wavelength	193nm	193nm
Pulse width	3ns	3ns
Fluence (energy density)	2-3 J/cm2	4.5 J/Cm^2
Energy distribution	Flat homogenised	Flat homogenised
Repetition rate	2HZ	10HZ
Carrier Gas	He (ca. 300ml/min), Ar make-up gas combined using a y-piece ca. 50% along sample line	He (ca. 300ml/min), Ar make-up gas combined using a y-piece ca. 50% along sample line
Ablation mode	static ablation	static ablation
Spot size	20-30µm	15-40µm
ICP parameters		
ICPMS	Agilent 7500cs (quadrupole)	Agilent 7500cs (quadrupole)
RF power	1300W	1200W
Acquisition parameters		
Scanning mode	Peak hopping	Peak hopping
Acquisition mode	time-resolved analysis	time-resolved analysis
Analysis time	20 s blank and 40 s ablation	20 s blank and 40 s ablation
Dwell time per isotope	202Hg-0.02 s,204Pb-0.02 s,206Pb-0.02 s,207Pb-0.04 s,208Pb-0.02 s,232Th-0.02 s 235U-0.03 s, 238U-0.02 s	information on the manuscript

Table 7 (Supplementary material). U-Pb isotopic data

Sample	Target	$^{238}U/^{206}Pb$	$^{238}U/^{206}Pb$ err(2σ)	$^{207}Pb/^{206}Pb$	$^{207}Pb/^{206}Pb$ err(2σ)
SSS1403	1403_1.4_20µm	2.36407	0.16766	0.36100	0.02800
SSS1403	1403_1.5_25µm	2.00803	0.11290	0.51700	0.03600
SSS1403	1403_15.3_25µm	2.47525	0.12866	0.37800	0.02700
SSS1403	1403_4.1_25µm	2.60417	0.16276	0.33800	0.02700
SSS1403	1403_12.3a_25µm	2.53807	0.16749	0.37000	0.03200
SSS15	6c_1_30µm	1.65837	0.08526	0.55000	0.02600
SSS15	20b_30µm	1.40845	0.06348	0.64500	0.03000
SSS15	1.1_25µm	1.92678	0.10395	0.50000	0.03300
SSS15	2.1_25µm	1.49701	0.09412	0.61700	0.04400
SSS15	3.1_25µm	1.51057	0.08443	0.66900	0.04700
SSS15	4.2_30µm	1.73913	0.07561	0.61300	0.03200
SSS15	6.2_25µm	0.56818	0.07102	0.83500	0.09000
SSS15	8.1_30µm	0.93023	0.06403	0.72700	0.04700
SSS15	11.2a_25µm	1.99601	0.13147	0.50900	0.04100
SSS15	11.2b_25µm	1.09290	0.10391	0.66600	0.04000
SSS15	26.2_25µm	0.78740	0.06820	0.88700	0.07500
SSS15	27.3a_30µm	0.55249	0.04273	0.90400	0.05200
SSS15	27.3b_30µm	0.72464	0.08927	0.82600	0.07100
SSS15	28.2_30µm	1.47275	0.06073	0.64300	0.03000
SSS15	29.1_25µm	1.13766	0.06989	0.67700	0.03300

Table 8 (Supplementary material; continue).

Trace element analysis	Eu/Eu*	Σ(Y+REE)	length (long axis in µm)
-	-	-	160
-	-	-	200
-	-	-	220
-	-	-	140
-	-	-	220
-	-	-	220
-	-	-	330
YES	0.697	10569.89927	190
-	-	-	145
YES	0.714	11644.17833	160
-	-	-	195
-	-	-	230
-	-	-	170
-	-	-	150
-	-	-	150
-	-	-	330
YES	0.667	6915.387	280
YES	0.667	6915.387	280
-	-	-	135
-	-	-	275

Table 9 (Supplementary material; continue).

SSS11B	7_2rim_20µm	1.53374	0.13644	0.60700	0.05000
SSS11B	10_3mantle_20µm	1.65289	0.11201	0.52300	0.04300
SSS11B	27_3_25µm?	1.80180	0.10389	0.56100	0.03700
SSS11B	31.2a_25µm	1.92308	0.10355	0.53100	0.03800
SSS11B	31.2b_25µm	1.82149	0.11612	0.59900	0.06700
SSS11A	2_3_30µm	1.76991	0.06892	0.57500	0.02300
SSS11A	3_4a_30µm	1.71233	0.07623	0.52000	0.02100
SSS11A	3_4b_30µm	2.08333	0.08681	0.47400	0.01900
SSS11A	4_2_30µm	1.72414	0.07134	0.56600	0.01900
SSS11A	5_2_30µm	1.60000	0.06400	0.63000	0.02800
SSS11A	6_2_30µm	1.72712	0.08352	0.54700	0.02400
SSS11A	8_4_30µm	1.96464	0.08492	0.51100	0.02200
SSS11A	11_2_30µm	1.85185	0.07545	0.53400	0.02000
SSS11A	12_3_30µm	1.67224	0.06991	0.54300	0.02000
SSS11A	13_3_30µm	1.24069	0.06927	0.66400	0.03400
SSS11A	14_4_30µm	1.51976	0.07622	0.60600	0.02600
SSS11A	15_2_30µm	1.70648	0.07863	0.56100	0.02400
SSS11A	17_2_30µm	1.89753	0.07561	0.48300	0.01900
SSS11A	20_3_30µm	2.04499	0.08364	0.49500	0.02200
SSS11A	21_2_30µm	1.60514	0.06956	0.59600	0.02700
SSS11A	22_1_30µm	1.79533	0.08380	0.53900	0.02600
SSS11A	25_4_30µm	1.76056	0.08059	0.55700	0.02200

Table 10 (Supplementary material; continue).

YES	0.801	3446.016001	80
YES	0.687	7726.505	165
–	–	–	175
–	–	–	310
–	–	–	310
YES	1.973	7723.346	260
YES	2.047	8911.702	290
YES	2.047	8911.702	290
YES	2.269	9206.478	450
YES	1.809	7686.190	130
YES	1.991	9230.891	260
YES	2.073	6181.195	240
–	–	–	390
YES	1.870	5069.254	500
YES	1.940	5302.165	320
–	–	–	290
–	–	–	140
–	–	–	170
YES	1.412	6081.411	245
–	–	–	160
–	–	–	230
YES	1.248	7506.098	190

Table 11 (Supplementary material; continue).

SSS03	2_1_30µm	1.11111	0.06049	0.73400	0.03300
SSS03	4_2_30µm	1.08932	0.05577	0.71500	0.03400
SSS03	5_2_30µm	1.48588	0.08831	0.64100	0.03500
SSS03	7_3_25µm	0.95877	0.08365	0.73400	0.05400
SSS03	11_2_25µm	0.70771	0.05009	0.80000	0.04100
SSS03	15_3a_30µm	0.98232	0.05693	0.71600	0.03300
SSS03	15_3b_25µm	1.32275	0.10148	0.72400	0.06000
SSS03	33c4a_20µm	1.16686	0.11846	0.74100	0.09300
SSS03	33c4b_20µm	0.80000	0.08960	0.87000	0.12000
SSS03	34_3_20µm	0.80000	0.07040	0.81900	0.06600
SSS03	3_3_30µm	1.27877	0.08340	0.64600	0.03700
SSSX18_4_2	X18_4_2	2.07039	0.13288	0.49400	0.03700
SSSX18_4_3	X18_4_3	2.34192	0.18099	0.38600	0.04100
SSS18_4	18_4_Target6.4-25µm	3.11236	0.15499	0.16210	0.00650

Table 12 (Supplementary material; continue).

-	-	-	300
-	-	-	95
YES	0.928	4716.445	140
-	-	-	125
-	-	-	150
YES	0.854	4228.252	140
YES	0.854	4228.252	140
-	-	-	135
-	-	-	135
YES	0.897	3446.831969	85
-	-	-	215
-	-	-	230
-	-	-	330
YES	0.775	13472.92419	240

Titanite and apatite trace element data are provided in the supplementary materials section in the online version of the manuscript "*Dating shear zones with plastically deformed titanite: New insights into the orogenic evolution of the Sudbury impact structure (Ontario, Canada)***" that has been published in the Journal **Precambrian Research.**

Chapter 5. Polyorogenic reworking of shear zones in the Southern Province during three accretionary episodes: A tell-tale story from *in-situ* U-Pb titanite geochronology

Konstantinos Papapavlou[1*], James R. Darling[1], Peter C. Lightfoot[2], Lisa Gibson[4], Robert Pelkey[4], Stephanie Lasalle[1], Craig D. Storey[1], Desmond Moser[3]

[1]School of Earth and Environmental Sciences, University of Portsmouth, Portsmouth, PO1 3QL, UK

[2]Harquail School of Earth Sciences, Laurentian University, Sudbury, Ontario, P3E 2C6, Canada

[3]Department of Earth Sciences, University of Western Ontario, London, Ontario, N6A 5B7, Canada

[4]VALE Technology Development (Canada) Limited, Brownfield Exploration, Copper Cliff P0M 1NO, Ontario, Canada

Abstract

Ductile shear zones at the deeper levels of the Creighton Mine (Sudbury, South Range) control the geometry and location of high metal tenor Ni-Cu-PGE sulphide ore bodies. *In – situ* U-Pb titanite age dating of shear-hosted titanite grains from three deep-seated epidote-amphibolite facies structures indicate reworking during three distinct orogenic events related with the Yavapai (ca. 1.77 – 1.7 Ga), Mazatzalian – Labradorian (1.7 – 1.6 Ga), and Chieflakian (1.5 – 1.4 Ga) events. No evidence of operation or reworking of the examined shear zones during the Penokean orogeny (1.9 – 1.8 Ga) is recorded in the examined titanite age populations. The ore-controlling character of the examined structures and new petrographic/microtectonic data indicate that the reworking of the shear zones during these events was accompanied by sulphide remobilization. At a regional scale, the recorded age populations show that the South Range of the Sudbury structure, and the Southern Province, exhibit a similar tectonothermal evolution to the accretionary provinces of the southwestern United States.

Keywords: Sudbury impact structure, Southern Province, Orogenesis, Shear zone, Sulphide remobilisation

1. Introduction

The 1.85 Ga Sudbury structure is a heavily mineralised, multi-ring impact crater, located at the crossroad of three Precambrian orogenic provinces, at the Southern edge of the Canadian shield (Krogh et al., 1982, Spray et al., 2004). During and after the impact event, the docking of continental and oceanic exotic terranes along a transcontinental convergent margin, which extended from Baltica to Australia, led to the accretionary growth and crustal assembly of the Laurentia craton (Karlstrom et al., 2001, Whitmeyer and Karlstrom., 2007). In the wider area of the Sudbury structure, geochronological data record five distinct events characterised as the: (a) Penokean (1.89 – 1.83 Ga ; Sims et al., 1989), (b) Yavapai (1.77 – 1.7 Ga ; Piercey et al., 2007) (c) Mazatzalian – Labradorian (1.7 – 1.6 Ga ; Bailey et al., 2004, Papapavlou et al., 2017), (d) Chieflakian (1.5 – 1.4 Ga ; Fueten and Redmond., 1997, Corfu and Easton., 2000) and (e) the long-lived Grenvillian orogeny (1.3 – 1.0 Ga ; Krogh, 1994). The influence of these events on the tectonothermal evolution of the Southern Province and the mineralised Sudbury impact structure are not fully recognised and remain under dispute (Riller and Schwerdtner., 1997, Raharimarefa et al., 2014). For instance, different generations of co-axial folds that have been characterised as Penokean structures, based strictly only on the structural geometry of the deformation fabrics, may be associated with significantly younger orogenic overprints (Schulz and Cannon, 2007). Thus, to resolve similar controversies, we test the hypothesis of polyorogenic activity at the South Range of the Sudbury structure through the age dating of different ductile shear zones. Drillcore samples from three ore-controlling high-strain shear zones from the heavily mineralized Creighton Mine, at the South Range of the Sudbury structure, were accessed in this study. The different shear zones were selected for petrographic-microtectonic analysis, accessory phase electron beam imaging (SEM/BSE), and *in-situ* U-Pb titanite geochronology. Thus, the main aims of this study are to: (a) bracket the timing of orogenic events that induced shear zone operation/reworking, (b) characterise in detail micro to meso-scale structural features and syn-kinematic assemblages of these uniquely exposed ore-controlling mylonitic shear zones and (c) place new temporal constraints, where possible, on the tectonic remobilization of shear-controlled Ni-Cu-PGE sulphide ore bodies at the South Range of the Sudbury structure.

2. Regional geology of the Sudbury impact structure

The Sudbury structure straddles the Superior, Southern, and Grenville orogenic provinces and is one of the largest and oldest impact structures on the planet that hosts vast reserves and resources of Ni-Cu-Platinum Group Elements (PGE) mineralisation (Ames and Farrow., 2007, **Figure 1a**). The Archean Superior province is the core of the North America craton, and was built by a collage of tectonostratigraphic terranes (i.e. sub-provinces) with distinct magmatic and tectonometamorphic histories (Card et al., 1990, Easton, 2000). At its southern margin, the Superior Province neighbours with the Southern Province that comprise chiefly plutonic bodies and Paleoproterozoic (2.5 – 2.2 Ga) supracrustal units of the Huronian Supergroup (**Figure 1b**) (Zolnai et al., 1983, Young et al., 2001). Further southwards, the Grenville Province (1.3 – 1.0 Ga) hosts deep-seated amphibolite to granulite facies crystalline rocks that record a protracted history of convergent-style orogenesis that dominated the south-eastern margin of Laurentia during the Mesoproterozoic (**Figure 1b**) (Tollo et al., 2004 and references therein). Three major impact-related units are recorded in the Sudbury structure (**Figure 1c**): (a) the pseudotachylitic Sudbury Breccia, (b) the Sudbury Igneous Complex and (c) the Sudbury Basin (Pye et al., 1984 and references therein). The northern margin of the Sudbury structure (North Range, **Figure 1c**) is bounded by a complex of Neo-Archean tonalitic gneisses (i.e. the Levack Gneiss Complex) whereas the Southern (South Range, **Figure 1c**) by a complex of plutons , volcanosedimentary, and siliciclastic units of the Huronian Supergroup in the Southern Province (Ames et al., 2008). The post-impact metamorphic evolution of the crater is characterised by greenschist to epidote-amphibolite facies conditions (Fleet et al., 1987). The maximum P-T conditions (P = 4-5 Kbar, T = 550 - 600°C) are recorded in the South Range, in spatial association with a crustal-scale system of moderately dipping, top-to-the-NW ductile thrusts that is named as the South Range Shear Zone (**Figure 1**)(Riller, 2005).

2.1 Shear zones in the Creighton Deep Mine: 118 and 315/Hodder families

Creighton Mine is located at the South Range of the impact structure within an embayment of the Sudbury Igneous Complex that hosts more than 200 Mt of Ni-Cu-PGE mineralization (**Figure 1c**) (Lightfoot, 2007). The majority of the magmatic ore bodies in Creighton are located either in the inclusion-bearing Sublayer unit at the base of the impact

melt sheet, or in association with Huronian metamafic and plutonic bodies of the footwall (**Figure 2**). Mylonitic shear zones are spatially associated with sulphide ore bodies at different depths of Creighton Mine (O'Donell, 1979). Specifically, at depths below 2.5 km borehole data indicate the presence of a steeply-dipping, ENE-striking, system of biotite-rich tectonites, that is named as the 118 system of shear zones (Snelling et al., 2013) (**Figure 2**). The 118 system intersects at low angle with the mineralised basal contact of the Sudbury Igneous Complex and comprises the following shear zones: (a) the Fresh Air Raise (FAR), (b) the Plum, (c) the 402, (d) the Return Air Raise (RAR), (d) the Northwest (NW) and (e) the North of NW shear zones (Snelling et al.,2013, Vale ltd pers. com). These shear zones are sub-parallel and have a spacing of approximately 60 meters, based on wireframe models and underground geological maps. A structurally distinct family of south-dipping mineralised shear zones with listric geometry, that becomes prevalent at the deeper levels of the Creighton Mine, is the Hodder/315 system. The present understanding, based on drillcore data and the orientation of shear fabrics, is that the Hodder/315 family of shear zones constitutes the down-dip extension of structures that define the contractional system of the South Range Shear Zone (**Figures 1 and 2**).

2 Structural framework of the Creighton Deep Mine

A drillcore-based wireframe model and the mesoscopic analysis of drillcore samples suggest that in the deeper levels of the Creighton Mine are recognised two phases of ductile deformation (D_1 – D_2). The presented wireframe model (**Figure 3**) is a 2D representation of a 3D model that has been constructed on Datamine using data from 2000 to 5000 boreholes (Lightfoot., 2016). Upright F_1 antiformal folds in footwall-hosted sulphide ore bodies were likely produced during the first increment of ductile strain (**Figure 3**). The D_1 deformation phase is expressed with a S_1 foliation defined chiefly by the shape-preferred orientation of biotite and hornblende grains axial planar to the F_1 antiformal folds. This S_1 foliation constitutes the main planar fabric in the S-L tectonites of the 118 shear zone system. A penetrative S_{1m} mylonitic fabric is observed preferentially in the biotite-rich domains of the 118 system indicating strain localization in rheollogically weaker, phyllosilicate-rich domains. Similarly with other mines of the South Range (e.g. Thayer Lindsley Mine, Bailey et al., 2004)

the basal contact of the Sudbury Igneous Complex in the Creighton Mine shows evidence of folding (**Figure 3, F2**

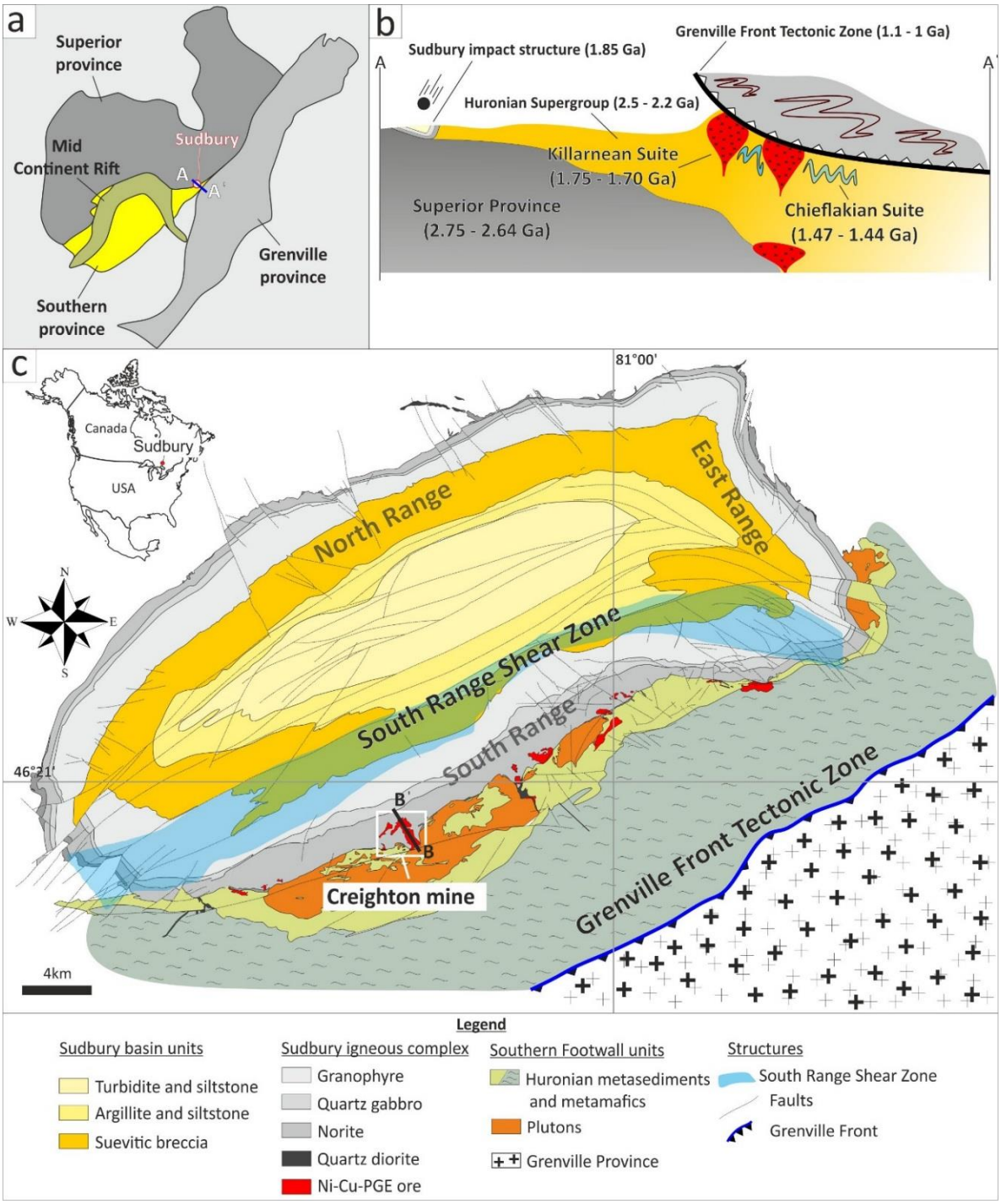

Figure 1. Synthetic figure that depicts : (a) The location of the Sudbury impact structure relative to the main orogenic provinces in North America. With A-A' is indicated a schematic crustal-scale cross section., (b) Schematic cross section A-A' that shows the location of the Sudbury impact structure relative to Superior, Southern, and Grenville provinces (modified from Crofu and Easton., 2000), (c) Simplified map of the Sudbury impact structure modified from Ames et al., 2008. With B-B' is indicated the cross section of Creighton Mine in **Figure 2**.

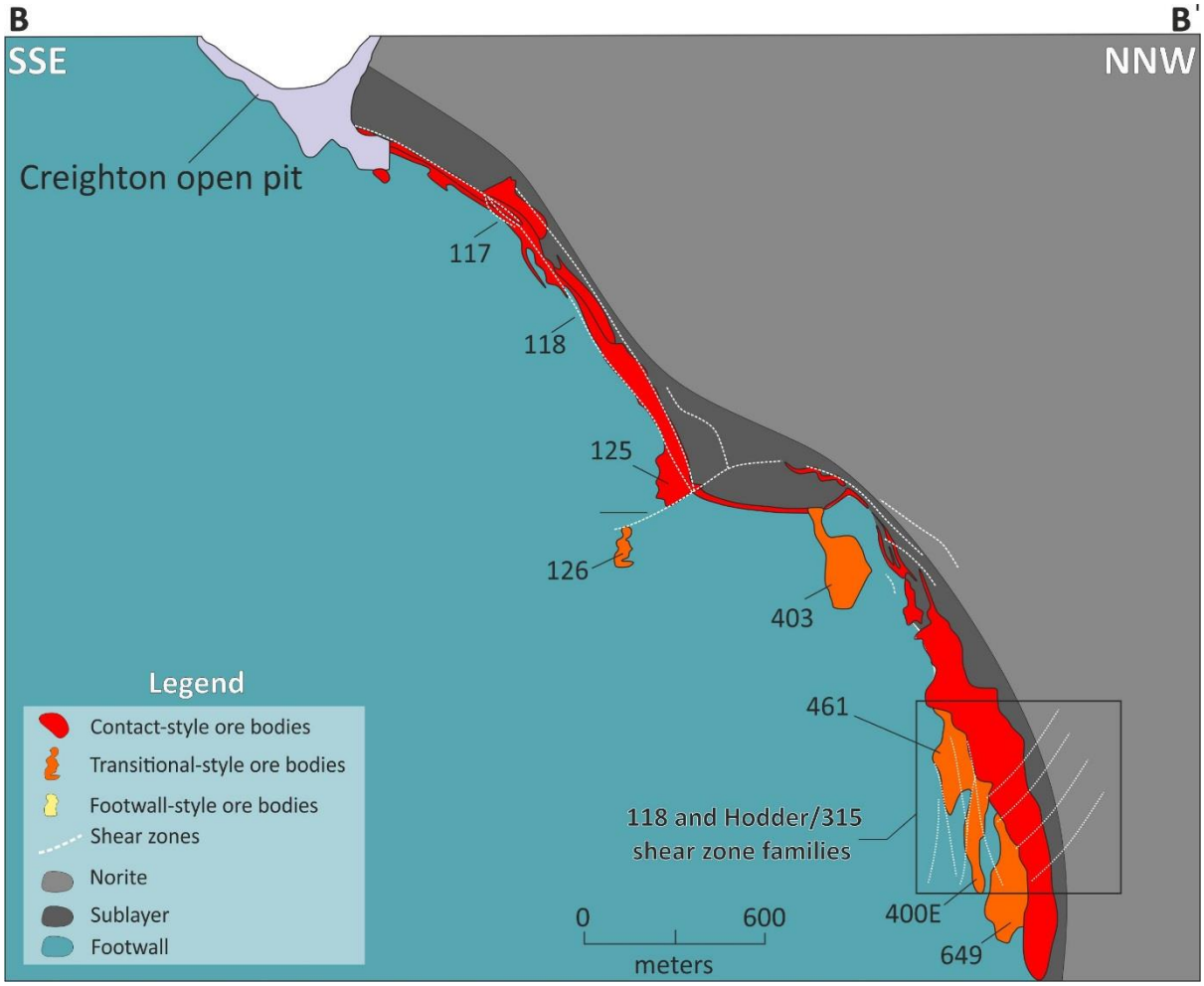

Figure 2. Cross section of Creighton Mine that depicts the relation of mylonitic shear zones with Ni-Cu-PGE sulphide ore bodies at the basal contact of the Sudbury Igneous Complex and the footwall of the South Range. In the rectangle is shown schematically the spatial relationship between the 118 and Hodder/315 shear zone systems.

folds). This folding episode is attributed to a D_2 deformation phase that produced moderately inclined open folds with south-dipping axial planes sub-parallel to the folded basal contact of the Sudbury Igneous Complex. Wireframe modelling shows that F_2 folds with similar geometric features are recorded also in footwall-hosted ore bodies (**Figure 3**). The F_2 folds host an axial planar S_2 fabric defined chiefly by biotite, that is locally transposed to the S_{2m} mylonitic fabric of the Hodder/315 shear zone system. In the wireframe model the movement of the D_2 shear zones induced a drag folding effect to the S_{1m} fabrics of the D_1 shear zones showing the overprinting relation between the two generations of shear fabrics (**Figure 3;**

relationship between plum and 315 shear zones). The target structures in this study have been classified into two families based on the orientation of the shear fabrics: (a) the steeply-dipping D_1 shear zones of the 118 family (RAR and Plum shear zones), and (b) the south-dipping D_2 shear zones of the Hodder/315 family (315 shear zone).

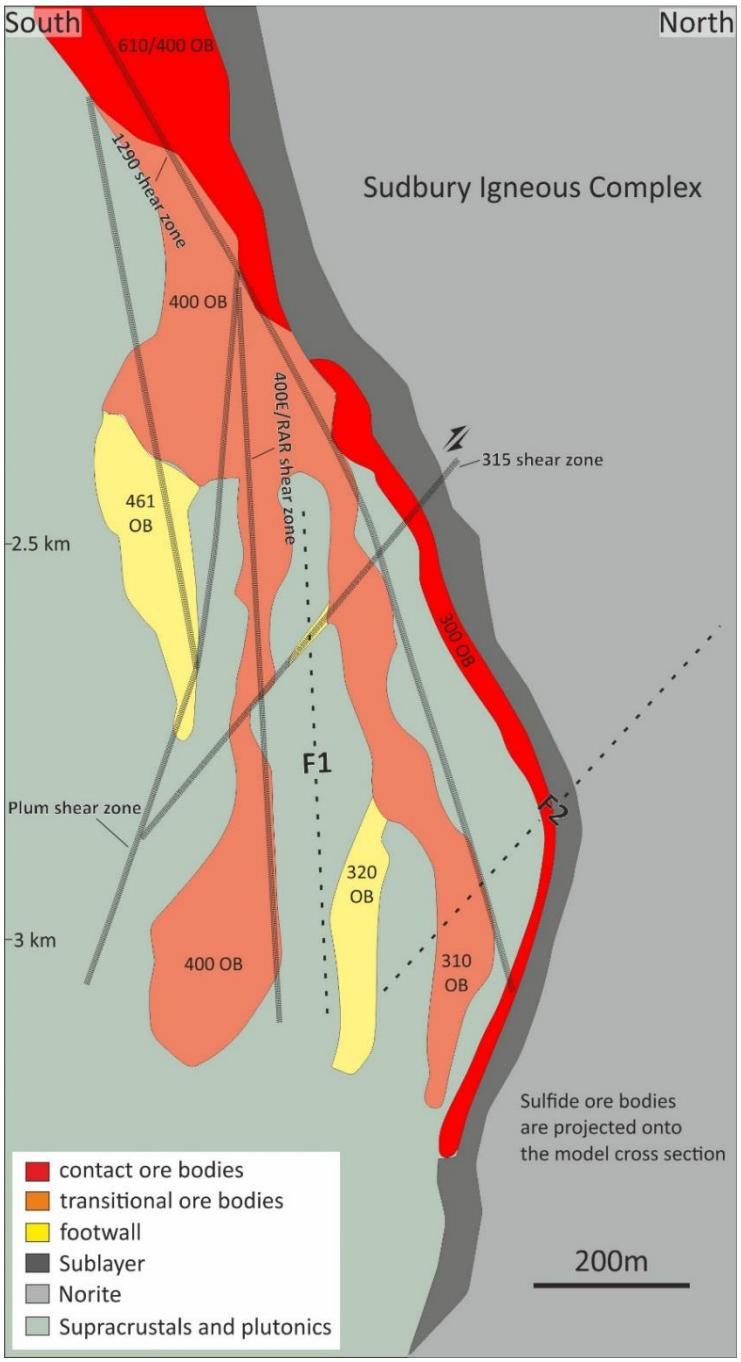

Figure 3. Model of Creighton Deep Mine constructed in DataMine that depicts the orientation relationships of the examined shear zones from the 118 and Hodder/315 families. The F1 denotes interpreted folds that produced during the deformation phase D_1 whereas with F2 folds that produced during the deformation phase D_2.

2.3 Mesoscale features of the shear zones

2.3.1 D_1 (steeply dipping) shear zones (Plum and RAR)

The Plum shear zone exhibits a steeply-dipping, ENE-striking structural grain with thickness that varies from 0.5 to 5 meters. Top-to-the-NW contractional shear fabrics in the Plum shear zone (i.e. sigmoids with thrust-sense of shear) are overprinted by brittle extensional faults (Snelling et al., 2013). The present understanding is that the operation of the Plum shear zone is associated with the modification and remobilization of the 461 and Plum ore bodies (**Figure 3**). Drillcore samples that intersect with the Plum shear zone can be classified based on lithological variations to quartzofeldspathic, biotite and amphibole-rich

domains. In the low-strain, quartzofeldspathic domains, is observed a S_1 foliation defined by the shape-preferred orientation of biotite flakes and stretched feldspars. Strain gradients in this domain are observed at the centimetre-scale (**Figure 4a**). Locally the S_1 foliation defines an axial planar fabric to isoclinally folded S_0 foliation defined by quartz and carbonate-rich veins (**Figure 4b**). Quartz sigmoids are observed preferentially to the biotite-rich domains (**Figure 4c**). The mineralised metamafic domains are characterised by a penetrative S_{1m} mylonitic fabric defined chiefly by calcic amphiboles. Fragments of wallrock clasts are observed preferentially in chalcopyrite-rich domains suggesting the presence of mechanical remobilization structures (durchbewegung sensu Marshall and Gilligan, 1989).

In the same orientation family, and below the 6500 level (i.e. 1.98 Km depth) of the Creighton Mine, the RAR shear zone exhibits NE-striking, steeply dipping S_1 shear fabrics (**Figure 3**). The intensity of the S_1 fabric varies within the shear zone resulting in the distinction of low and high-strain domains. In both domains, the S_2 fabric is defined predominantly by biotite and calcic amphiboles with ubiquitous development of foliation-parallel quartz and carbonate-rich veins. Quartz-rich porphyroclasts with anastomosing biotite folia are recorded in the meta-granitoid-hosted protomylonitic domains. Within the low-strain parts of the shear zone are recorded also amphibole-rich domains of foliated pseudotachylite. Within the higher strain biotite-rich mylonitic segments are observed shear sense indicators with orthorhombic (i.e. φ-type quartz porphyroclasts) and monoclinic symmetry (i.e. quartz sigmoids) (**Figure 4d-e**).

2.3.2 D_2 (south-dipping) shear zones (315 shear zone)

The 315 shear zone is an east-west striking, moderately dipping structure, with top-to-the-north, thrust-sense of shear, and listric geometry. A penetrative south-dipping S_{2m} fabric is defined by the shape preferred orientation of biotite laths and calcic amphiboles. Locally ultramylonitic bands are characterised by centimetre-scale alternation of biotite, amphibole and feldspar-rich domains (**Figure 4f**). Whole rock data and wireframe modelling show that this shear zone hosts high metal tenor Cu/Ni mineralization and controls the geometry of the 310 ore body. The structural features of the 315 shear zone suggest that it belongs to the contractional family of structures of the South Range Shear Zone.

3. Petrographic characterisation of shear zone samples

3.1 D_1 (steeply dipping) shear zones (RAR and Plum)

Biotite and hornblende grains dominate modally the assemblage (80-90%) and define the penetrative S_{2m} fabric in the RAR shear zone (**Figure 5a**). Within the lower strain domains of the shear zone are recorded cm-scale alternations of biotite and hornblende-rich bands. Euhedral epidotes with brown allanitic cores show sharp optical boundaries with the fabric-forming silicates. Titanite grains are observed as: (a) euhedral grains in textural equilibrium with hornblende and biotite grains in the high-strain domains and (b) as anhedral grains with ilmenite cores and patchy zoning in the low strain domains, **Figure 5b**). The zircon grains in the RAR shear zone exhibit spongy morphology, host silicate inclusions, and locally align with the high-strain fabric. Patchily zoned zircons with fragmental texture and apatite rims are observed also locally.

In the Plum shear zone are recognised quartzofeldspathic protomylonitic domains and meta-mafic mylonitic domains. The quartzofeldspathic domain is characterised by the assemblage: Qtz–Bt–Hbl–Pl–Ep±Aln±Ttn±Ap±Zrn±Po. Remnant feldspar porphyroclasts show core and mantle microstructures with localization of chalcopyrite grains in the recrystallized mantles (**Figure 5c**). Within the feldspar porphyroclasts are recorded also linear bands that show preferential recrystallization relative to adjacent intra-grain domains and host chalcopyrite grains. In the metamafic domains hornblende is the modally abundant phase and defines with chalcopyrite and pyrrhotite grains a folded S_2 fabric (**Figure 5d**). Titanite grains that overgrow ilmenite cores and have sharp optical contacts with the fabric-forming biotite grains were detected chiefly in the felsic domains. Sulphide grains (pyrrhotite-pentlandite-chalcopyrite) are observed mostly within the metamafic mylonitic domains and host polymineralic silicate inclusions.

3.2 D_2 (south - dipping) shear zones (315 shear zone)

The 315 shear zone comprise biotite-rich mylonites with the assemblage: Bt-Qtz-Hbl-Pl-Po-Cpy±Pn±Cal±Ttn±Zr. Biotite laths, calcic amphiboles and sulphide grains define a folded S_2 fabric (**Figure 5e**) that is locally transposed to a penetrative S_{2m} mylonitic fabric defined chiefly by biotite grains (**Figure 5f**). Titanite grains are observed mainly as anhedral masses with patchy zoning in reflected light and only locally are in textural equilibrium with fabric-

forming phases. Crystal-plastic microstructures are observed mostly in biotite (e.g. kink bands) and quartz grains (e.g. undulose extinction).

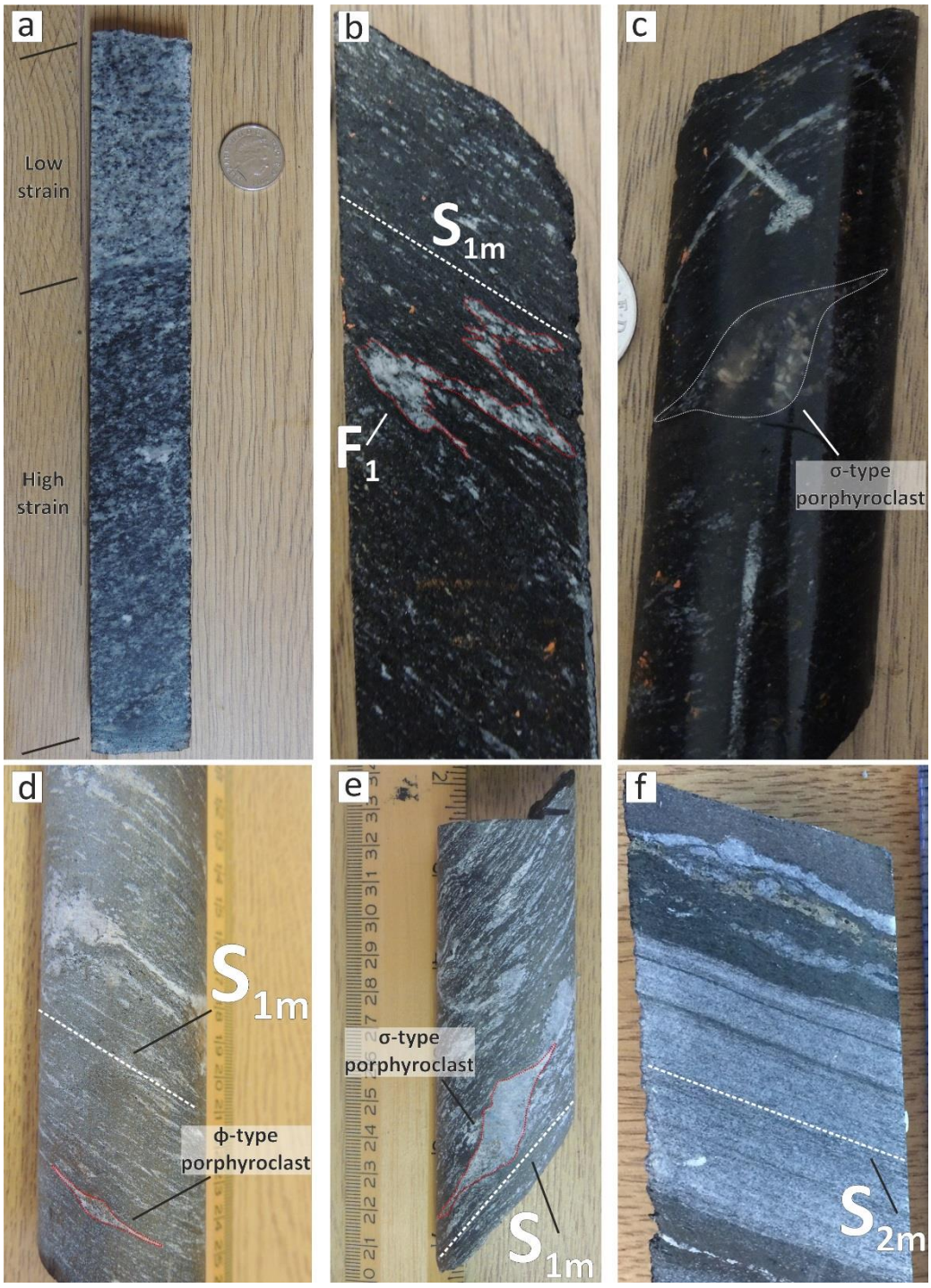

Figure 4. Drillcore samples from the Plum, RAR, and 315 shear zones of the Creighton Mine that depict : (a) Centimetre-scale strain gradients in quartzofeldspathic domains of the Plum shear zone. Note the intensification of the planar fabrics in the domain with higher modal abundance of biotite, (b) Isoclinally folded F_1 carbonate vein with development of the S_{1m} mylonitic fabric parallel to its axial plane, (c) Quartz sigmoid in the biotite-rich mylonitic domains of the Plum shear zone, (d) biotite-rich mylonitic domain of the RAR shear zone with ϕ-type porphyroclasts, (e) biotite-rich mylonitic domain of the RAR shear zone with σ-type quartz porphyroclasts, (f)

Ultramylonitic band in the 315 shear zone with alternation of feldspar, amphibole, and biotite-rich domains. Note the strong shape preferred orientation of chalcopyrite grains parallel to the high-strain S_{2m} fabric.

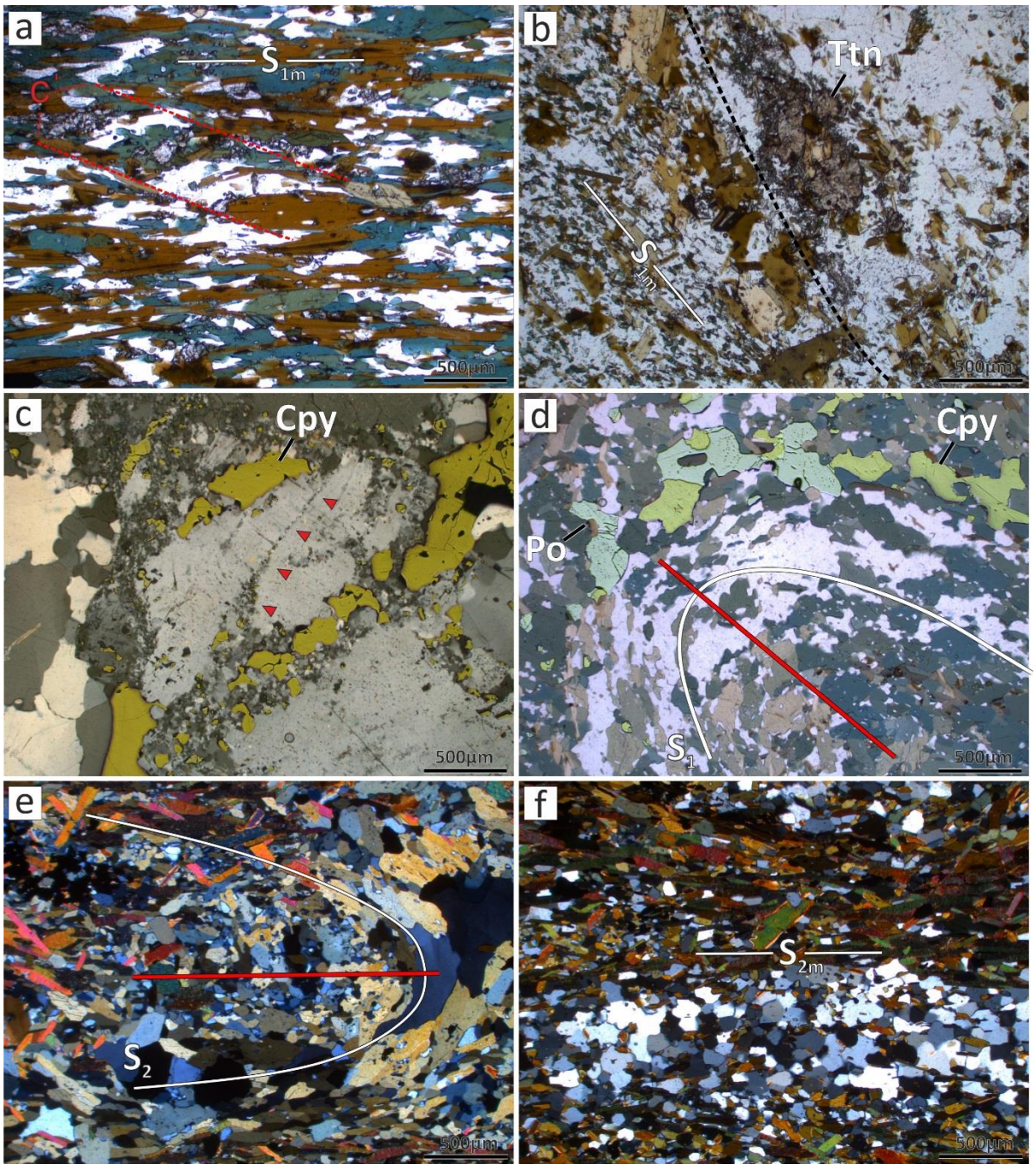

Figure 5. Phototomicrographs from the the RAR, Plum, and 315 shear zone samples that show : (a) A penetrative mylonitic fabric defined by hornblende and biotite grains in the RAR shear zone. Note the C' planes, indicated with red color, oblique to the high-strain S_{1m} fabric, (b) Boundary between two domains with different fabric intensity on the RAR shear zone. In the lower strain domain (right) is observed titanite porphyroclast with weak shape preferred orientation. In the higher strain domain with the higher abundance of biotite and amphibole grains (left) is observed a penetrative S_{1m} fabric, (c) Feldspar porphyroclast in the Plum shear zone that exhibits recrystallization in the rims. Recrystallized areas are observed also within linear intragrain bands (indicated with red triangles). Chalcopyrite grains are preferentially located along the dynamically recrystallized rims of the feldspar porphyroclasts (d) Folded S_1 fabric in the Plum shear zone defined by hornblende grains. Chalcopyrite

and pyrrhotite grains with strong shape preferred orientation define also the S_1 fabric, (e) S_2 folded fabric in the 315 shear zone defined by hornblende, quartz, and sulphide grains, (f) High-strain S_{2m} fabric defined by biotite in the 315 shear zone. Note the band of recrystallized feldspar at the lower part of the photograph.

4. Titanite as a chronometer in Creighton Mine shear zones

Titanite ($CaTiSiO_5$) is a common U-bearing accessory phase that has been used extensively as chronometer of magmatic, metamorphic and metasomatic events (Frost et al., 2000). The closure temperature of titanite to Pb diffusion is suggested to be in the range of 600°C to 750°C for typical geological cooling rates and grain size up to 210μm (Verts et al., 1996, Kirkland et al., 2016). Titanite incorporates initial Pb (i.e. non-radiogenic) in its crystal lattice and in order to interpret correctly age data from this phase a correction of initial lead is necessary. The correction can be made either by measuring the Pb isotopic composition of low uranium co-genetic minerals (e.g. feldspars) or using Pb isotopic composition values from crustal Pb evolution models (e.g. Stacey and Kramers., 1975).

Another approach to treat U-Pb isotopic data from phases with low radiogenic Pb /common Pb ratios is by plotting uncorrected data of co-genetic grains with spread in radiogenic Pb/common Pb components to a Terra-Wasserburg diagram ($^{207}Pb/^{206}Pb$ – $^{238}U/^{206}Pb$). The intersection of the regressed isochron with the Y axis ($^{207}Pb/^{206}Pb$) yields the isotopic composition of common lead whereas the lower intercept with the concordia curve yields the $^{238}U/^{206}Pb$ date (Chew et al., 2014). In this study the U-Pb isotopic data are presented on Terra-Wasserburg diagrams unconstrained to an upper intercept using the total $^{207}Pb/^{206}Pb$ and $^{238}U/^{206}Pb$ isotopic ratios uncorrected for common Pb.

Titanite was chosen for U-Pb isotopic microanalysis in Creighton Mine shear zones for the following reasons: (a) is the most abundant accessory phase within the examined shear zones, (b) the size of the fracture-free grains is large enough for LA-ICP-MS microanalysis using a spot size of at least 20μm, (c) texturally can be linked with metasomatic and fabric-forming events (Papapavlou et al., 2017) and (d) comparing with other accessory phases the selected grains does not show evidence of metamictic phenomena (e.g. allanite) and microstructural features indicative of a pre-impact origin (e.g. zircons).

5.Sampling and methodology

5.1 Sample selection and electron beam imaging

Forty eight samples (n = 48) were selected in total from different drillcores that intersect with the RAR, Plum and 315 shear zones at different depths below the 7800 level (2.37 km) of the Creighton Mine. Nine mylonitic samples (n = 9) were selected after detailed petrographic inspection for U-Pb titanite geochronology. For each sample, polished thin and thick sections were prepared, and mapped using transmitted and reflected light. Titanite grains with different aspect ratios were targeted from the reflected light maps for backscattered electron (BSE) imaging using either a Zeiss EVO MA 10 or a Philips XL30 CP scanning electron microscope at the University of Portsmouth (UK).

5.2 *In-situ* U-Pb titanite geochronology by laser ablation-inductively coupled plasma-mass spectrometry (LA-ICP-MS)

Fifty-six U-Pb isotopic analyses of the selected titanite grains were performed using an ASI RESOlution 193 nm ArF excimer laser coupled to a quadrupole Agilent 7500cs ICP-MS at the University of Portsmouth, UK. Fifty-five additional analyses (n=55) were performed using the same laser system attached to a quadrupole PlasmaQuant Elite ICP-MS. The analytical conditions and parameters of data collection are provided in **Tables 1 and 2 (Supplementary material).** All of the U-Pb isotopic analyses (**Tables 3 to 6, supplementary material**) were performed with laser fluence of 2 J/cm^2, frequency of 2 Hz, and three pulses of pre-ablation. The reduction of the raw U-Pb isotope data was performed with the Iolite software (Paton et al., 2011) using an exponential model for the correction of downhole elemental fractionation. The data were plotted on Terra-Wasserburg diagrams using the Isoplot v.4.1 software (Ludwig, 2012). Instrumental mass bias was corrected by sample-standard bracketing using the matrix-matched Khan titanite as the primary standard (ID-TIMS age of 522.2 ± 2.2 Ma, Heaman et al., 2009). The Sylvester pluton titanite (ID-TIMS age of 262 ± 2Ma, Gabrielse et al., 1993), the Fish Canyon Tuff titanite (ID-TIMS age of 28.40 ± 0.02 Ma, Schmitz and Bowring., 2001), the Bear Lake Ridge titanite (BLR-1; ID-TIMS age of 1047.1 ± 0.4 Ma, Aleinikoff et al., 2007) and the MKED1 titanite (Spandler et al., 2016, ID-TIMS age of 1517.32 ± 0.32 Ma) were variably included as secondary standards every four or five unknowns to monitor the accuracy and precision of the analyses.

In the first run of U-Pb analyses using the Agilent ICP-MS, the Fish Canyon Tuff and Sylvester Pluton secondary titanite standards yielded lower intercept dates in Terra-Wasserburg diagrams of 24 ± 7.3 Ma (2σ, n = 24, MSWD = 3.2) and 257 ± 13 Ma (2σ, n = 8, MSWD = 0.42), both of which are within uncertainty of the reference values above. During the second analytical session, using the PlasmaQuant Elite ICP-MS, U-Pb analyses on the Fish Canyon Tuff titanite yielded a lower intercept date in Terra-Wasserburg diagram of 27.5 ± 9.2 Ma (2σ, n = 7, MSWD = 2.8), and the Bear Lake Ridge, Sylvester Pluton, and MKED-1 secondary standards yielded lower intercept dates of 1051 ± 15 Ma (2σ, n = 12, MSWD = 3.4), 262.8 ± 9.2 Ma (2σ, n = 11,MSWD = 0.21) and 1524 ± 35 Ma (2σ, n = 20, MSWD = 0.61), respectively. The regressed isochrons on analyses of the Fish Canyon Tuff titanite were anchored to a $^{207}Pb/^{206}Pb$ value of 0.84 ± 0.05 based on the measured common Pb composition of leached sanidine feldspars (Schmitz and Bowring., 2001). In both sessions, the upper intercepts of the regressed isochrons on the Bear Lake Road titanite analyses were anchored to a $^{207}Pb/^{206}Pb$ value of 0.91 ± 0.05 based on initial Pb values from the crustal Pb evolution model of (Stacey and Kramers.,1975).

6. Results

6.1 Electron beam imaging of accessory phases (SEM/BSE)

6.1.1 D_1 RAR shear zone

Titanite grains in the RAR shear zone are classified to two populations based on distinct textural differences between the low and high-strain domains. Specifically, titanite grains within the low-strain domains are anhedral, show patchy zoning in BSE and host ilmenite inclusions (**Figure 6a**). Preliminary microstructural data (EBSD, Electron Backscatter Diffraction) from the titanite grains hosted within the low strain domains show that these grains exhibit dynamic recrystallization features. Within the high-strain domains the titanite grains are in textural equilibrium with fabric-forming silicates and host also ilmenite and apatite inclusions (**Figure 6b**). Locally, titanite grains within the high-strain parts show recrystallization and polycrystalline amalgamation. The zircon grains are commonly fractured, host silicate inclusions, and show in BSE sector and oscillatory zoning. Rarely, zircon overgrowths show sharp optical boundaries with fabric-forming biotite flakes. Epidote is a ubiquitous accessory phase and commonly hosts sector zoned allanitic cores. The epidote overgrowths are observed also in mutual contact with titanite and biotite grains.

6.1.2 D1 Plum shear zone

In the Plum shear zone, the titanite grains are characterised also by patchy zoning, ilmenite cores, and subhedral patchily zoned apatite inclusions (**Figure 6c**). Euhedral rims that are darker in BSE images show sharp boundaries with biotite flakes. Crystal-plastic microstructures are recorded locally in titanites such as sub-grains decorated by μm-scale darker films in BSE (**Figure 6d**). Other relatively abundant accessory phases that were detected are allanite grains with epidote rims and apatite grains. The allanite grains overgrow patchily zoned apatite grains and are observed also along intragranular fractures of apatite grains. The detected zircon grains are also intensely fractured, have spongy texture with silicate inclusions, and commonly exhibit darker subhedral cores with brighter overgrowths.

6.1.3 D_2 315 shear zone

Two textural populations of titanite are recognised in the 315 shear zone: (a) grains that exhibit overgrowth zoning (discontinuous core and rim domains with variable BSE response) (**Figure 6e**) and (b) grains with patchy zoning and ilmenite inclusions (**Figure 6f**). The patchily zoned grains locally show a strong shape preferred orientation and are observed in textural equilibrium with biotite flakes. Locally amalgamation of smaller patchily zoned euhedral grains is observed. Allanite grains are observed commonly in association with biotite grains.

7. U-Pb titanite geochronology

7.1 RAR shear zone

Forty U-Pb isotopic analyses (n=40) were performed on anhedral, patchily-zoned titanite grains from three samples hosted within the low-strain domains of the RAR shear zone. The analysed titanite grains show low uranium contents (U < 7 ppm), with average concentration of 3.2 ppm. The spread in U-Pb ratios defines a mixing array between radiogenic and common Pb components. The regressed U-Pb isochron line in Terra-Wasserburg diagram yields a lower intercept date of 1730 ± 66 Ma (2σ, MSWD = 2.2) (**Figure7, Upper panel left**). The intersection of this regression line with the y axis yields an initial $^{207}Pb/^{206}Pb$ isotopic ratio of 0.98 ± 0.04 (95% confidence). Euhedral titanite grains, from three samples within the higher strain domains of the shear zone show elevated uranium contents with maximum concentration of up to 25 ppm and average concentration of 14 ppm. Twenty-

eight analyses (n = 28) from these grains define a U-Pb isochron with a lower intercept date of 1622 ± 25 Ma (2σ, MSWD = 1.8) (**Figure 7, Upper panel right**). The initial $^{207}Pb/^{206}Pb$ composition is estimated at 0.85 ± 0.16 (95% confidence) and overlaps within uncertainty with that of the older population. The higher uncertainty on the initial $^{207}Pb/^{206}Pb$ composition of the younger population is attributed to the lower amounts of common Pb on the crystal lattice of the selected grains. The presence of two age populations corroborates also the detection of two textural populations within domains of variable fabric intensity in the RAR shear zone.

7.2 315 shear zone

Thirteen U-Pb isotopic analyses (n = 13) were performed totally from one sample of biotite-rich mylonite from the 315 shear zone. Eight analyses (n = 8) targeted on grains with patchy zoning, that show average uranium concentration of 21ppm, yield a lower intercept date of 1750 ± 39 (2σ, MSWD = 0.83) with an initial $^{207}Pb/^{206}Pb$ isotopic ratio estimated at 0.92 ± 0.14 (**Figure 7, Lower panel, left**). The titanite grains from the population with overgrowth zoning show lower uranium contents with average concentration of 15 ppm. Five analyses (n = 5) from core and rim domains of the titanite population with overgrowth zoning yield a lower intercept date of 1656 ± 41 Ma (2σ, MSWD = 0.43) with an initial $^{207}Pb/^{206}Pb$ ratio of 0.91 ± 0.09 (**Figure 7, Lower panel, right**).

7.3 Plum shear zone

Twenty-Eight U-Pb isotopic analyses (n=28) were performed on patchily zoned titanite grains with ilmenite cores from two quartzofeldspathic samples that are hosted within the low-strain domains of the Plum shear zone. The analysed grains are low in uranium, with average concentration of 7 ppm. The analytical points from these grains define on a Terra-Wasserburg diagram a single isochron with a regressed lower intercept of 1453±33 Ma (2σ, MSWD = 1.5) (**Figure 8**). The initial $^{207}Pb/^{206}Pb$ isotopic composition of the Pb reservoir where the titanite grains equilibrated is estimated at 0.96 ± 0.02 (95% confidence).

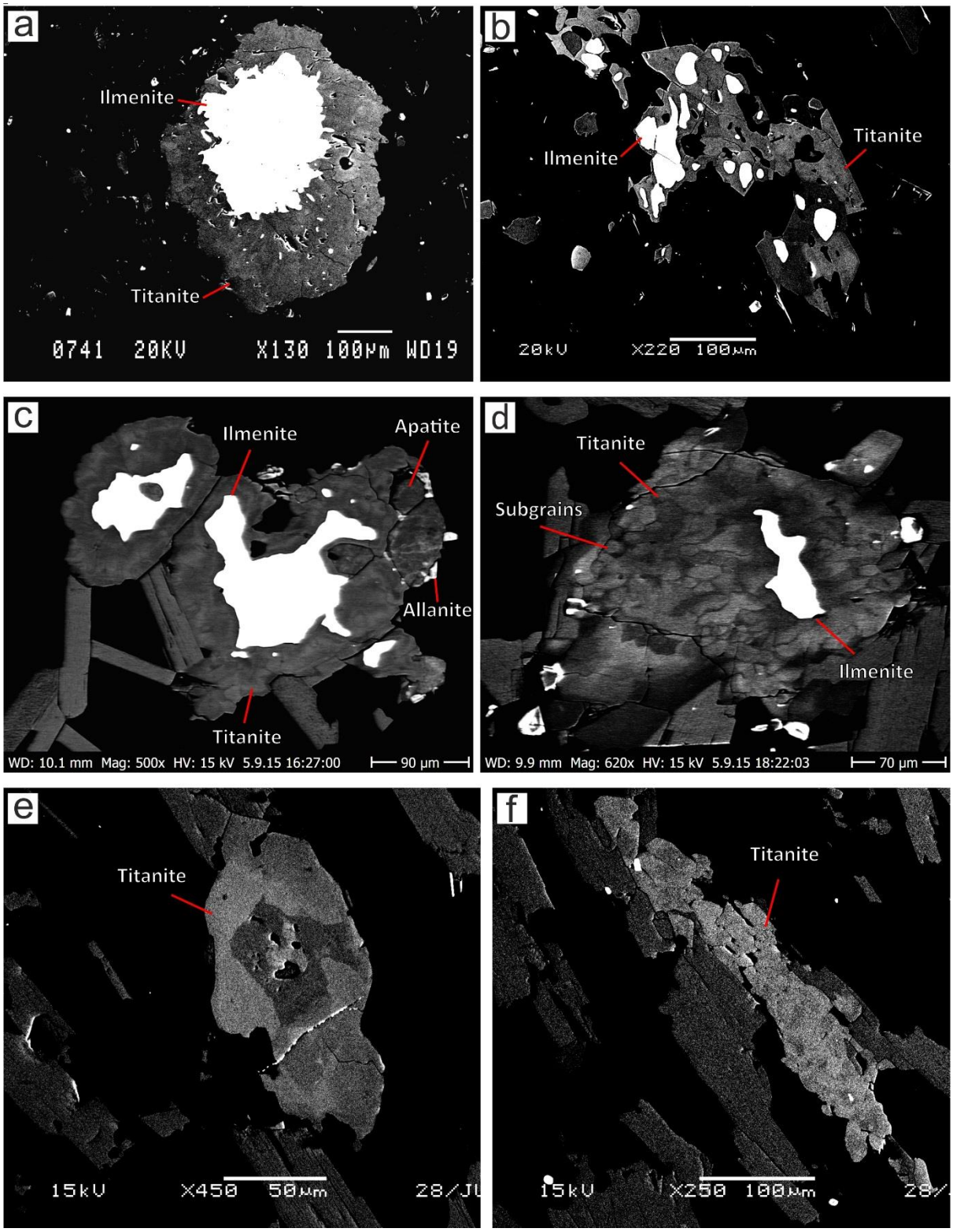

Figure 6. Backscatter electron (BSE) images of titanite grains from the RAR, Plum and 315 shear zones that show : (a) Anhedral titanite grain with patchy zoning and ilmenite core from the low-strain domains of the RAR shear zone, (b) titanite grain with ilmenite inclusions from the high-strain domains of the RAR shear zone that is in textural equilibrium with fabric-forming biotite. Note the sharp optical contacts between titanite and biotite matrix, (c) patchily zoned titanite grains with ilmenite and apatite inclusions from the Plum shear zone. The

apatite grains show also patchy zoning and are rimmed by allanite grains, (d) titanite grain with ilmenite inclusions from the Plum shear zone. The subgrains in this grain are decorated by darker films with anastomosing geometry, (e) Sector zoned titanite grain from the 315 shear zone with discontinuous core-mantle-rim domains with variable BSE response, (f) patchily zoned titanite grain with ilmenite inclusions from the 315 shear zone that shows a strong shape preferred orientation and is in textural equilibrium with the fabric-forming biotite.

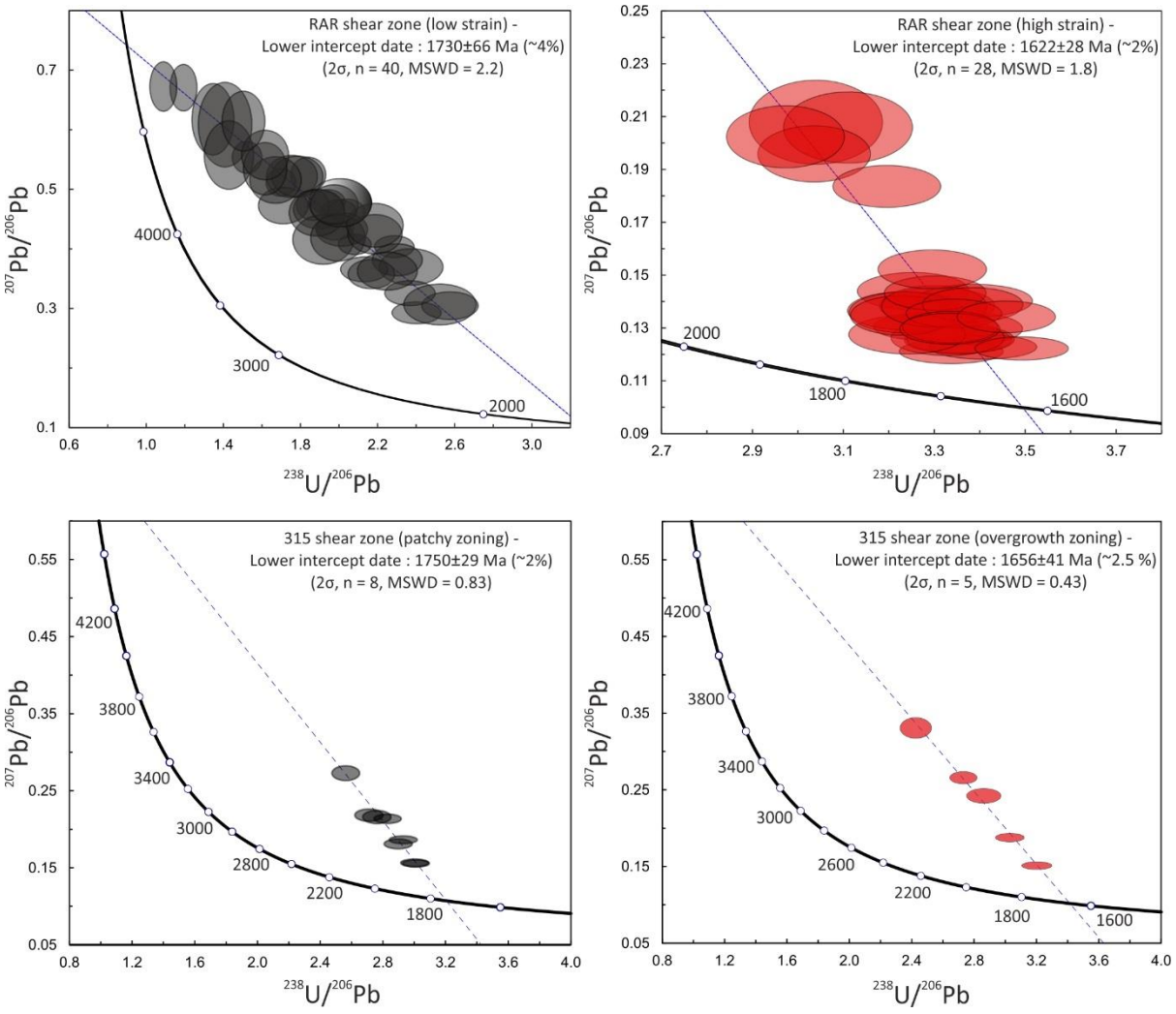

Figure 7. Terra-Wasserburg U-Pb concordia diagrams that show isotopic data from: (Upper panel left) titanite grains hosted within the low-strain domains of the RAR shear zone. The analysed grains are variably enriched in common Pb components and show spread. (Upper panel right) titanite grains hosted with the higher strain domains of the RAR shear zone. Note that this generation of grains is more radiogenic and does not show spread in Terra-Wasserburg space. (Lower panel – left) titanite grains with patchy zoning from the 315 shear zone. (Lower panel - right) titanite grains with sector zoning from the 315 shear zone.

8.1 Implications for the Proterozoic orogenic evolution of the Southern province

The *in-situ* U-Pb age dating of shear-hosted titanite grains from the South Range of the Sudbury structure indicates operation of the examined shear zones at ca. 1.75 Ga, 1.65 Ga, and 1.45 Ga. These three age populations demonstrate polyorogenic reworking of the South Range and the Huronian Supergroup during the three accretionary-collisional events that are discussed below.

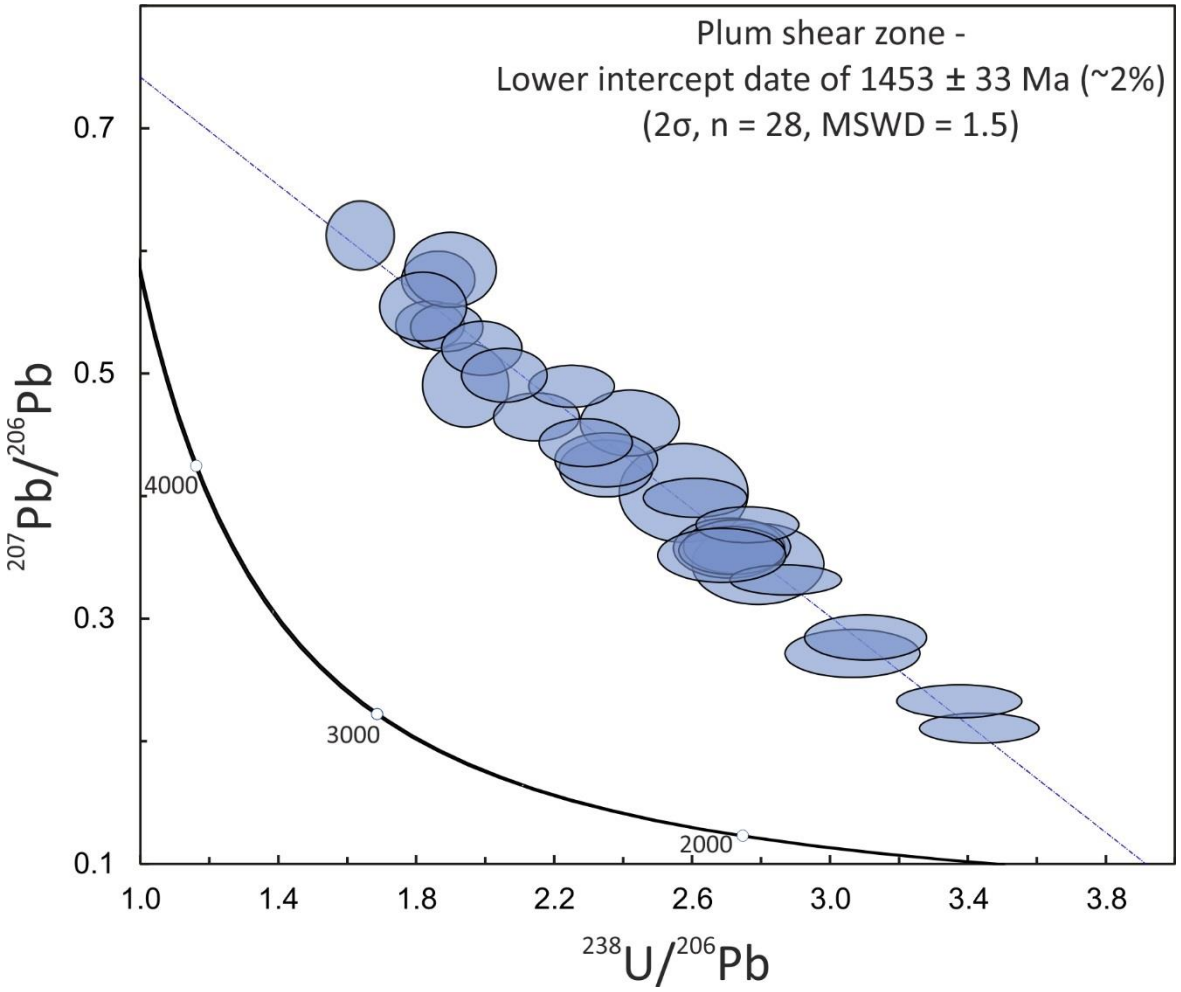

Figure 8. Terra-Wasserburg U-Pb concordia diagram that shows U-Pb isotopic data from titanite grains of the D_1 Plum shear zone.

8. Discussion

8.1.1 Yavapai event (1.77 – 1.7 Ga)

The oldest age population of ca. 1.75 Ga is recorded in patchily zoned titanite grains hosted within D_1 and D_2 amphibolite-facies shear zones. Looking at a broader scale, shear zone reworking accompanied by syn-tectonic fluid flow and ore upgrading is attributed to a thermal event at ca. 1.77 Ga in the Southern Lake Superior Region (Marquette Range, Northern Michigan, USA) (Rasmussen et al., 2016). This event is linked with the Yavapai-interval arc accretion and is characterised by Barrovian greenschist to amphibolite-facies metamorphism, gneiss dome formation, and reactivation at ca. 1.76 Ga of a Paleoarchean suture zone, the Great Lakes Tectonic zone, that extends eastwards to the Sudbury structure (Sims and Day., 1993, Tohver et al., 2007). The steeply dipping D_1 shear zones of Creighton Mine have been correlated genetically with a major transcurrent shear zone of the Southern Province, the Murray fault zone (Snelling et al., 2013). This fault zone is interpreted as the easternmost continuation of the Great Lakes Tectonic Zone (Sims et al., 1980, Riller et al., 1999,).

Recent studies in the Southern province show that the Yavapai event reached lower amphibolite facies conditions (P = 2.8 – 4 Kbar, T = 540 - 565°C) between 1744 ± 29 Ma and 1704 ± 13 Ma (Raharimarefa et al., 2014). The new U-Pb titanite age data from the RAR and Plum shear zone corroborate within analytical uncertainty these estimates. Taking in consideration the fluid-mediated features (see also Harlov et al., 2006, Harlov et al., 2011) and the strong shape preferred orientation in some of the selected grains (e.g. 315 shear zone, **Figure 6f**) we suggest that the formation of high-strain S_{1m} and S_{2m} fabrics facilitated the creation of permeability paths for the channelization of metamorphic/metasomatic fluids. Thus, the oldest age population of 1.75 Ga likely represents the timing of a syndeformational fluid-flow event during the Yavapai-interval accretion.

8.1.2 Mazatzalian – Labradorian event (1.7 – 1.6 Ga)

The age population of ca. 1.65 Ga, is recorded in titanite grains from both D_1 and D_2 shear zones. The analysed titanite grains from the RAR shear zone are in textural equilibrium with fabric-forming silicates showing that the date of ca. 1.65 Ga manifests titanite growth during the reworking of the shear fabrics. In the case of the 315 shear zone the analytical points that define the ca. 1.65 Ga isochron are located within core and rim domains of sector-

zoned grains. Thus, the single age population of ca. 1.65 Ga, that is defined from core and rim domains with variable BSE signature, likely denotes protracted growth of titanite during a single orogenic episode. Both age populations showcase that the examined structures record an orogenic event younger than the Yavapai-interval arc accretion named as the Mazatzalian – Labradorian event (ca. 1.7 – 1.6 Ga) corroborating recent studies in Creighton Mine (Papapavlou et al., 2017).

The Mazatzalian – Labradorian orogenic belt extends from Southwest United States (Mazatzal mountains, Arizona) up to Labrador in Canada and comprises a Northwest-vergent, thin-skinned, fold and thrust belt active between 1.67 Ga and 1.62 Ga (Gower et al., 1992, Amato et al., 2008, Duebendorfer et al., 2015). Previous U-Pb age dating of shear-hosted titanite grains, from the South Range of the Sudbury structure yielded a weighted mean $^{207}Pb/^{206}Pb$ date of 1658 ± 68 Ma that is interpreted as the timing of shear zone activity during this event (Bailey et al., 2004). Metasomatic mobilization of alkali elements and re-equilibration of the Sr isotope composition of footwall breccia from the North Range are attributed also to a thermal event at ca. 1.65 Ga (whole-rock Rb-Sr isochron) (Deutch et al., 1989). Further P-T-t constraints for this metasomatic episode are missing but the fluid-mediated textural features in the ca. 1.62 Ga titanite grains from the RAR shear zone (i.e. patchy zoning, ilmenite inclusions) indicate that metasomatism and fabric reworking temporally overlap during the Mazatzalian – Labradorian event.

8.1.3 Chieflakian event (1.47 – 1.44 Ga)

The 1.45 Ga titanite grains are hosted within quartzofeldspathic domains of the D_1 Plum shear zone and exhibit a variety of textural features indicative of fluid-mediated and recrystallization processes such as ilmenite cores, patchy zoning, and sub-grain boundaries. The nucleation of subgrains in a textural population of grains with metasomatic features suggests that the date of 1453±33 Ma brackets an event of syn-tectonic fluid percolation in the Plum shear zone. This age agrees remarkably well with previous studies (**Table 7, supplementary material**) that document a pre-Grenvillian thermal event, mainly in the Southern province and proximally to Grenville Front, better known as the Chieflakian event (Haggart et al., 1993, Dudas et al., 1994, Krogh, 1994, Corfu and Easton, 2000).

One scenario is that the Plum shear zone operated as a permeability pathway for the ingress of metasomatic fluids during the Chieflakian orogeny. These fluids led to metasomatic

removal and mobilisation of LREE (Light Rare Earth Elements) that sinked in the allanite coronas that armour patchily zoned apatite grains. The presence of apatite inclusions in the titanites could be another micro-textural line of evidence for the petrogenesis of accessory phases via fluid-mediated metasomatic reactions (Harlov et al., 2005, Harlov, 2011).

On the other hand, similar microtextural relationships between apatite and allanite have been described, after the breakdown of monazite (LREE-rich phosphate), in amphibolite-facies terranes and are associated with small-scale intergranular elemental redistribution (Finger et al., 1998). However, petrographic evidence for the formation or breakdown of monazite does not exist in the Plum shear zone. Overall, the uncommon textural relationships between REE-bearing phases in the Plum shear zone testify that mid-crustal shear zones are foci of crustal fluids that can enhance the mobility of relatively immobile elements (Rolland et al., 2003).

8.2 Temporal constraints of Ni-Cu-PGE sulphide remobilization in the South Range

The remobilization of Ni-Cu-PGE sulphides in the South Range of the Sudbury structure has been attributed to the Penokean (1.9 – 1.8 Ga) and Mazatzalian – Labradorian events (1.7 – 1.6 Ga) (Bailey et al., 2004, Dare et al., 2010, Mukwakwami et al., 2013, Papapavlou et al., 2017). The new petrographic and U-Pb titanite age data from the three ore-controlling shear zones of the Creighton Mine provide further insights on this ore-modifying process. The folded S_1 fabric defined by hornblende, chalcopyrite, and pyrrhotite grains shows that fabric-formation in amphibolite facies conditions accompanies sulphide movement. Further support for that is given by the localization of chalcopyrite grains at the recrystallized rims of feldspar porphyroclasts bracketing the deformation temperatures of sulphide kinesis between 450 - 600°C (Passchier and Trouw., 2005). These petrographic relationships demonstrate that the remobilization of sulphides took place in lower amphibolite facies conditions during the operation of the D_1 Plum shear zone.

The age populations of ca. 1.75, 1.65 and 1.45 Ga in the shear hosted titanites of the D_1 shear zones suggests that the movement of sulphides may have happened progressively during the different accretionary episodes, with a last pulse during the Chieflakian orogeny. U-Pb titanite age data from the 315 shear zone, that is member of the South Range Shear Zone, show reworking of the structure during the Yavapai (1.77 – 1.7 Ga) and Mazatzalian –

Labradorian (1.7 – 1.6 Ga) events and not during the Penokean event (1.9 – 1.8 Ga) that is traditionally regarded as the dominant tectonothermal event in the area. Consequently, is suggested that the three documented orogenic events possibly have a stronger impact on the remobilization of magmatic sulphides that was previously recognised.

8.3 Comparative orogenic evolution of Southern Province and Southwest United States

Geochronological studies demonstrate that the Proterozoic crust in North American midcontinent has similar tectonothermal evolution and is spatially connected with the Proterozoic crust in accretionary provinces of southwestern United States (Holm et al., 1998, Holm et al., 2005, Van Schmus et al., 2007). The two main orogenic pulses that are widely recognised in southwest United States (i.e. Arizona, New Mexico) are related with the Yavapai (ca. 1.75 – 1.7 Ga) and Mazatzal (ca. 1.65 Ga) events (Karlstrom and Bowring., 1988). A later episode of intracratonic tectonism that induced reworking of shear fabrics, syncontractional magmatism, and basin formation took place between 1.48 and 1.4 Ga (Nyman et al., 1994, Pedrick et al., 1998, Doe et al., 2012). Importantly, texturally-controlled total Pb monazite age dating of mylonitic fabrics from the Colorado mineral belt (SW USA) shows shear zone reactivation during two events at ca. 1.71 – 1.63 Ga and 1.45 – 1.38 Ga (Shaw et al., 2001, Jessup et al., 2006).

The three age populations of ca. 1.75, 1.65 and 1.45 Ga, in the three amphibolite-facies shear zones of Creighton Mine, document reactivation during the same orogenic events, named as Yavapai (1.77 – 1.7 Ga), Mazatzalian – Labradorian (1.7 – 1.6 Ga), and Chieflakian (1.47 – 1.44 Ga). Unfortunately, the character of the samples (i.e. non-oriented drillcores) inhibits the placing of any kinematic constraints on these reactivation events. The presence though of D_1 steeply dipping mylonitic fabrics and kinematic indicators of monoclinic and orthorhombic symmetry in the RAR shear zone may indicate kinematic partitioning and reworking in a setting of transpressional tectonism. The reactivation of the structures could be the response to far-field stress effects during the successive docking of the different accretionary provinces to the southeast-facing Laurentia convergent margin. This hypothesis though necessitates rigorous, field-based, structural analysis of different mylonitic shear zones of the Southern Province.

9. Conclusions

The new U-Pb titanite age data from the South Range of the Sudbury structure demonstrate that the Southern Province has a complex polyorogenic history. The three shear-hosted titanite age populations of ca. 1.75 Ga, 1.65 Ga and 1.45 Ga show that these events are related with the Yavapai (1.77 – 1.7 Ga), Mazatzalian – Labradorian (1.7 – 1.6 Ga) and Chieflakian (1.47 – 1.44 Ga) accretionary events. The absence of Penokean ages (1.9 – 1.8 Ga) indicates that the effects of this event on the tectonothermal evolution of the Southern Province and the Sudbury impact structure are overestimated. Overall, in accordance with previous studies in the Great Lakes region (Piercey et al., 2007, Holm et al., 2007) this study corroborates that the orogenic evolution of the Southern Province is linked with that of the Transcontinental Proterozoic Provinces in the southwestern United States.

Acknowledgements

K.P acknowledges a University of Portsmouth research studentship. Feedback on different aspects of Creighton Mine geology from Collin Mecke is greatly appreciated.

References

Aleinikoff, J. N., Wintsch, R. P., Tollo, R. P., Unruh, D. M., Fanning, C. M., & Schmitz, M. D. (2007). Ages and origins of rocks of the Killingworth dome, south-central Connecticut: Implications for the tectonic evolution of southern New England. *American Journal of Science*, *307*(1), 63–118. http://doi.org/10.2475/01.2007.04

Amato, J. M., Boullion, A. O., Serna, A. M., Sanders, A. E., Farmer, G. L., Gehrels, G. E., & Wooden, J. L. (2008). Evolution of the Mazatzal province and the timing of the Mazatzal orogeny: Insights from U-Pb geochronology and geochemistry of igneous and metasedimentary rocks in southern New Mexico. *Bulletin of the Geological Society of America*, *120*(3–4), 328–346. http://doi.org/10.1130/B26200.1

Ames, D. E., Davidson, A., & Wodicka, N. (2008). Geology of the giant Sudbury polymetallic mining camp, Ontario, Canda. *Economic Geology*, *103*(5), 1057–1077. http://doi.org/10.2113/gsecongeo.103.5.1057

Ames, D.E., and Farrow, C.E.G., (2007), Metallogeny of the Sudbury mining camp, Ontario, in Goodfellow, W.D., ed., Mineral Deposits of Canada: A Synthesis of Major Deposit-Types, District Metallogeny, the Evolution of Geological Provinces, and Exploration Methods: Geological Association of Canada, Mineral Deposits Division, Special Publication No. 5, p. 329-350

Bailey, J., Lafrance, B., McDonald, A. M., Fedorowich, J. S., Kamo, S., & W.J. Davis., D. A. A. (2004). Mazatzal–Labradorian-age (1.7–1.6 Ga) ductile deformation of the South Range Sudbury impact structure at the Thayer Lindsley mine, Ontario. *Canadian Journal of Earth Sciences* , *41*(12), 1491–1505. JOUR. http://doi.org/10.1139/e04-098

Bailey, J., McDonald, A. M., Lafrance, B., & Fedorowich, J. S. (2006). Variations in Ni content in sheared magmatic sulfide ore at the Thayer Lindsley Mine, Sudbury, Ontario. *Canadian Mineralogist*, *44*(5), 1063–1077. http://doi.org/10.2113/gscanmin.44.5.1063

Corfu, F., & Easton, R. M. (2001). U-Pb evidence for polymetamorphic history of Huronian rocks within the Grenville front tectonic zone east of Sudbury, Ontario, Canada. *Chemical Geology*, *172*(1–2), 149–171. http://doi.org/10.1016/S0009-2541(00)00241-2

Card, K. D. (1990). A review of the Superior Province of the Canadian Shield, a product of Archean accretion. *Precambrian Research*, *48*(1–2), 99–156. http://doi.org/10.1016/0301-9268(90)90059-Y

Chew, D. M., Petrus, J. A., & Kamber, B. S. (2014). U-Pb LA-ICPMS dating using accessory mineral standards with variable common Pb. *Chemical Geology*, *363*, 185–199. http://doi.org/10.1016/j.chemgeo.2013.11.006

Dare, S. A. S., Barnes, S. J., & Prichard, H. M. (2010). The distribution of platinum group elements (PGE) and other chalcophile elements among sulfides from the Creighton Ni-Cu-PGE sulfide deposit, Sudbury, Canada, and the origin of palladium in pentlandite. *Mineralium Deposita*, *45*(8), 765–793. http://doi.org/10.1007/s00126-010-0295-6

Deutsch, A., Lakomy, R., & Buhl, D. (1989). Strontium- and neodymium-isotopic characteristics of a heterolithic breccia in the basement of the Sudbury impact structure, Canada. *Earth and Planetary Science Letters*, *93*(3), 359–370. http://doi.org/10.1016/0012-821X(89)90035-6

Doe, M. F., Jones, J. V., Karlstrom, K. E., Thrane, K., Frei, D., Gehrels, G., & Pecha, M. (2012). Basin formation near the end of the 1.60-1.45 Ga tectonic gap in southern Laurentia: Mesoproterozoic Hess Canyon Group of Arizona and implications for ca. 1.5 Ga supercontinent configurations. *Lithosphere*, *4*(1), 77–88. http://doi.org/10.1130/L160.1

Duebendorfer, E. M., Williams, M. L., & Chamberlain, K. R. (2015). Case for a temporally and spatially expanded Mazatzal orogeny. *Lithosphere*, *7*(6), L412.1. http://doi.org/10.1130/L412.1

Dudas, F.O., Davidson, A., and Bethune, K.M., 1994: Age of the Sudbury diabase dykes and their metamorphism in the Grenville Province, Ontario; in Radiogenic Age and Isotopic Studies: Report 8; Geological Survey of Canada, Current Research 1994-F, p. 97-106

Easton, R. M. (2000). Metamorphism of the Canadian Shield, Ontario, Canada. II. Proterozoic metamorphic history. *Canadian Mineralogist*, *38*(2), 319–344

Fleet, M. E., Barnett, R. L., & Morris, W. A. (1987). Prograde Metamorphism of the Sudbury Igneous Complex. *Canadian Mineralogist*, *25*, 499–514

Finger, F., Broska, I., Roberts, M. P., & Schermaier, A. (1998). Replacement of primary monazite by apatite-allanite-epidote coronas in an amphibolite facies granite gneiss from the eastern Alps. *American Mineralogist*, *83*(3–4), 248–258.

Fueten, F., & Redmond, D. J. (1997). Documentation of a 1450 Ma contractional orogeny preserved between the 1850 Ma Sudbury impact structure and the 1 Ga Grenville orogenic front, Ontario. *Bulletin of the Geological Society of America*, *109*(3), 268–279. http://doi.org/10.1130/0016-7606(1997)109<0268:DOAMCO>2.3.CO;2

Gabrielse, H., Mortensen, J.K., Parrish, R.R., Harms, T.A., Nelson, J.L., and van der Heyden, P.,1993: Late Paleozoic plutons in the Sylvester Allochthon, northern British Columbia; inRadiogenic Age and Isotopic Studies: Report 7; Geological Survey of Canada, Paper 93-2,p.107-118

Gower, C. F., Schärer, U., & Heaman, L. M. (1992). The Labradorian orogeny in the Grenville Province, eastern Labrador, Canada. *Canadian Journal of Earth Sciences*, *29*(9), 1944–1957. http://doi.org/10.1139/e92-152

Haggart, M. J., Jamieson, R. a., Reynolds, P. H., Krogh, T. E., Beaumont, C., & Culshaw, N. G. (1993). Last Gasp of the Grenville Orogeny: Thermochronology of the Grenville Front Tectonic Zone near Killarney, Ontario. *The Journal of Geology*, *101*(5), 575–589. http://doi.org/10.1086/648250

Harlov, D. E., Wirth, R., & Förster, H. J. (2005). An experimental study of dissolution-reprecipitation in fluorapatite: Fluid infiltration and the formation of monazite. *Contributions to Mineralogy and Petrology*, *150*(3), 268–286. http://doi.org/10.1007/s00410-005-0017-8

Harlov, D., Tropper, P., Seifert, W., Nijland, T., & Förster, H. J. (2006). Formation of Al-rich titanite (CaTiSiO4O-CaAlSiO4OH) reaction rims on ilmenite in metamorphic rocks as a function of fH2O and fO2. *Lithos*, *88*(1–4), 72–84. http://doi.org/10.1016/j.lithos.2005.08.005

Harlov, D. (2011). Petrological and experimental application of REE- and actinide-bearing accessory minerals to the study of Precambrian high-grade gneiss terranes. In *Geological Society of America Memoirs* (Vol. 207, pp. 13–24). Geological Society of America. http://doi.org/10.1130/2011.1207(02)

Heaman, L. M. (2009). The application of U-Pb geochronology to mafic, ultramafic and alkaline rocks: An evaluation of three mineral standards. *Chemical Geology*, *261*(1–2), 42–51. http://doi.org/10.1016/j.chemgeo.2008.10.021

Holm, D. K., Darrah, K. S., & Lux, D. R. (1998). Evidence for widespread approximately 1760 Ma metamorphism and rapid crustal stabilization of the early Proterozoic (1870-1820 Ma) Penokean Orogen, Minnesota. *American Journal of Science*, *298*(1), 60–81. http://doi.org/10.2475/ajs.298.1.60

Holm, D. K., Van Schmus, W. R., MacNeill, L. C., Boerboom, T. J., Schweitzer, D., & Schneider, D. (2005). U-Pb zircon geochronology of Paleoproterozoic plutons from the northern midcontinent, USA: Evidence for subduction flip and continued convergence after geon 18 Penokean orogenesis. *Bulletin of the Geological Society of America*, *117*(3–4), 259–275. http://doi.org/10.1130/B25395.1

Holm, D. K., Anderson, R., Boerboom, T. J., Cannon, W. F., Chandler, V., Jirsa, M., … Van Schmus, W. R. (2007). Reinterpretation of Paleoproterozoic accretionary boundaries of the

north-central United States based on a new aeromagnetic-geologic compilation. *Precambrian Research*, *157*(1–4), 71–79. http://doi.org/10.1016/j.precamres.2007.02.023

Jessup, M. J., Jones III, J. V., Karlstrom, K. E., Williams, M. L., Connelly, J. N., & Heizler, M. T. (2006). Three Proterozoic Orogenic Episodes and an Intervening Exhumation Event in the Black Canyon of the Gunnison Region, Colorado. *The Journal of Geology*, *114*(5), 555–576. http://doi.org/10.1086/506160

Karlstrom, K. E., & Bowring, S. a. (1988). Early Proterozoic Assembly of Tectonostratigraphic Terranes in Southwestern North America. *The Journal of Geology*, *96*(5), 561–576. http://doi.org/10.1086/629252

Karlstrom, K. E., Åhäll, K. I., Harlan, S. S., Williams, M. L., McLelland, J., & Geissman, J. W. (2001). Long-lived (1.8-1.0 Ga) convergent orogen in southern Laurentia, its extensions to Australia and Baltica, and implications for refining Rodinia. *Precambrian Research*, *111*, 5–30. http://doi.org/10.1016/S0301-9268(01)00154-1

Krogh, T. E., McNutt, R. H., & Davis, G. L. (1982). Two high precision U–Pb zircon ages for the Sudbury Nickel Irruptive. *Canadian Journal of Earth Sciences*, *19*(4), 723–728. http://doi.org/10.1139/e82-061

Krogh, T. E. (1994). Precise U-Pb ages for Grenvillian and pre-Grenvillian thrusting of Proterozoic and Archean metamorphic assemblages in the Grenville Front tectonic zone, Canada. *Tectonics*, *13*(4), 963–982. http://doi.org/10.1029/94TC00801

Lightfoot, P. C. (2007). Advances in Ni-Cu-PGE Sulphide Deposit Models and Implications for Exploration Technologies. *Ore Deposits and Exploration Technology*, 629–646

Ludwig, K. R. (2012). User's Manual for Isoplot 3.75 - A Geochronological Toolkit for Microsoft Excel. *Berkeley Geochronology Center Special Publication*, (5), 75p

Marshall, B., & Gilligan, L. B. (1989). Durchbewegung structure, piercement cusps, and piercement veins in massive sulfide deposits; formation and interpretation. *Economic Geology*, *84*(8), 2311–2319. http://doi.org/10.2113/gsecongeo.84.8.2311

Mukwakwami, J., Lafrance, B., Lesher, C. M., Tinkham, D., Rayner, N., & Ames, D. (2014). Deformation, metamorphism, and mobilization of Ni–Cu–PGE sulfide ores at Garson Mine,

Sudbury. *Mineralium Deposita*, *49*(2), 175–198. JOUR. http://doi.org/10.1007/s00126-013-0479-y

Nyman, M. W., Karlstrom, K. E., Kirby, E., & Graubard, C. M. (1994). Mesoproterozoic contractional orogeny in western North America: evidence from ca. 1.4 Ga plutons. *Geology*. http://doi.org/10.1130/0091-7613(1994)022<0901:MCOIWN>2.3.CO;2

O'Donell. D., (1979). Creighton Mine orebody characteristics, Unpublished internal report to INCO, 88p

Passchier, C. W., & Trouw, R. R. A. J. (2005). *Microtectonics*. *Microtectonics*. http://doi.org/10.1007/978-3-662-08734-3

Paton, C., Hellstrom, J., Paul, B., Woodhead, J., Hergt, J., Kosler, J., … Wahba, G. (2011). Iolite: Freeware for the visualisation and processing of mass spectrometric data. *Journal of Analytical Atomic Spectrometry*, *26*(12), 2508. http://doi.org/10.1039/c1ja10172b

Pedrick, J. N., Karlstrom, K. E., & Bowring, S. A. (1998). Reconciliation of conflicting tectonic models for Proterozoic rocks of northern New Mexico. *Journal of Metamorphic Geology*, *16*(5), 687–707. http://doi.org/10.1111/j.1525-1314.1998.00165.x

Piercey, P., Schneider, D. A., & Holm, D. K. (2007). Geochronology of Proterozoic metamorphism in the deformed Southern Province, northern Lake Huron region, Canada. *Precambrian Research*, *157*(1–4), 127–143. http://doi.org/10.1016/j.precamres.2007.02.013

Raharimahefa, T., Lafrance, B., Tinkham, D. K., & Corfu, F. (2014). New structural, metamorphic, and U–Pb geochronological constraints on the Blezardian Orogeny and Yavapai Orogeny in the Southern Province, Sudbury, Canada. *Canadian Journal of Earth Sciences*, *51*(8), 750–774. http://doi.org/10.1139/cjes-2014-0025

Rasmussen, B., Zi, J.-W., Sheppard, S., Krapež, B., & Muhling, J. R. (2016). Multiple episodes of hematite mineralization indicated by U-Pb dating of iron-ore deposits, Marquette Range, Michigan, USA. *Geology*, *44*(7), 547–550. http://doi.org/10.1130/G37783.1

Riller, U., & Schwerdtner, W. M. (1997). Documentation of a 1450 Ma contractional orogeny preserved between the 1850 Ma Sudbury impact structure and the 1 Ga Grenville orogenic

front, Ontario: Discussion and Reply. *Geological Society of America Bulletin*, *109*(9), 1228–1230. http://doi.org/10.1130/0016-7606(1997)109<1228:DOAMCO>2.3.CO;2

Riller, U., Schwerdtner, W. M., Halls, H. C., & Card, K. D. (1999). Transpressive tectonism in the eastern Penokean orogen, Canada consequences for Proterozoic crustal kinematics and continental fragmentation. *Precambrian Research*, *93*, 51–70. http://doi.org/10.1016/S0301-9268(98)00097-7

Riller, U. (2005). Structural characteristics of the Sudbury impact structure, Canada: Impact-induced versus orogenic deformation-A review. *Meteoritics & Planetary Science*, *40*, 1723–1740. http://doi.org/10.1111/j.1945-5100.2005.tb00140.x

Rolland, Y., Cox, S., Boullier, A. M., Pennacchioni, G., & Mancktelow, N. (2003). Rare earth and trace element mobility in mid-crustal shear zones: Insights from the Mont Blanc Massif (Western Alps). *Earth and Planetary Science Letters*, *214*(1–2), 203–219. http://doi.org/10.1016/S0012-821X(03)00372-8

Schulz, K. J., & Cannon, W. F. (2007). The Penokean orogeny in the Lake Superior region. *Precambrian Research*, *157*, 4–25. http://doi.org/10.1016/j.precamres.2007.02.022

Schmitz, M. D., & Bowring, S. A. (2001). U-Pb zircon and titanite systematics of the Fish Canyon Tuff: An assessment of high-precision U-Pb geochronology and its application to young volcanic rocks. *Geochimica et Cosmochimica Acta*, *65*(15), 2571–2587. http://doi.org/10.1016/S0016-7037(01)00616-0

Shaw, C. A., Karlstrom, K. E., Williams, M. L., Jercinovic, M. J., & McCoy, A. M. (2002). Electron-microprobe monazite dating of ca. 1.71-1.63 Ga and ca. 1.45-1.38 Ga deformation in the Homestake shear zone, Colorado: Origin and early evolution of a persistent intracontinental tectonic zone. *Geology*, *29*(8), 739–742. http://doi.org/10.1130/0091-7613(2001)029<0739:EMMDOC>2.0.CO;2

Sims, P. K., Card, K. D., Morey, G. B., & Peterman, Z. E. (1980). The Great Lakes tectonic zone — A major crustal structure in central North America. *Geological Society of America Bulletin*, *91*(12), 690. http://doi.org/10.1130/0016-7606(1980)91<690:TGLTZA>2.0.CO;2

Sims, P. K., Schmus, W. R. Van, Schulz, K. J., & Peterman, Z. E. (1989). Tectono-stratigraphic evolution of the Early Proterozoic Wisconsin magmatic terranes of the Penokean Orogen. *Canadian Journal of Earth Sciences*. http://doi.org/10.1139/e89-180

Sims, P.K., and Day, W.C., 1993, The Great Lakes tectonic zone – Revisited: U.S. Geological Survey Bulletin 1904-S, 11 p

Snelling, P. E., Godin, L., & McKinnon, S. D. (2013). The role of geologic structure and stress in triggering remote seismicity in Creighton Mine, Sudbury, Canada. *International Journal of Rock Mechanics and Mining Sciences*, *58*, 166–179. http://doi.org/10.1016/j.ijrmms.2012.10.005

Spandler, C., Hammerli, J., Sha, P., Hilbert-Wolf, H., Hu, Y., Roberts, E., & Schmitz, M. (2016). MKED1: A new titanite standard for in situ analysis of Sm–Nd isotopes and U–Pb geochronology. *Chemical Geology*, *425*, 110–126. http://doi.org/10.1016/j.chemgeo.2016.01.002

Spray, J. G., Butler, H. R., & Thompson, L. M. (2004). Tectonic influences on the morphometry of the Sudbury impact structure: Implications for terrestrial cratering and modeling. *Meteoritics & Planetary Science*, *39*, 287–301. http://doi.org/10.1111/j.1945-5100.2004.tb00341.x

Stacey, J. S., & Kramers, J. D. (1975). Approximation of terrestrial lead isotope evolution by a two-stage model. *Earth and Planetary Science Letters*, *26*(2), 207–221. http://doi.org/10.1016/0012-821X(75)90088-6

Tohver, E., Holm, D. K., van der Pluijm, B. A., Essene, E. J., & Cambray, F. W. (2007). Late Paleoproterozoic (geon 18 and 17) reactivation of the Neoarchean Great Lakes Tectonic Zone, northern Michigan, USA: Evidence from kinematic analysis, thermobarometry and 40Ar/39Ar geochronology. *Precambrian Research*, *157*(1–4), 144–168. http://doi.org/10.1016/j.precamres.2007.02.014

Tollo, R.P., Corriveau, L., McLelland, J., and Bartholomew, M.J., 2004, Proterozoic tectonic evolution of the Grenville orogen in North America: An introduction, *in* Tollo, R.P., Corriveau, L., McLelland, J., and Bartholomew, M.J., eds., Proterozoic tectonic evolution of the Grenville

orogen in North America: Boulder, Colorado,Geological Society of America Memoir 197, p. 1–18

Van Schmus, W. R., Schneider, D. A., Holm, D. K., Dodson, S., & Nelson, B. K. (2007). New insights into the southern margin of the Archean–Proterozoic boundary in the north-central United States based on U–Pb, Sm–Nd, and Ar–Ar geochronology. *Precambrian Research*, *157*(1), 80–105. http://doi.org/10.1016/j.precamres.2007.02.011

Verts, L. A., Chamberlain, K. R., & Frost, C. D. (1996). U-Pb sphene dating of metamorphism: the importance of sphene growth in the contact aureole of the Red Mountain pluton, Laramie Mountains, Wyoming. *Contributions to Mineralogy and Petrology*, *125*(2–3), 186–199. http://doi.org/10.1007/s004100050215

Whitmeyer, S. J., & Karlstrom, K. E. (2007). Tectonic model for the Proterozoic growth of North America. *Geosphere*, *3*, 220–259. http://doi.org/10.1130/GES00055.1

Young, G. M., Long, D. G. F., Fedo, C. M., & Nesbitt, H. W. (2001). Paleoproterozoic Huronian basin: Product of a Wilson cycle punctuated by glaciations and a meteorite impact. *Sedimentary Geology*, *141-142*, 233–254. doi:10.1016/S0037-0738(01)00076-8

Zolnai, a. I., Price, R. a., & Helmstaedt, H. (1984). Regional cross section of the Southern Province adjacent to Lake Huron, Ontario: implications for the tectonic significance of the Murray Fault Zone. *Canadian Journal of Earth Sciences*, *21*(4), 447–456. doi:10.1139/e84-048

Supplementary material of Chapter 5

Table 13 (Supplementary material). LA-ICP-MS conditions with Agilent 7500cs)

Laser Ablation system	
Instrument model	RESOlution SE ArF (Argon-Fluoride)
Ablation cell	Laurin S155 (dual volume design)
Laser wavelength	193nm
Pulse width	3ns
Fluence (energy density)	ca. 2J/cm2
Energy distribution	Flat homogenised
Repetition rate	2HZ
	He (ca. 300ml/min), Ar make-up gas combined using a y-piece
Carrier Gas	ca. 50% along sample line
Ablation mode	static ablation
Spot size	20-30µm

ICP parameters	
ICPMS	Agilent 7500cs (quadrupole)
RF power	1300W

Acquisition parameters	
Scanning mode	Peak hopping
Acquisition mode	time-resolved analysis
Analysis time	20 s blank and 40 s ablation
Isotope	Dwell time
202Hg	0.02 s
204Pb	0.02 s
206Pb	0.02 s
207Pb	0.04 s
208Pb	0.02 s
232Th	0.02 s
235U	0.03 s
238U	0.02 s

Table 14 (Supplementary material). LA-ICP-MS conditions with Plasma Quant Elite

Laser Ablation system	
Instrument model	RESOlution SE ArF (Argon-Fluoride)
Ablation cell	Laurin S155 (dual volume design)
Laser wavelength	193nm
Pulse width	3ns
Preablation	3 pulses
Fluence (energy density)	2J/cm^2
Energy distribution	Flat homogenised
Repetition rate	2HZ
Carrier Gas	He (ca. 300ml/min), Ar make-up gas combined using a y-piece ca. 50% along sample line
Ablation mode	static ablation
Spot size	20-30µm

ICP parameters	
ICPMS	Plasma Quant Elite (quadrupole)
RF power	1200W

Acquisition parameters	
Scanning mode	peak hopping
Acquisition mode	time-resolved analysis
Analysis time	20 s blank and 40 s ablation
Isotope	Dwell time
202Hg	0.02s
204Pb	0.02s
206Pb	0.02s
207Pb	0.02s
208Pb	0.02s
232Th	0.02s
235U	0.03s
238U	0.02s

Table 15 (Supplementary material). U-Pb isotopic data from titanite of the RAR shear zone (low-strain domain)

Target	238/206	238/206err	207/206	207/206err
KPCM03_1	1.946	0.072	0.479	0.017
KPCM03_2	1.701	0.064	0.512	0.019
KPCM03_3	2.041	0.079	0.462	0.018
KPCM03_4	2.000	0.076	0.462	0.017
KPCM03_5	2.083	0.069	0.408	0.014
KPCM03_6	1.524	0.063	0.554	0.022
KPCM03_7	2.288	0.084	0.404	0.015
KPCM03_8	1.866	0.070	0.474	0.021
KPCM03_9	1.980	0.078	0.435	0.016
KPCM03_10	1.195	0.057	0.671	0.032
KPCM03_11	1.842	0.075	0.525	0.024
KPCM03_12	1.091	0.057	0.673	0.034
kpcm02a_1	1.757	0.108	0.522	0.029
kpcm02a_2	2.016	0.110	0.433	0.023
kpcm02a_3	1.712	0.106	0.473	0.025
kpcm03_1	1.786	0.108	0.522	0.028
kpcm03_2	1.348	0.089	0.618	0.049
kpcm03_3	1.898	0.108	0.467	0.027
st_1 (kpcm09)	1.919	0.129	0.416	0.034
st_2 (kpcm09)	1.887	0.117	0.461	0.032
st_3 (kpcm09)	2.375	0.135	0.370	0.025
KPCM03_1	1.672	0.109	0.516	0.032
KPCM03_2	2.304	0.106	0.382	0.022
KPCM03_3	2.132	0.100	0.366	0.017
KPCM03_4	1.996	0.116	0.419	0.032
KPCM03_5	1.410	0.113	0.609	0.058
KPCM03_6	2.188	0.115	0.425	0.027
KPCM03_7	1.431	0.104	0.558	0.047
KPCM03_8	1.618	0.092	0.535	0.036
KPCM03_9	2.169	0.099	0.358	0.020
KPCM03_10	2.188	0.120	0.440	0.030
KPCM03_11	1.618	0.099	0.558	0.034
KPCM03_12	1.976	0.102	0.475	0.027
KPCM03_14	1.506	0.091	0.615	0.041
KPCM03_15	2.404	0.104	0.293	0.015
kpcm09_1	2.577	0.120	0.305	0.019
kpcm09_2	2.370	0.107	0.326	0.017
kpcm09_3	2.252	0.127	0.363	0.026
kpcm09_4	2.525	0.153	0.307	0.028
kpcm09_6	2.008	0.133	0.478	0.033

Table 16 (Supplementary material). U-Pb isotopic data from titanite grains of the RAR shear zone (high-strain domain)

Target name	238/206	238/206 err	207/206	207/206err
PL17_6a	3.228	0.092	0.135	0.006
PL17_6b	3.300	0.095	0.138	0.006
PL17_6c	3.303	0.092	0.143	0.005
PL17_7a	3.385	0.091	0.139	0.005
PL17_7b	3.196	0.097	0.184	0.007
PL17_8a	3.493	0.084	0.122	0.004
PL17_8b	3.343	0.086	0.136	0.004
PL17_8c	3.296	0.098	0.152	0.006
PL17_9a	3.336	0.086	0.130	0.005
PL17_9b	3.334	0.090	0.130	0.005
PL17_10	3.459	0.089	0.134	0.005
PL18_1b	3.040	0.120	0.208	0.013
PL18_1b2	3.110	0.116	0.206	0.011
PL18_2b	3.338	0.094	0.121	0.004
PL18_2c	3.375	0.098	0.130	0.005
PL18_3b	3.254	0.101	0.144	0.006
PL18_3b2	3.307	0.104	0.138	0.006
PL18_3b4	3.036	0.101	0.196	0.009
PL18_4b2	2.973	0.106	0.203	0.010
PL18_6b	3.352	0.097	0.126	0.004
PL18_4b_2	3.389	0.104	0.140	0.005
PL18_10(2)	3.408	0.096	0.123	0.004
PL14_7a	3.284	0.096	0.131	0.004
PL14_12a	3.358	0.097	0.126	0.004
PL14_12b	3.330	0.102	0.126	0.006
PL14_10a	3.240	0.105	0.128	0.006
PL14_10b	3.236	0.104	0.137	0.006
PL14_13	3.233	0.098	0.136	0.006
PL17_1	3.218	0.124	0.128	0.006
PL17_3	3.229	0.125	0.136	0.007
PL14_2	3.172	0.131	0.133	0.006
PL18_1	3.394	0.138	0.156	0.008
PL18_2	3.364	0.124	0.124	0.005
PL18_3	3.174	0.141	0.139	0.007

Table 17 (Supplementary material). U-Pb isotopic data from titanite grains of the Plum shear zone

Target	238/206	238/206err	207/206	207/206err
X0113_1	2.793	0.156	0.345	0.027
X0113_2	3.067	0.160	0.272	0.016
X0113_3	3.435	0.142	0.211	0.010
X0113_5	2.577	0.153	0.403	0.033
X0113_6	2.353	0.111	0.423	0.019
X0113_4	2.710	0.132	0.358	0.020
X0113_8	2.732	0.127	0.359	0.018
X0113_9	3.377	0.148	0.233	0.011
X0113_11	1.946	0.102	0.491	0.028
X0113_12	2.421	0.117	0.460	0.022
X0113_10	3.106	0.145	0.285	0.015
X0113_13	2.717	0.126	0.356	0.016
X0115_1	1.866	0.087	0.577	0.019
X0115_2	2.611	0.123	0.399	0.013
X0115_3	1.842	0.081	0.540	0.016
X0115_4	1.639	0.081	0.613	0.023
X0115_5	2.151	0.102	0.465	0.016
X0115_6	1.890	0.086	0.538	0.016
X0115_7	1.901	0.108	0.585	0.025
X0115_8	2.252	0.101	0.490	0.014
X0115_9	2.874	0.132	0.332	0.010
X0115_10	2.762	0.122	0.377	0.012
X0115_11	1.821	0.103	0.555	0.023
X0115_12	2.353	0.122	0.430	0.018
X0115_13	2.294	0.110	0.444	0.016
X0115_14	1.992	0.095	0.521	0.018
X0115_15	2.058	0.102	0.499	0.018
X0115_16	2.688	0.152	0.352	0.018

Table 18 (Supplementary material). U-Pb isotopic data from the 315 shear zone

Target	238/206	238/206 err	207/206	207/206 err
0110_2c	2.565	0.072	0.273	0.008
0110_4h2	2.932	0.073	0.187	0.004
0110_4h3	3.013	0.070	0.156	0.004
0110_4h4	2.899	0.073	0.181	0.005
0110_4h5	2.712	0.074	0.219	0.007
0110_4h6	3.005	0.073	0.157	0.004
0110_4bd	2.763	0.074	0.216	0.007
0110_4bb	2.832	0.071	0.214	0.005
0110_3ba	3.031	0.075	0.188	0.005
0110_3bb	2.864	0.090	0.242	0.008
0110_3bc	2.427	0.082	0.331	0.011
0110_4bc	3.204	0.079	0.151	0.004
0110_4ba	2.733	0.072	0.266	0.007

Table 19 (Supplementary material). Geochronological data from the wider area of the Sudbury structure related with the ca. 1.45 Ga event (Cheieflakian)

Isotopic system	Mineral	Date	Location	Reference
Rb-Sr	Muscovite	ca. 1450 Ma	Chief lake complex (Grenville Front)	Krogh and Davis., 1968
Rb-Sr	Epidote-chlorite-actinolite	1430±15 Ma	North Range of Sudbury structure (Footwall Breccia)	Deutsch et al., 1989
U-Pb	Titanite	1454±8 Ma	Killarney (Grenville front)	Haggart et al., 1993
U-Pb	Titanite	1453±6 Ma	Killarney (Grenville front)	Krogh, 1994
U-Pb	Monazite and Zircon	ca. 1445	Tyson lake area (Grenville province)	Dudas et al., 1994
U-Pb	Zircon	1471±10 Ma	Street Township (Grenville front)	Corfu and Easton., 2000
Ar-Ar	Biotite	1477±8 Ma	South range of Sudbury structure (Thayer Lindsley)	Bailey et al., 2004
K-Ar	Biotite	1410-1490±60 Ma	South range of Sudbury structure (Victoria Mine)	Szentpeteri, 2009 (PhD thesis)
Ar-Ar	Biotite	1377-1482±7.8 Ma	South range of Sudbury structure (Victoria Mine)	Szentpeteri, 2009 (PhD thesis)

Chapter 6. Titanite as a recorder and chronometer of large meteorite impact events

Konstantinos Papapavlou[1], James R. Darling[1], Desmond E. Moser[2], Lee F. White[1], Ivan R. Barker[2], EIMF[3], Peter C. Lightfoot[4], Craig D. Storey[1], and Joseph N. Dunlop[1]

[1]School of Earth and Environmental Sciences, University of Portsmouth, Portsmouth, PO1 3QL, UK
[2]Department of Earth Sciences, University of Western Ontario, London, Ontario, N6A 5B7, Canada
[3]Edinburgh Ion Microprobe Facility, School of Geosciences, Grant Institute, University of Edinburgh, West Main Road, Edinburgh EH9 3JW, UK
[4] Harquail School of Earth Sciences, Laurentian University, Sudbury, Ontario, P3E 2C6, Canada

Abstract

Identifying large impact structures is challenging as many of the traditional shock indicator phases are readily recrystallized during post-shock metamorphism. Highly robust phases such as zircon, while faithful recorders of shock wave passage, may respond with only partial Pb loss and deliver imprecise impact ages. With a lower closer temperature than many other robust chronometers, titanite ($CaTiSiO_5$) could serve as both an indicator and chronometer of shock metamorphism. We examined titanite grains within two well constrained shock metamorphic gradients in the uplifted crater floors of the Sudbury (Ontario, Canada) and Vredefort (South Africa) impact structures using EBSD microstructural and SIMS U-Pb dating techniques. All grains host a variety of impact-induced microstructural features, most prominently crosscutting microtwin planes oriented 75°/<010> and 108°/<010> relative to the host, reported here for first time in natural specimens. Microtwin-bearing titanite sampled outside the contact metamorphic aureole of the impact-induced melt sheet is not re-set by the impact event whereas total re-setting has occurred within ~200m of the melt sheet base. It is notable that at Sudbury, shock microstructures and ages survive in cores of grains even when reworked by tectonic mylonitisation. Overall, the microstructural chronology of shocked titanite can be regarded as an additional and widespread tool for the detection and dating of large meteorite impact events.

1. Introduction

The limited number of precisely and accurately dated terrestrial impact structures demonstrates that impact chronology is a challenging task (Jourdan et al., 2009). Uranium and thorium-bearing accessory phases, such as zircon ($ZrSiO_4$), baddeleyite (ZrO_2), and monazite ((LREE) PO_4), show growing potential as chronometers and recorders of impact bombardment (Krogh et al.,1984, Moser, 1997, Darling et al., 2016, Erickson et al., 2016). The high closure temperature of these phases (Zircon T_c = > 900°C; baddeleyite T_c = > 900°C, Monazite T_c = 700 to > 800°C) means that most shocked geochronometers preserve either a crystallization or partially impact-reset age (i.e. Abramov et al., 2013), with only those exposed to the most intense melt-sheet induced heating recording a true age of shock metamorphism (Moser et al., 2011). Titanite ($CaTiSiO_5$) is a widely occurring accessory mineral in an array of terrestrial settings (Frost et al., 2001), contains significant concentrations of U (0.1 to 1000 ppm), and most importantly has a lower closure temperature to Pb diffusion (~600-650 ºC; Cherniak, 1993) than other U-Th-Pb chronometers. In addition, it has also been reported from a wide range of planetary materials, including Martian shergottites (Langenhorst and Poirrier, 2000), lunar breccia deposits (Grieve et al., 1975), ultramafic ureilites (Guan and Crozaz, 2000), and Vesta-derived eucrites (Delaney et al., 1983). Accordingly, titanite may be a powerful recorder and chronometer of shock events within a wide range of planetary materials. However, such applications are currently hampered by a poor understanding of the microstructural and chemical response of titanite to shock loading and annealing.

The only previous examples of shock-induced titanite microstructures come from laboratory-controlled shock loading experiments (Deutsch and Scharer, 1990) and artificially shocked granitoids during nuclear detonation events (Short, 1966; Borg, 1970). Specifically, experimental shock loading up to ~59 GPa produced lowering of birefringence and intense mosaicism with a minimal effect on the U-Pb isotope systematics of titanite (Deutsch and Scharer, 1990). Structural and phase shifts in titanite (i.e. P2/a to A2/a space group shift) have also been observed at increasing pressure and temperature conditions (Ghose et al., 1991, Kunz et al., 1996, Angel et al., 1996). Shocked and fractured titanite was reported from the relatively small (6km diameter) Gardnos impact structure in Norway however no microstructural data have been reported for these samples, and U-Pb ages reflect pre-and

post-impact regional metamorphism (Kalleson et al., 2009). Given the fundamental difference between natural and experimental shock loading regimes (principally duration of shock loading), ground truthing of naturally shocked titanite grains is necessary to reconcile observations between experimental and natural systems. In this study, we combine quantitative microstructural analysis (electron backscatter diffraction; EBSD) with high-spatial resolution geochronology (secondary ion mass spectrometry; SIMS) to document and date impact-induced microstructures in shock-metamorphosed titanite grains from the two largest and oldest accepted impact craters on Earth: the Sudbury and Vredefort impact structures.

2.Geological background and sample description

The Vredefort structure (South Africa) represents one of the oldest, largest, and most deeply eroded terrestrial impact craters. It is a product of collision between a < 15 km bolide impactor (Ivanov, 2005) and the Archean Kaapvaal craton, producing a 20km diameter ultra-high temperature metamorphic aureole at 2020 $\pm$ 3 Ma in the central uplift (Moser, 1997). The chosen sample (**Figure 1A**) is a relatively titanite-rich Archean syenogranite outcropping in a large (~100m) exposure on the Skietkop farm at a radial distance of ~7km from the geographic center of the impact. It is situated at the edge of the impact-generated thermal metamorphic aureole in a zone where quartz shock microstructures are partially recrystallized (Grieve, 1990) and zircon is not yet exhibiting strong Pb-loss due to impact (Moser et al., 2011). It's distance from the base of the Vredefort melt sheet is not known as it has been removed by erosion.

The Sudbury impact structure is a deformed 1850 Ma meteorite crater hosted by Archean and Proterozoic supracrustal target rocks (Krogh et al., 1984), with an original crater diameter estimated of at least 250 km (Riller., 2005). Two titanite-bearing samples, a greenschist-facies overprinted felsic granulite and a foliated (mylonitised) pseudotachylite, have been sampled from the North and South Range respectively (**Figure 1B**). The North Range sample is hosted within the Levack gneiss complex approximately 600m north of the impact melt sheet and is characterized by the assemblage Quartz – Feldspar – Chlorite – Actinolite – Epidote ± Zircon ± Titanite ± Apatite. The mylonitic sample was retrieved approximately 2.4 km underground from a borehole that intersects the ore-controlling "RAR" shear zone in the Creighton Mine. The sample is from the low-strain domains of the shear

zone and exhibits alternating biotite and amphibole-rich domains. The mineral assemblage is Hornblende – Biotite – K-Feldspar – Epidote – Quartz – Titanite (± Ilmenite ± Zircon ± Apatite). The sample occurs ~ 150m from the melt sheet base, and is thus presumed to contain the most melt sheet-proximal titanite in this study. Zircon grains from the mylonitic sample, but also from adjacent shear zone samples of the Creighton Mine, show the development of one or two sets of planar features. These zircon grains locally exhibit in BSE images polycrystalline domains with development of neoblastic crystallites (**Item DR3**).

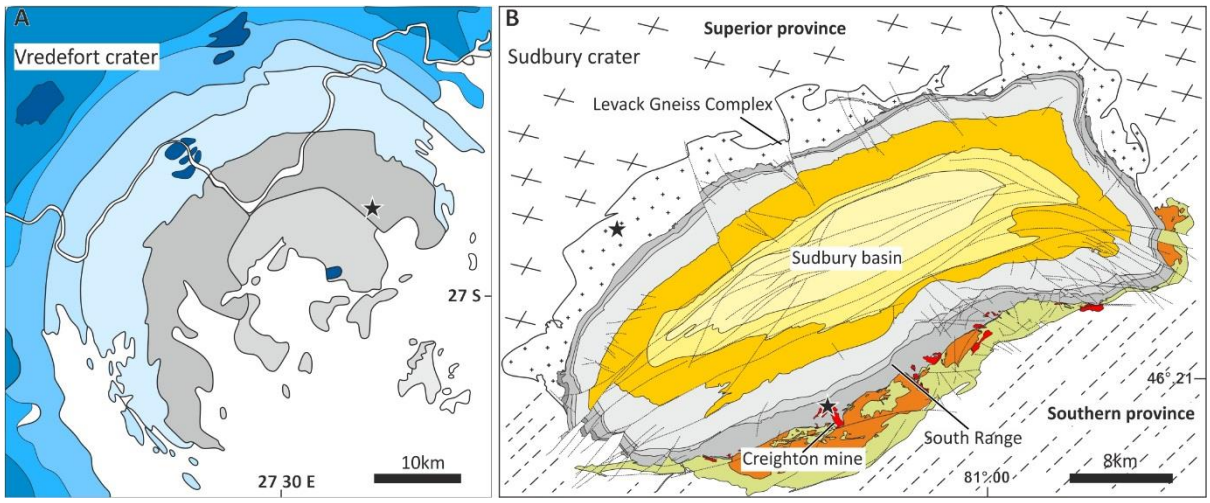

Figure 1. Simplified geological maps of the Vredefort (A) and Sudbury (B) impact structures. With black stars is denoted the location of the samples (look also Item DR1) examined in this study. Note that in Figure 1B, the sample of the South Range is projected at the surface.

3.Methodology

Titanite and zircon grains with different morphological features were detected *in-situ* on reflected light maps of polished thin, thick sections and grain mounts. The selected titanite grains from the Sudbury and Vredefort structures were imaged with backscattered electron (BSE) and forescattered electron (FSE) microscopy (**Items DR2 to DR5**) using different Scanning Electron Microscopes (SEM) at the University of Portsmouth (UK). After the electron beam imaging, selected titanite grains with features indicative of shock metamorphism were characterised microstructurally using the technique of electron backscatter diffraction (EBSD) at the University of Portsmouth (UK) and the ZAPLab (University of Western Ontario, CA). Analytical details for the collection of crystallographic data are provided in **Table DR1**. The *in-situ* U-Pb isotopic microanalysis of microstructurally characterised targets was performed at the Ion Microprobe Facility (University of Edinburgh, UK) using a Cameca 1270 SIMS.

Analytical conditions and data collection details of the Ion microprobe session are provided in **Item DR9** and **Table DR2**.

4.Results

4.1Titanite microstructures

4.1.1 Sudbury

Two major textural types of titanite grains are recognized in the North and South Range samples that we refer to as 'Type 1' and 'Type 2' grains. Type 1 grains exhibit crosscutting planar features whereas Type 2 titanite are characterised as patchily zoned grains that host ilmenite, apatite and biotite inclusions. Type 1 grains are present in the more pristine North Range gneisses, but are limited to inclusions within Type 2 grains in the tectonically overprinted sample from the South Range. The Type 1 grains from the South Range exhibit sector zoning and bright response in BSE images (**Item DR2**), and host one or two sets of equally spaced, parallel, planar features. In grains where two sets of planar features are observed, these cross-cut each other at 40° and 55°, in the North and South Range, respectively (**Figure 2A-D**). Band contrast maps of Type 1 grains show that the planar features in the backscatter electron images (**item DR2**) are twin lamellae with variable thickness (~ 1 μm to 5 μm) that laterally pinch out. These lamellae displace each other, an observation that indicates accommodated intracrystalline slip (**Figure 2A-D**). Strain-free neoblasts, likely produced by dynamic recrystallization during the tectonic deformation of the impact basin, are observed only in the Type 2 grains (**Figure 2C-D**).

High-resolution EBSD maps (i.e. step size = 100nm) of the inter-grain domains show that Type 1 inclusions operated as barriers to the propagation of recrystallization (**Figure 2C-D**). The Type 1 grains accommodate crystal-plastic strain up to 10° and in misorientation profiles across the twins show cumulative misorientation of ~74° relative to the host (**Items DR6 to DR8**). The isolated twin domains also record relative internal misorientations of up to 5°-6° (**Figure 2D**). Host and twins define overlapping point maxima in the (001) pole figure, thus the (001) is regarded as the glide plane. In terms of misorientation relationships, the St1 set of twins relative to the host shows 115°/<100>,75°/<010>, and 143°/101 whereas the St2 set of twins 68°/<100> and 108°/<010> and 43°/101 (**Figure 2, Pole figures**).

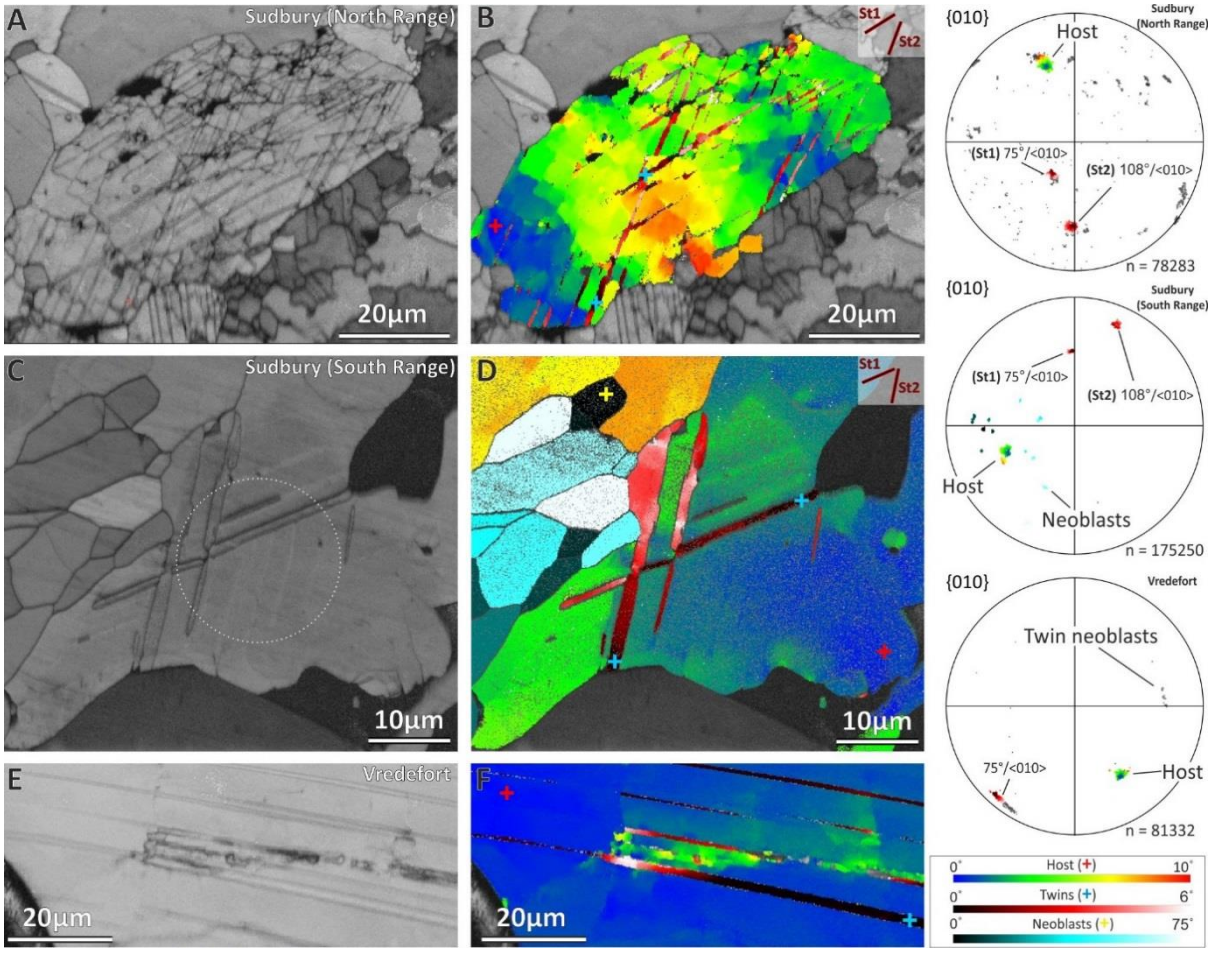

Figure 2. Collage of photographs that depicts in the first column band contrast maps (A,C,E), in the second misorientation maps (B,D,F), and in the third pole figures. In the first row the EBSD crystallographic data are from Type 1 titanite grains of the North Range, in the second row are depicted Type 1 and Type 2 grains from the South Range, and in the third Type 1 grains from the Vredefort structure.

4.1.2 Vredefort

High resolution maps (i.e. step size = 80nm) of the twin lamellae from the Vredefort grains show that the twin planes accommodated rotationally crystal-plastic strain up to the point of twin recrystallization and formation of neoblasts (**Figure 2E-F**). These plastically deformed twins and neoblastic, twin-related, crystallites follow small circle distributions (**Figure 2F, Pole figure**). In a grain with twin lamellae and planar features (target 15, **Item DR8**), the (001) is also recognized as the glide plane with misorientation relationships of 68°/<100>, 108°<010>, and 43°/<101> and cumulative misorientation across the twins of 74°. It is important to note that the St1 set of twins in Type 1 grains

from Sudbury and the twin lamellae from target 15 from Vredefort show identical misorientation relationships relative to their hosts (**Figure 2, Pole figures**).

5.*In-situ* U-Pb titanite geochronology

5.1 Sudbury

Six titanite grains from the RAR shear zone in the Sudbury structure, that host both Type 1 inclusions and Type 2 overgrowths were selected for microstructurally-targeted U-Pb age dating. Type 1 grains from the Sudbury structure contain up to 80 ppm U, and average Th/U = 0.95. Nine analyses (n = 9) targeted on twins or planar features, yield a weighted average $^{207}Pb/^{206}Pb$ age of 1851 ± 12 Ma (2σ, n = 9, MSWD = 0.76). In concordia space, U-Pb isotopic data from Type 1 grains yield a regressed upper intercept age of 1845 ± 14 Ma (2σ, n = 9, MSWD = 2.8) (**Figure 3A**). No systematic age variations related to the number of twins or planar features in each grain were observed. U-Pb isotopic data from grains with extremely low uranium contents (i.e. ~1 ppm), related with the type 2 dynamically recrystallized overgrowths, were not taken into consideration on the interpretation.

5.2 Vredefort

Seven grains from the Vredefort structure, with planar features and twin lamellae, were selected for U-Pb analysis Sixteen analyses (n = 16) were performed on different microstructural domains of the Vredefort grains. Two analyses with extremely high ^{204}Pb contents, relative to the rest, were rejected. The analysed grains have low concentrations of uranium (average 15 ppm) and twelve of them have average Th/U = 7.4. Two analyses located above recrystallized twins (target 6) show elevated Uranium contents (26 ppm) and decreased Th/U ratios (Th/U ~ 2). The U-Pb isotopic analyses yield a weighted average $^{207}Pb/^{206}Pb$ age of 2620±24 Ma (2σ, n = 14, MSWD = 20). A slightly younger $^{207}Pb/^{206}Pb$ age of 2441 ± 34 Ma, relative to the main age population, is recorded in only one case (target 12-1, **Table DR3**). In U-Pb concordia space the Vredefort titanites show a spread of $^{206}Pb/^{238}U$ ages between 2823 ± 33 Ma and 2378 ± 26 Ma defining a discordia line with upper intercept of 2636 ± 37 Ma and lower intercept of 1264 ± 490 Ma (2σ, n = 14, MSWD = 6.3) (**Figure 3B**).

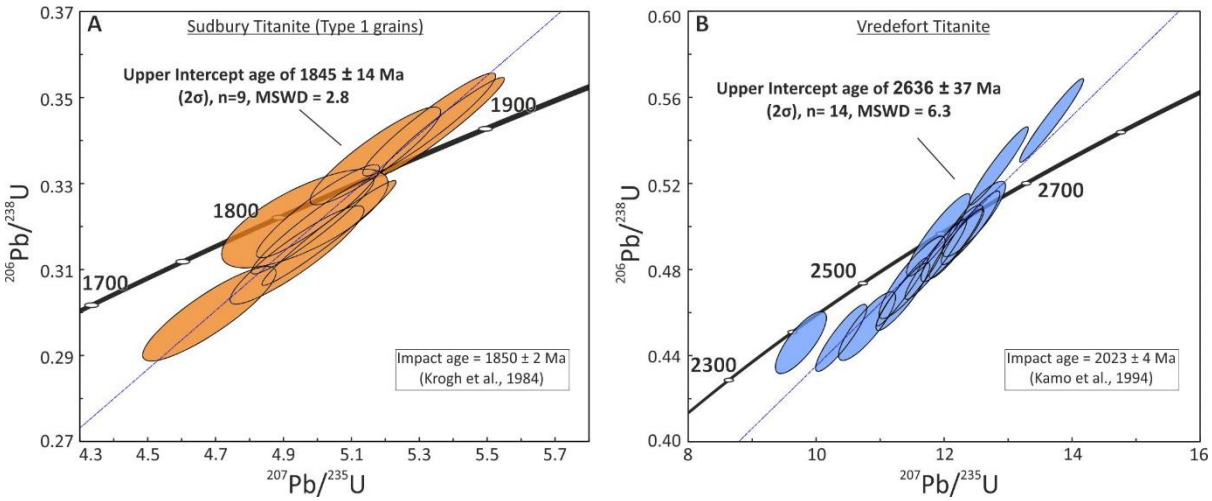

Figure 3. Wetherill – Concordia diagrams the depict U-Pb isotopic data from Type 1 titanite grains from the South Range of the Sudbury structure (diagram A) and the Vredefort structure (diagram B), respectively.

6.Discussion

6.1 Titanite microstructure as shock indicator

The only experimental microstructural data of shock loading in titanite, at ~2 GPa and T = 600-700°C, come from the Hardhat and Piledriver nuclear events in Nevada (Borg, 1972). In these events, initially untwinned titanite grains develop two sets of twins with the following elements: K1 (composition plane) irrational near {221} with η1 (shear direction) <110> and K2 {131} with η2 irrational. The two sets intersect each other at 55 ± 2° (Borg, 1970), in agreement with microtwin planes observed in the Type 1 grains from the Sudbury structure. The development of twin lamellae in the Sudbury grains induced a work-hardening effect that inhibited the propagation of brittle fracturing and dynamic recrystallization. This material behavior was critical on the preservation of the Type 1 grains as inclusions in the metasomatic/metamorphic, patchily zoned, Type 2 overgrowths.

Moreover, the common twin-host and cumulative misorientation relationships in twinned titanites from the Sudbury and Vredefort structures, and the newly reported microstructural phenomena suggest that the examined grains have genetic affinities and constitute the first microstructurally-justified examples of shock metamorphism in titanite. Similarities in the micro-scale geometrical features of the twin lamellae from both impact settings, and the presence within the same samples of zircons with shock-induced planar features support the initial hypothesis for the shock-induced deformation of these grains.

Taking into consideration these lines of evidence, and the absence of similar microstructures in titanite grains from other geological settings (Kennedy et al., 2010), we suggest that these shock microstructures can be used to ascertain meteoritic bombardment events in a wide range of titanite-bearing samples.

6.2 Implications for the U-Pb dating of impact events

Despite the textural similarities observed in titanite within both the Sudbury and Vredefort impact structures, the analysed U-Pb isotopic data from these grains yield different results. The protolith of the Vredefort titanite grains initially crystallized at around 3.4-3.1 Ga (Hart et al., 1999), thus the spread of U-Pb data observed here likely represents a partially age-reset grain population owing to Pb-loss induced by high-temperature metamorphism at ~2.7 Ga and/or the 2020 ± 3 Ma impact event itself (Moser, 1997). Conversely, titanite grains presenting crystallographically-similar twin domains from the South Range of the Sudbury structure yield an upper intercept U-Pb age of 1845 ± 14 Ma, in close agreement with high temporal resolution age constraints (ID-TIMS) placing the impact event at 1850 ± 2 Ma (Krogh et al., 1984). Remarkably, the $^{207}Pb/^{206}Pb$ and U-Pb dates from the Type 1 titanite population agree perfectly with the previous temporal constraints, suggesting complete radiogenic Pb-loss induced by the impact heating.

Although this age could theoretically be linked to an orogenic event during the impact (Penokean orogeny at 1.9 – 1.8 Ga, Sims et al., 1989), shear-hosted, Penokean-aged titanite grains from the South Range (1849 ± 6 Ma; Mukwakwami et al., 2014) are geochemically and texturally unrelated to the Type 1 shocked population of grains. Given the close proximity to the preserved impact melt sheet (150 – 200m), a plausible scenario is that the synergy of syn-impact mechanical twining and post-impact thermal metamorphism, with post-shock temperature estimates of ~ 850 to 1000°C (Lakomy, 1990), facilitated the complete age resetting of these grains. In comparison, the absence of high-temperature post-shock annealing within the more distal Vredefort sample likely prevented complete diffusion of radiogenic Pb. Instead the grains preserve evidence for partial Pb-loss and discordance due to a pre-impact 2.7 Ga thermal event likely related to the intrusion and cooling of Vetnersrdorp -age intrusions known to exist in the central uplift (Hart et al.,1999)

This new data mirrors age-resetting trends observed in zircon, where the generation of shock-induced features alone is not enough to induce age resetting, instead requiring post-

shock annealing to mobilize lead along impact-generated diffusion pathways (Moser et al., 2011). However, given the lower closure temperature of titanite (~650°C versus ~1000°C for zircon) we suggest that a larger abundance of titanite grains will record true impact ages, requiring less energy to encourage complete age resetting. This is particularly important when dating extra-terrestrial meteoritic material, where high shock pressures have facilitated ejection from the planetary surface before quenching in space. In these scenarios, zircon may be too resilient to Pb-loss, only recording resolved impact ages in rare, high-temperature granular domains and not in the more abundant microtwin planes observed in terrestrial (Moser et al., 2011) and Lunar samples (Cavosie et al., 2015). The age dating of impact-reset microstructures shows that titanite has great potential as a robust impact bombardment chronometer in lithologies lacking fully age-reset zircon.

Acknowledgements

K.P. acknowledges a University of Portsmouth research studentship. Vale ltd. is gratefully acknowledged for access to drillcore material. Vale geologists Lisa Gibson, Colin Mecke, Clarence Pickett and Rob Pelkey are thanked for the provided information and feedback.

References

Abramov, O., Kring, D. A., & Mojzsis, S. J. (2013). The impact environment of the Hadean Earth. *Chemie Der Erde - Geochemistry*, *73*(3), 227–248. http://doi.org/10.1016/j.chemer.2013.08.004

Angel, R. J., Ross, N. L., Seifert, F., & Fliervoet, T. F. (1996). Structural characterization of pentacoordinate silicon in a calcium silicate. *Nature*, *384*(6608), 441–444. http://doi.org/10.1038/384441a0

Borg, I. Y. (1970). Mechanical <110> twinning in shocked sphene. American Mineralogist, vol. 55, 1876-1888

Cavosie, A. J., Erickson, T. M., Timms, N. E., Reddy, S. M., Talavera, C., Montalvo, S. D., … Moser, D. (2015). A terrestrial perspective on using ex situ shocked zircons to date lunar impacts. *Geology*, *43*(11), 999–1002. http://doi.org/10.1130/G37059.1

Darling, J. R., Moser, D. E., Barker, I. R., Tait, K. T., Chamberlain, K. R., Schmitt, A. K., & Hyde, B. C. (2016). Variable microstructural response of baddeleyite to shock metamorphism in young basaltic shergottite NWA 5298 and improved U-Pb dating of Solar System events. *Earth and Planetary Science Letters*, *444*, 1–12. http://doi.org/10.1016/j.epsl.2016.03.032

Delaney, J. S., Takeda, H., Prinz, M., Nehru, C. E., & Harlow, G. E. (1983). The nomenclature of polymict basaltic achondrites. *Meteoritics*, *18*(2), 103–111. http://doi.org/10.1111/j.1945-5100.1983.tb00581.x

Deutsch, A., & Schärer, U. (1990). Isotope systematics and shock-wave metamorphism: I. U-Pb in zircon, titanite and monazite, shocked experimentally up to 59 GPa. *Geochimica et Cosmochimica Acta*, *54*(12), 3427–3434. http://doi.org/10.1016/0016-7037(90)90295-V

Erickson, T. M., Cavosie, A. J., Pearce, M. A., Timms, N. E., & Reddy, S. M. (2016). Empirical constraints on shock features in monazite using shocked zircon inclusions. *Geology*, *44*(8), 635–638. http://doi.org/10.1130/G37979.1

Frost, B. R., Chamberlain, K. R., & Schumacher, J. C. (2001). Sphene (titanite): Phase relations and role as a geochronometer. *Chemical Geology*, *172*(1–2), 131–148. http://doi.org/10.1016/S0009-2541(00)00240-0

Ghose, S., Ito, Y., & Hatch, D. (1991). Paraelectric-antiferroelectric phase transition in titanite, CaTiSiO5. *Physics and Chemistry of Minerals*, *17*(7), 591–603. http://doi.org/10.1007/BF00203838

Grieve, R. A., McKay, G. A., Smith, H. D., & Weill, D. F. (1975). Lunar polymict breccia 14321: a petrographic study. *Geochimica et Cosmochimica Acta*, *39*(3). http://doi.org/10.1016/0016-7037(75)90193-3

Grieve, R. A. F., Coderre, J. M., Robertson, P. B., & Alexopoulos, J. (1990). Microscopic planar deformation features in quartz of the Vredefort structure: Anomalous but still suggestive of an impact origin. *Tectonophysics*, *171*(1), 185–200. http://doi.org/10.1016/0040-1951(90)90098-S

Guan, Y. B., & Crozaz, G. (2000). Light rare earth element enrichments in ureilites: A detailed ion microprobe study. *Meteoritics & Planetary Science*, *35*(1), 131–144. http://doi.org/10.1111/j.1945-5100.2000.tb01980.x

Hart, R., Moser, D., & Andreoli, M. (1999). Archean age for the granulite facies metamorphism near the center of the Vredefort structure, South Africa. *Geology*, *27*(12), 1091–1094. http://doi.org/10.1130/0091-7613(1999)027<1091

Ivanov, B. A. (2005). Numerical modeling of the largest terrestrial meteorite craters. *Solar System Research*. http://doi.org/10.1007/s11208-005-0051-0

Jourdan, F., Renne, P. R., & Reimold, W. U. (2009). An appraisal of the ages of terrestrial impact structures. *Earth and Planetary Science Letters*, *286*(1–2), 1–13. http://doi.org/10.1016/j.epsl.2009.07.009

Kalleson, E., Corfu, F., & Dypvik, H. (2009). U–Pb systematics of zircon and titanite from the Gardnos impact structure, Norway: Evidence for impact at 546Ma? *Geochimica et Cosmochimica Acta*, *73*(10), 3077–3092. http://doi.org/10.1016/j.gca.2009.02.020

Kennedy, A. K., Kamo, S. L., Nasdala, L., & Timms, N. E. (2010). Grenville skarn titanite: Potential reference material for sims U-Th-Pb analysis. *Canadian Mineralogist*, *48*(6), 1423–1443. http://doi.org/10.3749/canmin.48.5.1423

Krogh, T.E., Davis, D.W. and Corfu, F. 1984. Precise U-Pb zircon and baddeleyite ages for the Sudbury area. In The Geology and Ore Deposits of the Sudbury Structure. Edited by E.G. Pye, A.J. Naldrett and P.E. Gilbin. Special Volume 1: 431-446, Ontario Geological Survey.

Kunz, M., Xirouchakis, D., Lindsley, D. H., & Hausermann, D. (1996). High-pressure phase transition in titanite (CaTiOSiO4). *American Mineralogist*, *81*(11–12), 1527–1530.

Lakomy, R. (1990). Implications for cratering mechanics from a study of the Footwall Breccia of the Sudbury impact structure, Canada. *Meteoritics*, *25*(3), 195–207. http://doi.org/10.1111/j.1945-5100.1990.tb00997.x

Langenhorst, F., & Poirier, J. P. (2000). “Eclogitic” minerals in a shocked basaltic meteorite. *Earth and Planetary Science Letters*, *176*(3–4), 259–265. http://doi.org/10.1016/S0012-821X(00)00028-5

Moser, D. E. (1997). Dating the shock wave and thermal imprint of the giant Vredefort impact, South Africa. *Geology*, *25*(1), 7–10. http://doi.org/10.1130/0091-7613(1997)025<0007:DTSWAT>2.3.CO;2

Moser, D. E., Cupelli, C. L., Barker, I. R., Flowers, R. M., Bowman, J. R., Wooden, J., & Hart, J. R. (2011). New zircon shock phenomena and their use for dating and reconstruction of large impact structures revealed by electron nanobeam (EBSD, CL, EDS) and isotopic U–Pb and (U–Th)/He analysis of the Vredefort domeThis article is one of a series of papers published in this Special Issue on the theme of Geochronology in honour of Tom Krogh. *Canadian Journal of Earth Sciences*, *48*(2), 117–139. JOUR. http://doi.org/10.1139/E11-011

Moser, D. E., Chamberlain, K. R., Tait, K. T., Schmitt, a K., Darling, J. R., Barker, I. R., & Hyde, B. C. (2013). Solving the Martian meteorite age conundrum using micro-baddeleyite and launch-generated zircon. *Nature*, *499*(7459), 454–7. http://doi.org/10.1038/nature12341

Mukwakwami, J., Lafrance, B., Lesher, C. M., Tinkham, D., Rayner, N., & Ames, D. (2014). Deformation, metamorphism, and mobilization of Ni–Cu–PGE sulfide ores at Garson Mine, Sudbury. *Mineralium Deposita*, *49*(2), 175–198. http://doi.org/10.1007/s00126-013-0479-y

Riller, U. (2005). Structural characteristics of the Sudbury impact structure, Canada: Impact-induced versus orogenic deformation-A review. *Meteoritics & Planetary Science*, *40*(11), 1723–1740. http://doi.org/10.1111/j.1945-5100.2005.tb00140.x

Short, N. M. (1966). Effects of shock pressures from a nuclear explosion on mechanical and optical properties of granodiorite. *Journal of Geophysical Research*, *71*(4), 1195–1215. http://doi.org/10.1029/JZ071i004p01195

Sims, P. K., Schmus, W. R. Van, Schulz, K. J., & Peterman, Z. E. (1989). Tectono-stratigraphic evolution of the Early Proterozoic Wisconsin magmatic terranes of the Penokean Orogen. *Canadian Journal of Earth Sciences*, *26*(10), 2145–2158. http://doi.org/10.1139/e89-180

Supplementary material of chapter 6

Titanite as recorder and chronometer of large meteorite impact events

Konstantinos Papapavlou[1a], James R. Darling[1], Desmond E. Moser[2], Lee F. White[1], Ivan R. Barker[2], Richard W. Hinton[3], Peter C. Lightfoot[4], Craig D. Storey[1] and Joseph N. Dunlop[1]

[1]School of Earth and Environmental Sciences, University of Portsmouth, Portsmouth, PO1 3QL, UK

[2]Department of Earth Sciences, University of Western Ontario, London, Ontario, N6A 5B7, Canada

[3]School of Geosciences, Grant Institute, University of Edinburgh, West Main Road, Edinburgh EH9 3JW, UK

[4] Harquail School of Earth Sciences, Laurentian University, Sudbury, Ontario, P3E 2C6, Canada

[a]Corresponding author: constantinepapapavlou@gmail.com

Contents

Item DR8. Electron Backscatter Diffraction (EBSD) Data of titanite grains from the Vredefort Impact structure

Item DR9. U-Pb Secondary Ion Microprobe Analysis (SIMS): Analytical details

Table DR1. Analytical conditions of EBSD data collection

Table DR2. U-Pb isotopic analyses of Sudbury titanite grains

Table DR3. U-Pb isotopic analyses of Vredefort titanite grains

Item DR1. **Location of the titanite-bearing samples examined in this study**

Sample's name	Location	Coordinates
KPCM09 (RAR shear zone)	Creighton Mine (Sudbury, South Range)	46°.47'67.75''N,81°.19'55.33''W
JD12SUD13	Levack Gneiss Complex (Sudbury, North Range)	46°36'21.90"N, 81°30'52.30"W
Vr_1	Vredefort	see text

Item DR2: Backscatter electron images of the two major titanite textural populations from the South Range of the Sudbury structure. The bright titanite cores with planar features are members of the type 1 grains. The grey overgrowths with patchy zoning and ilmenite inclusions are members of the type 2.

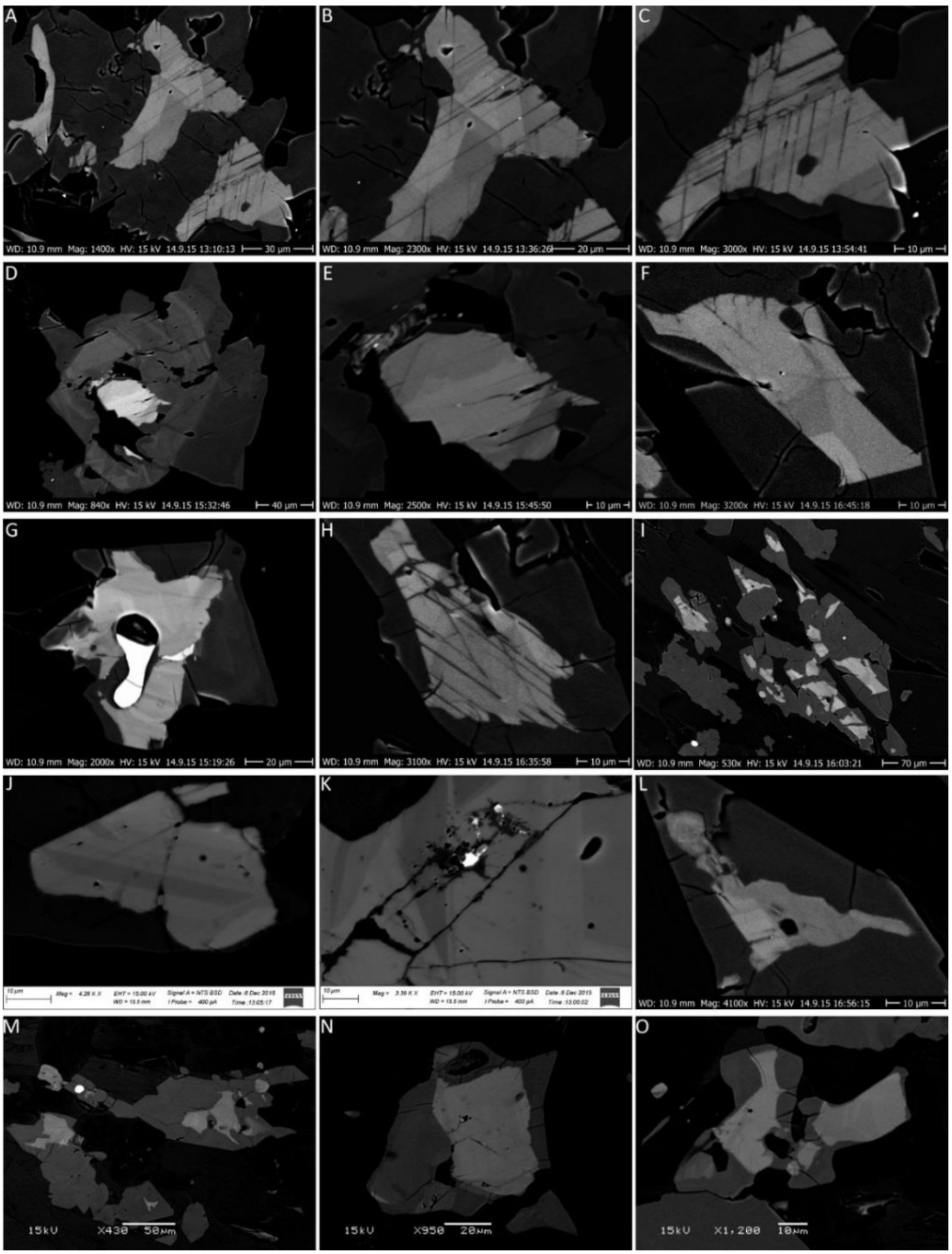

Item DR3: Backscatter electron images of zircons within shear zones of the South Range. The imaged grains are characterised by patchy zoning, at least two sets of planar features, intense fracturing, and locally show evidence of granulation (e.g. photomicrographs C and F). The photomicrographs A to I are from zircons grains located in the same sample that the bright titanite grains of the textural family a have been found. The photomicrographs J to O are from a shear zone adjacent to the RAR shear zone in the Creighton Mine.

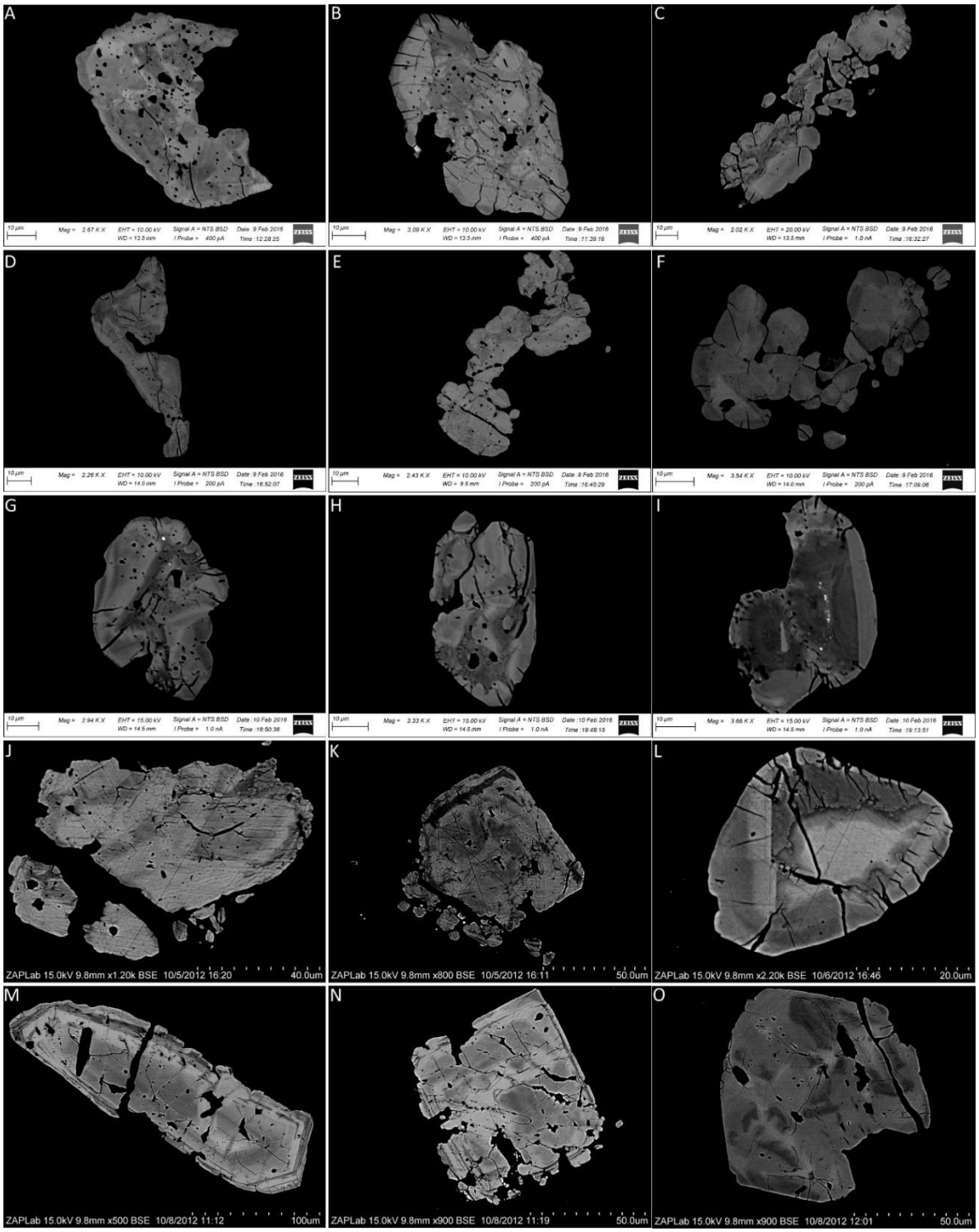

Item DR4: Backscatter electron images of titanite grains from the Vredefort impact structure. The grains show patchy zoning, planar features (e.g. photomicrographs A, D, and L), and orientated inclusion trails (e.g. photomicrographs A, B, G, and J). The oriented inclusions trails possibly denote the presence of annealed planar features.

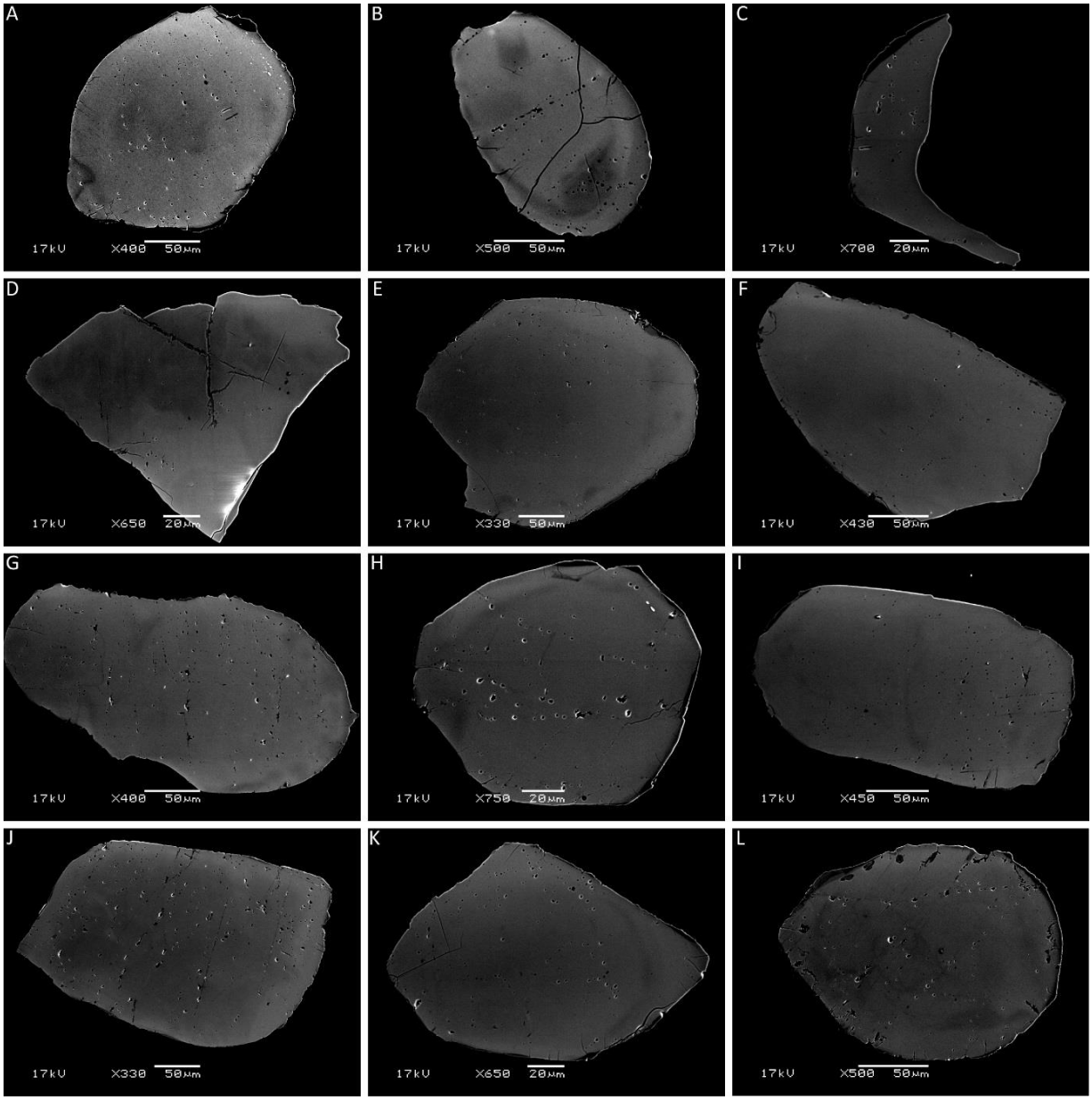

Item DR5: Forescatter electron images (FSD) that show orientation contrasts in the Vredefort titanite grains. Twins and planar features are expressed as lighter or darker bands in greyscale (e.g. photomicrographs D, E, F, and I).

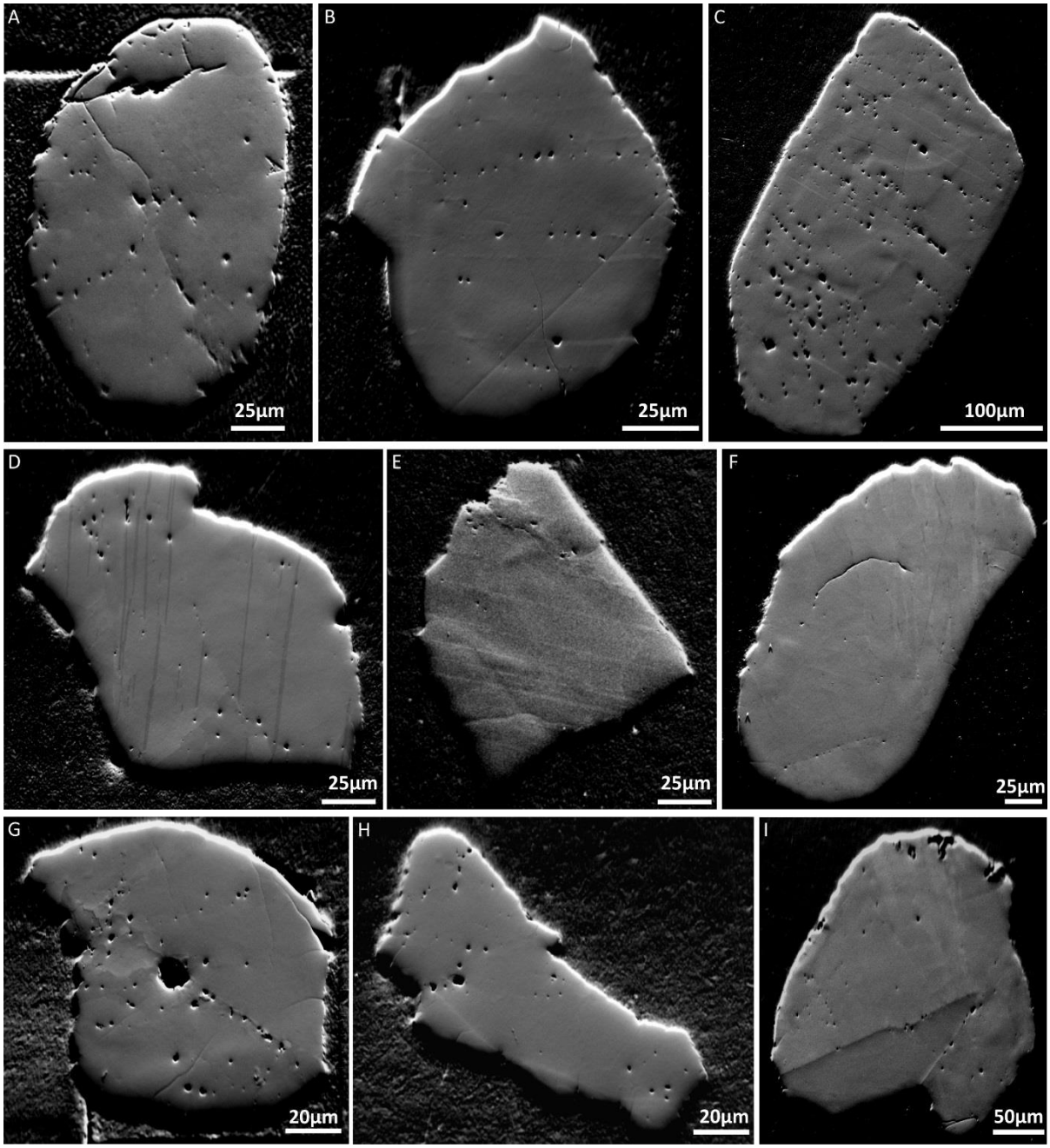

Items DR6 to DR8 : Upper panel – Band contrast and band slope maps. Lower panel – Misorientation and Euler maps. Below the maps are presented pole figures for each grain coloured based on the variations in misorientation values for each pixel.

Item DR6 (Target JD12SUD13_North Range of the Sudbury structure)

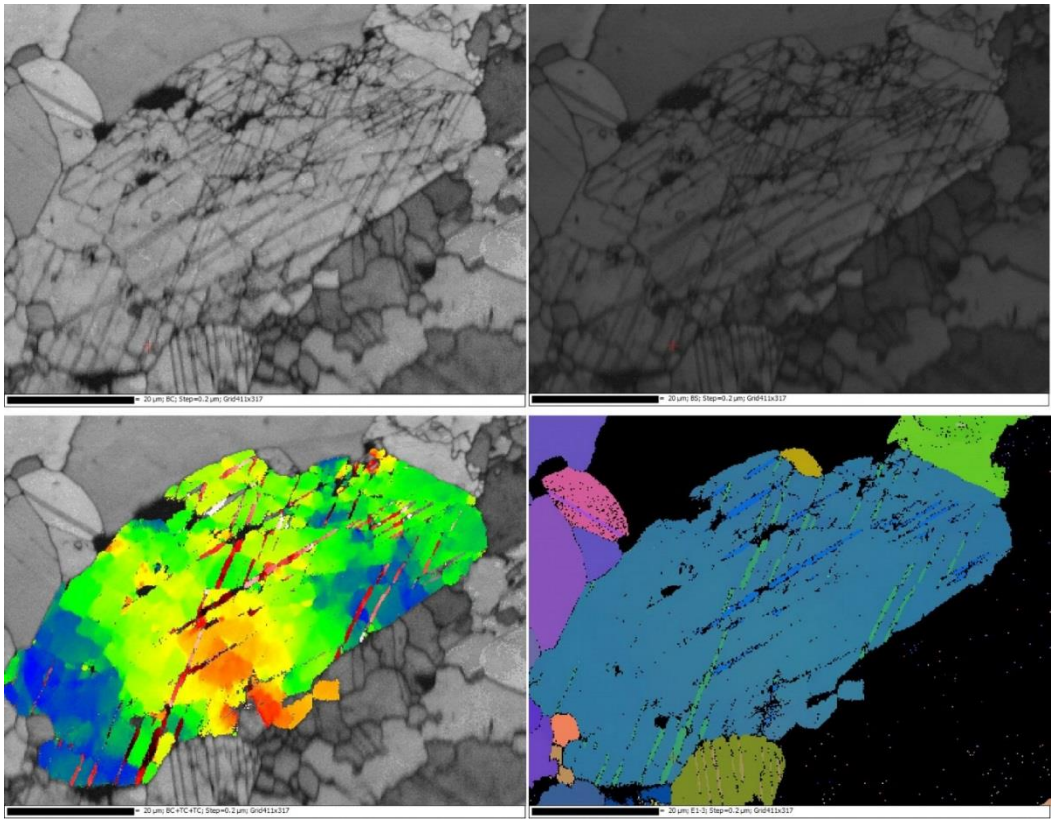

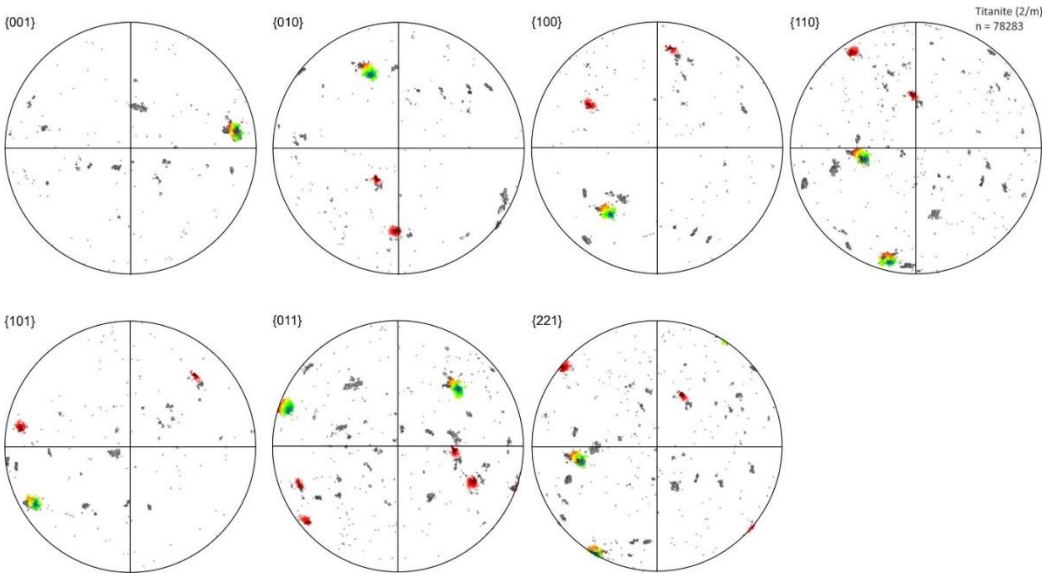

Item DR7 (Target 4_South Range of Sudbury structure)

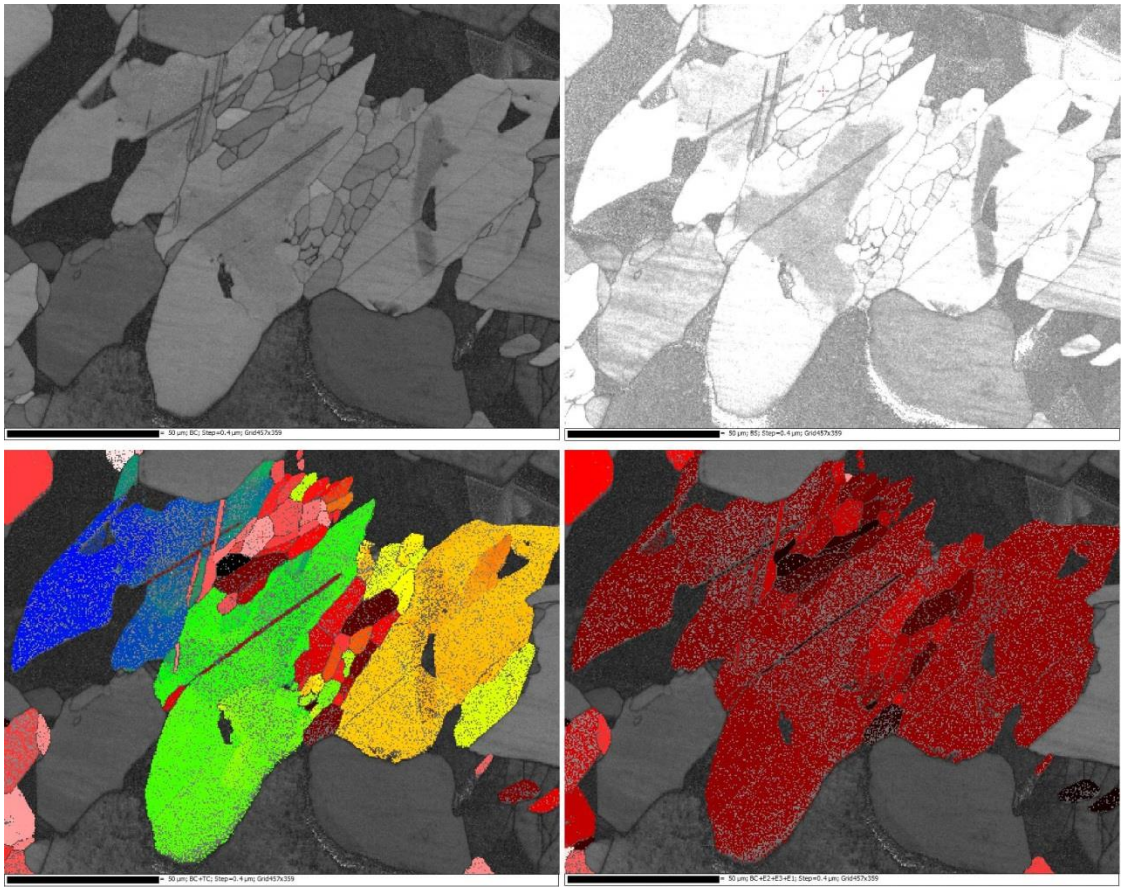

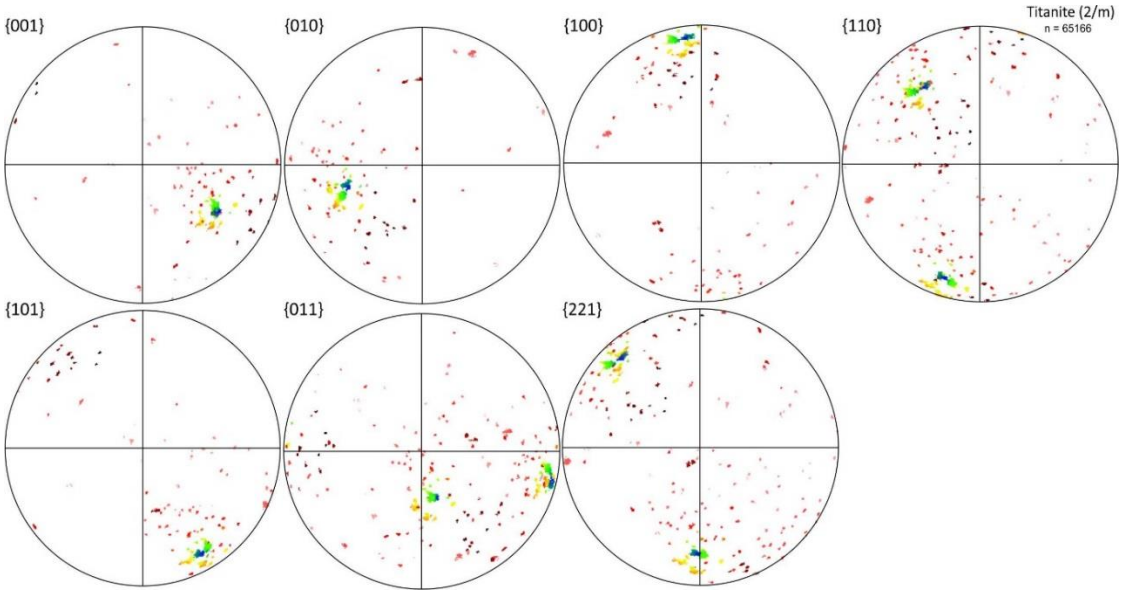

Item DR7 (Target 4HR_South Range of Sudbury structure):

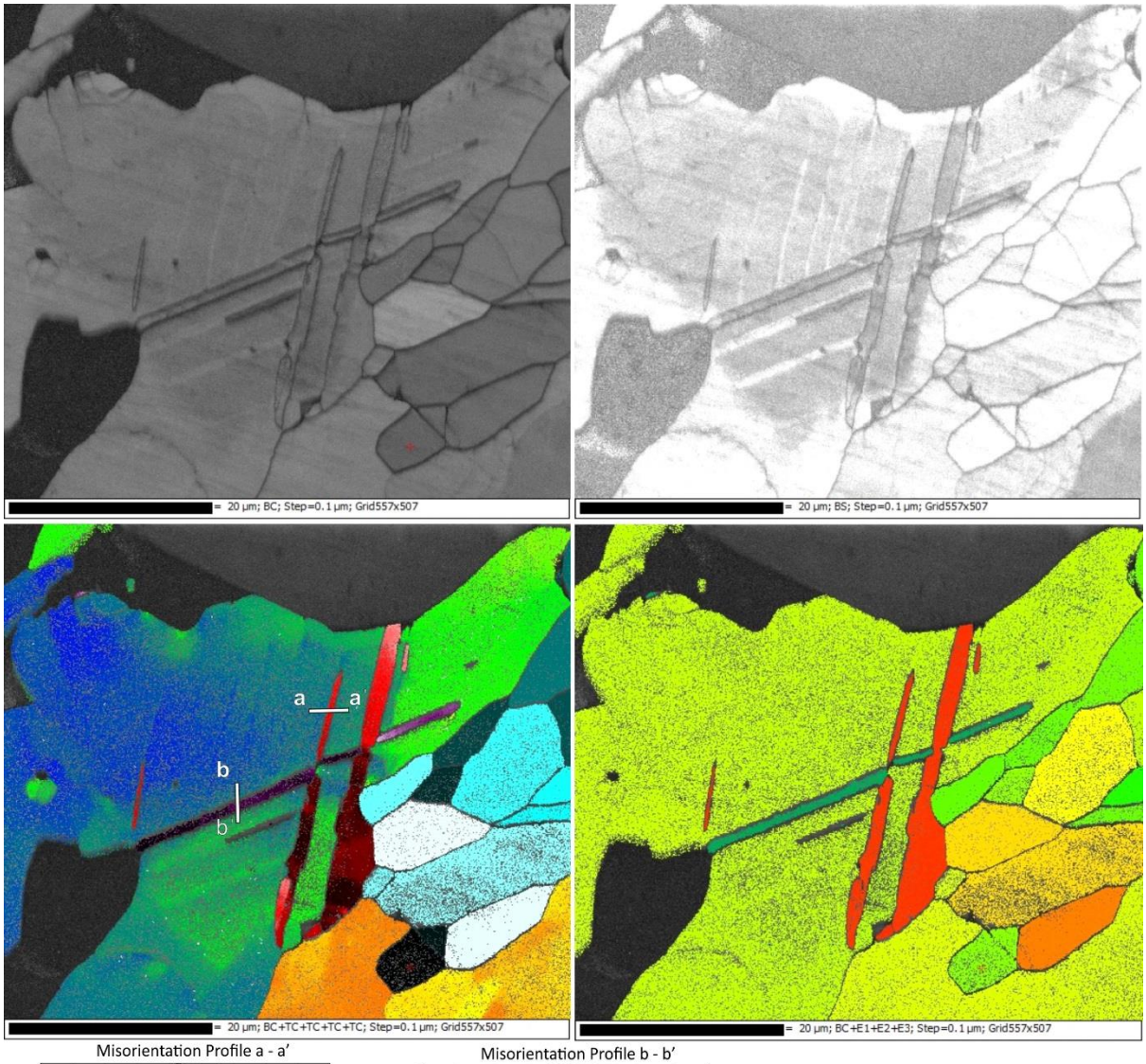

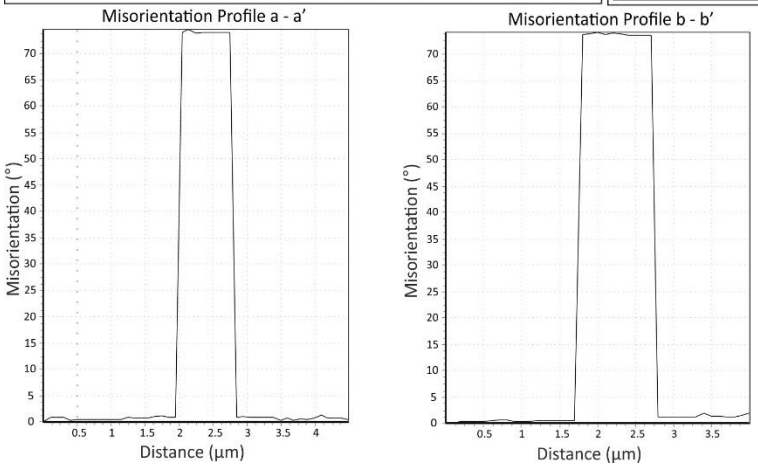

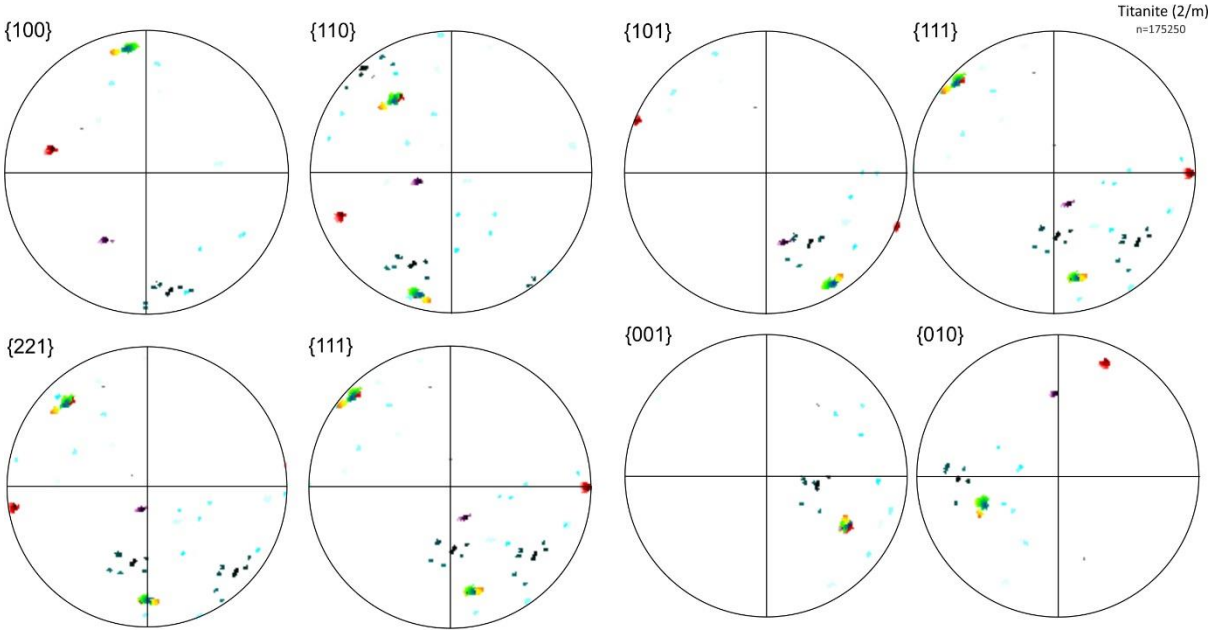

Item DR7 (Target 2_South Range of Sudbury structure)

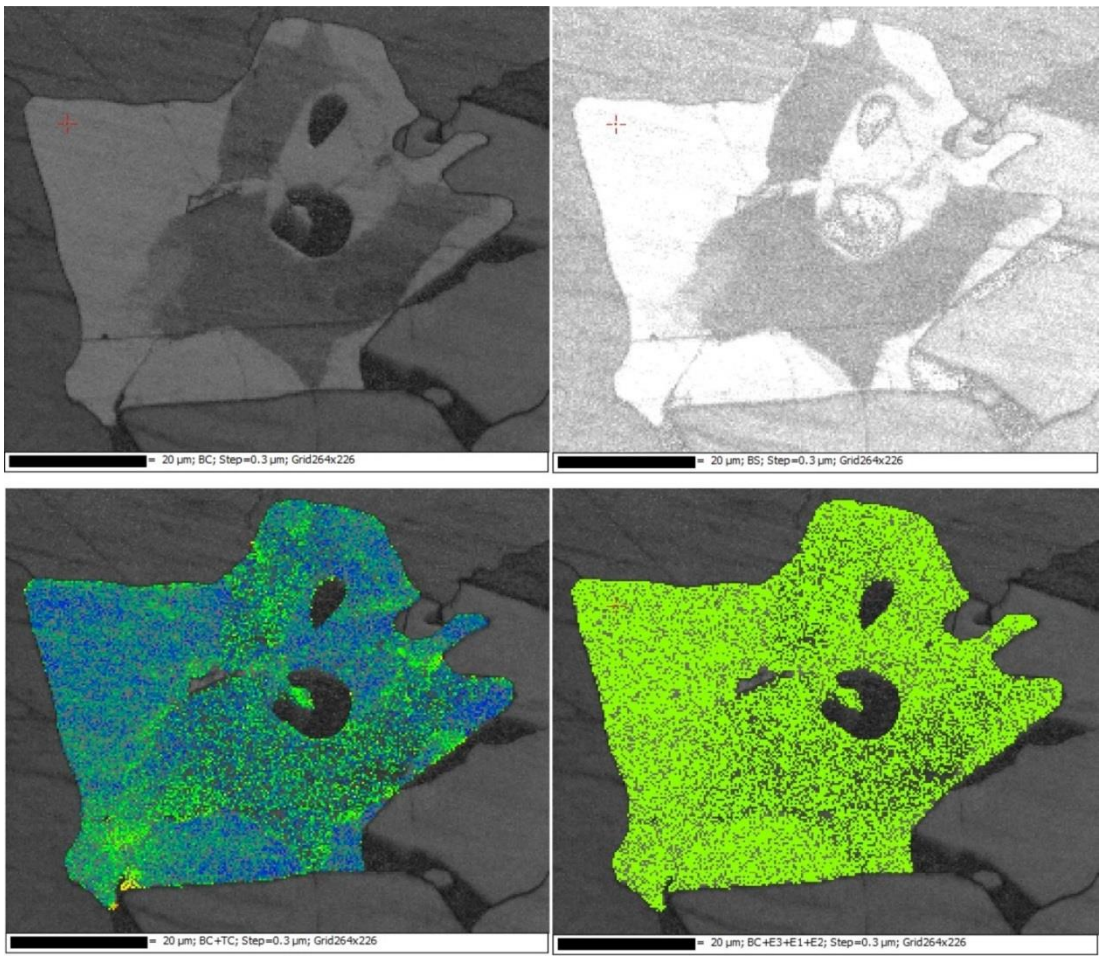

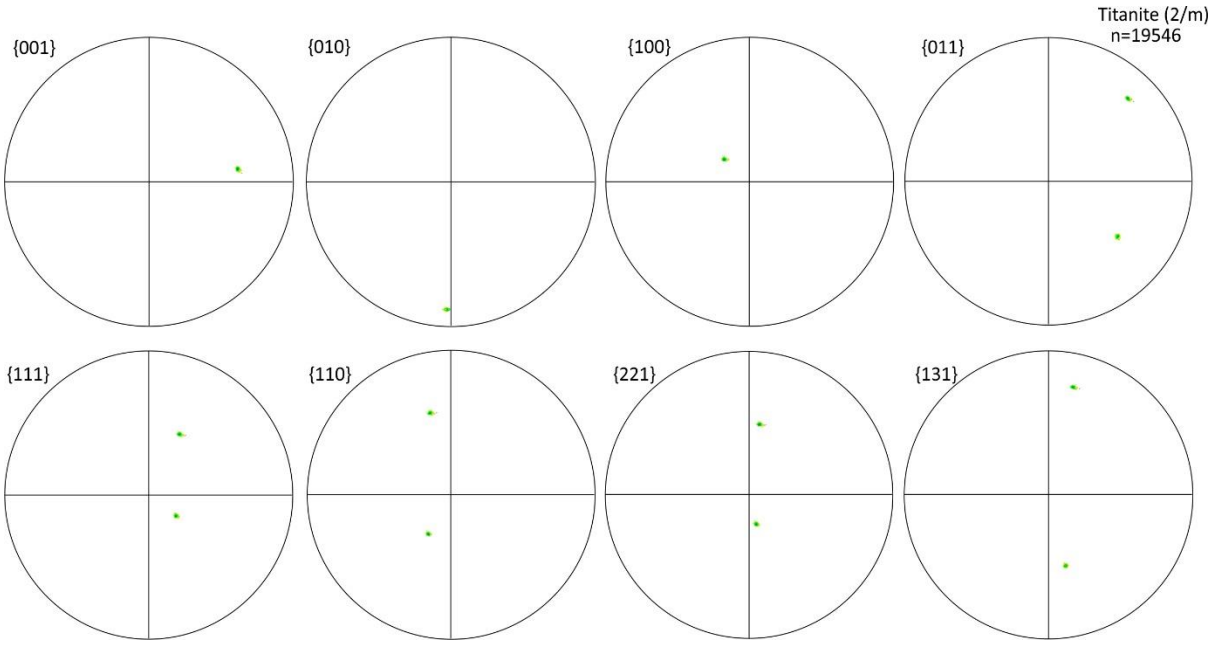

Item DR7 (Target 6-7_South Range of Sudbury structure)

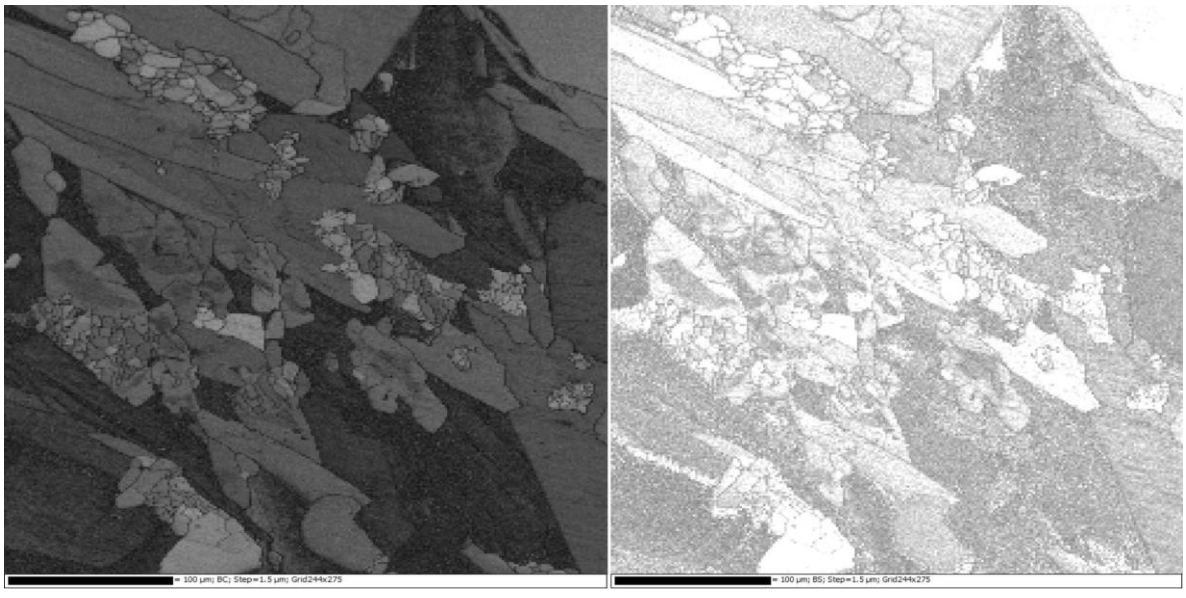

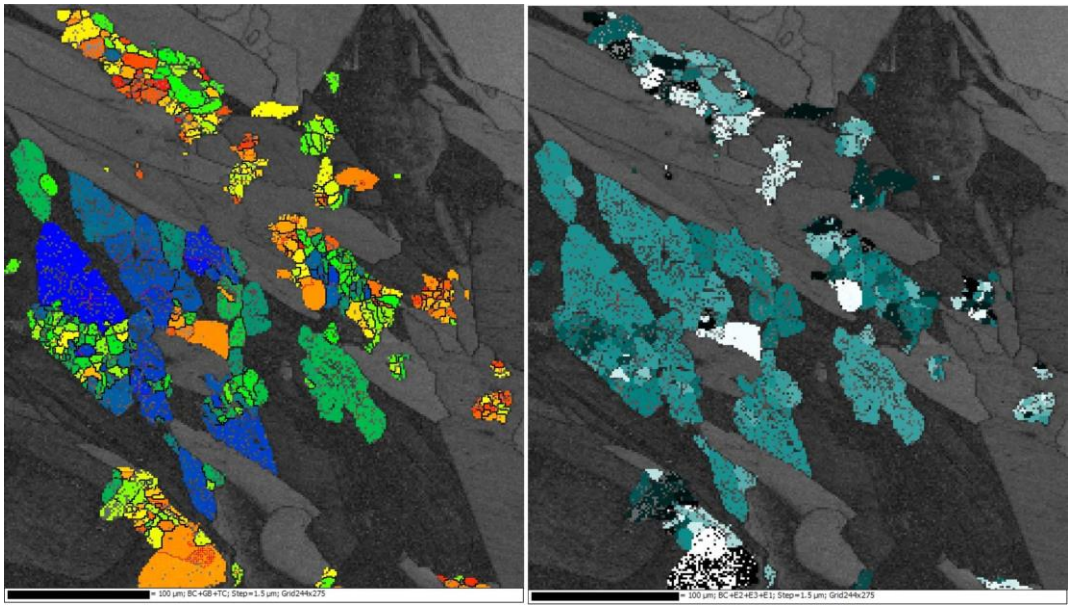

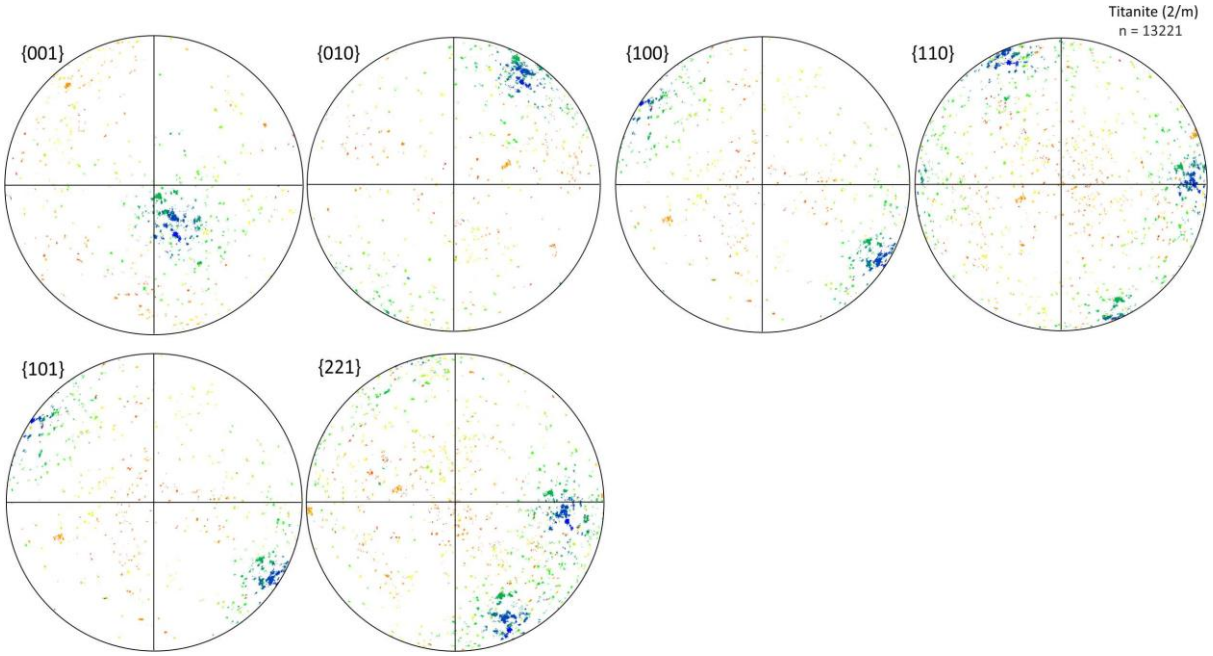
Titanite (2/m)
n = 13221
{001}
{010}
{100}
{110}
{101}
{221}

Item DR8 (Target 6_Vredefort structure)

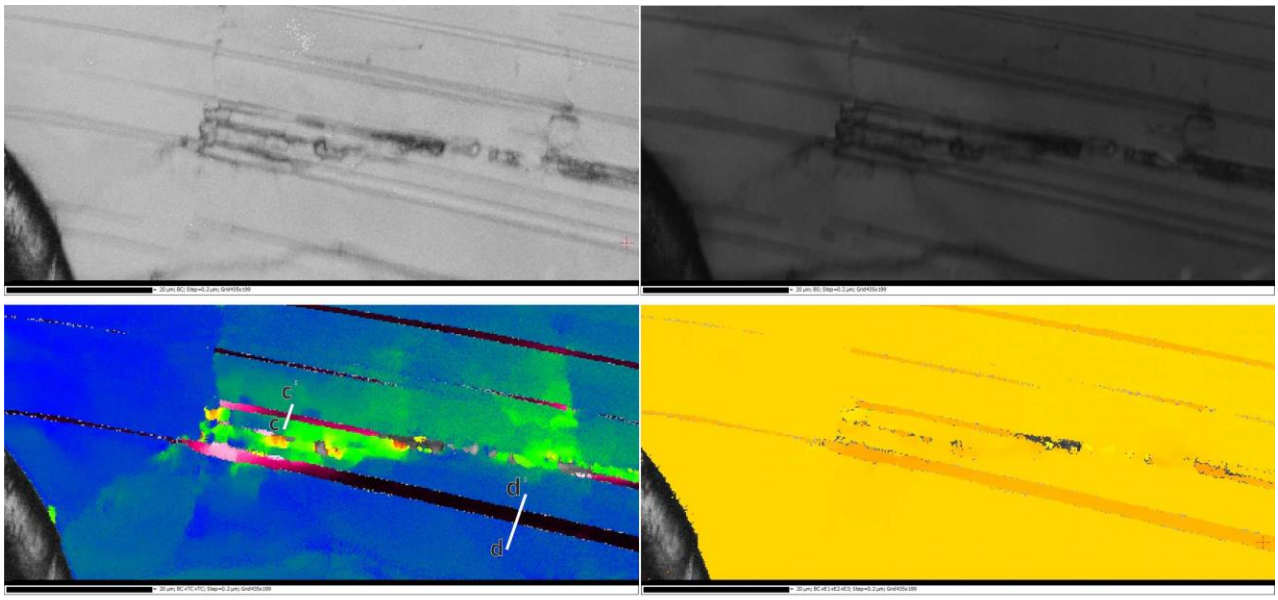

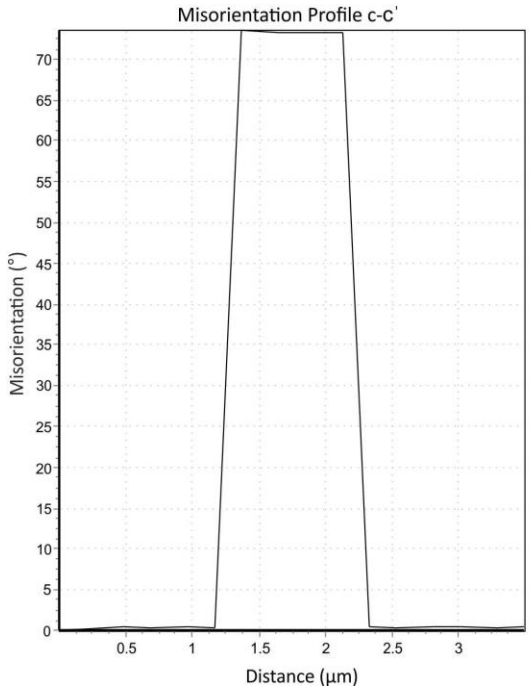

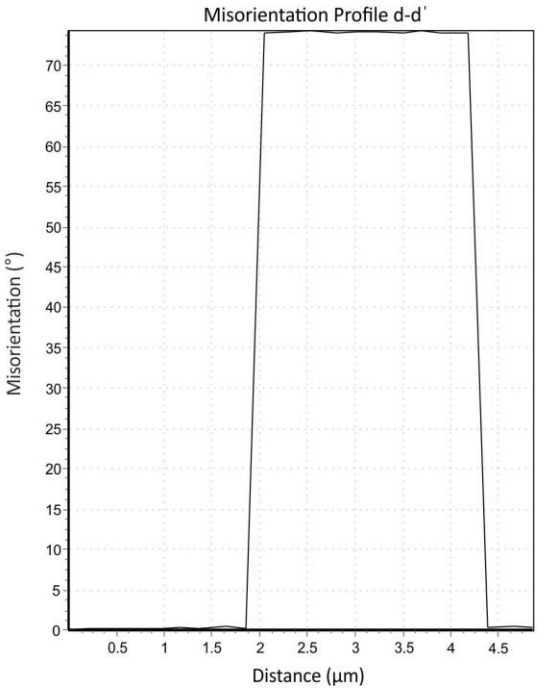

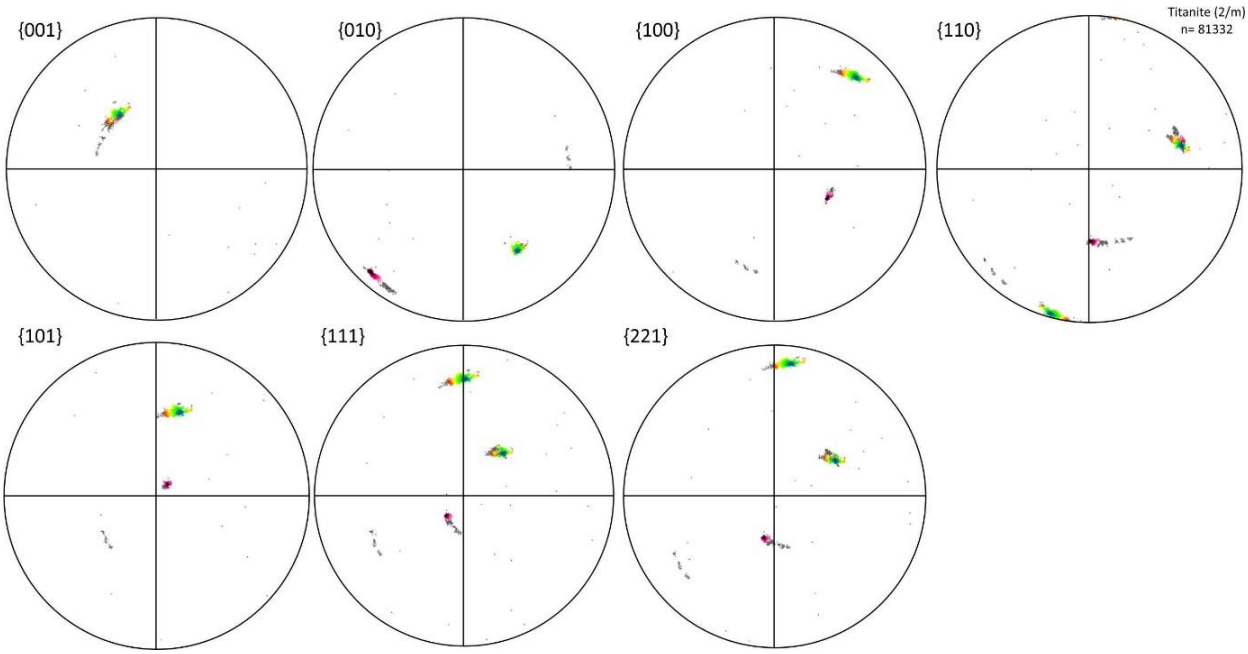

Item DR8 (Target 6HR_Vredefort structure)

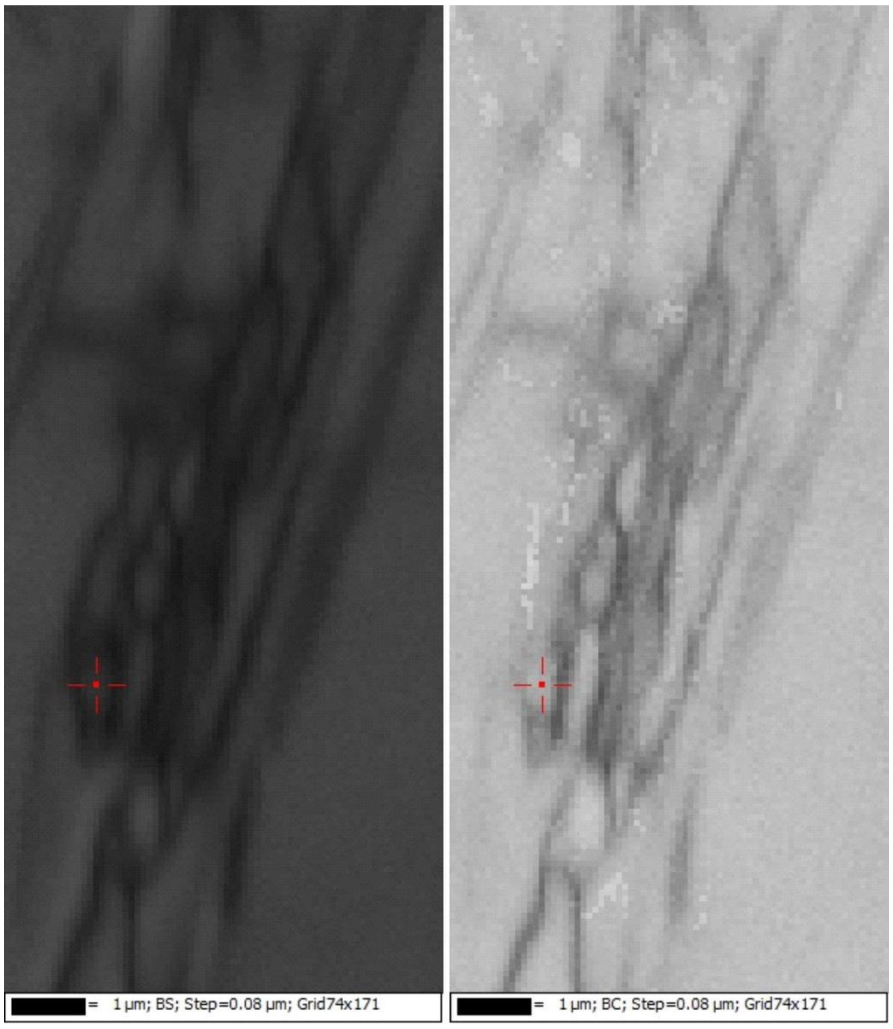

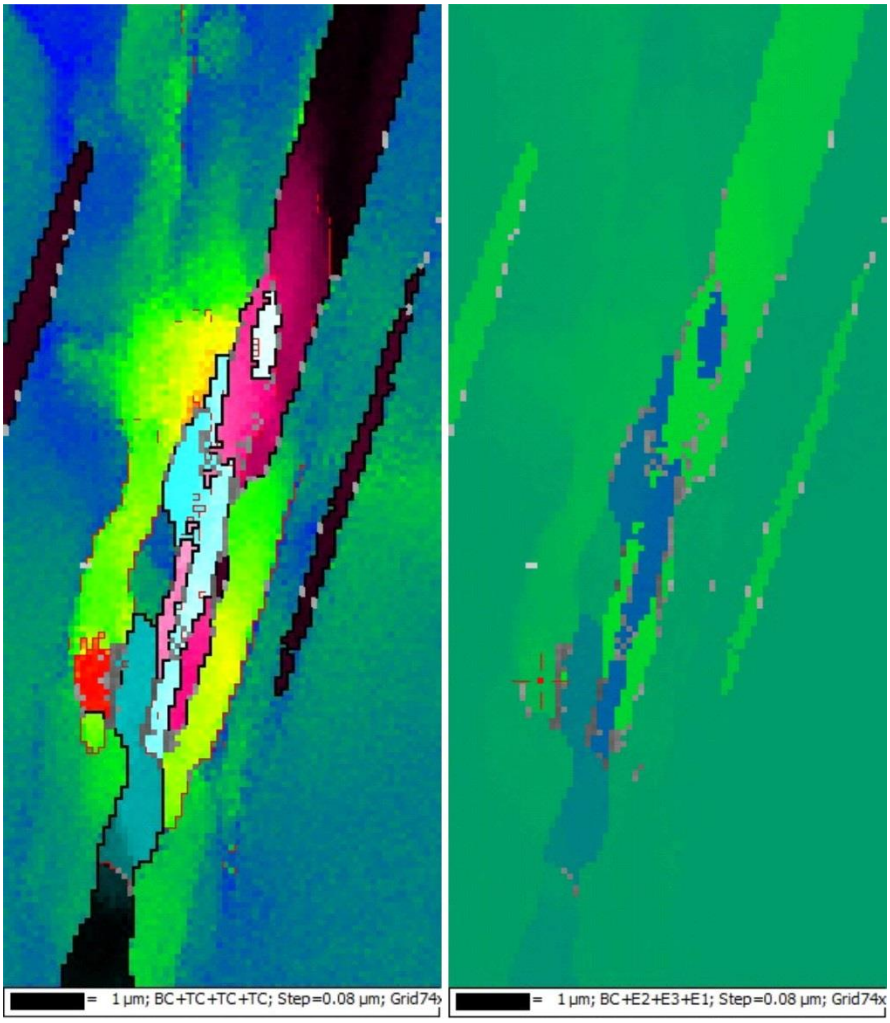
= 1 µm; BC+TC+TC+TC; Step=0.08 µm; Grid74
= 1 µm; BC+E2+E3+E1; Step=0.08 µm; Grid74x

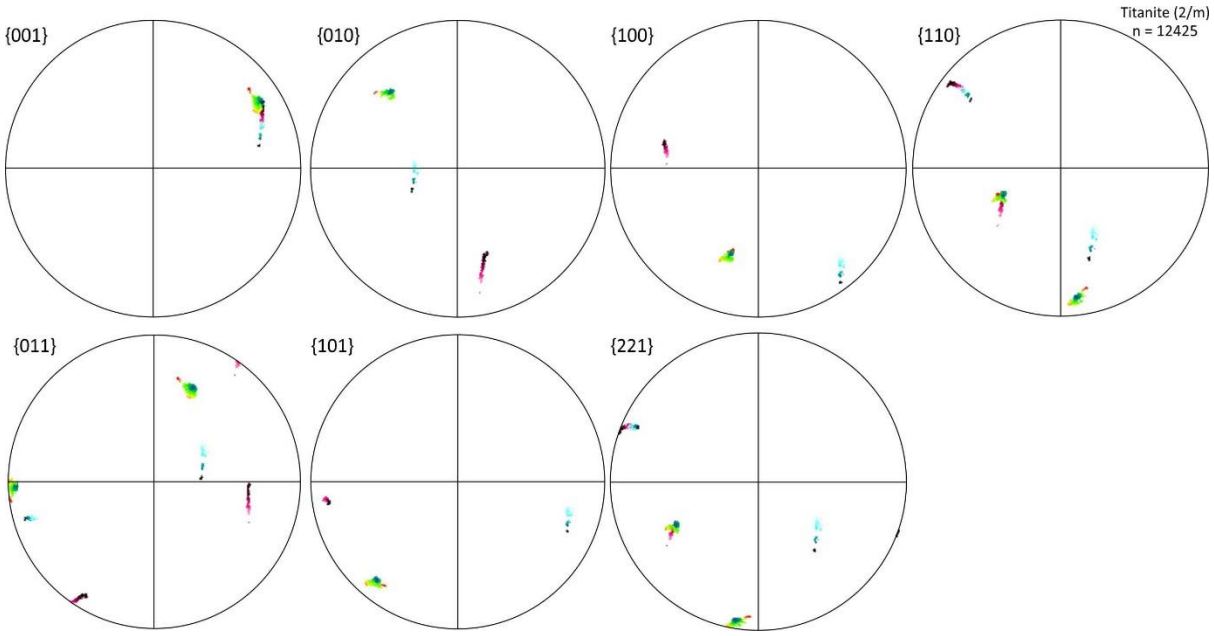
{001}
{010}
{100}
{110}
Titanite (2/m)
n = 12425
{011}
{101}
{221}

Item DR8 (Target 8_Vredefort structure)

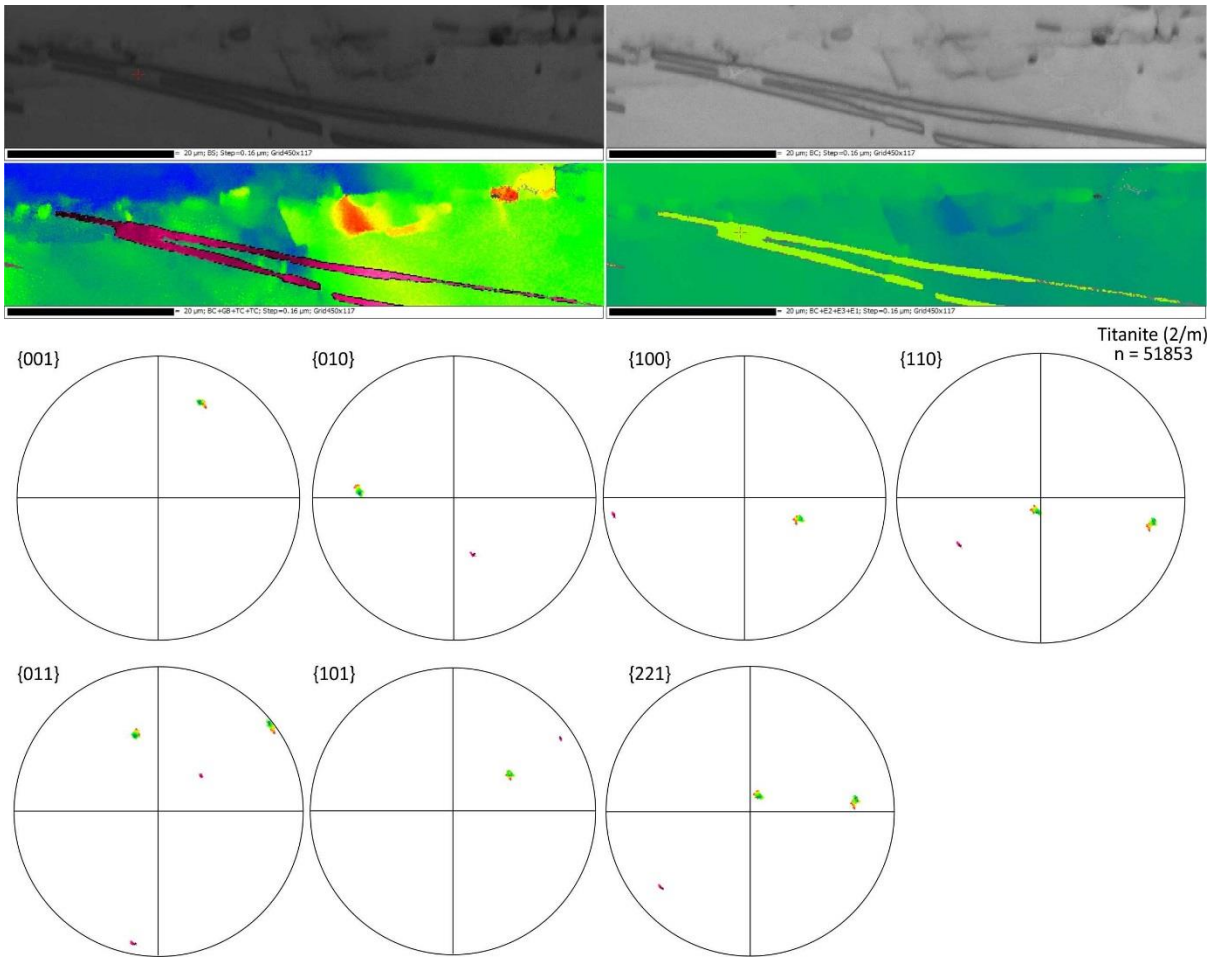

Item DR8 (Target 15_Vredefort structure)

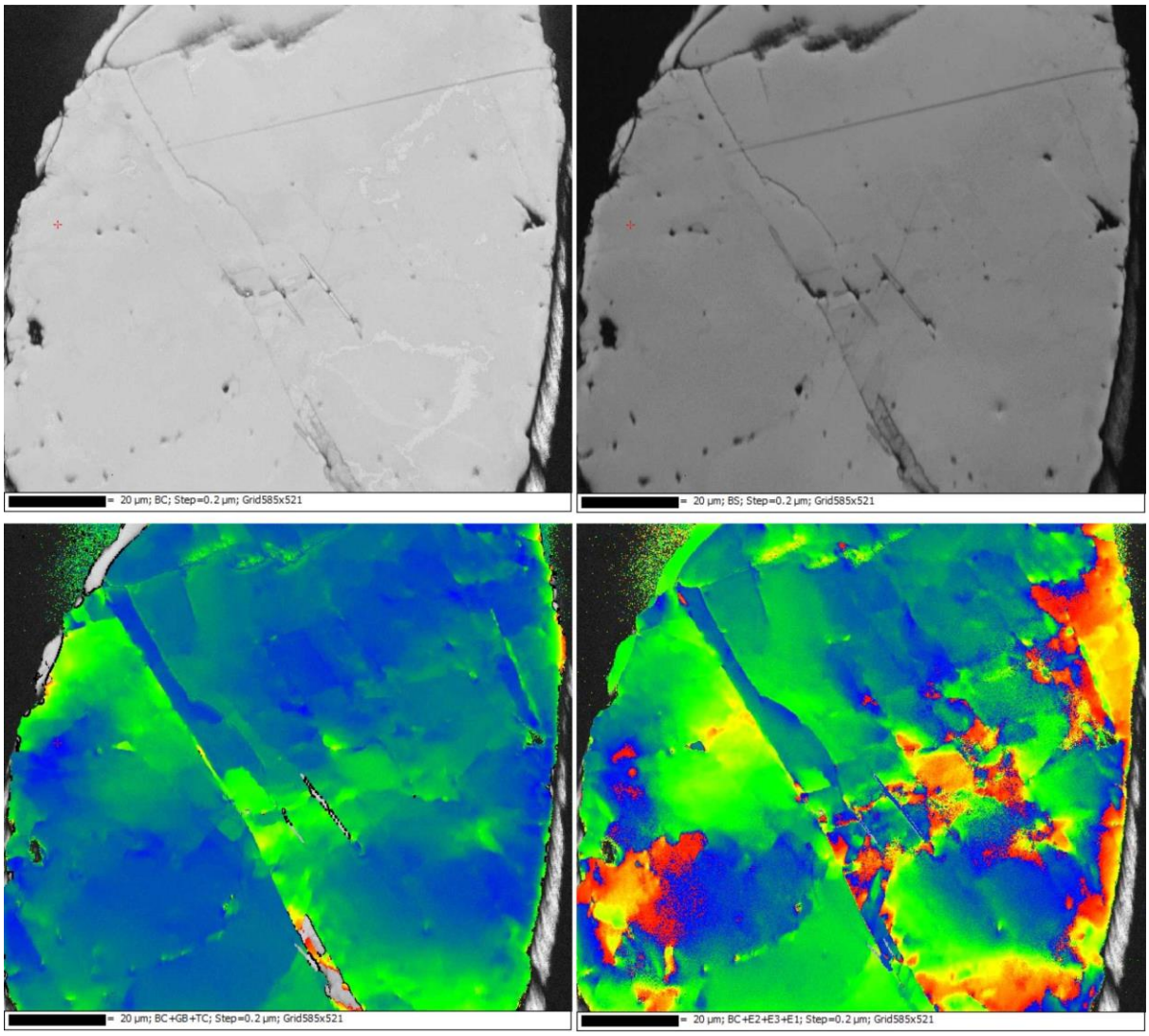

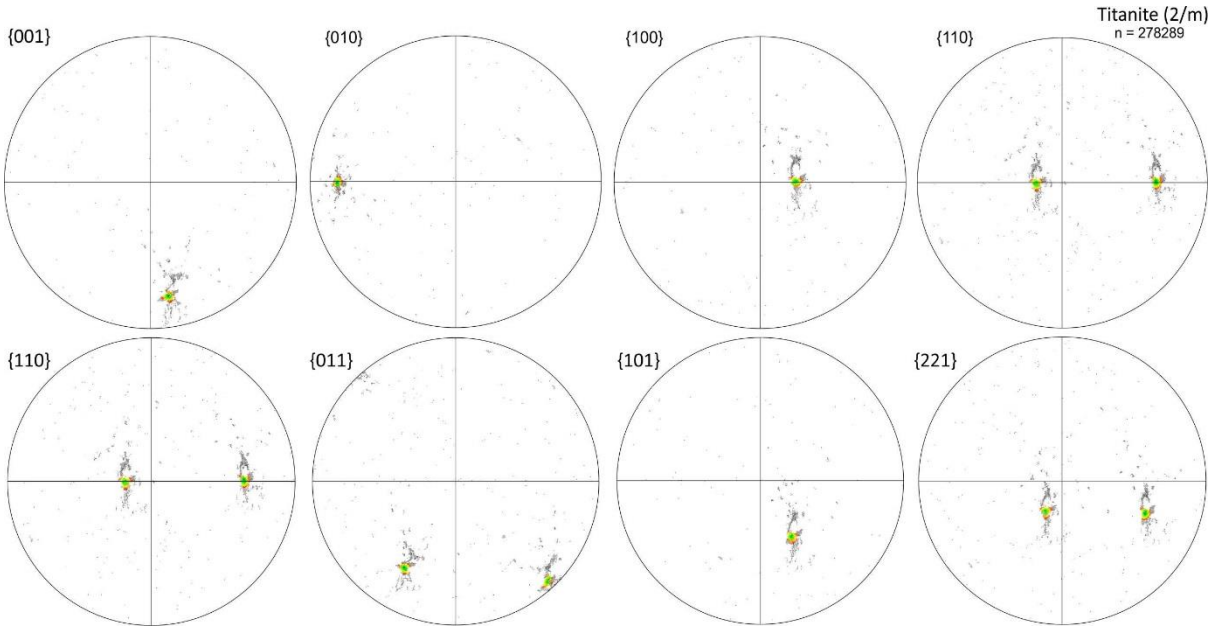

Item DR9. U-Pb Secondary Ion Microprobe Analysis (SIMS): Analytical details

During the U-Pb analytical session was followed the sample-standard bracketing technique with Khan titanite (ID-TIMS age of 522.2 ± 2.2 Ma, Heaman, 2009) as the primary bracketing standard. To check the accuracy and precision of the analyses MKED1 (ID-TIMS age of 1517.32 ± 0.32 Ma, Spandler et al., 2016) and Ontario – 2 (LA-ICP-MS age of 1053.3 ± 3.1 Ma, Spencer et al., 2013) were used as secondary standards. Six analyses of the MKED-1 secondary standard yielded an upper intercept age in concordia space of 1518 ± 11 (1σ, n = 6, MSWD = 1.16) with a weighted average $^{207}Pb/^{206}Pb$ age of 1515 ± 17 (1σ, n = 6, MSWD = 1.3). Five analyses of the Ontario – 2 secondary standard yielded a weighted average $^{207}Pb/^{206}Pb$ age of 1057 ± 67 (n = 5, MSWD = 6.5). The SIMS U-Pb isotopic data were collected with a spot size of 15 – 20µm, beam current of 6nA, and impact energy of 22keV.

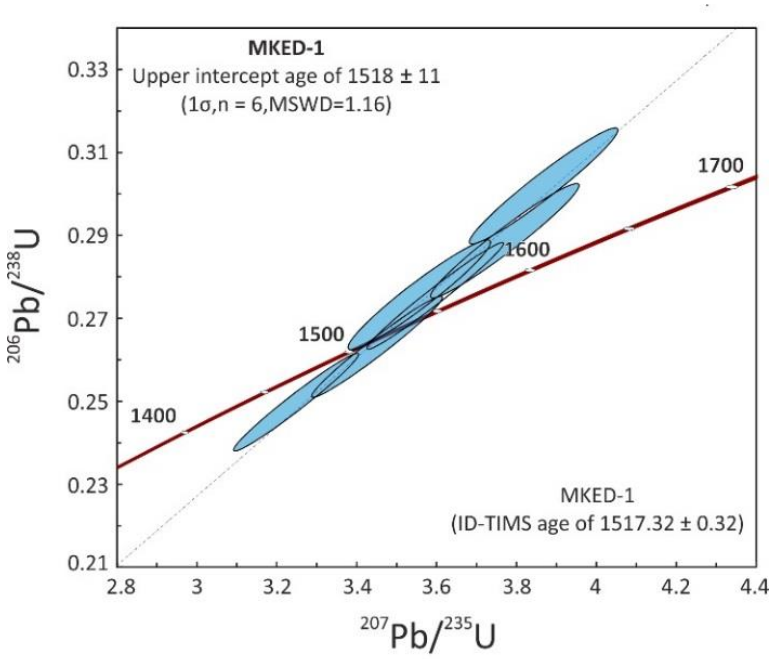

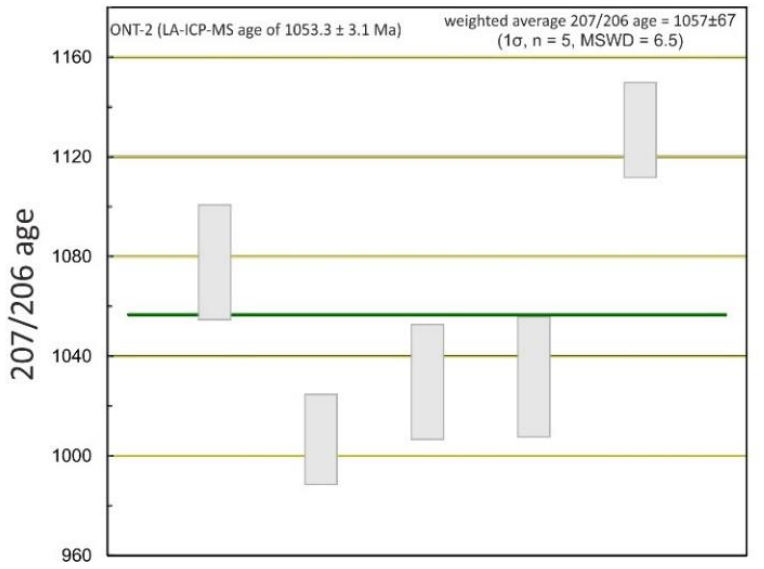

Item DR9. U-Pb isotopic data from the secondary standards MKED-1 and Ontario-2 plotted in concordia and weighted average Pb/Pb diagrams, respectively.

Table DR20. Analytical conditions of EBSD data collection

Instrumentation		
Host Institute	Western University	Portsmouth University
SEM Model	Hitachi SU6600 FEG-SEM (Schottky electron source)	Zeiss EVO MA10 (LaB6 electron source)
EBSD System	Oxford Instruments Nordlys EBSD detector	Oxford Instrument Nordlys-Nano EBSD detector
EBSD Software	HKL Channel 5	Oxford Instruments AZTEC
SEM settings		
Carbon coat (<5nm)	Yes	No
Acc. Voltage (kV)	20	20
Working distance (mm)	19	14 to 20
Probe current (nA)	8	1
Tilt (^{o})	70	70
EBSD data collection and processing		
EBSP collection time per frame (ms)	80	< 120
Background (frames)	64	64
EBSP noise reduction (frames)	7	5
EBSP noise reduction (binning)	4x4	2x2
EBSP noise reduction (gain)	High	High
Hough resolution	60	70
Band detection min/max	4 to 7	10 to 12
Step size (nm)	50 to 150	80 to 200
Noise reduction	wildspike only	wildspike only

Table DR2. U-Pb isotopic analyses from Sudbury titanite grains (Type 1 and Type 2 populations)

Target	Textural family	U(ppm)	Th(ppm)	Pb(ppm)	Th/U	f_{206}(%)	$^{207}Pb/^{235}U$	1σ	$^{206}Pb/^{238}U$	1σ	$^{207}Pb/^{206}Pb$	1σ
kpcm09_trgt1_1	Type 1	59.181	45.189	23.557	0.783	1.154	5.330	0.080	0.344	0.005	0.112	0.001
kpcm09_trgt1_2	Type 1	79.862	75.244	30.705	0.967	0.546	5.034	0.081	0.319	0.005	0.115	0.000
kpcm09_trgt1_3	Type 1	59.357	49.046	20.944	0.848	1.140	4.682	0.080	0.300	0.004	0.113	0.001
kpcm09_trgt2_2	Type 1	20.668	16.730	7.786	0.830	1.867	4.963	0.100	0.322	0.005	0.112	0.002
kpcm09_trgt3_2	Type 1	80.723	92.122	34.060	1.171	1.064	5.171	0.079	0.336	0.005	0.111	0.001
kpcm09_trgt3_3	Type 1	87.762	80.536	36.113	0.941	0.564	5.370	0.074	0.343	0.005	0.113	0.000
kpcm09a_1	Type 1	75.767	70.788	29.186	0.958	0.392	4.986	0.074	0.320	0.005	0.113	0.000
kpcm09a_2	Type 1	50.571	59.221	20.066	1.201	0.361	4.940	0.081	0.313	0.005	0.114	0.001
kpcm09a_3	Type 1	46.204	39.778	17.697	0.883	0.832	5.002	0.074	0.324	0.004	0.112	0.001
kpcm09_trgt2_1	Type 2	1.323	0.404	0.423	0.313	15.535	6.344	0.343	0.296	0.014	0.156	0.004
kpcm09_trgt3_1	Type 2	1.108	0.062	0.306	0.058	33.161	1.841	0.465	0.300	0.011	0.044	0.011

Table DR2 (continue)

ρ	$^{207}Pb/^{235}U$ date	1σ	$^{206}Pb/^{238}U$	1σ	Discordance (%)
0.946	1873.722	12.762	1839.000	9.000	3.584
0.974	1825.138	13.500	1782.685	24.297	-4.822
0.874	1763.994	14.247	1690.164	22.237	-8.738
0.721	1813.083	16.920	1799.132	22.797	-1.633
0.907	1847.913	12.861	1869.799	22.365	2.567
0.967	1880.102	11.759	1903.463	21.992	2.668
0.955	1816.965	12.454	1790.293	22.071	-3.070
0.912	1809.198	13.704	1757.663	22.890	-5.957
0.922	1819.722	12.470	1807.433	21.518	-1.395
0.852	2024.542	46.363	1670.835	67.430	-30.584
0.147	1060.157	153.785	1692.936	54.860	N/A

Table DR3. U-Pb isotopic data from Vredefort titanite grains

Target	Textural features	U(ppm)	Th(ppm)	Pb(ppm)	Th/U	f_{206}(%)	$^{207}Pb/^{235}U$	1σ	$^{206}Pb/^{238}U$	1σ
1-1	patchy zoning	16.145	119.020	21.806	7.563	3.173	11.498	0.211	0.476	0.008
1-2	patchy zoning	15.231	120.781	21.207	8.135	3.103	11.354	0.172	0.468	0.006
2-1	patchy zoning	11.377	79.778	15.692	7.193	4.659	12.465	0.202	0.504	0.007
6-1	patchy zoning with planar features	26.287	55.247	21.249	2.156	2.124	12.854	0.188	0.528	0.007
6-2	patchy zoning with planar features	24.230	47.693	19.952	2.019	2.014	13.679	0.204	0.549	0.008
6-3	patchy zoning with planar features	25.942	161.450	32.555	6.384	2.172	12.193	0.174	0.492	0.007
5-1	brighter domain in patchily zoned grain	10.353	70.693	13.829	7.005	4.727	11.910	0.204	0.496	0.008
9-1	patchy zoning with planar features	15.494	131.202	22.628	8.687	3.467	11.342	0.163	0.470	0.006
9-2	patchy zoning with planar features	15.822	121.840	22.680	7.900	2.991	12.120	0.198	0.492	0.007
12-1	patchy zoning with planar features	11.171	82.504	14.147	7.576	5.464	9.760	0.163	0.446	0.006
12-2	patchy zoning with planar features	12.586	88.612	15.770	7.223	4.308	10.794	0.182	0.454	0.007
12-3	patchy zoning	11.274	87.074	15.961	7.923	4.281	11.869	0.197	0.485	0.008
15-2	patchy zoning with planar features	11.236	73.274	13.253	6.690	4.934	10.390	0.164	0.448	0.006
15-3	patchy zoning	12.060	73.325	15.135	6.237	3.987	12.412	0.187	0.500	0.007

Table DR3 (Continue)

$^{207}Pb/^{206}Pb$	1σ	ρ	$^{207}Pb/^{235}U$ date	1σ	$^{206}Pb/^{238}U$	1σ	Discordance (%)
0.175	0.001	0.892	2564.447	16.990	2511.628	33.954	-3.621
0.176	0.001	0.905	2552.679	14.064	2472.776	28.148	-5.475
0.179	0.001	0.876	2640.057	15.147	2629.432	30.622	-0.701
0.176	0.001	0.957	2668.988	13.701	2734.414	31.164	4.407
0.181	0.001	0.969	2727.773	14.018	2822.877	32.950	6.203
0.180	0.001	0.938	2619.394	13.317	2580.022	28.426	-2.604
0.174	0.001	0.919	2597.360	15.927	2597.566	33.569	0.022
0.175	0.001	0.961	2551.653	13.298	2482.565	28.350	-4.773
0.179	0.001	0.907	2613.747	15.187	2580.677	31.378	-2.210
0.159	0.002	0.792	2412.393	15.247	2378.360	26.206	-2.566
0.173	0.002	0.849	2505.548	15.578	2412.192	28.800	-6.577
0.178	0.001	0.944	2594.128	15.446	2548.493	32.959	-3.062
0.168	0.001	0.899	2470.163	14.502	2388.024	28.239	-5.909
0.180	0.001	0.925	2636.097	14.085	2611.711	29.901	-1.593

(1) errors are presented at 1σ uncertainty level

(2) The f_{206}(%) indicates the percentage of ^{206}Pb that is common Pb

(3) Discordance 0% denotes a concordant analysis. Analyses with discordance values above 10% were not taken into consideration.

(4) The common Pb correction is based on the measured ^{204}Pb counts

Chapter 7. Mineral chemistry as a vectoring tool of shear-controlled mineralization: A comparative study from the Sudbury mining camp (Ontario, Canada)

1 Introduction

Shear zones are migration pathways of metal-bearing fluids and melts controlling different mineral systems worldwide. These include orogenic gold deposits (Groves et al., 1998), Ni-Cu-(PGE) deposits (Saumur and Cruden, 2016; Bailey et al., 2004), Pb-Zn-Ag deposits (Austin and Blenkinsop, 2009; Liu et al., 2016), Cu - Au deposits (Dora and Randive., 2015; Kitt et al., 2016), and Rare metal deposits (Partington, 1990 inter alia). A better understanding of their exploration potential, using quantitative microanalytical tools, would provide critical information on drilling campaigns, prioritizing exploration targets, and constraining better the empirical traits of shear-hosted mineral deposits. Despite though their significant role, few studies have documented mineral-chemistry from ore-controlling or prospective shear zones for exploration purposes.

Chemical microanalysis of different mineral phases, from major to trace element level, has revealed that concentration gradients of pathfinder elements can be used as vectoring tools for the detection of porphyry copper (Wilkinson et al., 2014, Cooke et al., 2014) and Ni-Cu-PGE deposits (Hanley and Bray, 2009, Warren et al., 2015). In this respect, the Sudbury impact structure as a multiply deformed mining district provides a globally unique site to compare mineral chemistry signatures of barren and ore-controlling segments of mylonitic shear zones. By presenting new mineral chemistry data from fabric-forming silicate minerals in shear zones of three heavily mineralised mines (i.e. Creighton, Copper Cliff and Garson mines; **Figure 1**) this study aims to: (a) characterise compositional variations in minerals from well characterised mylonitic shear zones and (b) test their vectoring potential as pathfinder tools of shear-hosted Ni-Cu-PGE mineralization.

2 Geological setting of the Sudbury mining camp

The world-class Sudbury mining camp hosts more than 1.7 billion tonnes of base and precious metals, including past and present resources, at average ore grade of 1% Ni, 1% Cu and 1g/t (Pt+Pd) (Farrow and Lightfoot., 2002, Lydon, 2007). The Sudbury structure is divided into the North, East, and South Range (**Figure 1)** and comprise the following three main units: (a) the Sudbury pseudotachylitic breccia, (b) the Sudbury Igneous Complex (SIC), and (c) the Sudbury basin (Pye et al., 1984). The Southern footwall of the Sudbury structure comprise supracrustals units of the Huronian Supergroup and plutonic bodies formed between 2.5 and 2.2 Ga (Scott and Spray., 2000). The North and East Ranges are bounded by a complex of Archean tonalitic gneisses named as the Levack Gneiss Complex (Card et al., 1990). The Sudbury Igneous Complex is divided into the following igneous components (Lightfoot et al., 2001, Therriault et al., 2002): (a) the Main mass that comprise the Norite (Lower unit), Quartz gabbro (transitional unit) and Granophyre units (Upper unit), (b) the Contact sublayer and (c) the radial and concentric quartz diorite offset dykes. The Main mass constitutes a chemically and density stratified impact melt sheet with granodioritic bulk composition and crustal affinity according to whole rock, Re-Os, Pb, Nd, and Sr isotope systematics (Walker et al., 1991, Dickin et al., 1996, Mungall et al., 2004).

The Contact sublayer is an inclusion-bearing Noritic unit, located in embayments at the base of the impact melt sheet, and hosts the majority of massive Ni-Cu-PGE sulphide ore bodies (**Figure 1**). The quartz diorite offset dykes record early injection phases of the impact melt sheet and are classified to mineralized (e.g. Copper Cliff offset dyke) and weakly mineralized systems (e.g. Foy offset dyke) (Lightfoot, 2007). The Sudbury basin is located stratigraphically on top of the igneous complex and comprise three main formations: (a) fallback breccia deposits of the Onaping formation, (b) pelitic units of the Onwatin formation, and (c) meta-turbidites of the Chelmsford formation (Pye et al., 1984 and references therein). The post-impact tectonometamorphic evolution of the impact crater is characterised by metamorphic overprints that reached greenschist to epidote-amphibolite facies conditions and localization of strain in a network of ductile and brittle-ductile shear zones, termed as the South Range Shear Zone (Fleet et al., Riller., 2005).

The three major styles of Ni-Cu-PGE mineralization that are recognized in the Sudbury mining camp are: (a) contact, (b) footwall, (c) offset-style, and (d) shear-hosted deposits. The

contact style deposits comprise massive and semi-massive Ni-Cu-PGE magmatic sulphides that are hosted mainly in the magmatic breccia of the contact sublayer. High metal tenor Cu-Ni-PGE footwall style deposits are classified to sharp-walled chalcopyrite-rich veins and low sulphide PGE deposits (Ames and Farrow., 2007). The third major style of mineralization, the offset-style deposits, are expressed as disseminated and blebby lenses in the inclusion-bearing quartz diorite dykes and exhibit Cu/Ni ratios of approximately 1 (Tuchscherer and Spray., 2002, Ames and Farrow., 2007).

2.1 Shear-hosted mineralization in the Sudbury mining camp (Ontario, Canada)

The polyphase deformed South Range of the Sudbury structure hosts greenschist to amphibolite facies shear zones that displaced and remobilised primary magmatic Ni-Cu-PGE ore bodies in Creighton, Garson, Thayer Lindsley, Lockerby, Cryderman, and Falconbridge East and West Mines (O'Donell, 1989, Bailey et al., 2006, Mukwakwami et al., 2013 and references therein). However, detailed investigations of the shear-hosted mineralization are available only for the Garson (Mukwakwami et al., 2014), Thayer Lindsley (Bailey et al., 2004), and Creighton Mines (O'Donell, 1981, Papapavlou et al, 2017). n Garson Mine, four brecciated sulphide ore bodies (i.e. #1, #2, #3, and #4 ore bodies) are hosted in steeply south-dipping amphibolite-facies shear zones. These ore bodies show meso-scale textures indicative of mechanical remobilization and exhibit elongation sub-parallel to the mylonitic stretching lineation (Mukwakwami et al., 2014). Whole-rock geochemical data from the shear-controlled sulphides of Garson Mine shows that these ore bodies have low Pd/Ir ratios and a restricted range of Fe/Ni ratios and Ni tenors. These geochemical features are attributed as evidence of a primary magmatic geochemical signature, weakly affected by later hydrothermal and deformation episodes (Mukwakwami et al., 2014). In contrast, sheared contact-style ore at the Thayer Lindsley mine shows a decrease in Ni contents and increase of Pt and Pd contents that is interpreted as result of syntectonic, fluid-induced, metal remobilization (Bailey et al., 2006). In Creighton Mine (Figure 7.1), biotite-rich shear zones exert a strong control on the remobilization of footwall-hosted deposits (Dare et al., 2010) but the influence of shearing and syn-tectonic fluid infiltration on the metal tenor of the ore bodies remains poorly constrained.

3. Target shear zones

Five shear zones that are exposed at the South Range of the Sudbury structure were selected for mineral-chemical analysis. These are: (a) the Cliff Lake Fault, that is hosted within the main mass of the Sudbury structure (**Figure 1**), (b) the Six Shaft Shear Zone that is exposed at the 5400 level of the Creighton Mine (), (c) the RAR Shear Zone that is exposed at the 7840 level of the Creighton Mine, (d) the X2 Fault exposed at the 4370 and the 4220 levels of the Copper Cliff Mine and (e) the 4 shear zone from the Garson Mine (**Figure 2**). The selected shear zones were selected for the following reasons: (a) they are related with different styles of mineralization, (b) have barren and ore-hosting domains, and (c) they are characterised by mineral assemblages with different fabric-forming silicates.

3.1 Meso-scale features of the examined shear zones

3.1.1 Cliff Lake Fault (Main Mass)

The Cliff Lake fault is a ENE-trending greenschist facies shear zone with sinuous geometry in plan view (**Figure 1**) and strike-parallel length of approximately 60 km (Little, 1990). The major strands of the shear are traced in the granophyric unit and at the contact with the transitional quartz gabbro unit. Field and borehole data indicate that the shear zone exhibits a strong reverse-sense component, with top-to-the-north sense of shear, juxtaposing footwall and main mass units (Figure 1, Cross section). In the quartz gabbro domains, the structure exhibits penetrative planar and linear fabrics L tectonites) defined chiefly by the shape preferred orientation of chlorite - biotite flakes and amphibole needles. A common feature, from thin section up to mesoscopic scale, is the development of foliation-parallel quartz veins. Locally, at the contact of the Upper unit with the transitional zone, cm-scale, strongly foliated anastomosed domains of the Cliff Lake fault are defined mostly by chlorite (chlorite abundance >90%). In the more felsic domains of the Upper granophyric unit a faintly developed foliation is recorded, with a well-developed stretching lineation defined by quartz and K-feldspar rods. The petrographic examination of different samples revealed the presence of mm-scale fabric gradients, C-C’/S composite fabrics, and quartz recrystallization microstructures (e.g. oblique foliations) indicative of sub-grain rotation recrystallization. From an exploration perspective, the Cliff Lake fault is regarded as barren structure at the upper domains but potentially displaces down-dip the basal ore-bearing contact of the main mass

hence can be characterised as a prospective structure at its deepest segments (personal communication with VALE).

3.1.2 Six Shaft Shear Zone (Creighton Mine) (see also chapter 4)

The Six Shaft Shear Zone is a km-scale mylonitic zone with top-to-the-SW sense of shear that is exposed underground at the 5400 level of the Creighton Mine (please look chapter 4). The mylonitic fabric is defined by the shape preferred orientation of biotite, hornblende, titanite and foliation-parallel, cm to meter-scale, mylonitic quartz veins. The Six Shaft Shear Zone is spatially related with contact, footwall-style, and mechanically remobilized Ni-Cu-PGE ore bodies. The shear zone is bounded marginally by a foliated meta-granitoid and exhibits a central, biotite-rich domain, with brecciated sulphide ore slivers.

3.1.3 RAR Shear Zone (Creighton Mine) (see also chapter 5)

The RAR shear zone is a NE-striking, steeply dipping structure that is exposed at the deeper levels of the Creighton mine (below the 6500 level, Figure with Creighton mine cross section) and belongs to the 118 system of the Creighton mine shear zones (Snelling et al., 2013). The mesoscopic analysis of drillcore samples that intersect with the RAR, at different structural levels, shows strongly foliated up to ultramylonitic quartz and biotite-rich bands. Locally, an alternation between cm-scale biotite and amphibole-rich domains is observed. The penetrative fabric in the RAR is defined predominantly by biotite and calcic amphiboles with ubiquitous presence of foliation-parallel quartz and carbonate-rich veins. In the biotite-rich mylonitic domains, are observed quartz porphyroclasts with orthorhombic (e.g. φ-type porphyroclasts) and monoclinic symmetry (e.g. quartz sigmoids). In the more felsic, meta-granitoid domain the biotite folia anastomose around the more competent quartz porphyroclasts.

(

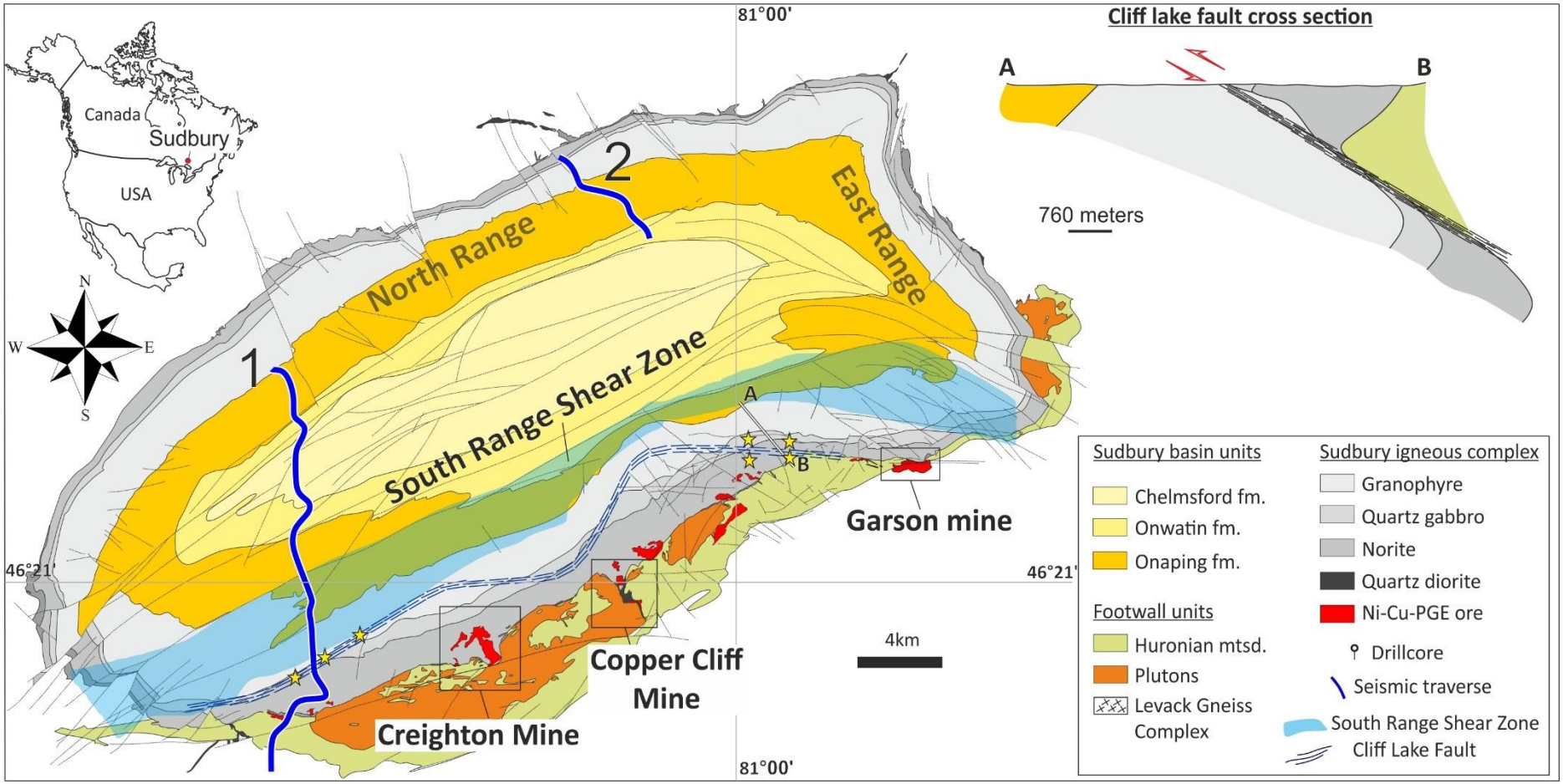

Figure 1. Simplified geological map of the Sudbury impact structure modified from Ames et al., (2005). With blue stitched lines is denoted the Cliff Lake Fault and with yellow stars the sampling locations of the structure. At the upper right part of the figure is depicted the simplified cross section A-B across the Cliff Lake fault. The cross section is modified from Vale internal report.

3.1.4 X2 Fault (Copper Cliff Mine)

The X2 fault is a NE-striking, biotite-rich, shear zone that extends down-dip up to the 5200 level of the Copper Cliff Mine (**Figure 2**). The mylonitic fabric in the shear zone is defined chiefly by the shape preferred orientation of biotite and chlorite laths. In the low strain domains of the shear zone are recorded also ptygmatic folds with thickened hinges and axial planes sub-parallel to the mylonitic foliation. At thin section scale, sulphide blebs are observed interspersed in the biotite and quartz-rich domains of the shear zone. The X2 fault is spatially related with different magmatic ore bodies and cross cuts down-dip the 890, 100 and 900 deposits (**Figure 2**).

3.1.5 #4 shear zone (Garson Mine)

Three main shear zones are recorded in the Garson Mine from the 1000 to 5000 levels. These shear zones are as the “#1 shear zone”, “#3 shear zone#, and the “#4 shear zone” (Mukwakwami et al., 2013). These shear zones are sub-parallel and host sulphide ore bodies (**Figure 2**). Recent studies suggest that these shear zones operated in amphibolite-facies conditions and are characterised by a strong dip-slip component. The #4 shear zone transects footwall-hosted metabasalts and noritic rocks and is displaced by ca. 1.25 Ga olivine diabase dykes (**Figure 2**).

4. Sampling

Twenty-four samples (n=24) were selected for mineral-chemical analysis from the examined shear zones. Specifically, from the Cliff Lake Fault, the seven analysed samples (n=7) were collected from different sites along-strike of the shear zone (**Figure 1**). From the Six Shaft Shear Zone, four samples (n=4) were collected from the mine drift walls of the 5400 level (**chapter 4**). The sampling traverse at the 5400 level transects obliquely, marginal lower strain and mineralized high-strain, biotite-rich domains, that are in proximity with a contact-style Ni-Cu-PGE ore body (**Figure 2**). Samples (number) from the RAR shear zone were selected based on existing 3D wireframe models of the shear zone taking in consideration the spatial relationship of the shear with proximal ore bodies. From the X2 Fault, of the Copper Cliff Mine, ten samples were collected (n=10) and three representative samples (n=3) were selected for mineral-chemical analysis.

5. Methodology (For more detail please see Chapter 2)

5.1 Electron beam imaging (SEM/BSE)

Rock-forming silicate and accessory phases were targeted on carbon-coated, polished thin sections, and imaged using a Philips XL30 CP Scanning Electron Microscope (SEM) coupled to an Oxfords instruments silicon drift X-max 80mm^2 energy dispersive X-ray spectrometer (EDS). The spectral analysis via EDS helped the identification and verification of the different targets and the potential presence of sulphide inclusions in the targeted micro-analytical volumes.

5.2 Mineral chemistry by Electron Probe Microanalysis (EPMA)

Major and minor element data were collected using a Cameca SX-100 at the University of Bristol (UK). The analyses were performed using the TAP wavelength dispersive crystal spectrometer for Na Kα, Si Kα, Al Kα, Mg Kα, and F Kα, the LPET for K Kα, Ca Kα, Ti Kα, Cr Kα and Cl Kα, and the LLIF for Fe Kα, Mn Kα, and Ni Kα. All the analyses were performed with a 10μm electron beam, at a voltage of 20kV, and 10nA beam current. Different in-house natural and synthetic materials were used as standards. The biotite analyses were recalculated based on 22 oxygens per formula unit whereas the amphiboles based on 23 oxygens following reference. The Fe^{+2}/Fe^{+3} estimation in the amphibole analyses was performed assuming 13 cations in total. The chlorite analyses were recalculated based on 28 oxygens with Fe^{+2}/Fe^{+3} and OH estimation assuming full site occupancy.

5.3 Trace element microanalysis by Laser Ablation Inductively Coupled Plasma Mass Spectrometry (LA-ICP-MS)

All the data were collected at the University of Portsmouth using an ASI RESOlution 193 nm ArF excimer laser coupled to a quadrupole Agilent 7500cs ICP-MS. The following isotopes were analysed ^{27}Al, ^{29}Si, ^{31}P, ^{43}Ca, ^{45}Sc, ^{49}Ti, ^{51}V, ^{53}Cr, ^{55}Mn, ^{59}Co, ^{60}Ni, ^{66}Zn, ^{69}Ga, ^{72}Ge, ^{85}Rb, ^{88}Sr, ^{89}Y, ^{90}Zr, ^{95}Mo, ^{118}Sn, ^{121}Sb, ^{137}Ba, ^{139}La, ^{140}Ce, ^{141}Pr, ^{146}Nd, ^{147}Sm, ^{151}Eu, ^{157}Gd, ^{159}Tb, ^{163}Dy, ^{165}Ho, ^{167}Er, ^{169}Tm, ^{173}Yb, ^{175}Lu, ^{177}Hf, ^{208}Pb, ^{232}Th, and ^{238}U. The following masses and isotopic ratios were monitored during the tuning of the instrument: ^{43}Ca, ^{202}Hg, ^{204}Hg, ^{51}V, ^{89}Y, ^{208}Pb, ^{232}Th, ^{235}U, ^{238}U, ^{238}U/^{232}Th, $^{238}U^{16}O^{+}/^{232}$Th, ^{140}Ce, and ^{177}Hf. The highest sensitivity levels in the masses of interest was recorded with Th/U ~ 1 and UO/O ~0.12. To correct for instrumental mass bias, the reference material the NIST 612 silica glass (Jochum et al., 2011)

to externally normalize sample analyses. TiO2 was used as the internal standard for biotite analyses using values from EPMA analyses. Analytical data were collected using a fluence of 4.5 J/cm^2, repetition rate of 4Hz and spotsize between 15 and 40µm.

6. Mineral-chemical data

In this section mineral-chemical data from the modally abundant fabric-forming phases (i.e. biotite and chlorite) in the four shear zones are presented from the studied shear zones (i.e. Six Shaft Shear Zone, Cliff Lake Fault, RAR Shear Zone, and X2 Fault). Detailed tables with mineral chemical data from all the sampled shear zones can be found in the **Appendix**.

6.1 Cliff Lake Fault

6.1.1 Biotite

From the western (i.e. Creighton Mine area) to the eastern (i.e. Kirkwood Mine area) segments of the shear zone (**Figure 1**) the fabric-forming biotites show a decrease in the magnesium number (X_{Mg} = Mg/(Fe+Mg)) from X_{Mg} = 0.50 to X_{Mg} = 0.19. At the central segments of the shear zone are recorded variations from X_{Mg} = 0.42 up to X_{Mg} = 0.25. Slight variations are recorded also in the abundance of MnO from 0.1 up to 0.5 Wt% in the same West – East trend. Regarding the concentration of halogens, fluorine varies from 0.1 up to 0.9 Wt% whereas smaller variations are observed in the abundance of chlorine from Cl = 0.1 up to 0.3 Wt%. The nickel content in these biotite grains is fairly low with average concentration of 7 ppm, and many analyses are below the detection limit. Importantly, the nickel abundance does not exhibit systematic variations relative to other major oxides (e.g. FeO, **Figure 3**).

6.1.2 Chlorite

Chlorite grains exhibit increasing X_{Fe} values and elevated MnO abundance in a west-east trend along strike of the shear zone. The X_{Fe} values vary from X_{Fe} = 0.47 at the western to X_{Fe} = 0.82 at the eastern segment of the shear zone. Reduced X_{Fe} values are recorded in the eastern segments of the shear zone in proximity to Sheppard and Blezard mines (X_{Fe} = 0.61 and 0.53). The Nickel abundance is low, average 30 ppm, and as with biotite grains are not observed systematic trends with major oxides (e.g. FeO, **Figure 4**)

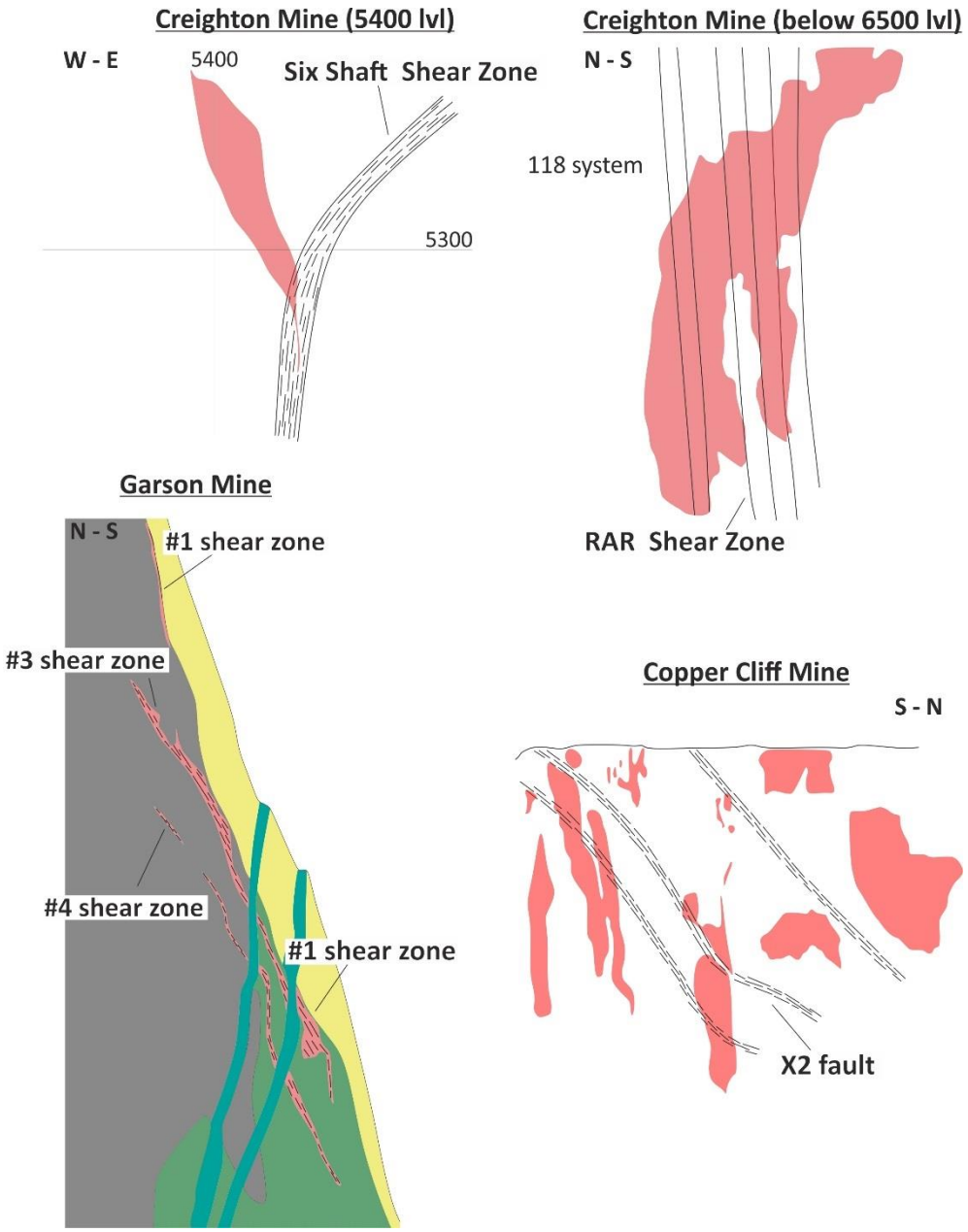

Figure 2. Schematic cross sections that depict the relationship of the examined shear zones with Ni-Cu-PGE sulphide ore bodies.

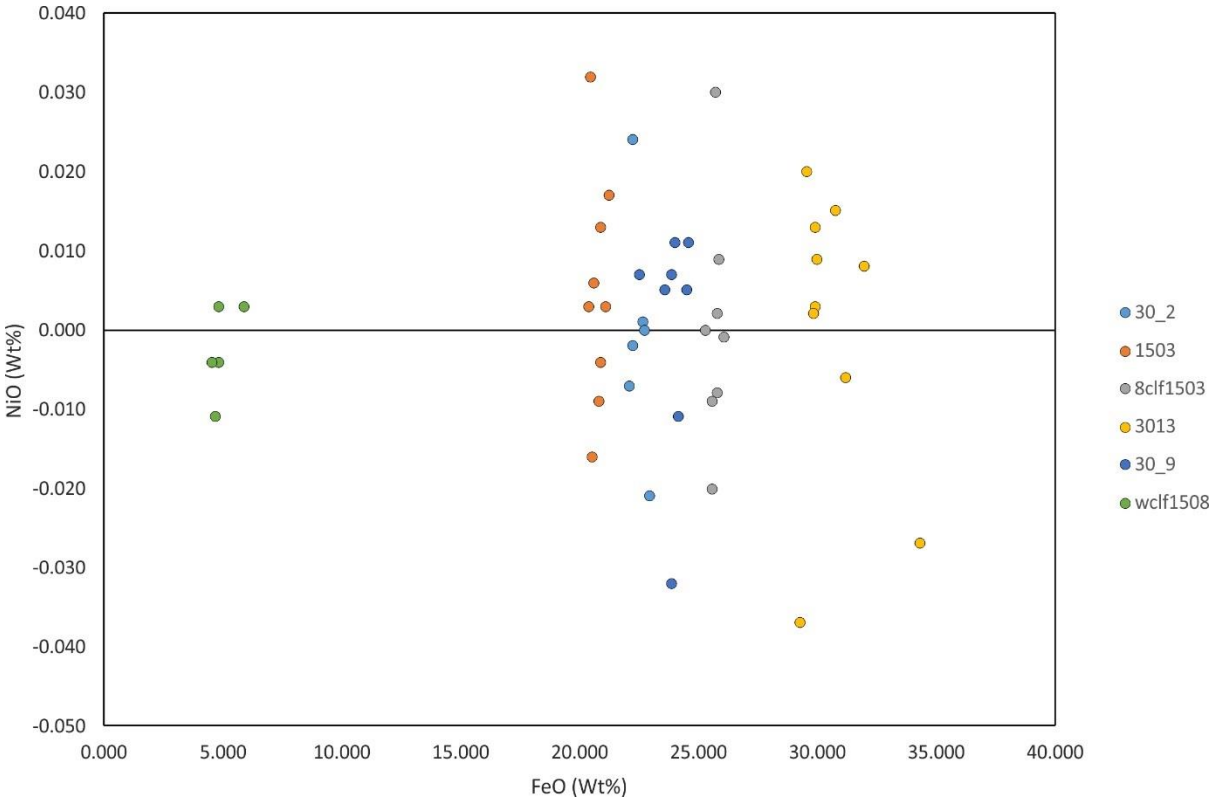

Figure 3. Plot that shows the relationship of Ni content relative to FeO in biotite grains from the Cliff Lake Fault

6.2 Six Shaft Shear Zone

6.2.1 Biotite (please see also chapter 4; Figure 4.7)

In the analysed biotite grains, along a transect oblique to the strike of the Six Shaft Shear Zone (**Figures 5-6**), is observed an order of magnitude increase in the concentration of nickel (**Figure 6**). The elevation in nickel concentration is accompanied by the decrease in FeO content in these grains (**Figure 7**). Slight increase along this transect is recorded also in the Co, Cr, Na_20, Sn, V, and Sc contents of the analysed biotite grains (see also **Appendix**; Trace element data). Along the examined transect is observed intensification of the biotite-defined mylonitic fabric and proximity to shear-hosted sulphides with mechanical remobilization meso-scale structures (**Figure 5**; see also chapter 4).

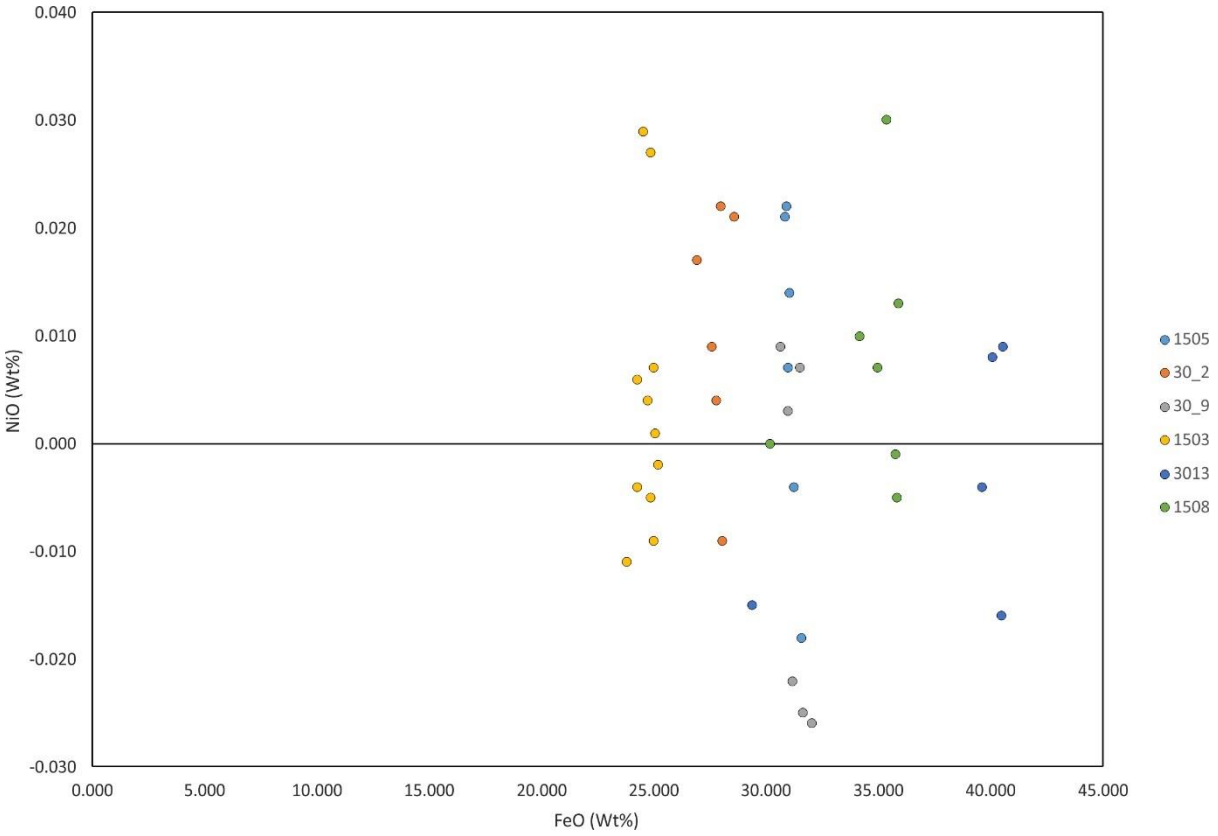

Figure 4. Plot that shows the relationship of Ni content relative to FeO in chlorite grains from the Cliff Lake Fault

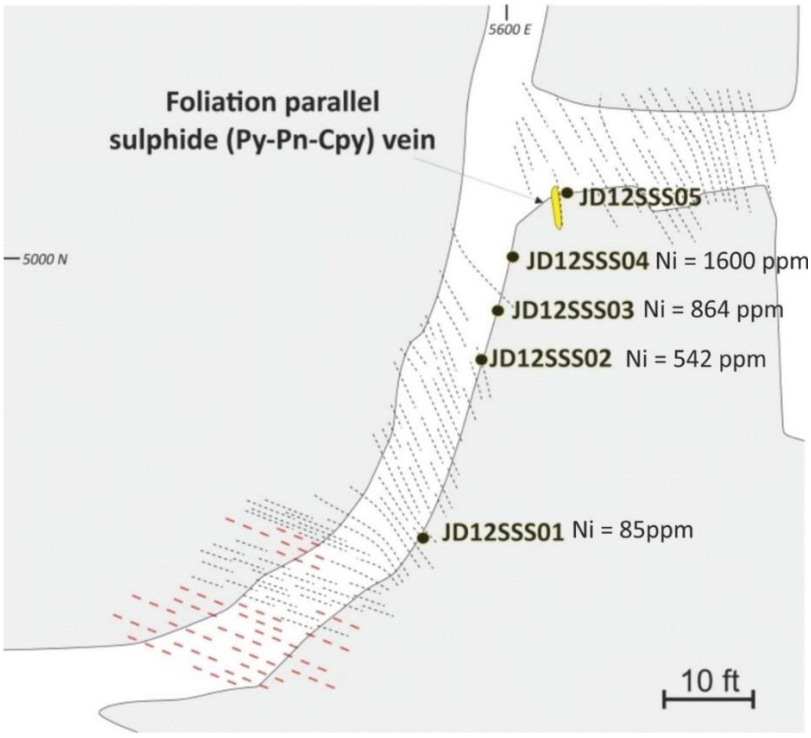

Figure 5. Simplified map of the Six Shaft Shear Zone that shows the location of the biotite-rich mylonitic samples studied for mineral-chemical analysis and the concentration of nickel in each sample

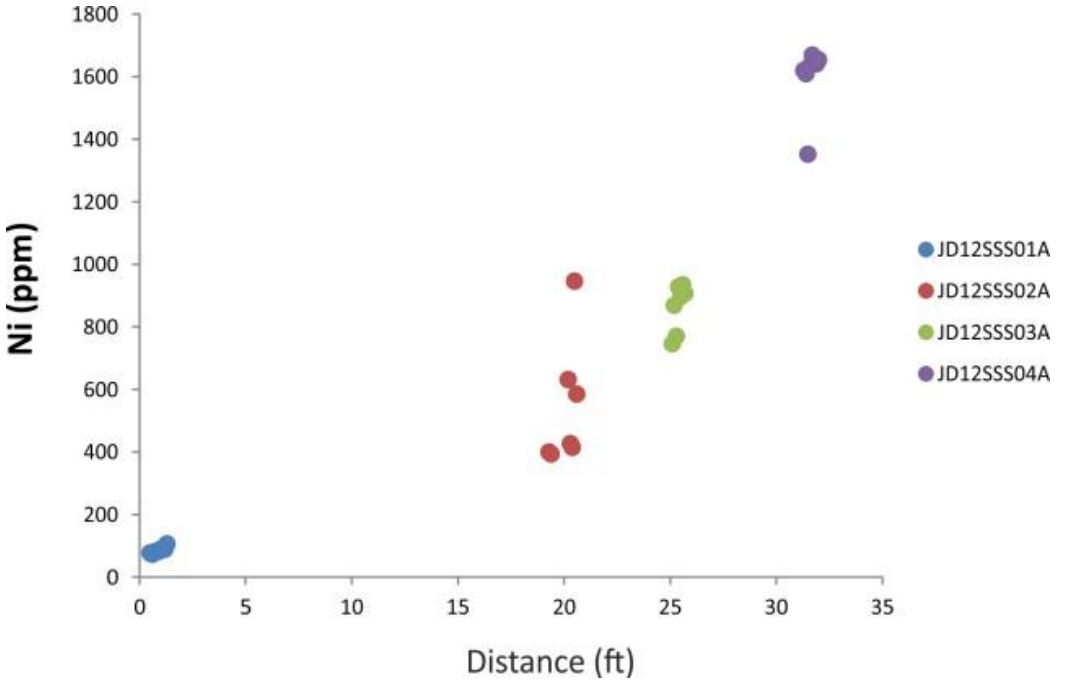

Figure 6. Plot that shows the nickel variation across strike of the Six Shaft Shear Zone

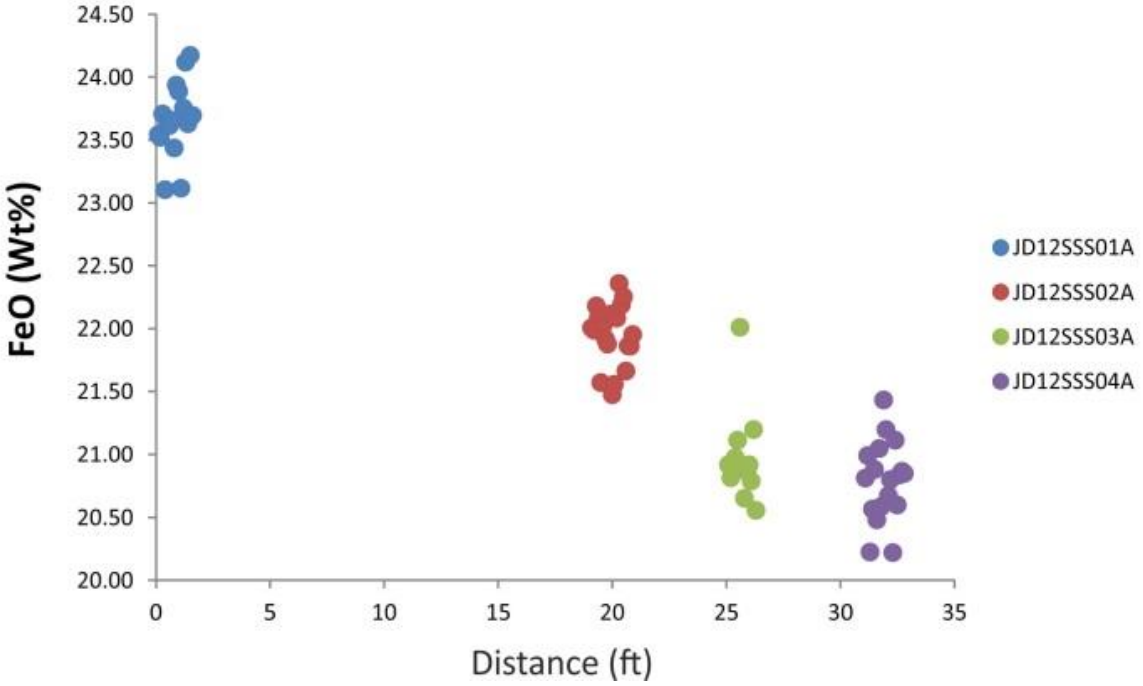

Figure 7. Plot that shows FeO variations in biotite grains of the Six Shaft Shear Zone

6.3 RAR Shear Zone

6.3.1 Biotite

The samples for mineral-chemical analysis from the RAR shear zone were selected based on 3D wireframe models of the shear zone and adjacent ore bodies. The main fabric forming phase in the shear is biotite with average nickel concentration of 585 ppm. Distinct compositional anomalies relative to the average nickel concentration is observed in two samples; the sample PL 19 and PL 3 (Figure 7.8) Specifically, in the sample PL 19 is recorded average nickel concentration of 3000 ppm whereas three analyses from the sample PL 13 show average nickel concentration of 36 ppm. Interestingly, in the samples that are recorded the highest nickel concentrations (PL 19, PL 7, and PL 4) are observed also the lowest chromium concentrations (**see Appendix; trace element data**). Independently of the location of the sample in the RAR shear zone are recorded slight variations in the concentration of zinc with average concentration of 330 ppm. The comparison of the nickel concentration relative to vanadium concentration shows that in grains with average nickel concentration of 600 ppm the vanadium concentrations vary from 200 to 300 ppm.

6.4 X2 Fault

6.4.1 Biotite

The three analysed samples are from exposures of the shear at the 4370 (PCL 1 and PCL 3) and 4220 levels (PCL 9) of the Copper Cliff Mine. Specifically, the analysed biotites from the sample PCL1 show small variations in X_{Fe} values (Fe^{+2}/Fe^{+2} + Mg) between X_{Fe} = 0.53-0.54. Interestingly, the biotite grains in the sample show elevated fluorine values up to 0.9 Wt% and small variations in the chlorine values from 0.1 to 0.26 Wt%. The nickel contents from eleven analyses on biotite grains vary from 1110 ppm to 1370 ppm with an average value of 1241 ppm (Figure 9). Similarly with the sample PCL1, the X_{Fe} values in biotite grains of the sample PCL3 vary from X_{Fe} = 0.50 – 0.51. Regarding the abundance of halogens, fluorine values in the biotite grains vary from F = 0.47 to 0.87 Wt% while chlorine values from Cl= 0.11 to 0.14 Wt%. Nickel values vary in abundance from 1080 to 1460 ppm with an average value of 1288 ppm **Figure 9**). The X_{Fe} values in biotite grains from the sample PCL9 vary from X_{Fe} = 0.55 up to X_{Fe} = 0.59. The halogens in the biotite grains of the sample show fluorine values from F = 0.24 – 0.66 Wt% and chlorine values from Cl = 0.19

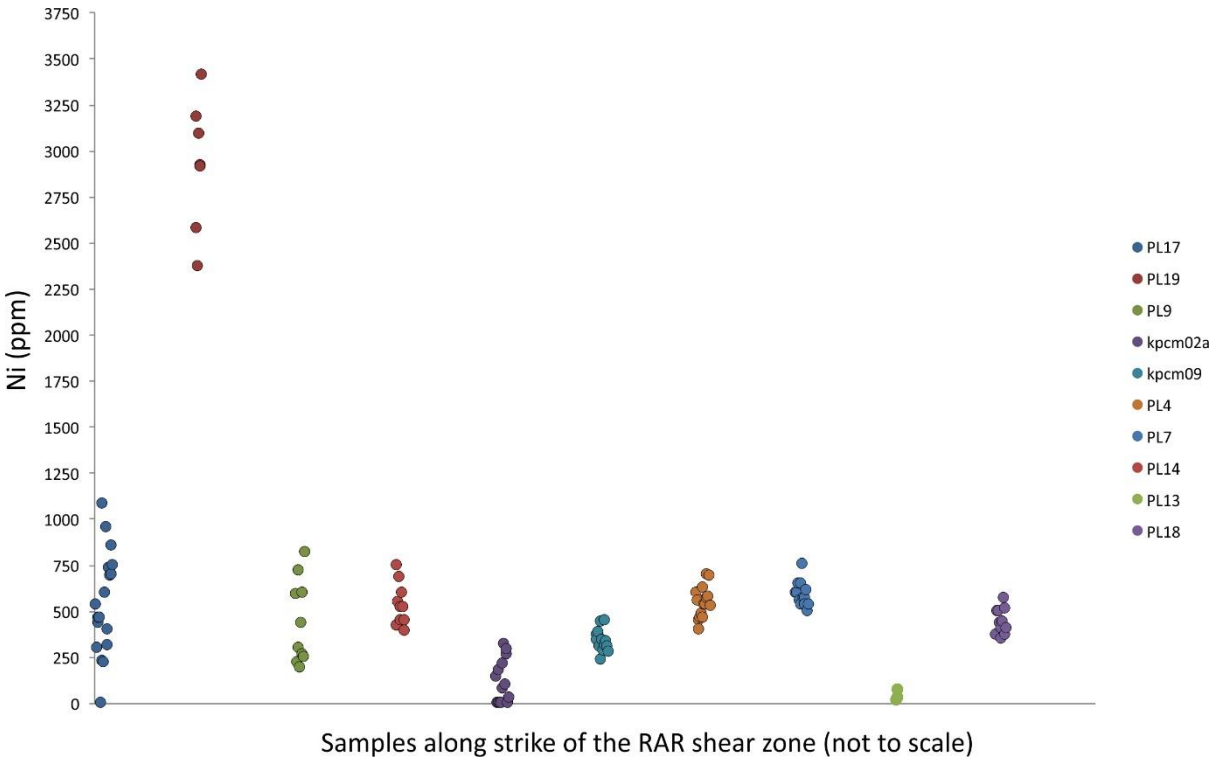

Figure 8. Plot that shows nickel variations in biotite grains of the RAR shear zone

– 0 .23 Wt%. The nickel contents in biotites of the sample are remarkably lower relative to the samples PCL1 and PCL3 and vary from 150 to 630 ppm.

6.4.2 Chlorite

Chlorite grains were analysed from two samples, the PCL3 and PCL 9 (**Figure 10**). Chlorite grains from the sample PCL 3 are compositionally characterised as ripidolites. The X_{Fe} values in the chlorites vary from X_{Fe} = 0.50 – 0.51. The fluorine values in the analysed chlorites varies from below detection limits up to F = 0.22 Wt%. The observed variations in the chlorine abundance are negligible and specifically vary from Cl = 0.01 – 0.02 Wt%. The nickel abundance in the chlorites varies from 1280 to 1660 ppm The chlorites in the sample PCL 9 are ripidolites with X_{Fe} values that vary from X_{Fe} = 0.56 – 0.58. The halogen values in the same grains show fluorine contents from F = 0.04 – 0.17 Wt % and chlorine from Cl = 0.02 – 0.04 Wt%.

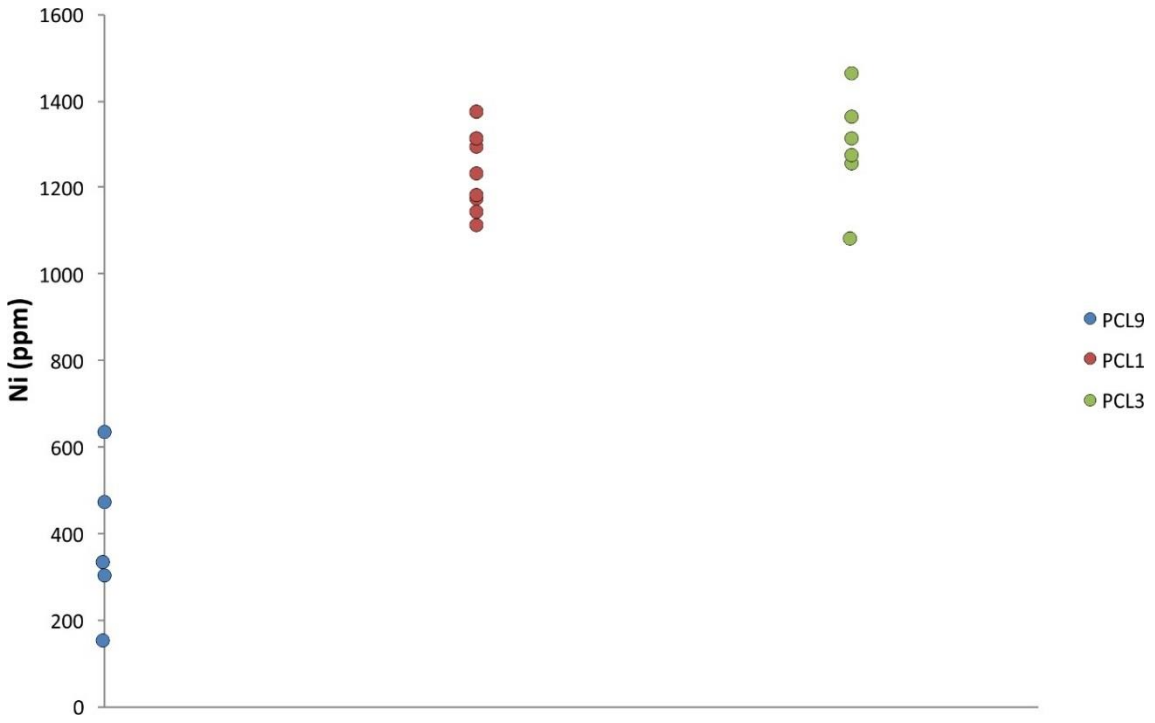

Figure 9. Plot that shows nickel variations in biotite grains from the X2 shear zone

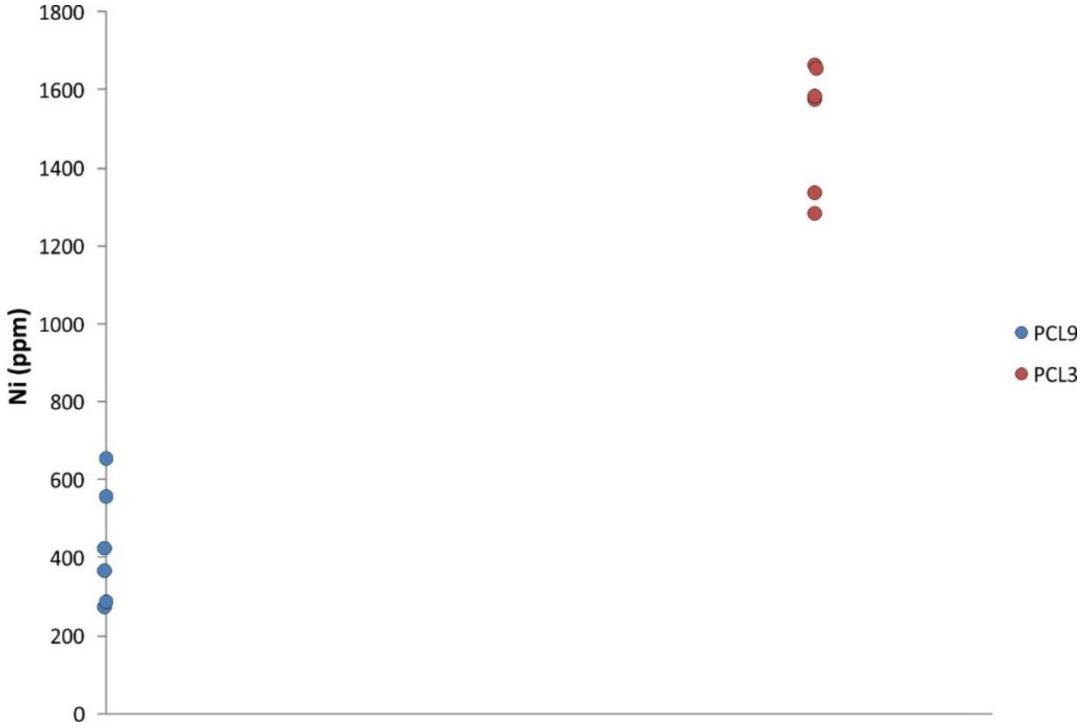

Figure 10. Plot that shows nickel variations in chlorite grains of the X2 shear zone

7. Discussion

The mineral-chemistry comparison of barren (i.e. Cliff Lake Fault) and ore-controlling shear zones shows that in the latter are observed up to two orders of magnitude increase in the nickel content of their fabric-forming silicates (mostly biotite). In comparison, biotite grains with phlogopitic composition (Mg-rich variety) from unmineralised settings exhibit median nickel concentrations up to 1700 ppm whereas Mg-biotites have typical median concentration of 178 ppm (Tischendorf et al., 2001). The analysed biotite grains from the Six Shaft Shear Zone with the highest nickel contents (i.e. average concentration 1600 ppm) are characterised as Mg-biotites demonstrating that this compositional anomaly resulted from the high nickel availability in proximity to a contact-style sulphide ore body.

In cases where a shear zone is hosted in a variety of lithologies, such as the RAR shear zone, the fabric-forming silicates show a high Ni/Cr geochemical signature but their vectoring potential towards shear-controlled mineralization remain less well understood. Further processing of the mineral-chemistry data using multivariable statistical methods (e.g. principal component analysis) can assist to understand better if certain pathfinder trace elements, from different mineral phases, can be used as a new geochemical exploration tool.

8. Conclusions

Preliminary analysis of mineral chemistry data from modally abundant fabric-forming silicates of barren and ore-controlling shear zones shows that the nickel content in phyllosilicates of the ore-controlling structures is elevated up to two orders of magnitude. Tentatively can be suggested that in shear zones where the fabric is defined chiefly by a single phase (e.g. biotite > 80 – 90 %) nickel variations show promise as a pathfinder tool of mineralization. This tool could provide significant insights at the targeting stage of prospective shear zones before the initiation of a drilling campaign.

References of Chapters 2, 3, and 7

Ames, D.E., Buckle, J., Davidson, A., and Card, K., 2005, Sudbury bedrock compilation: Geological Survey of Canada Open File 4570, geology, color map, and digital tables, scale 1:50,000.

Ames, D.E. and Farrow, C.E.G., 2007, Metallogeny of the Sudbury mining camp, Ontario, in Goodfellow W.D., ed., Mineral deposits of Canada: A synthesis of major deposit-types, district metallogeny, the evolution of geological provinces, and exploration methods: Geological Association of Canada, Mineral Deposits Division, Special Publication no. 5, p. 329–350.

Austin, J. R., & Blenkinsop, T. G. (2009). Local to regional scale structural controls on mineralisation and the importance of a major lineament in the eastern Mount Isa Inlier, Australia: Review and analysis with autocorrelation and weights of evidence. *Ore Geology Reviews*, *35*(3–4), 298–316. http://doi.org/10.1016/j.oregeorev.2009.03.004

Bailey, J., McDonald, A. M., Lafrance, B., & Fedorowich, J. S. (2006). Variations in Ni content in sheared magmatic sulfide ore at the Thayer Lindsley Mine, Sudbury, Ontario. *Canadian Mineralogist*, *44*(5), 1063–1077. http://doi.org/10.2113/gscanmin.44.5.1063

Bailey, J., Lafrance, B., McDonald, A. M., Fedorowich, J. S., Kamo, S., & W.J. Davis., D. A. A. (2004). Mazatzal–Labradorian-age (1.7–1.6 Ga) ductile deformation of the South Range Sudbury impact structure at the Thayer Lindsley mine, Ontario. *Canadian Journal of Earth Sciences* , *41*(12), 1491–1505. http://doi.org/10.1139/e04-098

Barnes, S.-J., & Lightfoot, P. C. (2005). Formation of magmatic nickel-sulfide ore deposits and processses affecting their copper and platinum-group element contents. *Economic Geology*, 179–213.

Berman, R.G. (1991) Thermobarometry using multi-equilibrium calculations: a new technique, with petrological applications; in, Quantitative methods in petrology: an issue in honor of Hugh J. Greenwood; Eds. Gordon, T M; Martin, R F. Canadian Mineralogist v. 29, 833-855.

Beaumont, C., Nguyen, M. H., Jamieson, R. A., & Ellis, S. (2006). Crustal flow modes in large hot orogens. *Geological Society, London, Special Publications*, *268*(1), 91–145. http://doi.org/10.1144/GSL.SP.2006.268.01.05

Becker, J. S. (2007). Inorganic Mass Spectrometry: Principles and Applications. John Willey and Sons. http://doi.org/10.1002/9780470517222

Bennett, G., Dressler, B.O. and Robertson, J.A. 1991. The Huronian Supergroup and associated intrusive rocks; in Geology of Ontario, Ontario Geological Survey, Special Volume 4, Part 1, p. 549-592.

Bleeker, W., Kamo, S.L., Ames, D.E., and Davis, D., (2015). New field observations and U-Pb ages in the Sudbury area: toward a detailed cross-section through the deformed Sudbury Structure, *In:* Targeted Geoscience Initiative 4: Canadian Nickel-Copper-Platinum Group Elements-Chromium Ore Systems – Fertility, Pathfinders, New and Revised Models, (ed.) D.E. Ames and M.G. Houle; Geological Survey of Canada, Open File 7856, p. 151–166.

Blonde J (1996) Petrology and metamorphism of Nipissing diabase of May Township, Ontario. M.Sc. thesis, Carleton University, 160 pp

Boerner, D. E., Milkereit, B., Wu, J., & Salisbury, M. (2000). Seismic images and three-dimensional architecture of a Proterozoic shear zone in the Sudbury Structure (Superior Province, Canada). *Tectonics*, *19*(2), 397–405. http://doi.org/10.1029/1999TC900060

Card, K. D. (1990). A review of the Superior Province of the Canadian Shield, a product of Archean accretion. *Precambrian Research*, *48*(1–2), 99–156. http://doi.org/10.1016/0301-9268(90)90059-Y

Card K. D. (1994) Geology of the Levack gneiss complex, the northern footwall of the Sudbury structure, Ontario. In *Current Research,* pp.269-278. Part C, Geol. Surv. Can.

Carr, S. D., Easton, R. M., Jamieson, R. A., & Culshaw, N. G. (2000). Geologic transect across the Grenville orogen of Ontario and New York. *Canadian Journal of Earth Sciences*, *37*(2–3), 193–216. http://doi.org/10.1139/e99-074

Clowes, R., Hynes, A., & Rivers, T. (2010). Protracted continental collision — evidence from the Grenville Orogen. This article is one of a series of papers published in this Special Issue on the theme *Lithoprobe — parameters, processes, and the evolution of a continent* . *Canadian Journal of Earth Sciences*, *47*(5), 591–620. http://doi.org/10.1139/E10-003

Cooke, D.R., Baker, M., Hollings, P., Sweet, G., Change, Z., Dnyushevsky, L., Gilbert, S., Zhou, T., White, N., Gemell, B., Inglis, S. (2014). New Advances in Detecting the Distal Geochemical Footprints of Porphyry Systems— Epidote Mineral Chemistry as a Tool for Vectoring and Fertility Assessments. In book: Building Exploration Capability for the 21st Century, Edition: Special Publication 18, Chapter: 7, Publisher: SOCIETY OF ECONOMIC GEOLOGISTS, INC., Editors: Karen D. Kelley, Howard C. Golden, pp.127–152

Corfu, F., & Llghtfoot, P. C. (1996). U-Pb geochronology of the Sublayer Environment, Sudbury Igneous Complex, Ontario. *Economic Geology*, *91*(7), 1263–1269. http://doi.org/10.2113/gsecongeo.91.7.1263

Culshaw, N. G., Jamieson, R. A., Ketchum, J. W. F., Wodicka, N., Corrigan, D., & Reynolds, P. H. (1997). Transect across the northwestern Grenville orogen, Georgian Bay, Ontario: Polystage convergence and extension in the lower orogenic crust. *Tectonics*, *16*(6), 966–982. http://doi.org/10.1029/97TC02285

Darling, J. R., Hawkesworth, C. J., Lightfoot, P. C., Storey, C. D., & Tremblay, E. (2010). Isotopic heterogeneity in the Sudbury impact melt sheet. *Earth and Planetary Science Letters*, *289*, 347–356. http://doi.org/10.1016/j.epsl.2009.11.023

Davis, D. W. (2008). Sub-million-year age resolution of Precambrian igneous events by thermal extraction–thermal ionization mass spectrometer Pb dating of zircon: Application to crystallization of the Sudbury impact melt sheet. *Geology*, *36*(5), 383. http://doi.org/10.1130/G24502A.1

Deutsch, A., Grieve, R. A. F., Avermann, M., Bischoff, L., Brockmeyer, P., Buhl, D., … Stoffler, D. (1995). The Sudbury Structure (Ontario, Canada): a tectonically deformed multi-ring impact basin. *Geologische Rundschau*, *84*(4), 697–709. http://doi.org/10.1007/BF00240561

Dora, M. L., & Randive, K. R. (2015). Chloritisation along the Thanewasna shear zone, Western Bastar Craton, Central India: Its genetic linkage to Cu-Au mineralisation. *Ore Geology Reviews*, *70*, 151–172. http://doi.org/10.1016/j.oregeorev.2015.03.018

Dressler B. O. 1984. The Effects of the Sudbury event and the intrusion of the Sudbury Igneous Complex on the Footwall rocks of the Sudbury structure. In *The geology and ore deposits of*

the Sudbury structure, edited by Pye E. G., Naldrett A. J., and Giblin P. E. Special Publication 1. Toronto: Ontario Geological Survey.pp. 97–136.

Engler, O., and Randle, V. (2010). Introduction to texture analysis: macrotexture, microtexture, and orientation mapping, 2nd edition. CRC press

Farrow, C.E.G., and Lightfoot, P.C., 2002, Sudbury PGE revisited: towards an integrated model: CIM Spec. Vol. 54, p. 273–297.

Fedo, C. M., Young, G. M., Nesbitt, H. W., & Hanchar, J. M. (1997). Potassic and sodic metasomatism in the Southern Province of the Canadian Shield: Evidence from the Paleoproterozoic Serpent Formation, Huronian Supergroup, Canada. *Precambrian Research*, *84*(1), 17–36. http://doi.org/10.1016/S0301-9268(96)00058-7

Fleet, M. E., Barnett, R. L., & Morris, W. A. (1987). Prograde Metamorphism of the Sudbury Igneous Complex. *Canadian Mineralogist*, *25*, 499–514.

Forsyth, D. A., Milkereit, B., Davidson, A., Hanmer, S., Hutchinson, D. R., Hinze, W. J., & Mereu, R. F. (1994). Seismic images of a tectonic subdivision of the Grenville Orogen beneath lakes Ontario and Erie. *Canadian Journal of Earth Sciences*, *31*(2), 229–242. http://doi.org/10.1139/e94-023

Gibson, A.M., Lightfoot, P.C., Evans, T.C., (2010). Contrasting styles of Low Sulphide High Precious Metal Mineralization in the 148 and 109 FW zones: North and South Ranges of the Sudbury Igneous Complex, Ontario, Canada. In Jugo, P.J., Lesher, C.M., and Mungall, J.E. (Eds): Abstracts, 11th International Platinum Symposium, Sudbury, Ontario, Canada. OGS Miscellaneous Release Data 269.

Gower, C. F., & Krogh, T. E. (2002). A U–Pb geochronological review of the Proterozoic history of the eastern Grenville Province. *Canadian Journal of Earth Sciences*, *39*(5), 795–829. http://doi.org/10.1139/e01-090

Goodhew, P. J., Humphreys, J., & Beanland, R. (2001). Electron Microscopy and Analysis. *Taylor and Francis*, *30*, 132. http://doi.org/10.1046/j.1365-2818.2001.0936b.x

Grieve, R. A. F., Ames, D. E., Morgan, J. V., & Artemieva, N. (2010). The evolution of the Onaping Formation at the Sudbury impact structure. *Meteoritics & Planetary Science*, *45*(5), 759–782. http://doi.org/10.1111/j.1945-5100.2010.01057.x

Groves, D. I., Goldfarb, R. J., Gebre-Mariam, M., Hagemann, S. G., & Robert, F. (1998). Orogenic gold deposits: a proposed classification in the context of their crustal distribution and relationship to other gold deposit types. *Ore Geology Reviews*, *13*(1–5), 7–27. http://doi.org/10.1016/S0169-1368(97)00012-7

Günther, D., & Hattendorf, B. (2005). Solid sample analysis using laser ablation inductively coupled plasma mass spectrometry. *Trends in Analytical Chemistry*, *24*(3), 255–265. http://doi.org/10.1016/j.trac.2004.11.017

Guillong, M., Horn, I., & Gunther, D. (2003). A comparison of 266 nm, 213 nm and 193 nm produced from a single solid state Nd:YAG laser for laser ablation ICP-MS. *Journal of Analytical Atomic Spectrometry*, *18*(10), 1224–1230. http://doi.org/10.1039/B305434A

Guillong, M., & Günther, D. (2002). Effect of particle size distribution on ICP-induced elemental fractionation in laser ablation-inductively coupled plasma-mass spectrometry. *Journal of Analytical Atomic Spectrometry*, *17*(8), 831–837. http://doi.org/10.1039/b202988j

Halter, W. E., Pettke, T., Heinrich, C. A., & Rothen-Rutishauser, B. (2002). Major to trace element analysis of melt inclusions by laser-ablation ICP-MS: Methods of quantification. *Chemical Geology*, *183*(1–4), 63–86. http://doi.org/10.1016/S0009-2541(01)00372-2

Hanley, J. J., & Bray, C. J. (2009). THE TRACE METAL CONTENT OF AMPHIBOLE AS A PROXIMITY INDICATOR FOR Cu-Ni-PGE MINERALIZATION IN THE FOOTWALL OF THE SUDBURY IGNEOUS COMPLEX, ONTARIO, CANADA. *Economic Geology*, *104*(1), 113–125. http://doi.org/10.2113/gsecongeo.104.1.113

Hoffman, P. (1988). United Plates Of America, The Birth Of A Craton: Early Proterozoic Assembly And Growth Of Laurentia. *Annual Review of Earth and Planetary Sciences*. http://doi.org/10.1146/annurev.earth.16.1.543

James, R.S., Sweeny, J.M., and Peredery, W., 1991, Thermobarometry of the Levack Gneisses-footwall rocks to the Sudbury Igneous Complex: Lithoprobe, Abitibi-Grenville Transect Report 32, p. 179–182.

Kamo, S. L., Reimold, W. U., Krogh, T. E., & Colliston, W. P. (1996). A 2.023 Ga age for the Vredefort impact event and a first report of shock metamorphosed zircons in pseudotachylitic breccias and Granophyre. *Earth and Planetary Science Letters*, *144*(3), 369–387. http://doi.org/10.1016/S0012-821X(96)00180-X

Keays, R. R., & Lightfoot, P. C. (2004). Formation of Ni-Cu-Platinum Group Element sulfide mineralization in the Sudbury impact melt sheet. *Mineralogy and Petrology*. http://doi.org/10.1007/s00710-004-0050-8

Kitt, S., Kisters, A., Steven, N., Maiden, K., & Hartmann, K. (2016). Shear-zone hosted copper mineralisation of the Omitiomire deposit - Structural controls of fluid flow and mineralisation during subduction accretion in the Pan-African Damara Belt of Namibia. *Ore Geology Reviews*, *75*, 1–15. http://doi.org/10.1016/j.oregeorev.2015.10.035

Krogh, T.E., Davis, D.W. and Corfu, F. 1984. Precise U-Pb zircon and baddeleyite ages for the Sudbury area. In The Geology and Ore Deposits of the Sudbury Structure. Edited by E.G. Pye, A.J. Naldrett and P.E. Gilbin. Special Volume 1: 431-446, Ontario Geological Survey

Krogh, T. E. (1994). Precise U-Pb ages for Grenvillian and pre-Grenvillian thrusting of Proterozoic and Archean metamorphic assemblages in the Grenville Front tectonic zone, Canada. *Tectonics*, *13*(4), 963–982. http://doi.org/10.1029/94TC00801

Lafrance, B., & Kamber, B. S. (2010). Geochemical and microstructural evidence for in situ formation of pseudotachylitic Sudbury breccia by shock-induced compression and cataclasis. *Precambrian Research*, *180*, 237–250. http://doi.org/10.1016/j.precamres.2010.04.006

Lightfoot, P. C. (2007). Advances in Ni-Cu-PGE Sulphide Deposit Models and Implications for Exploration Technologies. *Ore Deposits and Exploration Technology*, 629–646.

Lightfoot, P.C., and Zotov, I.A., 2005, Geology and geochemistry of the Sudbury Igneous Complex, Ontario, Canada: Origin of nickel sulphide mineralization associated with an impact-generated melt sheet: Geology of Ore Deposits. 47, p. 349–381.

Lightfoot, P. C., & Doherty, W. (2001). Chemical evolution and origin of nickel sulfide mineralization in the sudbury igneous complex, Ontario, Canada. *Economic Geology*, *96*, 1855–1875. http://doi.org/10.2113/gsecongeo.96.8.1855

Lightfoot, P. G., Keays, R. R., Morrison, G. G., Bite, A., & Farrell, K. P. (1997). Geochemical relationships in the sudbury igneous complex: Origin of the main mass and offset dikes. *Economic Geology*, *92*(3), 289–307. http://doi.org/10.2113/gsecongeo.92.3.289

Liu, C., Bagas, L., & Wang, F. (2016). Isotopic analysis of the super-large Shuangjianzishan Pb-Zn-Ag deposit in Inner Mongolia, China: Constraints on magmatism, metallogenesis, and tectonic setting. *Ore Geology Reviews*, *75*, 252–267. http://doi.org/10.1016/j.oregeorev.2015.12.019

Longerich H (2008) Laser ablation–inductively coupled plasma– mass spectrometry (LA–ICP–MS); an introduction. In Sylvester P ed. Laser ablation ICP-MS in the earth sciences: current practices and outstanding issues. (Short Course Series 40) Mineralogical Association of Canada, Vancouver, BC, 1–18

Long, D.G.F., 1992. Does the Sedimentology of the Chelmsford Formation Provide Evidence for a Meteorite Impact Origin of the Sudbury Structure? Abstracts of Papers Presented to the International Conference on Large Meteorite Impacts and Planetary Evolution, p48.

Maitland, T., & Sitzman, S. (2007). Electron Backscatterd Diffraction (EBSD) Technique and Materials Characterization Examples. *Scanning Microscopy for Nanotechnology : Techniques and Applications*, 41–76. http://doi.org/0387396209

McLennan, S. M., Simonetti, A., & Goldstein, S. L. (2000). Nd and Pb isotopic evidence for provenance and post-depositional alteration of the Paleoproterozoic Huronian Supergroup, Canada. *Precambrian Research*, *102*, 263–278. http://doi.org/10.1016/S0301-9268(00)00070-X

McLelland, J., Daly, J. S., & McLelland, J. M. (1996). The Grenville Orogenic Cycle (ca. 1350-1000 Ma): an Adirondack perspective. *Tectonophysics*, *265*(1), 1–28. http://doi.org/10.1016/S0040-1951(96)00144-8

Muir, T.L. and Peredery, W.V. 1984. The Onaping Formation; in The Geology and Ore Deposits of the Sudbury Structure, Ontario Geological Survey, Special Volume 1, p. 139-210.

Mukwakwami, J., Lafrance, B., Lesher, C. M., Tinkham, D., Rayner, N., & Ames, D. (2014). Deformation, metamorphism, and mobilization of Ni–Cu–PGE sulfide ores at Garson Mine, Sudbury. *Mineralium Deposita*, *49*(2), 175–198. http://doi.org/10.1007/s00126-013-0479-y

Mukwakwami, J., Lafrance, B., & Lesher, C. M. (2012). Back-thrusting and overturning of the southern margin of the 1.85Ga Sudbury Igneous Complex at the Garson mine, Sudbury, Ontario. *Precambrian Research*, *196–197*, 81–105. http://doi.org/10.1016/j.precamres.2011.10.020

Mungall, J. E., Ames, D. E., & Hanley, J. J. (2004). Geochemical evidence from the Sudbury structure for crustal redistribution by large bolide impacts. *Nature*, *429*(6991), 546–548. http://doi.org/10.1038/nature02577

Naldrett, A.J., and Hewins, R.H., 1984, The main mass of the Sudbury Igneous Complex: Ontario Geological Survey Special Volume 1, p. 235–251.

Newbury, D. E., & Ritchie, N. W. M. (2013). Is scanning electron microscopy/energy dispersive X-ray spectrometry (SEM/EDS) quantitative? *Scanning*, *35*(3), 141–168. http://doi.org/10.1002/sca.21041

Ostermann, M., Scharer, U., & Deutsch, A. (1996). Impact melt dikes in the Sudbury multi-ring basin (Canada): Implications from uranium-lead geochronology on the Foy Offset Dike. *Meteoritics & Planetary Science*, *31*(4), 494–501. http://doi.org/10.1111/j.1945-5100.1996.tb02091.x

Partington, G. A. (1990). Environment and structural controls on the intrusion of the giant rare metal Greenbushes pegmatite, Western Australia. *Economic Geology*. http://doi.org/10.2113/gsecongeo.85.3.437

Pattison, E. F. (1979). The Sudbury sublayer. *The Canadian Mineralogist*, *17*(2), 257–274. Retrieved from http://www.canmin.org/content/17/2/257.short

Percival, J.A. and Easton, R.M. 2007. Geology of the Canadian Shield in Ontario: an update; Ontario Geological Survey, Open File Report 6196, Geological Survey of Canada, Open File 5511, Ontario Power Generation, Report 06819-REP-01200-10158-R00, 65p.

Percival, J. A., Sanborn-Barrie, M., Skulski, T., Stott, G. M., Helmstaedt, H., & White, D. J. (2006). Tectonic evolution of the western Superior Province from NATMAP and Lithoprobe studies. *Canadian Journal of Earth Sciences*, *43*(7), 1085–1117. http://doi.org/10.1139/e06-062

Percival, J. A., & Williams, H. R. (1989). Late Archean Quetico accretionary complex, Superior province, Canada. *Geology*, *17*(1), 23. http://doi.org/10.1130/0091-7613(1989)017<0023:LAQACS>2.3.CO;2

Pettke, T., Oberli, F., Audétat, A., Guillong, M., Simon, A. C., Hanley, J. J., & Klemm, L. M. (2012). Recent developments in element concentration and isotope ratio analysis of individual fluid inclusions by laser ablation single and multiple collector ICP-MS. *Ore Geology Reviews*, *44*, 10–38. http://doi.org/10.1016/j.oregeorev.2011.11.001

Prior, D. J., Trimby, P. W., Weber, U. D., & Dingley, D. J. (1996). Orientation contrast imaging of microstructures in rocks using forescatter detectors in the scanning electron microscope. *Mineralogical Magazine*, *60*(403), 859–869. http://doi.org/10.1180/minmag.1996.060.403.01

Raharimahefa, T., Lafrance, B., & Tinkham, D. K. (2014). New structural, metamorphic, and U–Pb geochronological constraints on the Blezardian Orogeny and Yavapai Orogeny in the Southern Province, Sudbury, Canada. *Canadian Journal of Earth Sciences*, *51*(8), 750–774. http://doi.org/10.1139/cjes-2014-0025

Randle, V. (2000). Theoretical framework for electron backscatter diffraction. In *Electron Backscatter Diffraction in Materials Science* (pp. 19–30). Boston, MA: Springer US. http://doi.org/10.1007/978-1-4757-3205-4_2

Reddy, S. M., & Hough, R. M. (2013). Microstructural evolution and trace element mobility in Witwatersrand pyrite. *Contributions to Mineralogy and Petrology*, *166*(5), 1269–1284. http://doi.org/10.1007/s00410-013-0925-y

Reed, S.J.B., (2005). Electron Microprobe Analysis and Scanning Electron Microscopy in Geology. Cambridge University Press, 2nd edition.

Riller, U. (2005). Structural characteristics of the Sudbury impact structure, Canada: Impact-induced versus orogenic deformation-A review. *Meteoritics & Planetary Science*, *40*, 1723–1740. http://doi.org/10.1111/j.1945-5100.2005.tb00140.x

Riller, U., Schwerdtner, W. M., Halls, H. C., & Card, K. D. (1999). Transpressive tectonism in the eastern Penokean orogen, Canada consequences for Proterozoic crustal kinematics and

continental fragmentation. *Precambrian Research*, *93*, 51–70. http://doi.org/10.1016/S0301-9268(98)00097-7

Riller, U., & Schwerdtner, W. M. (1997). Mid-crustal deformation at the southern flank of the Sudbury Basin, central Ontario, Canada. *Geological Society of America Bulletin* , *109*(7), 841–854. http://doi.org/10.1130/0016-7606(1997)109<0841:MCDATS>2.3.CO;2

Rousell D. H. 1984. Onwatin and Chelmsford Formations. In The geology and ore deposits of the Sudbury structure, edited by Pye E. G., Naldrett A. J., and Giblin P. E. Special Publication 1. Toronto: Ontario Geological Survey. pp. 211–218.

Saumur, B. M., & Cruden, A. R. (2016). On the emplacement of the voisey's bay intrusion (Labrador, Canada). *Bulletin of the Geological Society of America*, *128*(1–2), 147–168. http://doi.org/10.1130/B31240.1

Schulz, K. J., & Cannon, W. F. (2007). The Penokean orogeny in the Lake Superior region. *Precambrian Research*, *157*, 4–25. http://doi.org/10.1016/j.precamres.2007.02.022

Schwarzer, R. A., Field, D. P., Adams, B. L., Kumar, M., & Schwartz, A. J. (2009). Present state of electron backscatter diffraction and prospective developments. In *Electron Backscatter Diffraction in Materials Science* (pp. 1–20). http://doi.org/10.1007/978-0-387-88136-2_1

Scott, R. G., & Spray, J. G. (1999). Magnetic fabric constraints on friction melt flow regimes and ore emplacement direction within the South Range Breccia Belt, Sudbury Impact Structure. *Tectonophysics*, *307*(1), 163–189. http://doi.org/10.1016/S0040-1951(99)00124-9

Sims, P. K., Schmus, W. R. Van, Schulz, K. J., & Peterman, Z. E. (1989). Tectono-stratigraphic evolution of the Early Proterozoic Wisconsin magmatic terranes of the Penokean Orogen. *Canadian Journal of Earth Sciences*. http://doi.org/10.1139/e89-180

Spencer, K. J., Hacker, B. R., Kylander-Clark, A. R. C., Andersen, T. B., Cottle, J. M., Stearns, M. A., … Seward, G. G. E. (2013). Campaign-style titanite U–Pb dating by laser-ablation ICP: Implications for crustal flow, phase transformations and titanite closure. *Chemical Geology*, *341*, 84–101. http://doi.org/10.1016/j.chemgeo.2012.11.012

Spray, J. G. (1997). Superfaults. *Geology*, *25*, 579–582. http://doi.org/10.1130/0091-7613(1997)025<0579:S>2.3.CO;2

Stipp, M., Stünitz, H., Heilbronner, R., & Schmid, S. M. (2002). The eastern Tonale fault zone: A “natural laboratory” for crystal plastic deformation of quartz over a temperature range from 250 to 700 °C. *Journal of Structural Geology*, *24*, 1861–1884. http://doi.org/10.1016/S0191-8141(02)00035-4

Stockwell, C.H. (1982). Proposals for the time classification and correlation of Precambrian rocks and events in Canada and adjacent areas of the Canadian Shield. Geological Survey of Canada, 80-19.

Stern R. A., (2009). Introduction to secondary ion mass spectrometry (SIMS) in geology, in Secondary Ion Mass Spectrometry in the Earth Sciences, ed.M. Fayek. Mineral. Assoc. Can., Short Course Series, , 41, 1–18.

Sylvester, P. J., & Jackson, S. E. (2016). A Brief History of Laser Ablation Inductively Coupled Plasma Mass Spectrometry (LA–ICP–MS). *Elements*, *12*(5), 307–310. http://doi.org/10.2113/gselements.12.5.307

Taylor, H. E. (2001). Inductively Coupled Plasma-Mass Spectrometry Practices and Techniques. Academic Press. http://doi.org/10.1016/B978-012683865-7/50010-7

Therriault, A. M., Fowler, A. D., & Grieve, R. A. F. (2002). The Sudbury Igneous Complex: A Differentiated Impact Melt Sheet. *Economic Geology*, *97*(7), 1521–1540. http://doi.org/Doi 10.2113/97.7.1521

Thomas, R. (2013). Practical Guide to ICP-MS: A Tutorial for Beginners, Third Edition. *Robert Thomas*, 446. http://doi.org/10.1017/CBO9781107415324.004

Thurston, P.C., 1991.Proterozoic Geology of Ontario: Introduction; *in* Geology of Ontario, Ontario Geological Survey, Special Volume 4, Part 1, p.543-548.

Tischendorf, G., Förster, H.-J., & Gottesmann, B. (2001). Minor- and trace-element composition of trioctahedral micas: a review. *Mineralogical Magazine*, *65*(2), 249–276. http://doi.org/10.1180/002646101550244

Thomson, M. L., Barnett, R. L., Fleet, M. E., & Kerrich, R. (1985). Metamorphic assemblages in the South-Range norite and footwall mafic rocks near the Kirkwood mine, Sudbury, Ontario. *Canadian Mineralogist*.

Tollo, R.P., Corriveau, L., McLelland, J., and Bartholomew, M.J., 2004, Proterozoic tectonic evolution of the Grenville orogen in North America: An introduction, *in* Tollo, R.P., Corriveau, L., McLelland, J., and Bartholomew, M.J., eds., Proterozoic tectonic evolution of the Grenville orogen in North America: Boulder, Colorado,Geological Society of America Memoir 197, p. 1–18.

Tohver, E., Holm, D. K., van der Pluijm, B. A., Essene, E. J., & Cambray, F. W. (2007). Late Paleoproterozoic (geon 18 and 17) reactivation of the Neoarchean Great Lakes Tectonic Zone, northern Michigan, USA: Evidence from kinematic analysis, thermobarometry and 40Ar/39Ar geochronology. *Precambrian Research*, *157*(1–4), 144–168. http://doi.org/10.1016/j.precamres.2007.02.014

Tuchscherer, M. G., & Spray, J. G. (2002). Geology, Mineralization, and Emplacement of the Foy OffsetDike, Sudbury Impact Structure. *Economic Geology*, *97*(7), 1377–1397. http://doi.org/10.2113/gsecongeo.97.7.1377

Walker, R. J., Morgan, J. W., Naldrett, A. J., Li, C., & Fassett, J. D. (1991). Re-Os isotope systematics of Ni-Cu sulfide ores, Sudbury Igneous Complex, Ontario: evidence for a major crustal component. *Earth and Planetary Science Letters*, *105*(4), 416–429. http://doi.org/10.1016/0012-821X(91)90182-H

Warren, M. R., Hanley, J. J., Ames, D. E., & Jackson, S. E. (2015). The Ni-Cr-Cu content of biotite as pathfinder elements for magmatic sulfide exploration associated with mafic units of the sudbury igneous complex, Ontario, Canada. *Journal of Geochemical Exploration*, *153*, 11–29. http://doi.org/10.1016/j.gexplo.2015.02.010

White, C.H., (2012). Low-Sulfide PGE-Cu-Ni Mineralization From Five Prospects Within The Footwall Of The Sudbury Igneous Complex, Ontario, Canada. PhD thesis, Department of Geology, University of Tronto.

Whitmeyer, S. J., & Karlstrom, K. E. (2007). Tectonic model for the Proterozoic growth of North America. *Geosphere*, *3*, 220–259. http://doi.org/10.1130/GES00055.1

Wilkinson, J. J., Chang, Z., Cooke, D. R., Baker, M. J., Wilkinson, C. C., Inglis, S., … Bruce Gemmell, J. (2015). The chlorite proximitor: A new tool for detecting porphyry ore deposits.

Journal of Geochemical Exploration, *152*, 10–26. http://doi.org/10.1016/j.gexplo.2015.01.005

Young, G. M., Long, D. G. F., Fedo, C. M., & Nesbitt, H. W. (2001). Paleoproterozoic Huronian basin: Product of a Wilson cycle punctuated by glaciations and a meteorite impact. *Sedimentary Geology*, *141–142*, 233–254. http://doi.org/10.1016/S0037-0738(01)00076-8

Zhang, J., Linnen, R., Lin, S., Davis, D., & Martin, R. (2014). Paleoproterozoic hydrothermal reactivation in a neoarchean orogenic lode-gold deposit of the southern abitibi subprovince: U-Pb monazite geochronological evidence from the young-davidson mine, Ontario. *Precambrian Research*, *249*, 263–272. http://doi.org/10.1016/j.precamres.2014.05.015

Zolnai, a. I., Price, R. a., & Helmstaedt, H. (1984). Regional cross section of the Southern Province adjacent to Lake Huron, Ontario: implications for the tectonic significance of the Murray Fault Zone. *Canadian Journal of Earth Sciences*, *21*(4), 447–456. http://doi.org/10.1139/e84-048

Chapter 8. Summary and future directions

This study had as its major aim the understanding of the post-impact orogenic evolution of the Sudbury structure through high-spatial resolution geochronology (LA-ICP-MS and SIMS) of shear-hosted accessory phases. Titanite ($CaTiSiO_5$) was the accessory mineral of choice, used to unravel the complex polyorogenic history of the Sudbury structure. The age dating of shear-hosted titanite grains from the Creighton Mine (South Range) indicates operation and/or reworking of the shear zones during three distinct orogenic pulses at ca. 1.75 Ga, 1.65 Ga, and 1.45 Ga. These three age populations are interpreted as evidence of shear zone operation during the Yavapai (ca. 1.8 – 1.7 Ga), Mazatzalian – Labradorian (ca. 1.7 – 1.6 Ga), and Chieflakian (ca. 1.5 – 1.4 Ga) events. The presence of titanite grains with shock-induced features in patchily zoned grains that belong to the 1.75 Ga age population suggests that the first orogenic event associated with the deformation of the South Range is the Yavapai orogeny (ca. 1.8 – 1.7 Ga). These three age populations suggest also that the southern province has a similar tectonothermal evolution with accretionary provinces in mid-continent and southwest United states corroborating previous studies.

In a focused petrochronologic study of a mylonitic shear zone from the Creighton Mine (Six Shaft Shear Zone, 5400 level) were recognised three textural populations of titanite grains (Group 1, Group 2, and Group 3). The Group 1 are interpreted as pre-tectonic grains since they define the cores of syndeformational patchily zoned grains. The latter show widespread evidence of crystal-plastic deformation and strong crystallographic preferred orientation (Group 2 grains). The blocky Group 3 grains are interpreted as post-tectonic and show chiefly brittle fracturing and weak effects of crystal plasticity. The three age populations show also variations in uranium contents, with the lowest amounts (< 4-5ppm) observed in the pre and post-tectonic grains. Diffuse crystallographic preferred orientation and annealing textures in plagioclase grains of the shear zone indicate that these grains were deformed via a dissolution-precipitation creep mechanism. The breakdown of plagioclase grains via dissolution-precipitation creep is recorded also in syn-tectonic titanite grains with positive europium anomalies. The age dating of the syn-tectonic titanite grains indicates that the examined shear zone operated during the Mazatzalian – Labradorian orogeny (1.7 – 1.6 Ga) and accommodated the local-scale mechanical remobilization of sulphide ore bodies.

As mentioned above, the 1.75 Ga titanite grains host as inclusions titanite grains with shock microstructures. The most prominent microstructural phenomena in these inclusions are cross-cutting microtwins, anastomosing microtwins, and twin recrystallization with neoblast formation. A ubiquitous shock indicator, both in Sudbury and Vredefort structures, is suggested to be the misorientation of shock microtwins relative to the host grains at 75°/<010> and 108°/<010>. The absence of dynamic recrystallization and brittle fracturing in titanite grains with shock features indicates that the shock wave induced a work hardening effect. This effect was critical for the survival of these grains in the polydeformed and polymetamorphosed South Range of the Sudbury structure. The age dating of shocked titanite grains located within 200m from the melt sheet yield the true impact ages whereas further away from the thermal metamorphic aureole only partial age resetting is observed. Both syn-impact mechanical twinning that generates fast diffusion pathways, and post-shock thermal annealing are necessary requirements for complete age resetting by an impact bombardment event.

The preliminary analysis of trace element data from fabric-forming silicates between ore-controlling and barren shear zones show interesting trends that can be used as exploration vectors. Specifically, in the case of the Six Shaft Shear Zone is observed an increase in nickel contents from the marginal to the core domains of the structure. Comparing these data, with data from barren exposures reveal that the metal-endowed shear zones exhibit specific trace element signatures. Further work will be pursued applying multivariable analysis (i.e. principal component analysis) in order to infer further information about the vectoring potential of different trace elements.

Regarding the absolute age dating of ductile deformation, future studies could focus on the integration of high temporal resolution techniques (ID-TIMS) in conjunction with quantitative microstructural analyses (EBSD) in order to place tighter constraints on events of crystal-plastic deformation. Moreover, in order to constrain better U-Pb age data from common lead-bearing phases a analytical protocol should be adopted for the measurement of the common lead isotopic composition using high precision techniques (e.g. MC-ICP-MS).

Appendix

Mineral chemistry data from the examined shear zones (see Chapter 7)

Biotite

Table 21

Locality	Garson Mine (5200 lvl)	Garson Mine (5200 lvl)	Garson Mine (5200 lvl)	Garson Mine (5200 lvl)	Garson Mine (5200 lvl)
Sample and analysis	kpgmd11-11 / 1 .	kpgmd11-12 / 1 .	kpgmd11-13 / 1 .	kpgmd11-14 / 1 .	kpgmd11-15 / 1 .
Mineral	Biotite	Biotite	Biotite	Biotite	Biotite
SiO2	36.618	36.426	36.503	36.138	36.401
TiO2	1.630	2.148	1.596	1.625	1.618
Al2O3	16.925	16.695	17.063	17.306	17.131
FeO	18.062	18.486	18.227	18.112	18.171
MnO	0.147	0.159	0.136	0.148	0.163
MgO	11.892	11.526	11.765	11.722	11.802
CaO	0.000	0.000	0.004	0.000	0.001
Na2O	0.064	0.133	0.060	0.039	0.073
K2O	9.602	9.509	9.516	9.575	9.364
Cl	0.094	0.083	0.088	0.070	0.054
Cr2O3	0.180	0.248	0.306	0.132	0.119
NiO	0.054	0.042	0.058	0.040	0.049
Total	95.267	95.455	95.321	94.906	94.945
Si	5.555	5.531	5.538	5.506	5.535
Al iv	2.445	2.469	2.462	2.494	2.465
Al vi	0.582	0.518	0.589	0.614	0.606
Ti	0.186	0.245	0.182	0.186	0.185
Cr	0.022	0.030	0.037	0.016	0.014
Fe	2.292	2.347	2.313	2.308	2.311
Mn	0.019	0.020	0.017	0.019	0.021
Mg	2.690	2.609	2.661	2.662	2.675
Ni	0.007	0.005	0.007	0.005	0.006
Ca	0.000	0.000	0.001	0.000	0.000
Na	0.019	0.039	0.018	0.011	0.022
K	1.858	1.841	1.842	1.861	1.816
OH*	3.976	3.979	3.977	3.982	3.986
Cl	0.024	0.021	0.023	0.018	0.014
Total	19.673	19.656	19.666	19.682	19.656
XFe	0.460	0.474	0.465	0.464	0.463
XMn	0.008	0.009	0.007	0.008	0.009

Table 22

Garson Mine (5200 lvl) kpgmd11-16 / 1 . Biotite	Garson Mine (5200 lvl) kpgmd11-17 / 1 . Biotite	Garson Mine (5200 lvl) kpgmd11-18 / 1 . Biotite	Garson Mine (5200 lvl) kpgmd11-19 / 1 . Biotite	Garson Mine (5200 lvl) kpgmd11-20 / 1 . Biotite
36.889	37.097	36.971	36.728	36.970
2.097	2.209	2.279	2.080	1.363
16.359	16.064	16.335	16.216	16.832
18.112	18.233	18.061	17.966	17.872
0.151	0.143	0.150	0.142	0.138
11.853	12.014	11.797	11.912	11.925
0.007	0.000	0.007	0.000	0.018
0.060	0.055	0.044	0.191	0.152
9.525	9.526	9.520	9.572	9.530
0.055	0.035	0.047	0.108	0.096
0.251	0.136	0.165	0.238	0.372
0.048	0.035	0.050	0.057	0.041
95.407	95.546	95.424	95.210	95.310
5.586	5.609	5.593	5.581	5.597
2.414	2.391	2.407	2.419	2.403
0.506	0.471	0.506	0.486	0.601
0.239	0.251	0.259	0.238	0.155
0.030	0.016	0.020	0.029	0.045
2.294	2.305	2.285	2.283	2.263
0.019	0.018	0.019	0.018	0.018
2.676	2.708	2.660	2.698	2.691
0.006	0.004	0.006	0.007	0.005
0.001	0.000	0.001	0.000	0.003
0.018	0.016	0.013	0.056	0.045
1.840	1.837	1.837	1.855	1.840
3.986	3.991	3.988	3.972	3.975
0.014	0.009	0.012	0.028	0.025
19.629	19.627	19.606	19.670	19.666
0.462	0.460	0.462	0.458	0.457
0.008	0.008	0.008	0.008	0.008

Table 23

Locality	Garson Mine (5200 lvl)	Garson Mine (5200 lvl)	Garson Mine (5200 lvl)	Garson Mine (5200 lvl)	Garson Mine (5200 lvl)
Sample and analysis	kpgmd12-21 / 1 .	kpgmd12-22 / 1 .	23 / 1 .	kpgmd12-24 / 1 .	25 / 1 .
Mineral	Biotite	Biotite	Biotite	Biotite	Biotite
SiO2	36.731	36.370	36.334	36.406	36.281
TiO2	1.042	0.820	1.200	1.035	1.215
Al2O3	18.095	17.849	17.525	17.507	17.553
FeO	16.904	16.889	17.489	17.105	17.357
MnO	0.135	0.142	0.147	0.150	0.144
MgO	11.620	12.117	11.942	12.227	11.981
CaO	0.013	0.002	0.002	0.011	0.001
Na2O	0.056	0.108	0.071	0.073	0.099
K2O	9.629	9.572	9.564	9.682	9.491
Cl	0.088	0.040	0.041	0.083	0.018
Cr2O3	0.240	0.221	0.138	0.105	0.166
NiO	0.039	0.049	0.061	0.054	0.048
Total	94.592	94.178	94.513	94.438	94.354
Si	5.568	5.543	5.536	5.546	5.531
Al iv	2.432	2.457	2.464	2.454	2.469
Al vi	0.802	0.749	0.683	0.690	0.685
Ti	0.119	0.094	0.138	0.119	0.139
Cr	0.029	0.027	0.017	0.013	0.020
Fe	2.143	2.153	2.229	2.179	2.213
Mn	0.017	0.018	0.019	0.019	0.019
Mg	2.626	2.753	2.712	2.777	2.723
Ni	0.005	0.006	0.007	0.007	0.006
Ca	0.002	0.000	0.000	0.002	0.000
Na	0.017	0.032	0.021	0.022	0.029
K	1.862	1.861	1.859	1.881	1.846
OH*	3.977	3.990	3.990	3.979	3.995
Cl	0.023	0.010	0.010	0.021	0.005
Total	19.621	19.693	19.684	19.708	19.680
XFe	0.449	0.439	0.451	0.440	0.448
XMn	0.008	0.008	0.008	0.009	0.008

Table 24

Garson Mine (5200 lvl) kpgmd12-26 / 1 . Biotite	Garson Mine (5200 lvl) 27 / 1 . Biotite	Garson Mine (5200 lvl kpgmd12-28 / 1 . Biotite	Garson Mine (5200 kpgmd12-29 / 1 . Biotite	Garson Mine (5200 lvl) kpgmd12-30 / 1 . Biotite
34.856	35.805	35.508	36.019	36.095
0.987	1.075	0.978	0.940	1.013
17.055	17.482	17.295	17.406	17.115
17.636	17.448	17.561	17.210	17.176
0.143	0.140	0.149	0.150	0.156
12.226	11.977	12.124	12.135	12.197
0.005	0.001	0.006	0.030	0.007
0.076	0.079	0.060	0.049	0.066
9.670	9.462	9.562	9.563	9.571
0.088	0.057	0.060	0.073	0.056
0.269	0.168	0.154	0.164	0.174
0.053	0.052	0.039	0.046	0.046
93.064	93.746	93.495	93.786	93.671
5.436	5.506	5.489	5.532	5.550
2.564	2.494	2.511	2.468	2.450
0.572	0.675	0.640	0.683	0.652
0.116	0.124	0.114	0.109	0.117
0.033	0.020	0.019	0.020	0.021
2.300	2.244	2.270	2.211	2.209
0.019	0.018	0.020	0.020	0.020
2.842	2.746	2.794	2.778	2.796
0.007	0.006	0.005	0.006	0.006
0.001	0.000	0.001	0.005	0.001
0.023	0.024	0.018	0.015	0.020
1.924	1.856	1.885	1.873	1.877
3.977	3.985	3.984	3.981	3.986
0.023	0.015	0.016	0.019	0.014
19.837	19.714	19.764	19.718	19.719
0.447	0.450	0.448	0.443	0.441
0.008	0.008	0.009	0.009	0.009

Table 25

Locality	Garson Mine (5200 lvl)	Garson Mine (5200 lvl)	Garson Mine (5200 lvl)	Garson Mine (5200 lvl)	Garson Mine (5200 lvl)
Sample and analysis	kpgmd13-15 / 1 .	kpgmd13-16 / 1 .	kpgmd13-17 / 1 .	kpgmd13-18 / 1 .	kpgmd13-19 / 1 .
Mineral	Biotite	Biotite	Biotite	Biotite	Biotite
SiO2	36.945	37.167	36.365	36.544	37.075
TiO2	1.051	1.031	1.009	1.028	1.016
Al2O3	17.128	17.278	17.418	17.314	16.934
FeO	16.774	16.694	16.875	16.601	16.499
MnO	0.142	0.151	0.150	0.141	0.138
MgO	13.062	13.007	12.687	12.789	13.142
CaO	0.016	0.011	0.000	0.010	0.031
Na2O	0.049	0.089	0.058	0.038	0.096
K2O	9.408	9.451	9.506	9.420	9.439
Cl	0.072	0.049	0.090	0.043	0.085
Cr2O3	0.179	0.207	0.243	0.262	0.245
NiO	0.061	0.044	0.051	0.071	0.051
Total	94.887	95.180	94.451	94.260	94.751
Si	5.578	5.588	5.531	5.555	5.602
Al iv	2.422	2.412	2.469	2.445	2.398
Al vi	0.627	0.650	0.654	0.657	0.618
Ti	0.119	0.117	0.115	0.117	0.115
Cr	0.021	0.025	0.029	0.031	0.029
Fe	2.118	2.099	2.147	2.110	2.085
Mn	0.018	0.019	0.019	0.018	0.018
Mg	2.940	2.915	2.876	2.898	2.960
Ni	0.007	0.005	0.006	0.009	0.006
Ca	0.003	0.002	0.000	0.002	0.005
Na	0.014	0.026	0.017	0.011	0.028
K	1.812	1.813	1.844	1.826	1.819
OH*	3.982	3.987	3.977	3.989	3.978
Cl	0.018	0.013	0.023	0.011	0.022
Total	19.680	19.671	19.708	19.680	19.684
XFe	0.419	0.419	0.427	0.421	0.413
XMn	0.009	0.009	0.009	0.009	0.008

Table 26

Garson Mine (5200 lvl) kpgmd13-20 / 1 . Biotite	Garson Mine (5200 lvl) kpgmd13-21 / 1 . Biotite	Garson Mine (5200 lvl) kpgmd13-22 / 1 . Biotite	Garson Mine (5200 lvl) kpgmd13-23 / 1 . Biotite	Garson Mine (5200 lvl) kpgmd13-24 / 1 . Biotite
37.060	36.608	36.582	36.287	36.141
1.118	1.336	1.335	1.572	1.503
17.342	16.886	16.999	17.022	16.867
16.832	17.111	17.441	17.164	17.102
0.168	0.162	0.171	0.160	0.159
12.691	12.753	12.650	12.512	12.832
0.023	0.017	0.006	0.001	0.010
0.079	0.232	0.081	0.093	0.079
9.355	9.274	9.432	9.561	9.535
0.088	0.131	0.100	0.075	0.044
0.238	0.185	0.162	0.107	0.147
0.042	0.054	0.069	0.051	0.066
95.035	94.748	95.027	94.604	94.483
5.585	5.556	5.544	5.523	5.509
2.415	2.444	2.456	2.477	2.491
0.665	0.576	0.581	0.578	0.540
0.127	0.153	0.152	0.180	0.172
0.028	0.022	0.019	0.013	0.018
2.121	2.172	2.211	2.185	2.180
0.021	0.021	0.022	0.021	0.021
2.851	2.885	2.858	2.839	2.916
0.005	0.007	0.008	0.006	0.008
0.004	0.003	0.001	0.000	0.002
0.023	0.068	0.024	0.028	0.023
1.798	1.795	1.823	1.856	1.854
3.977	3.966	3.974	3.981	3.989
0.023	0.034	0.026	0.019	0.011
19.645	19.702	19.699	19.705	19.733
0.427	0.429	0.436	0.435	0.428
0.010	0.010	0.010	0.009	0.009

Table 27

Locality	Garson Mine (5200 lvl)	Garson Mine (5200 lvl)	Garson Mine (5200 lvl)	Garson Mine (5200 lvl)	Garson Mine (5200 lvl)
Sample and analysis	kpgmd14-1 / 1 .	kpgmd14-2 / 1 .	kpgmd14-3 / 1 .	kpgmd14-4 / 1 .	kpgmd14-6 / 1 .
Mineral	Biotite	Biotite	Biotite	Biotite	Biotite
SiO2	35.204	35.015	35.116	35.369	35.425
TiO2	1.862	2.180	1.629	1.814	1.803
Al2O3	16.802	16.592	17.112	16.739	16.603
FeO	21.976	22.110	22.075	22.590	22.429
MnO	0.176	0.167	0.175	0.184	0.171
MgO	9.192	9.046	9.303	8.835	9.235
CaO	0.040	0.026	0.007	0.004	0.011
Na2O	0.104	0.183	0.264	0.067	0.149
K2O	9.200	9.116	9.460	9.293	9.073
Cl	0.150	0.264	0.196	0.448	0.230
Cr2O3	0.132	0.152	0.127	0.158	0.184
NiO	0.087	0.107	0.108	0.103	0.114
Total	94.924	94.958	95.574	95.604	95.426
Si	5.478	5.461	5.442	5.497	5.495
Al iv	2.522	2.539	2.558	2.503	2.505
Al vi	0.560	0.512	0.568	0.564	0.530
Ti	0.218	0.256	0.190	0.212	0.210
Cr	0.016	0.019	0.016	0.019	0.023
Fe	2.860	2.884	2.861	2.936	2.909
Mn	0.023	0.022	0.023	0.024	0.022
Mg	2.132	2.103	2.149	2.047	2.135
Ni	0.011	0.013	0.014	0.013	0.014
Ca	0.007	0.004	0.001	0.001	0.002
Na	0.031	0.055	0.079	0.020	0.045
K	1.826	1.814	1.870	1.842	1.795
OH*	3.960	3.930	3.948	3.882	3.940
Cl	0.040	0.070	0.052	0.118	0.060
Total	19.684	19.683	19.772	19.679	19.686
XFe	0.573	0.578	0.571	0.589	0.577
XMn	0.008	0.008	0.008	0.008	0.008

Table 28

Garson Mine (5200 lvl) kpgmd14-7 / 1 . Biotite	Garson Mine (5200 lvl) kpgmd14-8 / 1 . Biotite	Garson Mine (5200 lvl) kpgmd14-9 / 1 . Biotite
35.481	35.493	35.636
1.847	1.735	1.856
16.354	16.711	16.814
22.868	22.570	22.231
0.194	0.173	0.174
8.935	9.134	8.762
0.005	0.015	0.043
0.134	0.183	0.695
9.262	9.376	9.321
0.446	0.364	0.476
0.191	0.177	0.152
0.102	0.111	0.085
95.819	96.043	96.244
5.512	5.489	5.502
2.488	2.511	2.498
0.507	0.535	0.561
0.216	0.202	0.215
0.023	0.022	0.019
2.971	2.919	2.870
0.026	0.023	0.023
2.069	2.106	2.016
0.013	0.014	0.011
0.001	0.003	0.007
0.040	0.055	0.208
1.835	1.850	1.835
3.883	3.905	3.876
0.117	0.095	0.124
19.701	19.727	19.766
0.589	0.581	0.587
0.009	0.008	0.008

Table 29

Locality	Garson Mine (5200 lvl)	Garson Mine (5200 lvl)	Garson Mine (5200 lvl)	Garson Mine (5200 lvl)	Garson Mine (5200 lvl)
Sample and analysis	kpgmd16-37 / 1 .	kpgmd16-38 / 1 .	kpgmd16-39 / 1 .	kpgmd16-40 / 1 .	kpgmd16-41 / 1 .
Mineral	Biotite	Biotite	Biotite	Biotite	Biotite
SiO2	34.541	34.558	34.476	34.431	34.326
TiO2	1.835	1.922	1.728	1.811	1.860
Al2O3	16.838	16.864	16.878	16.806	16.794
FeO	20.933	20.688	21.215	20.967	21.457
MnO	0.188	0.192	0.197	0.186	0.194
MgO	9.901	9.889	10.067	10.004	9.863
CaO	0.000	0.000	0.004	0.017	0.014
Na2O	0.096	0.102	0.066	0.157	0.164
K2O	9.395	9.297	9.428	9.442	9.404
Cl	0.103	0.108	0.088	0.099	0.088
Cr2O3	0.055	0.034	0.048	0.047	0.090
NiO	0.100	0.107	0.129	0.114	0.115
Total	93.985	93.762	94.322	94.082	94.368
Si	5.417	5.423	5.396	5.401	5.382
Al iv	2.583	2.577	2.604	2.599	2.618
Al vi	0.530	0.543	0.511	0.509	0.485
Ti	0.216	0.227	0.203	0.214	0.219
Cr	0.007	0.004	0.006	0.006	0.011
Fe	2.746	2.715	2.777	2.751	2.813
Mn	0.025	0.026	0.026	0.025	0.026
Mg	2.315	2.314	2.349	2.339	2.305
Ni	0.013	0.014	0.016	0.014	0.014
Ca	0.000	0.000	0.001	0.003	0.002
Na	0.029	0.031	0.020	0.048	0.050
K	1.880	1.861	1.882	1.889	1.881
OH*	3.973	3.971	3.977	3.974	3.977
Cl	0.027	0.029	0.023	0.026	0.023
Total	19.761	19.734	19.791	19.797	19.807
XFe	0.543	0.540	0.542	0.540	0.550
XMn	0.009	0.009	0.009	0.009	0.009

Table 30

Garson Mine (5200 lvl) kpgmd16-42 / 1 . Biotite	Garson Mine (5200 lvl) kpgmd16-43 / 1 . Biotite	Garson Mine (5200 lvl) kpgmd16-44 / 1 . Biotite	Garson Mine (5200 lvl) kpgmd16-45 / 1 . Biotite	Garson Mine (5200 lvl) kpgmd16-46 / 1 . Biotite	Garson Mine (5200 lvl) kpgmd16-47 / 1 . Biotite
34.861	34.640	34.113	34.111	34.369	34.539
1.253	1.193	1.421	1.327	1.256	1.990
17.424	17.681	17.251	17.274	17.067	17.027
20.765	21.290	20.994	21.050	21.265	20.883
0.186	0.188	0.181	0.189	0.180	0.191
10.280	9.992	10.043	9.992	10.070	9.757
0.002	0.007	0.000	0.000	0.000	0.000
0.040	0.046	0.077	0.079	0.063	0.112
9.645	9.339	9.564	9.465	9.531	9.342
0.080	0.111	0.079	0.136	0.162	0.123
0.391	0.420	0.336	0.353	0.401	0.115
0.094	0.087	0.099	0.095	0.107	0.108
95.020	94.995	94.157	94.070	94.472	94.187
5.401	5.375	5.353	5.359	5.384	5.403
2.599	2.625	2.647	2.641	2.616	2.597
0.583	0.609	0.544	0.558	0.534	0.542
0.146	0.139	0.168	0.157	0.148	0.234
0.048	0.052	0.042	0.044	0.050	0.014
2.691	2.763	2.755	2.766	2.786	2.732
0.024	0.025	0.024	0.025	0.024	0.025
2.374	2.311	2.349	2.340	2.351	2.275
0.012	0.011	0.012	0.012	0.014	0.014
0.000	0.001	0.000	0.000	0.000	0.000
0.012	0.014	0.023	0.024	0.019	0.034
1.906	1.848	1.914	1.897	1.904	1.864
3.979	3.971	3.979	3.964	3.957	3.967
0.021	0.029	0.021	0.036	0.043	0.033
19.797	19.774	19.832	19.823	19.830	19.735
0.531	0.544	0.540	0.542	0.542	0.546
0.009	0.009	0.009	0.009	0.008	0.009

Table 31

Garson Mine (5200 lvl) kpgmd16-48 / 1 . Biotite	Garson Mine (5200 lvl) kpgmd16-49 / 1 . Biotite	Garson Mine (5200 lvl) kpgmd16-50 / 1 . Biotite	Garson Mine (5200 lvl) kpgmd16-51 / 1 . Biotite
34.217	34.110	34.324	34.710
1.961	1.915	1.758	1.511
17.089	17.022	17.046	17.270
20.778	21.314	21.100	20.719
0.197	0.196	0.196	0.187
9.773	9.769	9.994	10.118
0.000	0.000	0.000	0.000
0.077	0.087	0.060	0.126
9.339	9.216	9.486	9.529
0.097	0.134	0.107	0.116
0.030	0.043	0.234	0.288
0.112	0.114	0.088	0.095
93.670	93.919	94.392	94.668
5.382	5.366	5.371	5.400
2.618	2.634	2.629	2.600
0.550	0.522	0.515	0.567
0.232	0.227	0.207	0.177
0.004	0.005	0.029	0.035
2.733	2.804	2.761	2.696
0.026	0.026	0.026	0.025
2.292	2.291	2.331	2.347
0.014	0.014	0.011	0.012
0.000	0.000	0.000	0.000
0.023	0.027	0.018	0.038
1.874	1.849	1.893	1.891
3.974	3.964	3.972	3.970
0.026	0.036	0.028	0.030
19.748	19.765	19.792	19.787
0.544	0.550	0.542	0.535
0.009	0.009	0.009	0.009

Table 32

Locality	Blezard	Blezard	Blezard	Blezard	Blezard	Blezard
Sample and analysis	clf30_2_st5_bt1	clf30_2_st5_bt2	clf30_2_st5_bt3	clf30_2_st5_bt4	clf30_2_st5_bt5	clf30_2_st5_bt6
Mineral	Biotite	Biotite	Biotite	Biotite	Biotite	Biotite
SiO2	34.733	36.243	36.325	34.935	34.939	35.962
TiO2	1.292	1.120	1.484	1.349	1.557	1.763
Al2O3	16.530	15.671	16.205	16.121	15.385	15.594
FeO	22.132	22.235	22.663	22.240	22.755	22.998
MnO	0.190	0.184	0.200	0.166	0.268	0.195
MgO	9.108	9.268	9.637	9.723	9.239	9.156
CaO	0.051	1.489	0.003	0.028	0.062	0.123
Na2O	0.077	0.174	0.039	0.078	0.151	0.050
K2O	8.623	7.944	9.511	8.817	8.688	9.168
F	0.215	0.554	0.439	0.387	0.458	0.136
Cl	0.226	0.194	0.147	0.140	0.283	0.288
Cr2O3	0.028	0.014	0.014	0.011	0.013	0.025
NiO	-0.007	-0.002	0.001	0.024	0.000	-0.021
Total	93.197	95.089	96.669	94.018	93.798	95.438
Si	5.516	5.643	5.583	5.514	5.561	5.602
Al iv	2.484	2.357	2.417	2.486	2.439	2.398
Al vi	0.610	0.519	0.518	0.512	0.447	0.465
Ti	0.154	0.131	0.172	0.160	0.186	0.207
Cr	0.004	0.002	0.002	0.001	0.002	0.003
Fe	2.939	2.895	2.913	2.935	3.029	2.996
Mn	0.026	0.024	0.026	0.022	0.036	0.026
Mg	2.156	2.151	2.208	2.287	2.192	2.126
Ni	-0.001	0.000	0.000	0.003	0.000	-0.003
Ca	0.009	0.248	0.000	0.005	0.011	0.021
Na	0.024	0.053	0.012	0.024	0.047	0.015
K	1.747	1.578	1.864	1.775	1.764	1.822
OH*	3.831	3.676	3.748	3.769	3.693	3.857
F	0.108	0.273	0.213	0.193	0.231	0.067
Cl	0.061	0.051	0.038	0.037	0.076	0.076
Total	19.666	19.602	19.715	19.726	19.714	19.677
XFe	0.577	0.574	0.569	0.562	0.580	0.585
XMn	0.009	0.008	0.009	0.008	0.012	0.009

Table 33

Locality	Creighton	Creighton	Creighton	Creighton	Creighton
Sample and analysis	clf1503_st8_bt1	clf1503_st8_bt2	clf1503_st8_bt3	clf1503_st8_bt4	clf1503_st8_bt5
Mineral	biotite	biotite	biotite	biotite	biotite
SiO2	36.051	36.472	37.054	36.181	36.211
TiO2	1.910	1.952	2.037	1.843	1.901
Al2O3	15.906	16.118	16.124	16.109	15.605
FeO	20.540	20.526	20.619	21.164	20.852
MnO	0.048	0.092	0.102	0.108	0.118
MgO	10.644	10.797	11.008	10.837	10.554
CaO	0.033	0.020	0.021	0.028	0.033
Na2O	0.074	0.029	0.082	0.053	0.017
K2O	9.108	9.374	9.153	8.956	8.929
F	0.090	0.371	0.052	0.035	0.368
Cl	0.167	0.160	0.212	0.135	0.227
Cr2O3	0.022	0.018	0.028	0.019	0.029
NiO	-0.016	0.032	0.006	0.003	-0.009
Total	94.576	95.960	96.498	95.471	94.834
Si	5.581	5.580	5.607	5.552	5.613
Al iv	2.419	2.420	2.393	2.448	2.387
Al vi	0.483	0.487	0.482	0.465	0.465
Ti	0.222	0.225	0.232	0.213	0.222
Cr	0.003	0.002	0.003	0.002	0.004
Fe	2.659	2.626	2.609	2.716	2.703
Mn	0.006	0.012	0.013	0.014	0.015
Mg	2.456	2.463	2.483	2.479	2.439
Ni	-0.002	0.004	0.001	0.000	-0.001
Ca	0.005	0.003	0.003	0.005	0.005
Na	0.022	0.009	0.024	0.016	0.005
K	1.798	1.829	1.767	1.753	1.766
OH*	3.912	3.779	3.921	3.948	3.760
F	0.044	0.180	0.025	0.017	0.180
Cl	0.044	0.041	0.054	0.035	0.060
Total	19.654	19.660	19.617	19.662	19.623
XFe	0.520	0.516	0.512	0.523	0.526
XMn	0.002	0.005	0.005	0.005	0.006

Table 34

Creighton clf1503_st8_bt6 biotite	Creighton clf1503_st4_bt7 biotite	Creighton clf1503_st4_bt8 biotite	Creighton clf1503_st4_bt9 biotite
36.309	36.649	36.310	36.242
1.431	2.088	2.084	2.155
16.054	16.175	15.872	15.917
20.431	21.272	20.947	20.916
0.103	0.129	0.113	0.048
11.477	10.621	10.261	10.073
0.044	0.009	0.036	0.060
0.063	0.058	0.079	0.034
8.662	9.493	9.094	9.124
0.364	-0.054	0.119	0.306
0.116	0.119	0.184	0.154
0.025	0.038	0.040	0.037
0.003	0.017	-0.004	0.013
95.081	96.615	95.135	95.078
5.582	5.563	5.598	5.600
2.418	2.437	2.402	2.400
0.491	0.456	0.483	0.498
0.165	0.238	0.242	0.250
0.003	0.005	0.005	0.005
2.627	2.700	2.701	2.703
0.013	0.017	0.015	0.006
2.630	2.403	2.358	2.320
0.000	0.002	0.000	0.002
0.007	0.001	0.006	0.010
0.019	0.017	0.024	0.010
1.699	1.838	1.788	1.798
3.793	3.995	3.894	3.810
0.177	-0.026	0.058	0.150
0.030	0.031	0.048	0.040
19.655	19.677	19.621	19.602
0.500	0.529	0.534	0.538
0.005	0.006	0.005	0.002

Table 35

Locality	Vermillion Lake	Vermillion Lake	Vermillion Lake	Vermillion Lake	Vermillion Lake
Sample and analysis	8clf1503_st1.1_bt1	8clf1503_st1.1_bt2	8clf1503_st1.1_bt3	8clf1503_st1.1_bt4	8clf1503_st1.1_bt5
Mineral	Biotite	Biotite	Biotite	Biotite	Biotite
SiO2	35.393	34.686	34.641	32.306	35.416
TiO2	1.903	1.779	1.793	1.911	1.870
Al2O3	15.649	15.378	15.276	13.874	15.350
FeO	25.918	25.349	25.840	25.754	26.112
MnO	0.225	0.273	0.241	0.237	0.249
MgO	7.200	7.509	7.381	6.882	7.837
CaO	0.036	0.011	0.045	0.058	0.023
Na2O	0.026	0.081	0.063	0.070	0.022
K2O	9.167	8.741	8.737	8.746	8.905
F	0.635	0.281	0.465	0.931	0.240
Cl	0.178	0.208	0.165	0.181	0.189
Cr2O3	0.003	0.004	-0.001	-0.010	0.000
NiO	0.009	0.000	-0.008	0.030	-0.001
Total	96.342	94.299	94.638	90.971	96.212
Si	5.568	5.548	5.543	5.478	5.556
Al iv	2.432	2.452	2.457	2.522	2.444
Al vi	0.470	0.448	0.425	0.251	0.394
Ti	0.225	0.214	0.216	0.244	0.221
Cr	0.000	0.001	0.000	-0.001	0.000
Fe	3.410	3.391	3.458	3.652	3.426
Mn	0.030	0.037	0.033	0.034	0.033
Mg	1.689	1.791	1.761	1.740	1.833
Ni	0.001	0.000	-0.001	0.004	0.000
Ca	0.006	0.002	0.008	0.011	0.004
Na	0.008	0.025	0.020	0.023	0.007
K	1.840	1.783	1.783	1.892	1.782
OH*	3.637	3.801	3.720	3.449	3.831
F	0.316	0.142	0.235	0.499	0.119
Cl	0.047	0.056	0.045	0.052	0.050
Total	19.679	19.692	19.702	19.849	19.699
XFe	0.669	0.654	0.663	0.677	0.651
XMn	0.009	0.011	0.009	0.009	0.010

Table 36

Vermillion Lake 8clf1503_st1.1_bt6 Biotite	Vermillion Lake 8clf1503_st1.1_bt7 Biotite	Vermillion Lake 8clf1503_st1.1_bt8 Biotite
33.818	32.794	35.297
1.866	1.775	1.807
14.926	14.160	15.627
25.622	25.829	25.608
0.216	0.239	0.229
7.055	6.669	7.431
0.027	0.005	0.038
0.059	0.022	0.095
8.988	9.249	8.803
0.271	0.595	0.993
0.161	0.174	0.168
-0.011	0.009	0.000
-0.020	0.002	-0.009
92.979	91.521	96.086
5.521	5.508	5.572
2.479	2.492	2.428
0.394	0.312	0.479
0.229	0.224	0.215
-0.001	0.001	0.000
3.499	3.628	3.381
0.030	0.034	0.031
1.717	1.670	1.749
-0.003	0.000	-0.001
0.005	0.001	0.006
0.019	0.007	0.029
1.872	1.982	1.772
3.816	3.634	3.459
0.140	0.316	0.496
0.045	0.050	0.045
19.759	19.859	19.661
0.671	0.685	0.659
0.008	0.009	0.009

Table 37

Locality	Kirkwood	Kirkwood	Kirkwood	Kirkwood	Kirkwood
Sample and analysis	clf3013_bt8_st2	clf3013_Bt9_st2	clf3013_Bt10_st2	clf3013_Bt11_st2	clf3013_Bt1_st1
Mineral	Biotite	Biotite	Biotite	Biotite	Biotite
SiO2	33.948	32.946	35.658	32.564	33.964
TiO2	1.617	1.61	1.572	1.355	1.512
Al2O3	15.419	15.491	15.941	14.985	15.494
FeO	29.918	31.213	30.784	32.015	29.599
MnO	0.372	0.422	0.431	0.451	0.377
MgO	4.017	4.192	4.246	4.17	4.16
CaO	0.003	-0.009	0.025	0.005	0.023
Na2O	0.028	-0.002	0.064	0.036	0.083
K2O	8.751	7.702	8.88	7.911	8.817
F	0.427	0.624	0.557	0.464	0.694
Cl	0.199	0.192	0.198	0.195	0.195
Cr2O3	0.001	0	-0.006	0.011	0.003
NiO	0.003	-0.006	0.015	0.008	0.02
Total	94.703	94.376	98.366	94.17	94.94
Si	5.552	5.437	5.601	5.422	5.551
Al iv	2.448	2.563	2.399	2.578	2.449
Al vi	0.524	0.450	0.552	0.362	0.535
Ti	0.199	0.200	0.186	0.170	0.186
Cr	0.000	0.000	-0.001	0.001	0.000
Fe	4.092	4.308	4.044	4.458	4.045
Mn	0.052	0.059	0.057	0.064	0.052
Mg	0.979	1.031	0.994	1.035	1.013
Ni	0.000	-0.001	0.002	0.001	0.003
Ca	0.001	-0.002	0.004	0.001	0.004
Na	0.009	-0.001	0.019	0.012	0.026
K	1.825	1.621	1.779	1.680	1.838
OH*	3.724	3.621	3.671	3.701	3.587
F	0.221	0.326	0.277	0.244	0.359
Cl	0.055	0.054	0.053	0.055	0.054
Total	19.681	19.667	19.637	19.783	19.703
XFe	0.807	0.807	0.803	0.812	0.800
XMn	0.012	0.014	0.014	0.014	0.013

Table 38

Kirkwood clf3013_Bt2_st1 Biotite	Kirkwood clf3013_Bt3_st1 Biotite	Kirkwood clf3013_Bt4_st1 Biotite	Kirkwood clf3013_Bt5_st1 Biotite	Kirkwood clf3013_Bt6_st1 Biotite
33.537	35.026	33.701	33.429	29.691
1.537	1.471	1.357	1.437	0.98
15.052	15.921	15.351	15.229	16.834
29.978	29.946	29.853	29.289	34.383
0.324	0.369	0.36	0.35	0.531
4.076	4.214	4.156	3.959	4.635
0.002	0.014	0.01	0.081	0.024
0.057	0.081	0.05	0.165	0.222
8.652	8.937	8.319	8.58	4.874
0.164	0.448	0.389	0.55	0.307
0.181	0.212	0.21	0.196	0.169
0.01	-0.001	0.003	0.005	0.005
0.009	0.013	0.002	-0.037	-0.027
93.578	96.649	93.759	93.234	92.629
5.547	5.590	5.557	5.557	5.022
2.453	2.410	2.443	2.443	2.978
0.481	0.585	0.541	0.542	0.378
0.191	0.177	0.168	0.180	0.125
0.001	0.000	0.000	0.001	0.001
4.147	3.997	4.117	4.072	4.864
0.045	0.050	0.050	0.049	0.076
1.005	1.002	1.022	0.981	1.169
0.001	0.002	0.000	-0.005	-0.004
0.000	0.002	0.002	0.014	0.004
0.018	0.025	0.016	0.053	0.073
1.825	1.819	1.750	1.819	1.052
3.863	3.717	3.738	3.656	3.787
0.086	0.226	0.203	0.289	0.164
0.051	0.057	0.059	0.055	0.048
19.716	19.659	19.666	19.707	19.737
0.805	0.799	0.801	0.806	0.806
0.011	0.012	0.012	0.012	0.015

Table 39

Locality	Sheppard	Sheppard	Sheppard	Sheppard	Sheppard
Sample and analysis	clf30_9_st1_bt1	clf30_9_st1_bt2	clf30_9_st1_bt3	clf30_9_st1_bt4	clf30_9_st1_bt5
Mineral	Biotite	Biotite	Biotite	Biotite	Biotite
SiO2	34.612	35.512	35.037	35.075	35.434
TiO2	1.442	1.455	1.374	1.435	1.384
Al2O3	16.018	16.043	16.328	15.949	16.151
FeO	24.63	23.891	23.641	23.87	24.156
MnO	0.316	0.303	0.342	0.332	0.327
MgO	8.184	7.897	7.957	7.775	7.941
CaO	0.026	0.008	-0.007	0.011	0.035
Na2O	0.04	0.016	0.062	0.086	0.029
K2O	8.581	9.272	9.471	9.139	9.034
F	0.437	0.475	0.139	-0.054	0.038
Cl	0.253	0.212	0.221	0.193	0.219
Cr2O3	0.01	0.015	-0.001	0.012	-0.002
NiO	0.011	0.007	0.005	-0.032	-0.011
Total	94.56	95.107	94.567	93.79	94.734
Si	5.504	5.599	5.544	5.581	5.583
Al iv	2.496	2.401	2.456	2.419	2.417
Al vi	0.507	0.580	0.590	0.573	0.582
Ti	0.172	0.173	0.164	0.172	0.164
Cr	0.001	0.002	0.000	0.002	0.000
Fe	3.276	3.150	3.129	3.177	3.183
Mn	0.043	0.040	0.046	0.045	0.044
Mg	1.940	1.856	1.877	1.844	1.865
Ni	0.001	0.001	0.001	-0.004	-0.001
Ca	0.004	0.001	-0.001	0.002	0.006
Na	0.012	0.005	0.019	0.027	0.009
K	1.741	1.865	1.912	1.855	1.815
OH*	3.712	3.707	3.871	3.975	3.923
F	0.220	0.237	0.070	-0.027	0.019
Cl	0.068	0.057	0.059	0.052	0.058
Total	19.698	19.672	19.735	19.691	19.666
XFe	0.628	0.629	0.625	0.633	0.631
XMn	0.013	0.013	0.014	0.014	0.014

Table 40

Sheppard clf30_9_st1_bt6 Biotite	Sheppard clf30_9_st1_bt7 Biotite	Sheppard clf30_9_st1_bt8 Biotite
34.878	35.48	41.912
1.497	1.503	1.357
16.006	16.093	14.265
24.569	24.042	22.559
0.303	0.306	0.294
7.93	7.89	7.502
0.025	-0.004	0.024
0.025	0.049	0.063
8.774	9.201	8.724
0.183	0.292	0.413
0.239	0.212	0.293
-0.001	0.017	0.009
0.005	0.011	0.007
94.431	95.091	97.423
5.537	5.586	6.270
2.463	2.414	1.730
0.532	0.572	0.786
0.179	0.178	0.153
0.000	0.002	0.001
3.262	3.165	2.823
0.041	0.041	0.037
1.877	1.852	1.673
0.001	0.001	0.001
0.004	-0.001	0.004
0.008	0.015	0.018
1.777	1.848	1.665
3.844	3.798	3.730
0.092	0.145	0.195
0.064	0.057	0.074
19.679	19.673	19.160
0.635	0.631	0.628
0.012	0.013	0.013

Table 41

Locality	Whitson Lake	Whitson Lake	Whitson Lake	Whitson Lake	Whitson Lake
Sample and analysis	wclf1508_st2.2_bt1	wclf1508_st2.2_bt2	wclf1508_st2.2_bt3	wclf1508_st2.2_bt4	wclf1508_st2.2_bt5
Mineral	Biotite	Biotite	Biotite	Biotite	Biotite
SiO2	46.552	47.976	45.829	47.06	46.507
TiO2	0.23	0.214	0.463	0.185	0.462
Al2O3	30.156	29.985	29.044	29.445	29.71
FeO	4.859	5.961	4.747	4.852	4.567
MnO	0.039	0.01	0.028	0.016	0.028
MgO	1.287	1.875	1.375	1.638	1.398
CaO	-0.006	0.03	0.03	0.011	0.021
Na2O	0.199	0.134	0.126	0.115	0.165
K2O	10.621	10.352	10.458	10.707	10.508
F	0.04	0.323	0.136	0.133	-0.173
Cl	0.003	0.017	0.003	0.001	0.01
Cr2O3	0.002	-0.004	-0.003	0.003	-0.001
NiO	-0.004	0.003	-0.011	0.003	-0.004
Total	93.978	96.876	92.226	94.169	93.198
Si	6.411	6.442	6.440	6.474	6.433
Al iv	1.589	1.558	1.560	1.526	1.567
Al vi	3.307	3.188	3.251	3.248	3.277
Ti	0.024	0.022	0.049	0.019	0.048
Cr	0.000	0.000	0.000	0.000	0.000
Fe	0.560	0.669	0.558	0.558	0.528
Mn	0.005	0.001	0.003	0.002	0.003
Mg	0.264	0.375	0.288	0.336	0.288
Ni	0.000	0.000	-0.001	0.000	0.000
Ca	-0.001	0.004	0.005	0.002	0.003
Na	0.053	0.035	0.034	0.031	0.044
K	1.866	1.773	1.874	1.879	1.854
OH*	3.982	3.859	3.939	3.942	4.073
F	0.017	0.137	0.060	0.058	-0.076
Cl	0.001	0.004	0.001	0.000	0.002
Total	18.077	18.068	18.060	18.075	18.046
XFe	0.679	0.641	0.660	0.624	0.647
XMn	0.008	0.002	0.006	0.003	0.006

Table 42

Locality	Creighton Mine (7840 lvl)	Creighton Mine (7840 lvl)	Creighton Mine (7840 lvl)	Creighton Mine (7840 lvl)	Creighton Mine (7840 lvl)
Sample and analysis	kpcm02a_bt1	kpcm02a_bt2	kpcm02a_bt3	kpcm02a_bt4	kpcm02a_bt5
Mineral	Biotite	Biotite	Biotite	Biotite	Biotite
SiO2	35.886	36.097	36.288	36.712	36.369
TiO2	1.683	1.666	1.620	1.562	1.639
Al2O3	15.789	15.782	15.825	15.927	15.767
FeO	23.437	23.265	23.372	23.422	23.304
MnO	0.348	0.305	0.325	0.367	0.345
MgO	8.684	8.642	8.601	8.740	8.830
CaO	0.006	0.013	0.028	0.005	0.072
Na2O	0.021	0.070	0.066	0.091	0.071
K2O	9.313	9.122	9.202	9.448	9.426
F	0.430	0.424	0.502	0.629	0.559
Cl	0.235	0.199	0.242	0.211	0.208
Cr2O3	0.011	0.015	0.024	0.018	0.033
NiO	0.014	-0.010	-0.007	0.018	-0.006
Total	95.856	95.591	96.089	97.151	96.617
Si	5.597	5.628	5.637	5.647	5.626
Al iv	2.403	2.372	2.363	2.353	2.374
Al vi	0.500	0.528	0.535	0.535	0.501
Ti	0.197	0.195	0.189	0.181	0.191
Cr	0.001	0.002	0.003	0.002	0.004
Fe	3.057	3.033	3.036	3.013	3.015
Mn	0.046	0.040	0.043	0.048	0.045
Mg	2.019	2.008	1.992	2.004	2.036
Ni	0.002	-0.001	-0.001	0.002	-0.001
Ca	0.001	0.002	0.005	0.001	0.012
Na	0.006	0.021	0.020	0.027	0.021
K	1.853	1.814	1.823	1.854	1.860
OH*	3.726	3.738	3.690	3.639	3.672
F	0.212	0.209	0.247	0.306	0.273
Cl	0.062	0.053	0.064	0.055	0.055
Total	19.683	19.643	19.645	19.667	19.684
XFe	0.602	0.602	0.604	0.601	0.597
XMn	0.015	0.013	0.014	0.016	0.015

Table 43

Creighton Mine (7840 lvl) kpcm02a_bt6 Biotite	Creighton Mine (7840 lvl) kpcm02a_bt7 Biotite	Creighton Mine (7840 lvl) kpcm02a_bt8 Biotite	Creighton Mine (7840 lvl) kpcm02a_bt9 Biotite	Creighton Mine (7840 lvl) kpcm02a_bt10 Biotite	Creighton Mine (7840 lvl) kpcm02a_bt11 Biotite
36.436	36.586	36.198	36.725	36.242	35.990
1.555	1.679	1.565	1.652	1.588	1.546
16.053	15.956	15.875	15.779	15.898	15.905
23.209	23.556	23.523	23.494	23.564	23.192
0.353	0.335	0.370	0.297	0.331	0.371
8.804	8.670	8.603	8.772	8.753	8.705
0.016	0.008	0.025	0.036	0.015	0.018
0.107	0.096	0.046	0.055	0.019	0.083
9.281	9.205	9.079	9.308	9.389	9.332
0.482	0.703	0.476	0.416	0.501	0.494
0.225	0.237	0.231	0.208	0.238	0.220
0.016	0.024	0.013	0.025	0.017	0.023
-0.002	0.021	0.008	0.032	0.010	0.026
96.536	97.077	96.013	96.798	96.565	95.906
5.626	5.635	5.627	5.654	5.612	5.607
2.374	2.365	2.373	2.346	2.388	2.393
0.547	0.532	0.536	0.518	0.514	0.528
0.181	0.194	0.183	0.191	0.185	0.181
0.002	0.003	0.002	0.003	0.002	0.003
2.997	3.034	3.058	3.025	3.052	3.022
0.046	0.044	0.049	0.039	0.043	0.049
2.026	1.991	1.994	2.013	2.021	2.022
0.000	0.003	0.001	0.004	0.001	0.003
0.003	0.001	0.004	0.006	0.002	0.003
0.032	0.029	0.014	0.016	0.006	0.025
1.828	1.808	1.800	1.828	1.855	1.854
3.706	3.596	3.705	3.743	3.692	3.698
0.235	0.342	0.234	0.203	0.245	0.243
0.059	0.062	0.061	0.054	0.062	0.058
19.662	19.639	19.641	19.643	19.681	19.690
0.597	0.604	0.605	0.600	0.602	0.599
0.015	0.014	0.016	0.013	0.014	0.016

Table 44

Creighton Mine (7840 lvl) kpcm02a_bt12 Biotite	Creighton Mine (7840 lvl) kpcm02a_bt13 Biotite	Creighton Mine (7840 lvl) kpcm02a_bt14 Biotite
36.458	36.205	36.138
1.602	1.590	1.525
15.692	16.000	15.756
23.169	23.557	23.127
0.325	0.375	0.342
8.665	8.843	8.607
0.010	0.026	0.071
0.068	0.055	0.039
9.293	9.381	9.230
0.554	0.277	0.649
0.196	0.239	0.227
0.012	0.025	0.015
0.029	-0.006	0.003
96.073	96.565	95.730
5.661	5.594	5.642
2.339	2.406	2.358
0.533	0.508	0.542
0.187	0.185	0.179
0.001	0.003	0.002
3.009	3.044	3.020
0.043	0.049	0.045
2.006	2.037	2.003
0.004	-0.001	0.000
0.002	0.004	0.012
0.020	0.016	0.012
1.841	1.849	1.838
3.676	3.802	3.619
0.272	0.135	0.320
0.052	0.063	0.060
19.645	19.695	19.653
0.600	0.599	0.601
0.014	0.016	0.015

Table 45

Locality	Creighton Mine (7840 lvl)	Creighton Mine (7840 lvl)	Creighton Mine (7840 lvl)	Creighton Mine (7840 lvl)	Creighton Mine (7840 lvl)
Sample and analysis	kpcm09-31 / 1 .	kpcm09-32 / 1 .	kpcm09-33 / 1 .	kpcm09-34 / 1 .	kpcm09-35 / 1 .
Mineral	Biotite	Biotite	Biotite	Biotite	Biotite
SiO2	36.125	36.023	35.771	36.023	35.952
TiO2	1.491	1.380	1.315	1.376	1.358
Al2O3	16.271	16.267	16.211	16.404	16.417
FeO	22.318	21.999	22.268	22.122	22.135
MnO	0.251	0.241	0.246	0.239	0.251
MgO	9.995	10.174	10.138	10.275	9.972
CaO	0.000	0.000	0.000	0.000	0.018
Na2O	0.079	0.082	0.063	0.072	0.115
K2O	9.227	9.251	9.221	9.184	9.075
Cl	0.223	0.239	0.251	0.229	0.247
Cr2O3	0.184	0.134	0.096	0.088	0.144
NiO	0.047	0.044	0.049	0.039	0.056
Total	96.209	95.834	95.630	96.049	95.738
Si	5.548	5.549	5.533	5.534	5.543
Al iv	2.452	2.451	2.467	2.466	2.457
Al vi	0.493	0.502	0.489	0.505	0.526
Ti	0.172	0.160	0.153	0.159	0.157
Cr	0.022	0.016	0.012	0.011	0.018
Fe	2.866	2.834	2.881	2.842	2.854
Mn	0.033	0.031	0.032	0.031	0.033
Mg	2.288	2.336	2.338	2.353	2.292
Ni	0.006	0.005	0.006	0.005	0.007
Ca	0.000	0.000	0.000	0.000	0.003
Na	0.024	0.024	0.019	0.021	0.034
K	1.807	1.817	1.819	1.800	1.785
OH*	3.942	3.938	3.934	3.940	3.936
Cl	0.058	0.062	0.066	0.060	0.064
Total	19.712	19.727	19.749	19.727	19.709
XFe	0.556	0.548	0.552	0.547	0.555
XMn	0.011	0.011	0.011	0.011	0.011

Table 46

Creighton Mine (7840 lvl) kpcm09-41 / 1 . Biotite	Creighton Mine (7840 lvl) kpcm09-42 / 1 . Biotite	Creighton Mine (7840 lvl) kpcm09-43 / 1 . Biotite	Creighton Mine (7840 lvl) kpcm09-44 / 1 . Biotite	Creighton Mine (7840 lvl) kpcm09-45 / 1 . Biotite	Creighton Mine (7840 lvl) kpcm09-46 / 1 . Biotite	Creighton Mine (7840 lvl) kpcm09-47 / 1 . Biotite	Creighton Mine (7840 lvl) kpcm09-48 / 1 . Biotite
36.059	35.639	35.843	35.594	35.883	35.832	36.023	36.038
1.476	1.402	1.407	1.367	1.413	1.326	1.338	1.317
16.474	16.478	16.419	16.623	16.333	16.542	16.481	16.510
21.739	22.079	22.128	21.985	21.923	21.775	21.851	21.797
0.236	0.228	0.229	0.226	0.225	0.232	0.236	0.219
10.081	9.936	10.105	10.019	10.159	10.021	10.034	10.028
0.005	0.005	0.000	0.000	0.000	0.017	0.013	0.010
0.088	0.105	0.081	0.098	0.073	0.081	0.061	0.004
9.313	9.078	9.249	9.250	9.189	9.243	9.303	9.212
0.189	0.230	0.242	0.235	0.223	0.239	0.215	0.212
0.029	0.045	0.056	0.041	0.047	0.028	0.036	0.033
0.030	0.043	0.036	0.040	0.057	0.043	0.039	0.035
95.718	95.268	95.797	95.479	95.526	95.381	95.630	95.413
5.549	5.522	5.527	5.506	5.541	5.539	5.553	5.561
2.451	2.478	2.473	2.494	2.459	2.461	2.447	2.439
0.537	0.532	0.511	0.537	0.514	0.554	0.548	0.564
0.171	0.163	0.163	0.159	0.164	0.154	0.155	0.153
0.004	0.006	0.007	0.005	0.006	0.003	0.004	0.004
2.798	2.861	2.854	2.844	2.831	2.815	2.817	2.813
0.031	0.030	0.030	0.030	0.029	0.030	0.031	0.029
2.313	2.295	2.323	2.310	2.339	2.309	2.306	2.307
0.004	0.005	0.004	0.005	0.007	0.005	0.005	0.004
0.001	0.001	0.000	0.000	0.000	0.003	0.002	0.002
0.026	0.031	0.024	0.029	0.022	0.024	0.018	0.001
1.828	1.794	1.819	1.825	1.810	1.823	1.829	1.813
3.951	3.940	3.937	3.938	3.942	3.937	3.944	3.945
0.049	0.060	0.063	0.062	0.058	0.063	0.056	0.055
19.711	19.719	19.736	19.744	19.722	19.721	19.716	19.690
0.547	0.555	0.551	0.552	0.548	0.549	0.550	0.549
0.011	0.010	0.010	0.010	0.010	0.011	0.011	0.010

Table 47

Locality	Creighton Mine (7840 lvl)	Creighton Mine (7840 lvl)	Creighton Mine (7840 lvl)	Creighton Mine (7840 lvl)	Creighton Mine (7840 lvl)	Creighton Mine (7840 lvl)	Creighton Mine (7840 lvl)
Sample and analysis	Pl4-52 / 1 .	Pl4-53 / 1 .	Pl4-54 / 1 .	Pl4-55 / 1 .	Pl4-56 / 1 .	Pl4-57 / 1 .	Pl4-58 / 1 .
Mineral	Biotite	Biotite	Biotite	Biotite	Biotite	Biotite	Biotite
SiO2	34.781	34.749	35.226	34.880	34.253	34.528	34.651
TiO2	2.147	2.122	2.052	2.153	2.060	2.019	1.967
Al2O3	16.491	16.531	16.675	16.440	16.358	16.535	16.001
FeO	26.411	26.272	26.238	26.417	26.146	26.351	26.465
MnO	0.263	0.275	0.261	0.276	0.274	0.284	0.303
MgO	6.608	6.720	6.699	6.675	6.801	6.596	6.628
CaO	0.002	0.000	0.005	0.010	0.002	0.006	0.830
Na2O	0.060	0.033	0.060	0.069	0.091	0.045	0.086
K2O	9.071	9.229	9.070	9.065	9.188	9.137	8.790
Cl	0.292	0.299	0.297	0.310	0.273	0.305	0.322
Cr2O3	0.011	0.014	0.014	0.007	0.002	0.003	0.005
NiO	0.076	0.070	0.057	0.050	0.059	0.062	0.059
Total	96.212	96.314	96.654	96.351	95.505	95.870	96.105
Si	5.464	5.455	5.493	5.471	5.431	5.450	5.467
Al iv	2.536	2.545	2.507	2.529	2.569	2.550	2.533
Al vi	0.518	0.515	0.558	0.511	0.488	0.527	0.442
Ti	0.254	0.251	0.241	0.254	0.246	0.240	0.233
Cr	0.001	0.002	0.002	0.001	0.000	0.000	0.001
Fe	3.470	3.450	3.422	3.466	3.467	3.479	3.492
Mn	0.035	0.037	0.035	0.037	0.037	0.038	0.040
Mg	1.548	1.573	1.557	1.561	1.607	1.552	1.559
Ni	0.010	0.009	0.007	0.006	0.008	0.008	0.008
Ca	0.000	0.000	0.001	0.002	0.000	0.001	0.140
Na	0.018	0.010	0.018	0.021	0.028	0.014	0.026
K	1.818	1.848	1.804	1.814	1.858	1.840	1.769
OH*	3.922	3.920	3.922	3.918	3.927	3.918	3.914
Cl	0.078	0.080	0.078	0.082	0.073	0.082	0.086
Total	19.672	19.693	19.644	19.672	19.738	19.698	19.710
XFe	0.692	0.687	0.687	0.689	0.683	0.691	0.691
XMn	0.010	0.010	0.010	0.010	0.011	0.011	0.011

Table 48

Creighton Mine (7840 lvl) Pl4-59 / 1 . Biotite	Creighton Mine (7840 lvl) Pl4-60 / 1 . Biotite	Creighton Mine (7840 lvl) Pl4-61 / 1 . Biotite	Creighton Mine (7840 lvl) Pl4-62 / 1 . Biotite	Creighton Mine (7840 lvl) Pl4-63 / 1 . Biotite	Creighton Mine (7840 lvl) Pl4-64 / 1 . Biotite	Creighton Mine (7840 lvl) Pl4-65 / 1 . Biotite	Creighton Mine (7840 lvl) Pl4-66 / 1 . Biotite
35.445	34.896	35.143	35.312	35.579	33.670	34.160	35.021
2.086	1.955	1.959	2.187	2.070	1.723	2.089	2.054
16.692	16.416	16.607	16.602	17.138	16.467	16.289	16.645
26.623	26.380	26.280	26.275	25.416	26.506	26.385	26.139
0.278	0.280	0.277	0.280	0.211	0.268	0.262	0.276
6.416	6.901	6.571	6.496	6.404	6.625	6.444	6.691
0.000	0.012	0.000	0.009	0.014	0.013	0.000	0.003
0.045	0.036	0.075	0.059	0.089	0.065	0.085	0.053
9.036	9.124	9.056	9.150	9.166	9.122	9.268	9.161
0.321	0.270	0.314	0.291	0.321	0.318	0.302	0.311
0.004	0.002	0.008	0.016	0.007	0.008	0.000	0.017
0.080	0.068	0.068	0.072	0.088	0.073	0.088	0.067
97.026	96.338	96.356	96.749	96.502	94.858	95.371	96.436
5.512	5.473	5.502	5.504	5.529	5.396	5.437	5.480
2.488	2.527	2.498	2.496	2.471	2.604	2.563	2.520
0.571	0.508	0.567	0.554	0.668	0.506	0.493	0.550
0.244	0.231	0.231	0.256	0.242	0.208	0.250	0.242
0.001	0.000	0.001	0.002	0.001	0.001	0.000	0.002
3.462	3.460	3.441	3.425	3.303	3.553	3.512	3.421
0.037	0.037	0.037	0.037	0.028	0.036	0.035	0.037
1.487	1.613	1.534	1.509	1.483	1.583	1.529	1.561
0.010	0.009	0.009	0.009	0.011	0.009	0.011	0.008
0.000	0.002	0.000	0.002	0.002	0.002	0.000	0.000
0.014	0.011	0.023	0.018	0.027	0.020	0.026	0.016
1.792	1.825	1.809	1.819	1.817	1.865	1.881	1.828
3.915	3.928	3.917	3.923	3.915	3.914	3.919	3.918
0.085	0.072	0.083	0.077	0.085	0.086	0.081	0.082
19.617	19.697	19.650	19.632	19.581	19.783	19.739	19.665
0.700	0.682	0.692	0.694	0.690	0.692	0.697	0.687
0.010	0.011	0.011	0.011	0.008	0.010	0.010	0.011

Table 49

Locality	Creighton Mine (7840 lvl)	Creighton Mine (7840 lvl)	Creighton Mine (7840 lvl)	Creighton Mine (7840 lvl)	Creighton Mine (7840 lvl)	Creighton Mine (7840 lvl)	Creighton Mine (7840 lvl)
Sample and analysis	PI7-13 / 1 .	PI7-14 / 1 .	PI7-15 / 1 .	PI7-16 / 1 .	PI7-17 / 1 .	PI7-18 / 1 .	PI7-19 / 1 .
Mineral	Biotite	Biotite	Biotite	Biotite	Biotite	Biotite	Biotite
SiO2	34.863	34.342	34.875	33.346	35.173	34.589	33.638
TiO2	1.766	1.761	1.771	1.686	1.726	1.764	1.698
Al2O3	16.749	16.538	17.127	16.691	16.957	16.555	16.646
FeO	26.527	26.627	25.979	26.197	26.037	26.772	26.285
MnO	0.315	0.315	0.319	0.304	0.312	0.306	0.305
MgO	6.361	6.574	6.328	6.542	6.446	6.590	6.698
CaO	0.001	0.010	0.005	0.008	0.010	0.001	0.005
Na2O	0.098	0.056	0.013	0.034	0.066	0.069	0.048
K2O	9.372	9.482	9.380	9.187	9.398	9.372	9.494
Cl	0.363	0.359	0.377	0.404	0.309	0.325	0.310
Cr2O3	0.009	0.010	0.000	0.005	0.009	0.006	0.012
NiO	0.076	0.076	0.082	0.071	0.082	0.068	0.096
Total	96.500	96.148	96.257	94.474	96.525	96.416	95.235
Si	5.476	5.432	5.473	5.370	5.499	5.448	5.375
Al iv	2.524	2.568	2.527	2.630	2.501	2.552	2.625
Al vi	0.576	0.515	0.641	0.538	0.624	0.521	0.510
Ti	0.209	0.209	0.209	0.204	0.203	0.209	0.204
Cr	0.001	0.001	0.000	0.001	0.001	0.001	0.002
Fe	3.484	3.522	3.410	3.528	3.404	3.526	3.513
Mn	0.042	0.042	0.042	0.041	0.041	0.041	0.041
Mg	1.489	1.550	1.480	1.570	1.502	1.547	1.595
Ni	0.010	0.010	0.010	0.009	0.010	0.009	0.012
Ca	0.000	0.002	0.001	0.001	0.002	0.000	0.001
Na	0.030	0.017	0.004	0.011	0.020	0.021	0.015
K	1.878	1.913	1.878	1.887	1.874	1.883	1.935
OH*	3.903	3.904	3.900	3.890	3.918	3.913	3.916
Cl	0.097	0.096	0.100	0.110	0.082	0.087	0.084
Total	19.719	19.781	19.675	19.791	19.682	19.758	19.828
XFe	0.701	0.694	0.697	0.692	0.694	0.695	0.688
XMn	0.012	0.012	0.012	0.012	0.012	0.011	0.012

Table 50

Creighton Mine (7840 lvl) Pl7-20 / 1 . Biotite	Creighton Mine (7840 lvl) Pl7-21 / 1 . Biotite	Creighton Mine (7840 lvl) Pl7-22 / 1 . Biotite	Creighton Mine (7840 lvl) Pl7-23 / 1 . Biotite	Creighton Mine (7840 lvl) Pl7-24 / 1 . Biotite	Creighton Mine (7840 lvl) Pl7-25 / 1 . Biotite
34.895	34.893	34.757	34.415	33.922	34.810
1.699	1.671	1.639	1.558	1.641	1.676
16.849	16.771	16.743	16.687	16.633	16.682
26.102	26.525	26.296	26.361	26.235	26.880
0.302	0.313	0.313	0.312	0.293	0.309
6.560	6.560	6.587	6.645	6.618	6.460
0.010	0.012	-0.001	0.007	0.008	0.004
0.045	0.083	0.051	0.042	0.023	0.054
9.424	9.365	9.441	9.468	9.425	9.318
0.307	0.369	0.349	0.396	0.322	0.376
0.009	0.006	0.001	0.003	0.005	0.000
0.072	0.073	0.068	0.078	0.063	0.068
96.274	96.639	96.244	95.971	95.188	96.637
5.478	5.471	5.470	5.445	5.413	5.468
2.522	2.529	2.530	2.555	2.587	2.532
0.596	0.571	0.576	0.557	0.541	0.556
0.201	0.197	0.194	0.185	0.197	0.198
0.001	0.001	0.000	0.000	0.001	0.000
3.427	3.478	3.461	3.488	3.501	3.531
0.040	0.042	0.042	0.042	0.040	0.041
1.535	1.533	1.545	1.567	1.574	1.513
0.009	0.009	0.009	0.010	0.008	0.009
0.002	0.002	0.000	0.001	0.001	0.001
0.014	0.025	0.016	0.013	0.007	0.016
1.887	1.873	1.895	1.911	1.918	1.867
3.918	3.902	3.907	3.894	3.913	3.900
0.082	0.098	0.093	0.106	0.087	0.100
19.712	19.731	19.738	19.775	19.788	19.732
0.691	0.694	0.691	0.690	0.690	0.700
0.012	0.012	0.012	0.012	0.011	0.012

Table 51

Locality	Creighton Mine (7840 lvl)	Creighton Mine (7840 lvl)	Creighton Mine (7840 lvl)	Creighton Mine (7840 lvl)	Creighton Mine (7840 lvl)
Sample and analysis	PL9_Bt1	PL9_Bt2	PL9_Bt3	PL9_Bt4	PL9_Bt5
Mineral	Biotite	Biotite	Biotite	Biotite	Biotite
SiO2	39.165	35.791	34.828	34.403	35.873
TiO2	1.700	1.764	1.732	1.802	1.735
Al2O3	17.342	16.116	15.567	15.477	15.655
FeO	25.464	25.931	26.259	25.968	25.064
MnO	0.340	0.375	0.348	0.326	0.313
MgO	7.839	7.018	6.568	6.598	6.695
CaO	0.023	0.001	0.034	0.027	0.030
Na2O	0.182	0.049	0.107	0.100	0.142
K2O	8.733	9.090	9.079	8.928	9.143
F	0.674	0.354	0.403	1.120	0.855
Cl	0.344	0.331	0.377	0.385	0.344
Cr2O3	-0.001	0.001	0.012	0.006	0.007
NiO	0.059	0.022	0.030	0.072	0.019
Total	101.864	96.844	95.342	95.212	95.874
Si	5.720	5.582	5.560	5.541	5.667
Al iv	2.280	2.418	2.440	2.459	2.333
Al vi	0.705	0.545	0.490	0.479	0.582
Ti	0.187	0.207	0.208	0.218	0.206
Cr	0.000	0.000	0.002	0.001	0.001
Fe	3.110	3.382	3.506	3.498	3.311
Mn	0.042	0.050	0.047	0.044	0.042
Mg	1.707	1.632	1.563	1.584	1.577
Ni	0.007	0.003	0.004	0.009	0.002
Ca	0.004	0.000	0.006	0.005	0.005
Na	0.052	0.015	0.033	0.031	0.043
K	1.627	1.808	1.849	1.834	1.842
OH*	3.604	3.738	3.694	3.324	3.481
F	0.311	0.175	0.203	0.570	0.427
Cl	0.085	0.088	0.102	0.105	0.092
Total	19.440	19.641	19.707	19.704	19.612
XFe	0.646	0.675	0.692	0.688	0.677
XMn	0.013	0.014	0.013	0.013	0.012

Table 52

Creighton Mine (7840 lvl)	Creighton Mine (7840 lvl)	Creighton Mine (7840 lvl)	Creighton Mine (7840 lvl)	Creighton Mine (7840 lvl)
PL9_Bt6	PL9_Bt7	PL9_Bt8	PL9_Bt9	PL9_Bt10
Biotite	Biotite	Biotite	Biotite	Biotite
35.231	35.569	35.513	35.261	34.853
1.871	1.833	1.691	1.721	1.668
15.772	15.969	15.912	15.860	15.578
26.089	25.772	26.040	26.136	26.215
0.306	0.338	0.345	0.299	0.310
6.865	6.821	6.752	6.771	6.799
0.000	0.014	0.013	0.030	0.012
0.077	0.035	0.043	0.067	0.066
9.088	9.140	9.101	9.101	9.031
0.465	0.627	0.664	0.589	0.435
0.289	0.334	0.395	0.342	0.391
0.007	0.006	0.007	0.003	-0.007
0.043	0.026	0.060	0.025	0.082
96.105	96.484	96.537	96.205	95.432
5.561	5.588	5.590	5.570	5.557
2.439	2.412	2.410	2.430	2.443
0.495	0.545	0.543	0.522	0.485
0.222	0.217	0.200	0.204	0.200
0.001	0.001	0.001	0.000	-0.001
3.444	3.386	3.428	3.453	3.496
0.041	0.045	0.046	0.040	0.042
1.615	1.597	1.584	1.594	1.616
0.005	0.003	0.008	0.003	0.011
0.000	0.002	0.002	0.005	0.002
0.024	0.011	0.013	0.021	0.020
1.830	1.831	1.827	1.834	1.837
3.691	3.600	3.564	3.614	3.675
0.232	0.312	0.331	0.294	0.219
0.077	0.089	0.105	0.092	0.106
19.676	19.638	19.653	19.676	19.708
0.681	0.679	0.684	0.684	0.684
0.012	0.013	0.013	0.011	0.012

Table 53

Locality	Creighton Mine (7840 lvl)	Creighton Mine (7840 lvl)	Creighton Mine (7840 lvl)	Creighton Mine (7840 lvl)	Creighton Mine (7840 lvl)	Creighton Mine (7840 lvl)	Creighton Mine (7840 lvl)
Sample and analysis	Pl13-27 / 1 .	Pl13-28 / 1 .	Pl13-29 / 1 .	Pl18-43 / 1 .	Pl18-44 / 1 .	Pl18-45 / 1 .	Pl18-46 / 1 .
Mineral	Biotite	Biotite	Biotite	Biotite	Biotite	Biotite	Biotite
SiO2	34.376	34.218	33.891	35.851	35.436	36.667	35.714
TiO2	2.023	2.043	2.287	1.449	1.511	1.510	1.494
Al2O3	16.544	16.537	16.294	16.100	16.018	16.212	16.023
FeO	26.283	26.504	26.700	20.399	20.730	20.218	21.317
MnO	0.192	0.175	0.213	0.178	0.172	0.176	0.184
MgO	6.740	6.679	6.518	11.102	11.158	11.049	11.122
CaO	0.022	0.020	0.003	0.001	0.014	0.013	0.005
Na2O	0.098	0.067	0.071	0.098	0.110	0.111	0.102
K2O	9.100	9.041	9.071	9.188	9.264	9.303	9.076
Cl	0.436	0.458	0.442	0.253	0.253	0.242	0.274
Cr2O3	0.007	0.007	0.007	0.037	0.087	0.102	0.068
NiO	0.001	0.004	0.009	0.047	0.063	0.063	0.055
Total	95.823	95.751	95.504	94.702	94.816	95.666	95.434
Si	5.434	5.420	5.398	5.549	5.499	5.601	5.510
Al iv	2.566	2.580	2.602	2.451	2.501	2.399	2.490
Al vi	0.517	0.508	0.457	0.486	0.429	0.520	0.424
Ti	0.240	0.243	0.274	0.169	0.176	0.173	0.173
Cr	0.001	0.001	0.001	0.005	0.011	0.012	0.008
Fe	3.475	3.511	3.557	2.640	2.690	2.583	2.751
Mn	0.026	0.023	0.029	0.023	0.023	0.023	0.024
Mg	1.588	1.577	1.548	2.561	2.581	2.516	2.558
Ni	0.000	0.000	0.001	0.006	0.008	0.008	0.007
Ca	0.004	0.003	0.000	0.000	0.002	0.002	0.001
Na	0.030	0.021	0.022	0.030	0.033	0.033	0.031
K	1.835	1.827	1.843	1.814	1.834	1.813	1.786
OH*	3.883	3.877	3.881	3.934	3.933	3.937	3.928
Cl	0.117	0.123	0.119	0.066	0.067	0.063	0.072
Total	19.716	19.716	19.731	19.734	19.788	19.683	19.764
XFe	0.686	0.690	0.697	0.508	0.510	0.507	0.518
XMn	0.007	0.007	0.008	0.009	0.008	0.009	0.009

Table 54

Creighton Mine (7840 lvl) Pl18-53 / 1 . Biotite	Creighton Mine (7840 lvl) Pl18-54 / 1 . Biotite	Creighton Mine (7840 lvl) Pl18-55 / 1 . Biotite	Creighton Mine (7840 lvl) Pl18-56 / 1 . Biotite	Creighton Mine (7840 lvl) Pl18-57 / 1 . Biotite	Creighton Mine (7840 lvl) Pl18-58 / 1 . Biotite	Creighton Mine (7840 lvl) Pl18-60 / 1 . Biotite
36.288	35.767	36.250	35.258	35.931	35.923	35.391
1.514	1.524	1.504	1.501	1.585	1.517	1.505
16.252	16.212	16.016	15.960	16.092	16.225	16.382
20.511	20.182	20.886	20.920	20.475	20.292	21.087
0.173	0.175	0.166	0.167	0.161	0.160	0.178
11.024	10.869	10.946	10.963	10.968	11.106	11.118
0.014	0.013	0.012	0.020	0.000	0.055	0.037
0.077	0.083	0.112	0.137	0.121	0.121	0.084
9.304	9.166	9.248	9.243	9.326	9.156	8.358
0.242	0.270	0.247	0.267	0.230	0.245	0.251
0.102	0.074	0.066	0.088	0.079	0.082	0.098
0.052	0.045	0.056	0.072	0.065	0.047	0.052
95.553	94.378	95.511	94.595	95.031	94.929	94.539
5.563	5.550	5.571	5.494	5.547	5.541	5.484
2.437	2.450	2.429	2.506	2.453	2.459	2.516
0.500	0.515	0.472	0.426	0.475	0.491	0.476
0.175	0.178	0.174	0.176	0.184	0.176	0.175
0.012	0.009	0.008	0.011	0.010	0.010	0.012
2.630	2.619	2.684	2.726	2.643	2.618	2.733
0.022	0.023	0.022	0.022	0.021	0.021	0.023
2.519	2.514	2.508	2.547	2.524	2.554	2.568
0.006	0.006	0.007	0.009	0.008	0.006	0.006
0.002	0.002	0.002	0.003	0.000	0.009	0.006
0.023	0.025	0.033	0.041	0.036	0.036	0.025
1.819	1.814	1.813	1.837	1.836	1.801	1.652
3.937	3.929	3.936	3.930	3.940	3.936	3.934
0.063	0.071	0.064	0.070	0.060	0.064	0.066
19.709	19.705	19.724	19.798	19.737	19.722	19.677
0.511	0.510	0.517	0.517	0.512	0.506	0.516
0.008	0.009	0.008	0.008	0.008	0.008	0.008

Table 55

Locality	Creighton Mine (7840 lvl)	Creighton Mine (7840 lvl)	Creighton Mine (7840 lvl)	Creighton Mine (7840 lvl)	Creighton Mine (7840 lvl)
Sample and analysis	PL14_Bt1	PL14_Bt2	PL14_Bt3	PL14_Bt4	PL14_Bt5
Mineral	Biotite	Biotite	Biotite	Biotite	Biotite
SiO2	36.88	36.898	37.092	36.514	37.267
TiO2	1.527	1.548	1.58	1.502	1.479
Al2O3	16.108	15.988	15.935	16.014	16.081
FeO	19.92	19.358	19.895	19.479	19.648
MnO	0.179	0.156	0.146	0.174	0.18
MgO	11.363	11.338	11.452	11.279	11.426
CaO	0.025	0.006	0.003	0.018	-0.006
Na2O	0.128	0.169	0.143	0.098	0.106
K2O	9.07	9.092	9.012	9.062	9.24
F	0.539	0.403	0.419	0.495	0.513
Cl	0.233	0.215	0.233	0.243	0.219
Cr2O3	0.054	0.063	0.05	0.051	0.042
NiO	0.075	0.042	0.055	0.068	0.045
Total	96.1	95.278	96.016	94.997	96.24
Si	5.621	5.649	5.645	5.623	5.659
Al iv	2.379	2.351	2.355	2.377	2.341
Al vi	0.515	0.535	0.503	0.530	0.537
Ti	0.175	0.178	0.181	0.174	0.169
Cr	0.007	0.008	0.006	0.006	0.005
Fe	2.539	2.479	2.532	2.509	2.495
Mn	0.023	0.020	0.019	0.023	0.023
Mg	2.582	2.588	2.598	2.589	2.586
Ni	0.009	0.005	0.007	0.008	0.005
Ca	0.004	0.001	0.000	0.003	-0.001
Na	0.038	0.050	0.042	0.029	0.031
K	1.763	1.776	1.749	1.780	1.790
OH*	3.680	3.749	3.738	3.695	3.697
F	0.260	0.195	0.202	0.241	0.246
Cl	0.060	0.056	0.060	0.063	0.056
Total	19.654	19.639	19.638	19.651	19.641
XFe	0.496	0.489	0.494	0.492	0.491
XMn	0.009	0.008	0.007	0.009	0.009

Table 56

Creighton Mine (7840 lvl) PL14_Bt6 Biotite	Creighton Mine (7840 lvl) PL14_Bt7 Biotite	Creighton Mine (7840 lvl) PL14_Bt8 Biotite	Creighton Mine (7840 lvl) PL14_Bt9 Biotite	Creighton Mine (7840 lvl) PL14_Bt10 Biotite
36.614	36.042	36.955	34.4	37.063
1.492	1.602	1.491	1.495	1.475
15.838	15.812	16.183	30.615	15.982
19.857	19.474	19.854	17.742	19.576
0.156	0.179	0.152	0.152	0.156
11.462	11.026	11.375	13.061	11.529
0.013	0.112	0.002	0.139	-0.001
0.103	0.074	0.089	0.097	0.092
9.075	8.907	9.215	6.38	9.239
0.451	0.457	0.333	0.196	0.458
0.239	0.232	0.233	0.226	0.225
0.039	0.083	0.084	0.058	0.071
0.052	0.06	0.052	0.045	0.039
95.392	94.061	96.018	104.604	95.904
5.622	5.610	5.624	4.614	5.647
2.378	2.390	2.376	3.386	2.353
0.488	0.511	0.527	1.454	0.517
0.172	0.188	0.171	0.151	0.169
0.005	0.010	0.010	0.006	0.009
2.550	2.535	2.527	1.990	2.495
0.020	0.024	0.020	0.017	0.020
2.623	2.558	2.581	2.611	2.619
0.006	0.008	0.006	0.005	0.005
0.002	0.019	0.000	0.020	0.000
0.031	0.022	0.026	0.025	0.027
1.777	1.768	1.789	1.091	1.796
3.719	3.714	3.780	3.865	3.721
0.219	0.225	0.160	0.083	0.221
0.062	0.061	0.060	0.051	0.058
19.675	19.642	19.656	19.371	19.656
0.493	0.498	0.495	0.432	0.488
0.008	0.009	0.008	0.009	0.008

Table 57

Locality	Creighton Mine (7840 lvl)	Creighton Mine (7840 lvl)	Creighton Mine (7840 lvl)	Creighton Mine (7840 lvl)	Creighton Mine (7840 lvl)	Creighton Mine (7840 lvl)	Creighton Mine (7840 lvl)
Sample and analysis	PL17_Bt1	PL17_Bt2	PL17_Bt3	PL17_Bt4	PL17_Bt5	PL17_Bt7	PL17_Bt8
Mineral	Biotite	Biotite	Biotite	Biotite	Biotite	Biotite	Biotite
SiO2	36.616	37.604	37.796	37.647	36.759	36.996	37.775
TiO2	1.542	1.522	1.527	1.495	1.521	1.445	1.503
Al2O3	16.001	16.27	16.367	16.36	15.89	16.095	16.577
FeO	20.029	20.436	20.237	20.129	19.921	19.452	19.951
MnO	0.154	0.207	0.172	0.212	0.163	0.181	0.183
MgO	11.234	11.632	11.433	11.674	11.429	11.42	11.984
CaO	0.018	0.034	0.004	-0.002	-0.002	0.006	-0.007
Na2O	0.051	0.131	0.137	0.111	0.099	0.113	0.11
K2O	9.092	9.066	9.335	9.398	9.151	9.002	9.41
F	0.568	0.22	0.378	0.484	0.314	0.295	0.297
Cl	0.2	0.236	0.236	0.236	0.211	0.206	0.215
Cr2O3	0.073	0.07	0.054	0.074	0.071	0.075	0.053
NiO	0.053	0.03	0.043	0.046	0.046	0.108	0.023
Total	95.632	97.459	97.718	97.865	95.573	95.394	98.075
Si	5.615	5.631	5.652	5.630	5.624	5.648	5.615
Al iv	2.385	2.369	2.348	2.370	2.376	2.352	2.385
Al vi	0.507	0.502	0.536	0.514	0.490	0.545	0.519
Ti	0.178	0.171	0.172	0.168	0.175	0.166	0.168
Cr	0.009	0.008	0.006	0.009	0.009	0.009	0.006
Fe	2.569	2.559	2.531	2.518	2.549	2.484	2.480
Mn	0.020	0.026	0.022	0.027	0.021	0.023	0.023
Mg	2.568	2.596	2.548	2.603	2.607	2.599	2.655
Ni	0.007	0.004	0.005	0.006	0.006	0.013	0.003
Ca	0.003	0.005	0.001	0.000	0.000	0.001	-0.001
Na	0.015	0.038	0.040	0.032	0.029	0.033	0.032
K	1.778	1.732	1.780	1.793	1.786	1.753	1.784
OH*	3.673	3.836	3.761	3.711	3.793	3.804	3.806
F	0.275	0.104	0.179	0.229	0.152	0.142	0.140
Cl	0.052	0.060	0.060	0.060	0.055	0.053	0.054
Total	19.653	19.643	19.641	19.668	19.671	19.626	19.670
XFe	0.500	0.496	0.498	0.492	0.494	0.489	0.483
XMn	0.008	0.010	0.009	0.011	0.008	0.009	0.009

Table 58

Creighton Mine (7840 lvl)	Creighton Mine (7840 lvl)	Creighton Mine (7840 lvl)	Creighton Mine (7840 lvl)	Creighton Mine (7840 lvl)	Creighton Mine (7840 lvl)	Creighton Mine (7840 lvl)	Creighton Mine (7840 lvl)
PL17_Bt9	PL17_Bt10	PL17_Bt11	PL17_Bt12	PL17_Bt13	PL17_Bt14	PL17_Bt15	PL17_Bt16
Biotite	Biotite	Biotite	Biotite	Biotite	Biotite	Biotite	Biotite
37.258	36.979	35.903	37.521	37.146	36.097	36.297	32.449
1.488	1.432	1.433	1.457	1.49	1.465	1.473	1.544
16.056	15.993	15.954	16.194	16.252	15.844	15.851	15.911
19.644	19.264	20.309	19.7	19.707	19.438	19.591	20.784
0.173	0.182	0.158	0.176	0.163	0.173	0.167	0.189
11.517	11.584	11.766	11.584	11.401	11.309	11.545	11.615
0.013	0.003	0.005	0.035	-0.009	0.008	0.012	0.152
0.157	0.157	0.074	0.114	0.128	0.057	0.044	0.146
9.237	9.227	8.662	9.226	9.316	9.254	9.315	7.975
0.267	0.415	0.357	0.329	0.546	0.483	0.257	0.742
0.23	0.215	0.218	0.221	0.215	0.227	0.209	0.208
0.047	0.09	0.095	0.052	0.099	0.103	0.093	0.079
0.022	0.06	0.095	0.031	0.04	0.073	0.069	0.07
96.107	95.6	95.03	96.641	96.494	94.531	94.923	91.864
5.652	5.645	5.538	5.659	5.633	5.600	5.595	5.259
2.348	2.355	2.462	2.341	2.367	2.400	2.405	2.741
0.523	0.523	0.439	0.537	0.537	0.497	0.474	0.298
0.170	0.164	0.166	0.165	0.170	0.171	0.171	0.188
0.006	0.011	0.012	0.006	0.012	0.013	0.011	0.010
2.492	2.459	2.620	2.485	2.499	2.522	2.525	2.817
0.022	0.024	0.021	0.022	0.021	0.023	0.022	0.026
2.605	2.636	2.706	2.604	2.577	2.615	2.653	2.806
0.003	0.007	0.012	0.004	0.005	0.009	0.009	0.009
0.002	0.000	0.001	0.006	-0.001	0.001	0.002	0.026
0.046	0.046	0.022	0.033	0.038	0.017	0.013	0.046
1.787	1.797	1.704	1.775	1.802	1.831	1.831	1.649
3.813	3.744	3.769	3.787	3.683	3.703	3.820	3.563
0.128	0.200	0.174	0.157	0.262	0.237	0.125	0.380
0.059	0.056	0.057	0.056	0.055	0.060	0.055	0.057
19.656	19.668	19.702	19.638	19.659	19.699	19.711	19.875
0.489	0.483	0.492	0.488	0.492	0.491	0.488	0.501
0.009	0.009	0.008	0.009	0.008	0.009	0.009	0.009

Table 59

Creighton Mine (7840 lvl) PL17_Bt17 Biotite	Creighton Mine (7840 lvl) PL17_Bt18 Biotite
36.038	36.272
1.409	1.463
16.057	15.83
19.739	20.06
0.211	0.133
11.539	11.187
0.17	0.039
0.235	0.182
8.556	9.196
0.556	0.475
0.21	0.221
0.064	0.082
0.085	0.075
94.869	95.213
5.564	5.598
2.436	2.402
0.487	0.478
0.164	0.170
0.008	0.010
2.549	2.589
0.028	0.017
2.656	2.574
0.011	0.009
0.028	0.006
0.070	0.054
1.685	1.810
3.674	3.710
0.272	0.232
0.055	0.058
19.685	19.719
0.490	0.501
0.011	0.007

Table 60

Locality	Creighton Mine_7840 lvl	Creighton Mine_7840 lvl	Creighton Mine_7840 lvl	Creighton Mine_7840 lvl	Creighton Mine_7840 lvl	Creighton Mine_7840 lvl	Creighton Mine_7840 lvl
Sample and analysis	PL19_Bt1	PL19_Bt2	PL19_Bt3	PL19_Bt4	PL19_Bt5	PL19_Bt6	PL19_Bt7
Mineral	Biotite	Biotite	Biotite	Biotite	Biotite	Biotite	Biotite
SiO2	35.030	35.218	35.623	35.019	35.340	34.232	34.966
TiO2	1.790	1.823	1.708	1.826	1.938	1.927	1.529
Al2O3	17.547	17.151	17.346	17.525	17.496	16.873	17.254
FeO	27.835	26.933	27.817	27.679	28.265	27.504	27.592
MnO	0.305	0.265	0.333	0.316	0.296	0.258	0.298
MgO	4.761	4.651	4.808	4.542	4.732	4.504	4.654
CaO	-0.004	0.014	0.005	0.006	-0.014	0.021	0.037
Na2O	-0.033	0.007	0.010	0.015	0.000	0.049	0.037
K2O	9.457	9.089	9.275	9.163	9.247	9.193	9.159
F	0.397	0.477	0.476	0.369	0.264	0.340	0.813
Cl	0.411	0.327	0.387	0.399	0.534	0.552	0.429
Cr2O3	0.008	0.012	0.011	0.001	0.010	0.005	0.007
NiO	0.258	0.318	0.237	0.309	0.292	0.291	0.341
Total	97.761	96.286	98.036	97.167	98.401	95.748	97.117
Si	5.480	5.563	5.545	5.500	5.491	5.485	5.526
Al iv	2.520	2.437	2.455	2.500	2.509	2.515	2.474
Al vi	0.716	0.757	0.728	0.745	0.695	0.672	0.740
Ti	0.211	0.217	0.200	0.216	0.226	0.232	0.182
Cr	0.001	0.001	0.001	0.000	0.001	0.001	0.001
Fe	3.642	3.558	3.621	3.636	3.673	3.686	3.647
Mn	0.040	0.035	0.044	0.042	0.039	0.035	0.040
Mg	1.110	1.095	1.116	1.063	1.096	1.076	1.096
Ni	0.032	0.040	0.030	0.039	0.036	0.038	0.043
Ca	-0.001	0.002	0.001	0.001	-0.002	0.004	0.006
Na	-0.010	0.002	0.003	0.005	0.000	0.015	0.011
K	1.887	1.831	1.842	1.836	1.833	1.879	1.846
OH*	3.695	3.674	3.664	3.710	3.730	3.678	3.479
F	0.196	0.238	0.234	0.183	0.130	0.172	0.406
Cl	0.109	0.088	0.102	0.106	0.141	0.150	0.115
Total	19.629	19.540	19.585	19.582	19.597	19.636	19.613
XFe	0.766	0.765	0.764	0.774	0.770	0.774	0.769
XMn	0.011	0.010	0.012	0.011	0.010	0.009	0.011

Table 61

Locality	X2 Fault-4220 lvl Copper Cliff	X2 Fault-4220 lvl Copper Cliff	X2 Fault-4220 lvl Copper Cliff	X2 Fault-4220 lvl Copper Cliff	X2 Fault-4220 lvl Copper Cliff	X2 Fault-4220 lvl Copper Cliff
Sample and analysis	pcl9_bt1	pcl9_bt2	pcl9_bt3	pcl9_bt4	pcl9_bt5	pcl9_bt6
Mineral	Biotite	Biotite	Biotite	Biotite	Biotite	Biotite
SiO2	34.897	35.981	36.485	37.113	36.015	35.402
TiO2	1.358	1.394	1.458	1.436	1.431	1.487
Al2O3	15.072	15.824	15.551	15.222	15.554	15.095
FeO	23.079	23.534	23.284	22.120	22.757	23.167
MnO	0.233	0.235	0.226	0.208	0.228	0.217
MgO	8.836	9.490	9.454	9.909	9.133	9.432
CaO	0.009	0.011	0.010	0.017	-0.005	0.016
Na2O	0.084	0.038	0.111	0.029	0.067	0.080
K2O	8.915	8.486	9.131	9.000	9.087	8.755
F	0.478	0.405	0.669	0.642	0.644	0.242
Cl	0.234	0.236	0.220	0.191	0.221	0.233
Cr2O3	0.023	0.030	0.032	0.028	0.028	0.027
NiO	0.015	0.033	0.033	0.030	0.047	0.063
Total	93.233	95.697	96.662	95.945	95.210	94.214
Si	5.605	5.591	5.636	5.726	5.641	5.599
Al iv	2.395	2.409	2.364	2.274	2.359	2.401
Al vi	0.458	0.489	0.467	0.494	0.513	0.413
Ti	0.164	0.163	0.169	0.167	0.169	0.177
Cr	0.003	0.004	0.004	0.003	0.003	0.003
Fe	3.100	3.058	3.008	2.854	2.981	3.064
Mn	0.032	0.031	0.030	0.027	0.030	0.029
Mg	2.116	2.198	2.177	2.279	2.133	2.224
Ni	0.002	0.004	0.004	0.004	0.006	0.008
Ca	0.002	0.002	0.002	0.003	-0.001	0.003
Na	0.026	0.011	0.033	0.009	0.020	0.025
K	1.826	1.682	1.799	1.771	1.816	1.766
OH*	3.693	3.739	3.616	3.637	3.622	3.816
F	0.243	0.199	0.327	0.313	0.319	0.121
Cl	0.064	0.062	0.058	0.050	0.059	0.062
Total	19.729	19.642	19.693	19.611	19.670	19.711
XFe	0.594	0.582	0.580	0.556	0.583	0.579
XMn	0.010	0.010	0.010	0.009	0.010	0.009

Table 62

Locality	X2 Fault-4370 lvl Copper Cliff	X2 Fault-4370 lvl Copper Cliff	X2 Fault-4370 lvl Copper Cliff	X2 Fault-4370 lvl Copper Cliff	X2 Fault-4370 lvl Copper Cliff	X2 Fault-4370 lvl Copper Cliff	X2 Fault-4370 lvl Copper Cliff
Sample and analysis	pcl1_st1_bt1	pcl1_st1_bt2	pcl1_st1_bt3	pcl1_st1_bt4	pcl1_st1_bt5	pcl1_st1_bt6	pcl1_st1_bt7
Mineral	Biotite	Biotite	Biotite	Biotite	Biotite	Biotite	Biotite
SiO2	36.691	36.569	32.911	36.399	35.239	36.656	36.819
TiO2	1.450	1.626	1.215	1.528	1.302	1.519	1.515
Al2O3	15.753	15.985	15.267	16.040	16.009	16.137	16.041
FeO	20.946	21.205	20.780	21.986	21.596	21.226	21.179
MnO	0.194	0.232	0.201	0.182	0.224	0.225	0.228
MgO	10.355	10.153	10.176	10.262	10.680	10.277	10.339
CaO	0.028	0.018	0.109	0.004	0.019	0.000	0.018
Na2O	0.296	0.189	0.343	0.161	0.154	0.132	0.093
K2O	8.938	9.101	7.192	9.038	8.014	9.257	9.366
F	0.848	0.616	0.568	0.840	0.736	0.659	0.763
Cl	0.191	0.097	0.263	0.148	0.164	0.118	0.131
Cr2O3	0.019	0.028	0.044	0.030	0.035	0.037	0.024
NiO	0.118	0.117	0.129	0.111	0.123	0.137	0.131
Total	95.826	95.936	89.198	96.728	94.295	96.379	96.647
Si	5.658	5.624	5.462	5.586	5.524	5.617	5.632
Al iv	2.342	2.376	2.538	2.414	2.476	2.383	2.368
Al vi	0.521	0.522	0.449	0.488	0.483	0.531	0.525
Ti	0.168	0.188	0.152	0.176	0.154	0.175	0.174
Cr	0.002	0.003	0.006	0.004	0.004	0.004	0.003
Fe	2.701	2.727	2.884	2.822	2.831	2.720	2.710
Mn	0.025	0.030	0.028	0.024	0.030	0.029	0.030
Mg	2.380	2.328	2.518	2.348	2.496	2.347	2.358
Ni	0.015	0.014	0.017	0.014	0.016	0.017	0.016
Ca	0.005	0.003	0.019	0.001	0.003	0.000	0.003
Na	0.089	0.056	0.110	0.048	0.047	0.039	0.028
K	1.758	1.785	1.523	1.769	1.603	1.809	1.828
OH*	3.537	3.675	3.628	3.554	3.592	3.650	3.597
F	0.414	0.300	0.298	0.408	0.365	0.319	0.369
Cl	0.050	0.025	0.074	0.039	0.044	0.031	0.034
Total	19.664	19.658	19.706	19.693	19.666	19.673	19.673
XFe	0.532	0.540	0.534	0.546	0.531	0.537	0.535
XMn	0.009	0.011	0.010	0.008	0.010	0.011	0.011

Table 63

X2 Fault-4370 lvl Copper Cliff pcl1_st1_bt8 Biotite	X2 Fault-4370 lvl Copper Cliff pcl1_st1_bt9 Biotite	X2 Fault-4370 lvl Copper Cliff pcl1_st1_bt10 Biotite	X2 Fault-4370 lvl Copper Cliff pcl1_st1_bt11 Biotite
36.278	34.212	36.355	36.573
1.596	1.540	1.453	1.490
16.050	16.230	16.024	16.033
21.614	21.471	20.973	20.749
0.198	0.225	0.201	0.223
10.264	11.325	10.413	10.502
-0.010	0.003	-0.012	0.005
0.099	0.058	0.111	0.096
9.261	7.157	9.307	9.207
0.903	0.497	0.500	0.733
0.129	0.128	0.142	0.182
0.037	0.038	0.020	0.028
0.131	0.137	0.114	0.118
96.550	93.019	95.601	95.939
5.580	5.405	5.609	5.625
2.420	2.595	2.391	2.375
0.491	0.428	0.522	0.532
0.185	0.183	0.169	0.172
0.005	0.005	0.002	0.003
2.781	2.837	2.706	2.669
0.026	0.030	0.026	0.029
2.354	2.667	2.395	2.408
0.016	0.017	0.014	0.015
-0.002	0.001	-0.002	0.001
0.030	0.018	0.033	0.029
1.817	1.442	1.831	1.806
3.527	3.717	3.719	3.596
0.439	0.248	0.244	0.357
0.034	0.034	0.037	0.047
19.701	19.628	19.697	19.665
0.542	0.515	0.531	0.526
0.009	0.011	0.010	0.011

Table 64

Locality	X2 Fault-4370 lvl Copper Cliff	X2 Fault-4370 lvl Copper Cliff	X2 Fault-4370 lvl Copper Cliff	X2 Fault-4370 lvl Copper Cliff	X2 Fault-4370 lvl Copper Cliff	X2 Fault-4370 lvl Copper Cliff
Sample and analysis	pcl3_bt5	pcl3_bt6	pcl3_bt7	pcl3_bt8	pcl3_bt9	pcl3_bt10
Mineral	Biotite	Biotite	Biotite	Biotite	Biotite	Biotite
SiO2	36.392	37.552	36.521	37.801	36.711	37.315
TiO2	1.265	1.240	1.179	1.384	1.232	1.184
Al2O3	16.239	16.539	16.484	17.081	16.533	16.977
FeO	20.286	20.460	20.466	20.300	19.898	20.612
MnO	0.179	0.221	0.189	0.165	0.158	0.214
MgO	10.630	10.934	10.755	10.813	10.753	10.992
CaO	0.000	0.011	-0.006	-0.013	-0.007	-0.007
Na2O	0.049	0.032	0.028	0.008	0.050	0.050
K2O	9.306	9.099	9.397	9.294	9.451	9.411
F	0.563	0.810	0.775	0.475	0.750	0.603
Cl	0.128	0.127	0.149	0.148	0.115	0.131
Cr2O3	0.075	0.048	0.043	0.081	0.069	0.067
NiO	0.108	0.125	0.136	0.127	0.146	0.131
Total	95.218	97.200	96.116	97.664	95.859	97.680
Si	5.618	5.666	5.601	5.648	5.625	5.605
Al iv	2.382	2.334	2.399	2.352	2.375	2.395
Al vi	0.572	0.607	0.581	0.656	0.611	0.611
Ti	0.147	0.141	0.136	0.156	0.142	0.134
Cr	0.009	0.006	0.005	0.010	0.008	0.008
Fe	2.619	2.582	2.625	2.537	2.550	2.589
Mn	0.023	0.028	0.025	0.021	0.021	0.027
Mg	2.446	2.459	2.459	2.408	2.456	2.461
Ni	0.013	0.015	0.017	0.015	0.018	0.016
Ca	0.000	0.002	-0.001	-0.002	-0.001	-0.001
Na	0.015	0.009	0.008	0.002	0.015	0.015
K	1.832	1.751	1.838	1.771	1.847	1.803
OH*	3.692	3.581	3.585	3.738	3.607	3.680
F	0.275	0.387	0.376	0.224	0.363	0.286
Cl	0.033	0.032	0.039	0.037	0.030	0.033
Total	19.677	19.600	19.693	19.574	19.667	19.663
XFe	0.517	0.512	0.516	0.513	0.509	0.513
XMn	0.009	0.011	0.009	0.008	0.008	0.010

Chlorite

Table 65

Locality	Garson Mine (5200lvl)	Garson Mine (5200lvl)	Garson Mine (5200lvl)	Garson Mine (5200lvl)	Garson Mine (5200lvl)
Sample and analysis	kpgmd11-1 / 1 .	kpgmd11-2 / 1 .	kpgmd11-3 / 1 .	kpgmd11-4 / 1 .	kpgmd11-5 / 1 .
Mineral	Chlorite	Chlorite	Chlorite	Chlorite	Chlorite
SiO2	25.424	25.965	25.470	25.374	25.785
TiO2	0.048	0.039	0.041	0.061	0.079
Al2O3	21.409	21.161	20.917	21.152	21.325
FeO	22.860	22.950	22.843	22.913	23.387
MnO	0.264	0.264	0.279	0.265	0.295
MgO	17.420	17.819	17.506	17.669	17.463
CaO	0.042	0.033	0.036	0.028	0.009
Na2O	0.100	0.130	0.127	0.081	0.042
K2O	0.062	0.088	0.052	0.031	0.017
Cl	0.029	0.042	0.030	0.039	0.027
Cr2O3	0.554	0.376	0.643	0.634	0.329
NiO	0.066	0.064	0.044	0.052	0.059
Total	88.278	88.932	87.986	88.299	88.817
Si	5.252	5.315	5.280	5.242	5.305
Al iv	2.748	2.685	2.720	2.758	2.695
Al vi	2.486	2.445	2.415	2.416	2.489
Ti	0.008	0.006	0.006	0.009	0.012
Cr	0.091	0.061	0.105	0.104	0.054
Fe+3	0.000	0.000	0.000	0.000	0.000
Fe+2	4.029	4.017	4.055	4.057	4.080
Mn	0.046	0.046	0.049	0.046	0.051
Mg	5.364	5.438	5.409	5.442	5.356
Ni	0.011	0.011	0.007	0.009	0.010
Ca	0.009	0.007	0.008	0.006	0.002
Na	0.080	0.103	0.102	0.065	0.033
K	0.033	0.046	0.027	0.016	0.009
Cl	0.020	0.029	0.021	0.028	0.019
OH*	15.980	15.971	15.979	15.972	15.981
Total	36.156	36.180	36.185	36.171	36.096
XFe	0.429	0.425	0.428	0.427	0.432

Table 66

Garson Mine (5200lvl) kpgmd11-6 / 1 . Chlorite	Garson Mine (5200lvl) kpgmd11-7 / 1 . Chlorite	Garson Mine (5200lvl) kpgmd11-8 / 1 . Chlorite	Garson Mine (5200lvl) kpgmd11-9 / 1 . Chlorite	Garson Mine (5200lvl) kpgmd11-10 / 1 . Chlorite
25.530	25.454	25.640	25.535	25.412
0.040	0.044	0.066	0.033	0.011
21.449	21.206	21.515	21.395	21.421
23.128	23.249	22.942	22.987	23.098
0.281	0.278	0.266	0.266	0.273
17.724	17.484	17.633	17.565	17.797
0.013	0.031	0.010	0.025	0.004
0.028	0.043	0.071	0.078	0.022
0.020	0.041	0.029	0.038	0.016
0.017	0.019	0.054	0.025	0.012
0.495	0.757	0.436	0.399	0.386
0.058	0.068	0.062	0.064	0.058
88.785	88.674	88.724	88.409	88.511
5.248	5.249	5.268	5.266	5.236
2.752	2.751	2.732	2.734	2.764
2.463	2.422	2.496	2.487	2.460
0.006	0.007	0.010	0.005	0.002
0.080	0.123	0.071	0.065	0.063
0.000	0.000	0.000	0.000	0.000
4.061	4.096	4.006	4.046	4.082
0.049	0.049	0.046	0.046	0.048
5.431	5.374	5.401	5.400	5.467
0.010	0.011	0.010	0.011	0.010
0.003	0.007	0.002	0.005	0.001
0.022	0.034	0.057	0.062	0.018
0.011	0.021	0.015	0.020	0.009
0.012	0.013	0.037	0.018	0.008
15.988	15.987	15.963	15.982	15.992
36.136	36.146	36.115	36.148	36.158
0.428	0.433	0.426	0.428	0.428

Table 67

Locality	Garson Mine (5200lvl)	Garson Mine (5200lvl)	Garson Mine (5200lvl)	Garson Mine (5200lvl)	Garson Mine (5200lvl)	Garson Mine (5200lvl)	Garson Mine (5200lvl)
Sample and analysis	kpgmd12-31 / 1 .	kpgmd12-32 / 1 .	kpgmd14-5 / 1 .	kpgmd14-1 / 1 .	kpgmd14-2 / 1 .	kpgmd14-3 / 1 .	kpgmd14-4 / 1 .
Mineral	Chlorite	Chlorite	Chlorite	Chlorite	Chlorite	Chlorite	Chlorite
SiO2	25.596	25.299	24.8811	23.9173	25.3819	24.9086	25.1362
TiO2	0.051	0.157	0.0864	0.0374	0.0338	0.03	0.0551
Al2O3	21.565	21.316	21.6307	21.2956	21.1668	21.8609	21.3122
FeO	23.187	22.642	27.9802	23.3811	27.9727	28.5421	27.7886
MnO	0.278	0.287	0.3576	0.3265	0.3688	0.3676	0.3583
MgO	17.107	17.471	13.6772	13.668	14.0483	13.6268	13.8835
CaO	0.108	0.120	0.0241	0.0138	0.037	0.0534	0.0351
Na2O	0.054	0.126	0.0651	0.1789	0.1381	0.0276	0.0077
K2O	0.037	0.033	0.0444	0.0364	0.0157	0.0038	0.0142
Cl	0.013	0.002	0.0268	0.0197	0.06	0.0126	0.0367
Cr2O3	0.221	0.359	0.1179	0.071	0.0834	0.0698	0.0599
NiO	0.053	0.069	0.1258	0.1001	0.1251	0.1366	0.1281
Total	88.270	87.881	89.017	83.046	89.432	89.640	88.816
Si	5.296	5.244	5.241	5.294	5.312	5.220	5.305
Al iv	2.704	2.756	2.759	2.706	2.688	2.780	2.695
Al vi	2.566	2.474	2.624	2.865	2.552	2.633	2.612
Ti	0.008	0.025	0.014	0.006	0.005	0.005	0.009
Cr	0.036	0.059	0.020	0.012	0.014	0.012	0.010
Fe+3	0.000	0.000	0.000	0.067	0.000	0.000	0.000
Fe+2	4.056	4.017	4.974	4.261	4.953	5.058	4.924
Mn	0.049	0.050	0.064	0.061	0.065	0.065	0.064
Mg	5.276	5.398	4.294	4.510	4.383	4.257	4.368
Ni	0.009	0.011	0.021	0.018	0.021	0.023	0.022
Ca	0.024	0.027	0.005	0.003	0.008	0.012	0.008
Na	0.044	0.101	0.053	0.154	0.112	0.022	0.006
K	0.019	0.017	0.024	0.021	0.008	0.002	0.008
Cl	0.009	0.002	0.019	0.015	0.043	0.009	0.026
OH*	15.991	15.998	15.981	15.985	15.957	15.991	15.974
Total	36.087	36.180	36.093	35.978	36.122	36.089	36.030
XFe	0.435	0.427	0.537	0.490	0.531	0.543	0.530

Table 68

Garson Mine (5200lvl) kpgmd14-5 / 1 . Chlorite	Garson Mine (5200lvl) kpgmd14-6 / 1 . Chlorite	Garson Mine (5200lvl) kpgmd14-7 / 1 . Chlorite	Garson Mine (5200lvl) kpgmd14-8 / 1 . Chlorite	Garson Mine (5200lvl) kpgmd14-9 / 1 . Chlorite	Garson Mine (5200lvl) kpgmd14-10 / 1 . Chlorite
24.9923	25.0692	24.8387	24.8702	25.2511	25.742
0.0446	0.0386	0.1036	0.0386	0.0633	0.244
21.6818	21.6169	21.3807	21.8921	20.9303	21.2495
28.0771	28.3198	28.1006	28.5825	28.3264	27.5602
0.376	0.3549	0.3726	0.3449	0.3628	0.3559
13.7236	13.6553	13.9654	13.3157	13.7933	13.3324
0.0158	0.0512	0.0258	0.0305	0.037	0.0083
0.1329	0.151	0.195	0.0886	0.1042	0.0681
0.0116	0.0158	0.0434	0.0102	0.1947	0.8681
0.0346	0.0608	0.0733	0.0697	0.0621	0.0496
0.0741	0.1015	0.0907	0.1032	0.1477	0.0916
0.1319	0.1416	0.1326	0.1167	0.1277	0.1448
89.296	89.577	89.322	89.463	89.401	89.715
5.243	5.248	5.205	5.225	5.298	5.361
2.757	2.752	2.795	2.775	2.702	2.639
2.623	2.602	2.519	2.659	2.502	2.612
0.007	0.006	0.016	0.006	0.010	0.038
0.012	0.017	0.015	0.017	0.025	0.015
0.000	0.000	0.000	0.000	0.000	0.000
4.985	5.020	5.039	5.059	5.057	4.852
0.067	0.063	0.066	0.061	0.064	0.063
4.292	4.261	4.363	4.170	4.314	4.139
0.022	0.024	0.022	0.020	0.022	0.024
0.004	0.011	0.006	0.007	0.008	0.002
0.108	0.123	0.158	0.072	0.085	0.055
0.006	0.008	0.023	0.005	0.104	0.461
0.025	0.043	0.052	0.050	0.044	0.035
15.975	15.957	15.948	15.950	15.956	15.965
36.126	36.135	36.228	36.077	36.191	36.261
0.537	0.541	0.536	0.548	0.540	0.540

Table 69

Locality	Vermillion Lake	Vermillion Lake	Vermillion Lake	Vermillion Lake	Vermillion Lake	Vermillion Lake
Sample and analysis	8clf1505_st1_chl1	8clf1505_st1_chl2	8clf1505_st1_chl3	8clf1505_st1_chl4	8clf1505_st1_chl5	8clf1505_st1_chl6
Mineral	Chlorite	Chlorite	Chlorite	Chlorite	Chlorite	Chlorite
SiO2	24.523	24.823	25.130	24.720	24.925	25.071
TiO2	0.040	0.037	0.048	0.043	0.055	0.051
Al2O3	20.916	21.096	20.366	20.921	20.305	20.302
FeO	31.603	30.867	31.043	31.244	30.908	31.020
MnO	0.219	0.193	0.196	0.235	0.234	0.203
MgO	11.181	11.490	11.436	11.122	11.420	11.484
CaO	0.029	0.026	0.034	0.043	0.019	0.019
Na2O	0.000	0.030	0.007	-0.019	-0.002	-0.033
K2O	0.011	0.013	0.045	0.015	0.033	0.008
F	0.027	-0.100	0.118	0.100	-0.072	0.072
Cl	0.018	0.025	0.026	0.024	0.024	0.021
Cr2O3	-0.004	0.002	0.001	0.000	0.005	-0.006
NiO	-0.018	0.021	0.014	-0.004	0.022	0.007
Total	88.546	88.525	88.464	88.445	87.875	88.219
Si	5.300	5.346	5.405	5.328	5.418	5.413
Al iv	2.700	2.654	2.595	2.672	2.582	2.587
Al vi	2.632	2.700	2.583	2.655	2.618	2.588
Ti	0.007	0.006	0.008	0.007	0.009	0.008
Cr	-0.001	0.000	0.000	0.000	0.001	-0.001
Fe+3	0.000	0.000	0.055	0.051	0.000	0.052
Fe+2	5.724	5.570	5.529	5.581	5.619	5.549
Mn	0.040	0.035	0.036	0.043	0.043	0.037
Mg	3.602	3.689	3.667	3.574	3.701	3.696
Ni	-0.003	0.004	0.002	-0.001	0.004	0.001
Ca	0.007	0.006	0.008	0.010	0.004	0.004
Na	0.000	0.025	0.006	-0.016	-0.002	-0.028
K	0.006	0.007	0.025	0.008	0.018	0.004
F	0.037	-0.136	0.161	0.136	-0.099	0.098
Cl	0.013	0.018	0.019	0.018	0.018	0.015
OH*	15.950	16.118	15.821	15.846	16.081	15.886
Total	36.013	36.043	35.918	35.913	36.016	35.911
XFe	0.614	0.602	0.604	0.612	0.603	0.602

Table 70

Locality	Blezard	Blezard	Blezard	Blezard	Blezard	Blezard
Sample and analysis	clf30_2_st2_chl6	clf30_2_st2_chl7	clf30_2_st2_chl8	clf30_2_st2_chl9	clf30_2_st2_chl10	clf30_2_st2_chl11
Mineral	Chlorite	Chlorite	Chlorite	Chlorite	Chlorite	Chlorite
SiO2	25.669	25.848	26.144	25.591	25.142	25.399
TiO2	0.036	0.034	0.040	0.041	0.036	0.021
Al2O3	21.207	21.220	20.289	20.074	19.470	20.595
FeO	28.093	28.608	28.036	27.611	27.779	26.957
MnO	0.391	0.345	0.354	0.341	0.390	0.384
MgO	13.598	13.524	13.950	13.444	13.259	13.963
CaO	0.236	0.279	0.267	0.193	0.185	0.292
Na2O	0.035	0.012	0.008	0.025	-0.005	-0.005
K2O	0.006	0.008	0.012	0.046	-0.003	0.014
F	0.421	0.114	-0.004	0.121	0.262	0.273
Cl	0.024	0.034	0.039	0.032	0.029	0.025
Cr2O3	0.006	0.018	0.014	0.021	0.002	0.007
NiO	-0.009	0.021	0.022	0.009	0.004	0.017
Total	89.710	90.064	89.171	87.549	86.550	87.943
Si	5.325	5.379	5.495	5.466	5.444	5.373
Al iv	2.675	2.621	2.505	2.534	2.556	2.627
Al vi	2.550	2.597	2.525	2.536	2.436	2.533
Ti	0.006	0.005	0.006	0.007	0.006	0.003
Cr	0.001	0.003	0.002	0.004	0.000	0.001
Fe+3	0.118	0.049	0.024	0.062	0.067	0.078
Fe+2	4.756	4.930	4.904	4.870	4.963	4.691
Mn	0.069	0.061	0.063	0.062	0.072	0.069
Mg	4.205	4.195	4.371	4.281	4.280	4.403
Ni	-0.002	0.004	0.004	0.002	0.001	0.003
Ca	0.052	0.062	0.060	0.044	0.043	0.066
Na	0.028	0.010	0.007	0.021	-0.004	-0.004
K	0.003	0.004	0.006	0.025	-0.002	0.008
F	0.552	0.150	-0.005	0.163	0.359	0.365
Cl	0.017	0.024	0.028	0.023	0.021	0.018
OH*	15.431	15.826	15.978	15.813	15.620	15.617
Total	35.787	35.920	35.972	35.913	35.861	35.851
XFe	0.537	0.543	0.530	0.535	0.540	0.520

Table 71

Locality	Sheppard	Sheppard	Sheppard	Sheppard	Sheppard	Sheppard
Sample and analysis	clf30_9_st3_chl7	clf30_9_st3_chl8	clf30_9_st3_chl9	clf30_9_st3_chl10	clf30_9_st3_chl11	clf30_9_st3_chl12
Mineral	Chlorite	Chlorite	Chlorite	Chlorite	Chlorite	Chlorite
SiO2	25.224	27.055	25.57	25.49	25.15	26.105
TiO2	0.066	0.031	0.007	0.06	0.071	0.009
Al2O3	19.878	18.411	19.4	20.268	20.204	17.841
FeO	30.696	32.085	31.64	31.218	31.007	31.555
MnO	0.561	0.671	0.669	0.59	0.559	0.625
MgO	11.172	11.287	10.633	11.263	10.936	10.727
CaO	0.067	0.125	0.129	0.075	0.149	0.174
Na2O	0.04	-0.015	0.002	0.014	0.007	0.052
K2O	0.008	0.022	0.006	0.02	0.013	0.052
F	0.066	0.037	0	0.037	0.082	-0.077
Cl	0.029	0.061	0.053	0.022	0.029	0.07
Cr2O3	0.01	0.002	0.009	0.01	0	0.008
NiO	0.009	-0.026	-0.025	-0.022	0.003	0.007
Total	87.825	89.747	88.091	89.043	88.211	87.148
Si	5.472	5.758	5.562	5.460	5.437	5.754
Al iv	2.528	2.242	2.438	2.540	2.563	2.246
Al vi	2.567	2.391	2.544	2.587	2.600	2.394
Ti	0.011	0.005	0.001	0.010	0.012	0.001
Cr	0.002	0.000	0.002	0.002	0.000	0.001
Fe+3	0.063	0.120	0.073	0.055	0.075	0.050
Fe+2	5.506	5.591	5.683	5.538	5.532	5.767
Mn	0.103	0.121	0.123	0.107	0.102	0.117
Mg	3.613	3.581	3.448	3.597	3.525	3.525
Ni	0.002	-0.004	-0.004	-0.004	0.001	0.001
Ca	0.016	0.029	0.030	0.017	0.035	0.041
Na	0.034	-0.012	0.002	0.012	0.006	0.044
K	0.004	0.012	0.003	0.011	0.007	0.029
F	0.091	0.050	0.000	0.050	0.112	-0.107
Cl	0.021	0.044	0.039	0.016	0.021	0.052
OH*	15.888	15.906	15.961	15.934	15.867	16.055
Total	35.919	35.833	35.904	35.930	35.893	35.971
XFe	0.607	0.615	0.625	0.609	0.614	0.623

Table 72

Locality	Creighton	Creighton	Creighton	Creighton	Creighton
Sample and analysis	clf1503_st1_chl1	clf1503_st1_chl2	clf1503_st1_chl2b	clf1503_st1_chl3	clf1503_st1_chl4
Mineral	Chlorite	Chlorite	Chlorite	Chlorite	Chlorite
SiO2	25.47	25.728	26.21	25.526	25.901
TiO2	0.059	0.07	0.059	0.06	0.052
Al2O3	20.918	20.712	21.341	20.615	21.152
FeO	24.885	24.996	25.012	24.545	25.078
MnO	0.167	0.198	0.19	0.195	0.198
MgO	15.192	15.226	15.498	15.276	15.559
CaO	0.069	0.019	0.064	0.038	0.026
Na2O	0.007	0.018	-0.007	0.026	-0.004
K2O	0.041	0.055	0.069	0.014	0.003
F	-0.085	0.095	0.189	0.103	0.032
Cl	0.018	0.015	0.019	0.017	0.02
Cr2O3	0.022	0.022	0.016	0.02	0.02
NiO	-0.005	0.007	-0.009	0.029	0.001
Total	86.758	87.161	88.651	86.464	88.038
Si	5.420	5.433	5.416	5.425	5.415
Al iv	2.580	2.567	2.584	2.575	2.585
Al vi	2.665	2.603	2.639	2.605	2.635
Ti	0.009	0.011	0.009	0.010	0.008
Cr	0.004	0.004	0.003	0.003	0.003
Fe+3	0.020	0.070	0.121	0.073	0.057
Fe+2	4.409	4.345	4.202	4.290	4.327
Mn	0.030	0.035	0.033	0.035	0.035
Mg	4.819	4.793	4.774	4.840	4.849
Ni	-0.001	0.001	-0.001	0.005	0.000
Ca	0.016	0.004	0.014	0.009	0.006
Na	0.006	0.015	-0.006	0.021	-0.003
K	0.022	0.030	0.036	0.008	0.002
F	-0.114	0.127	0.247	0.138	0.042
Cl	0.013	0.011	0.013	0.012	0.014
OH*	16.101	15.862	15.740	15.849	15.944
Total	35.999	35.910	35.824	35.899	35.919
XFe	0.479	0.479	0.475	0.474	0.475

Table 73

Creighton clf1503_st1_chl5 Chlorite	Creighton clf1503_st2_chl6 Chlorite	Creighton clf1503_st2_chl7 Chlorite	Creighton clf1503_st2_chl8 Chlorite	Creighton clf1503_st2_chl9 Chlorite	Creighton clf1503_st2_chl10 Chlorite
25.833	26.461	25.934	26.472	26.032	25.934
0.079	0.125	0.066	0.08	0.077	0.074
21.18	20.763	20.861	21.34	21.582	21.706
24.256	24.776	24.859	24.291	23.823	25.206
0.183	0.175	0.176	0.147	0.188	0.191
15.728	15.251	15.681	16.219	15.781	15.641
0.034	0.019	0.012	0.008	0.022	0.02
0.017	-0.028	0.039	0.008	0.015	-0.004
0.02	0.39	0.02	0.008	0.009	0.023
0.037	0.181	0.139	0.032	-0.088	0.031
0.013	0.032	0.017	0.002	0.017	0.011
0.041	0.016	0.014	0.014	0.008	0.023
-0.004	0.004	0.027	0.006	-0.011	-0.002
87.419	88.162	87.844	88.627	87.454	88.854
5.415	5.495	5.421	5.459	5.441	5.370
2.585	2.505	2.579	2.541	2.559	2.630
2.659	2.609	2.578	2.656	2.762	2.675
0.012	0.020	0.010	0.012	0.012	0.012
0.007	0.003	0.002	0.002	0.001	0.004
0.072	0.125	0.068	0.090	0.088	0.054
4.180	4.177	4.278	4.099	4.076	4.311
0.032	0.031	0.031	0.026	0.033	0.033
4.915	4.721	4.886	4.985	4.917	4.828
-0.001	0.001	0.005	0.001	-0.002	0.000
0.008	0.004	0.003	0.002	0.005	0.004
0.014	-0.023	0.032	0.006	0.012	-0.003
0.011	0.207	0.011	0.004	0.005	0.012
0.049	0.238	0.184	0.042	-0.116	0.041
0.009	0.023	0.012	0.001	0.012	0.008
15.942	15.740	15.804	15.957	16.104	15.952
35.910	35.874	35.904	35.884	35.909	35.929
0.464	0.477	0.471	0.457	0.459	0.475

Table 74

Locality	Kirkwood	Kirkwood	Kirkwood	Kirkwood	Kirkwood
Sample and analysis	clf3013_chl1_st2	clf3013_chl2_st2	clf3013_chl3_st2	clf3013_chl4_st2	clf3013_chl5_st2
Mineral	Chlorite	Chlorite	Chlorite	Chlorite	Chlorite
SiO2	23.579	23.615	23.488	34.458	24.001
TiO2	0.047	0.044	0.298	1.695	0.046
Al2O3	19.842	19.501	19.623	15.439	19.963
FeO	40.119	40.488	39.61	29.379	40.583
MnO	0.784	0.74	0.766	0.353	0.764
MgO	4.477	4.51	4.3	4.25	4.419
CaO	0.037	0.002	0.292	0.011	-0.006
Na2O	0.016	0.014	0.089	0.033	0.054
K2O	0.067	0.021	0.013	8.855	0.014
F	0.262	0.068	0.002	0.41	0.099
Cl	0.023	0.036	0.032	0.188	0.025
Cr2O3	-0.004	0.007	-0.005	-0.001	-0.001
NiO	0.008	-0.016	-0.004	-0.015	0.009
Total	89.257	89.031	88.505	95.055	89.97
Si	5.308	5.361	5.350	6.727	5.370
Al iv	2.692	2.639	2.650	1.273	2.630
Al vi	2.600	2.587	2.627	2.461	2.650
Ti	0.008	0.008	0.051	0.249	0.008
Cr	-0.001	0.001	-0.001	0.000	0.000
Fe+3	0.074	0.016	0.033	0.190	0.059
Fe+2	7.478	7.671	7.513	4.607	7.534
Mn	0.149	0.142	0.148	0.058	0.145
Mg	1.502	1.526	1.460	1.237	1.474
Ni	0.001	-0.003	-0.001	-0.002	0.002
Ca	0.009	0.000	0.071	0.002	-0.001
Na	0.014	0.012	0.079	0.025	0.047
K	0.038	0.012	0.008	4.410	0.008
F	0.373	0.098	0.003	0.506	0.140
Cl	0.018	0.028	0.025	0.124	0.019
OH*	15.609	15.875	15.972	15.369	15.841
Total	35.874	35.973	35.987	37.237	35.924
XFe	0.834	0.834	0.838	0.795	0.837

Table 75

Locality	Whitson Lake	Whitson Lake	Whitson Lake	Whitson Lake	Whitson Lake	Whitson Lake	Whitson Lake
Sample and analysis	wclf1508_st1.1_chl1	wclf1508_st1.1_chl2	wclf1508_st1.1_chl3	wclf1508_st1.1_chl4	wclf1508_st1.1_chl5	wclf1508_st1.1_chl6	wclf1508_st1.1_chl7
Mineral	Chlorite	Chlorite	Chlorite	Chlorite	Chlorite	Chlorite	Chlorite
SiO2	24.899	31.358	26.765	25.777	24.687	25.284	24.221
TiO2	0.041	0.987	0.381	0.020	0.045	0.035	0.080
Al2O3	19.265	16.736	17.997	19.900	19.215	18.530	18.820
FeO	35.764	30.234	34.191	35.903	35.854	34.980	35.367
MnO	0.584	0.350	0.500	0.565	0.542	0.517	0.519
MgO	8.100	6.607	7.636	8.392	7.921	8.204	7.764
CaO	0.062	0.041	0.055	0.064	0.037	0.069	0.051
Na2O	0.005	0.038	-0.017	0.029	-0.002	0.017	0.011
K2O	0.030	5.822	1.790	0.028	0.062	0.008	0.153
F	0.087	0.179	0.111	0.096	0.066	0.055	0.167
Cl	0.008	0.068	0.029	0.018	0.014	0.017	0.015
Cr2O3	0.002	-0.005	0.002	-0.002	0.015	-0.002	0.007
NiO	-0.001	0.000	0.010	0.013	-0.005	0.007	0.030
Total	88.846	92.415	89.450	90.802	88.449	87.719	87.203
Si	5.493	6.378	5.802	5.530	5.481	5.625	5.454
Al iv	2.507	1.622	2.198	2.470	2.519	2.375	2.546
Al vi	2.514	2.520	2.453	2.579	2.519	2.498	2.467
Ti	0.007	0.151	0.062	0.003	0.008	0.006	0.014
Cr	0.000	-0.001	0.000	0.000	0.003	0.000	0.001
Fe^{+3}	0.049	0.092	0.053	0.102	0.037	0.100	0.032
Fe^{+2}	6.550	5.051	6.146	6.339	6.621	6.408	6.627
Mn	0.109	0.060	0.092	0.103	0.102	0.097	0.099
Mg	2.664	2.003	2.468	2.684	2.622	2.721	2.606
Ni	0.000	0.000	0.002	0.002	-0.001	0.001	0.005
Ca	0.015	0.009	0.013	0.015	0.009	0.016	0.012
Na	0.004	0.030	-0.014	0.024	-0.002	0.015	0.010
K	0.017	3.021	0.990	0.015	0.035	0.005	0.088
F	0.121	0.230	0.152	0.130	0.093	0.077	0.238
Cl	0.006	0.047	0.021	0.013	0.011	0.013	0.011
OH*	15.873	15.723	15.826	15.857	15.897	15.910	15.751
Total	35.928	36.936	36.263	35.866	35.952	35.867	35.961
XFe	0.712	0.720	0.715	0.706	0.717	0.705	0.719

Table 76

Locality	Copper Cliff (4370 lvl)	Copper Cliff (4370 lvl)	Copper Cliff (4370 lvl)	Copper Cliff (4370 lvl)	Copper Cliff (4370 lvl)	Copper Cliff (4370 lvl)
Sample and analysis	pcl3_chl1	pcl3_chl2	pcl3_chl3	pcl3_chl4	pcl3_chl5	pcl3_chl6
Mineral	Chlorite	Chlorite	Chlorite	Chlorite	Chlorite	Chlorite
SiO2	26.187	27.316	26.165	26.286	27.25	27.044
TiO2	0.046	0.04	0.052	0.042	0.081	0.075
Al2O3	21.24	21.645	21.054	19.971	21.575	21.32
FeO	27.241	26.767	26.742	26.742	27.132	26.664
MnO	0.4	0.408	0.355	0.348	0.354	0.367
MgO	14.247	14.96	14.406	14.641	14.487	14.652
CaO	0.019	0.035	0.04	0.026	0.011	0.013
Na2O	-0.008	-0.004	0.024	0.011	0.016	0.026
K2O	0.016	0.023	0.162	0.027	0.243	0.251
F	-0.038	0.076	0.228	0.117	0.169	0.009
Cl	0.019	0.04	0.026	0.013	0.027	0.022
Cr2O3	0.063	0.064	0.035	0.068	0.099	0.118
NiO	0.133	0.157	0.128	0.158	0.166	0.165
Total	89.565	91.527	89.418	88.45	91.609	90.726
Si	5.447	5.505	5.418	5.523	5.493	5.515
Al iv	2.553	2.495	2.582	2.477	2.507	2.485
Al vi	2.658	2.667	2.586	2.483	2.650	2.657
Ti	0.007	0.006	0.008	0.007	0.012	0.012
Cr	0.010	0.010	0.006	0.011	0.016	0.019
Fe+3	0.059	0.147	0.096	0.066	0.148	0.094
Fe+2	4.679	4.365	4.536	4.633	4.426	4.454
Mn	0.070	0.070	0.062	0.062	0.060	0.063
Mg	4.417	4.495	4.447	4.585	4.353	4.454
Ni	0.022	0.025	0.021	0.027	0.027	0.027
Ca	0.004	0.008	0.009	0.006	0.002	0.003
Na	-0.006	-0.003	0.019	0.009	0.013	0.021
K	0.008	0.012	0.086	0.014	0.125	0.131
F	-0.050	0.097	0.299	0.155	0.215	0.012
Cl	0.013	0.027	0.018	0.009	0.018	0.015
OH*	16.037	15.876	15.683	15.835	15.766	15.973
Total	35.931	35.801	35.876	35.903	35.832	35.934
XFe	0.518	0.501	0.510	0.506	0.512	0.505

Table 77

Locality	Copper Cliff (4220 lvl)	Copper Cliff (4220 lvl)	Copper Cliff (4220 lvl)	Copper Cliff (4220 lvl)	Copper Cliff (4220 lvl)	Copper Cliff (4220 lvl)
Sample and analysis	pcl9_chl1	pcl9_chl2	pcl9_chl3	pcl9_chl4	pcl9_chl5	pcl9_chl6
Mineral	Clorite	Clorite	Clorite	Clorite	Clorite	Clorite
SiO2	26.266	24.626	26.276	25.780	25.503	25.509
TiO2	0.041	0.033	0.054	0.027	0.050	0.038
Al2O3	20.881	20.124	20.601	20.818	20.656	20.659
FeO	29.909	29.936	29.668	29.704	29.587	29.303
MnO	0.476	0.441	0.415	0.483	0.378	0.435
MgO	12.788	11.837	12.636	12.286	12.237	12.401
CaO	0.021	0.019	0.028	0.038	0.005	0.019
Na2O	0.033	0.018	0.040	0.118	0.027	0.030
K2O	0.098	0.040	0.060	0.035	0.063	0.009
F	0.123	0.117	0.178	0.045	0.118	0.034
Cl	0.026	0.033	0.041	0.041	0.035	0.022
Cr2O3	0.033	0.035	0.021	0.035	0.025	0.007
NiO	0.027	0.042	0.036	0.055	0.065	0.028
Total	90.723	87.300	90.056	89.465	88.749	88.494
Si	5.453	5.363	5.482	5.439	5.420	5.437
Al iv	2.547	2.637	2.518	2.561	2.580	2.563
Al vi	2.581	2.540	2.574	2.631	2.613	2.637
Ti	0.006	0.005	0.008	0.004	0.008	0.006
Cr	0.005	0.006	0.003	0.006	0.004	0.001
Fe+3	0.071	0.009	0.115	0.051	0.078	0.062
Fe+2	5.122	5.444	5.061	5.191	5.181	5.161
Mn	0.084	0.081	0.073	0.086	0.068	0.079
Mg	3.958	3.843	3.930	3.864	3.877	3.940
Ni	0.005	0.007	0.006	0.009	0.011	0.005
Ca	0.005	0.004	0.006	0.009	0.001	0.004
Na	0.027	0.015	0.032	0.097	0.022	0.025
K	0.052	0.022	0.032	0.019	0.034	0.005
F	0.162	0.161	0.235	0.060	0.159	0.046
Cl	0.018	0.024	0.029	0.029	0.025	0.016
OH*	15.820	15.814	15.736	15.911	15.816	15.938
Total	35.915	35.978	35.842	35.967	35.898	35.925
XFe	0.568	0.587	0.568	0.576	0.576	0.570

Amphiboles

Table 78. kpgmd 12

Locality	Garson Mine (5200 lvl)	Garson Mine (5200 lvl)	Garson Mine (5200 lvl)	Garson Mine (5200 lvl)
Sample and analysis	kpgmd12-33 / 1 .	kpgmd12-34 / 1 .	kpgmd12-35 / 1 .	kpgmd12-36 / 1 .
Mineral	Amphibole	Amphibole	Amphibole	Amphibole
SiO2	50.550	47.430	46.182	52.902
TiO2	0.170	0.334	0.318	0.058
Al2O3	4.973	8.529	9.148	1.845
FeO	12.862	14.231	14.347	11.875
MnO	0.298	0.300	0.291	0.292
MgO	14.558	12.657	12.174	16.552
CaO	12.313	12.147	12.130	12.625
Na2O	0.600	0.918	1.037	0.170
K2O	0.091	0.174	0.169	0.013
Cr2O3	0.117	0.188	0.079	0.054
NiO	0.035	0.014	0.026	0.041
Cl	0.005	0.000	0.007	0.013
Total	96.572	96.921	95.906	96.439
Si	7.353	6.935	6.847	7.637
Al_{iv}	0.647	1.065	1.153	0.314
Al_{vi}	0.206	0.404	0.446	0.000
Ti	0.019	0.037	0.035	0.006
Cr	0.013	0.022	0.009	0.006
Fe^{+3}	0.366	0.468	0.443	0.437
Fe^{+2}	1.198	1.272	1.336	0.996
Mn	0.037	0.037	0.037	0.036
Mg	3.157	2.759	2.691	3.562
Ni	0.004	0.002	0.003	0.005
Ca	1.919	1.903	1.927	1.953
Na	0.169	0.260	0.298	0.048
K	0.017	0.032	0.032	0.002
OH*	1.999	2.000	1.998	1.997
Cl	0.001	0.000	0.002	0.003
Total	17.105	17.195	17.257	17.003
X_{Mg}	0.725	0.684	0.668	0.781
X_{Fe}	0.275	0.316	0.332	0.219
$(Na+K)_{(A)}$	0.105	0.195	0.257	0.003
$Fe^{+3}/(Fe^{+3}+Al_{vi})$	0.641	0.537	0.498	1.000

Table 79. kpgmd13

Locality	Garson Mine (5200 lvl)	Garson Mine (5200 lvl)	Garson Mine (5200 lvl)	Garson Mine (5200 lvl)	Garson Mine (5200 lvl)	Garson Mine (5200 lvl)
Sample and analysis	25 / 1 .	26 / 1 .	27 / 1 .	28 / 1 .	29 / 1 .	30 / 1 .
Mineral	Amphibole	Amphibole	Amphibole	Amphibole	Amphibole	Amphibole
SiO2	54.855	53.942	47.478	53.673	50.318	50.240
TiO2	0.045	0.041	0.842	0.037	0.521	0.412
Al2O3	1.383	1.879	7.293	1.978	4.836	4.954
FeO	11.046	11.682	14.746	12.111	11.655	13.109
MnO	0.321	0.320	0.318	0.382	0.295	0.343
MgO	17.159	16.535	12.919	16.230	15.952	14.649
CaO	12.495	12.416	10.770	12.220	12.275	12.395
Na2O	0.209	0.244	0.669	0.405	0.566	0.553
K2O	0.016	0.030	1.588	0.031	0.384	0.381
Cr2O3	0.116	0.433	0.573	0.505	0.112	0.136
NiO	0.020	0.029	0.041	0.039	0.033	0.039
Cl	0.023	0.020	0.148	0.039	0.123	0.119
Total	97.688	97.570	97.386	97.650	97.068	97.329
Si	7.775	7.685	6.931	7.658	7.244	7.288
Al_{iv}	0.225	0.315	1.069	0.333	0.756	0.712
Al_{vi}	0.006	0.001	0.186	0.000	0.064	0.135
Ti	0.005	0.004	0.092	0.004	0.056	0.045
Cr	0.013	0.049	0.066	0.057	0.013	0.016
Fe^{+3}	0.341	0.393	0.779	0.432	0.551	0.393
Fe^{+2}	0.969	0.999	1.022	1.013	0.852	1.197
Mn	0.039	0.039	0.039	0.046	0.036	0.042
Mg	3.626	3.512	2.811	3.452	3.423	3.168
Ni	0.002	0.003	0.005	0.004	0.004	0.005
Ca	1.897	1.895	1.684	1.868	1.893	1.926
Na	0.057	0.067	0.189	0.112	0.158	0.155
K	0.003	0.005	0.296	0.006	0.070	0.071
OH*	1.994	1.995	1.963	1.991	1.970	1.971
Cl	0.006	0.005	0.037	0.009	0.030	0.029
Total	16.958	16.968	17.170	16.986	17.122	17.152
X_{Mg}	0.789	0.778	0.733	0.773	0.801	0.726
X_{Fe}	0.211	0.222	0.267	0.227	0.199	0.274
$(Na+K)_{(A)}$	0.003	0.005	0.296	0.006	0.122	0.152
$Fe^{+3}/(Fe^{+3}+Al_{vi})$	0.982	0.998	0.808	1.000	0.895	0.745

Table 80. kpgmd14

Locality	Garson Mine (5200 lvl)	Garson Mine (5200 lvl	Garson Mine (5200 lvl)	Garson Mine (5200 lvl)	Garson Mine (5200 lvl)
Sample and analysis	kpgmd14-10 / 1 .	kpgmd14-11 / 1 .	kpgmd14-12 / 1 .	kpgmd14-13 / 1 .	kpgmd14-14 / 1 .
Mineral	Amphibole	Amphibole	Amphibole	Amphibole	Amphibole
SiO2	43.071	43.8375	40.5208	41.263	41.8588
TiO2	0.2674	0.2362	0.3004	0.2736	0.3112
Al2O3	13.0983	11.7542	15.8647	15.0872	14.8697
FeO	18.6701	19.1862	19.6659	19.686	19.3765
MnO	0.2963	0.2999	0.3063	0.2848	0.2853
MgO	8.0846	8.4688	6.2405	6.6328	6.9609
CaO	11.9804	11.9502	11.7918	11.7958	11.7271
Na2O	1.2538	1.0904	1.485	1.2376	1.3989
K2O	0.3578	0.4319	0.617	0.515	0.5369
Cr2O3	0.0724	0.1363	0.126	0.119	0.1384
NiO	0.0703	0.0542	0.0445	0.064	0.0588
Cl	0.1317	0.156	0.345	0.12	0.3147
Total	97.3541	97.6018	97.3079	97.0788	97.8372
Si	6.455	6.555	6.155	6.238	6.284
Al_{iv}	1.545	1.445	1.845	1.762	1.716
Al_{vi}	0.769	0.626	0.995	0.927	0.915
Ti	0.030	0.027	0.034	0.031	0.035
Cr	0.009	0.016	0.015	0.014	0.016
Fe^{+3}	0.427	0.523	0.372	0.475	0.432
Fe^{+2}	1.913	1.876	2.126	2.014	2.000
Mn	0.038	0.038	0.039	0.036	0.036
Mg	1.806	1.888	1.413	1.495	1.558
Ni	0.008	0.007	0.005	0.008	0.007
Ca	1.924	1.914	1.919	1.911	1.886
Na	0.364	0.316	0.437	0.363	0.407
K	0.068	0.082	0.120	0.099	0.103
OH*	1.967	1.960	1.911	1.969	1.920
Cl	0.033	0.040	0.089	0.031	0.080
Total	17.357	17.313	17.476	17.373	17.396
X_{Mg}	0.486	0.502	0.399	0.426	0.438
X_{Fe}	0.514	0.498	0.601	0.574	0.562
$(Na+K)_{(A)}$	0.357	0.313	0.476	0.373	0.396
$Fe^{+3}/(Fe^{+3}+Al_{vi})$	0.357	0.455	0.272	0.339	0.321

Table 81.CLF 38A

Locality	Creighton	Creighton	Creighton	Creighton	Creighton
Sample and analysis	Clf38a-1.1	Clf38a-1.2	Clf38a-1.3	Clf38a-1.4	Clf38a-1.5
Mineral	Amphibole	Amphibole	Amphibole	Amphibole	Amphibole
SiO2	46.500	43.690	43.240	41.550	44.310
TiO2	0.270	0.260	0.200	0.160	0.240
Al2O3	11.310	13.690	15.340	14.600	13.850
FeO	21.990	22.200	22.210	21.430	22.300
MnO	0.380	0.360	0.410	0.290	0.420
MgO	8.350	6.910	6.520	7.170	7.120
CaO	11.980	12.250	12.020	11.530	11.980
Na2O	1.510	1.630	1.710	1.410	1.670
K2O	0.230	0.320	0.300	0.350	0.260
Cr2O3	-0.020	0.020	0.020	0.010	-0.020
NiO	0.020	0.010	-0.030	0.040	0.050
Total	102.520	101.340	101.940	98.540	102.180
Si	6.629	6.366	6.239	6.154	6.368
Al iv	1.371	1.634	1.761	1.846	1.632
Al vi	0.529	0.717	0.847	0.702	0.714
Ti	0.029	0.028	0.022	0.018	0.026
Cr	-0.002	0.002	0.002	0.001	-0.002
Fe+3	0.668	0.512	0.619	0.977	0.666
Fe+2	1.954	2.193	2.061	1.678	2.014
Mn	0.046	0.044	0.050	0.036	0.051
Mg	1.775	1.501	1.402	1.583	1.525
Ni	0.002	0.001	-0.003	0.005	0.006
Ca	1.830	1.912	1.858	1.830	1.845
Na	0.417	0.461	0.478	0.405	0.465
K	0.042	0.059	0.055	0.066	0.048
OH*	2.000	2.000	2.000	2.000	2.000
Total	17.289	17.432	17.392	17.301	17.358
X_{Mg}	0.476	0.406	0.405	0.485	0.431
X_{Fe}	0.524	0.594	0.595	0.515	0.569
$(Na+K)_{(A)}$	0.289	0.432	0.392	0.301	0.358
$Fe^{+3}/(Fe^{+3}+Al_{vi})$	0.558	0.417	0.422	0.582	0.483

Table .RAR KPCM09

Locality	Creighton Mine (7840 lvl)	Creighton Mine (7840 lvl)	Creighton Mine (7840 lvl)	Creighton Mine (7840 lvl)
Sample and analysis	kpcm09-36 / 1 .	kpcm09-37 / 1 .	kpcm09-38 / 1 .	kpcm09-39 / 1 .
Mineral	Amphibole	Amphibole	Amphibole	Amphibole
SiO2	48.265	43.797	46.818	51.183
TiO2	0.196	0.177	0.299	0.115
Al2O3	7.000	7.277	7.648	3.161
FeO	17.656	22.526	18.031	16.082
MnO	0.371	0.334	0.377	0.386
MgO	11.227	10.188	10.558	13.385
CaO	12.431	11.492	12.338	12.555
Na2O	0.673	0.696	0.794	0.291
K2O	0.376	0.407	0.486	0.169
Cr2O3	0.114	0.092	0.055	0.072
NiO	0.034	0.079	0.037	0.034
Cl	0.067	0.090	0.074	0.023
Total	98.410	97.153	97.515	97.456
Si	7.082	6.548	6.974	7.492
Al_{iv}	0.918	1.282	1.026	0.508
Al_{vi}	0.293	0.000	0.317	0.038
Ti	0.022	0.020	0.033	0.013
Cr	0.013	0.011	0.006	0.008
Fe^{+3}	0.398	1.610	0.375	0.384
Fe^{+2}	1.768	1.206	1.871	1.584
Mn	0.046	0.042	0.048	0.048
Mg	2.456	2.271	2.345	2.921
Ni	0.004	0.009	0.004	0.004
Ca	1.954	1.841	1.969	1.969
Na	0.191	0.202	0.229	0.082
K	0.070	0.078	0.092	0.032
OH*	1.983	1.977	1.981	1.994
Cl	0.017	0.023	0.019	0.006
Total	17.216	17.120	17.291	17.083
X_{Mg}	0.581	0.653	0.556	0.648
X_{Fe}	0.419	0.347	0.444	0.352
$(Na+K)_{(A)}$	0.216	0.120	0.291	0.083
$Fe^{+3}/(Fe^{+3}+Al_{vi})$	0.576	1.000	0.542	0.911

Table 82. RAR KPCM09 (Continue)

Creighton Mine (7840 lvl) kpcm09-40 / 1 . Amphibole	Creighton Mine (7840 lvl) kpcm09-49 / 1 . Amphibole	Creighton Mine (7840 lvl) kpcm09-50 / 1 . Amphibole	Creighton Mine (7840 lvl) kpcm09-51 / 1 . Amphibole
46.073	45.427	43.275	45.111
0.246	0.370	0.366	0.315
8.264	9.158	11.295	9.973
18.363	19.017	19.973	19.059
0.377	0.398	0.361	0.377
10.316	9.617	8.310	9.094
12.265	12.202	12.115	12.255
0.822	0.950	1.035	0.909
0.479	0.636	0.828	0.702
0.101	0.029	0.021	0.042
0.019	0.005	0.018	0.028
0.088	0.092	0.152	0.119
97.412	97.900	97.749	97.985
6.873	6.780	6.520	6.743
1.127	1.220	1.480	1.257
0.326	0.391	0.525	0.500
0.028	0.042	0.042	0.035
0.012	0.003	0.002	0.005
0.485	0.444	0.497	0.359
1.806	1.929	2.019	2.023
0.048	0.050	0.046	0.048
2.294	2.140	1.866	2.026
0.002	0.001	0.002	0.003
1.960	1.951	1.956	1.963
0.238	0.275	0.302	0.264
0.091	0.121	0.159	0.134
1.978	1.977	1.961	1.970
0.022	0.023	0.039	0.030
17.289	17.347	17.417	17.360
0.560	0.526	0.480	0.500
0.440	0.474	0.520	0.500
0.289	0.347	0.417	0.360
0.598	0.532	0.486	0.418

Table 83

Locality	Creighton Mine (7840 lvl)	Creighton Mine (7840 lvl)	Creighton Mine (7840 lvl)	Creighton Mine (7840 lvl)	Creighton Mine (7840 lvl)
Sample and analysis	Pl13-26 / 1 .	Pl13-30 / 1 .	Pl13-31 / 1 .	Pl13-32 / 1 .	Pl13-33 / 1 .
Mineral	Amphibole	Amphibole	Amphibole	Amphibole	Amphibole
SiO2	38.464	38.649	38.445	38.367	38.352
TiO2	0.560	0.414	0.590	0.467	0.607
Al2O3	14.379	14.116	14.245	15.163	14.198
FeO	25.539	25.081	25.170	23.948	25.188
MnO	0.363	0.374	0.371	0.343	0.379
MgO	4.119	4.306	4.133	3.992	4.225
CaO	11.454	11.505	11.486	11.522	11.460
Na2O	1.483	1.415	1.453	1.262	1.415
K2O	1.215	1.204	1.220	1.167	1.184
Cr2O3	0.024	-0.001	0.015	-0.001	0.013
NiO	0.008	0.008	0.008	0.011	0.015
Cl	0.596	0.574	0.554	0.563	0.569
Total	98.201	97.643	97.690	96.803	97.606
Si	5.977	6.031	6.006	6.019	5.989
Al_{iv}	2.023	1.969	1.994	1.981	2.011
Al_{vi}	0.610	0.627	0.628	0.823	0.602
Ti	0.065	0.049	0.069	0.055	0.071
Cr	0.003	0.000	0.002	0.000	0.002
Fe^{+3}	0.778	0.731	0.698	0.557	0.766
Fe^{+2}	2.541	2.542	2.590	2.585	2.524
Mn	0.048	0.049	0.049	0.046	0.050
Mg	0.954	1.002	0.962	0.934	0.983
Ni	0.001	0.001	0.001	0.001	0.002
Ca	1.907	1.923	1.922	1.937	1.917
Na	0.447	0.428	0.440	0.384	0.428
K	0.241	0.240	0.243	0.234	0.236
OH*	1.843	1.848	1.853	1.850	1.849
Cl	0.157	0.152	0.147	0.150	0.151
Total	17.595	17.591	17.606	17.554	17.582
X_{Mg}	0.273	0.283	0.271	0.265	0.280
X_{Fe}	0.727	0.717	0.729	0.735	0.720
$(Na+K)_{(A)}$	0.595	0.591	0.606	0.554	0.582
$Fe^{+3}/(Fe^{+3}+Al_{vi})$	0.560	0.538	0.526	0.404	0.560

Table 84

Creighton Mine (7840 lvl) Pl13-34 / 1 . Amphibole	Creighton Mine (7840 lvl) Pl13-36 / 1 . Amphibole	Creighton Mine (7840 lvl) Pl13-37 / 1 . Amphibole	Creighton Mine (7840 lvl) Pl13-38 / 1 . Amphibole	Creighton Mine (7840 lvl) Pl13-39 / 1 . Amphibole	Creighton Mine (7840 lvl) Pl13-40 / 1 . Amphibole
38.468	38.747	38.878	39.868	38.797	38.257
0.590	0.471	0.601	0.751	0.452	0.584
14.869	15.240	14.941	13.806	14.668	14.457
24.533	24.850	24.599	24.673	25.267	25.136
0.376	0.341	0.351	0.365	0.370	0.359
4.057	3.961	4.047	4.555	4.084	4.104
11.498	11.557	11.651	11.546	11.373	11.393
1.277	1.294	1.326	1.189	1.598	1.590
1.224	1.045	1.164	1.003	1.223	1.244
0.019	0.019	0.028	0.012	0.000	0.011
-0.003	-0.006	0.005	0.002	-0.002	-0.001
0.566	0.586	0.589	0.475	0.587	0.578
97.473	98.104	98.180	98.245	98.417	97.712
6.001	5.993	6.026	6.137	6.008	5.979
1.999	2.007	1.974	1.863	1.992	2.021
0.735	0.771	0.756	0.642	0.684	0.641
0.069	0.055	0.070	0.087	0.053	0.069
0.002	0.002	0.003	0.001	0.000	0.001
0.650	0.699	0.576	0.685	0.708	0.696
2.551	2.515	2.613	2.492	2.564	2.589
0.050	0.045	0.046	0.048	0.049	0.048
0.944	0.913	0.935	1.045	0.943	0.956
0.000	-0.001	0.001	0.000	0.000	0.000
1.922	1.915	1.935	1.904	1.887	1.908
0.386	0.388	0.398	0.355	0.480	0.482
0.243	0.206	0.230	0.197	0.242	0.248
1.850	1.846	1.845	1.876	1.846	1.847
0.150	0.154	0.155	0.124	0.154	0.153
17.552	17.510	17.564	17.456	17.608	17.637
0.270	0.266	0.264	0.296	0.269	0.270
0.730	0.734	0.736	0.704	0.731	0.730
0.552	0.510	0.564	0.456	0.608	0.637
0.469	0.475	0.432	0.516	0.509	0.521

Table 85

Creighton Mine (7840 lvl) Pl13-41 / 1 . Amphibole	Creighton Mine (7840 lvl) Pl13-42 / 1 . Amphibole
39.002	38.963
0.618	0.619
14.701	14.167
25.052	25.388
0.360	0.362
4.074	4.249
11.521	11.482
1.326	1.345
1.216	1.186
0.000	0.009
0.002	0.020
0.550	0.556
98.421	98.346
6.027	6.028
1.973	1.972
0.705	0.612
0.072	0.072
0.000	0.001
0.673	0.770
2.565	2.515
0.047	0.047
0.939	0.980
0.000	0.002
1.907	1.903
0.397	0.403
0.240	0.234
1.856	1.854
0.144	0.146
17.544	17.541
0.268	0.280
0.732	0.720
0.544	0.541
0.488	0.557

Table 86

Locality	Creighton Mine (7840 lvl)	Creighton Mine (7840 lvl)	Creighton Mine (7840 lvl)	Creighton Mine (7840 lvl)	Creighton Mine (7840 lvl)
Sample and analysis	PL17-11 / 1 .	PL17-12 / 1 .	PL17-13 / 1 .	PL17-14 / 1 .	PL17-23 / 1 .
Mineral	Amphibole	Amphibole	Amphibole	Amphibole	Amphibole
SiO2	50.842	48.522	46.306	48.533	51.476
TiO2	0.185	0.31	0.357	0.354	0.277
Al2O3	4.776	8.562	9.721	7.65	4.944
FeO	14.379	16.077	16.678	15.252	14.451
MnO	0.357	0.353	0.326	0.344	0.39
MgO	13.758	11.746	10.5	12.213	13.828
CaO	12.233	12.11	12.142	11.927	12.069
Na2O	0.529	0.994	0.912	0.92	0.55
K2O	0.116	0.288	0.348	0.262	0.187
Cr2O3	0.014	0.01	0.037	0.034	0.05
NiO	-0.003	0.017	0.038	0.082	0.008
Cl	0.041	0.075	0.1	0.059	0.018
F	0.055	0.272	0.245	0.222	0.124
Total	97.282	99.336	97.71	97.852	98.372
Si	7.389	6.999	6.843	7.076	7.387
Al_{iv}	0.611	1.001	1.157	0.924	0.613
Al_{vi}	0.207	0.455	0.536	0.391	0.223
Ti	0.020	0.034	0.040	0.039	0.030
Cr	0.002	0.001	0.004	0.004	0.006
Fe^{+3}	0.383	0.403	0.365	0.416	0.425
Fe^{+2}	1.365	1.536	1.696	1.444	1.309
Mn	0.044	0.043	0.041	0.042	0.047
Mg	2.981	2.526	2.313	2.655	2.958
Ni	0.000	0.002	0.005	0.010	0.001
Ca	1.905	1.872	1.922	1.863	1.856
Na	0.149	0.278	0.261	0.260	0.153
K	0.022	0.053	0.066	0.049	0.034
OH*	1.965	1.858	1.860	1.883	1.939
F	0.025	0.124	0.115	0.102	0.056
Cl	0.010	0.018	0.025	0.015	0.004
Total	17.075	17.203	17.249	17.172	17.043
X_{Mg}	0.686	0.622	0.577	0.648	0.693
X_{Fe}	0.314	0.378	0.423	0.352	0.307
$(Na+K)_{(A)}$	0.075	0.203	0.249	0.172	0.043
$Fe^{+3}/(Fe^{+3}+Al_{vi})$	0.650	0.470	0.405	0.516	0.656

Table 87

Creighton Mine (7840 lvl) PL17-24 / 1 . Amphibole	Creighton Mine (7840 lvl) PL17-25 / 1 . Amphibole	Creighton Mine (7840 lvl) PL17-26 / 1 . Amphibole	Creighton Mine (7840 lvl) PL17-27 / 1 . Amphibole	Creighton Mine (7840 lvl) PL17-28 / 1 . Amphibole
50.615	49.76	52.631	49.178	47.158
0.396	0.336	0.103	0.324	0.349
6.29	6.339	3.475	8.29	10.075
15.219	15.116	13.778	16.355	16.593
0.327	0.333	0.293	0.365	0.369
13.257	12.752	14.712	12.069	11.161
12.289	12.222	12.243	12.13	12.062
0.685	0.65	0.375	0.923	1.142
0.25	0.266	0.057	0.297	0.378
0.053	0.032	0.037	0.016	-0.003
0.052	0.051	-0.021	0.009	0.046
0.038	0.039	0.015	0.072	0.107
0.148	0.058	0.21	-0.115	0.407
99.619	97.954	97.908	99.913	99.844
7.217	7.229	7.559	7.011	6.800
0.783	0.771	0.441	0.989	1.200
0.274	0.314	0.147	0.404	0.512
0.042	0.037	0.011	0.035	0.038
0.006	0.004	0.004	0.002	0.000
0.429	0.342	0.385	0.500	0.497
1.385	1.494	1.269	1.450	1.504
0.039	0.041	0.036	0.044	0.045
2.818	2.762	3.150	2.565	2.399
0.006	0.006	-0.002	0.001	0.005
1.877	1.902	1.884	1.853	1.863
0.189	0.183	0.104	0.255	0.319
0.045	0.049	0.010	0.054	0.070
1.924	1.964	1.901	2.034	1.788
0.067	0.027	0.095	-0.052	0.186
0.009	0.010	0.004	0.017	0.026
17.112	17.135	16.999	17.162	17.252
0.670	0.649	0.713	0.639	0.615
0.330	0.351	0.287	0.361	0.385
0.112	0.135	0.010	0.162	0.252
0.611	0.521	0.724	0.553	0.493

Table 88

Locality	Creighton Mine (7840 lvl)	Creighton Mine (7840 lvl)	Creighton Mine (7840 lvl)
Sample and analysis	Pl18-47 / 1 .	Pl18-48 / 1 .	Pl18-49 / 1 .
Mineral	Amphibole	Amphibole	Amphibole
SiO2	46.677	44.765	44.712
TiO2	0.353	0.460	0.466
Al2O3	8.600	9.757	10.363
FeO	16.747	16.796	17.503
MnO	0.330	0.293	0.297
MgO	11.174	10.730	10.151
CaO	12.122	11.902	11.826
Na2O	0.958	1.158	1.231
K2O	0.303	0.384	0.435
Cr2O3	0.033	0.026	0.029
NiO	0.033	0.028	0.042
Cl	0.085	0.104	0.127
Total	97.413	96.403	97.181
Si	6.890	6.693	6.654
Al_{iv}	1.110	1.307	1.346
Al_{vi}	0.386	0.413	0.472
Ti	0.039	0.052	0.052
Cr	0.004	0.003	0.003
Fe^{+3}	0.477	0.565	0.558
Fe^{+2}	1.590	1.535	1.620
Mn	0.041	0.037	0.037
Mg	2.459	2.392	2.252
Ni	0.004	0.003	0.005
Ca	1.917	1.907	1.886
Na	0.274	0.336	0.355
K	0.057	0.073	0.083
OH*	1.979	1.974	1.968
Cl	0.021	0.026	0.032
Total	17.248	17.316	17.323
X_{Mg}	0.607	0.609	0.582
X_{Fe}	0.393	0.391	0.418
$(Na+K)_{(A)}$	0.248	0.316	0.323
$Fe^{+3}/(Fe^{+3}+Al_{vi})$	0.553	0.578	0.542

Table 89

Creighton Mine (7840 lvl) Pl18-50 / 1 . Amphibole	Creighton Mine (7840 lvl) Pl18-51 / 1 . Amphibole	Creighton Mine (7840 lvl) Pl18-52 / 1 . Amphibole	Creighton Mine (7840 lvl) Pl18-59 / 1 . Amphibole
46.202	45.374	45.615	46.360
0.347	0.439	0.399	0.400
8.673	9.398	9.201	9.172
16.678	16.994	16.737	16.781
0.289	0.283	0.274	0.284
11.321	10.863	11.089	11.104
11.946	11.930	11.913	11.939
1.014	1.121	1.110	1.148
0.299	0.328	0.305	0.313
0.019	0.019	0.051	0.071
0.042	0.036	0.019	0.032
0.083	0.107	0.087	0.107
96.913	96.891	96.799	97.710
6.841	6.744	6.771	6.819
1.159	1.256	1.229	1.181
0.354	0.390	0.381	0.409
0.039	0.049	0.044	0.044
0.002	0.002	0.006	0.008
0.588	0.581	0.586	0.526
1.477	1.531	1.492	1.538
0.036	0.036	0.035	0.035
2.499	2.407	2.454	2.435
0.005	0.004	0.002	0.004
1.895	1.900	1.895	1.881
0.291	0.323	0.319	0.327
0.056	0.062	0.058	0.059
1.979	1.973	1.978	1.973
0.021	0.027	0.022	0.027
17.243	17.285	17.272	17.268
0.629	0.611	0.622	0.613
0.371	0.389	0.378	0.387
0.243	0.285	0.272	0.268
0.624	0.599	0.606	0.562

Epidote

Table 90

Locality	Creighton Mine (5400 lvl)	Creighton Mine (5400 lvl)	Creighton Mine (5400 lvl)	Creighton Mine (5400 lvl)	Creighton Mine (5400 lvl)	Creighton Mine (5400 lvl)	Creighton Mine (5400 lvl)
Sample and analysis	SSS01-16 / 1 .	SSS01-17 / 1 .	SSS01-18 / 1 .	SSS01-19 / 1 .	SSS01-20 / 1 .	SSS01-21 / 1 .	SSS01-22 / 1 .
Mineral	Epidote	Epidote	Epidote	Epidote	Epidote	Epidote	Epidote
SiO2	36.051	37.642	37.613	37.654	37.417	37.568	37.773
TiO2	0.092	0.054	0.066	0.042	0.048	0.097	0.061
Al2O3	23.243	24.306	22.947	23.509	23.727	23.139	23.321
Fe2O3	0.000	0.000	0.000	0.000	0.000	0.000	0.000
MnO	0.139	0.138	0.203	0.182	0.095	0.207	0.161
FeO	0.000	0.000	0.000	0.000	0.000	0.000	0.000
CaO	21.015	23.149	23.395	23.567	23.561	23.287	23.470
MgO	0.033	0.019	0.010	0.006	0.000	0.010	0.000
La2O3	1.250	0.184	0.020	0.000	0.055	0.053	0.000
Ce2O3	1.988	0.463	0.062	0.000	0.063	0.120	0.017
Pr2O3	0.101	0.131	0.000	0.043	0.000	0.000	0.058
Nd2O3	0.731	0.258	0.035	0.014	0.048	0.054	0.003
ThO2	0.000	0.000	0.000	0.000	0.000	0.009	0.000
Total	84.643	86.344	84.351	85.017	85.014	84.544	84.864
Si	3.288	3.286	3.343	3.316	3.297	3.334	3.333
∑ Tsite	3.288	3.286	3.343	3.316	3.297	3.334	3.333
Al	2.499	2.500	2.404	2.440	2.464	2.420	2.425
Mg	0.004	0.002	0.001	0.001	bdl	0.001	
Ti	0.006	0.004	0.004	0.003	0.003	0.006	0.004
∑ M1-3-site	2.510	2.506	2.410	2.443	2.467	2.428	2.429
Na	0.0540	0.0083	0.0300	0.0076	0.0062	0.0179	0.0021
Ca	2.0539	2.1649	2.2281	2.2236	2.2241	2.2145	2.2190
Mn^{2+}	0.0107	0.0102	0.0153	0.0136	0.0071	0.0156	0.0120
La	0.0421	0.0059	0.0007	bdl	0.0018	0.0017	bdl
Ce	0.0664	0.0148	0.0020	bdl	0.0020	0.0039	0.0005
Pr	0.0034	0.0042	bdl	0.0014	bdl	bdl	0.0019
Nd	0.0238	0.0080	0.0011	0.0004	0.0015	0.0017	0.0001
Th	0.0000	0.0000	0.0000	0.0000	0.0000	0.000	0.0000
∑A1-2 site	2.254	2.216	2.277	2.247	2.243	2.255	2.236
∑REE	0.136	0.033	0.004	0.002	0.005	0.007	0.003

Table 91

Creighton Mine (5400 lvl) SSS01-12 / 1 . Epidote	Creighton Mine (5400 lvl) SSS01-13 / 1 . Epidote	Creighton Mine (5400 lvl) SSS01-14 / 1 . Epidote	Creighton Mine (5400 lvl) SSS01-15 / 1 . Epidote	Creighton Mine (5400 lvl) SSS01-6 / 1 . Epidote	Creighton Mine (5400 lvl) SSS01-8 / 1 . Epidote	Creighton Mine (5400 lvl) SSS01-9 / 1 . Epidote	Creighton Mine (5400 lvl) SSS01-10 / 1 . Epidote
36.777	35.728	37.636	37.436	31.565	35.585	36.471	36.549
0.068	0.063	0.071	0.054	0.527	0.123	0.066	0.053
23.891	21.256	22.899	23.481	13.060	19.445	21.838	22.318
0.000	0.000	0.000	0.000	0.000	0.000	0.000	0.000
0.141	0.227	0.179	0.149	0.548	0.345	0.235	0.218
0.000	0.000	0.000	0.000	0.000	0.000	0.000	0.000
22.458	20.464	23.120	23.402	12.529	18.793	21.642	21.183
0.007	0.105	0.013	0.003	0.165	0.098	0.038	0.052
0.389	0.951	0.132	0.000	6.097	1.618	0.918	0.849
0.938	2.186	0.269	0.014	10.540	3.641	1.414	1.711
0.104	0.191	0.071	0.002	0.793	0.437	0.083	0.152
0.511	1.098	0.101	0.039	2.972	1.458	0.317	0.650
0.009	0.090	0.033	0.000	1.057	0.505	0.103	0.122
85.293	82.359	84.524	84.580	79.853	82.048	83.125	83.857
3.273	3.373	3.349	3.313	3.642	3.466	3.364	3.355
3.273	3.373	3.349	3.313	3.642	3.466	3.364	3.355
2.506	2.365	2.402	2.449	1.776	2.232	2.374	2.415
0.001	0.015	0.002	0.000	0.028	0.014	0.005	0.007
0.005	0.004	0.005	0.004	0.046	0.009	0.005	0.004
2.511	2.384	2.408	2.453	1.850	2.255	2.384	2.426
0.0016	0.0095	0.0050	0.0150	0.0190	0.0125	0.0039	0.0076
2.1416	2.0701	2.2046	2.2192	1.5489	1.9611	2.1390	2.0836
0.0106	0.0182	0.0135	0.0112	0.0536	0.0285	0.0184	0.0170
0.0128	0.0331	0.0043	bdl	0.2595	0.0581	0.0312	0.0287
0.0306	0.0756	0.0088	0.0005	0.4452	0.1298	0.0478	0.0575
0.0034	0.0066	0.0023	0.0001	0.0333	0.0155	0.0028	0.0051
0.0162	0.0370	0.0032	0.0012	0.1225	0.0507	0.0104	0.0213
0.000	0.002	0.001		0.028	0.011	0.002	0.003
2.217	2.252	2.242	2.247	2.510	2.267	2.256	2.223
0.063	0.152	0.019	0.002	0.861	0.254	0.092	0.113

Table 92

Creighton Mine (5400 lvl) SSS01-11 / 1 . Epidote	Creighton Mine (5400 lvl) SSS01-2 / 1 . Epidote	Creighton Mine (5400 lvl) SSS01-3 / 1 . Epidote	Creighton Mine (5400 lvl) SSS01-4 / 1 . Epidote	Creighton Mine (5400 lvl) SSS01-5 / 1 . Epidote
37.746	31.511	30.512	36.217	37.972
0.047	1.862	1.040	0.082	0.039
24.034	9.238	12.113	21.695	24.119
0.000	0.000	0.000	0.000	0.000
0.250	0.375	0.481	0.237	0.192
0.000	0.000	0.000	0.000	0.000
23.471	9.555	12.378	20.176	23.370
0.000	0.806	0.184	0.087	0.000
0.040	6.667	6.018	1.629	0.023
0.031	12.466	10.906	2.734	0.016
0.024	0.976	0.921	0.161	0.000
0.054	3.572	2.926	0.762	0.010
0.000	2.096	1.632	0.255	0.000
85.697	79.124	79.111	84.035	85.741
3.299	3.886	3.612	3.377	3.314
3.299	3.886	3.612	3.377	3.314
2.475	1.343	1.690	2.384	2.481
	0.148	0.032	0.012	bdl
0.003	0.173	0.093	0.006	0.003
2.478	1.664	1.815	2.402	2.484
0.0157	0.0304	0.0187	0.0108	0.0188
2.1977	1.2626	1.5702	2.0159	2.1855
0.0185	0.0392	0.0482	0.0187	0.0142
0.0013	0.3033	0.2628	0.0560	0.0007
0.0010	0.5628	0.4727	0.0933	0.0005
0.0008	0.0439	0.0397	0.0055	0.0000
0.0017	0.1573	0.1237	0.0254	0.0003
	0.059	0.044	0.005	0.000
2.237	2.458	2.580	2.231	2.220
0.005	1.067	0.899	0.180	0.002

Table 93

Locality	Creighton Mine (5400 lvl)	Creighton Mine (5400 lvl)	Creighton Mine (5400 lvl)	Creighton Mine (5400 lvl)	Creighton Mine (5400 lvl)	Creighton Mine (5400 lvl)	Creighton Mine (5400 lvl)
Sample and analysis	SSS02-37 / 1 .	SSS02-38 / 1 .	SSS02-39 / 1 .	SSS02-40 / 1 .	SSS02-41 / 1 .	SSS02-42 / 1 .	SSS02-43 / 1 .
Mineral	Epidote	Epidote	Epidote	Epidote	Epidote	Epidote	Epidote
SiO2	30.550	37.506	31.802	34.777	37.017	33.354	37.902
TiO2	1.592	0.282	1.202	0.233	0.063	0.213	0.050
Al2O3	14.750	24.188	15.578	21.192	23.756	20.215	24.592
Fe2O3	0.000	0.000	0.000	0.000	0.000	0.000	0.000
MnO	0.373	0.088	0.331	0.271	0.095	0.453	0.145
FeO	0.000	0.000	0.000	0.000	0.000	0.000	0.000
CaO	10.911	22.882	12.164	19.079	23.154	13.332	23.375
MgO	0.635	0.027	0.351	0.097	0.034	1.344	0.005
La2O3	6.037	0.387	5.175	1.699	0.165	1.825	0.021
Ce2O3	10.480	0.606	10.144	3.303	0.355	3.047	0.053
Pr2O3	0.885	0.026	1.041	0.461	0.000	0.263	0.000
Nd2O3	3.101	0.225	3.668	1.244	0.157	1.011	0.004
ThO2	1.445	0	1.434	0.66	0.161	1.837	0.016
Total	80.759	86.217	82.890	83.016	84.957	76.894	86.163
Si	3.482	3.286	3.491	3.333	3.280	3.457	3.291
∑ Tsite	3.482	3.286	3.491	3.333	3.280	3.457	3.291
Al	1.981	2.498	2.016	2.394	2.481	2.469	2.517
Mg	0.108	0.004	0.057	0.014	0.004	0.208	0.001
Ti	0.136	0.019	0.099	0.017	0.004	0.017	0.003
∑ M1-3-site	2.226	2.520	2.172	2.424	2.489	2.693	2.521
Na	0.0057	0.0148	0.0026		0.0046		
Ca	1.3323	2.1480	1.4309	1.9591	2.1981	1.4803	2.1748
Mn^{2+}	0.0360	0.0065	0.0308	0.0220	0.0071	0.0398	0.0107
La	0.254	0.013	0.210	0.060	0.005	0.070	0.001
Ce	0.437	0.019	0.408	0.116	0.012	0.116	0.002
Pr	0.037	0.001	0.042	0.016		0.010	
Nd	0.126	0.007	0.144	0.043	0.005	0.037	0.000
Th	0.037		0.036	0.014	0.003	0.043	0.000
∑A1-2 site	2.266	2.209	2.303	2.230	2.235	1.796	2.188
∑REE	0.854	0.040	0.803	0.235	0.022	0.233	0.002

Table 94

Creighton Mine (5400 lvl) SSS02-44 / 1 . Epidote	Creighton Mine (5400 lvl) SSS02-30 / 1 . Epidote	Creighton Mine (5400 lvl) SSS02-31 / 1 . Epidote	Creighton Mine (5400 lvl) SSS02-33 / 1 . Epidote	Creighton Mine (5400 lvl) SSS02-34 / 1 . Epidote	Creighton Mine (5400 lvl) SSS02-35 / 1 . Epidote	Creighton Mine (5400 lvl) SSS02-36 / 1 . Epidote	Creighton Mine (5400 lvl) SSS02-45 / 1 . Epidote
36.618	34.053	36.720	37.290	37.486	36.484	36.986	33.730
0.094	1.248	0.120	0.027	0.278	0.091	0.098	0.102
21.979	15.199	23.934	24.042	24.510	23.007	23.597	20.492
0.000	0.000	0.000	0.000	0.000	0.000	0.000	0.000
0.304	0.401	0.116	0.274	0.065	0.213	0.198	0.331
0.000	0.000	0.000	0.000	0.000	0.000	0.000	0.000
19.838	12.821	22.974	23.145	23.538	20.818	22.103	15.918
0.254	0.798	0.027	0.016	0.023	0.085	0.140	0.152
0.709	3.452	0.073	0.084	0.061	1.032	0.346	3.750
1.344	6.743	0.157	0.132	0.093	1.973	0.669	6.076
0.093	0.579	0.049	0.113	0.000	0.211	0.000	0.462
0.497	1.964	0.061	0.042	0.041	0.726	0.270	1.844
0.965	2.291	0.301	0.026	0.064	0.372	0.177	0
82.695	79.549	84.532	85.191	86.159	85.012	84.584	82.857
3.410	3.690	3.263	3.284	3.259	3.322	3.304	3.374
3.410	3.690	3.263	3.284	3.259	3.322	3.304	3.374
2.412	1.941	2.506	2.495	2.511	2.469	2.484	2.416
0.035	0.129	0.004	0.002	0.003	0.012	0.019	0.023
0.007	0.102	0.008	0.002	0.018	0.006	0.007	0.008
2.454	2.172	2.518	2.499	2.532	2.487	2.509	2.446
0.0036	0.0398	0.0082		0.0418	0.0227	0.0250	0.0184
1.9791	1.4887	2.1871	2.1838	2.1924	2.0309	2.1154	1.7059
0.0240	0.0368	0.0087	0.0204	0.0048	0.0164	0.0150	0.0280
0.024	0.138	0.002	0.003	0.002	0.035	0.011	0.138
0.046	0.268	0.005	0.004	0.003	0.066	0.022	0.222
0.003	0.023	0.002	0.004		0.007		0.017
0.017	0.076	0.002	0.001	0.001	0.024	0.009	0.066
0.020	0.056	0.006	0.001	0.001	0.008	0.004	
2.117	2.126	2.221	2.217	2.246	2.209	2.201	2.196
0.090	0.504	0.011	0.012	0.006	0.131	0.042	0.444

Table 95

Creighton Mine (5400 lvl) SSS02-46 / 1 . Epidote	Creighton Mine (5400 lvl) SSS02-47 / 1 . Epidote	Creighton Mine (5400 lvl) SSS02-48 / 1 . Epidote	Creighton Mine (5400 lvl) SSS02-49 / 1 . Epidote	Creighton Mine (5400 lvl) SSS02-50 / 1 . Epidote	Creighton Mine (5400 lvl) SSS02-51 / 1 . Epidote	Creighton Mine (5400 lvl) SSS02-52 / 1 . Epidote	Creighton Mine (5400 lvl) SSS02-53 / 1 . Epidote
36.914	36.208	37.716	37.266	37.548	35.829	37.723	36.501
0.064	0.088	0.032	0.072	0.048	0.097	0.023	1.101
23.670	23.007	24.410	24.304	24.382	21.156	24.592	20.732
0.000	0.000	0.000	0.000	0.000	0.000	0.000	0.000
0.135	0.192	0.083	0.129	0.107	0.362	0.071	0.168
0.000	0.000	0.000	0.000	0.000	0.000	0.000	0.000
22.276	20.893	23.335	23.106	23.500	19.500	23.542	12.449
0.154	0.389	0.041	0.291	0.040	0.320	0.000	4.176
0.398	0.646	0.126	0.104	0.064	1.355	0.039	0.033
0.751	1.230	0.232	0.189	0.119	2.604	0.104	0.098
0.055	0.189	0.06	0.006	0	0.127	0.036	0
0.320	0.434	0.098	0.087	0.051	0.983	0.041	0.017
0.124	0.411	0.064	0.051	0	0.885	0	0
84.861	83.687	86.197	85.605	85.859	83.218	86.171	75.275
3.290	3.301	3.285	3.260	3.273	3.367	3.277	3.579
3.290	3.301	3.285	3.260	3.273	3.367	3.277	3.579
2.486	2.472	2.506	2.506	2.505	2.343	2.518	2.396
0.020	0.053	0.005	0.038	0.005	0.045		0.610
0.004	0.006	0.002	0.005	0.003	0.007	0.002	0.081
2.511	2.531	2.513	2.548	2.513	2.395	2.519	3.087
	0.032	0.006		0.060	0.012	0.064	0.022
2.127	2.041	2.178	2.166	2.195	1.963	2.191	1.308
0.010	0.015	0.006	0.010	0.008	0.029	0.005	0.014
0.013	0.022	0.004	0.003	0.002	0.047	0.001	0.001
0.025	0.041	0.007	0.006	0.004	0.090	0.003	0.004
0.002	0.006	0.002	0.000		0.004	0.001	
0.010	0.014	0.003	0.003	0.002	0.033	0.001	0.001
0.003	0.009	0.001	0.001		0.019		
2.189	2.179	2.207	2.188	2.270	2.197	2.268	1.349
0.050	0.083	0.016	0.012	0.007	0.174	0.007	0.005

Table 96

Creighton Mine (5400 lvl) SSS02-54 / 1 . Epidote	Creighton Mine (5400 lvl) SSS02-55 / 1 . Epidote	Creighton Mine (5400 lvl) SSS02-23 / 1 . Epidote	Creighton Mine (5400 lvl) SSS02-24 / 1 . Epidote	Creighton Mine (5400 lvl) SSS02-25 / 1 . Epidote	Creighton Mine (5400 lvl) SSS02-26 / 1 . Epidote	Creighton Mine (5400 lvl) SSS02-27 / 1 . Epidote	Creighton Mine (5400 lvl) SSS02-28 / 1 . Epidote	Creighton Mine (5400 lvl) SSS02-29 / 1 . Epidote
37.593	37.685	31.543	31.630	37.657	37.613	37.546	32.995	36.001
0.059	0.056	1.478	1.438	0.678	0.111	0.658	0.288	0.146
23.055	24.782	14.538	14.474	23.737	24.220	23.760	18.430	23.067
0.000	0.000	0.000	0.000	0.000	0.000	0.000	0.000	0.000
0.175	0.090	0.381	0.369	0.078	0.116	0.154	0.396	0.231
0.000	0.000	0.000	0.000	0.000	0.000	0.000	0.000	0.000
21.271	23.465	13.598	13.591	23.319	23.440	22.833	13.415	20.614
0.102	0.014	0.209	0.226	0.045	0.039	0.054	1.107	0.083
0.504	0.041	5.797	5.658	0.023	0.032	0.265	3.749	1.388
0.93	0.075	9.78	9.782	0.04	0.065	0.482	6.158	2.305
0.073	0	0.837	0.781	0.019	0.009	0.14	0.509	0.156
0.394	0.03	2.444	2.452	0.047	0.009	0.204	1.634	0.696
0.222	0.046	1.417	1.631	0.074	0.211	0.122	1.367	0.513
84.378	86.284	82.022	82.032	85.717	85.865	86.218	80.048	85.200
3.387	3.268	3.484	3.493	3.299	3.282	3.294	3.465	3.288
3.387	3.268	3.484	3.493	3.299	3.282	3.294	3.465	3.288
2.448	2.533	1.892	1.884	2.451	2.491	2.457	2.281	2.483
0.014	0.002	0.034	0.037	0.006	0.005	0.007	0.173	0.011
0.004	0.004	0.123	0.119	0.045	0.007	0.043	0.023	0.010
2.466	2.538	2.050	2.041	2.501	2.503	2.507	2.477	2.504
0.002	0.004	0.019	0.028	0.001	0.002	0.002	0.010	0.001
2.054	2.180	1.609	1.608	2.189	2.191	2.146	1.509	2.017
0.013	0.007	0.036	0.035	0.006	0.009	0.011	0.035	0.018
0.017	0.001	0.236	0.230	0.001	0.001	0.009	0.145	0.047
0.031	0.002	0.395	0.396	0.001	0.002	0.015	0.237	0.077
0.002		0.034	0.031	0.001	0.000	0.004	0.019	0.005
0.013	0.001	0.096	0.097	0.001	0.000	0.006	0.061	0.023
0.005	0.001	0.036	0.041	0.001	0.004	0.002	0.033	0.011
2.136	2.197	2.461	2.466	2.201	2.210	2.197	2.050	2.198
0.063	0.005	0.762	0.754	0.004	0.004	0.035	0.463	0.152

Table 97

Locality	Creighton Mine (5400 lvl)	Creighton Mine (5400 lvl)	Creighton Mine (5400 lvl)	Creighton Mine (5400 lvl)	Creighton Mine (5400 lvl)
Sample and analysis	SSS03-57 / 1 .	SSS03-58 / 1 .	SSS03-59 / 1 .	SSS03-60 / 1 .	SSS03-61 / 1 .
Mineral	Epidote	Epidote	Epidote	Epidote	Epidote
SiO2	37.834	36.143	37.662	35.703	35.772
TiO2	0.079	0.116	0.180	0.091	0.103
Al2O3	25.289	24.076	24.179	22.917	23.213
Fe2O3	0.000	0.000	0.000	0.000	0.000
MnO	0.118	0.225	0.187	0.278	0.268
FeO	0.000	0.000	0.000	0.000	0.000
CaO	23.712	21.798	23.547	19.623	20.141
MgO	0.034	0.079	0.019	0.110	0.092
La2O3	0.018	0.537	0.039	0.972	0.915
Ce2O3	0.004	0.984	0.049	1.955	1.739
Pr2O3	0.053	0.012	0.000	0.173	0.209
Nd2O3	0.011	0.380	0.000	0.890	0.709
ThO2	0.000	0.369	0.005	0.704	0.598
Total	87.152	84.719	85.867	83.416	83.759
Si	3.245	3.239	3.283	3.317	3.292
∑ Tsite	3.245	3.245	3.245	3.245	3.245
Al	2.556	2.543	2.484	2.509	2.518
Mg	0.004	0.011	0.002	0.015	0.013
Ti	0.005	0.008	0.012	0.006	0.007
∑ M1-3-site	2.565	2.562	2.498	2.531	2.537
Na	0.054	0.054	1.054	2.054	3.054
Ca	2.179	2.093	2.199	1.953	1.986
Mn^{2+}	0.009	0.017	0.014	0.022	0.021
La	0.001	0.018	0.001	0.033	0.031
Ce	0.000	0.032	0.002	0.066	0.059
Pr	0.002	0.000		0.006	0.007
Nd	0.000	0.012		0.030	0.023
Th		0.008	0.000	0.015	0.013
∑A1-2 site	2.244	2.234	3.270	4.179	5.193
∑REE	0.003	0.063	0.003	0.135	0.120

Table 98

Creighton Mine (5400 lvl) SSS03-62 / 1 . Epidote	Creighton Mine (5400 lvl) SSS03-63 / 1 . Epidote	Creighton Mine (5400 lvl) SSS03-64 / 1 . Epidote	Creighton Mine (5400 lvl) SSS03-56 / 1 . Epidote	Creighton Mine (5400 lvl) SSS03-65 / 1 . Epidote	Creighton Mine (5400 lvl) SSS03-66 / 1 . Epidote
35.504	35.486	37.622	34.741	35.840	31.135
0.081	0.094	0.145	0.118	0.128	0.064
23.832	23.672	24.845	22.783	23.532	17.581
0.000	0.000	0.000	0.000	0.000	0.000
0.243	0.342	0.204	0.308	0.268	0.542
0.000	0.000	0.000	0.000	0.000	0.000
22.139	20.347	23.293	19.338	20.235	11.935
0.044	0.079	0.018	0.127	0.399	0.267
0.227	0.949	0.039	1.216	0.636	5.130
0.386	1.882	0.075	2.323	1.239	10.222
0.093	0.203	0.017	0.242	0.127	1.055
0.182	0.805	0.013	0.905	0.508	3.857
0.443	0.191	0.059	0.787	0.459	0.000
83.174	84.050	86.330	82.888	83.371	81.788
3.213	3.248	3.263	3.268	3.276	3.415
3.245	3.245	3.245	3.245	3.245	3.245
2.542	2.554	2.540	2.526	2.535	2.272
0.006	0.011	0.002	0.018	0.054	0.044
0.006	0.006	0.009	0.008	0.009	0.005
2.554	2.571	2.552	2.552	2.598	2.321
4.054	5.054	6.054	7.054	8.054	9.054
2.147	1.996	2.165	1.949	1.982	1.402
0.019	0.027	0.015	0.025	0.021	0.050
0.008	0.032	0.001	0.042	0.021	0.208
0.013	0.063	0.002	0.080	0.041	0.410
0.003	0.007	0.001	0.008	0.004	0.042
0.006	0.026	0.000	0.030	0.017	0.151
0.009	0.004	0.001	0.017	0.010	
6.258	7.208	8.239	9.206	10.150	11.318
0.029	0.128	0.005	0.161	0.084	0.811

Table 99

Locality	Creighton Mine (5400 lvl)	eighton Mine (5400 lv	Creighton Mine (5400 lvl)	Creighton Mine (5400 lvl)	Creighton Mine (5400 lvl)	Creighton Mine (5400 lvl)	Creighton Mine (5400 lvl)
Sample and analysis	SSS04-67 / 1 .	SSS04-68 / 1 .	SSS04-69 / 1 .	SSS04-70 / 1 .	SSS04-71 / 1 .	SSS04-72 / 1 .	SSS04-73 / 1 .
Mineral	Epidote	Epidote	Epidote	Epidote	Epidote	Epidote	Epidote
SiO2	35.164	34.925	35.106	34.747	37.572	37.876	38.088
TiO2	0.102	0.122	0.097	0.104	0.094	0.132	0.108
Al2O3	23.236	23.105	23.307	22.749	24.701	25.204	25.238
Fe2O3	0.000	0.000	0.000	0.000	0.000	0.000	0.000
MnO	0.249	0.273	0.251	0.337	0.212	0.139	0.212
FeO	0.000	0.000	0.000	0.000	0.000	0.000	0.000
CaO	19.656	19.206	19.382	18.445	23.364	23.612	23.522
MgO	0.153	0.170	0.175	0.240	0.005	0.019	0.007
La2O3	1.145	1.168	1.088	1.460	0.014	0.061	0.020
Ce2O3	2.407	2.470	2.315	3.016	0.043	0.114	0.019
Pr2O3	0.212	0.153	0.217	0.290	0.000	0.001	0.000
Nd2O3	1.178	1.284	1.136	1.503	0.005	0.045	0.031
ThO2	0.023	0.024	0.029	0.157	0	0.009	0.001
Total	83.525	82.900	83.103	83.048	86.010	87.212	87.246
Si	3.267	3.273	3.271	3.280	3.267	3.250	3.264
∑ Tsite	3.267	3.273	3.271	3.280	3.267	3.250	3.264
Al	2.544	2.552	2.559	2.531	2.532	2.549	2.549
Mg	0.021	0.024	0.024	0.034	0.001	0.002	0.001
Ti	0.007	0.009	0.007	0.007	0.006	0.009	0.007
∑ M1-3-site	2.572	2.584	2.590	2.572	2.538	2.560	2.557
Na	10.054	11.054	12.054	13.054	14.054	15.054	16.054
Ca	1.956	1.929	1.935	1.866	2.177	2.171	2.160
Mn^{2+}	0.020	0.022	0.020	0.027	0.016	0.010	0.015
La	0.0392	0.0404	0.0374	0.0508	0.0004	0.0019	0.0006
Ce	0.0819	0.0847	0.0790	0.1042	0.0014	0.0036	0.0006
Pr	0.0072	0.0052	0.0074	0.0100		0.0000	
Nd	0.0391	0.0430	0.0378	0.0507	0.0002	0.0014	0.0009
Th	0.000	0.001	0.001	0.003		0.000	0.000
∑A1-2 site	12.198	13.178	14.171	15.166	16.248	17.242	18.231
∑REE	0.1674	0.1733	0.1615	0.2157	0.0020	0.0069	0.0022

Table 100

Creighton Mine (5400 lvl) SSS04-74 / 1 . Epidote	Creighton Mine (5400 lvl) SSS04-75 / 1 . Epidote	Creighton Mine (5400 lvl) SSS04-76 / 1 . Epidote	Creighton Mine (5400 lvl) SSS04-77 / 1 . Epidote	Creighton Mine (5400 lvl) SSS04-78 / 1 . Epidote	Creighton Mine (5400 lvl) SSS04-79 / 1 . Epidote
33.958	38.076	37.105	35.682	34.375	34.963
0.155	0.112	0.098	0.074	0.131	0.106
22.679	26.102	24.540	23.463	22.894	23.252
0.000	0.000	0.000	0.000	0.000	0.000
0.315	0.200	0.238	0.321	0.318	0.262
0.000	0.000	0.000	0.000	0.000	0.000
20.148	23.425	22.246	19.442	18.725	19.437
0.225	0.016	0.054	0.133	0.181	0.140
0.892	0.052	0.365	1.011	1.390	1.315
1.762	0.102	0.687	2.122	2.806	2.626
0.061	0.000	0.050	0.159	0.254	0.133
0.811	0.051	0.362	1.028	1.290	1.225
0.066	0	0	0	0.156	0.059
81.072	88.136	85.745	83.435	82.520	83.518
3.212	3.231	3.269	3.309	3.253	3.256
3.212	3.231	3.269	3.309	3.253	3.256
2.528	2.610	2.548	2.564	2.554	2.552
0.032	0.002	0.007	0.018	0.026	0.019
0.011	0.007	0.006	0.005	0.009	0.007
2.571	2.619	2.562	2.588	2.588	2.579
17.054	18.054	19.054	20.054	21.054	22.054
2.042	2.129	2.100	1.932	1.899	1.939
0.025	0.014	0.018	0.025	0.025	0.021
0.0311	0.0016	0.0119	0.0346	0.0485	0.0452
0.0610	0.0032	0.0222	0.0720	0.0972	0.0895
0.0021		0.0016	0.0054	0.0088	0.0045
0.0274	0.0015	0.0114	0.0340	0.0436	0.0407
0.001				0.003	0.001
19.244	20.204	21.219	22.157	23.180	24.195
0.1216	0.0063	0.0470	0.1460	0.1981	0.1799

Table 101

Creighton Mine (5400 lvl) SSS04-80 / 1 . Epidote	Creighton Mine (5400 lvl) SSS04-81 / 1 . Epidote	Creighton Mine (5400 lvl) SSS04-82 / 1 . Epidote	Creighton Mine (5400 lvl) SSS04-83 / 1 . Epidote	Creighton Mine (5400 lvl) SSS04-84 / 1 . Epidote	Creighton Mine (5400 lvl) SSS04-85 / 1 . Epidote
37.793	34.873	34.574	33.743	37.180	37.720
0.106	0.110	0.117	0.137	0.088	0.090
24.629	22.872	22.572	22.119	24.946	25.604
0.000	0.000	0.000	0.000	0.000	0.000
0.215	0.295	0.259	0.340	0.200	0.183
0.000	0.000	0.000	0.000	0.000	0.000
22.554	19.323	18.573	17.259	22.249	23.628
0.215	0.223	0.259	0.272	0.045	0.006
0.207	1.219	1.514	1.765	0.400	0.058
0.384	2.397	2.996	3.529	0.827	0.106
0.032	0.189	0.372	0.350	0.099	0.000
0.208	1.126	1.406	1.664	0.447	0.073
0	0.121	0.064	0.047	0	0
86.343	82.748	82.706	81.225	86.481	87.468
3.289	3.269	3.276	3.290	3.255	3.226
3.289	3.269	3.276	3.290	3.255	3.226
2.526	2.527	2.521	2.541	2.574	2.581
0.028	0.031	0.037	0.040	0.006	0.001
0.007	0.008	0.008	0.010	0.006	0.006
2.561	2.566	2.566	2.591	2.586	2.587
23.054	25.054	26.054	27.054	28.054	29.054
2.103	1.941	1.886	1.803	2.087	2.165
0.016	0.023	0.021	0.028	0.015	0.013
0.0066	0.0421	0.0529	0.0635	0.0129	0.0018
0.0122	0.0823	0.1039	0.1260	0.0265	0.0033
0.0010	0.0065	0.0128	0.0124	0.0032	
0.0065	0.0377	0.0476	0.0579	0.0140	0.0022
	0.003	0.001	0.001		
25.199	27.189	28.179	29.146	30.213	31.240
0.0264	0.1686	0.2173	0.2598	0.0566	0.0074

Table 102

Creighton Mine (5400 lvl) SSS04-86 / 1 . Epidote	Creighton Mine (5400 lvl) SSS04-87 / 1 . Epidote	Creighton Mine (5400 lvl) SSS04-88 / 1 . Epidote	Creighton Mine (5400 lvl) SSS04-89 / 1 . Epidote	Creighton Mine (5400 lvl) SSS04-90 / 1 . Epidote	Creighton Mine (5400 lvl) SSS04-91 / 1 . Epidote
38.010	38.256	37.100	37.211	34.781	37.462
0.134	0.112	0.102	0.081	0.136	0.133
25.753	26.327	25.259	25.008	23.070	24.812
0.000	0.000	0.000	0.000	0.000	0.000
0.200	0.148	0.193	0.198	0.301	0.199
0.000	0.000	0.000	0.000	0.000	0.000
23.108	23.755	22.684	21.874	18.161	23.323
0.028	0.012	0.050	0.056	0.229	0.140
0.181	0.000	0.232	0.668	1.473	0.028
0.391	0.000	0.504	1.327	2.961	0.064
0.000	0.000	0.000	0.154	0.294	0.009
0.216	0.010	0.260	0.657	1.434	0.043
0.014	0	0	0	0.138	0.005
88.035	88.620	86.384	87.234	82.978	86.218
3.243	3.222	3.231	3.255	3.283	3.250
3.243	3.222	3.231	3.255	3.283	3.250
2.590	2.613	2.593	2.578	2.567	2.537
0.004	0.002	0.006	0.007	0.032	0.018
0.009	0.007	0.007	0.005	0.010	0.009
2.602	2.622	2.606	2.591	2.609	2.563
30.054	31.054	32.054	33.054	34.054	35.054
2.113	2.144	2.117	2.050	1.837	2.168
0.014	0.011	0.014	0.015	0.024	0.015
0.0057		0.0075	0.0216	0.0513	0.0009
0.0122		0.0161	0.0425	0.1023	0.0020
			0.0049	0.0101	0.0003
0.0066	0.0003	0.0081	0.0205	0.0483	0.0013
0.000				0.003	0.000
32.206	33.208	34.217	35.208	36.130	37.241
0.0245	0.0003	0.0316	0.0895	0.2121	0.0045

Table 103

Creighton Mine (5400 lvl) SSS04-92 / 1 . Epidote	Creighton Mine (5400 lvl) SSS04-93 / 1 . Epidote	Creighton Mine (5400 lvl) SSS04-94 / 1 . Epidote	reighton Mine (5400 lv SSS04-95 / 1 . Epidote	reighton Mine (5400 lvl) SSS04-96 / 1 . Epidote	Creighton Mine (5400 lvl) SSS04-97 / 1 . Epidote
33.782	37.435	36.966	34.906	37.291	38.012
0.110	0.120	0.106	0.097	0.061	0.198
22.407	25.027	24.358	23.222	24.719	25.682
0.000	0.000	0.000	0.000	0.000	0.000
0.355	0.210	0.172	0.318	0.134	0.150
0.000	0.000	0.000	0.000	0.000	0.000
18.380	23.723	22.219	18.875	23.432	23.925
0.212	0.008	0.046	0.214	0.008	0.002
1.412	0.009	0.542	1.269	0.093	0.000
2.789	0.000	1.011	2.627	0.218	0.000
0.295	0.000	0.090	0.190	0.000	0.000
1.319	0.000	0.432	1.234	0.111	0.017
0.181	0	0.011	0.233	0.01	0
81.242	86.532	85.953	83.185	86.077	87.986
3.251	3.233	3.266	3.263	3.248	3.228
3.251	3.233	3.266	3.263	3.248	3.228
2.541	2.547	2.537	2.559	2.537	2.571
0.030	0.001	0.006	0.030	0.001	0.000
0.008	0.008	0.007	0.007	0.004	0.013
2.580	2.556	2.550	2.595	2.542	2.583
36.054	37.054	38.054	39.054	40.054	41.054
1.895	2.195	2.103	1.891	2.187	2.177
0.029	0.015	0.013	0.025	0.010	0.011
0.0501	0.0003	0.0177	0.0438	0.0030	
0.0983		0.0327	0.0899	0.0070	
0.0103		0.0029	0.0065		
0.0453		0.0136	0.0412	0.0035	0.0005
0.004		0.000	0.005	0.000	
38.186	39.265	40.237	41.156	42.264	43.242
0.2040	0.0003	0.0669	0.1813	0.0134	0.0005

Table 104

Creighton Mine (5400 lvl) SSS04-98 / 1 . Epidote	Creighton Mine (5400 lvl) SSS04-108 / 1 . Epidote	Creighton Mine (5400 lvl) SSS04-109 / 1 . Epidote	Creighton Mine (5400 lvl) SSS04-110 / 1 . Epidote	:reighton Mine (5400 lvl SSS04-111 / 1 . Epidote	Creighton Mine (5400 lvl) SSS04-112 / 1 . Epidote
33.760	34.875	38.199	37.035	35.347	37.018
0.140	0.117	0.148	0.079	0.113	0.151
21.746	22.688	25.238	24.900	22.950	23.990
0.000	0.000	0.000	0.000	0.000	0.000
0.379	0.286	0.135	0.246	0.287	0.218
0.000	0.000	0.000	0.000	0.000	0.000
19.091	19.136	23.677	21.982	18.858	21.726
0.162	0.179	0.020	0.077	0.198	0.151
1.248	1.414	0.009	0.427	1.184	0.029
2.455	2.703	0.016	0.874	2.320	0.045
0.209	0.221	0.020	0.018	0.233	0.000
1.253	1.210	0.002	0.432	1.172	0.006
0.154	0.04	0	0.044	0	0
80.597	82.869	87.464	86.114	82.662	83.334
3.264	3.280	3.265	3.256	3.317	3.322
3.264	3.280	3.265	3.256	3.317	3.322
2.478	2.515	2.543	2.580	2.538	2.538
0.023	0.025	0.003	0.010	0.028	0.020
0.010	0.008	0.010	0.005	0.008	0.010
2.512	2.548	2.555	2.595	2.574	2.568
42.054	43.054	44.054	45.054	46.054	47.054
1.978	1.929	2.169	2.071	1.896	2.089
0.031	0.023	0.010	0.018	0.023	0.017
0.0445	0.0491	0.0003	0.0138	0.0410	0.0010
0.0869	0.0931	0.0005	0.0281	0.0797	0.0015
0.0074	0.0076	0.0006	0.0006	0.0080	
0.0433	0.0406	0.0001	0.0136	0.0393	0.0002
0.003	0.001		0.001		
44.248	45.197	46.234	47.200	48.141	49.162
0.1821	0.1904	0.0015	0.0561	0.1679	0.0026

Table 105

reighton Mine (5400 lv	Creighton Mine (5400 lvl)	Creighton Mine (5400 lvl	Creighton Mine (5400 lvl)	Creighton Mine (5400 lvl)	Creighton Mine (5400 lvl)
SSS04-99 / 1 .	SSS04-100 / 1 .	SSS04-101 / 1 .	SSS04-102 / 1 .	SSS04-103 / 1 .	SSS04-104 / 1 .
Epidote	Epidote	Epidote	Epidote	Epidote	Epidote
34.544	37.676	37.047	35.481	38.639	37.687
0.125	0.342	0.082	0.102	0.095	0.068
22.867	24.872	24.712	23.492	26.313	26.004
0.000	0.000	0.000	0.000	0.000	0.000
0.303	0.210	0.178	0.268	0.190	0.209
0.000	0.000	0.000	0.000	0.000	0.000
18.835	23.696	22.830	18.799	23.687	21.740
0.200	0.029	0.020	0.225	0.057	0.217
1.268	0.000	0.276	1.368	0.014	0.494
2.556	0.005	0.525	2.767	0.057	0.876
0.227	0.000	0.010	0.391	0.000	0.060
1.250	0.000	0.228	1.326	0.045	0.388
0.084	0	0.058	0.095	0.011	0
82.259	86.830	85.966	84.314	89.108	87.743
3.266	3.246	3.247	3.285	3.240	3.247
3.266	3.246	3.247	3.285	3.240	3.247
2.548	2.525	2.553	2.563	2.601	2.641
0.028	0.004	0.003	0.031	0.007	0.028
0.009	0.022	0.005	0.007	0.006	0.004
2.585	2.551	2.561	2.602	2.614	2.673
49.054	50.054	51.054	52.054	53.054	54.054
1.908	2.187	2.144	1.865	2.128	2.007
0.024	0.015	0.013	0.021	0.013	0.015
0.0442		0.0089	0.0467	0.0004	0.0157
0.0885	0.0002	0.0168	0.0938	0.0018	0.0276
0.0078		0.0003	0.0132		0.0019
0.0422		0.0071	0.0438	0.0013	0.0119
0.002		0.001	0.002	0.000	
51.171	52.257	53.246	54.139	55.200	56.133
0.1827	0.0002	0.0332	0.1975	0.0035	0.0572

Table 106

Creighton Mine (5400 lvl) SSS04-105 / 1 . Epidote	Creighton Mine (5400 lvl) SSS04-106 / 1 . Epidote	Creighton Mine (5400 lvl) SSS04-107 / 1 . Epidote
36.853	34.119	34.684
0.099	0.164	0.185
24.560	22.525	23.087
0.000	0.000	0.000
0.240	0.327	0.287
0.000	0.000	0.000
21.667	18.559	19.463
0.055	0.322	0.553
0.624	1.379	0.952
1.189	2.814	1.887
0.170	0.380	0.168
0.582	1.396	0.852
0	0.196	0.109
86.039	82.181	82.227
3.264	3.250	3.241
3.264	3.250	3.241
2.563	2.529	2.543
0.007	0.046	0.077
0.007	0.012	0.013
2.577	2.587	2.633
55.054	56.054	57.054
2.056	1.894	1.949
0.018	0.026	0.023
0.0204	0.0485	0.0328
0.0385	0.0981	0.0646
0.0055	0.0132	0.0057
0.0184	0.0475	0.0284
	0.004	0.002
57.211	58.186	59.159
0.0828	0.2073	0.1315

Table 107

Locality	Creighton Mine (7840 lvl)	Creighton Mine (7840 lvl)	Creighton Mine (7840 lvl)	Creighton Mine (7840 lvl)	Creighton Mine (7840 lvl)	Creighton Mine (7840 lvl)	Creighton Mine (7840 lvl)
Sample and analysis	Pl19-36 / 1 .	Pl19-37 / 1 .	Pl19-38 / 1 .	Pl19-39 / 1 .	Pl19-40 / 1 .	Pl9-23 / 1 .	Pl9-24 / 1 .
Mineral	Epidote	Epidote	Epidote	Epidote	Epidote	Epidote	Epidote
SiO2	38.647	37.799	38.108	38.430	38.688	38.658	35.078
TiO2	0.054	0.071	0.116	0.235	0.072	0.073	0.095
Al2O3	25.935	25.752	25.662	25.681	26.174	25.175	25.113
Fe2O3	10.149	9.977	10.317	9.311	9.814	11.138	9.050
MnO	0.200	0.160	0.227	0.208	0.139	0.195	0.138
FeO	0.239	0.000	0.000	1.786	0.000	0.058	2.218
CaO	24.095	23.694	23.899	22.127	24.184	24.057	19.660
MgO	0.017	0.004	0.011	0.391	0.013	0.008	0.204
K2O	0.004	0.006	0.018	0.711	0.016	0.002	0.068
NaO	0.047	0.010	0.013	0.002	-0.011	-0.006	0.022
Cr2O3	0.004	0.012	0.015	0.005	-0.003	0.013	0.017
NiO	-0.036	0.007	0.009	-0.022	0.000	-0.015	0.022
F	-0.058	0.117	-0.050	-0.188	0.038	-0.127	0.607
Cl	0.010	0.002	0.010	0.070	0.000	0.001	0.019
Total	99.307	97.611	98.355	98.747	99.124	99.230	92.311
Si	2.996	2.986	2.988	3.019	3.005	3.010	2.956
Al	0.004	0.014	0.012				0.044
∑ T-site	3.000	3.000	3.000	3.019	3.005	3.010	3.000
Al	2.366	2.384	2.359	2.377	2.396	2.310	2.450
Mg	0.002	0.000	0.001	0.046	0.002	0.001	0.026
Ti	0.003	0.004	0.007	0.014	0.004	0.004	0.006
Fe3+	0.592	0.593	0.609	0.550	0.574	0.653	0.574
Fe2+	0.016			0.117		0.004	0.156
∑ M1-3-site	2.978	2.982	2.975	3.105	2.975	2.972	3.212
Na	0.054	0.008	0.030	0.008	0.006	0.008	0.016
Ca	2.001	2.006	2.008	1.862	2.013	2.007	1.775
Mn2+	0.013	0.011	0.015	0.014	0.009	0.013	0.010
∑ A1-2-site	2.069	2.025	2.053	1.884	2.028	2.027	1.801
Xczo	0.794	0.800	0.793	0.766	0.805	0.777	0.763
Xferriep	0.199	0.199	0.205	0.177	0.193	0.220	0.179

Table 108

Creighton Mine (7840 lvl) PI9-25 / 1 . Epidote	Creighton Mine (7840 lvl) PI9-26 / 1 . Epidote	Creighton Mine (7840 lvl) PI9-27 / 1 . Epidote	Creighton Mine (7840 lvl) PI9-28 / 1 . Epidote	Creighton Mine (7840 lvl) PI9-29 / 1 . Epidote	Creighton Mine (7840 lvl) PI9-30 / 1 . Epidote	Creighton Mine (7840 lvl) PI9-31 / 1 . Epidote	Creighton Mine (7840 lvl) kpcm02a-66 / 1 . Epidote
37.867	38.168	38.204	37.620	37.972	38.420	38.052	38.439
0.081	0.086	0.055	0.082	0.051	0.065	0.118	0.081
24.094	24.821	24.333	23.917	24.637	24.791	24.513	24.834
11.964	11.197	11.405	11.638	11.105	11.151	12.066	11.139
0.134	0.144	0.150	0.173	0.161	0.121	0.227	0.162
0.000	0.267	0.253	0.225	0.003	0.260	0.000	0.172
23.781	23.797	23.613	23.411	23.717	23.683	23.594	23.760
-0.016	0.000	-0.009	0.010	0.006	0.024	0.004	0.015
-0.001	0.011	0.020	0.000	0.010	0.024	0.031	0.011
0.026	-0.015	0.019	-0.004	-0.016	0.033	0.021	0.000
0.013	0.013	0.002	0.000	-0.003	0.001	0.000	0.024
-0.021	0.009	0.001	-0.006	0.000	0.018	-0.009	0.004
0.116	-0.203	0.203	-0.248	-0.061	0.011	-0.013	0.029
-0.001	0.000	0.003	-0.008	0.003	0.000	0.014	0.006
98.037	98.295	98.253	96.810	97.585	98.602	98.618	98.676
3.001	3.002	3.021	3.008	3.010	3.017	2.995	3.017
						0.005	
3.001	3.002	3.021	3.008	3.010	3.017	3.000	3.017
2.250	2.301	2.268	2.254	2.301	2.294	2.270	2.298
-0.002		-0.001	0.001	0.001	0.003	0.000	0.002
0.005	0.005	0.003	0.005	0.003	0.004	0.007	0.005
0.713	0.663	0.679	0.700	0.662	0.659	0.715	0.658
	0.018	0.017	0.015	0.000	0.017		0.011
2.967	2.986	2.965	2.975	2.968	2.977	2.992	2.973
0.030	0.019	0.011	0.019	0.006	0.015	0.003	
2.019	2.005	2.001	2.006	2.014	1.993	1.990	1.998
0.009	0.010	0.010	0.012	0.011	0.008	0.015	0.011
2.059	2.034	2.022	2.036	2.031	2.015	2.008	2.009
0.759	0.770	0.765	0.758	0.775	0.771	0.759	0.773
0.240	0.222	0.229	0.235	0.223	0.221	0.239	0.221

Table 109

Creighton Mine (7840 lvl) kpcm02a-67 / 1 . Epidote	Creighton Mine (7840 lvl) kpcm02a-68 / 1 . Epidote	Creighton Mine (7840 lvl) kpcm02a-69 / 1 . Epidote	Creighton Mine (7840 lvl) kpcm02a-70 / 1 . Epidote	Creighton Mine (7840 lvl) kpcm02a-73 / 1 . Epidote	Creighton Mine (7840 lvl) kpcm02a-74 / 1 . Epidote	Creighton Mine (7840 lvl) kpcm02a-75 / 1 . Epidote
38.388	38.225	39.277	38.548	38.330	38.310	39.446
0.081	0.066	0.071	0.098	0.063	0.090	0.082
24.574	24.474	25.210	24.949	24.526	24.432	25.601
10.378	11.123	10.416	11.081	10.296	10.931	8.613
0.208	0.203	0.163	0.179	0.210	0.210	0.203
0.616	0.437	1.168	0.070	0.761	0.246	1.698
23.559	23.495	23.776	23.928	23.652	23.802	23.344
0.001	-0.030	0.004	0.008	-0.002	-0.003	0.042
0.059	0.011	0.021	0.023	-0.004	0.017	0.072
-0.012	-0.006	-0.033	0.005	0.013	-0.010	-0.002
0.031	0.025	0.027	0.017	0.031	0.049	0.046
-0.040	0.013	-0.021	-0.025	-0.038	-0.011	-0.015
-0.019	0.181	0.302	-0.098	0.179	0.327	0.144
-0.001	-0.002	-0.008	0.006	-0.001	0.006	0.006
97.823	98.215	100.374	98.789	98.017	98.396	99.280
3.037	3.023	3.038	3.016	3.030	3.027	3.069
3.037	3.023	3.038	3.016	3.030	3.027	3.069
2.291	2.281	2.299	2.301	2.285	2.275	2.348
0.000	-0.004	0.000	0.001	0.000	0.000	0.005
0.005	0.004	0.004	0.006	0.004	0.005	0.005
0.618	0.662	0.606	0.653	0.612	0.650	0.504
0.041	0.029	0.076	0.005	0.050	0.016	0.110
2.954	2.973	2.985	2.965	2.951	2.946	2.972
0.005			0.004	0.040	0.008	
1.997	1.991	1.971	2.006	2.003	2.015	1.946
0.014	0.014	0.011	0.012	0.014	0.014	0.013
2.015	2.005	1.981	2.022	2.057	2.037	1.959
0.775	0.767	0.770	0.776	0.774	0.772	0.790
0.209	0.223	0.203	0.220	0.208	0.221	0.170

Apatite

Table 110

Locality	Creighton Mine (5400 lvl)	Creighton Mine (5400 lvl)	Creighton Mine (5400 lvl)	Creighton Mine (5400 lvl)	Creighton Mine (5400 lvl)	Creighton Mine (5400 lvl)
Sample and analysis	sss01_15b_3	sss01_9b_1	sss01_16c_1	sss01_16b_3	sss01_27c_2	sss01_29d
Mineral	Apatite	Apatite	Apatite	Apatite	Apatite	Apatite
P2O5	41.891	42.144	42.671	42.893	41.739	41.939
SiO2	0.01	0.078	-0.002	0.165	0.701	0.009
Na2O	-0.04	-0.002	0	-0.04	-0.01	0.001
CaO	54.648	54.671	55.703	55.704	54.749	54.995
Al2O3	-0.011	0.034	0.016	0.121	0.242	0.016
La2O3	0.028	-0.048	-0.008	0.009	0.009	-0.013
Ce2O3	0.001	0.022	0.016	-0.048	-0.007	-0.005
SO2	-0.003	0	0.002	0.005	0.002	-0.006
ThO2	0.001	0.021	-0.004	-0.022	-0.012	-0.004
UO2	-0.016	0.005	0.016	0.009	0.031	0.001
F	2.745	3.07	2.664	2.821	2.765	2.897
Cl	0.07	0.065	0.099	0.061	0.056	0.077
H2O	0.394	0.244	0.46	0.404	0.407	0.323
Total	99.786	100.355	101.647	102.192	100.702	100.257
O=F , Cl	1.172	1.307	1.144	1.202	1.177	1.237
Total	98.615	99.048	100.503	100.99	99.525	99.02

Table 111

Locality	Creighton Mine (5400 lvl)	Creighton Mine (5400 lvl)	Creighton Mine (5400 lvl)	Creighton Mine (5400 lvl)	Creighton Mine (5400 lvl)
Sample and analysis	sss11b_3.3	sss11b_2b_4	sss11b_1_5_1	sss11b_1_5_2	sss11b_1_6
Mineral	Apatite	Apatite	Apatite	Apatite	Apatite
P2O5	43.371	42.761	42.435	41.959	43.270
SiO2	-0.009	0.007	0.019	0.008	0.008
Na2O	-0.030	-0.002	-0.015	-0.013	0.004
CaO	56.255	55.895	55.659	55.288	56.159
Al2O3	0.006	0.001	0.018	-0.007	0.012
La2O3	-0.007	-0.008	-0.010	-0.007	0.016
Ce2O3	0.010	0.053	0.013	0.003	0.007
SO2	0.005	0.005	0.005	0.003	0.010
ThO2	0.003	-0.001	-0.009	0.003	0.041
UO2	-0.026	0.006	0.031	-0.020	-0.047
F	2.945	2.671	2.784	2.813	2.905
Cl	0.069	0.086	0.083	0.087	0.076
H2O	0.354	0.464	0.399	0.366	0.369
Total	103.018	101.950	101.445	100.529	102.878
O=F , Cl	1.256	1.144	1.191	1.204	1.240
Total	101.762	100.806	100.254	99.325	101.637

Table 112

Creighton Mine (5400 lvl) sss11b_1_3 Apatite	Creighton Mine (5400 lvl) sss11b_10_2 Apatite	Creighton Mine (5400 lvl) sss11b_24_1_1 Apatite	Creighton Mine (5400 lvl) sss11b_24_1_2 Apatite	Creighton Mine (5400 lvl) sss11b_30_1 Apatite
43.255	42.746	42.905	42.968	42.838
0.037	0.001	-0.006	-0.003	0.008
-0.021	-0.039	-0.017	-0.048	-0.007
55.585	55.567	56.150	55.820	55.988
0.055	-0.014	0.004	-0.005	0.019
-0.028	-0.006	-0.006	0.008	0.013
0.010	0.019	0.010	0.011	-0.002
0.005	0.004	0.002	-0.005	0.000
0.014	-0.029	0.000	0.006	0.008
-0.019	-0.036	0.005	0.012	-0.043
2.848	2.970	2.720	2.656	2.935
0.088	0.079	0.074	0.062	0.061
0.387	0.314	0.450	0.482	0.344
102.285	101.699	102.321	102.024	102.216
1.219	1.268	1.162	1.132	1.250
101.066	100.431	101.159	100.892	100.966

Table 113

Locality	Creighton Mine (5400 lvl)	Creighton Mine (5400 lvl)	Creighton Mine (5400 lvl)	Creighton Mine (5400 lvl)	Creighton Mine (5400 lvl)	Creighton Mine (5400 lvl)	Creighton Mine (5400 lvl)
Sample and analysis	sss20_trgt9	sss20_trgt10	sss20_trgt8	sss20_trgt7	sss20_trgt2	sss20_trgt3	sss20_trgt4
Mineral	Apatite	Apatite	Apatite	Apatite	Apatite	Apatite	Apatite
P2O5	42.928	42.799	42.506	43.229	42.736	42.393	42.034
SiO2	-0.002	0.002	0.004	0.024	0.201	0.016	0.011
Na2O	-0.007	-0.005	0.008	-0.015	-0.041	-0.026	-0.027
CaO	56.213	56.181	55.709	55.759	55.819	56.081	55.921
Al2O3	0.018	0.049	0.035	0.006	0.089	-0.015	-0.011
La2O3	0.007	0.022	-0.039	0.005	-0.013	0.027	-0.055
Ce2O3	0.046	0.024	0.009	0.006	0.02	0.01	-0.002
SO2	0.006	0.001	0	0.003	0.005	0.004	0.007
ThO2	-0.008	0.01	-0.01	-0.001	-0.003	-0.017	-0.04
UO2	-0.005	0.021	-0.001	0.021	0.011	-0.025	0.019
F	2.941	2.964	2.673	2.777	2.698	2.706	2.626
Cl	0.083	0.087	0.086	0.097	0.092	0.101	0.07
H2O	0.341	0.325	0.455	0.42	0.455	0.436	0.473
Total	102.581	102.484	101.485	102.348	102.126	101.773	101.16
O=F , Cl	1.257	1.268	1.145	1.191	1.157	1.162	1.121
Total	101.325	101.217	100.34	101.156	100.969	100.611	100.039

Table 114

Locality	Creighton Mine (5400 lvl)	Creighton Mine (5400 lvl)	Creighton Mine (5400 lvl)	Creighton Mine (5400 lvl)	Creighton Mine (5400 lvl)
Sample and analysis	sss1403_18_1	sss1403_18b	sss1403_10_1	sss1403_10_2	sss1403_trgt8
Mineral	Apatite	Apatite	Apatite	Apatite	Apatite
P2O5	42.107	43.321	42.993	42.334	42.740
SiO2	0.072	0.309	0.009	0.013	0.015
Na2O	0.014	-0.015	-0.019	-0.016	-0.009
CaO	55.688	55.628	56.227	55.059	56.043
Al2O3	0.002	0.140	-0.008	-0.001	0.008
La2O3	0.009	-0.006	-0.013	0.021	0.003
Ce2O3	-0.001	-0.012	-0.006	0.028	0.004
SO2	0.005	0.001	-0.004	0.006	-0.001
ThO2	-0.030	0.032	-0.004	0.019	0.013
UO2	0.002	0.021	-0.001	0.011	0.002
F	3.014	3.112	2.843	2.550	2.876
Cl	0.057	0.068	0.094	0.091	0.087
H2O	0.285	0.273	0.387	0.502	0.364
Total	101.255	102.905	102.552	100.634	102.155
O=F , Cl	1.282	1.326	1.218	1.094	1.231
Total	99.973	101.579	101.334	99.540	100.924

Trace element data (RAR and SIX SHAFT SHEAR ZONE)

Biotite

Table 115

Locality	Creighton Mine (5400 lvl)	Creighton Mine (5400 lvl)	Creighton Mine (5400 lvl)	Creighton Mine (5400 lvl)	Creighton Mine (5400 lvl)	Creighton Mine (5400 lvl)	Creighton Mine (5400 lvl)	Creighton Mine (5400 lvl)
Sample and analysis	SSS01A_site04_bt_01	SSS01A_site04_bt_01	SSS01A_site04_bt_02	SSS01A_site04_bt_04	SSS01A_site07_bt_01	SSS01A_site07_bt_02	SSS01A_site07_bt_03	SSS01A_site07_bt_04
Mineral	Biotite	Biotite	Biotite	Biotite	Biotite	Biotite	Biotite	Biotite
P31	20.994	18.282	bdl	bdl	bdl	75.612	bdl	68.470
Sc45	1.071	1.036	1.192	5.476	0.737	bdl	0.667	0.521
Ti49	9274.570	9343.198	9628.220	8041.659	10302.913	10335.620	9220.997	9933.201
V51	211.522	209.221	220.829	209.332	200.878	201.133	202.205	148.251
Cr52	77.327	84.780	63.762	69.150	17.616	21.762	49.459	42.386
Mn55	1904.697	1858.407	2094.031	2025.425	2043.195	2024.427	2062.150	2233.637
Co59	65.317	64.271	69.872	65.497	68.902	68.136	70.056	72.077
Ni60	77.142	72.413	80.446	81.147	89.273	89.368	88.888	105.819
Zn66	415.243	408.852	420.864	442.977	409.392	420.762	414.179	453.932
Ga69	39.926	38.699	40.949	44.988	32.007	31.229	34.560	36.365
Ge72	0.753	0.683	bdl	bdl	bdl	bdl	bdl	bdl
As75	<0.5	bdl	bdl	bdl	bdl	bdl	bdl	bdl
Rb85	891.871	910.335	905.222	882.037	869.822	907.623	817.062	868.655
Sr88	0.338	0.252	1.047	68.071	0.514	0.416	0.510	0.615
Y89	0.028	bdl	bdl	23.395	bdl	bdl	0.065	bdl
Zr90	0.293	bdl	0.538	0.689	bdl	bdl	bdl	bdl
Nb93	11.814	13.940	7.591	6.043	5.567	10.207	5.297	5.560
Mo95	bdl	bdl	bdl	bdl	bdl	bdl	bdl	bdl
Sn118	0.858	0.737	1.158	1.775	1.016	0.872	0.781	0.825
Ba137	429.108	475.482	742.903	658.392	460.847	334.554	558.011	601.212
Hf177	bdl	bdl	bdl	bdl	bdl	bdl	bdl	bdl
Ta181	0.111	0.192	bdl	0.071	bdl	bdl	0.091	0.169
W182	0.366	0.251	bdl	0.320	bdl	bdl	0.319	0.550
Pb208	3.575	2.242	12.145	27.851	6.216	3.202	23.050	21.377
Th232	bdl	bdl	bdl	11.015	bdl	bdl	bdl	bdl
U238	0.071	0.040	0.720	2.932	bdl	bdl	0.524	0.639

Table 116

Locality	Creighton Mine (5400 lvl)	Creighton Mine (5400 lvl)	Creighton Mine (5400 lvl)	Creighton Mine (5400 lvl)	Creighton Mine (5400 lvl)	Creighton Mine (5400 lvl)	Creighton Mine (5400 lvl)
Sample and analysis	SSS02A_site04a_bt_01	SSS02A_site04a_bt_02	SSS02A_site10_bt_01	SSS02A_site10_bt_02	SSS02A_site10_bt_03	SSS02A_site10_bt_04	SSS02A_site10_bt_05
Mineral	Biotite	Biotite	Biotite	Biotite	Biotite	Biotite	Biotite
P31	bdl	bdl	bdl	76.67800557	bdl	bdl	bdl
Sc45	2.356	2.090	2.474	3.475	2.460	3.038	4.057
Ti49	10677.418	10345.511	28932.386	10487.422	10755.073	10775.164	9740.325
V51	242.780	245.025	188.257	167.611	163.209	182.404	163.613
Cr52	60.695	58.082	28.080	28.319	18.688	21.168	12.111
Mn55	1480.208	1434.554	1385.749	1488.475	1462.484	1503.661	1426.350
Co59	68.463	68.492	73.241	72.888	72.658	79.504	69.480
Ni60	399.490	393.713	631.374	426.622	414.758	945.679	584.579
Zn66	346.243	322.932	331.589	339.280	325.881	348.583	322.912
Ga69	62.452	57.047	57.315	61.021	59.473	57.326	56.887
Ge72	bdl	bdl	bdl	bdl	bdl	bdl	bdl
As75	bdl	bdl	bdl	bdl	bdl	bdl	bdl
Rb85	497.320	464.249	432.990	476.635	479.590	467.691	443.818
Sr88	0.214	0.448	1.585	0.317	0.316	0.406	2.068
Y89	0.663	1.879	82.351	0.373	0.343	bdl	bdl
Zr90	bdl	0.185	2.537	bdl	bdl	bdl	0.128
Nb93	14.180	16.058	144.765	8.413	9.094	7.165	8.932
Mo95	bdl	bdl	bdl	bdl	bdl	bdl	bdl
Sn118	2.611	1.870	1.310	1.334	1.398	1.973	1.808
Ba137	2257.371	2132.593	1908.949	2242.152	2264.532	2100.207	2166.743
Hf177	bdl	bdl	bdl	bdl	bdl	bdl	bdl
Ta181	0.3419	0.3630	9.8489	bdl	0.1590	0.0988	0.0985
W182	1.0355	0.4377	1.3623	0.8701	bdl	0.6315	0.7901
Pb208	2.6058	2.5586	3.1653	2.1885	2.4509	4.3222	2.8894
Th232	bdl	0.054	0.212	bdl	bdl	0.342	0.174
U238	bdl	0.341	0.926	bdl	bdl	0.767	0.113

Table 117

Locality	Creighton Mine (5400 lvl)	Creighton Mine (5400 lvl)	Creighton Mine (5400 lvl)	Creighton Mine (5400 lvl)	Creighton Mine (5400 lvl)	Creighton Mine (5400 lvl)	Creighton Mine (5400 lvl)
Sample and analysis	SSS03A_site01_bt_01	SSS03A_site01_bt_02	SSS03A_site01_bt_03	SSS03A_site01_bt_04	SSS03A_site01_bt_05	SSS03A_site01_bt_06	SSS03A_site01_bt_07
Mineral	Biotite	Biotite	Biotite	Biotite	Biotite	Biotite	Biotite
P31	33.554	bdl	bdl	41.581	28.789	35.500	40.223
Sc45	6.721	8.181	9.108	7.511	6.757	11.497	11.222
Ti49	9615.293	11295.407	9565.212	11789.791	11651.536	11583.957	11461.216
V51	281.703	247.203	270.668	326.076	321.691	268.806	258.555
Cr52	30.204	135.427	24.244	88.437	95.453	159.640	178.932
Mn55	1293.551	1463.969	1342.460	1528.189	1542.731	1543.053	1523.325
Co59	63.175	71.555	64.658	74.832	74.696	72.974	72.398
Ni60	745.651	868.733	770.358	927.639	896.980	934.344	906.504
Zn66	306.686	336.444	318.158	379.803	372.267	367.495	366.133
Ga69	39.652	42.724	41.202	47.455	46.521	47.163	45.385
Ge72	1.374	bdl	2.793	2.525	1.543	1.212	bdl
As75	bdl	bdl	bdl	bdl	bdl	bdl	bdl
Rb85	412.763	461.231	416.184	506.300	499.054	486.703	480.337
Sr88	52.302	14.989	48.299	0.465	0.484	0.562	0.708
Y89	0.112	bdl	0.090	bdl	bdl	0.338	0.437
Zr90	bdl	bdl	bdl	bdl	0.059	bdl	bdl
Nb93	16.920	14.929	16.167	20.342	20.406	14.505	12.655
Mo95	bdl	bdl	bdl	bdl	bdl	bdl	bdl
Sn118	1.928	1.700	1.848	2.568	2.461	2.196	1.930
Ba137	1648.008	1873.886	1564.975	1921.983	1891.407	1986.264	1938.323
Hf177	bdl	bdl	bdl	bdl	bdl	bdl	bdl
Ta181	0.858	1.470	0.841	0.869	1.104	1.197	0.958
W182	0.338	bdl	bdl	0.533	0.430	0.528	0.478
Pb208	4.896	3.845	4.232	2.774	2.581	2.841	2.696
Th232	bdl	bdl	bdl	bdl	bdl	0.026	0.067
U238	bdl	bdl	0.075	bdl	0.084	0.101	0.134

Table 118

Locality	Creighton Mine (5400 lvl)	Creighton Mine (5400 lvl)	Creighton Mine (5400 lvl)	Creighton Mine (5400 lvl)	Creighton Mine (5400 lvl)	Creighton Mine (5400 lvl)	Creighton Mine (5400 lvl)
Sample and analysis	SSS04A_site01_bt_01	SSS04A_site01_bt_02	SSS04A_site01_bt_03	SSS04A_site01_bt_04	SSS04A_site01_bt_05	SSS04A_site01_bt_07	SSS04A_site01_bt_08
Mineral	Biotite	Biotite	Biotite	Biotite	Biotite	Biotite	Biotite
P31	bdl	bdl	86.108	52.689	32.749	32.253	38.401
Sc45	36.942	36.798	58.901	31.669	34.385	31.357	32.936
Ti49	11061.294	11018.064	9214.113	11743.774	12146.900	11741.628	11971.161
V51	381.643	381.633	316.892	389.281	395.628	393.969	393.692
Cr52	230.486	250.108	178.124	165.040	189.400	205.791	209.874
Mn55	1646.047	1720.460	1470.711	1798.713	1848.111	1804.812	1855.829
Co59	94.674	96.966	77.429	94.142	98.692	95.222	95.733
Ni60	1619.550	1608.996	1351.397	1633.917	1668.192	1640.753	1653.456
Zn66	400.200	400.641	335.869	422.775	441.211	418.888	415.759
Ga69	57.882	57.071	48.892	56.436	57.185	58.719	56.798
Ge72	bdl	2.600	bdl	1.980	2.118	2.007	2.112
As75	bdl	bdl	bdl	bdl	bdl	bdl	bdl
Rb85	581.329	590.872	484.458	582.142	593.958	591.977	590.852
Sr88	0.236	0.573	1.055	0.404	0.363	0.857	0.363
Y89	0.255	2.345	311.530	0.105	0.075	0.043	0.353
Zr90	bdl	0.512	94511.723	6.667	2.964	bdl	4.246
Nb93	7.959	7.889	7.571	10.765	11.093	10.149	7.553
Mo95	bdl	bdl	bdl	bdl	bdl	bdl	bdl
Sn118	2.949	2.556	2.691	2.358	2.281	3.651	2.287
Ba137	2305.479	2391.008	1850.628	2463.025	2423.714	2380.502	2424.566
Hf177	bdl	bdl	2387.222	0.139	bdl	bdl	0.151
Ta181	0.086	0.083	0.801	0.133	0.094	0.140	0.102
W182	0.386	1.203	0.498	0.532	0.589	0.571	0.882
Pb208	1.437	2.598	7.535	2.768	2.338	2.944	2.554
Th232	bdl	bdl	32.031	bdl	bdl	bdl	bdl
U238	bdl	bdl	70.614	bdl	bdl	0.067	0.064

Table 119

Locality	Creighton Mine (7840 lvl)	Creighton Mine (7840 lvl)	Creighton Mine (7840 lvl)	Creighton Mine (7840 lvl)	Creighton Mine (7840 lvl)	Creighton Mine (7840 lvl)	Creighton Mine (7840 lvl)
Sample and analysis	KPCM09_St1_Trgt1_Bt	KPCM09_St1_Trgt3_Bt	KPCM09_St1_Trgt4_Bt	KPCM09_St1_Trgt5_Bt	KPCM09_St2_Trgt2_Bt	KPCM09_St2_Trgt3_Bt	KPCM09_St2_Trgt4_Bt
Mineral	Biotite	Biotite	Biotite	Biotite	Biotite	Biotite	Biotite
SiO2	41.447	39.787	40.859	41.805	40.074	41.287	39.883
TiO2	1.491	1.315	1.376	1.358	1.402	1.407	1.367
MnO	0.231	0.228	0.225	0.238	0.216	0.219	0.215
MgO	8.918	8.644	8.816	8.919	8.600	8.864	8.715
CaO	bdl	bdl	bdl	bdl	bdl	bdl	0.040
K2O	11.360	11.052	11.235	11.571	11.214	11.559	10.995
Sc45	4.244	3.929	4.034	3.683	2.524	2.391	2.492
V51	165.992	160.119	162.781	167.114	210.977	212.021	208.927
Cr53	971.775	658.076	532.679	1030.993	294.921	419.576	304.117
Co59	86.248	84.126	84.351	88.005	83.889	85.909	83.441
Ni60	374.237	360.003	367.838	374.463	359.546	357.646	352.482
Cu63	bdl	bdl	bdl	bdl	bdl	bdl	bdl
Zn66	344.457	328.726	333.500	338.691	315.032	338.861	326.438
Rb85	614.611	587.561	610.116	604.163	591.416	601.760	551.599
Sr88	0.324	0.332	0.265	0.347	0.694	0.350	0.406
Nb93	14.521	6.049	8.296	5.658	4.140	3.990	3.649
Mo95	0.184	0.170	bdl	0.215	0.234	0.222	0.176
Sn118	1.171	0.939	1.245	0.985	1.168	1.191	1.016
Ta181	0.179	0.081	0.092	0.060	0.018	0.031	0.029
Pb208	1.686	1.171	1.634	1.307	1.416	1.202	1.415

Table 120

Creighton Mine (7840 lvl) KPCM09_St2_Trgt5_Bt Biotite	Creighton Mine (7840 lvl) KPCM09_St3_Trgt1_Bt Biotite	Creighton Mine (7840 lvl) KPCM09_St3_Trgt3_Bt Biotite
39.856	50.040	40.558
1.413	1.326	1.317
0.213	0.300	0.220
8.552	10.366	8.996
bdl	2.444	0.044
10.637	10.929	11.391
2.676	28.000	4.355
213.053	351.437	256.784
239.054	173.844	153.111
81.965	94.202	84.171
352.501	355.100	325.607
bdl	bdl	bdl
323.690	367.799	315.964
553.224	563.988	583.328
0.338	1.798	1.046
4.381	3.557	2.914
bdl	0.403	bdl
1.049	1.880	0.913
0.028	bdl	bdl
1.355	1.877	1.342

Table 121

Locality	Creighton Mine (7840 lvl)	Creighton Mine (7840 lvl)	Creighton Mine (7840 lvl)	Creighton Mine (7840 lvl)	Creighton Mine (7840 lvl)	Creighton Mine (7840 lvl)	Creighton Mine (7840 lvl)
Sample and analysis	PL4_St1_Trgt1_Bt	PL4_St1_Trgt2_Bt	PL4_St1_Trgt3_Bt	PL4_St1_Trgt4_Bt	PL4_St1_Trgt5_Bt	PL4_St1_Trgt6_Bt	PL4_St1_Trgt7_Bt
Mineral	Biotite	Biotite	Biotite	Biotite	Biotite	Biotite	Biotite
SiO2	39.630	39.882	38.890	39.251	42.570	41.355	36.940
TiO2	2.147	2.122	2.052	2.153	2.060	2.019	1.966
MnO	0.271	0.274	0.266	0.266	0.279	0.278	0.264
MgO	6.047	6.178	6.014	5.922	6.043	5.963	5.574
CaO	bdl	bdl	bdl	bdl	0.138	bdl	bdl
K2O	10.928	11.098	10.739	10.752	10.933	10.997	10.184
Sc45	17.062	16.614	16.949	13.138	13.717	17.317	17.725
V51	202.149	206.077	197.958	195.543	200.218	217.651	190.224
Cr53	24.982	24.888	32.938	51.568	22.723	28.560	29.732
Co59	68.557	67.326	66.317	67.743	70.591	68.616	64.792
Ni60	601.951	623.622	598.704	589.683	615.073	616.083	556.236
Cu63	bdl	0.379	bdl	bdl	0.380	bdl	bdl
Zn66	359.937	361.026	344.051	332.021	352.139	359.553	328.688
Rb85	584.772	596.237	573.494	576.504	587.259	585.878	542.646
Sr88	0.468	0.563	0.485	0.504	16.576	0.484	0.550
Nb93	54.788	48.975	36.618	33.495	24.765	22.626	20.504
Mo95	bdl	bdl	0.189	bdl	0.229	bdl	0.235
Sn118	2.397	2.833	2.137	2.126	2.386	2.142	2.237
Ta181	1.662	1.392	0.951	0.863	0.284	0.277	0.229
Pb208	3.865	3.754	3.666	3.384	4.107	2.843	2.558

Table 122

Creighton Mine (7840 lvl) PL4_St1_Trgt8_Bt Biotite	Creighton Mine (7840 lvl) PL4_St1_Trgt9_Bt Biotite	Creighton Mine (7840 lvl) PL4_St1_Trgt10_Bt Biotite	Creighton Mine (7840 lvl) PL4_St2_Trgt1_Bt Biotite	Creighton Mine (7840 lvl) PL4_St2_Trgt2_Bt Biotite	Creighton Mine (7840 lvl) PL4_St2_Trgt3_Bt Biotite	Creighton Mine (7840 lvl) PL4_St2_Trgt4_Bt Biotite	Creighton Mine (7840 lvl) PL4_St2_Trgt5_Bt Biotite
40.188	39.787	39.233	40.366	40.206	36.334	38.821	39.193
2.086	1.955	1.959	2.187	2.070	1.723	2.089	2.054
0.282	0.272	0.273	0.282	0.248	0.254	0.263	0.276
5.964	5.970	6.075	6.154	6.080	5.644	5.943	6.056
bdl	0.098	bdl	0.090	bdl	0.059	bdl	bdl
10.959	10.852	10.787	11.135	10.949	10.020	10.748	10.900
19.390	17.032	16.786	20.124	20.208	19.762	18.487	18.501
204.378	199.070	212.561	185.274	180.521	173.884	178.572	181.937
27.265	31.894	33.510	36.496	23.981	31.141	22.888	38.360
69.603	68.618	69.736	68.366	67.771	62.562	65.329	67.371
606.322	600.502	604.899	629.358	618.290	570.749	604.930	622.824
bdl	bdl	bdl	bdl	bdl	bdl	bdl	bdl
362.997	352.827	358.669	373.190	336.915	327.341	347.774	349.882
584.239	576.051	564.900	587.376	581.065	529.908	567.403	577.135
0.659	0.868	0.453	0.711	0.512	0.546	0.440	0.430
23.825	24.195	28.316	48.761	37.992	29.638	31.758	45.945
bdl	0.148	0.273	bdl	bdl	0.211	bdl	0.256
2.382	30.406	2.701	2.735	2.588	2.570	2.415	2.383
0.323	0.373	0.408	1.536	1.047	0.413	0.864	1.606
3.137	3.846	2.976	3.393	3.057	2.653	3.402	3.206

Table 123

Locality	Creighton Mine (7840 lvl)	Creighton Mine (7840 lvl)	Creighton Mine (7840 lvl)	Creighton Mine (7840 lvl)	Creighton Mine (7840 lvl)	Creighton Mine (7840 lvl)	Creighton Mine (7840 lvl)
Sample and analysis	PL7_St1_Trgt1_Bt	PL7_St1_Trgt2_Bt	PL7_St1_Trgt3_Bt	PL7_St1_Trgt4_Bt	PL7_St1_Trgt5_Bt	PL7_St1_Trgt6_Bt	PL7_St1_Trgt7_Bt
Mineral	Biotite	Biotite	Biotite	Biotite	Biotite	Biotite	Biotite
SiO2	39.576	40.907	39.145	38.665	39.343	39.291	40.658
TiO2	1.766	1.760	1.770	1.686	1.725	1.764	1.698
MnO	0.304	0.313	0.300	0.294	0.295	0.295	0.299
MgO	5.963	6.085	5.891	5.761	5.853	5.928	5.926
CaO	bdl	bdl	0.088	bdl	bdl	bdl	bdl
K2O	11.353	11.612	11.063	11.206	11.181	11.301	11.587
Sc45	7.938	5.988	5.661	6.055	5.572	6.253	5.320
V51	282.148	294.806	289.631	286.824	278.175	289.912	282.022
Cr53	5.802	8.249	14.270	12.872	4.176	bdl	bdl
Co59	73.954	76.554	73.233	74.340	73.243	73.992	75.841
Ni60	580.904	604.931	586.735	583.432	577.731	581.191	598.024
Cu63	bdl	bdl	bdl	bdl	bdl	bdl	bdl
Zn66	361.209	371.817	356.855	359.704	349.772	357.369	364.302
Rb85	725.387	728.593	651.261	650.369	725.021	718.888	707.882
Sr88	0.391	1.109	0.846	0.455	0.380	0.395	0.408
Nb93	19.322	15.825	14.361	14.256	15.630	14.758	15.164
Mo95	0.231	0.264	0.206	0.263	bdl	0.177	bdl
Sn118	2.370	2.512	2.605	2.400	2.535	2.983	2.686
Ta181	0.234	0.076	0.039	0.061	0.058	0.050	0.065
Pb208	3.098	11.864	13.434	3.560	3.521	3.361	3.250

Table 124

Creighton Mine (7840 lvl) PL7_St1_Trgt8_Bt Biotite	Creighton Mine (7840 lvl) PL7_St1_Trgt9_Bt Biotite	Creighton Mine (7840 lvl) PL7_St1_Trgt10_Bt Biotite	Creighton Mine (7840 lvl) PL7_St1_Trgt11_Bt Biotite	Creighton Mine (7840 lvl) PL7_St1_Trgt12_Bt Biotite	Creighton Mine (7840 lvl) PL7_St1_Trgt13_Bt Biotite
39.738	39.933	39.916	40.004	39.727	39.817
1.699	1.671	1.639	1.558	1.641	1.676
0.289	0.292	0.291	0.290	0.289	0.309
5.856	5.859	5.888	5.910	5.914	6.141
bdl	bdl	bdl	bdl	bdl	0.049
11.268	11.327	11.413	11.360	11.319	11.531
4.798	4.987	5.053	4.666	4.920	4.948
278.113	288.580	286.933	280.741	283.878	291.511
9.127	4.742	8.888	10.242	6.460	14.097
73.298	74.064	74.779	75.947	72.749	76.423
590.148	590.980	606.934	600.806	595.305	614.075
bdl	bdl	bdl	bdl	bdl	0.546
342.025	355.072	346.827	362.976	363.141	372.634
719.778	724.281	724.346	709.813	726.047	729.858
0.359	0.374	0.376	0.389	0.403	0.840
15.827	14.889	15.458	13.560	14.306	13.137
0.240	bdl	0.233	0.199	bdl	0.204
2.028	2.925	2.535	2.336	2.363	2.565
0.066	0.058	0.061	0.047	0.057	0.039
4.095	3.285	3.309	2.706	3.355	7.173

Table 125

Locality	Creighton Mine (7840 lvl)	Creighton Mine (7840 lvl)	Creighton Mine (7840 lvl)
Sample and analysis	PL13_St1_Trgt2_Bt	PL13_St1_Trgt3_Bt	PL13_St1_Trgt4_Bt
Mineral	Biotite	Biotite	Biotite
SiO2	43.341	41.963	43.182
TiO2	2.022	2.043	2.287
MnO	0.205	0.177	0.225
MgO	6.337	6.202	6.347
CaO	bdl	bdl	bdl
K2O	12.080	11.495	11.951
Sc45	2.986	3.042	3.548
V51	134.269	125.352	130.236
Cr53	90.576	60.118	108.234
Co59	86.006	84.692	81.598
Ni60	69.459	67.008	67.633
Cu63	bdl	bdl	bdl
Zn66	375.444	342.789	341.171
Rb85	611.439	577.703	585.103
Sr88	0.630	1.004	0.765
Nb93	27.066	26.277	30.337
Mo95	bdl	bdl	0.267
Sn118	bdl	2.163	1.542
Ta181	0.113	0.088	0.087
Pb208	3.375	3.008	3.003

Table 126

Locality	Creighton Mine (7840 lvl)	Creighton Mine (7840 lvl)	Creighton Mine (7840 lvl)	Creighton Mine (7840 lvl)	Creighton Mine (7840 lvl)	Creighton Mine (7840 lvl)	Creighton Mine (7840 lvl)
Sample and analysis	PL17_Bt_Trgt1	PL17_Bt_Trgt2	PL17_Bt_Trgt3	PL17_Bt_Trgt4	PL17_Bt_Trgt5	PL17_Bt_Trgt6	PL17_Bt_Trgt7
Mineral	Biotite	Biotite	Biotite	Biotite	Biotite	Biotite	Biotite
SiO2	41.161	41.803	41.435	42.216	41.863	41.300	39.616
TiO2	1.542	1.522	1.527	1.495	1.521	1.500	1.445
MnO	0.183	0.182	0.184	0.186	0.183	0.182	0.176
MgO	9.604	9.881	9.738	9.860	9.928	9.801	9.366
CaO	bdl	bdl	bdl	bdl	bdl	bdl	bdl
K2O	11.372	11.441	11.326	11.574	11.414	11.306	10.815
Sc45	3.738	3.564	3.207	3.840	4.374	3.628	3.879
V51	215.539	217.124	214.231	222.849	228.186	222.393	211.874
Cr53	485.134	545.504	415.754	478.914	497.274	541.573	489.329
Co59	90.775	92.636	91.007	92.217	89.496	93.763	81.849
Ni60	503.485	515.490	507.796	507.980	505.686	525.483	484.474
Cu63	bdl	bdl	bdl	bdl	bdl	bdl	bdl
Zn66	302.907	309.219	302.437	308.427	296.914	305.309	278.068
Rb85	670.070	650.869	640.382	645.250	666.521	638.975	636.775
Sr88	0.494	0.382	0.466	0.333	0.424	0.314	0.446
Nb93	3.950	1.872	1.918	1.428	2.175	1.381	2.194
Mo95	0.168	bdl	bdl	bdl	bdl	0.230	0.159
Sn118	1.293	1.404	1.295	1.273	1.611	1.301	1.274
Ta181	0.049	0.020	bdl	bdl	0.016	bdl	0.024
Pb208	1.543	1.501	1.528	1.231	1.557	1.335	1.827

Table 127

Creighton Mine (7840 lvl) PL17_Bt_Trgt8 Biotite	Creighton Mine (7840 lvl) PL17_Bt_Trgt9 Biotite	Creighton Mine (7840 lvl) PL17_Bt_Trgt10 Biotite	Creighton Mine (7840 lvl) PL17_Bt_Trgt11 Biotite	Creighton Mine (7840 lvl) PL17_Bt_Trgt12 Biotite	Creighton Mine (7840 lvl) PL17_Bt_Trgt13 Biotite	Creighton Mine (7840 lvl) PL17_Bt_Trgt14 Biotite	Creighton Mine (7840 lvl) PL17_Bt_Trgt15 Biotite
41.687	42.197	40.002	41.447	39.702	43.032	47.553	40.784
1.503	1.488	1.432	1.433	1.457	1.490	1.465	1.473
0.183	0.187	0.169	0.189	0.179	0.197	0.190	0.184
9.791	9.999	9.456	9.930	9.500	10.062	10.087	9.606
bdl	bdl	bdl	bdl	bdl	0.564	0.173	bdl
11.429	11.597	11.004	11.001	10.900	11.107	11.068	11.191
4.186	3.549	3.863	4.335	4.289	7.755	4.394	4.143
217.122	215.552	212.382	215.834	213.196	234.753	220.009	223.231
413.436	254.302	585.692	656.547	461.624	706.086	644.021	635.438
83.896	96.287	90.165	94.735	88.362	93.268	93.995	92.099
476.313	529.512	507.458	535.624	507.823	541.374	533.081	523.565
bdl	bdl	bdl	bdl	bdl	bdl	0.539	bdl
286.196	317.987	290.083	320.159	292.980	314.591	311.925	304.527
674.602	677.704	629.859	621.287	631.708	614.280	631.036	647.255
0.448	0.409	0.340	1.498	0.467	0.653	28.258	0.489
2.147	3.003	1.449	1.309	1.742	1.412	2.122	1.524
0.142	0.172	bdl	bdl	bdl	bdl	0.256	0.129
1.702	1.598	1.553	1.320	1.365	1.466	1.478	1.580
0.018	0.025	0.009	bdl	0.015	bdl	0.035	bdl
1.630	1.574	1.513	1.235	1.333	1.388	2.057	1.359

Table 128

Creighton Mine (7840 lvl) PL17_Bt_Trgt16 Biotite	Creighton Mine (7840 lvl) PL17_Bt_Trgt17 Biotite
43.075	39.558
1.544	1.409
0.192	0.178
10.134	9.308
bdl	bdl
11.809	10.783
3.894	3.232
224.878	203.789
474.411	362.550
96.161	86.934
542.800	488.146
bdl	0.375
325.101	289.959
687.839	617.659
0.611	0.519
2.167	1.427
bdl	bdl
1.771	1.147
bdl	bdl
1.548	1.642

Table 129

Locality	Creighton Mine (7840 lvl)	Creighton Mine (7840 lvl)	Creighton Mine (7840 lvl)	Creighton Mine (7840 lvl)
Sample and analysis	PL18_St1_Trgt1_Bt	PL18_St1_Trgt2_Bt	PL18_St1_Trgt3_Bt	PL18_St1_Trgt4_Bt
Mineral	Biotite	Biotite	Biotite	Biotite
SiO2	39.360	40.666	40.779	41.419
TiO2	1.448	1.510	1.510	1.493
MnO	0.165	0.167	0.169	0.172
MgO	9.139	9.456	9.512	9.772
CaO	bdl	bdl	bdl	bdl
K2O	10.569	11.214	11.201	11.483
Sc45	3.368	3.412	3.456	3.569
V51	219.826	240.675	240.568	243.445
Cr53	255.572	576.292	596.873	531.498
Co59	88.604	92.852	91.980	94.533
Ni60	406.583	431.318	429.055	439.976
Cu63	bdl	bdl	0.384	bdl
Zn66	274.854	277.996	278.907	295.366
Rb85	557.077	544.616	572.122	583.311
Sr88	0.806	0.494	0.445	0.521
Nb93	5.808	3.636	2.367	2.617
Mo95	0.130	bdl	bdl	bdl
Sn118	1.463	1.458	1.295	1.439
Ta181	0.033	0.027	bdl	bdl
Pb208	1.956	1.930	1.703	1.431

Creighton Mine (7840 lvl) PL18_St1_Trgt6_Bt Biotite	Creighton Mine (7840 lvl) PL18_St1_Trgt7_Bt Biotite	Creighton Mine (7840 lvl) PL18_Site2_Trgt1_Bt Biotite	Creighton Mine (7840 lvl) PL18_St2_Trgt2_Bt Biotite	Creighton Mine (7840 lvl) PL18_St2_Trgt5_Bt Biotite
40.289	42.525	39.723	41.922	36.684
1.513	1.524	1.500	1.584	1.505
0.166	0.175	0.165	0.170	0.161
9.338	9.691	9.303	9.762	8.831
bdl	0.063	bdl	bdl	0.156
11.018	11.604	10.849	11.531	9.228
3.380	3.493	3.957	3.915	3.912
237.269	241.556	238.470	246.734	230.917
601.330	575.096	555.756	564.219	500.967
90.676	92.908	92.220	96.589	79.989
423.824	448.605	427.324	456.331	401.191
bdl	bdl	bdl	bdl	0.289
278.001	286.533	279.031	293.732	246.622
574.568	589.421	552.578	587.054	490.061
0.718	0.472	0.541	0.437	1.766
3.476	2.151	2.869	3.128	2.270
bdl	bdl	bdl	bdl	bdl
1.377	1.697	1.241	1.351	1.165
0.040	bdl	0.024	0.021	0.010
2.009	1.618	1.611	2.047	1.265

Trace element data

Amphibole

Table 130

Locality	Creighton Mine (7840 lvl)	Creighton Mine (7840 lvl)	Creighton Mine (7840 lvl)	Creighton Mine (7840 lvl)
Sample and analysis	KPCM09_St2_Trgt2_Amp	KPCM09_St2_Trgt3_Amp	KPCM09_St2_Trgt5_Amp	KPCM09_St3_Trgt2_Amp
Mineral	Amphibole	Amphibole	Amphibole	Amphibole
SiO2	32.510	49.999	69.799	71.879
TiO2	0.177	0.299	0.246	0.366
MnO	0.235	0.371	0.484	0.392
MgO	5.730	8.732	12.750	9.370
CaO	8.261	12.528	17.633	13.971
K2O	0.379	0.702	0.614	1.096
Sc45	36.696	53.904	77.719	131.548
V51	191.752	284.283	360.024	570.699
Cr53	498.340	544.848	781.602	124.472
Co59	35.200	56.173	73.955	59.693
Ni60	133.192	206.052	284.794	196.914
Cu63	0.336	0.357	0.384	0.503
Zn66	146.712	232.104	302.750	241.768
Rb85	0.775	1.634	1.187	10.212
Sr88	4.907	7.903	8.741	7.745
Zr90	2.035	3.555	3.718	3.719
Nb93	1.664	2.591	2.358	2.331
Mo95	0.183	0.303	0.255	0.228
Sn118	2.090	3.388	3.449	3.688
La139	0.043	0.179	0.192	0.061
Ce140	0.367	0.856	0.901	0.406
Pr141	0.113	0.195	0.230	0.123
Nd146	0.770	1.503	1.530	0.888
Sm147	0.523	0.726	0.800	0.731
Eu151	0.159	0.247	0.219	0.157
Gd157	1.097	1.759	1.588	1.433
Tb159	0.244	0.370	0.324	0.316
Dy163	1.736	2.991	2.485	2.194
Ho165	0.447	0.748	0.600	0.621
Er167	1.456	2.591	2.045	1.831
Tm169	0.213	0.347	0.264	0.262
Yb172	1.500	2.445	1.535	1.757
Lu175	0.231	0.407	0.255	0.317
Ta181	0.018	bdl	0.039	0.021
Pb208	1.175	2.073	2.861	2.658
Bi209	bdl	bdl	bdl	bdl

Table 131

Locality	Creighton Mine (7840 lvl)	Creighton Mine (7840 lvl)	Creighton Mine (7840 lvl)	Creighton Mine (7840 lvl)
Sample and analysis	PL13_St1_Trgt1_Amp	PL13_St1_Trgt5_Amp	PL13_St1_Trgt6_Amp	PL13_St1_Trgt7_Amp
Mineral	Amphibole	Amphibole	Amphibole	Amphibole
SiO2	43.850	44.902	44.984	47.087
TiO2	0.560	0.414	0.590	0.467
MnO	0.333	0.338	0.348	0.307
MgO	3.596	3.740	3.690	3.188
CaO	11.294	11.377	11.569	10.949
K2O	1.430	1.442	1.479	1.272
Sc45	110.132	15.259	81.415	61.400
V51	262.523	24.600	193.329	153.177
Cr53	69.055	bdl	bdl	7.671
Co59	40.632	41.433	41.854	38.487
Ni60	27.220	27.801	29.733	25.627
Cu63	bdl	0.666	bdl	0.866
Zn66	223.307	218.913	215.472	177.952
Rb85	3.462	3.749	4.339	2.912
Sr88	12.129	12.538	13.588	68.578
Zr90	4.498	5.791	4.781	3.572
Nb93	17.629	23.124	23.384	13.790
Mo95	bdl	bdl	0.311	bdl
Sn118	6.040	6.248	5.390	4.832
La139	0.112	0.220	0.070	0.048
Ce140	0.627	1.001	0.482	0.527
Pr141	0.224	0.247	0.206	0.184
Nd146	1.708	2.287	1.497	1.535
Sm147	2.375	2.320	1.459	1.519
Eu151	0.623	1.011	0.479	0.353
Gd157	6.573	6.208	5.385	4.452
Tb159	1.996	2.114	1.871	1.354
Dy163	20.079	21.678	20.037	13.285
Ho165	5.461	5.752	5.938	3.715
Er167	20.156	20.484	22.167	13.600
Tm169	3.134	3.087	3.599	2.235
Yb172	20.088	21.783	25.569	16.824
Lu175	3.252	3.189	3.870	2.508
Ta181	0.217	0.596	0.348	0.171
Pb208	3.510	3.511	3.894	5.426
Bi209	bdl	bdl	0.178	bdl

Table 132

Creighton Mine (7840 lvl) PL13_St1_Trgt8_Amp Amphibole	Creighton Mine (7840 lvl) PL13_St1_Trgt9_Amp Amphibole	Creighton Mine (7840 lvl) PL13_St2_Trgt2_Amp Amphibole	Creighton Mine (7840 lvl) PL13_St2_Trgt3_Amp Amphibole	Creighton Mine (7840 lvl) PL13_St2_Trgt4_Amp Amphibole
68.171	45.270	52.814	56.852	60.083
0.607	0.590	0.601	0.751	0.452
0.520	0.348	0.390	0.428	0.453
5.697	3.600	4.082	4.903	4.648
16.988	11.424	13.117	14.076	15.221
1.970	1.480	1.689	1.580	1.910
95.191	101.218	133.073	159.329	64.428
177.255	255.939	359.444	404.788	73.581
bdl	115.751	121.652	134.763	bdl
61.746	43.574	51.607	54.654	54.561
45.634	27.732	35.187	34.650	31.407
1.096	0.565	bdl	bdl	bdl
321.092	215.256	235.221	247.404	287.150
4.051	3.295	4.263	6.463	4.530
16.640	12.118	13.290	15.640	12.554
5.747	4.560	4.889	8.953	4.429
19.710	15.361	20.116	30.070	20.737
bdl	0.473	bdl	1.442	bdl
8.433	5.859	6.370	6.542	6.902
0.075	0.062	1.842	19.373	0.110
0.719	0.419	5.293	77.835	0.433
0.211	0.134	0.641	15.932	0.167
2.075	1.237	2.894	84.568	0.811
1.832	1.387	2.376	24.609	1.459
0.765	0.402	0.621	1.169	0.329
5.770	4.166	6.147	28.605	3.717
1.930	1.329	1.875	4.190	1.106
20.392	13.867	19.399	30.452	12.693
6.160	4.200	5.133	6.821	3.771
23.355	15.674	18.597	22.016	15.349
4.034	2.763	2.816	2.915	2.570
30.021	21.247	20.142	20.593	19.537
4.559	3.358	2.753	3.017	3.300
0.178	0.138	0.241	0.563	0.189
7.794	4.757	5.034	7.782	4.998
bdl	bdl	bdl	bdl	bdl

Table 133

Creighton Mine (7840 lvl) PL13_St2_Trgt5_Amp Amphibole	Creighton Mine (7840 lvl) PL13_St2_Trgt6_Amp Amphibole	Creighton Mine (7840 lvl) PL13_St2_Trgt7_Amp Amphibole
42.333	53.009	50.270
0.584	0.618	0.619
0.324	0.392	0.389
3.401	4.055	4.066
10.713	13.497	12.784
1.379	1.689	1.689
103.830	131.634	110.391
253.995	311.836	212.152
44.402	35.343	12.564
39.612	49.663	46.270
29.646	32.038	32.273
0.655	0.859	1.041
206.766	233.810	247.663
3.855	3.989	4.586
13.883	13.977	14.404
5.066	5.533	5.632
22.548	22.395	23.803
bdl	bdl	bdl
5.716	7.133	7.146
0.134	0.349	0.078
0.611	0.742	0.650
0.196	0.197	0.219
1.463	1.737	1.881
1.944	1.648	1.979
0.563	0.417	0.516
5.758	4.780	6.123
1.680	1.544	2.220
18.489	17.812	23.381
5.424	5.082	6.714
20.037	19.325	24.849
3.322	3.185	3.961
23.523	23.504	28.501
3.520	3.418	4.519
0.351	0.260	0.356
3.994	5.404	4.933
bdl	bdl	bdl

Table 134

Locality	Creighton Mine (7840 lvl)	Creighton Mine (7840 lvl)	Creighton Mine (7840 lvl)	Creighton Mine (7840 lvl)	Creighton Mine (7840 lvl)
Sample and analysis	PL18_Site1_Trgt1b_Amp	PL18_St1_Trgt2b_Amp	PL18_St1_Trgt4b_Amp	PL18_St1_Trgt5b_Amp	PL18_St2_Trgt4_Amp
Mineral	Amphibole	Amphibole	Amphibole	Amphibole	Amphibole
SiO2	50.567	49.780	52.532	49.898	55.433
TiO2	0.460	0.465	0.438	0.398	0.399
MnO	0.292	0.292	0.300	0.282	0.274
MgO	9.611	9.125	10.008	9.565	9.389
CaO	12.331	12.171	13.053	12.347	12.294
K2O	0.431	0.442	0.407	0.376	0.375
Sc45	50.240	52.875	55.471	55.638	55.454
V51	321.107	344.467	367.812	366.442	360.487
Cr53	114.322	187.485	196.972	425.829	441.266
Co59	64.897	63.006	69.121	64.197	61.275
Ni60	262.750	255.529	285.355	265.491	255.427
Cu63	0.563	0.467	0.444	0.577	1.038
Zn66	175.012	176.482	188.203	177.278	162.498
Rb85	1.715	1.056	0.937	1.047	1.694
Sr88	11.105	11.132	9.847	9.667	68.910
Zr90	4.535	4.337	3.920	3.507	3.274
Nb93	2.891	3.242	4.242	2.001	3.316
Mo95	0.170	bdl	0.188	0.257	0.279
Sn118	5.431	5.429	6.401	4.837	5.087
La139	0.156	0.211	0.159	0.116	0.124
Ce140	1.335	1.392	1.169	0.879	0.903
Pr141	0.404	0.416	0.375	0.288	0.246
Nd146	3.391	3.246	3.567	2.126	2.499
Sm147	2.407	2.330	3.673	1.510	2.367
Eu151	0.740	0.758	1.221	0.493	0.807
Gd157	4.401	4.415	7.944	2.660	4.943
Tb159	0.785	0.845	1.697	0.503	1.096
Dy163	5.929	6.456	12.866	3.828	8.607
Ho165	1.482	1.619	2.885	0.911	1.974
Er167	4.766	4.991	9.024	3.207	6.512
Tm169	0.712	0.766	1.408	0.461	0.961
Yb172	5.134	5.501	9.314	3.605	6.697
Lu175	0.816	0.910	1.310	0.684	1.084
Ta181	0.035	0.042	0.204	0.019	0.104
Pb208	1.129	1.139	1.011	0.866	2.359
Bi209	bdl	bdl	0.080	0.053	bdl

University of Portsmouth

Certificate of Ethics Review

Project Title:	Petrochronology and mineral-chemistry of mid-crustal shear zones : new tools for tectonics and mineral exploration
User ID:	716315
Name:	Konstantinos Papapavlou
Application Date:	14/11/2016 14:28:24

You must download your certificate, print a copy and keep it as a record of this review.

It is your responsibility to adhere to the University Ethics Policy and any Department/School or professional guidelines in the conduct of your study including relevant guidelines regarding health and safety of researchers and University Health and Safety Policy.

It is also your responsibility to follow University guidance on Data Protection Policy:

- General guidance for all data protection issues
- University Data Protection Policy

You are reminded that as a University of Portsmouth Researcher you are bound by the UKRIO Code of Practice for Research; any breach of this code could lead to action being taken following the University's Procedure for the Investigation of Allegations of Misconduct in Research.

Any changes in the answers to the questions reflecting the design, management or conduct of the research over the course of the project must be notified to the Faculty Ethics Committee. **Any changes that affect the answers given in the questionnaire, not reported to the Faculty Ethics Committee, will invalidate this certificate.**

This ethical review should not be used to infer any comment on the academic merits or methodology of the project. If you have not already done so, you are advised to develop a clear protocol/proposal and ensure that it is independently reviewed by peers or others of appropriate standing. A favourable ethical opinion should not be perceived as permission to proceed with the research; there might be other matters of governance which require further consideration including the agreement of any organisation hosting the research.

GovernanceChecklist
A1-BriefDescriptionOfProject: Ductile shear zones in the Sudbury Ni-Cu-PGE mining camp are new exploration targets but the timing of operation and their ore bearing potential are poorly constrained. Accessory phase geochronology using novel microanalytical tools (LA-ICP-MS) and microchemical analysis of fabric forming phases, combining SEM/EDS and EMP, aim to fill these gaps. Isotopic age constraints from shear zone hosted accessory minerals will ascribe these deformation zones in orogenic context. In addition, microchemical analysis will be utilized to test if trends in the trace element

composition of modally abundant phases can be used to vector new ore bodies.

A2-Faculty: Science
A3-VoluntarilyReferToFEC: No
A5-AlreadyExternallyReviewed: No
B1-HumanParticipants: No
HumanParticipantsDefinition
B2-HumanParticipantsConfirmation: Yes
C6-SafetyRisksBeyondAssessment: No
D2-PhysicalEcologicalDamage: No
D4-HistoricalOrCulturalDamage: No
E1-ContentiousOrIllegal: No
E2-SociallySensitiveIssues: No
F1-InvolvesAnimals: No
F2-HarmfulToThirdParties: No
G1-ConfirmReadEthicsPolicy: Confirmed
G2-ConfirmReadUKRIOCodeOfPractice: Confirmed
G3-ConfirmReadConcordatToSupportResearchIntegrity: Confirmed
G4-ConfirmedCorrectInformation: Confirmed

FORM UPR16

Research Ethics Review Checklist

Please include this completed form as an appendix to your thesis (see the Postgraduate Research Student Handbook for more information

Postgraduate Research Student (PGRS) Information			**Student ID:**	716315
PGRS Name:	Konstantinos Papapavlou			
Department:	SEES	**First Supervisor:**	Dr. James Darling	
Start Date: (or progression date for Prof Doc students)		**1 October 2013**		
Study Mode and Route:	Part-time ☐ Full-time ☐	MPhil ☐ PhD ☒	MD ☐ Professional Doctorate ☐	

Title of Thesis:	Petrochronology and mineral chemistry of mid-crustal shear zones : new tools for tectonics and mineral exploration
Thesis Word Count: (excluding ancillary data)	50495

If you are unsure about any of the following, please contact the local representative on your Faculty Ethics Committee for advice. Please note that it is your responsibility to follow the University's Ethics Policy and any relevant University, academic or professional guidelines in the conduct of your study

Although the Ethics Committee may have given your study a favourable opinion, the final responsibility for the ethical conduct of this work lies with the researcher(s).

UKRIO Finished Research Checklist: (If you would like to know more about the checklist, please see your Faculty or Departmental Ethics Committee rep or see the online version of the full checklist at: http://www.ukrio.org/what-we-do/code-of-practice-for-research/)	
a) Have all of your research and findings been reported accurately, honestly and within a reasonable time frame?	YES ☒ NO ☐
b) Have all contributions to knowledge been acknowledged?	YES ☒ NO ☐
c) Have you complied with all agreements relating to intellectual property, publication and authorship?	YES ☒ NO ☐
d) Has your research data been retained in a secure and accessible form and will it remain so for the required duration?	YES ☒ NO ☐
e) Does your research comply with all legal, ethical, and contractual requirements?	YES ☒ NO ☐

Candidate Statement:	
I have considered the ethical dimensions of the above named research project, and have successfully obtained the necessary ethical approval(s)	
Ethical review number(s) from Faculty Ethics Committee (or from NRES/SCREC):	
If you have *not* submitted your work for ethical review, and/or you have answered 'No' to one or more of questions a) to e), please explain below why this is so:	

Signed *(PGRS)*:		**Date:** 13 November 2016